ANNUAL REPORTS ON NMR SPECTROSCOPY

Volume 34

- Multidimensional NMR methods for elucidating structure and dynamics of polymers
- Structure and dynamics of polymer gel systems viewed using NMR spectroscopy
- NMR studies of cross-linked polymers
- The conformational connection between the microstructures of polymers and their NMR spectra
- A review of high resolution NMR studies of vulcanized elastomers
- Structural analysis of oriented polymers by solid state NMR

ACADEMIC PRESS

ANNUAL REPORTS ON

NMR SPECTROSCOPY

Edited by

G. A. WEBB

Department of Chemistry, University of Surrey, Guildford, Surrey, England

I. ANDO

Department of Polymer Chemistry, Tokyo Institute of Technology, Ookayama, Meguro-ku, Tokyo, Japan

VOLUME 34

ACADEMIC PRESS

San Diego • London • Boston
New York • Sydney • Tokyo • Toronto

This book is printed on acid-free paper.

Academic Press, Inc.
525 B Street, Suite 1900, San Diego, California 92101-4495, USA
http://www.apnet.com

Academic Press Limited
24–28 Oval Road, London NW1 7DX, UK
http://www.hbuk.co.uk/ap/

ISBN 0-12-505334-7

A catalogue record for this book is available from the British Library

Typeset by Keyset Composition, Colchester, Essex
Printed in Great Britain by Hartnolls Ltd, Bodmin, Cornwall

97 98 99 00 01 02 EB 9 8 7 6 5 4 3 2 1

List of Contributors

Isao Ando, *Department of Polymer Chemistry, Tokyo Institute of Technology, Ookayama, Meguro-ku, Tokyo 152, Japan.*

Tetsuo Asakura, *Department of Biotechnology, Tokyo University of Agriculture and Technology, Koganei, Tokyo 184, Japan.*

Makoto Demura, *Department of Biotechnology, Tokyo University of Agriculture and Technology, Koganei, Tokyo 184, Japan.*

Masatoshi Kobayashi, *Department of Polymer Chemistry, Tokyo Institute of Technology, Ookayama, Meguro-ku, Tokyo 152, Japan.*

Jack L. Koenig, *Department of Macromolecular Science, Case Western Reserve University, Cleveland, Ohio 44106-7202, USA.*

Hiromichi Kurosu, *Department of Polymer Chemistry, Tokyo Institute of Technology, Ookayama, Meguro-ku, Tokyo 152, Japan.*

Shingo Matsukawa, *Department of Polymer Chemistry, Tokyo Institute of Technology, Ookayama, Meguro-ku, Tokyo 152, Japan.*

Makio Mori, *Department of Macromolecular Science, Case Western Reserve University, Cleveland, Ohio 44106–7202, USA.*

Naoki Nishikawa, *Department of Biotechnology, Tokyo University of Agriculture and Technology, Koganei, Tokyo 184, Japan.*

H. W. Spiess, *Max-Planck-Institut für Polymerforschung, Ackermannweg 10, D-55128 Mainz, Germany.*

Alan E. Tonelli, *Fiber and Polymer Science Program, College of Textiles, North Carolina State University, PO Box 8301, Raleigh, North Carolina 27695-8301, USA.*

Andrew K. Whittaker, *Centre for Magnetic Resonance, University of Queensland, Queensland, 4072, Australia.*

Hidekazu Yasunaga, *Kyoto Institute of Technology, Department of Chemistry and Materials Technology, Faculty of Engineering and Design, Goshokaido-cho, Matsugasaki, Sakyo-ku, Kyoto 606, Japan.*

Preface

It is a very great pleasure for me to welcome my longstanding co-worker and friend, Professor I. Ando of the Tokyo Institute of Technology, as co-editor of this volume of *Annual Reports on NMR Spectroscopy*, which represents the third in the series of special issues. The theme of this volume is applications of NMR in polymer science. The lambent insight into the structure and dynamics of molecules afforded by NMR techniques is well established. Volume 34 of *Annual Reports on NMR Spectroscopy* consists of six chapters covering a wide range of polymer topics, each one demonstrating the unique ability of NMR to provide information of both general and special interests.

Multidimensional NMR methods for elucidating structure and dynamics of polymers are covered by Professor H. W. Spiess; structure and dynamics of polymer gel systems are reported on by Professor I. Ando together with Drs H. Yasunaga, M. Kobayashi, S. Matsukawa and H. Kurosu; NMR studies of crosslinked polymers are reviewed by Dr A. K. Whittaker; Professor A. E. Tonelli deals with the conformational connection between the microstructures of polymers and their NMR spectra; a review of high-resolution NMR studies of vulcanized elastomers is provided by Dr M. Mori and Professor J. L. Koenig; the volume is completed with an account of the structural analysis of oriented polymers by solid-state NMR from Professor T. Asakura, Dr M. Demura and Dr N. Nishikawa.

My thanks go to all of these contributors, and to my co-editor and the production staff at Academic Press (London), for their very generous cooperation in the genesis of this volume.

University of Surrey
Guildford, Surrey
England

G. A. WEBB
October 1996

This Page Intentionally Left Blank

Contents

Multidimensional NMR Methods for Elucidating Structure and Dynamics of Polymers

H. W. SPIESS

Max-Planck-Institut für Polymerforschung, Postfach 3148 D – 55021 Mainz, Germany

This report describes new developments in multidimensional solid-state NMR, which is evolving as an indispensable tool for polymer characterization. After a short introduction, the unique information available by solid-state NMR is demonstrated by specific examples of structural studies of chain conformation, advanced aspects of chain dynamics, phase separation and interfacial effects, as well as non-linear plastic deformation in polymers. Emphasis is placed on the new development of high-resolution multiple-quantum NMR spectroscopy of abundant nuclei in solids with first experimental examples on the location of hydrogen positions in organic solids and chain order in polymer melts and elastomers.

1. INTRODUCTION

The study of structure and dynamics of polymers by NMR can be viewed as part of a more general endeavour of materials science, aimed at establishing structure–property relationships in order to improve known and

ANNUAL REPORTS ON NMR SPECTROSCOPY
VOLUME 34 ISBN 0-12-505334-7

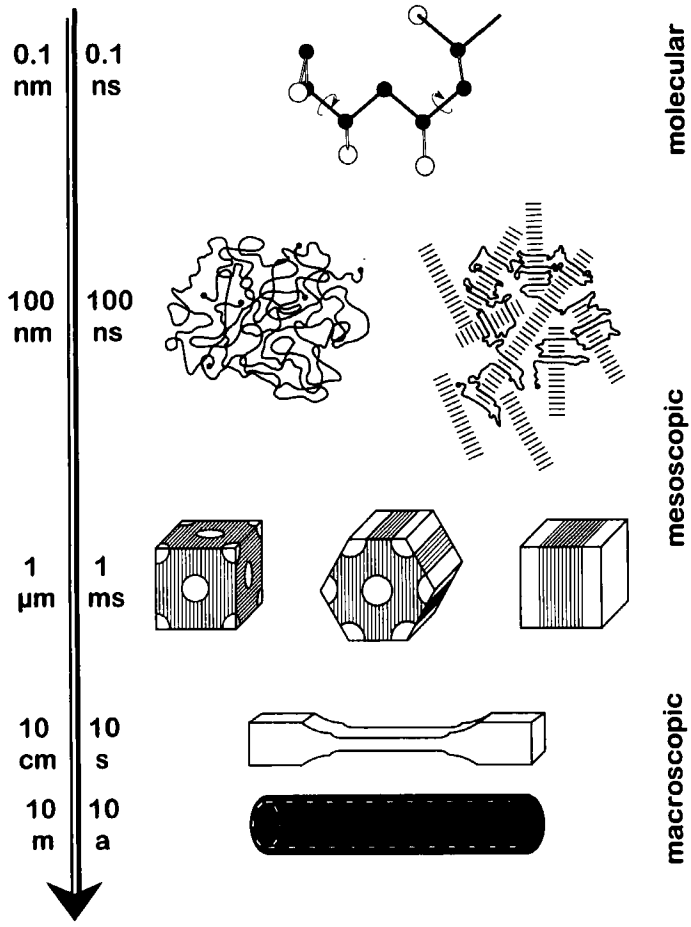

Fig. 1. Length- and timescales of polymer materials showing (from top to bottom) a conformational unit, random coils of amorphous and lamellae of semicrystalline polymers, phase separated structures, a testing bar for mechanical measurements and part of a tube as final product.

design new materials. Polymer behaviour depends on both the molecular structure and the organization of the macromolecules in the solid state.[1] Therefore, it involves enormous length- and timescales as indicated in Fig. 1. Most polymers are amorphous, where the chains form random coils on mesoscopic scales. Stereoregular macromolecules can partially crystallize to form ordered lamellar structures separated by non-crystalline regions. Multicomponent polymer systems are phase separated in most cases to form micellar, cylindrical or lamellar structures, depending on the fraction of the

Table 1. Methods of polymer characterization.

Method	Type
Microscopy	Light, electron, scanning tunnel, force
Spectroscopy	NMR, EPR, IR/Raman, UV/VIS
Scattering	Light, X-ray, neutron
Relaxation	Dielectric, mechanical
Simulation	Computer

different components. On a macroscopic level the mechanical behaviour is typically probed by a tensile bar and the final product might be a large-scale tube.

Therefore, polymer characterization must cover these wide length- and timescales. This calls for powerful analytical tools and, in fact, all variants of microscopy, spectroscopy, scattering, relaxation and computer simulation techniques as collected in Table 1 are used in this area. In view of the fact that these methods are generally far advanced and well established in polymer physics the question may arise: do we need yet another tool, such as solid-state NMR? The answer will be yes only if NMR compares favourably with the other techniques and yields important information which cannot be obtained in an easier way. Indeed, NMR spectroscopy offers several advantages, such as:

- unique selectivity;
- exceptionally high versatility;
- high potential for further developments.

These are demonstrated here through recent examples from our laboratory covering a wide range of length- and timescales, probing the local chain conformation, advanced aspects of chain dynamics, phase separation in multicomponent systems, and immobilization due to non-linear mechanical deformation.

2. SOLID-STATE NMR

Before describing specific examples we briefly review the techniques used in these applications. Most of them involve concepts of two-dimensional spectroscopy.[2] A full treatment is available in our extended monograph on multidimensional solid-state NMR and polymers.[3]

NMR clearly outranks the other techniques of polymer characterization as far as *selectivity* is concerned. First of all, NMR is highly site-selective, since the precession (Larmor) frequency is vastly different for the nuclei of

different elements or even for different isotopes of the same element. Furthermore, internal couplings of the nuclei to their surroundings render NMR sensitive to the details of the chemical structure. The enormous signal contrast due to the differences of natural abundance for the different isotopes provides a route of further increasing selectivity by isotopic labelling. The build-up of magnetization, which can subsequently be utilized in the NMR experiment, requires exchange of energy between the nuclear spins and their surroundings (spin–lattice relaxation, time constant T_1). This process strongly depends on the molecular dynamics. Likewise, the free induction decay (FID) (transverse relaxation, time constant T_2) depends on the strength and the fluctuations of the couplings the nuclear spins experience. Thus "relaxation filters" can be applied to record selectively NMR spectra of mobile or rigid parts of a heterogeneous polymer material. Last, but not least, after recording multidimensional data sets, repeated Fourier transformation (FT) yields multidimensional NMR spectra. They offer fundamental advantages over conventional (one-dimensional, 1D) spectra, such as increase of spectral resolution and routes to new information, unavailable from 1D NMR even in the limit of highest resolution.

2.1. One-dimensional NMR

NMR spectra are site-selective, because the magnetic fields that the nuclei experience are slightly different from the external field $\mathbf{B}_0$ due to the magnetic shielding by the surrounding electrons. The *chemical shift* spans about 10 ppm for ^{1}H and 200 ppm for ^{13}C in different functional groups. In solids, several anisotropic couplings of nuclear spins with their surroundings exist[2,3] which can be used to provide angular dependent information. In particular, the magnetic *dipole–dipole coupling* of nuclei among themselves leads to broad NMR lines covering approximately 50 kHz for ^{1}H–^{1}H homonuclear coupling and approximately 25 kHz for ^{1}H–^{13}C heteronuclear coupling. The *anisotropy* of the *chemical shift* results in powder patterns, which for ^{13}C cover approximately 15 kHz at a field strength of 7 T. In addition to these magnetic interactions, nuclei with spin $I > 1/2$ can also have electric quadrupole moments and are subject to *quadrupole coupling* to the electric field gradient at the nuclear site. For ^{2}H ($I = 1$) in C–^{2}H bonds this leads to spectral splittings of approximately 250 kHz. Since C–H bonds are common in polymers, ^{2}H labelling is particularly useful.

The angular dependence of the NMR frequency in high magnetic fields is alike for all couplings and is given by

$$\omega = \omega_L + \tfrac{1}{2}\Delta(3\cos^2\vartheta - 1 - \eta\,\sin^2\vartheta\,\cos 2\,\varphi) \qquad (1)$$

Here ω_L is the Larmor frequency including isotropic chemical shifts and Δ

describes the strength of the anisotropic coupling, i.e. anisotropic chemical shift or ^{13}C–^{1}H dipole–dipole coupling for ^{13}C and quadrupole coupling for ^{2}H. The asymmetry parameter η describes the deviation of the anisotropic coupling from axial symmetry ($0 \leq \eta \leq 1$). The angles ϑ, φ are the polar angles of the magnetic field $\mathbf{B}_0$ in the principal axes system of the coupling tensor. This in turn is often related in a simple way to the molecular geometry: the unique axis (z) is along a ^{13}C–^{1}H bond (dipole–dipole coupling), or a C–^{2}H bond (quadrupole coupling) or perpendicular to an sp^2 plane as for ^{13}C chemical shift tensors in aromatic rings etc. If one of the above-mentioned couplings dominates, either because of its strength, or because the others have been suppressed by decoupling, the NMR spectra are particularly simple. Depending on the total spin involved, signals described by equation (1) and their mirror images with respect to ω_L may be superimposed and in powder samples, spectra for all orientations are added to yield the powder line shape (e.g., the Pake pattern for ^{2}H with spin $I = 1$). Thus, advanced solid-state NMR techniques make use of the fact that the orientation of molecules is directly reflected in the *position* of the respective line in a suitably recorded NMR spectrum.

These anisotropic interactions are averaged out in liquids due to the rapid isotropic rotational motions of the molecules, and only the isotropic chemical shift remains. This yields much better resolved spectra. In solids a similar averaging effect can be achieved by mechanically rotating the sample at the "magic" angle of θ_M relative to $\mathbf{B}_0$, for which the angular function $(3\cos^2\theta_M - 1)$ vanishes. Such magic angle spinning (MAS) yields liquid-like spectra if the spinning frequency ω_R is significantly larger than the width of the anisotropic powder pattern ($\omega_R \gg \Delta$). In the slow spinning regime, $\omega_R < \Delta$, the centre band at the isotropic chemical shift is flanked by sidebands at multiples of ω_R, thus retaining information about the anisotropic coupling.

A few examples of 1D NMR spectra exemplifying the information they provide about structure and dynamics of polymers are collected in Fig. 2, displaying single ^{13}C-lines at the isotropic chemical shifts (Fig. 2(a)), a chemical shift powder pattern for ^{13}C in a carbonyl group and its relation to the molecular geometry (Fig. 2(b)), a ^{13}C MAS sideband pattern (Fig. 2(c)), and ^{2}H NMR line shapes for an isotropic powder (Pake pattern, Fig. 2(d)), a uniaxially drawn fibre (Fig. 2(e)), and a phenyl ring with motional averaging due to flipping about the axis shown (Fig. 2(f)).

2.2. Two-dimensional NMR

A 2D NMR spectrum[2,3] is generated by recording a two-dimensional data set following pulsed irradiation as a function of two time variables, as shown schematically in Fig. 3(a), and subsequent double Fourier transformation.

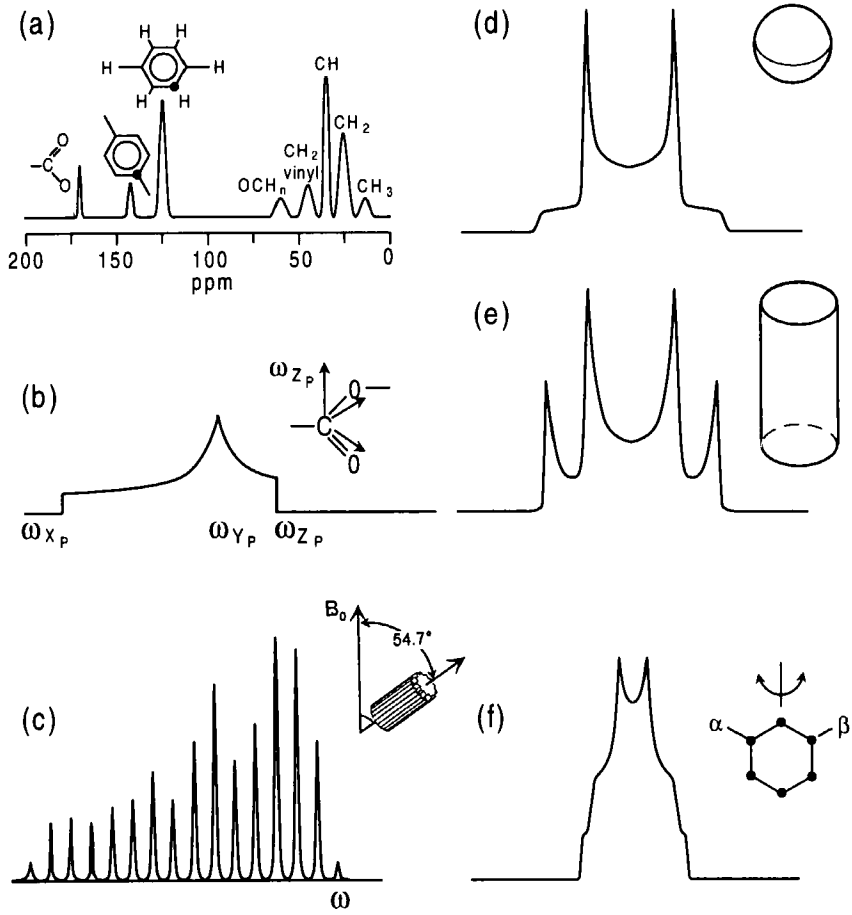

Fig. 2. Examples of solid-state NMR spectra. (a) ^{13}C CP MAS spectrum displaying isotropic chemical shifts of different functional groups. (b) ^{13}C powder pattern for a carbonyl group, governed by the chemical shift anisotropy and relation of the principal axes system of the shielding tensor to the molecular framework. (c) ^{13}C sidebands due to anisotropic chemical shift and slow MAS. (d) ^{2}H-NMR line shape for a rigid isotropic powder (Pake pattern). (e) ^{2}H-NMR line shape for a uniaxial fibre. (f) ^{2}H-NMR line shape for flipping phenyl rings.

The development of the nuclear spin system in the *evolution period* with incremented time t_1 at the beginning of the pulse sequence provides the basis for the first frequency dimension ω_1. The NMR signal is detected in the *detection period* with time t_2 at the end of the pulse sequence, providing the basis for the second frequency dimension ω_2. In *exchange experiments*, a variable *mixing period* of duration t_m, during which dynamic processes can take place, is inserted between evolution and detection.

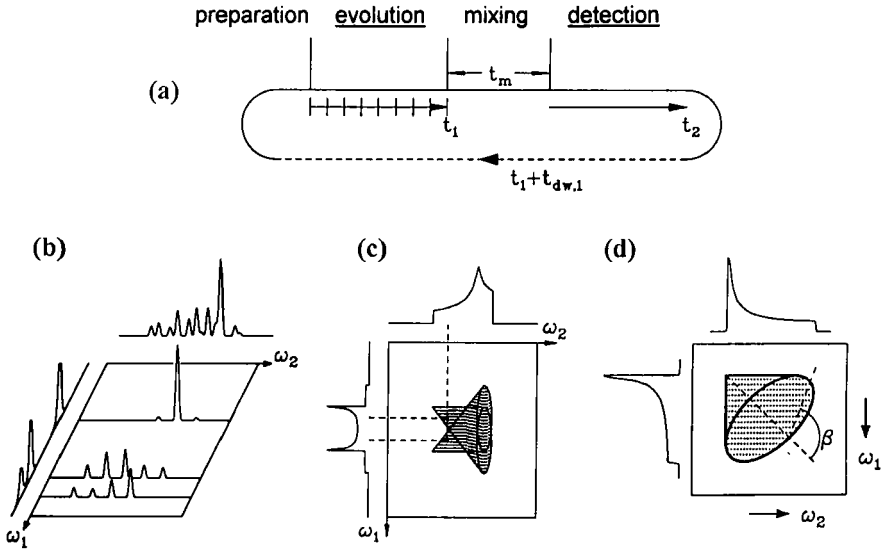

Fig. 3. Principles of 2D-NMR spectroscopy. (a) Basic pulse sequence consisting of preparation, evolution, mixing and detection periods. Prior to this, relaxation filters can be applied in the preparation period to distinguish from, e.g. molecular motion. (b) Separation of isotropic and anisotropic chemical shift sideband patterns. (c) Correlation of anisotropic chemical shift and dipolar interaction. (d) 2D exchange spectrum revealing the reorientation of a polymer segment about the angle β through an elliptical exchange ridge.

The most important aspects of 2D NMR are exemplified in Fig. 3(b)–(d). First, 2D NMR is often used to *increase the spectral resolution* of solid-state NMR spectra by *separating* different interactions. As an example, consider 1D sideband patterns. Their analysis is often hampered by a severe loss of spectral resolution due to overlapping sidebands of ^{13}C with different isotropic chemical shifts. This loss of resolution is circumvented at the expense of a new frequency dimension as demonstrated in Fig. 3(b), where sideband patterns for different sites experiencing different isotropic chemical shifts are separated from each other.

Other 2D NMR techniques aim at obtaining new information by *correlating* different interactions. As a specific example, Fig. 3(c) displays a 2D NMR spectrum correlating a ^{13}C chemical shift with a ^{13}C–^{1}H dipolar powder pattern. Since the dipole–dipole coupling is well-understood in terms of bond lengths and angles, such spectra provide valuable information about the orientation of the principal axes of the chemical shift tensor in relation to structural units such as CH_2-groups etc.

As far as applications to polymers are concerned, 2D *exchange* NMR proves to be particularly valuable.[3] First of all, by varying the mixing time

t_m, slow dynamic processes in the range of milliseconds to seconds can be followed in *real time*. Moreover, 2D exchange NMR spectra yield unique and model-independent information about the *geometry* of rotational motions. In fact, for axially symmetric tensors, ubiquitous in ^2H NMR of polymers, the 2D exchange spectrum yields elliptical ridge patterns from which the angle about which the segments have rotated can be read off with a ruler (Fig. 3(d)).

3. SPECIFIC EXAMPLES

3.1. Conformational effects on ^{13}C chemical shifts

The packing behaviour of polymers strongly depends on their chain microstructure.[4] A schematic representation of the carbon-backbone of an amorphous polymer is depicted in Fig. 4(a). In order to specify the conformation of a polymer segment one must know the bond length **l**, the valence angle θ and the rotational states Φ_i. The rotational potential $E(\Phi_i)$ around the central C–C bond in an *n*-butane unit is plotted in Fig. 4(b). The minima for the *gauche* conformers are higher than that of the *trans* by about 3.5 kJ mol^{-1}. Since this energy difference is comparable to the thermal energy at ambient temperatures, a large number of conformations is normally present in an amorphous polymer. Therefore experimental techniques are needed which can check the conformational statistics.

Glassy solid-state amorphous polymers typically display broad ^{13}C Cross-Polarization Magic Angle Spinning (CP MAS) NMR lines, due to an inhomogenous superposition of contributions from different conformations. These conformational effects on ^{13}C chemical shifts have traditionally been attributed to the shielding of a reference carbon C^0 by the γ-substituent C^γ, (Fig. 4(b)), in a semiempirical fashion ("*γ-gauche* effect").[4] As a specific example, Fig. 5(a) shows the ^{13}C CP MAS spectrum of atactic poly(propylene) (aPP) with the assignment of the CH_2 resonance to specific conformations of a tetrameric unit, displayed in Fig. 5(b).[5] This assignment is readily made by comparison with the chemical shifts in crystalline isotactic and syndiotactic polypropylene. The conformational effects are particularly strong for the CH_2 group. They should not be confused with the configurational splittings in the NMR spectra of polymers in solution, well-established in determining the chain microstructure.[4]

A complete analysis of such spectra in terms of structural information is now possible, since the conformational effects can be calculated on an *ab initio* level.[6–8] Our approach combines conformational statistics,[9] geometry optimization from molecular mechanics calculations[10] and *ab initio* calculations of the chemical shifts based on individual Gauges for Localized Orbitals

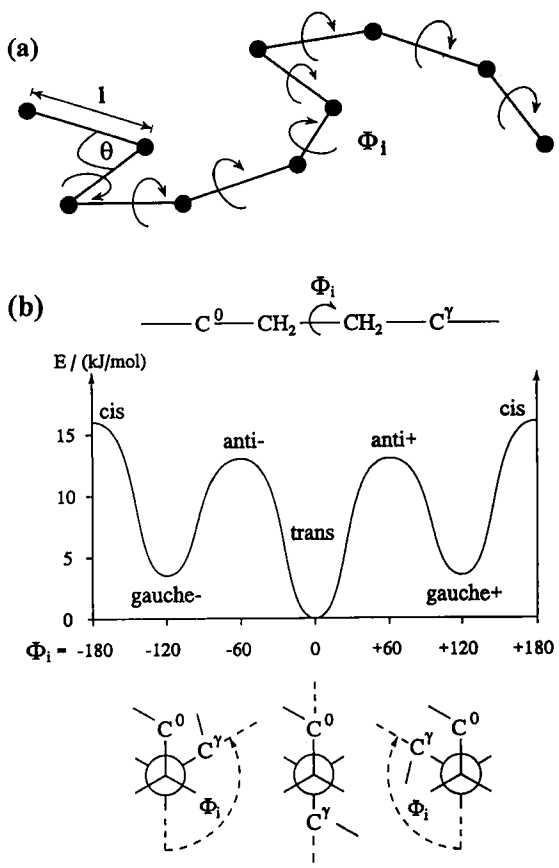

Fig. 4. (a) Schematic representation of a carbon-backbone polymer chain in the amorphous state. (b) The potential energy E for rotation about the central carbon of a butane unit in a polymer chain together with Newman projections illustrating the different interactions between the atom C^0 and its *γ-gauche* substituent C^γ for the conformations *gauche*− (g−), *trans* (t) and *gauche*+ (g+).

(IGLO).[11] The simulations for the different groups are plotted in Fig. 5(a) below the experimental spectrum. The fine lines display the contributions of the various geometries. The envelopes of the respective patterns are in remarkable agreement with experiment. The absolute heights of the resonance are adjusted arbitrarily, as the different groups have different CP-efficiencies. The absolute positions of the bands for the respective groups are not correctly reproduced by the quantum chemical calculation, since a small atomic basis set was employed in order to save computational time. It has been shown[7] that this does not seriously affect the simulation of conformational effects.

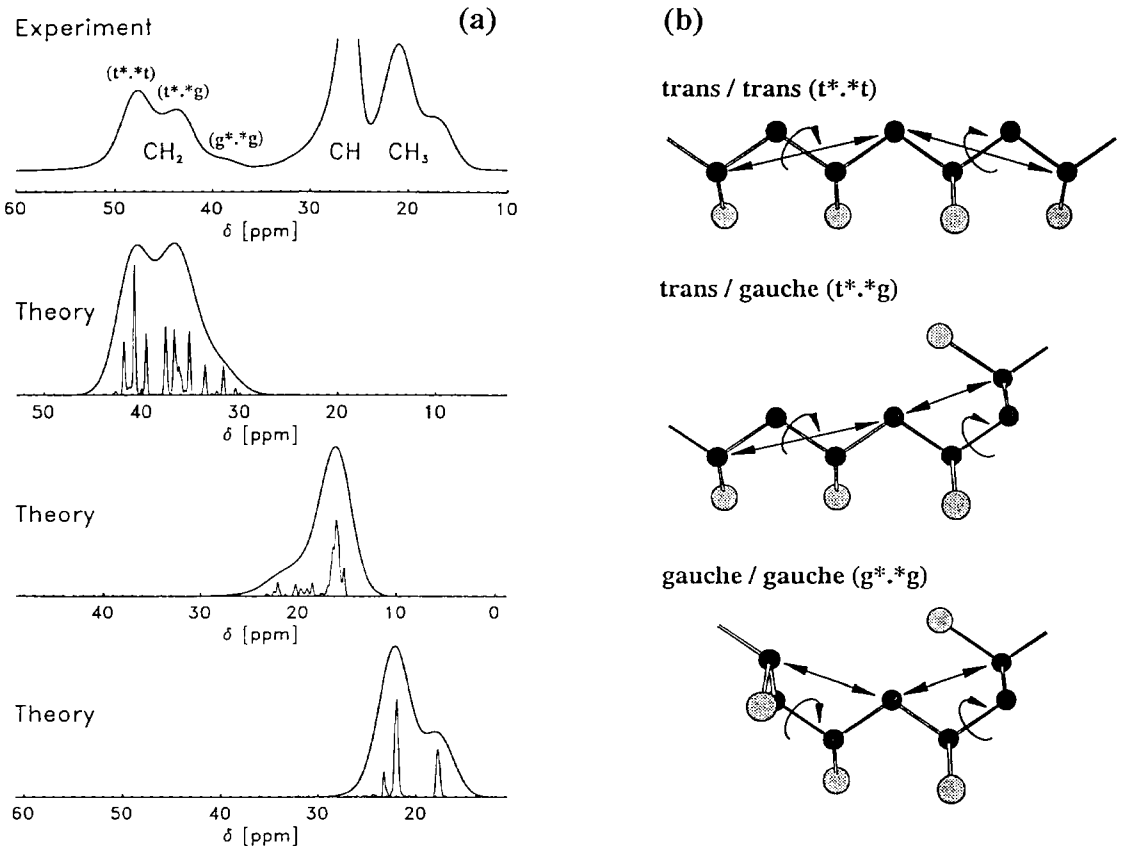

Fig. 5. (a) Experimental ^{13}C CP MAS spectrum of amorphous poly(propylene) (top) and simulations for the various bands.[8] (b) Schematic representation of the conformations of a tetrameric unit in poly(propylene) relevant for the *γ-gauche* effect of the methylene group C^0H_2. One particular configuration, the *mrr* tetrad, is selected, here. The abbreviation t*.*g stands for a conformational unit around a carbon centre denoted by *.* with undefined conformations of the neighbouring bonds and t and g conformations of the next neighbouring bonds.

Similar calculations have been performed for a variety of polymers with different structural features.[7,8] In general, remarkable agreement between experiment and simulation has been observed. Correlations between chemical shifts and geometrical factors such as bond lengths, dihedral angles and defect structures[12] have been established and ways to improve the quantum chemical calculations by more advanced techniques are discussed in an extensive review on the subject.[13] Thus, similar to the use for biopolymers,[14] the chemical shift of synthetic polymers in the solid state emerges as an important source of structural information.

3.2. High-resolution double-quantum NMR spectroscopy of solids

The local conformation of amorphous polymers is an example of a more general problem, namely our lack of knowledge about the detailed structure of disordered materials on the molecular level. Since disordered systems do not contain well-developed periodic structures which are needed for precise structural determination by X-ray or neutron scattering, alternatives are needed. Here solid-state NMR is highly attractive, since it allows direct measurement of structural parameters such as internuclear distances by making use of the dipole–dipole interaction. The couplings are particularly strong among the protons. In solids this leads to a many-body problem, because all spins are coupled with each other. Therefore, it is generally believed that one cannot study specific spin pairs in a solid, unless they are structurally isolated as, e.g., in crystal water, or isotopically diluted rare spins.[15] For this reason, substantial effort has been placed recently on introducing isolated ^{13}C–^{13}C or ^{13}C–^{15}N spin pairs by double isotopic labelling and then measuring the distance between the labelled positions.[16] If this procedure is repeated for a sufficient number of sites the structure can eventually be solved. Most of this work is devoted to solid biopolymers, where the molecular structures are complex but usually well defined. In addition, a few studies aimed at determining torsional angles[17,18] and interchain packing[19,20] in amorphous polymers have been reported. Clearly, the total work needed would substantially be reduced, if the structural information could be obtained by resolving the abundant ^{1}H–^{1}H or ^{1}H–^{13}C dipolar couplings in solids. Thus, high-resolution dipolar spectroscopy of solids represents a major challenge for NMR spectroscopy.

High-resolution NMR of solids inevitably involves sample spinning. Today, fast MAS with spinning frequencies in the range of 15 kHz is almost routine. These frequencies are still lower than those of the strong dipole–dipole coupling between, e.g. the two protons in a CH_2 group, but higher than those between protons belonging to different groups. This suggests that one can reach a regime where the weak couplings between remote spins are essentially spun out, while the strong couplings between nearby spins are

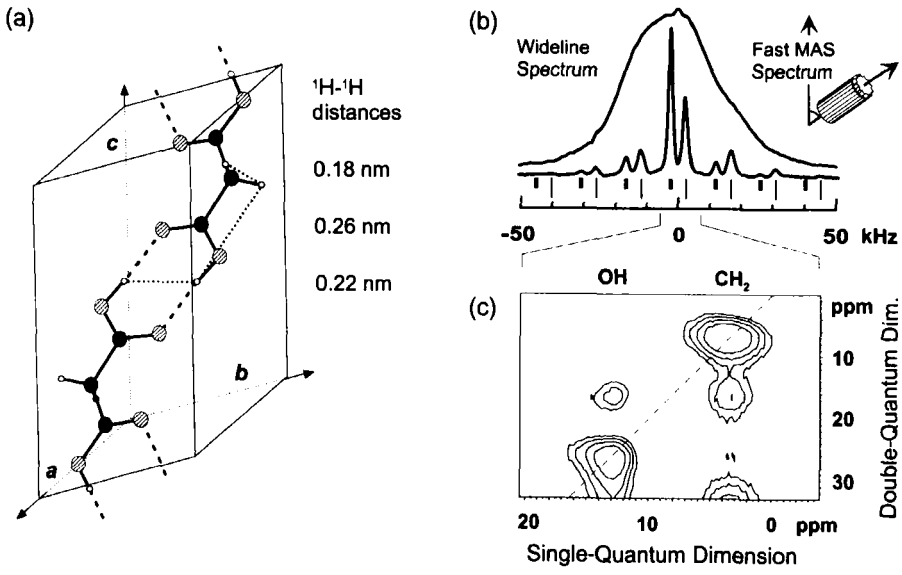

Fig. 6. Structural studies of solids by multiple-quantum NMR spectroscopy. (a) Crystal structure of malonic acid. (b) ^{1}H wideline and fast MAS spectrum at 500 MHz. (c) Part of high-resolution double-quantum NMR spectrum.[21]

retained. This then should lead to spinning sideband patterns from which the ^{1}H–^{1}H dipolar coupling can quantitatively be obtained. In a recent study of a model compound we showed that this is indeed the case.[21] Figure 6 displays the crystal structure of malonic acid (Fig. 6(a)) together with its ^{1}H wideline spectrum as well as its fast MAS spectrum, recorded with ν_R = 14 kHz at an ^{1}H Larmor frequency of 500 MHz (Fig. 6(b)). The spinning sideband patterns of the aliphatic and the carboxylic protons are clearly resolved and the ^{1}H–^{1}H distances derived from them are in full accord with the crystal structure determined by neutron scattering.[21]

The ease with which these ^{1}H–^{1}H distances are obtained by our approach on a powder sample and a measuring time of only a few minutes should be appreciated. Nevertheless, measurement of strong couplings alone will typically not provide sufficient insight into the structure, since the internuclear distances between the protons of functional groups are well known. Thus, in order to solve a structure, the connectivity between protons of different groups has to be established. This can be achieved by double-quantum (DQ) NMR spectroscopy.

Multiple-quantum (MQ) NMR spectroscopy is well-established for structural studies in liquids and highly mobile solutes in liquid crystals.[2,22,23] Here

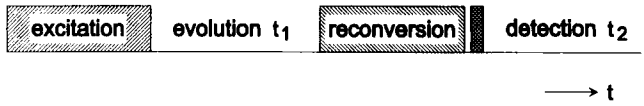

Fig. 7. Basic scheme of multiple-quantum NMR spectroscopy involving preparation, evolution, reconversion and detection periods.

we use it for strongly coupled solids under fast MAS.[21,24] The basic pulse sequence of MQ NMR spectroscopy is depicted in Fig. 7. At first, MQ coherence is excited by a proper pulse sequence, then it evolves during an evolution time t_1. Since this coherence cannot directly be detected, it is subsequently reconverted into detectable single-quantum coherence. Multiple-quantum NMR spectroscopy thus requires at least two-dimensional spectroscopy. The nature of the corresponding 2D spectra is illustrated in Fig. 8. Here we consider two kinds of pairs of spins, labelled 1 and 2, with different chemical shifts. The excitation of DQ coherence is based on the dipole–dipole coupling between the two spins involved. The DQ coherence frequency is the sum of the individual single-quantum frequencies of the two spins. Thus, if the two kinds of groups are separated (Fig. 8(a)), DQ signals can only occur at $2\omega_1$ and $2\omega_2$ along the DQ dimension, i.e. on the skewed diagonal of a 2D plot with proper frequency scaling. Note that distinct from the INADEQUATE experiment in isotropic liquids based on the isotropic scalar couplings[2] the intragroup coherences occur despite the fact that the isotropic chemical shifts of the two spins are equal. This is due to the fact that in solids the DQ coherence is generated by the anisotropic dipole–dipole coupling. These signals reflect the dipolar couplings within the respective groups. If the groups are intermixed (Fig. 8(b)), DQ coherences between spins of different groups can also be excited. As a consequence, a pair of lines occurs at the sum frequency $\omega_1 + \omega_2$ in the DQ dimension at frequencies ω_1 and ω_2 in the single-quantum dimension. Thus, such a pair of lines maps the connectivity between group 1 and group 2 directly in the 2D-NMR spectrum. For short excitation times the intensities of the DQ signals are proportional to Δ_{ij}^2, where Δ_{ij} describes the dipole–dipole coupling between the two spins involved, cf. equation (1).

Indeed, a pattern as described here is observed in the DQ spectrum of malonic acid, displayed in Fig. 6(c). Moreover, the quantitative analysis of the intensities in relation to those for the CH_2 group and OH groups yield a closest distance of 0.26 nm between a carboxylic and an aliphatic proton[21] in full agreement with the neutron diffraction study. Thus, our study of a crystalline model compound shows that intra- and intergroup ^1H–^1H distances in strongly coupled dipolar solids can be measured quantitatively by double-quantum NMR spectroscopy.

The method is not restricted to crystalline compounds. In fact, the first

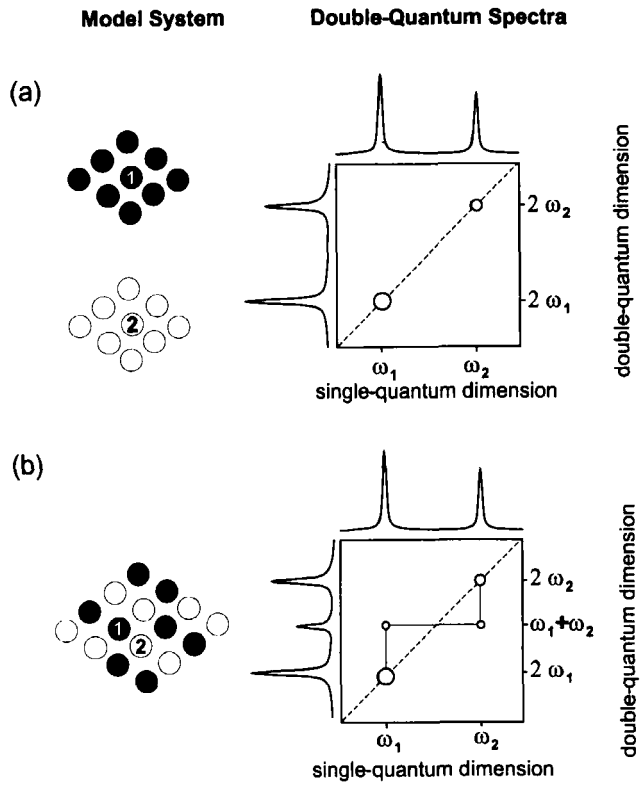

Fig. 8. Scheme of double-quantum spectra. (a) Model system with spin pairs separated. Signals appear only at $2\omega_1$ and $2\omega_2$ in the double-quantum dimension. (b) The double-quantum coherence of spins belonging to different groups leads to an additional pair of signals at the sum frequency $\omega_1 + \omega_2$ in the double-quantum dimension. The connectivity is indicated by a solid line.

DQ spectrum for a rigid solid was recorded for amorphous polycarbonate[24] and showed the connectivity between the methyl- and phenylprotons. For improved spectral resolution heteronuclear DQ spectra, involving ^{13}C–^{1}H coherences have been recorded.[25] An inherent feature of MQ spectra under MAS are spinning sidebands which may easily extend beyond the width of the static powder spectra. They result mainly from rotor encoding of the DQ Hamiltonian under MAS.[21,26,27] Last, but not least, the spectral resolution in the single-quantum dimension can be improved by combining fast MAS with multiple pulse line narrowing.[28] Thus, it is clear that high-resolution multiple-quantum NMR of solids, exploiting the dipole–dipole interaction between specific spin pairs of a strongly coupled spin system emerges as a powerful tool for structural elucidation of amorphous systems. Moreover, as will be shown below, multiple-quantum NMR also provides unique

information about the chain dynamics of macromolecules, since dipolar couplings between adjacent groups along a chain can be exploited.

3.3. Advanced aspects of chain dynamics from multidimensional exchange NMR

Polymer dynamics is of central importance for establishing structure–property relationships. In order to provide the basis for a better understanding of the mechanical and rheological behaviour of polymer materials, slow motions with correlation times longer then 1 ms are most valuable. They occur, e.g. in dense polymer melts associated with the glass transition of these amorphous systems. Of the great variety of molecular motions possible in polymers (e.g. translations, rotations and vibrations), rotations have the most pronounced effects on NMR spectra and relaxation parameters. Thus multidimensional NMR provides, in particular, unique information about rotational motions.[3] A major advantage of this technique is its ability to separate the information about the *geometry* and the *time dependence* of the chain dynamics. Most informative are 3D or 4D spectra, which probe the orientation of a given group at three or even four subsequent times, between which dynamic processes can take place. From such studies, described in chapter 8 of our monograph,[3] a picture for the molecular motion (Fig. 9) emerges. The chain dynamics as probed by an individual group involves small angle fluctuations as well as large angle jumps, due to conformational transitions of the chain. By multidimensional exchange NMR we can then tackle the following questions concerning the detailed geometry of the motions as well as memory effects:

- What are the mean amplitudes of the small angle fluctuations and the jumps?
- Does the probability of undergoing a jump change after the group has performed a jump?
- What is the probability of forward jumps as distinct from a jump back to the starting position?

Recording complete 3D, let alone 4D, spectra of solids is extremely time consuming. Therefore, reduced versions, where projections of the spectra on lower dimensional planes are recorded, should be considered.[3] Here, we recently introduced a new experiment, denoted as Difference Correlated exchange spectroscopy (DICO),[29] which allows us to answer the first question. The corresponding pulse sequence is plotted in Fig. 10(a). By setting the two first evolution times equal, $t_1 = t_2 = t_{12}$, a projection of the 3D exchange spectrum onto the body diagonal of the 3D cube is achieved (Fig. 10(b)). Thus, the frequency of the group in the detection period, ω_3, is correlated with the *difference* of the frequencies $\omega_d = \omega_2 - \omega_1$ the same

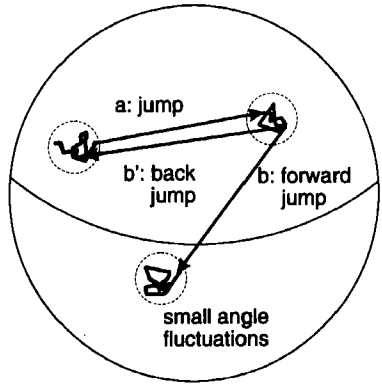

Fig. 9. Scheme of complex rotational motion as probed by multidimensional NMR.

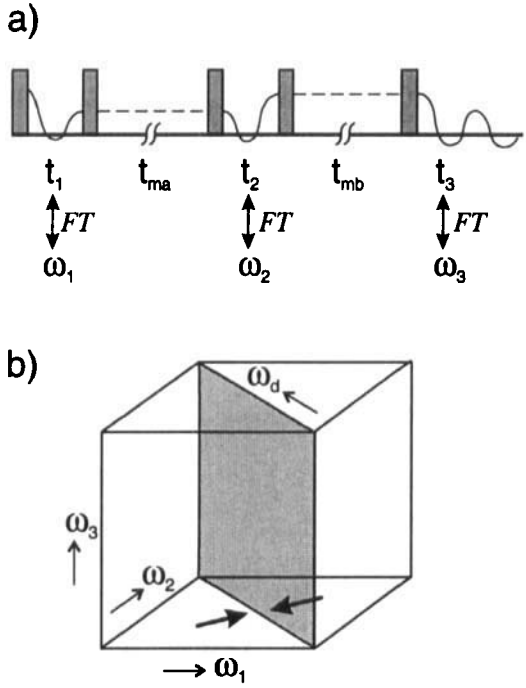

Fig. 10. (a) General scheme of 3D exchange NMR. (b) Projection plane in the 3D frequency cube recorded in the DICO experiment by incrementing t_1 and t_2 simultaneously.[29]

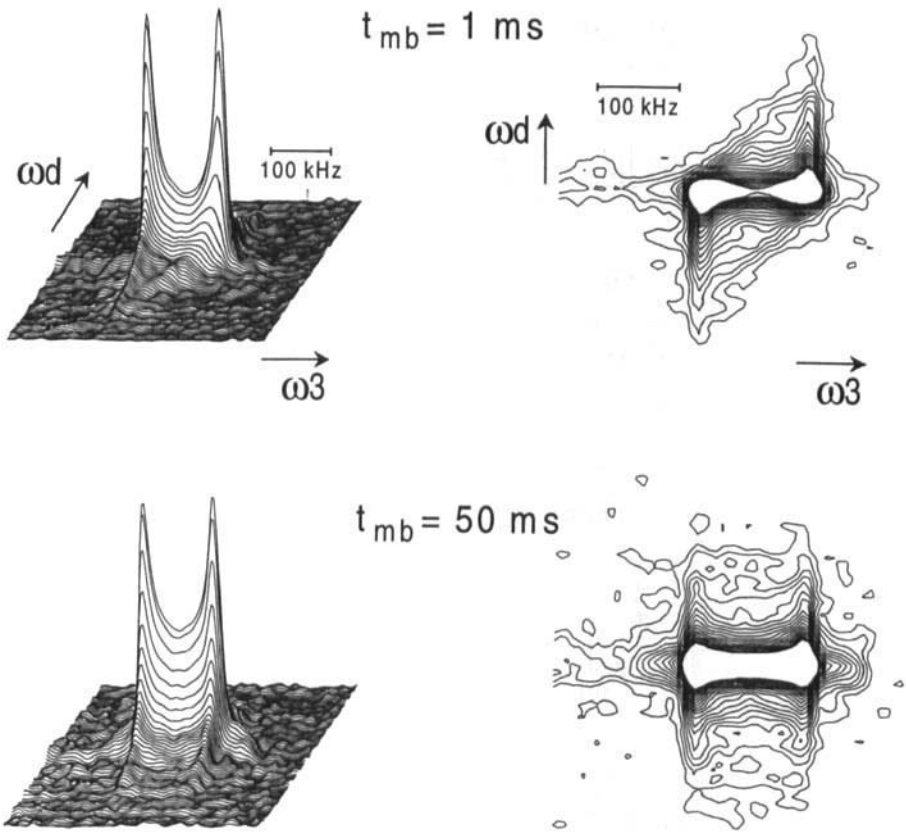

Fig. 11. Experimental ^{2}H DICO spectra for polystyrene at $T = 386$ K with $t_{ma} = 10$ ms and two different values of t_{mb} as indicated.[29]

group had at the end and at the beginning for the first mixing time t_{ma}. A series of ^{2}H-DICO spectra probing the chain dynamics of poly(styrene) is plotted in Fig. 11. For short t_{mb} the spectra show skewed, asymmetric shapes and become symmetric with respect to $\omega_d = 0$ for longer t_{mb}. As shown in detail elsewhere[29] this symmetrization can quantitatively be analysed in terms of the probability of undergoing a jump during t_{mb} and a *dynamic order parameter* $\langle P_2(t) \rangle$. The latter is the $L = 2$ coefficient in the expansion of the reorientational angle distribution describing the group motion[3] in terms of Legendre polynamids P_L. Notably, two contributions to $\langle P_2(t) \rangle$ can be distinguished. The first corresponds to slow small angle fluctuations with a mean amplitude of 10°, whereas the second corresponds to about 30°–40° for a single jump, eventually leading to anisotropic motion. The low value of the mean jump angle found here is rather surprising, since conformational

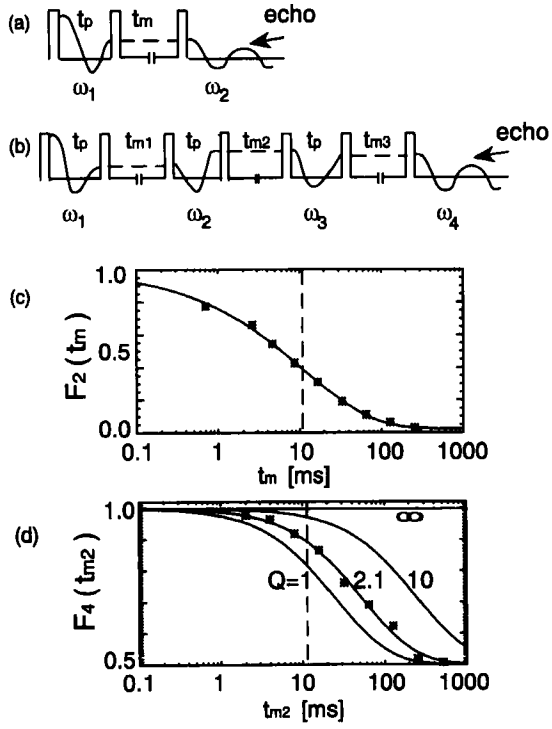

Fig. 12. Pulse sequences for reduced multidimensional NMR experiments: (a) 2D echo; (b) 4D echo. Results for ^{13}C–NMR of poly(vinylacetate) at $T = 320$ K: (c) 2D echo, F_2, (d) 4D echo, F_4.[30]

transitions are a prominent aspect of chain dynamics. If they would occur in a fixed potential, jump angles of 109° would result.

The remaining two questions raised above concern rate and orientational memory effects. They can be tackled with reduced 4D NMR methods, where the echo signals after a three-pulse, 2D echo, F_2 (Fig. 12(a)) and a seven-pulse sequence, 4D echo, F_4 (Fig. 12(b)) are compared. As a first example we studied the rate memory of structural relaxation for poly(vinylacetate) (PVAc) slightly above the glass transition temperature T_g.[30] In Fig. 12(c), F_2 (t_m) for the ^{13}C resonance of the ester group is plotted on a logarithmic scale. The data can be fitted nicely with a stretched exponential exp $[-(t/\tau_o)^\beta]$ with $\beta = 0.52$. In Fig. 12(d) below $F_4(t_{m2})$ with $t_{m1} = t_{m3} = 16$ ms ($\approx\tau_o$) is plotted versus the intermediate mixing time t_{m2}. The solid lines in Fig. 12(d) represent theoretical curves of the decay of F_4 for different values of the so-called rate memory parameter $Q \geq 1$.[31] It counts the number of jumps until a typical slow segment, which at the beginning had a correlation time longer than the average, changes its motional rate such

that in the detection period its correlation time is shorter than the average. This rate memory parameter is close to its minimum $Q = 1$, where the probability of undergoing a jump changes after each jump. This indicates a strong coupling of the motion of the group studied to its surroundings. Similar behaviour was observed for the chain motion in poly(styrene) probed by ^{2}H-NMR.[32] These studies aimed at characterizing complex dynamics with varying rates have triggered a number of investigations including theoretical work,[33] optical techniques[34–36] and non-linear dielectric relaxation.[37]

The last question can be answered by comparing the ratio of the 2D echo $F_2(t)$ with a 4D echo for $t_{m2} = t_{m3} = t/2$ and $t_{m2} = 0$. For poly(styrene) the probability of jumping back to the angular region close to starting position was found to be about 10–15%, higher than one would expect from pure statistics. This defines the *orientational memory*. It is relatively high since we apply a rather coarse graining of orientation in the echo experiment. If we ask for strict return jumps by full 3D spectra, the orientational memory is found to be very low (see chapter 8 of ref. 3).

The results from multidimensional exchange NMR provide unprecedented details about the differences between the simple chain dynamics in crystalline regions and the complex dynamics at the glass transition of amorphous polymers. The former occur in well-defined potentials, with fixed jump angles and high rate, as well as orientational, memory.[3] The latter occur in a time-dependent potential, which apparently can change after each jump. This is due to the strong coupling between the group undergoing a motional process and its surroundings. This coupling leads to low rate and orientational memory and is also responsible for the large deviation of the mean jump angle from that expected from conformational transitions in a fixed potential. All these findings together suggest a picture for the complex chain dynamics at the glass transition, where the motion of a group is strongly coupled to the dynamics of its surroundings. Thereby, the environment apparently adjusts in such a way that a group, despite being involved in a conformational transition, is displaced as little as possible.

3.4. Motional parameters involving adjacent groups along the chain

In the previous section the motion of individual groups was followed step by step on a timescale of tens of milliseconds. At somewhat higher temperatures, about 50 K or more above T_g, these chain motions are rapid enough to effectively average the anisotropic couplings that were used to monitor the orientation of the individual groups. Then, NMR can probe the motional behaviour of the average chain structure. Contrary to low molar mass liquids the chain motion in polymers is not completely isotropic, resulting in residual spin-dependent anisotropic couplings. Numerous ways have been proposed to relate these residual couplings to characteristic chain

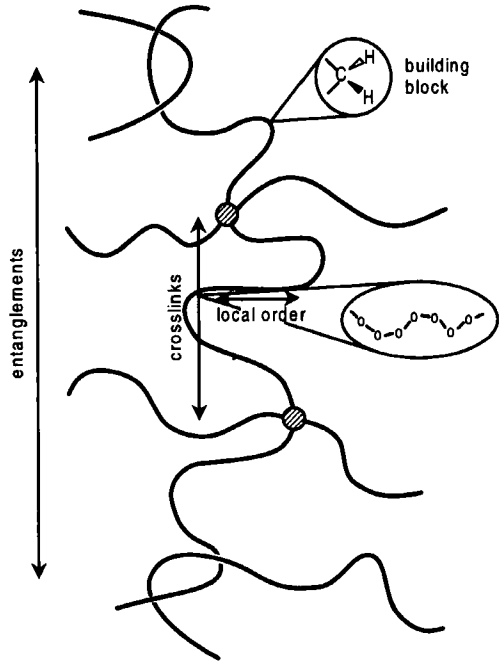

Fig. 13. Sketch of lengthscales reflected in the non-isotropic chain motion in polymer melts and elastomers: locally ordered regions, e.g. stretched conformations, crosslinks and entanglements.

parameters. The most fruitful concept involves a hierarchy of length- and timescales (Fig. 13). Restrictions of the chain motion result from local chain order due, e.g., to the presence of extended local conformations or stiffening structural elements on a shorter scale and entanglements as well as crosslinks on a longer scale. Then the autocorrelation function

$$S(t) = \tfrac{1}{2}\langle 3\cos^2\theta - 1\rangle \tag{2}$$

where θ is the angle between the orientation of a vector $\mathbf{r}$ fixed to a structural unit of the chain at time zero, $\mathbf{r}(0)$ and time t, $\mathbf{r}(t)$, will not simply decay to zero, but at intermediate times level at some finite plateau value reflecting the anisotropy of the motion as shown in Fig. 14. On a longer timescale isotropization occurs. The height of the intermediate plateau can then be considered as a dynamic order parameter of the chain motion, since it persists for a large number of conformational transitions. Such dynamic order parameters have mainly been considered in elastomers by measuring residual ^1H–^1H couplings of CH_2 groups[38,39] or ^2H residual quadrupolar couplings[40] and it was concluded that they are typically very small, i.e. below 5%.

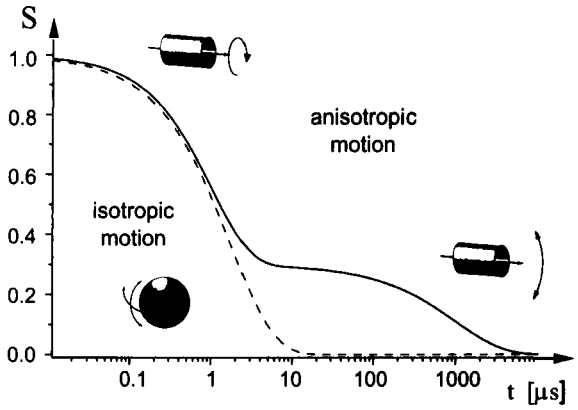

Fig. 14. Scheme of a two-step decay of an $S = \langle P2(t) \rangle$ correlation function of a unit undergoing an anisotropic motion as opposed to a one-step decay of isotropic motion.

Recently, the different approaches commonly used to measure the residual dipolar couplings in elastomers, such as the free induction decay, ^{13}C-edited ^{1}H transverse relaxation, and crosspolarization built-up curves were compared and the couplings related to the crosslink density.[41] This study also clearly separated the contribution of the chemical crosslinks from those of the intrinsic local order of the polymer chain. All these methods, however, probe the chain order via anisotropic couplings whose primary directions are *transverse* to the local chain axis. Thus, they primarily probe the axial motion (Fig. 14). The chain order can much better be characterized if residual couplings *along* the carbon–carbon bonds can be determined.

This has recently been achieved by determining the residual dipole–dipole coupling between the CH_2 and the adjacent CH group in the polybutadiene segment of a crosslinked poly(styrene-cobutadiene) (SBR) elastomer (Fig. 15(a)) from 2D exchange NMR.[42] A much more complete dataset is provided by the double-quantum spectrum of such a system recorded under fast MAS (Fig. 15(b)). In order to excite DQ coherences the dipolar coupling which is essentially spun out under fast MAS has to be recoupled. Here a number of rotor-synchronized multiple pulse sequences are available.[43–46] In the DQ spectrum of the elastomer virtually all connectivities of protons within a group and to those of adjacent groups are resolved. The connectivity within the butadiene moiety is indicated by solid lines. It is immediately obvious that the intensity of the intergroups peaks is similar to those of the intragroup couplings. Thus, the respective residual dipolar couplings $\bar{\Delta}_{ij}$ must be similar. They depend on both the respective internuclear distance r_{ij} and the respective dynamic order parameter S_{ij}, according to $\bar{\Delta}_{ij} \propto S_{ij}/r_{ij}^3$. The internuclear distances of protons separated by a carbon–carbon bond are

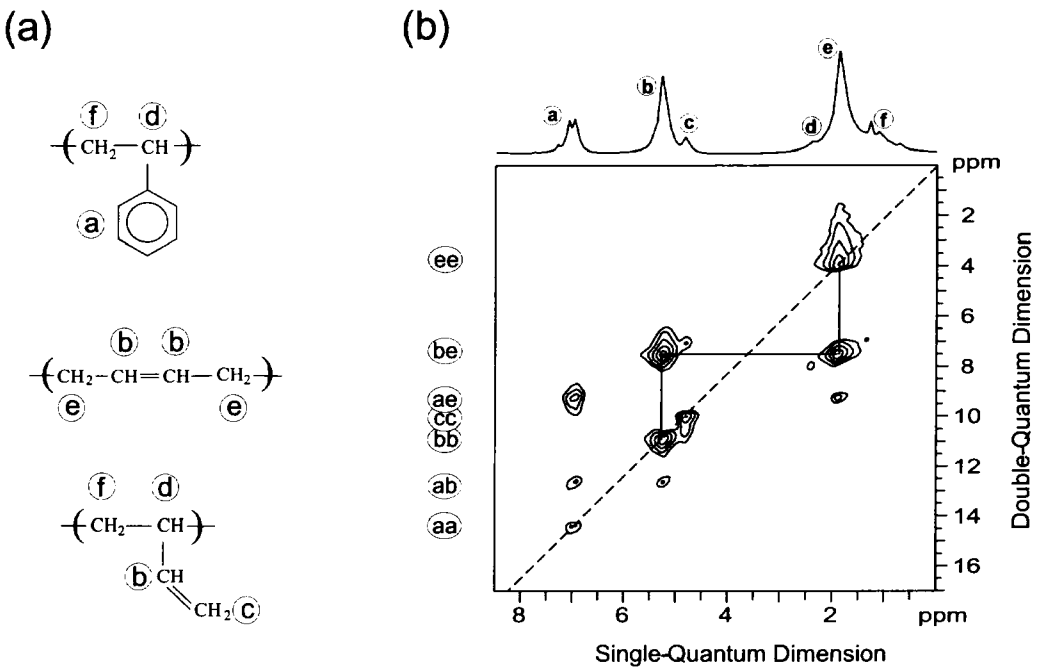

Fig. 15. (a) Structural elements of an SBR elastomer. (b) ^{1}H-double-quantum NMR spectrum at 500 MHz and room temperature with assignment to the structural elements. The connectivity between the CH_2 and the CH protons is indicated by a solid line.

2.7–3.0 Å rather than 1.8 Å for the protons in a CH_2-group. Therefore, based on the r^{-3} dependence of the dipole–dipole coupling the intergroup couplings have so far been neglected.[36–41] The DQ spectrum, however, clearly shows that they are comparable to the intragroup couplings. This is only possible if the dynamic order parameter for directions *along* the chain are much higher than those for transverse directions. Quantitative analysis of our DQ data show that the dynamic order parameter for the C=C bond in the butadiene unit of elastomers can be as high as 0.3–0.4, about an order of magnitude higher than anticipated. Thus, this new type of NMR spectroscopy provides a route to new categories of information that had been completely out of reach. This also allows us to test advanced theoretical concepts. Indeed, significant differences of the time constants of the decay of autocorrelation functions for directions transverse and along the hydrocarbon chain have been noticed in recent computer simulations of simple alkanes.[47,48]

This suggests that dynamic order parameter for macromolecular chain units should be considered as a new parameter in order to get a better understanding of the rheological behaviour of polymer melts on a molecular level. This parameter apparently strongly varies for different polymers. In fact, extremely high values were previously found in poly(alkylmethacrylate)s by ^{13}C-NMR at temperatures about 50 K above T_g.[49] In poly(ethylmethacrylate) $S = 0.7$ and in poly(methylmethacrylate) $S = 0.35$.

3.5. Phase separation and interfacial structures in core–shell latexes

NMR spectroscopy as a local method yields especially clear-cut results on the molecular level. However, solid-state NMR can also provide information about domain sizes and interface structures in heterogeneous polymers on mesoscopic scales by means of spin diffusion, i.e. the diffusion of nuclear magnetization through the sample without transport of material. It is mediated by dipolar couplings and, therefore, is most efficient among protons.[3] Figure 16 demonstrates schematically the connection between the spatial distribution of proton magnetization within the sample and the solid-state NMR spectra for a two-phase system with spatially constant proton density. In equilibrium, the proton polarization is spatially constant and the relative signal intensities in an NMR spectrum reflect the integral chemical composition of the sample. Differences in the chemical structure or in local molecular mobility can be used to select the proton magnetization in one component (A) and suppress it in the other (B) (Fig. 16(a)). The subsequent redistribution of magnetization by ^{1}H spin diffusion is monitored by NMR spectroscopy (Fig. 16(b)). For short times the mean-square distance $\langle x^2 \rangle$ the magnetization moves within the time t is given by $\langle x^2 \rangle = aDt$, where D is the spin diffusion constant of the system under study. The prefactor a

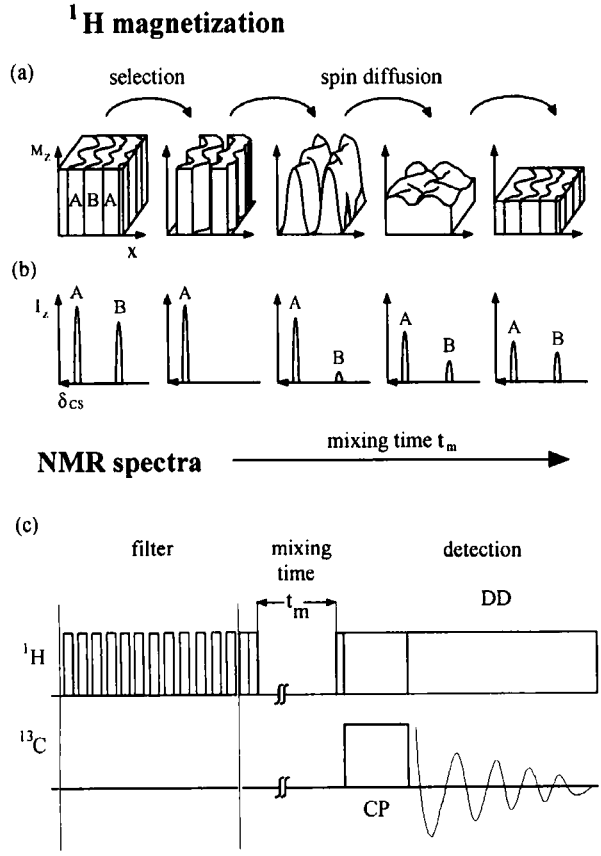

Fig. 16. Schematic representation of ^{1}H spin diffusion studies in a two-phase system (A, B) with spatially constant proton density. (a) Spatial distribution of ^{1}H magnetization. (b) NMR spectra for different mixing times t_m. (c) Pulse sequence for selection of the mobile fraction by the dipolar filter.

depends on the geometry of the packing, e.g., lamellar, cylindrical, or spherical. The spin diffusion constant D is related to the strength of the dipolar coupling as reflected in the width of the ^{1}H NMR spectrum and has been calibrated for polymers of different molecular mobility by comparing spin diffusion data with direct measurements of domain sizes by X-ray scattering and electron microscopy.[50,51] (For more elaborate treatments of spin diffusion see refs 3, 50, 52.) The selection is typically achieved on the basis of mobility differences by use of the dipolar filter, depicted in Fig. 16(c). It consists of twelve ^{1}H 90° pulses separated by a delay time t_d. By increasing t_d and/or repeating the sequence the filter can be made stronger, i.e. more selective against small differences in mobility.

A particularly interesting class of heterogeneous polymers are core–shell systems produced by emulsion polymerization.[53,54] Such latexes are of considerable technological importance as paints, adhesives, coatings or high-impact modifiers of engineering plastics. It is known, however, that depending on the reaction conditions or crosslinking of the core, the morphology deviates from the ideal core–shell structure depicted in Fig. 17(a). For instance, inhomogeneities in the core (Fig. 17(b)), or interfaces with microdomains (Fig. 17(c)) or with a concentration gradient (Fig. 17(d)) may result. These substructures may have pronounced effects on the performance of the core–shell particles, e.g. their ability to form uniform films. Whereas the overall size of the particle can be well characterized by transmission electron microscopy (TEM),[54] solid-state NMR spin diffusion techniques are particularly sensitive regarding the substructures.[55]

In a recent study, differences in the interface structure of core–shell latexes prepared at different temperatures were characterized in considerable detail.[56] The latexes are based on a mobile core of poly(butyl acrylate) (PBuA) and a rigid shell of poly(methyl methacrylate) (PMMA). Two systems were studied, for which the polymerization of the latter was performed at 20°C or at 72°C. The resulting core–shell systems are referred to as low- and high-temperature systems, respectively. Figure 18 displays the 2D-WISE (*Wi*deline *Se*paration) spectrum[3] of the low-temperature system. It probes the dynamics as revealed in the width of the ^1H dipolar spectra along one dimension separated for the different functional groups according to their ^{13}C chemical shifts along the second dimension. As expected, the slices at the PMMA chemical shifts exhibit broad ^1H spectra, since the chains are immobilized below T_g. Contrary to this, the slices at the PBuA chemical shifts exhibit partially narrowed spectra, reflecting high chain mobility above its T_g. However, these slices also show considerable broadening, which is attributed to PBuA chains being immobilized in the interface with a concentration gradient. Indeed, mobilized PMMA can likewise be detected by application of the dipolar filter and subsequent crosspolarization.[56]

Quantitative analysis of the interface structure is possible by spin diffusion studies with ^1H detection. In Fig. 19(a) we compare the spin diffusion behaviour of a core–shell system with complete phase separation and an interface with microdomains with a core–shell system with incomplete phase separation resulting in an interface with a concentration gradient. The intensity of the selected mobile fraction is plotted as a function of the square root of the mixing time t_m. After selection of the mobile component the spin diffusion curves should level at the stoichiometric ratio for the former. For the latter, a fraction of the mobile component is immobilized and cannot pass the filter. Therefore, the spin diffusion curve will level below the stoichiometric ratio.

Information about the size and the distances between the microdomains can be deduced from analysis of the decay of the spin diffusion curve, as

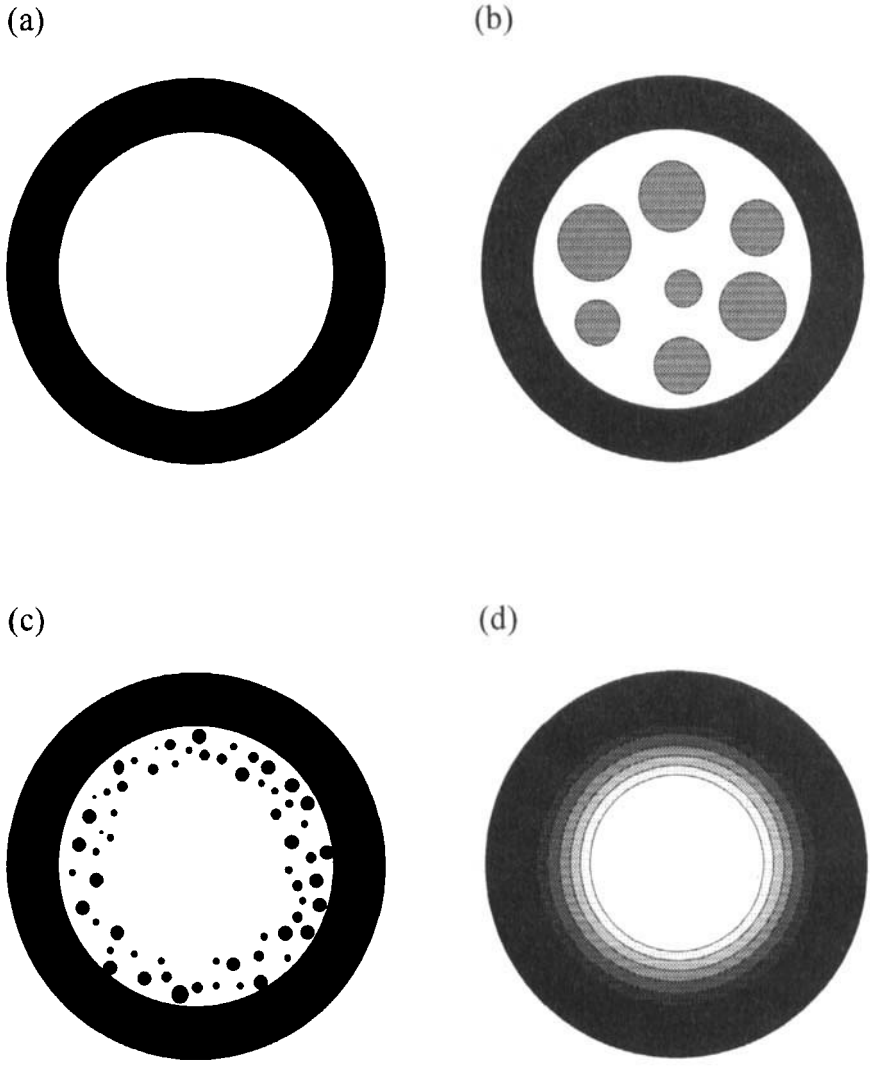

Fig. 17. Morphologies of core–shell latexes. (a) Ideal structure. (b) Inhomogeneities in the core, (c) Interface with small microdomains. (d) Interface with concentration gradient.

depicted in Fig. 19(b). For an ideal core–shell system the decay will be very slow, since spin diffusion has to cover the full size of the particle, which might be larger than 100 nm in diameter. In the interface with microdomains, distances of the order of only 10 nm have to be covered before the rigid phase is reached. This leads to fast spin diffusion. In a real system, of course, both diffusion processes will be superposed.

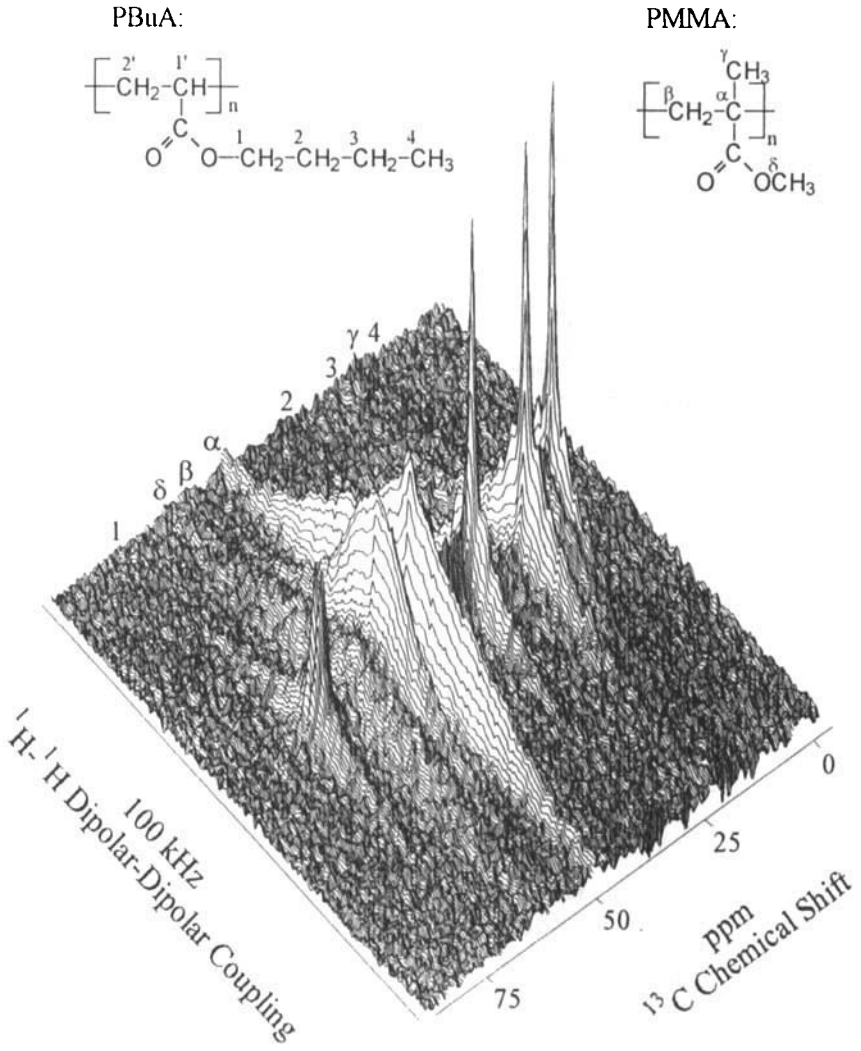

Fig. 18. 2D-WISE spectrum of the low-temperature latex system of PBuA and PMMA with assignment of ^{13}C chemical shifts.[56]

It is important to note that neither of the experiments alone can provide a full description of such complex structures. Moreover, the temperature of the experiment should be adjusted in order to achieve optimum discrimination against small differences in mobility.[57] However, taken together, and combining NMR with conventional techniques like TEM, different interface structures can clearly be distinguished. For instance, in our study of the PBuA–PMMA system[56] the low-temperature latex was found to have a broad

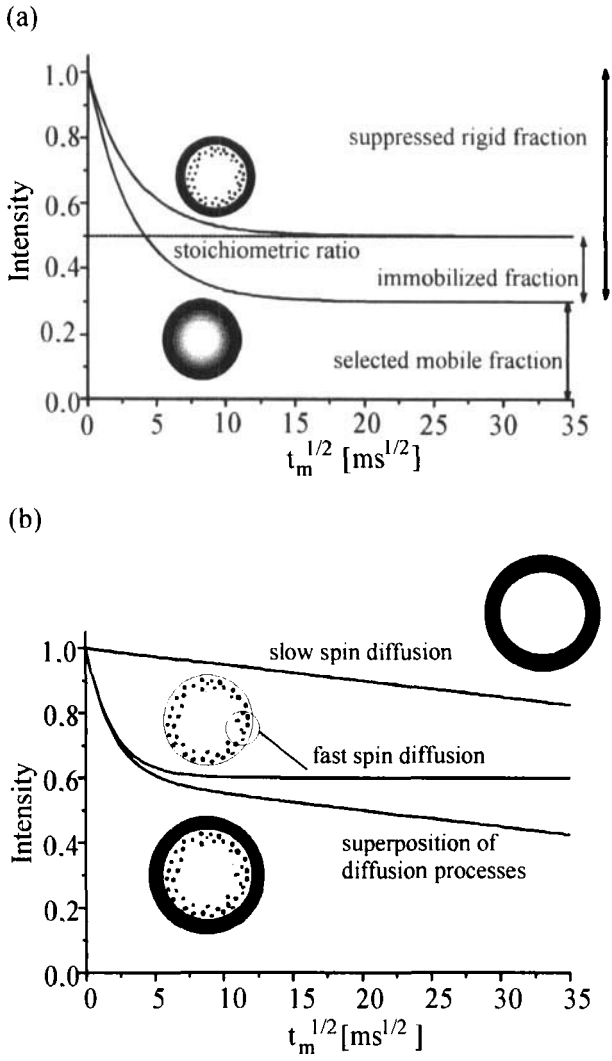

Fig. 19. Schematic representation of spin diffusion studies of the interface structure in core–shell systems. (a) Comparison of microphase separated and concentration gradient interface. (b) Comparison of ideal structure and interface with microdomains.

interface with a concentration gradient, whereas the interface of the high-temperature latex consists predominantly of small microdomains.

Thus, solid-state NMR emerges as an important tool to characterize the phase separation of heterogeneous polymers such as core–shell latexes or dialysis membranes.[58]

3.6. Spatially resolved NMR

Eventually one would like to obtain the information about the chain order and dynamics accessible by solid-state NMR, not only for the sample as a whole, but spatially resolved. For instance, one would like to distinguish the molecular parameters in regions close to the surface or in regions of non-linear plastic deformation[59] from those in the bulk. By applying pulsed field gradients, the concepts of multidimensional NMR can also be used to generate spatial dimensions in multidimensional spectra through Fourier imaging.[2,60] As a first example, spatially resolved ^{13}C-NMR spectra of injection-moulded syndiotactic poly(propylene) were recorded.[61] In such samples it is known that the skin and core layers possess different melting behaviour and mechanical properties due to differences in molecular order, orientation and morphology. Indeed, differences in density and chain alignment could be unravelled in the spatially resolved ^{13}C NMR spectra, demonstrating that spectroscopic NMR imaging is possible.

Even more challenging is to spatially resolve differences in molecular motions in regions of non-linear plastic deformation of polymers, such as the necking region or shearbands. This has recently been achieved by parameter imaging of cold drawn polycarbonate.[62,63] For highest signal intensity ^{1}H NMR was used. Since the spatial resolution is inversely proportional to the line-width multiple-pulse line narrowing[3] was employed. In parameter imaging an appropriate spectroscopy parameter such as a relaxation rate is recorded as a function of spatial dimensions. For polycarbonate, the effective transverse relaxation rate $T_{2\text{eff}}^{-1}$ measured via the Ostroff–Waugh (OW-4) sequence[64] was found to provide the highest contrast. It is sensitive to slow thermal motions in the kilohertz region. The $T_{2\text{eff}}$ decay for polycarbonate is non-exponential and can be decomposed into two components, where the short time decay results predominantly from the phenylene rings and is assigned to small angle motions and main-chain wiggling.[65]

The pulse sequence for two-dimensional parameter imaging is shown in Fig. 20.[66] It starts with the parameter selection OW-sequence in t_1, followed by the imaging part applying line narrowing by the magic sandwich echo sequence.[67,68] It consists of a phase-encoding part in the indirect dimension t_2, followed by a frequency-encoding sequence with stroboscopic detection during t_3. As shown in Fig. 21a, the relaxation rate in the deformed region of a cold drawn sample is roughly twice as large as in the undeformed part of the specimen, indicating immobilization in the deformed regions.[62]

In order to reconcile the changes in mobility detected here $T_{2\text{eff}}^{-1}$ was also measured as a function of temperature in undeformed polycarbonate. This shows that the changes in this relaxation rate due to the drawing correspond to a temperature shift of about 85 K. On the other hand, the slowing down of the phenylene flip rate due to drawing to $\lambda = 1.7$ corresponds to a temperature shift of only 10 K, in accordance with the slight change in density

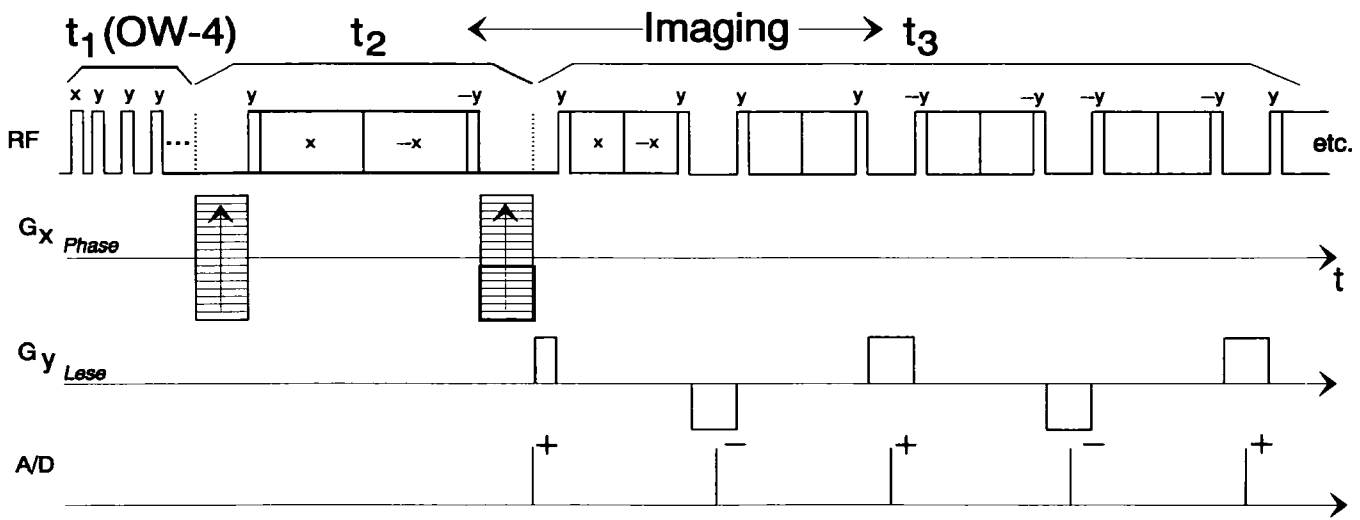

Fig. 20. Pulse sequence for two-dimensional parameter imaging of solids.[66]

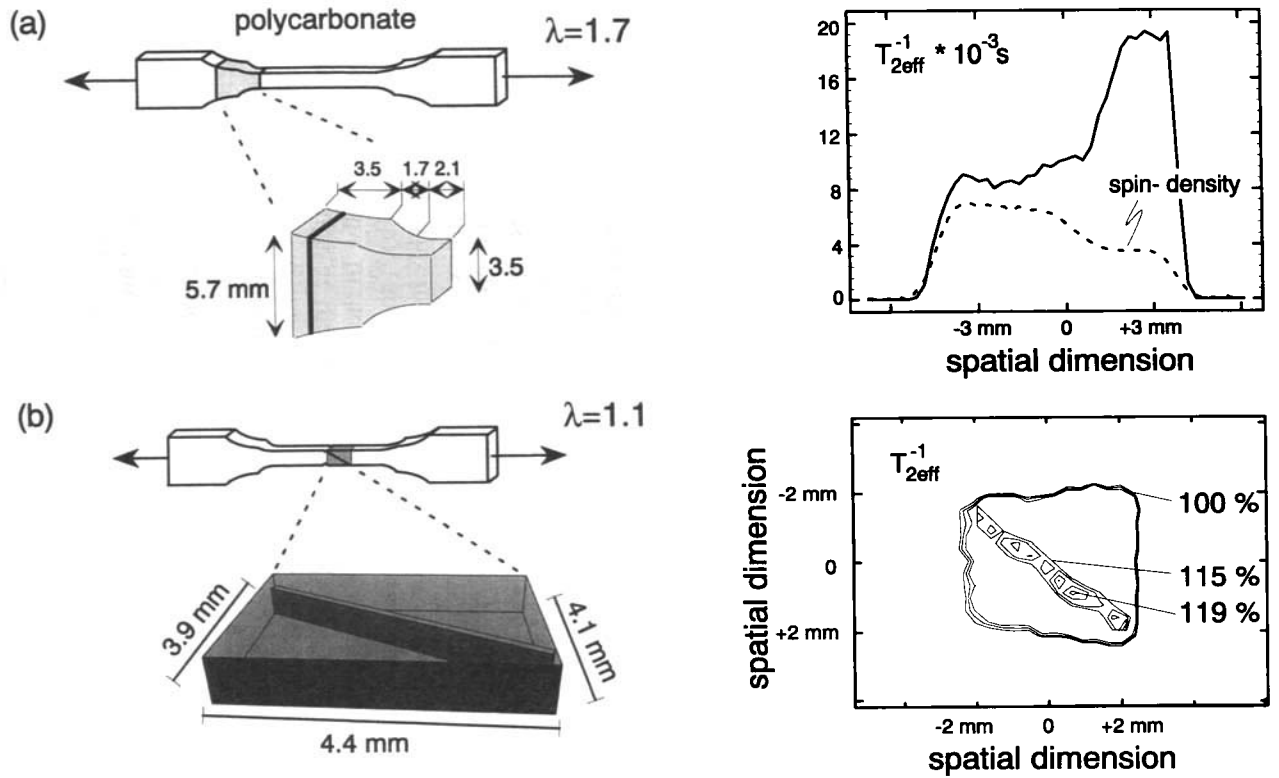

Fig. 21. Visualization of immobilization of polycarbonate by mechanical deformation with NMR parameter imaging; sketches of the samples on the left. (a) Effective transverse relaxation rate T_{2eff}^{-1} as a function of space in the necking region.[62] (b) Two-dimensional T_{2eff}^{-1} image of a shearband. The relaxation rate in the shearband is increased by 19% compared to the surrounding material as indicated.[63]

between the deformed and undeformed regions.[69] Thus, these spatially resolved NMR measurements of the molecular dynamics indicate that the packing in the cold drawn region must be different from that of the glassy polymer itself, since large amplitude motions and the overall density on one hand, and small amplitude motions on the other hand, are affected differently by the mechanical deformation.

The sensitivity of NMR to changes in mobility is high enough to even detect differences in immobilization within the deformed regions. For instance, in shearbands the inhomogeneities of plastic deformation are further localized.[59] Such shearbands can be produced by cold drawing a specimen with a fine scratch at the surface, as indicated in Fig. 21(b), and can be identified optically. In the $T_{2\text{eff}}^{-1}$ parameter image of the polycarbonate sample shown in Fig. 21(b),[63] the shearband can clearly be seen as a region of further immobilization. This image convincingly demonstrates that advanced solid-state NMR can indeed establish relations between macroscopic behaviour (shearbands) and microscopic parameters (molecular dynamics) of polymers. Similarly, images of stress in deformed elastomers have recently been obtained from DQ images of deuterated oligomers dissolved in them.[70] In another study[71] the spatial distribution of domain sizes has been determined by spatially resolved spin diffusion studies.

3.7. Further applications of solid-state NMR of polymers

This report concentrates on selected aspects of multidimensional solid-state NMR. In order to be more general, this section briefly reviews other recent applications. In fact, a number of reviews on solid-state NMR and polymers have been published, e.g. on the local dynamics of polymers above and below T_g by various relaxation techniques,[72] NMR imaging of solids,[73] solid-state NMR techniques for the study of polymer–polymer miscibility[74] and 2D exchange spectroscopy in polymer research.[75]

One- and two-dimensional NMR was used to determine the structure of spider dragline silk in order to understand its extraordinary mechanical properties.[76,77] In synthetic fibres from industrial process lines the orientational distribution was determined as a function of processing conditions by 2D MAS NMR for hot drawn nylon 6[78] and poly(ethylene terephthalate) (PET).[79] In drawn fibres of the same material, slow phenylene flips were observed and attributed to ordered non-crystalline layers of the crystals.[80] The effect of mechanical deformation on the molecular dynamics in poly(*p*-phenylene terephthalamide) fibres was examined by ^{2}H-2D exchange NMR.[81] A pulse sequence for increased spectral resolution of the synchronized 2D MAS experiment for determining molecular order[3] has been developed.[82]

Two-dimensional exchange NMR methods have been applied, e.g. to study

conformational transitions of the flexible spacers in main-chain liquid crystalline polymers,[83] the anion dynamics of glassy polyelectrolytes,[84] rotational diffusion of PMMA latexes[85] and the compositional dependence of segmented dynamics in polyisoprene–poly(vinylethylene) blends.[86] Moreover, 2D WISE NMR and spin diffusion techniques were used to study the phase separation and molecular motions in polystyrene–poly (2,6-dimethyl-*p*-phenylene oxide)[87] and polyurethane elastomers.[88] The same method revealed that in cellulose–poly(vinyl alcohol) blends exposed to moisture, the water is predominantly associated with the cellulose backbone.[89] Last, but not least, new double-quantum NMR techniques for determining torsional angles in the solid state have been introduced[90,91] utilizing ^{13}C labelled materials.

4. CONCLUSIONS AND OUTLOOK

The recent examples described in this review demonstrate the advantages of solid-state NMR as an advanced tool of polymer characterization. Its unique selectivity allows us to distinguish specific chemical sites in a polymer structure and also regions of different mobility. By combining NMR spectroscopy with spin diffusion techniques and imaging, enormous lengthscales can be covered from the molecular to the macroscopic level. NMR also outranks other techniques as far as versatility is concerned. For instance, it can probe the conformational statistics in glassy polymers, dynamic order phenomena in polymer melts and elastomers, interface structures in structured heterogeneous polymers and immobilization in regions of non-linear plastic deformation. In most of these cases the information provided by multidimensional solid-state NMR is also unique, i.e. it has not been available before by other techniques. This holds in particular as far as dynamic aspects are concerned, where multidimensional exchange NMR provides higher-order correlation functions which can separate the geometry of the motion from its time dependence. This allows us to probe memory effects of complex chain dynamics, e.g. at the glass transition of amorphous polymers. This information is of fundamental importance and provides the basis of a better understanding of polymer behaviour. At the same time, advanced NMR methods are applied to industrial samples, such as core–shell latexes, elastomers and dialysis membranes. In fact, the results obtained from multidimensional NMR have already been used to achieve dramatic improvement of the long-time stability of poly(ethylene) tubes.[92]

High-resolution multiple-quantum NMR spectroscopy of abundant nuclei in strongly coupled solids opens up an enormous potential for further development, since structure and dynamics can now be probed via connectivities between different functional groups. It has been pointed out[3] that

close analogies exist between multidimensional solid-state NMR and X-ray or neutron scattering. Multiple-quantum NMR will provide information equivalent to that of quasielastic *coherent* neutron scattering, albeit for much slower processes in the regime of milliseconds to seconds.

Thus, rather than asking "Do we need solid-state NMR?", we hope that in the future the question will be "How could we ever do without it?"

ACKNOWLEDGEMENTS

Most of the examples presented here were obtained by our research group within the last three years. I would like to specifically thank my coworkers, Christine Boeffel, Ralf Born, Dan Demco, Helen Geen, Carsten Fülber, Johannes Gottwald, Robert Graf, Siegfried Hafner, Andreas Heuer, Sigrid Kuebler, Katharina Landfester, Stefan Spiegel, Jeremy Titman, Frank Weigand, Ulrich Wiesner and Manfred Wilhelm. Stimulating discussions with Profs Bernhard Blümich, Klaus Schmidt-Rohr and Hans Sillescu are gratefully acknowledged.

REFERENCES

1. J. I. Kroschwitz (ed.), *Concise Encyclopedia of Polymer Science and Technology*, J. Wiley & Sons, New York, 1990.
2. R. R. Ernst, G. Bodenhausen and A. Wokaun, *Principles of Nuclear Magnetic Resonance in One and Two Dimensions*, Oxford University Press, Oxford, 1987.
3. K. Schmidt-Rohr and H. W. Spiess, *Multidimensional Solid-State NMR and Polymers*, Academic Press, London, 1994.
4. A. E. Tonelli, *NMR Spectroscopy and Polymer Microstructure: The Conformational Connection*, VCH Publ., New York, 1989.
5. K. Zemke, K. Schmidt-Rohr and H. W. Spiess, *Acta Polym.*, 1994, **45**, 148.
6. H. Kurosu, I. Ando and G. A. Webb, *Magn. Reson. Chem.*, 1993, **31**, 399.
7. R. Born, H. W. Spiess, W. Kutzelnigg, U. Fleischer and M. Schindler, *Macromolecules*, 1994, **27**, 1500.
8. R. Born and H. W. Spiess, *Macromolecules*, 1995, **28**, 7785.
9. W. L. Mattice and U. W. Suter, *Conformational Theory of Large Molecules*, J. Wiley and Sons, New York, 1994.
10. K. B. Lipkowitz and D. B. Boyd (eds), *Reviews in Computational Chemistry*, Vol. 2, VCH, Weinheim, New York, 1991.
11. W. Kutzelnigg, U. Fleischer and M. Schindler, *NMR Basic Principles. Progr.*, 1991, **23**, 165.
12. F. Auriemma, R. Born, H. W. Spiess, C. De Rosa and P. Corradini, *Macromolecules*, 1995, **28**, 6902.
13. R. Born and H. W. Spiess, *NMR Basic Princip. Progr.*, 1997, **35**, 1.
14. A. C. de Dios and E. Oldfield, *Solid State NMR*, 1996, **6**, 101.
15. A. Abragam, *The Principles of Nuclear Magnetism*, Oxford University Press, London, 1961.
16. A. E. Bennett, R. G. Griffin and S. Vega, *NMR Basic Princip. Progr.*, 1994, **33**, 1.

17. G. Dabbagh, D. P. Wekily and R. Tycko, *Macromolecules*, 1994, **27**, 6183.
18. M. Tomaselli, P. Robyr, B. H. Meier, C. Grob-Pisano, R. R. Ernst and U. W. Suter, *Mol. Phys.*, in press.
19. A. Schmidt, T. Kowalewski and J. Schaefer, *Macromolecules*, 1993, **26**, 1729.
20. P. Robyr, M. Tomaselli, J. Straka, C. Grob-Pisano, U. W. Suter, B. H. Meier and R. R. Ernst, *Mol. Phys.*, 1995, **84**, 995.
21. J. Gottwald, D. E. Demco, R. Graf and H. W. Spiess, *Chem. Phys. Lett.*, 1995, **243**, 314.
22. D. P. Weitekamp, *Adv. Magn. Reson.*, 1993, **11**, 111.
23. M. Munowitz and A. Pines, *Adv. Chem. Phys.*, 1987, **66**, 1.
24. H. Geen, J. J. Titman, J. Gottwald and H. W. Spiess, *Chem. Phys. Lett.*, 1994, **227**, 79.
25. W. Sommer, J. Gottwald, D. E. Demco and H. W. Spiess, *J. Magn. Reson.*, 1995, **A112**, 131.
26. H. Geen, J. J. Titman, J. Gottwald and H. W. Spiess, *J. Magn. Reson.*, 1995, **A114**, 264.
27. R. Graf, D. E. Demco, J. Gottwald, S. Hafner and H. W. Spiess, *J. Chem. Phys.*, 1997, **106**, 885.
28. S. Hafner and H. W. Spiess, *J. Magn. Reson.*, 1996, **A121**, 160.
29. A. Heuer, J. Leisen, S. C. Kuebler and H. W. Spiess, *J. Chem. Phys.*, 1996, **105**, 7088.
30. A. Heuer, M. Wilhelm, H. Zimmermann and H. W. Spiess, *Phys. Rev. Lett.*, 1995, **75**, 2851.
31. A. Heuer, *Phys. Rev. E.*, 1997, in press.
32. S. C. Kuebler, A. Heuer and H. W. Spiess, *Phys. Rev. E.*, submitted.
33. H. Sillescu, *J. Chem. Phys.*, 1996, **104**, 4877.
34. R. Richert, *Chem. Phys. Lett.*, 1993, **216**, 223.
35. M. T. Cicerone, F. R. Blackburn and M. D. Ediger, *Macromolecules*, 1995, **28**, 8825.
36. M. T. Cicerone and M. D. Ediger, *J. Chem. Phys.*, 1995, **103**, 5684.
37. B. Schiener, A. Loidl, R. Böhmer and R. V. Chamberlin, *Science*, 1996, **274**, 752.
38. J. P. Cohen-Addad, in *Progress in NMR Spectroscopy* (ed. J. W. Emsley, J. Feeney and L. H. Sutcliffe), 1993, **25**, 1.
39. M. G. Brereton, *Macromolecules*, 1990, **23**, 1119.
40. P. Sotta and B. Deloche, *Macromolecules*, 1990, **23**, 1999.
41. P. Sotta, C. Fülber, D. E. Demco, B. Blümich and H. W. Spiess, *Macromolecules*, 1996, **29**, 6222.
42. D. E. Demco, S. Hafner, C. Fülber, R. Graf and H. W. Spiess, *J. Chem. Phys.*, 1996, **105**, 11285.
43. R. Tycko and G. Dabbagh, *Chem. Phys. Lett.*, 1990, **173**, 461.
44. Y. K. Lee, N. D. Kurur, M. Helmle, O. G. Johannessen, N. C. Nnielsen and M. H. Levitt, *Chem. Phys. Lett.*, 1995, **242**, 304.
45. B.-Q. Sun, P. R. Costa, D. Kocsiko, P. T. Lansbury and R. G. Griffin, *J. Chem. Phys.*, 1995, **102**, 702.
46. M. Feike, D. E. Demco, R. Graf, J. Gottwald, S. Hafner and H. W. Spiess, *J. Magn. Reson.*, 1996, in press.
47. H. Takeuchi and R.-J. Roe, *J. Chem. Phys.*, 1991, **94**, 7446, 7458.
48. G. D. Smith, D. Y. Yoon, W. Zhu and M. D. Ediger, *Macromolecules*, 1994, **27**, 5563.
49. A. S. Kulik, D. Radloff and H. W. Spiess, *Macromolecules*, 1994, **27**, 3111.
50. J. Clauss, K. Schmidt-Rohr and H. W. Spiess, *Acta Polym.*, 1993, **44**, 1.
51. S. Spiegel, K. Schmidt-Rohr, C. Boeffel and H. W. Spiess, *Polymer*, 1993, **34**, 4566.
52. D. L. VanderHart, *Macromolecules*, 1994, **27**, 2837.
53. M. Okumo, *Makromol. Chem., Makromol. Symp.*, 1990, **35/36**, 307.

54. Y. C. Chen, V. Dimonie and M. S. El-Aasser, *Macromolecules*, 1991, **24**, 3779.
55. S. Spiegel, K. Landfester, G. Lieser, C. Boeffel, H. W. Spiess and N. Eidam, *Makromol. Chem.*, 1995, **196**, 985.
56. K. Landfester, C. Boeffel, M. Lambla and H. W. Spiess, *Macromolecules*, 1996, **29**, 5972.
57. K. Landfester and H. W. Spiess, *Macromol. Chem., Rapid. Comm.*, 1996, **17**, 875.
58. R. H. Lewis, U. Wiesner, S. Lehmann and H. W. Spiess, *J. Biomater. Sci. Polym. Edn.*, 1994, **6**, 565.
59. R. N. Haward, *The Physics of Glassy Polymers*, Applied Science, London, 1973.
60. B. Blümich and W. Kuhn (eds), *Magnetic Resonance Microscopy: Methods and Applications in Materials Science, Agriculture and Biomedicine*, VCH, Weinheim, 1992.
61. E. Günther, B. Blümich and H. W. Spiess, *Macromolecules*, 1992, **25**, 3315.
62. F. Weigand and H. W. Spiess, *Macromolecules*, 1995, **28**, 6361.
63. F. Weigand, U. Wiesner and H. W. Spiess, *Adv. Mater.*, 1996, **8**, 481.
64. E. D. Ostroff and J. S. Waugh, *Phys. Rev. Lett.*, 1966, **16**, 1097.
65. J. Schaefer, E. O. Stejskal, D. Perchak, J. Skolnick and R. Yaris, *Macromolecules*, 1985, **18**, 368.
66. F. Weigand, S. Hafner and H. W. Spiess, *J. Magn. Reson.*, 1996, **A120**, 210.
67. H. Schneider and H. Schmiedel, *Phys. Lett.*, 1969, **A30**, 298.
68. W.-K. Rhim, A. Pines and J. S. Waugh, *Phys. Rev. Lett.*, 1970, **25**, 218.
69. M. T. Hansen, B. Blümich, C. Boeffel, H. W. Spiess, L. Morbitzer and A. Zembrod, *Macromolecules*, 1992, **25**, 5542.
70. M. Klinkenberg, B. Blümler and B. Blümich, *J. Magn. Reson.*, 1996, **A119**, 197.
71. F. Weigand, D. E. Demco, B. Blümich and H. W. Spiess, *J. Magn. Reson.*, 1996, **A120**, 190.
72. F. Laupretere, *NMR Basic Princip. Progr.*, 1994, **30**, 63.
73. P. Blümler and B. Blümich, *NMR Basic Princip. Progr.*, 1994, **30**, 209.
74. W. S. Veeman and W. E. J. R. Maas, *NMR Basic Princip. Progr.*, 1994, **32**, 127.
75. H. W. Beckham and H. W. Spiess, *NMR Basic Princip. Progr.*, 1994, **32**, 163.
76. A. Simmons, E. Ray and L. W. Jelinski, *Macromolecules*, 1994, **27**, 5235.
77. J. Kümmerlen, J. D. van Beek, F. Vollrath and B. H. Meier, *Macromolecules*, 1996, **29**, 2920.
78. D. L. Tzou, H. W. Spiess and S. Curran, *J. Polym. Sci. Poly. Phys. Ed.*, 1994, **32**, 1521.
79. W. Gabrielse, H. Angad Gaur and W. S. Veeman, *Macromolecules*, 1996, **29**, 4125.
80. M. Wilhelm and H. W. Spiess, *Macromolecules*, 1996, **29**, 1088.
81. D. J. Schaefer, R. J. Schadt, K. H. Gardner, V. Gabara, S. R. Allen and A. D. English, *Macromolecules*, 1995, **28**, 1152.
82. Z. Song, O. N. Atzukin, A. Rupprecht and M. H. Levitt, *Chem. Phys. Lett.*, 1996, **253**, 349.
83. J. Leisen, C. Boeffel, H. W. Spiess, D. Y. Yoon, M. H. Sherwood, M. Kawasumi and V. Percec, *Macromolecules*, 1995, **28**, 6937.
84. R. R. Rietz, K. Schmidt-Rohr, W. H. Meyer, H. W. Spiess and G. Wegner, *Solid State Ionics*, 1994, **68**, 151.
85. G. A. Barrall, K. Schmidt-Rohr, V. K. Lee, K. Landfester, H. Zimmermann, G. C. Chingas and A. Pines, *J. Chem. Phys.*, 1996, **104**, 509.
86. G. C. Chung, J. A. Kornfield and S. D. Smith, *Macromolecules*, 1994, **27**, 5729.
87. S. Li, D. M. Rice and F. E. Karasz, *Macromolecules*, 1996, **29**, 2211.
88. H.-J. Tao, D. M. Rice, W. J. MacKnight and S. L. Hsu, *Macromolecules*, 1995, **28**, 4036.
89. D. Radloff, C. Boeffel and H. W. Spiess, *Macromolecules*, 1996, **29**, 1528.
90. K. Schmidt-Rohr, *Macromolecules*, 1996, **29**, 3975.

91. X. Feng, Y. K. Lee, D. Sandström, M. Edén, A. Sebald and M. H. Levitt, *Chem. Phys. Lett.*, 1996, **257**, 314.
92. L. L. Böhm, H. F. Enderle and M. Fleissner, in *Catalyst Design for Taylor-made Polyolefins*, p. 351. Kodansha Ltd, Tokyo, 1994.

This Page Intentionally Left Blank

Structures and Dynamics of Polymer Gel Systems Viewed Using NMR Spectroscopy

HIDEKAZU YASUNAGA

Department of Chemistry and Materials Technology, Kyoto Institute of Technology, Goshokaido-cho, Matsugasaki, Sakyo-ku, Kyoto 606, Japan

MASATOSHI KOBAYASHI, SHINGO MATSUKAWA, HIROMICHI KUROSU and ISAO ANDO

Department of Polymer Chemistry, Tokyo Institute of Technology, Ookayama, Meguro-ku, Tokyo 152, Japan

ANNUAL REPORTS ON NMR SPECTROSCOPY
VOLUME 34 ISBN 0-12-505334-7

Recent fundamental research on hydro-polymer gel systems by means of NMR techniques such as pulse NMR, pulsed field-gradient spin-echo NMR, solid-state high-resolution NMR and NMR imaging methods have been reviewed. Such NMR techniques have elucidated structures and dynamics of gel systems as a function of the degree of crosslinking and their response process by an application of stimulus such as change in temperature, stress and electric field. It has been demonstrated that NMR techniques are powerful means of determining micro- and macroscopic structures and dynamics of more complicated systems with mobile components such as gel systems.

1. INTRODUCTION

Polymer gels have attracted considerable attention from the point of view of various physical and chemical properties.[1] For example, hydro-polyelectrolyte gels show a dramatic change in volume in response to change in solvent composition, pH, ionic strength, and temperature. They contract upon application of electric fields and work as electrically-activated devices. Water-swollen polymer gels can convert chemical energy into mechanical energy.[2] These lead to the vitality of polymer research and development of a diversity of interests on polymer gel materials. In order to develop new polymer materials, polymer gel design has been performed on the basis of advanced polymer science and technology. The properties of polymers are closely related to their structures and dynamics. For this reason, the establishment of methods for determining the structures and dynamics is very important for making reliable polymer gel design and for developing new advanced polymer gels.

Recently, various new NMR techniques such as pulse NMR, solid-state high-resolution NMR, NMR imaging, etc. have been developed to obtain useful information about the structures and dynamics of polymers in solution and in the solid state.[3] These techniques should be applied to polymer gel systems to get detailed information on the structure and dynamics.

This review covers recent fundamental research work on the structure and dynamics of hydro-polymer gel systems by means of some NMR techniques.

2. POLYMER GEL PREPARATIONS

Polymer gels may be classified as chemical gels or physical gels by the manner of the linkages between polymer chains.[1] In the former case, the linkages between polymer chains occur by covalent bonds whereas in the latter case, gels occur by physical interactions such as van der Waals interactions, hydrogen bonds, Coulombic interactions, etc.

2.1. Chemical gels

Chemical gels are prepared by radical polymerization of monomers with multifunctionalities. In particular, hydrogels are often polymerized with water-soluble monomers which have ionic groups, hydroxyl groups, amide groups or ethylene ether groups such as acrylic acids, hydroxyethyl acrylates, alkylacrylamides, poly(ethylene acrylate), etc. The functional groups such as hydroxyl groups, carboxylic acid groups, epoxyl groups, etc. can be easily introduced into the gel networks. Radical reactions using initiators such as redox catalysts of organic peroxide/amine systems are so strong that highly crosslinked gels can be obtained even at low temperature. The degree of crosslinking varies with the amount of multifunctional monomer used and is increased as the amount of multifunctional monomer is increased. The distribution of chain lengths between neighbouring crosslinking points in the obtained gel is very large.

The degree of swelling of a polymer gel (q) is defined as the ratio of the mass of swollen polymer gel (M_{swollen}) to the mass of dried polymer (M_{dry}):

$$q = M_{\text{swollen}}/M_{\text{dry}} \tag{1}$$

For example, the q values of poly(N,N′-dimethylacrylamide) (PDMAA) gels are plotted against the mole fraction of N,N′-methylene-bis(acrylamide) (MBAA) as crosslinking agent for DMAA (f_c) in Fig. 1(a).[33]

As seen from this figure, swollen PDMAA gel samples are in the range of $q = 7.5$ to 50, where a decrease in q relates to an increase in crosslinking. At a state of equilibrium swelling, the relation between the density of crosslinking point (N_c) and q is given by[4]

$$N_c \approx q^{-5/3} \tag{2}$$

The efficiency of crosslinking (N_c/f_c) is plotted against f_c in Fig. 1(b) assuming that $N_c/f_c = 1.0$ at $q = 50$, which corresponds to the ratio of the amount of MBAA contributing to crosslinking points to that of MBAA added. It is found that the efficiency of crosslinking decreases with an increase in f_c because it becomes more difficult in highly crosslinked gels for both vinyl groups of MBAA to react.

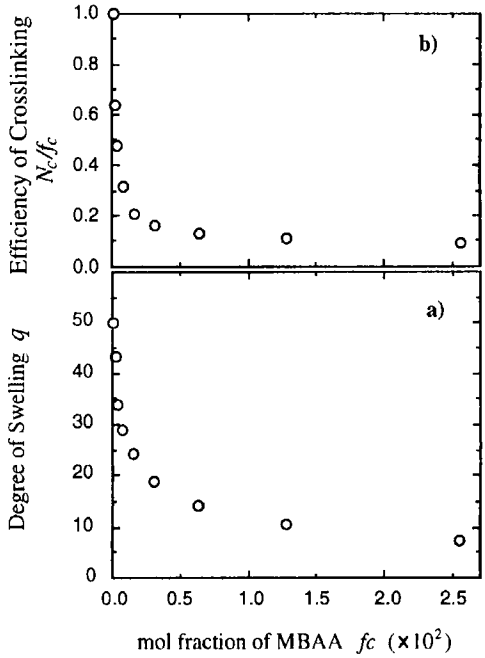

Fig. 1. (a) Dependence of the degree of swelling (q) of PDMAA gel on f_c at 303 K, where f_c is the mole fraction of MBAA used as crosslinking reagent. (b) Plot of the ratio of N_c/f_c against f_c assuming that $N_c/f_c = 1.0$ at $f_c = 0.01$. N_c is calculated from the experimental values of q using equation (2).

Ionic polymerization can be used to prepare gels in organic solvents which have no reactive groups such as a hydroxyl group or an amino group. The distribution of the sizes of network in the gel is relatively narrow.

The direct crosslinking reaction between polymer chains is also used to prepare chemical gels. In this case, the polymer chains must have functional groups in a polymer chain to allow crosslinking. The sizes of network can be controlled to give a narrow distribution.

The crosslinking points formed by covalent bonds are generally stable to heating, pH and the composition of solvent. Therefore, such chemical gels do not have the sol–gel transition which is often observed for physical gels, with the exception of some chemical gels containing reversible covalent bonds such as poly(vinyl alcohol)–borate complex.[5]

2.2. Physical gels

In physical gels, crosslinking points are formed by strong intermolecular interactions such as Coulombic, dipole–dipole, van der Waals, charge

transfer, hydrophobic and hydrogen bonding interactions. Some physical gels become thermo-reversible gels, which have a transition from gel to sol with increasing temperature, or in some cases transition from sol to gel.[6]

Synthetic polymers such as poly(vinyl alcohol) (PVA), poly(N-isopropylacrylamide) (PNIPAM), etc. become physical gels under specified conditions. The gelation of PVA arises by the formation of hydrogen bonds between its interchains and PNIPAM by hydrophobic interactions. Aqueous PVA solution can form a gel by undergoing freeze–thaw cycles. Aqueous PNIPAM solution can form a gel by increasing the temperature above 32°C.

There are some types of physical gels formed from biopolymers, such as polysaccharides and proteins etc.[7,8] A number of polysaccharides in aqueous solution can transform into gels under various specified conditions. κ-Carrageenan consists of two galactose units such as α-1,3-linked galactose-4-sulphate and β-1,4-linked 3,6-anhydrogalactose. The gelation of κ-carrageenan is enhanced by the presence of cations such as K^+, Rb^+ and Cs^+. Gellan is a linear anionic heteropolysaccharide with a tetrasaccharide repeat unit, the gelation of which depends on the type and concentration of associated cations. Starch gels may be regarded as phase-separated or composite gels. Amylose and amylopectin are components of starch. The gelation of amylose involves the phase separation of an amylose-rich amorphous network in which crystallization occurs. Gelatin is a protein which is prepared from partial hydrolytic degradation of collagen. Gel formation and the melting behaviour of gelatin strongly depend on temperature, concentration and composition of the gelatin sample.

3. MICROSCOPIC ASPECTS OF STRUCTURES AND DYNAMICS OF POLYMER GEL SYSTEMS

3.1. ^{1}H pulse NMR approaches for elucidating structure and dynamics

Spin–lattice relaxation time (T_1) and spin–spin relaxation time (T_2) give information about microscopic dynamics of solvents[9–12] or of polymers in gels.[13] From the relaxation times, the correlation time τ_c of the molecular motion can be estimated by using the Bloembergen–Purcell–Pound (BPP) theory[14] if the relaxation times are predominantly affected by dipole–dipole interactions. The relaxation times for solvents in gels are closely associated with microscopic molecular motion and structure of the gel. The understanding of structure and dynamics for gel systems is important not only for fundamental research work, but practical research work such as drug delivery systems, separation technology and applications for soft actuators.

3.1.1. Sol–gel transition of aqueous PNIPAM solution viewed using ^1H T_1 and T_2

It is known that PNIPAM in water undergoes a phase transition from sol to gel at around 31°C.[15] ^1H pulse NMR experiments provide useful information about molecular motion of the polymer and solvent in the solution and gel state. The abrupt change of molecular motion for solvent in the gel is caused by the formation of gel structure at the phase transition temperature and therefore, the changes in relaxation time sensitively reflects the changes in state.

Figure 2 shows plots of the ^1H T_2 values against temperature for water in 1, 2.5, 5 and 10% wt/v PNIPAM/water solutions and for neat water at atmospheric pressure.[13] The PNIPAM was prepared by radical polymerization and fractionated to have narrow distribution of molecular weight. The T_2 value increases slowly as the temperature is increased up to 30°C. (As expected, the T_2 value of neat water increases linearly with temperature up to 50°C.) At the gelation temperature (about 31°C), the T_2 value in all of the polymer solutions transitionally decreases. As the temperature is further increased, the T_2 value increases again. This implies that the mobility of water increases with increasing temperature up to 30°C, then decreases transitionally at about 31°C due to the gelation of the system and increases again with a further increase of temperature. This trend is very different from the case of neat water. Furthermore, Fig. 2 shows that increasing the polymer concentration leads to a decrease in ^1H T_2 for water. This means that the molecular motion of water is more severely restricted by an increase of the intermolecular interactions between the polymer chains and water molecules. It is further found that as the polymer concentration increases up to 5% at the gelation temperature, the magnitude of the decrease for the T_2 value (ΔT_2) is larger, meaning the phase transition becomes sharper. However, as the polymer concentration is further increased up to 10% wt/v, the ΔT_2 value decreases. Such a situation may result from a balance between the contribution to the restrictions of molecular motion caused by an increase of the polymer concentration and the generation of a three-dimensional network structure.

Figure 3 shows a plot of the ^1H T_1 value of water molecules in 5% wt/v PNIPAM–water solution at atmospheric pressure as a function of temperature. The T_1 value slowly increases as the temperature is increased. At the gelation temperature, the T_1 value transitionally decreases. As the temperature is further increased, the T_1 value slowly increases. This behaviour is very similar to that for T_2. As seen from the observed T_1 and T_2 behaviours, the water molecules are in the fast motion region ($\omega\tau_c << 1$, where ω is the resonance frequency). Similar results were obtained at 1, 2.5, and 10% wt/v solutions. Therefore, the T_1 and T_2 values for water in the PNIPAM–water system are very sensitive to the phase transition and provide dynamic information.

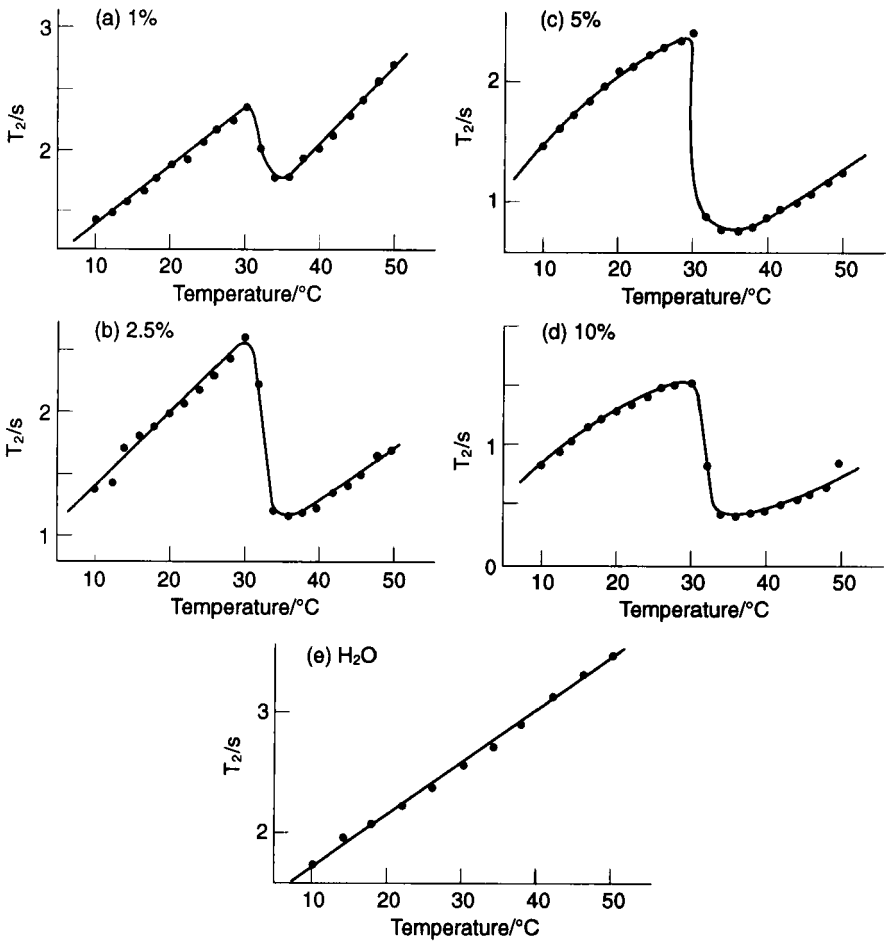

Fig. 2. Temperature dependence of ^1H T_2 for water in PNIPAM–water solution with the concentration of (a) 1, (b) 2.5, (c) 5 and (d) 10% wt/v and for (e) neat water at atmospheric pressure.

The application of pressure on the PNIPAM–water system will change the situation around network polymer and solvent. Therefore, intermolecular interactions between water and PNIPAM must change and so the dynamics of phase transition for the system change at high pressure. The information about the change of dynamics will be obtained by T_1 and T_2. Figure 4 shows the temperature dependence of ^1H T_2 for water in 10% wt/v PNIPAM–water solution at pressures of 100, 200, 300, and 400 kg cm^{-2}. The temperature for the phase transition is almost independent of pressure. At pressures of 100 and 200 kg cm^{-2} the T_2 value decreases transitionally and then sharply at the gelation temperature. However, at pressures of 300 and 400 kg cm^{-2}, the T_2

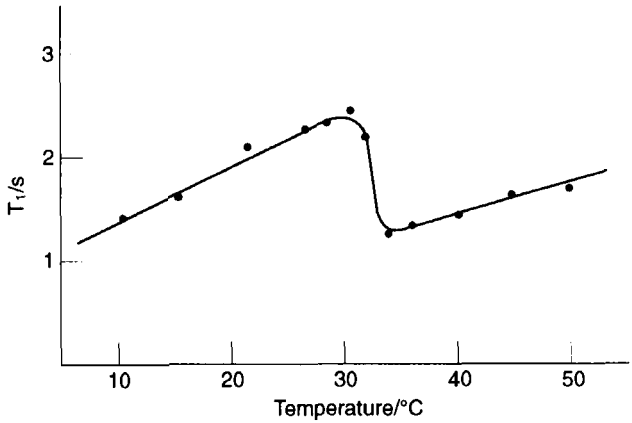

Fig. 3. Temperature dependence of ^1H T_1 for water in 5% wt/v PNIPAM–water solution at atmospheric pressure.

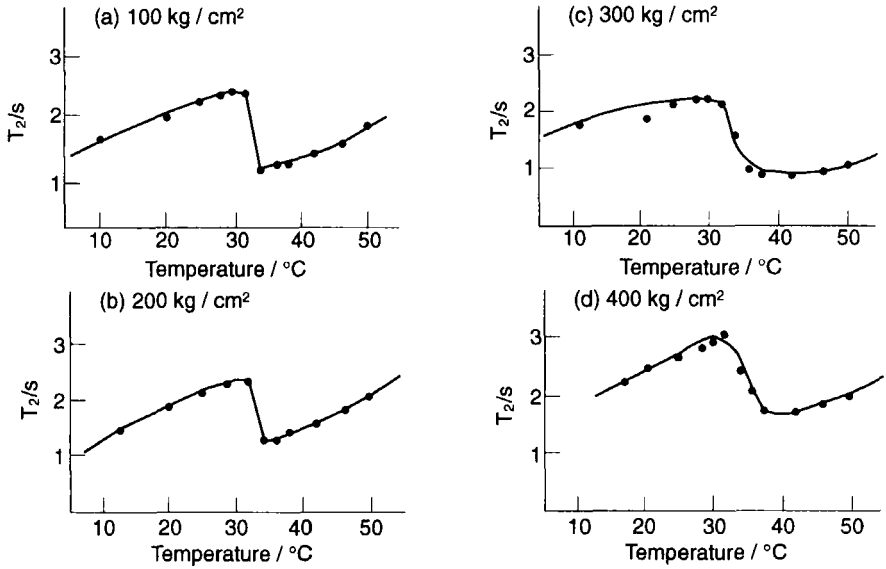

Fig. 4. Temperature dependence of ^1H T_2 for water in 5% wt/v PNIPAM–water solution under pressure of (a) 100, (b) 200, (c) 300, and (d) 400 kg cm^{-2}.

value decreases transitionally but slowly at the gelation temperature. Therefore, the sharpness of the phase transition decreases as the pressure is increased. This means that the gelation of the system occurs slowly under high pressure, and the application of high pressures prevents gelation.

Figure 5 shows the pressure dependence of ^1H T_2 for water in 5% wt/v

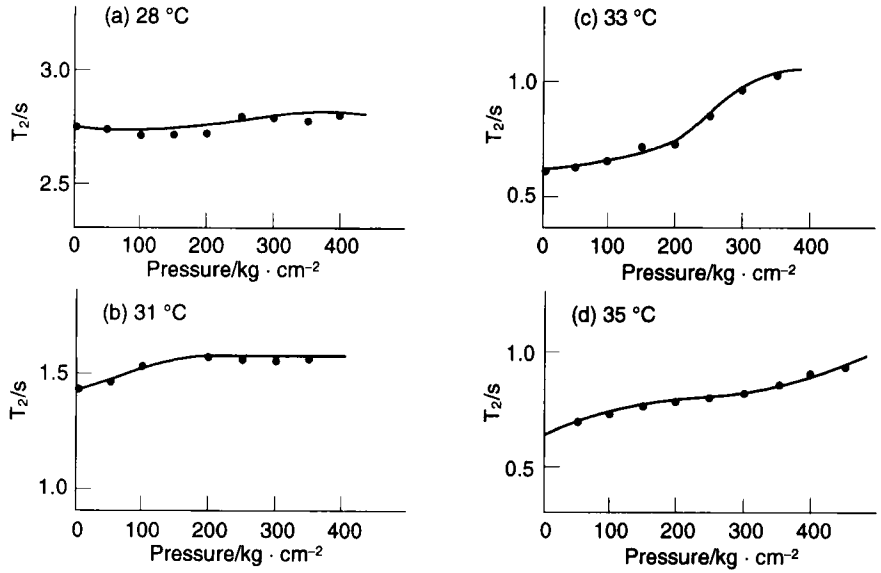

Fig. 5. Pressure dependence of ^1H T_2 for water in 5% wt/v PNIPAM–water solution at temperature of (a) 28, (b) 31, (c) 33, and (d) 35°C.

PNIPAM–water solution at temperatures of 28, 31, 33, and 35°C. The dependencies change as a function of temperature. At 28°C the T_2 value is almost independent of pressure. However, at 31°C the T_2 value slightly increases as the pressure is increased. At 33°C the T_2 value increases significantly as the pressure is increased and at 35°C the pressure dependence of the T_2 value returns to the smaller scale. Therefore, the relatively large T_2 change occurs at the gelation temperature. However, at temperatures higher or lower than the gelation temperature, the T_2 change is very small. At the gelation temperature, the large increase of T_2, correspond to a large increase of molecular motion, means that the application of pressure inhibits gelation. At 35°C, after a stable gel is formed, pressure does not greatly influence gel structure or the molecular motion of water in the gel network.

3.1.2. Phase transition of a PNIPAM gel viewed using ^1H T_2

Figure 6 shows the degree of swelling (q) of a PNIPAM gel in water as a function of temperature, where PNIPAM gel was prepared by radical polymerization of NIPAM and MBAA using a redox initiator of $K_2S_2O_8$/N,N,N′,N′-tetramethylethylenediamine and swollen in water. The q value and volume change transitionally around 33–34°C, as described already.[16] Such transitions are viewed from dynamics through the observation

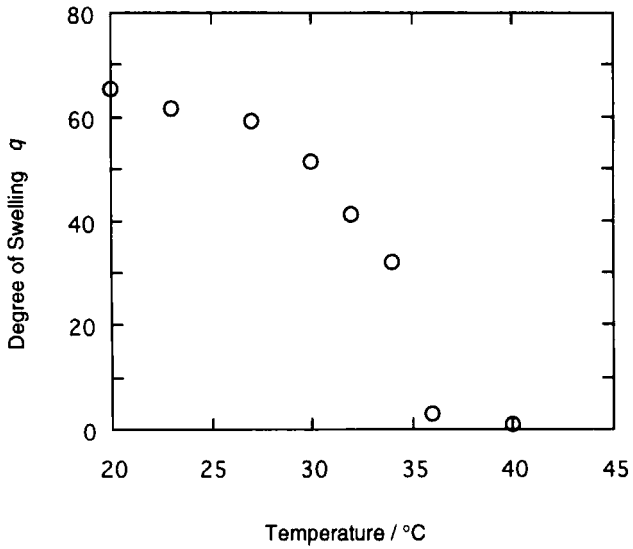

Fig. 6. Temperature dependence for the volume of PNIPAM gel at the state of equilibrium swelling.

of ^1H T_2 values.[68] The ^1H T_2 values as a function of temperature for a PNIPAM gel (q = 30 at 20°C) and for neat water are shown in Fig. 7. During the NMR measurements, the gel shrinks with an increase in temperature and exuded water is wiped away. The T_2 value increased as the temperature was increased up to 33°C. At the volume-phase transition temperature (33°C), the T_2 value transitionally decreased. As the temperature was further increased, the T_2 value increased again. This implies that the mobility of water in the gel increases with increasing temperature up to 33°C in spite of the relatively gentle change of the q value, in a similar manner to the mobility of neat water. It then decreases transitionally at 33°C due to the steep decrease of the q value and increases again with a further increase in temperature during which the q value does not change.

In the shrinkage process of gels induced by elevating temperature over the transition temperature, a PNIPAM gel often forms a skin structure where the unshrunk inner layer is surrounded by the shrunk outer layer, and so it takes a long time to complete the shrinkage process. Figure 8 shows the time dependencies of the ^1H T_2 values for sample Gel-A with q = 30 by rapid change of temperature from 20 to 40°C and for sample Gel-B with q = 13 at 20°C. The shape of its gel changes as illustrated in Fig. 9. As the temperature is increased, the T_2 value for the gel decreases with a decrease in q, while the T_2 value of neat water increases linearly. Furthermore, it was found from the T_2 curve that there were two components with different mobilities in sample Gel-A after the temperature was raised. A short T_2

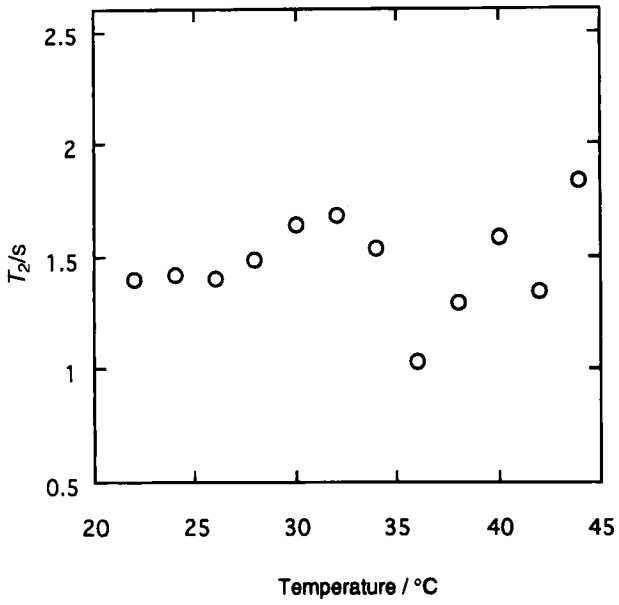

Fig. 7. Temperature dependence of ^1H T_2 for PNIPAM gel.

component corresponds to the shrunk outer layer and a long T_2 component to the unshrunk inner layer. This result is supported by the ^1H NMR imaging experiment for a PNIPAM gel with a skin structure (see Section 4). The value of the long T_2 component decreased slowly after 20 minutes, while that of the short T_2 component was independent of the elapsed time. This shows that the q value of the unshrunk inner layer decreases after the formation of skin structure.

3.2. Pulsed field gradient spin echo (PGSE) ^1H NMR approaches for elucidating self-diffusion of solvent in a gel

Pulsed field gradient spin echo (PGSE) ^1H NMR is a powerful method for studying self-diffusion in polymer systems. It gives direct information about molecular dynamics. In PGSE ^1H NMR the ($\pi/2$–τ–π) pulse sequence and two field gradient pulses are used as shown in Fig. 10, where τ is the pulse interval. Thus, the relationship between echo signal intensity and pulse field gradient parameters is given by

$$\ln\left(\frac{A(\delta)}{A(0)}\right) = -\frac{2\tau}{T_2} - \gamma^2 G^2 D\delta^2\left(\Delta - \frac{\delta}{3}\right) \tag{3}$$

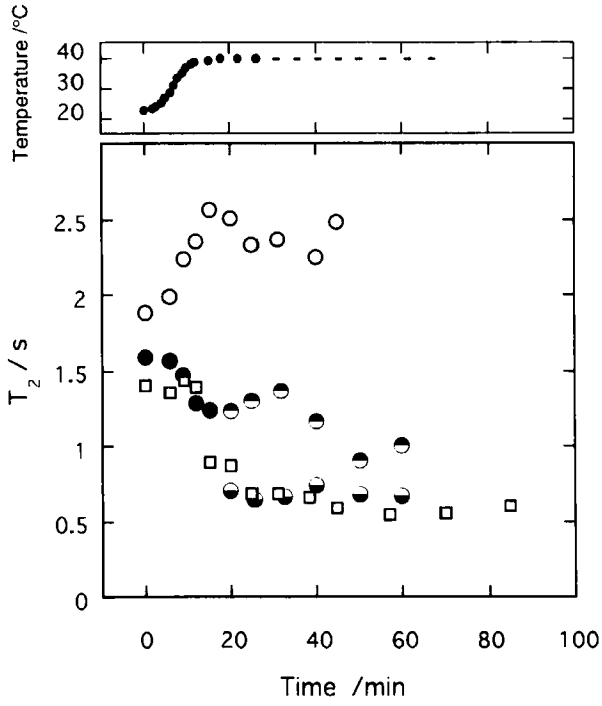

Fig. 8. Time courses of ^1H T_2 for water: neat water (○); sample Gel-A (●); sample Gel-B (□). After elevation of temperature, Gel-A had two components of T_2 (◓), (◒).

where $A(\delta)$ and $A(0)$ are echo signal intensities at $t = 2\tau$ with and without the magnetic field gradient pulse length δ, respectively, γ is the gyromagnetic ratio of the proton, G the field gradient strength, D the self-diffusion coefficient and Δ the gradient pulse interval. The diffusion coefficient (D) closely relates to the mean square displacement ($<z^2(\Delta)>$) of molecules considered along the direction of field gradient in the PGSE NMR experiment as[17]

$$<z^2(\Delta)> = 2D\Delta \tag{4}$$

where Δ is the observation time.

3.2.1. Self-diffusion of solvent in a PMAA gel

Poly(methacrylic acid) (PMAA) gel is a well-known hydro-polyelectrolyte gel. In general, hydro-polyelectrolyte gels have unique physical and chemical properties. For example, they show a drastic volume change in response to

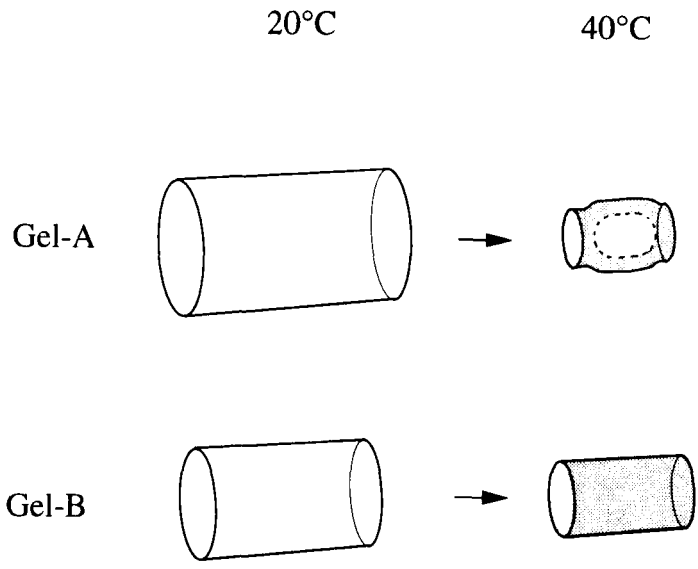

Fig. 9. Illustration of shape change for samples Gel-A and Gel-B with varying temperature.

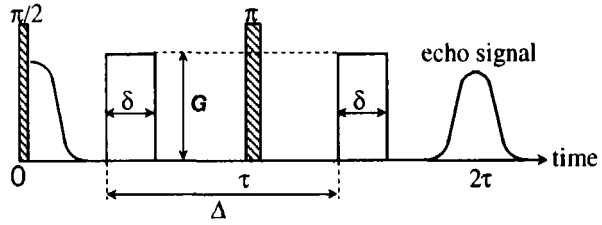

Fig. 10. Pulsed field gradient pulse sequence for measuring the diffusion coefficient D.

change in solvent composition,[16] pH,[19] ionic strength[20] and temperature,[21] and the application of an electric field.[22,23] In these reaction processes, the hydro-polyelectrolyte gels change their volume by releasing or absorbing water. In such processes, water molecules play a significant role. In order to reveal the role of water in the gels, it is important to understand the dynamic behaviour of water contained in hydro-polyelectrolyte gels associated with the polymer network structure.

To understand the translational motion of water contained in a PMAA gel caused by a change in the degree of crosslinking, the diffusion coefficient of H_2O molecules (D_{H_2O}) has been determined by the PGSE ^1H NMR method at 300 K as listed in Table 1, where the PMAA gel was prepared by radical polymerization of MAA and MBAA using $K_2S_2O_8$ as initiator and

Table 1. Determined ^{1}H T_1, ^{1}H T_2 and D_{H_2O} values of water in PMAA gel as a function of the degree of swelling (q).

q	^{1}H T_1 (s)	^{1}H T_2 (s)	D_{H_2O} (10^{-5} cm^2 s^{-1})
3.4	0.09	0.006	1.37
3.6	0.93	0.010	1.37
4.7	1.03	0.020	1.53
21.7	2.06	0.191	1.90
59.4	3.29	0.577	2.16
105.8	3.78	1.095	2.19

put in water at the state of equilibrium swelling.[9] As seen from Table 1, D_{H_2O} increases as q increases. Therefore, an increase in q leads to an increase in mobility of water molecules. As seen from the plot of D_{H_2O} against $q^{1/3}$ in Fig. 11, D_{H_2O} increases linearly from 1.37×10^{-5} to 2.19×10^{-5} cm^2 s^{-1} with increasing $q^{1/3}$. This shows that the translational motion of water molecules in the PMAA gel increases with an increase in the degree of swelling. The determined D_{H_2O} value for neat water at 300 K is 2.5×10^{-5} cm^2 s^{-1}. Therefore, it can be said that the translational motion of water molecules in the gel is more restrained than that of neat water because of intermolecular interactions with the polymer network.

It should be profitable to compare the D_{H_2O} with relaxation times for water in a PMAA gel. ^{1}H T_1 and T_2 values for water in the PMAA gel may be sensitive to a change in the degree of crosslinking in the gel. ^{1}H T_1 and T_2 values for water in the PMAA gel have been determined at 300 K as a function of q, as shown in Table 1. From this table, it is seen that the ^{1}H T_1 and T_2 values increase as q increases. This means that the molecular motion of water molecules increases with an increase in q. If the ^{1}H T_1 and T_2 values for water in the PMAA gel are plotted against $q^{1/3}$, a linear relationship is obtained (Fig. 12). From these results, it can be said that an increase in $q^{1/3}$ leads to a linear increase in molecular motion of water molecules in the gel, and that the molecular motion is in the fast motion region ($\omega\tau_c << 1$) in the BPP theory.[13]

In order to understand the hydrodynamic behaviour of water in a PMAA gel, the relationship between q and the radius of a water cluster has been studied. In the case of water molecules, the ^{1}H T_1 is predominantly governed by dipole–dipole interactions.[24,25] The equation for ^{1}H T_1 is expressed as[25,26]

$$\frac{1}{T_1} = \left(\frac{a}{b}\right)^2 \left(\frac{\gamma^4 h^2}{12\pi^2 b^4 D_{H_2O}}\right) \left(1 + \frac{3\pi N b^6}{5a^3}\right) \tag{5}$$

where b is the distance between protons of a water molecule (b = 1.58 Å),

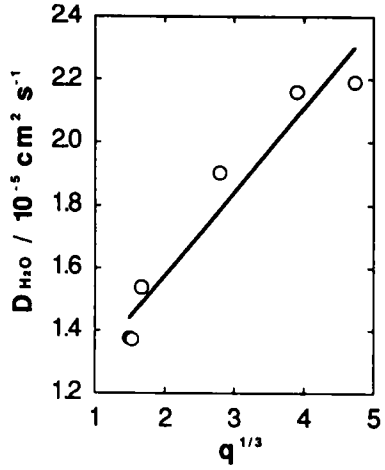

Fig. 11. Plots of the diffusion coefficients of water (D_{H_2O}) in PMAA gel against $q^{1/3}$ at 300 K.

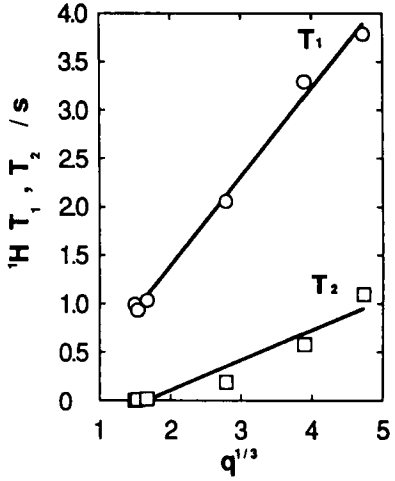

Fig. 12. Plots of ^{1}H T_1 and T_2 values for water in PMAA gel against $q^{1/3}$ at 300 K.

γ the gyromagnetic ratio of water, h is Planck's constant and N the number of proton spins of water molecules per cubic centimetre. a is the radius of a water cluster corresponding to a hard sphere in the Stokes–Einstein model. Figure 13 shows a plot of the a values calculated from equation (3) against $q^{1/3}$. It is found that a linearly decreases from 3.4×10^{-8} to 1.9×10^{-8} cm with increasing $q^{1/3}$. This shows that the radius of a water cluster in the PMAA gel decreases with an increase of the degree of swelling, i.e. the

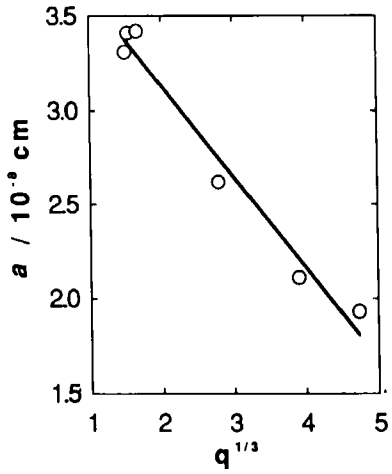

Fig. 13. Plots of the radius (a) of a water cluster corresponding to a hard sphere in the Stokes–Einstein model against $q^{1/3}$.

translational motion of water molecules in the gel is decreased by an increase of the density of the network polymer.

3.2.2. Self-diffusion of solvent in a PNIPAM gel

PNIPAM gel, as mentioned above, undergoes a volume phase transition at about 33°C. Such behaviour is understood from a dynamical aspect.[27] The D values of HDO (D_{HDO}) in a PNIPAM gel swollen with deuterated water (D_2O), in which a small amount of HDO is contained (<1%), have been determined under the state of equilibrium swelling at 23°C as a function of q (Fig. 14).[68] The D_{HDO} value for a PNIPAM gel at high q value (>40) is very close to the D_{HDO} value in neat D_2O. For gels with q values smaller than 40, the D_{HDO} value of HDO in the gel decreases as the q value decreases.

The molecular motion of solvent during the volume phase transition has been clarified through the observation of D_{HDO}. The D_{HDO} values for water in a PNIPAM gel (q = 66 at 20°C) and for neat water are plotted against temperature in Fig. 15. During the NMR experiments, water is exuded and wiped away. The D_{HDO} value increases as the temperature is increased up to 34°C. At the volume phase transition temperature (about 34°C), the D_{HDO} value transitionally decreases.

This implies that the mobility of water in the gel increases with an increase in temperature up to 34°C in spite of the decrease in q from 66 to *ca.* 30 (as shown in Fig. 6), and decreases transitionally at 34°C due to the steep

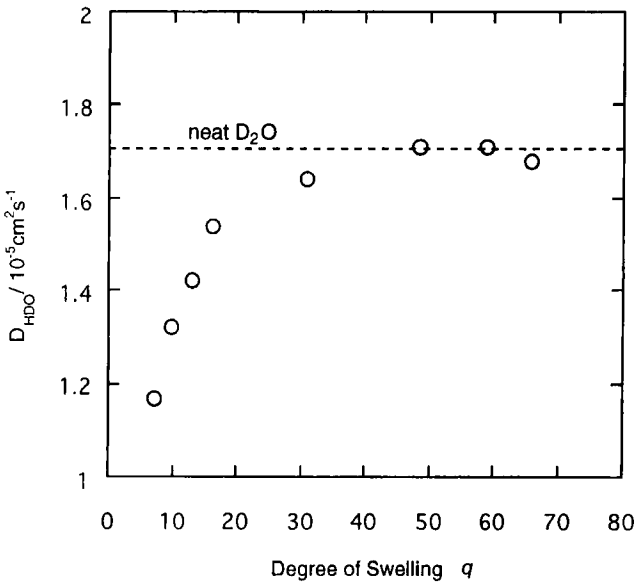

Fig. 14. Dependence of the diffusion coefficient of water molecule (D_{HDO}) on the degree of swelling (q) in a PNIPAM gel. The dashed line indicates the diffusion coefficient of a small amount of HDO contained in neat D_2O.

decrease of the q value. After the transition, the high-resolution PGSE ^1H NMR spectrum cannot be obtained due to a large decrease in molecular motion as a result of a large shrinkage of the gel.

The change in molecular motion of solvent in the gel over the phase transition temperature without a change in q has been studied. A PNIPAM gel in the shrunk part is put in an NMR tube to determine D_{HDO} at various temperatures by heating or cooling, as shown in Fig. 15. During the NMR experiment, the volume of the gel is kept constant. As shown in Fig. 15, D_{HDO} decreases largely at the transition temperature. Such a decrease of D_{HDO} is caused by the large decrease of the mobility of polymer networks which are formed by physical crosslinking at the transition temperature. This process is reversible for heating and cooling, as seen from Fig. 15.

3.3. PGSE ^1H NMR approaches for elucidating self-diffusion of solvent and probe polymer in a PDMAA gel

A deep understanding of the diffusional behaviour of low- and high-molecular-weight (Mw) molecules in a polymer gel is needed for the development of fundamental research work as well as practical work.[28–32]

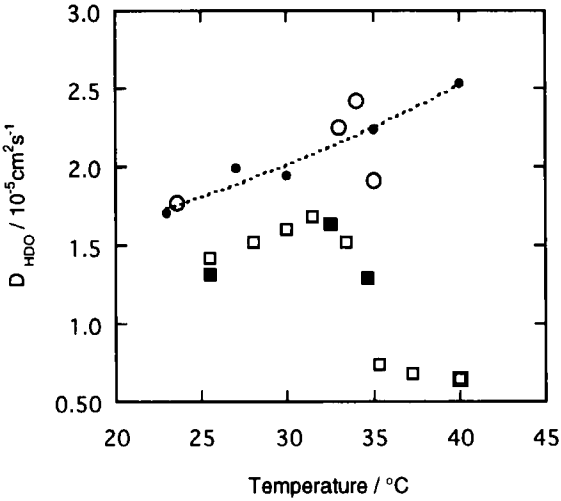

Fig. 15. Temperature dependence of the diffusion coefficients of water molecules (D_{HDO}) in neat D_2O (●), in a PNIPAM gel at the state of equilibrium swelling (q = 66 at 20°C) (○) and in a PNIPAM gel obtained after heating at 40°C (q = 4) (□) in going from 20 to 40°C. In the last sample, the NMR measurements were carried out in a cooling process from 40 to 20°C (■).

For example, PGSE ^1H NMR spectra of a PDMAA (q = 46.3) gel containing poly(ethylene glycohol) (PEG) (Mw = 20 000) as probe polymer and D_2O containing a small amount of HDO are shown as a function of magnetic field gradient pulse length (δ) in Fig. 16, where the PDMAA gel was prepared by radical polymerization of DMAA, PEG (1% wt/v) and MBAA using $K_2S_2O_8$ as initiator and was swollen in aqueous 1% PEG D_2O solution.[33]

Peaks at 4.73, 3.72 and 2.93 ppm can be straightforwardly assigned to HDO, the methylene protons of PEG, and the methyl protons of PDMAA, respectively, by comparison with reference data on PEG solution and PDMAA gel without PEG. The peak intensity is influenced by the velocity of diffusion of the corresponding molecule. Peaks at 4.73 and 3.72 ppm quickly decay, but the peak at 2.93 ppm does not. The decay for water as solvent and PEG as probe polymer comes from fast translational motion through the networks. On the other hand, the displacement for the PDMAA network by molecular motion is much smaller compared with solvent and PEG because the PDMAA network is not in translational motion but random fluctuating motion. Therefore, the lack of decay of the peak is due to insufficient strength of the field gradient in the instrument used to measure such displacement. For the peaks at 4.73 and 3.72 ppm, the $\ln[A(\delta)/A(0)]$ values against $\gamma^2G^2\delta^2[\Delta - (\delta/3)]$ are plotted in Fig. 17. It is seen that the experimental data lie on a straight line. This implies that there is a single

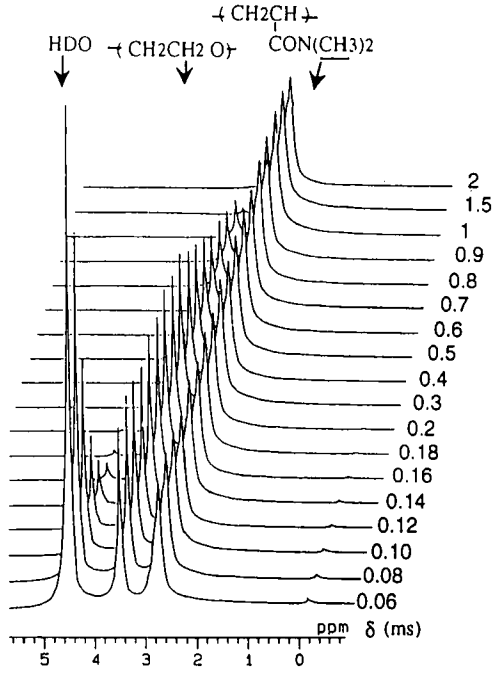

Fig. 16. Spin echo ^{1}H NMR spectra of PDMAA gel with $q = 46.3$ containing PEG with Mw = 20 000 as probe polymer and HDO as solvent, observed by varying field gradient pulse duration (δ).

component of molecular motion for individual diffusants of HDO and PEG in the gel in the observation time range. From the slope of the obtained straight lines, the diffusion coefficients of HDO (D_{HDO}) and PEG (D_{PEG}) were determined to be 2.02×10^{-5} and 1.96×10^{-7} cm^2 s^{-1}, respectively. The former is larger than the latter by a factor of about 100.

3.3.1. Self-diffusion of solvent in PDMAA gels

The determined D_{HDO} values in PDMAA gels with various q values were plotted against q as shown in Fig. 18.[33] It can be seen that D_{HDO} increases as q increases and is almost independent of the molecular weight of PEG contained in the PDMAA gel. The change of D_{HDO} in the small q region is much larger than that in the large q region. The D_{HDO} value in the large q region approaches asymptotically that for HDO contained in neat D_2O (2.2×10^{-5} cm^2 s^{-1}). Therefore it can be said that intermolecular interactions between water and polymer network, of which the strength depends on the size of network, restrain translational motion of water molecules and there are almost no significant interactions between probe polymer and

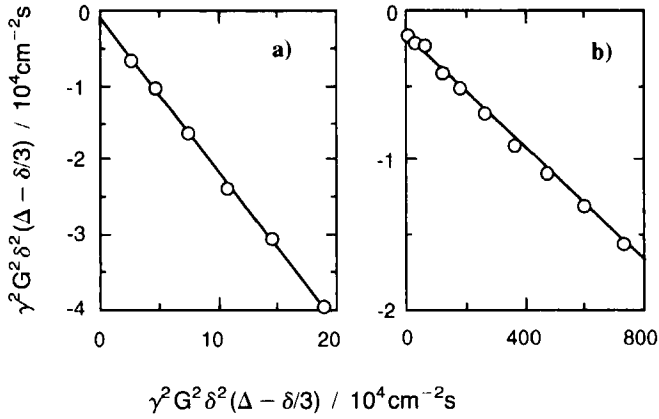

Fig. 17. Diffusional spin echo attenuation of HDO (a) and PEG with Mw = 20 000 (b) in a PDMAA gel with $q = 46.3$ and varying field gradient pulse duration (δ). From the slopes of the straight lines, D_{HDO} and D_{PEG} are obtained to be 2.02×10^{-5} cm^2 s^{-1} and 1.96×10^{-7} cm^2 s^{-1}, respectively.

solvent. This leads to the above experimental finding that the molecular motion of HDO is independent of the molecular weight of PEG contained in the gel.

We can understand more clearly the diffusional behaviour of water in the gel system using the following equation obtained from the modified free volume theory proposed by Fujita,[34]

$$D_{HDO} = D_{HDO}^{neat} \exp\left(\frac{1}{f_{solv} - q(f_{solv}^2/\beta)}\right) \tag{6}$$

where D_{HDO}^{neat} is the diffusion coefficient for HDO in neat liquid D_2O, f_{solv} is the fractional free volume for neat liquid D_2O, and β is the characteristic constant associated with volume fraction of solvent. The solid curve obtained from a least-squares fitting to the experimental data using equation (6) with $D_{HDO}^{neat} = 2.2 \times 10^{-5}$ cm^2 s^{-1} is shown in Fig. 18. The experimental data lie on the theoretical curve. From this result, the diffusion coefficient for an HDO molecule in bulk PDMAA ($q \rightarrow 1$) is obtained to be 3.5×10^{-8} cm^2 s^{-1}.[35,36] It can be said that the rapid decrease of D_{HDO} in the small q region can be explained by the decrease in free volume.

3.3.2. Self-diffusion of probe polymer in a PDMAA gel

In order to investigate the translational motion of PEG as probe polymer contained in a PDMAA gel, the diffusion coefficient of PEG (D_{PEG}) was determined at 303 K varying q and molecular weight of PEG contained in

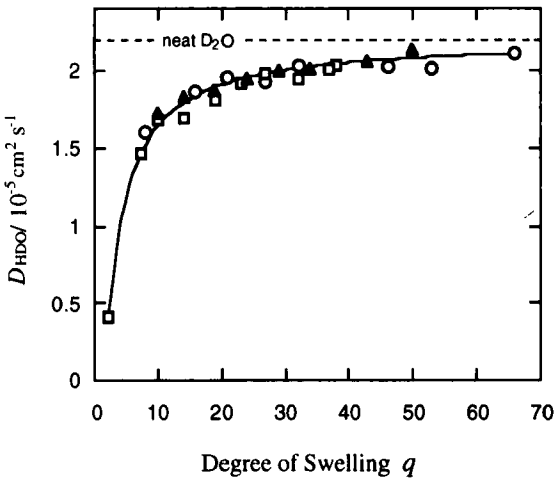

Fig. 18. Dependence of the diffusion coefficient of water molecule (D_{HDO}) on the degree of swelling (q) in a PDMAA gel containing PEG with Mw = 4250 (□), 10 890 (▲) and 20 000 (○) at 303 K.

the gel. The D_{PEG} values obtained were plotted against q as shown in Fig. 19(a).[33] It was found that D_{PEG} increased as q was increased and depends on the molecular weight of PEG. The D_{PEG} value in gels is smaller than that at 1 wt% solution (D_{PEG}^{soln}) at 303 K as shown in Fig. 19(b). Therefore, it can be said that the translational motion of PEG in the gel is more restrained by large intermolecular interactions with the polymer network than that of PEG in solution, and that PEG with higher molecular weight is more strongly restrained.

The relationship between the degree of restraint and the ratio of the screening length of polymer network to the size of probe polymer has been studied. If the interchain hydrodynamic interaction in the gel is thought to be more important than the topological constraint, D_{PEG} is expressed by

$$\frac{D_{PEG}}{D_{PEG}^{0}} = \exp(-\kappa R) \tag{7}$$

where D_{PEG}^{0} is the diffusion coefficient of an isolated PEG, κ^{-1} the dynamical screening length of polymer chains and R is the hydrodynamic radius of probe polymer.[21,31] When the D_{PEG}^{0} value is determined from the diffusion coefficient of PEG in aqueous dilute solution (D_{PEG}^{soln}), the change for local friction of polymer must be taken into account.[37] Then, D_{PEG}^{0} is given by

$$D_{PEG}^{0} = \frac{D_{PEG}^{soln}}{(D_{HDO}^{neat}/D_{HDO})} \tag{8}$$

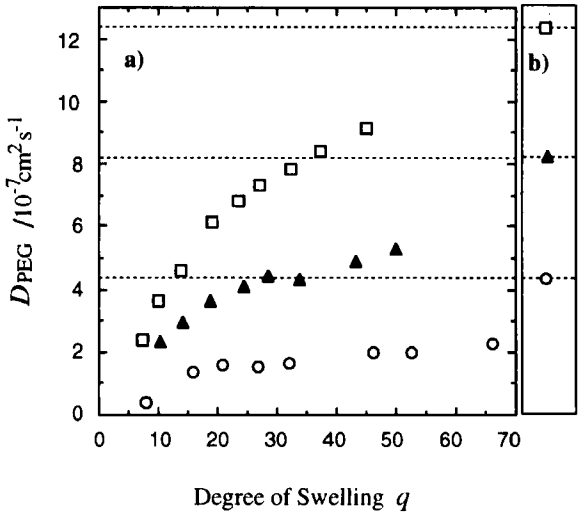

Fig. 19. (a) Dependence of the diffusion coefficient of PEG in PDMAA gel on the degree of swelling (q) at 303 K. (b) The diffusion coefficients of PEG in 1 wt% aqueous solution at 303 K; Mw = 4250 (□), 10 890 (▲) and 20 000 (○).

The dynamical screening length (κ^{-1}) is related to the concentration of network polymer (c) and is expressed by

$$\kappa^{-1} = c^{u} = q^{-u} \tag{9}$$

where u is expected to be a constant in the range 0.5–1.0 and depends largely on the polymer species.[38] From substitution of equations (8) and (9) into equation (7), the following equation is obtained:

$$\ln\left(-\ln\frac{D_{PEG}D_{HDO}^{neat}}{D_{PEG}^{soln}D_{HDO}}\right) = u\ \ln\ q + \ln R \tag{10}$$

The experimental data shown in Fig. 19 are given as log–log plots of $-\ln[D_{PEG}D_{HDO}^{neat}/(D_{PEG}^{soln}D_{HDO})]$ against the degree of swelling (q), as shown in Fig. 20. The three straight lines for PEG with different molecular weights have almost the same slope and different intercept. As R in solution is assumed to be the same as that in the gel, we have

$$R = \frac{kT}{6\pi\eta_s D_{PEG}^{soln}} \tag{11}$$

where η_s is the viscosity of solvent in solution, k is the Boltzmann constant and T is the absolute temperature. The substitution of equation (11) into equation (10) gives

$$\ln\left[\left(-\ln\frac{D_{PEG}D_{HDO}^{neat}}{D_{PEG}^{soln}D_{HDO}}\right)D_{PEG}^{soln}\right] = u\ln q + \ln\left(\frac{kT}{6\pi\eta_s}\right) \tag{12}$$

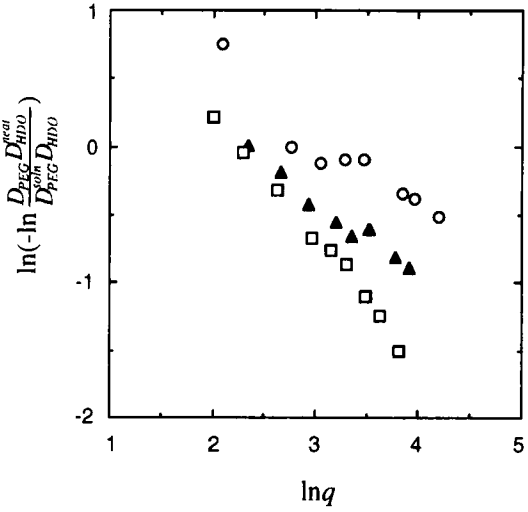

Fig. 20. Plots of $\ln[-\ln(D_{PEG}D^{neat}_{HdO}/(D^{soln}_{PEG}D_{HDO})]$ against $\ln q$ at 303 K; PEG Mw = 4250 (□), 10 890 (▲), and 20 000 (○).

In Fig. 21, the $\ln[-\ln(D_{PEG}\, D^{neat}_{HDO}/(D^{soln}_{PEG}\, D_{HDO}))\, D^{soln}_{PEG}]$ values calculated using the experimental data are plotted against $\ln q$. A straight line with a slope of $-3/4$ is obtained and so $u = -3/4$. Therefore, we have $\kappa^{-1} = q^{3/4} = c^{-3/4}$. de Gennes[39] proposed that for flexible polymer chains in a gel with good solvent the relation $\kappa^{-1} \approx c^{-3/4}$ is obtained. This prediction is in good agreement with the experimental results.

3.3.3. Self-diffusion of probe polymer in a PAA gel

Poly(acrylic acid) (PAA) interacts strongly with PEG.[40] Therefore, a PAA gel will shrink at any specified PEG concentration. In this case, the diffusion of PEG in a PAA gel may be more restrained than that in the PDMAA gel. In Fig. 22, the D_{PEG} values obtained for a PAA gel with aqueous 0.05 wt% PEG (Mw = 4250) solution are plotted against q together with those for PDMAA gels.[41] The D_{PEG} value in a PAA gel is much smaller than that in a PDMAA gel because the translational motion of PEG in PAA gel is more restrained compared with that in the PDMAA gel. From these results, it can be said that there are strong interactions between the PAA network and PEG. It was also found that the addition of a small amount of HCl (0.1 mM) leads to the decrease of D_{PEG} together with a slight decrease in q, because the dissociation of carboxyl groups in PAA is depressed and so the formation of the complex between PEG and PDMAA was facilitated. The ^{1}H T_2 values of PEG in a PDMAA gel and in a PAA gel at the same concentration have been determined to be 0.4 s and 0.2 s, respectively. This

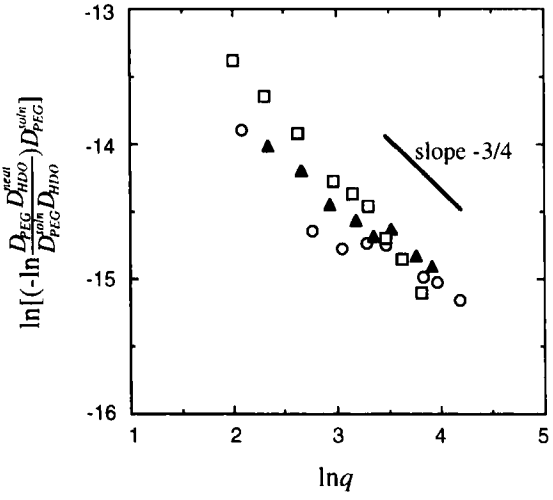

Fig. 21. Plots of $\ln[-\ln(D_{PEG}D^{neat}_{HDO}/(D^{soln}_{PEG}D_{HDO}))D^{soln}_{PEG}]$ against $\ln q$ at 303 K; Mw = 4250 (□), 10 890 (▲), and 20 000 (○).

indicates that the segmental motion of PEG in a PAA gel is also more restrained than that in a PDMAA gel. These results agree with the above-mentioned diffusional behaviour.

3.4. Solid-state high-resolution ^{13}C NMR approaches for elucidating the mechanism of gel formation

It is very important for understanding the properties of polymer gels to elucidate the mechanism of the gel formation. In this section, we are concerned with the structure and mechanism of poly(vinyl alcohol) (PVA) gel and the mechanism of gel formation.[42] PVA gel prepared by repeating freeze–thaw cycles is representative of physical gels and thermoreversible gels.

It is known that PVA in aqueous solution forms a gel when undergoing freeze–thaw cycles. The gelation is the result of network formation, and at the beginning of the gelation, phase separation into polymer-rich and polymer-poor regions arises.[43] It has been suggested that the cause of the gel formation in PVA may be due to the formation of intermolecular hydrogen bonds.[44] However, it is not clearly understood.

It has been demonstrated that solid-state high-resolution NMR spectroscopy is a useful means to obtain information about the structure of solid polymers. This may suggest that solid-state high-resolution NMR spectroscopy can provide structural information about the immobile component of polymer gels in addition to the mobile component.

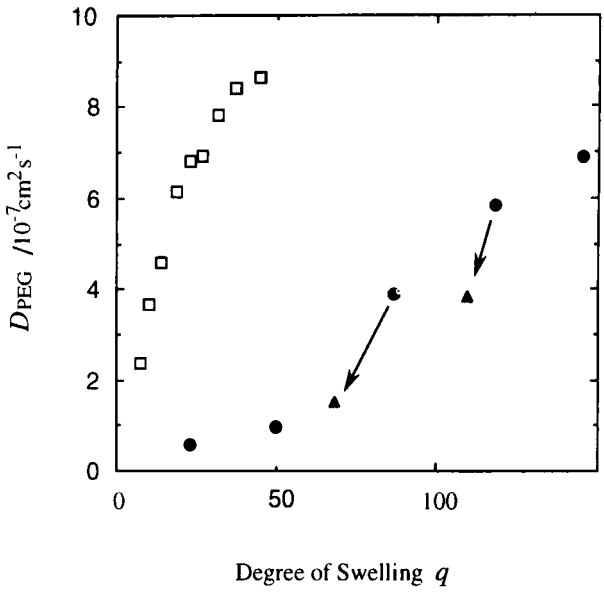

Fig. 22. Dependence of the diffusion coefficient of PEG in PAA gel (●) and in PDMAA (□) on the degree of swelling (q) at 303 K. By addition of HCl, D_{PEG} is decreased from ● to ▲ as indicated by the arrow.

Solid-state high-resolution ^{13}C NMR spectra of PVA gels have been measured by the CP/MAS (cross-polarization/magic angle spinning) and PST/MAS (pulse saturation transfer) methods.[42] In this study, the degree of polymerization and the degree of saponification of PVA were 1700 and 99.9%, respectively. The PVA gel was prepared from PVA–water solution (9% wt/wt) by repeating freeze–thaw cycles four times (frozen at −20°C for 20 h, melted at 25°C and kept at 25°C for 4 h). In the CP method, enhancement of ^{13}C magnetization is effective for solids whereas in the PST method, the nuclear Overhauser effect (NOE) enhances ^{13}C magnetization in mobile components such as gels. The PVA gel sample was contained in a cylinder-type rotor with a rubber O-ring. The use of an O-ring prevented loss of water from the gel during the high-speed spinning of the rotor.

Figure 23 shows ^{13}C NMR spectra of PVA in the solution, gel and solid states as measured by some NMR methods.[42] In the solution-state ^{13}C NMR spectrum of PVA aqueous solution (Fig. 23(A)), each of the ^{13}C signals for the CH_2 and CH carbons have split into multiple peaks due to stereochemical configuration. The three split peaks for the CH carbon can be assigned to *mm*, *mr* and *rr* triads from high frequency[45] and further, each of the triad peaks have split into pentad peaks, where *m* and *r* indicate meso and racemo dyads, respectively. The split peaks for the CH_2 carbon come from tetrad

configurations. In the solution-state ^{13}C NMR spectrum of PVA gel, as shown in Fig. 23(B), the ^{13}C signals for the CH carbons have split into three peaks due to triad configurations. In the case of PVA solution, the ^{13}C signals for the CH and CH_2 carbons have become a broad peak because the PVA–water system changes from solution state to gel state and so dipole–dipole interactions between ^{1}H and ^{13}C nuclei are increased. The ^{13}C PST/MAS NMR spectrum of PVA gel, as shown in Fig. 23(C), is very similar to the solution-state ^{13}C NMR spectrum of PVA gel (Fig. 23(B)). In the PST method, NOE enhancement has been used to obtain the ^{13}C signal with a repetition time of 5 s. In this case, the PST method effectively enhances peak intensity for mobile regions. This means that only the mobile component of PVA gel is observed in both of the spectra.

In the ^{13}C CP/MAS NMR spectrum of solid PVA, the ^{13}C signal for the CH carbon has three split peaks as shown in Fig. 23(C).[42] In the CP method, cross-polarization is used to obtain the ^{13}C signal. The CP method effectively enhances peak intensity for rigid regions. The chemical shift difference between these peaks is considerably larger than the splitting due to stereochemical configuration. Terao *et al.*[46] explained such a splitting by the number of intramolecular hydrogen bonds with neighbouring hydroxyl groups. By assuming that the ^{13}C signal of the CH carbon is to high frequency by 6 ppm per intramolecular hydrogen bond, the most deshielded peak (peak I) can be assigned to the *mm* triad with two intramolecular hydrogen bonds, the central peak (peak II) to the *mm* and *mr* triads with one intramolecular hydrogen bond and the most shielded peak (peak III) to the *mm*, *mr* and *rr* triads with no intramolecular hydrogen bonds (Fig. 24). This assignment becomes reference data for understanding the ^{13}C CP/MAS NMR spectra of PVA gel as shown below.[42]

In the ^{13}C CP/MAS spectrum of PVA gel (Fig. 23(D)), the CH signal is composed of the three split peaks corresponding to the triad configurations together with the three split peaks as in the ^{13}C CP/MAS spectrum of solid PVA.[42] This means that both the immobile and mobile components of PVA gel are observed.

In order to clarify such a situation, ^{13}C CP/MAS experiments on PVA gels with different polymer concentrations were carried out.[42] Water in a PVA gel sample prepared by freeze–thaw cycles was gradually taken out by evaporation. By this procedure, four kinds of PVA gel samples with different polymer concentrations were prepared. Figure 25 shows ^{13}C CP/MAS NMR spectra of PVA in the gel state, where the original gel (A) prepared by freeze–thaw cycles and three other gels (B, C and D) prepared by the dehydration of gel A were used. The polymer concentrations of gel samples A, B, C and D are 9.1%, 11.8%, 13.8% and 35.0% wt/wt, respectively. The relative peak intensities for the ^{13}C spectra of four kinds of PVA gel samples and solid PVA are shown in Table 2. As shown in Fig. 25 and Table 2, as the water fraction of PVA gel decreases, the intensities of the three split peaks

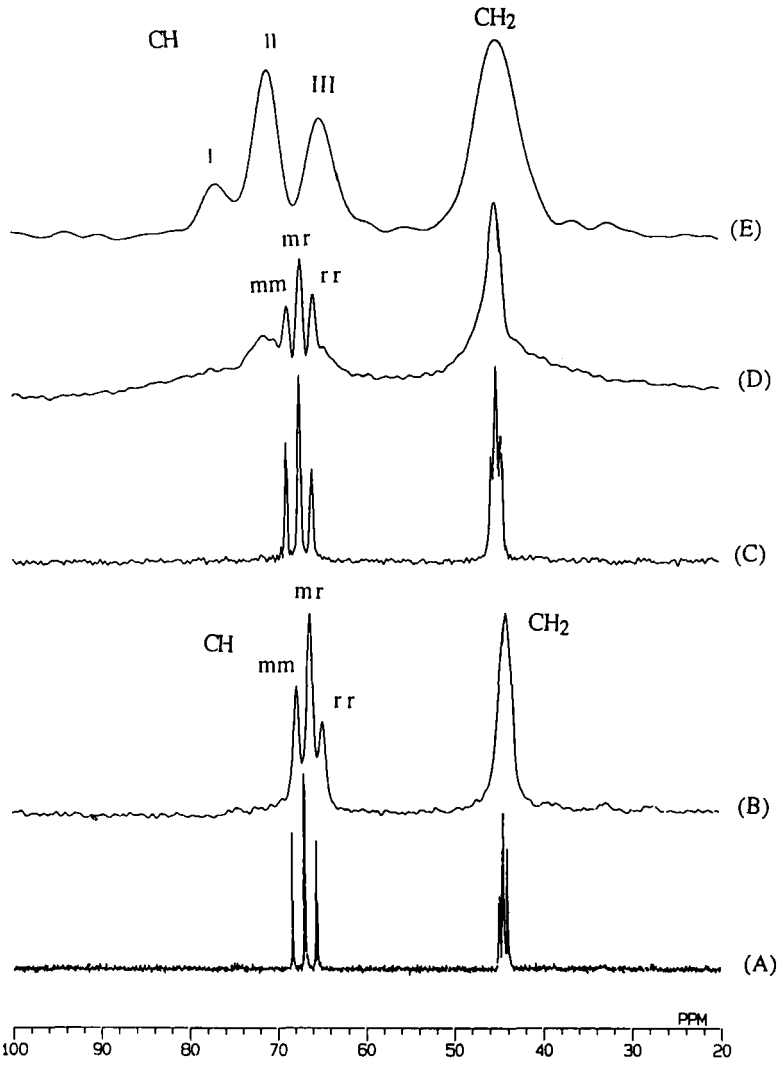

Fig. 23. ^{13}C NMR spectra of PVA in the solution, gel and solid states as measured by some NMR methods. Solution-state NMR method:(A) in PVA/D_2O solution and (B) in the gel state. Solid-state NMR method: in the gel state (C) (PST/MAS) and (D) (CP/MAS), and in the solid state (E) (CP/MAS).

due to stereochemical configurations decrease and the intensities of the three peaks I, II and III increase. In sample D, with high polymer concentration, the three peaks due to stereochemical configurations completely disappear. On the basis of the Terao's assignment for solid PVA, peaks I, II and III may be assigned to the CH carbons with two (intermolecular or

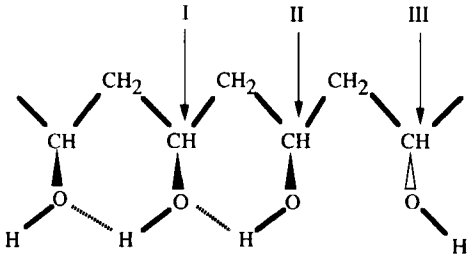

Fig. 24. Schematic diagram for intramolecular hydrogen bonding of solid PVA. The ^{13}C chemical shift of the CH carbon is assumed to move downfield by 6 ppm per an intramolecular hydrogen bond.[46] According to this, the most unshielded peak (peak I) is assigned to the *mm* triad with two intramolecular hydrogen bonds, the central peak (peak II) to the *mm* and *mr* triads with one intramolecular hydrogen bond and the most shielded peak (peak III) to the *mm*, *mr* and *rr* triads with no intramolecular hydrogen bonds.

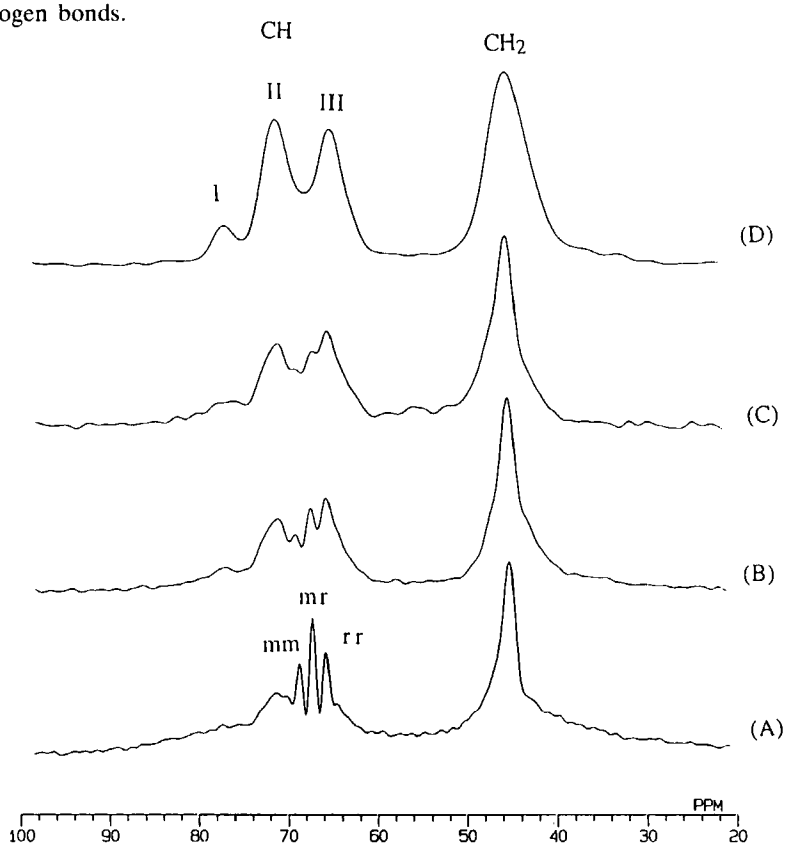

Fig. 25. 67.8 MHz ^{13}C CP/MAS NMR spectra of PVA in the gel state. (A) Original gel prepared by freeze–thaw cycles. (B)–(D) Gels prepared by dehydration of gel A. The polymer concentrations of samples A, B, C and D are 9.1%, 11.8%, 13.8% and 35.0% wt/wt, respectively.

Table 2. Relative ^{13}C peak intensities for the CH carbons in PVA.

Samples	Intensity fraction of peaks					
	I	II	III	*mm*	*mr*	*rr*
Gel at polymer concentration (% wt/wt) of						
9.1	0.05	0.33	0.27	0.09	0.17	0.09
11.8	0.07	0.36	0.33	0.05	0.11	0.08
13.8	0.09	0.36	0.35	0.04	0.10	0.06
35.0	0.09	0.50	0.41	—	—	—
Solid	0.14	0.49	0.37			
Solution at −50°C	0.05	0.27	0.68			

intramolecular) hydrogen bonds, one (intermolecular or intramolecular) hydrogen bond and no hydrogen bonds, respectively. The ^{13}C CP/MAS NMR spectrum of sample D is very similar to that of solid PVA except the intensity of peak III in the former is somewhat larger than that in the latter. These experimental results show that as the water fraction decreases, the fraction of the immobile component of PVA gel increases and the amount of CH carbons with no hydrogen bonds in sample D is somewhat larger than that in solid PVA.

In the PVA gel, there exist CH carbons forming only one hydrogen bond at low polymer concentration. At high polymer concentration there are two types of CH carbons, those forming two hydrogen bonds and those forming one hydrogen bond. As shown in Table 2, the ratio of the number of CH carbons forming two hydrogen bonds to that forming one hydrogen bond is 9:50 for the PVA gel at high polymer concentration and 14:49 for solid PVA.

Figure 26 shows ^{13}C PST/MAS NMR spectra of the four kinds of PVA gel samples. The spectra of samples A, B and C are very similar to each other and the CH signal splits into three peaks corresponding to the triad configurations. However, in the spectrum of sample D, the CH signal becomes a broad peak because the molecular motion is restrained by an increase in polymer concentration and so dipole–dipole interactions do not vanish. This result means that in samples A, B and C there exists the mobile component, but in sample D the mobile component disappears.

Further, the ^{13}C CP/MAS spectrum of PVA solution at −50°C has been measured as shown in Fig. 27.[42] On the basis of the obtained results, the mechanism of gel formation by freeze–thaw cycles was elucidated. The three peaks which arise from the splittings by stereochemical configurations completely disappear. Instead, peaks I, II and III appear. In PVA solution at −50°C, some hydroxyl groups form hydrogen bonds as in PVA gel and

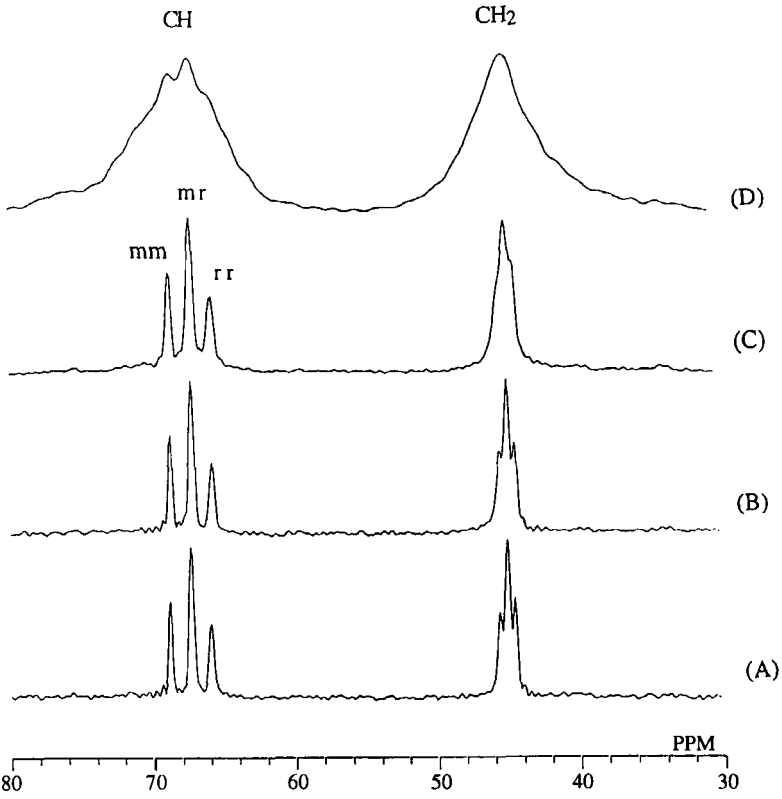

Fig. 26. 67.8 MHz ^{13}C PST/MAS NMR spectra of PVA in the gel state. (A) original gel prepared by freeze–thaw cycles. (B)–(D) Gels prepared by dehydration of gel A. The polymer concentrations of samples A, B, C and D are 9.1%, 11.8%, 13.8% and 35.0% w/w, respectively.

so the crosslinked structure is formed. This means that gel formation is induced in going from room temperature to −50°C. From these experimental findings, it can be said that the procedure of freeze–thaw cycles leads to an increase in the amount of crosslinked structure by hydrogen bonding as shown in Fig. 28.

The ^{13}C T_1 values of PVA in the gel state have been measured in order to clarify the dynamics of PVA gel.[47] Figure 29 shows the partially relaxed ^{13}C spectra of PVA gel, obtained by using the inversion–recovery pulse sequence combined with the PST/MAS technique. It was found that the CH signal, which has three split peaks corresponding to the triad configurations (*mm*, *mr* and *rr*), recovers in the same manner as τ increases. These indicate that the three peaks due to the triad configurations have almost the same relaxation time. Figure 30 shows the partially relaxed ^{13}C spectra of PVA

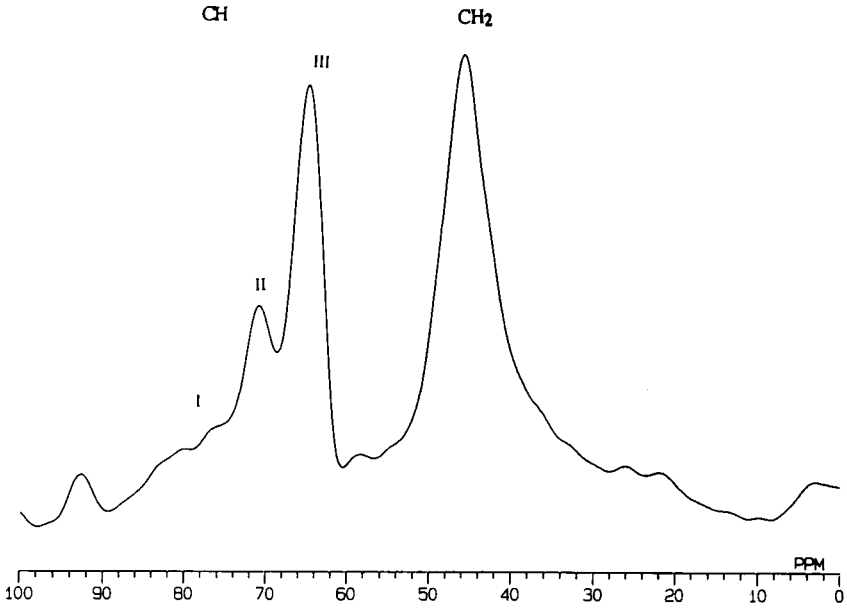

Fig. 27. 67.8 MHz ^{13}C CP/MAS NMR spectrum of PVA gel at −50°C.

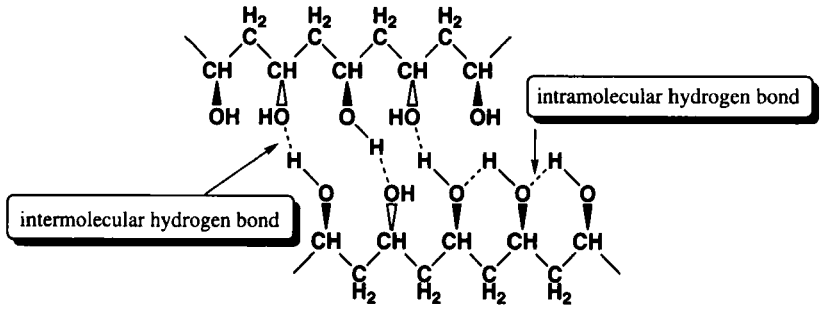

Fig. 28. The crosslinked structure of PVA gel formed by inter- and intramolecular hydrogen bonds.

gel obtained by using Torchia's pulse sequence.[48] It was found that peaks II and III still remain at $\tau = 5$ s, but the three peaks due to the triad configurations disappear as τ increases. This indicates that the T_1 values of peaks II and III are longer than those of the *mm*, *mr* and *rr* triad peaks. The ^{13}C T_1 values of PVA gel obtained by the above procedures are summarized in Table 3. These experimental results show that two types of CH carbons exist, with different molecular motion. One is the

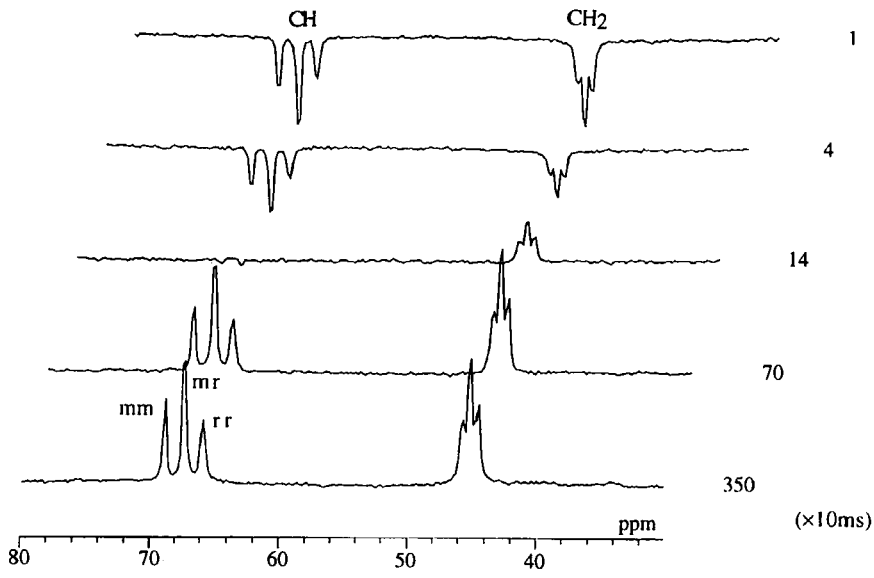

Fig. 29. Partially relaxed ^{13}C spectra of PVA gel, obtained by the inversion–recovery pulse sequence. The magnetization is enhanced by the PST/MAS method.

Table 3. Determined ^{13}C T_1 values of PVA gel.

	^{13}C T_1 (s)					
	CH					
Method	*mm*	*mr*	*rr*	II	III	CH_2
Torchia's pulse sequence (CP method)	0.64[a]	0.25[a]	0.27[a]	7.8	7.6	5.2
Inversion–recovery pulse sequence (PST method)	0.37	0.28	0.32			0.16

[a] ^{13}C T values of CH (*mm*, *mr*, *rr*) obtained by Torchia's pulse sequence are not sufficiently accurate because of the poor signal/noise ratio.

mobile component with a T_1 value of about 0.3 s, and another is the immobile component with a T_1 value of about 7–8 s. The ^{13}C T_1 values of the immobile component of PVA gel were measured by the Torchia pulse sequence. The ^{13}C T_1 value of the mobile component of PVA gel was obtained accurately by the inversion–recovery pulse sequence combined with the PST/MAS technique.

From the above results, it can be noted that hydrogen bonding plays an

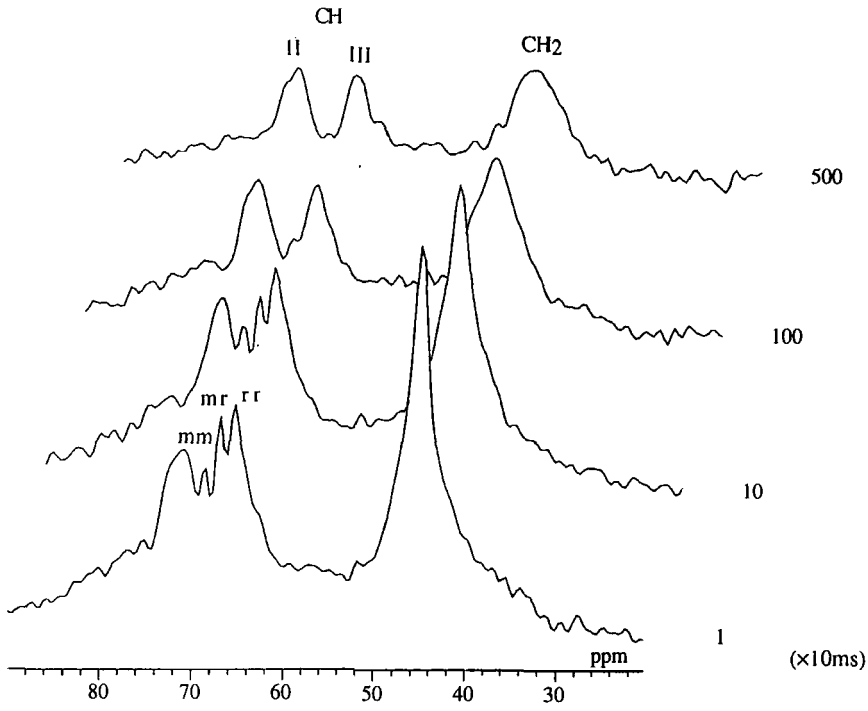

Fig. 30. Partially relaxed ^{13}C spectra of PVA gel obtained by the Torchia pulse sequence.

important role the formation of PVA gel by formation of crosslinking between interchains.

4. MACROSCOPIC ASPECTS OF STRUCTURES AND DYNAMICS OF POLYMER GEL SYSTEMS

4.1. Image analysis of stress–strain in a polymer gel

Crosslinked polyelectrolyte gels contract upon application of electric fields[20] and work as electrically activated devices.[23,49] Water-swollen polymer gels can convert chemical energy into mechanical energy.[2] In contrast to this, chemical reactions are caused in polymer gels by applied mechanical energy. Ionization of the carboxylic groups of water-swollen PMAA gels occurs upon application of stress.[49] It is important to clarify the mechanism of the contraction on polymer gel under an electric field (energy conversion from electrochemical to mechanical) and of the chemical reaction induced by the application of stress (energy conversion from mechanical to chemical).

Polyelectrolyte gels consist of a network polymer and water as solvent. Water molecules which specifically interact with polymer chains play a significant role in the above-mentioned energy conversion of polymer gels. To evaluate the properties of water contained in polymer gels and elucidate such interactions, many investigations have been undertaken using DSC,[50] NMR[11,51] etc. Yasunaga *et al.* have studied the structure and dynamics of water molecules in polymer gels by NMR spectroscopy by measuring and calculating the ^{1}H NMR chemical shift values, relaxation times and self-diffusion coefficients.[9,53,54] Attention was also paid to the structure and dynamics of the network polymer of gels which were studied by solid-state high-resolution NMR spectroscopies.[44,55,56] Moreover, it has been recognized that the importance of research from a macroscopic point of view with microscopic information at the molecular level is paramount to understand the unique behaviour of gels under an electric field and stress as well as other properties.

Recently, NMR imaging[52] has been widely used for obtaining information on the spatial distribution of the spin density and the relaxation times in living systems containing a mobile component such as water.[57–60] However, without special techniques, it is not easy to obtain such spatial information with high resolution for solid samples, due to the short T_2, the large dipolar broadening and the chemical shift anisotropy of them. For this reason, NMR imaging has only been applied to bulk polymer systems containing small molecules with high mobility to obtain information about their diffusion and relaxation times,[61,62] except for some work on solid polymer materials using the MAS method.[63] Through these investigations, the NMR imaging technique has been demonstrated to be a powerful means to characterize the spatial distribution of the spin density and the molecular motion of the mobile component in polymer systems, for which dipolar broadening is negligible.

NMR imaging has been employed to study the structure and dynamics of polymer gels macroscopically on the basis of microscopic, spatial and dynamic information. The ^{1}H NMR imaging patterns of the spatial distribution of the ^{1}H spin density and the ^{1}H T_2 of water molecules in crosslinked water-swollen PMAA gel with applied stress[64] and an electric field[65,66] have been analysed. PMAA gel was prepared by radical polymerization of MAA (3.0 mol dm^{-3}) and MBAA (9.4×10^{-3} mol dm^{-3}) in aqueous solution at 333 K as reported.[64]

^{1}H NMR imaging measurements[64–67] were carried out by means of a JEOL GSX-270 NMR spectrometer operating at 270.1 MHz with a JEOL NM-GIM 270 imaging system at 300 K. The imaging pulse sequence used was based on the spin echo pulse sequence[67] of Hahn.[68] The data processing for a two-dimensional image was performed by the Fourier imaging method.[69] The pulse sequence is shown in Fig. 31. The slice selection gradient (G_z) and selective RF pulse determine the position of the region to be observed. The

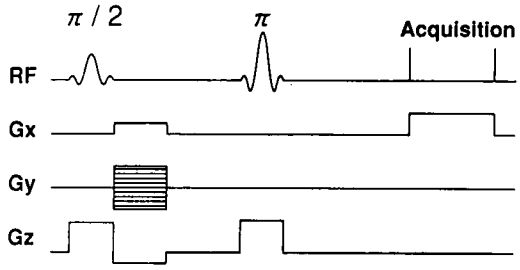

Fig. 31. A diagram for the spin echo ^{1}H imaging pulse sequence for the spin density image.

phase-encoding gradient (G_y) which was varied in intensity systematically, serves to obtain the differentiation of the volume elements in the y-direction.[70] The phase-encoding period was fixed to be constant. The readout gradient (G_x) was applied in the x-direction, and during the phase-encoding period the reversed gradient ($-G_z$) was also applied to refocus the selectively excited magnetization. During the acquisition period, the readout gradient (G_x) was applied to disperse the volume elements in the x-direction.

In the ^{1}H NMR imaging experiments, the gradient strengths used for the slice selection, phase-encoding and read-out were 19, 20 and 20 mT m^{-1}, respectively, and the slice thickness was 2.0 mm. The used $\pi/2$ and π RF pulse lengths were 1.5 μs, but the strength of a $\pi/2$ pulse was half that of a π pulse. The echo time was 36 ms, the phase-encoding time was 4 ms and the repetition time was 2–15 s. The number of data points was 256. The number of accumulations was four to obtain ^{1}H NMR image signals with a reasonable signal-to-noise ratio. The spin echo method based on Hahn pulse sequence was also used to obtain ^{1}H T_2 enhanced images. In this case the echo time is longer than that used for the spin density measurement.

A cylindrical PMAA gel sample with a diameter of 15.0 mm and a height of 5.3 mm at $q = 22$ was placed in a cylindrical sealed glass cell with an inside diameter of 22.0 mm and a height of 25.0 mm. The stress on the gel sample was applied by a glass piston, with a circular top of diameter 7.7 mm. The amount of stress was controlled by a weight on the piston. The distance between the centre of the circular surface of the PMAA gel with diameter of 15 mm and the centre of the circular piston with diameter of 7.7 mm was 1.8 mm. A PMAA gel sample with a diameter of 4.0 mm at $q = 89$ was inserted in a glass NMR sample tube with an inner diameter of 5.0 mm.

A ^{1}H spin density NMR imaging experiment of a PMAA gel swollen by D_2O ($q = 22$) was carried out, but no image was obtained. Throughout the experiments described, no ^{1}H signals of the polymer network of the PMAA gel at $q = 22$ could be detected by imaging due to its extensive dipolar broadening, but ^{1}H signals of water contained in the gel could be successfully

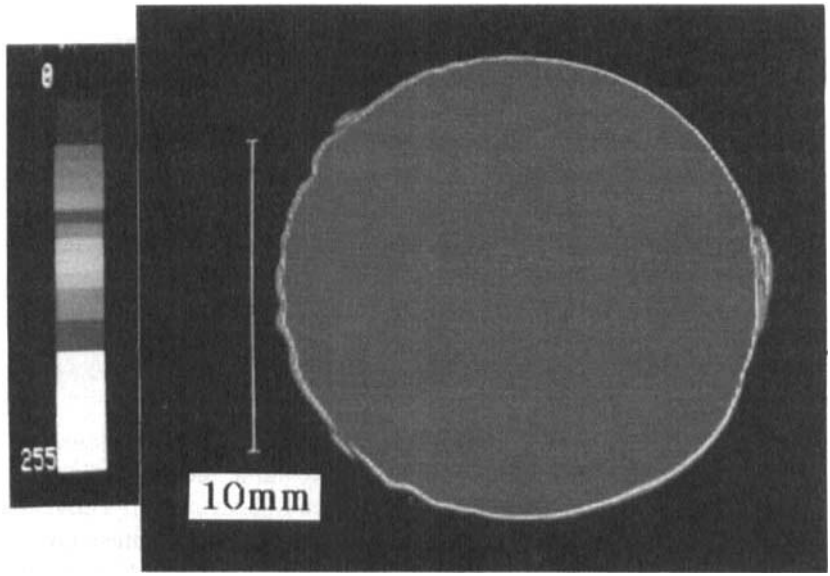

Fig. 32. Observed transverse ^{1}H spin density image of PMAA gel at $q = 22$ without stress at a depth of 1.9 mm from the top surface. The colour signal variation is 10 steps.

observed due to fast molecular motion. Figure 32 shows the observed transverse ^{1}H spin density image of water in the PMAA gel at $q = 22$ with no stress, where the direction of the cross-sectional profile is perpendicular to the direction along a used glass cell. The magnitude of ^{1}H spin density is differentiated using 256 steps, and the observed ^{1}H spin density image is represented by colours from white, representing the highest density, to dark blue representing the lowest density. The colour intensity scale is shown on the left (reproduced here in black and white). The ^{1}H spin density distribution of the obtained image is approximately homogeneous. This shows that the water molecules are homogeneously distributed in the gel, and are undergoing fast molecular motion.

The transverse ^{1}H spin density images of water in the PMAA gel at $q = 22$ under stress of 4.8 kPa are shown in Figs 33(a) and (b),[64] where the latter image is of a slice below the top surface of the gel for comparison with the former. The circular portion (blue) in Fig. 33(a) shows the compressed region to which stress is applied. In Fig. 33(b), there are white regions at the top and the bottom of the image, and coloured semicircular bands appear towards the compressed region in the order white → light pink → pink → red → orange → bright orange, and the innermost portion (yellow) appears in the compressed region. The periphery of the gel image

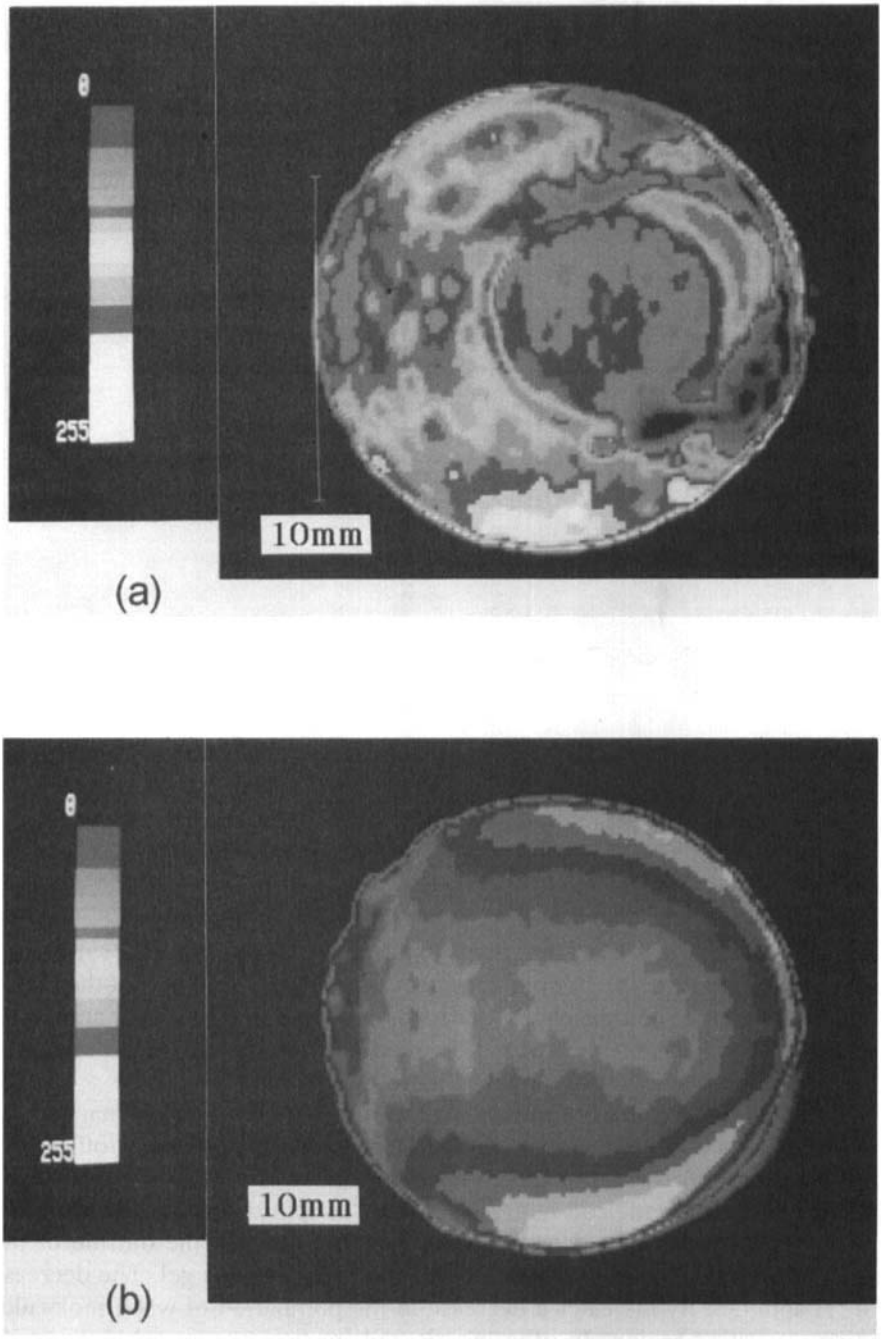

Fig. 33. Observed transverse ^{1}H spin density image of PMAA gel at $q = 22$ under a stress of 4.8 kPa at a depth of (a) 1.0 mm and (b) 1.9 mm from the top surface.

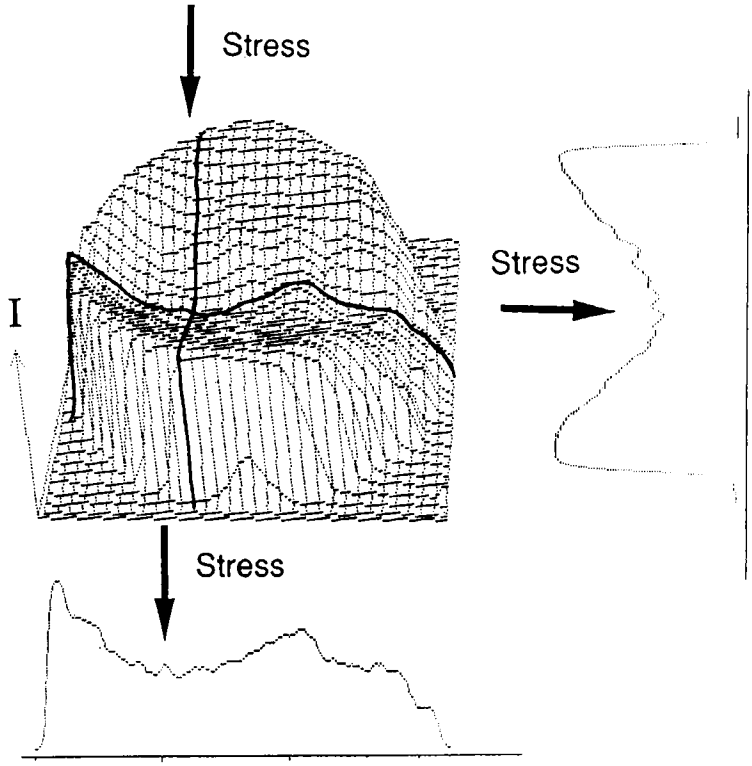

Fig. 34. Intensity profile of the transverse ^{1}H image of PMAA gel at $q = 22$ at a depth of 1.9 mm from the top surface under a stress of 4.8 kPa.

is blue. Further, it is seen that the ^{1}H spin density pattern as shown in Fig. 33(b) is asymmetric, the ^{1}H spin density of water in the right part of the image (the white region) being higher than that in the left part (the yellow and green regions). The fact that the stress is applied at a distance from the centre of the gel induces such an asymmetric pattern.

Detailed ^{1}H spin density profiles of the image with a longitudinal section and a cross-section are shown in Fig. 34. As seen from these profiles, the ^{1}H spin density of water in the compressed region is lower than that of the uncompressed region, and a stress-induced ^{1}H spin density gradient occurs in the gel. The ^{1}H spin density becomes higher towards the outside of the gel and becomes lower in the vicinity of the surface of the gel. The decrease of ^{1}H spin density indicates a decrease in the population of water molecules in any specified region. In other words, the fraction of network polymer in any specified region is increased. In the white region the population of water and the fraction of network polymer are higher and lower, respectively, than

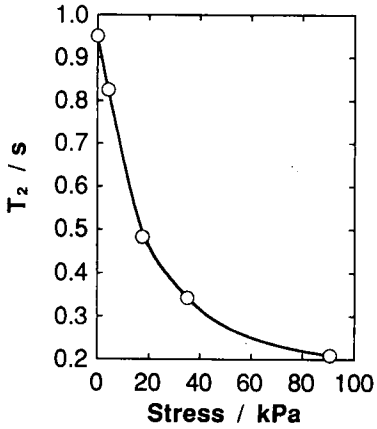

Fig. 35. Dependence of ^1H T_2 for water in PMAA gel at $q = 89$ on the applied stress at a resonance frequency of 500.1 MHz.

those in the other regions. This shows that by deformation of the PMAA gel sample due to stress, the uncompressed part of the top surface of the gel rises up slightly, and water molecules excluded from the compressed region migrate to the surrounding region.

Before studying the ^1H T_2 enhanced image of the PMAA gel, it may be significant to have some information about the ^1H T_2 of water in the gel, in order to understand the dynamical behaviour of water in the gel under homogeneous stress. The ^1H T_2 value of water in the PMAA gel ($q = 89$) compressed homogeneously was measured by means of 500 MHz ^1H pulse NMR. The ^1H T_2 of water in the PMAA gel was measured using the CPMG method.

The obtained ^1H T_2 values are plotted against the strength of the applied stress in Fig. 35. It is shown that the T_2 value decreases with increasing stress, and the T_2 value under a stress of 17.6 kPa is half the value under no stress. This shows that the molecular motion of water in the PMAA gel is restrained by the strain induced by stress. Therefore, it is expected that the ^1H T_2 enhanced imaging of water in the gel provides useful information on the spatial distribution change for the molecular motion of water by the application of stress.

Figures 36(a) and (b) show coronal ^1H T_2 enhanced images of water in the PMAA gel at $q = 22$, where the word "coronal" means that the cross-sectional profile is parallel to the direction of the applied stress. In this image, the relative magnitude of the ^1H T_2 value of the water is represented by colours. White represents the longest T_2 value and dark blue the shortest T_2 value. The colour scale is shown on the left. In the gel with no stress the ^1H T_2 distribution is homogeneous, but in the gel with a stress of 4.8 kPa

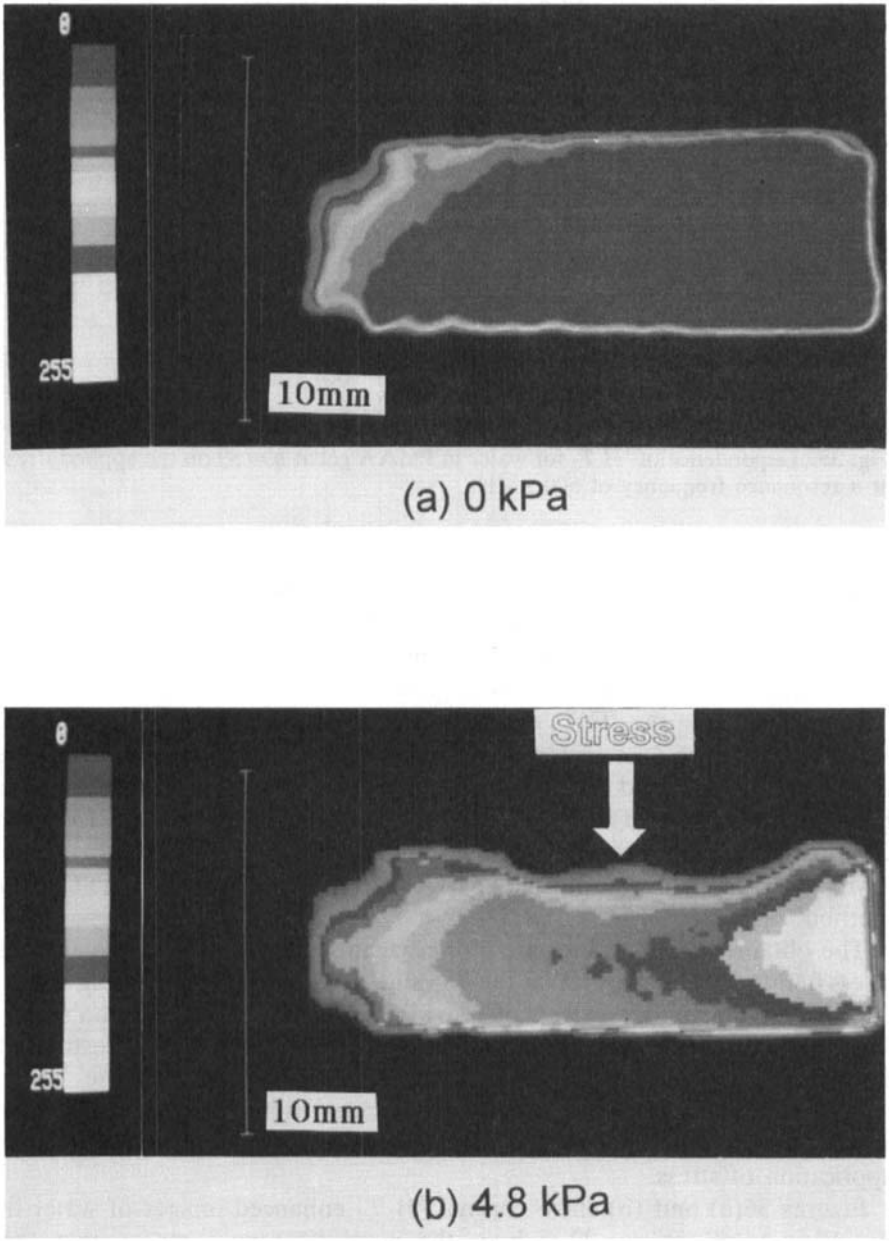

Fig. 36. Observed coronal ^{1}H T_2 enhanced image of PMAA gel at $q = 22$ (a) without stress and (b) under a stress of 4.8 kPa.

a gradient pattern in the T_2 distribution is obtained, where the stress is applied at a distance from the centre of the gel. The ^1H T_2 value of the top surface is small (dark blue or blue). The colour in the compressed region changes from the top of the gel towards the bottom in the order dark blue → blue → green → light green → yellowish green → yellow → bright orange → orange → red → orange → bright orange → yellow → blue → dark blue. This indicates that the ^1H T_2 value of water in the compressed region increases from the top surface of the gel towards the inner part and decreases from the inner part towards the bottom. The ^1H T_2 value increases from the left end of the gel to the right end, the colour changing in the order dark blue → blue → green → light green → yellowish green → yellow → bright orange → orange → red → pink → light pink → white. As seen from the above results, the propagation of the strain induced in the gel can be observed as the ^1H T_2 distribution. In the compressed region, the experimental findings that the ^1H T_2 value is not constant from the top of the gel to the bottom comes from the inhomogeneous strain distribution of the network of the gel. The ^1H T_2 value in the right part of the image is longer than that of the left part as shown in Fig. 36(b). As mentioned above, the fact that the stress is applied at a distance from the centre of the gel induces such an asymmetric ^1H T_2 pattern.

The ^1H T_2 enhanced images of the gel as a function of stress are shown in Fig. 37. As seen from this figure, the gradient pattern of spatial distribution on ^1H T_2 changes with increasing stress. The red and orange regions in the compressed region become narrow with increasing stress, and the bright orange and yellow regions become wide. The white region becomes wide with an increase of the strength of stress from 12.7 to 28.4 kPa. As seen from these results, the molecular motion of water molecules in the compressed region is more strongly restrained with an increase of stress. Further, in the uncompressed region (the right and left parts of the gel) the population of water molecules which are undergoing relatively fast molecular motion increases with increasing stress. This shows that the migration of water in the gel is increased with an increase of stress, and the difference in molecular motion of water in between the compressed and the uncompressed regions becomes large. The central cross-sectional ^1H T_2 profiles of the images along a glass cell are shown in Fig. 38. The slope of the right wall for the T_2 gradient pattern of the gel to which the stress is applied becomes steep with increasing stress, while the slope of the left wall does not change so considerably. This shows that the molecular motion of water molecules in the region near the top surface is strongly restrained with an increase of stress. The spatial distribution of molecular motion of water molecules is not homogeneous from the top surface of the gel towards the bottom in the compressed region. This shows that the deformation of the network by the stress is not homogeneous in the compressed region.

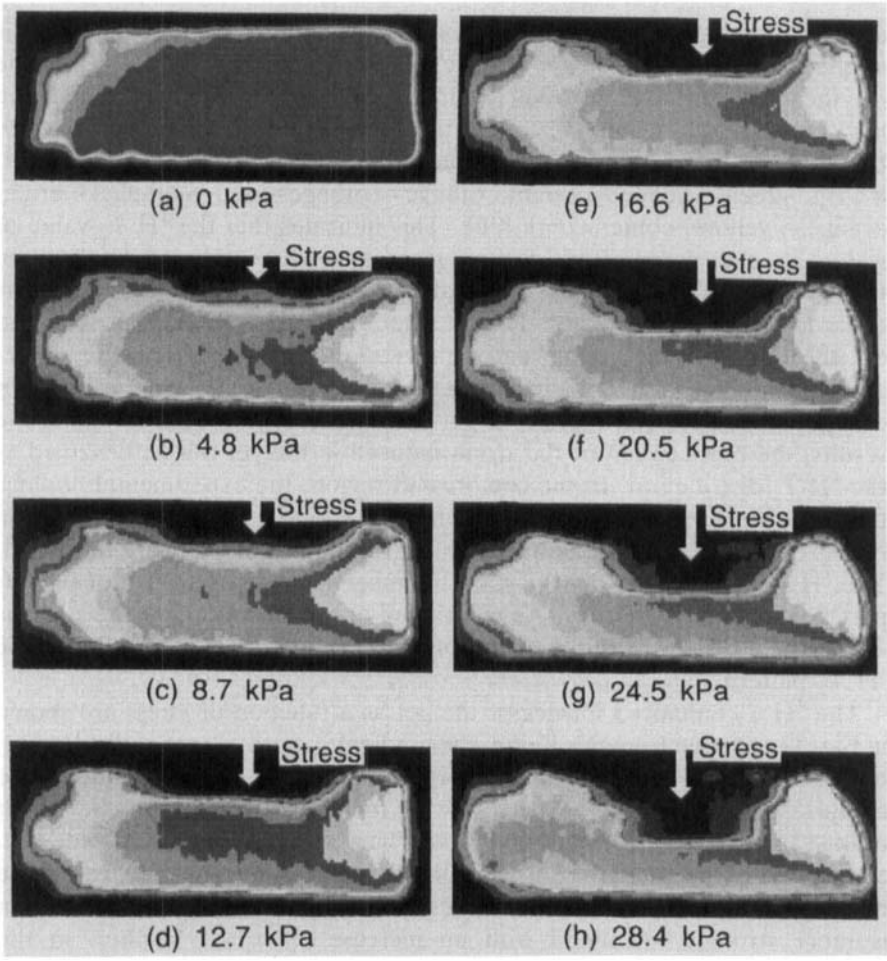

Fig. 37. Observed coronal ^1H T_2 enhanced image of PMAA gel at $q = 22$ as a function of stress.

4.2. Shrinkage analysis of a homogeneous polymer gel under the application of an electric field

Water-swollen crosslinked polymer gels deform under the application of an electric field because they can convert chemical, electrical and thermal energies into mechanical energy. Such a reaction is termed the chemomechanical system. The first observation of electric-field induced deformation was made by Tanaka *et al.*[22] A rod-like gel of a copolymer of acrylic acid-acrylamide was found to shrink under the application of an electric field to the gel. A similar phenomenon was also observed by other

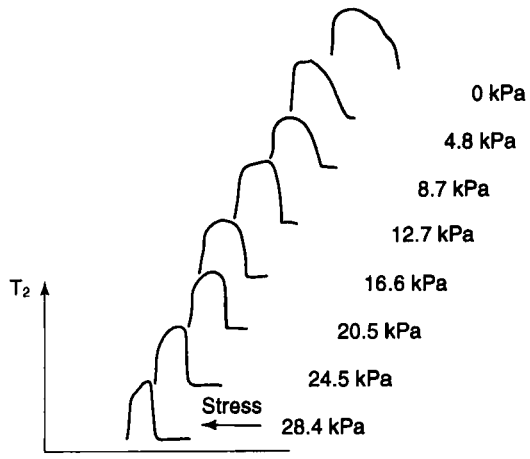

Fig. 38. Intensity profiles from the ^1H T_2 enhanced image of PMAA gel as a function of stress obtained from Fig. 37.

workers.[23] Recently, applications of polymer gels to electrically-activated devices have been studied widely using these deformation properties. Although a great deal of effort has been made in investigations of the mechanism, it seems that a fundamental approach at the molecular level has rarely been taken. Therefore, it is important to clarify the macroscopic structure and dynamics of small molecules in a polymer gel through the observation of microscopic information at the molecular level.

Shibuya *et al.*[65] have measured ^1H NMR imaging patterns of the spatial distribution of ^1H spin density and ^1H T_2 of water molecules in crosslinked PMAA gel under an electric stimulus, to clarify the behaviour of water molecules in a PMAA gel during the shrinkage process induced by the application of an electric field. This is carried out using the obtained results on the spatial distribution change of ^1H spin density and the molecular motion of water molecules. A cylindrical PMAA gel ($q = 40$) obtained was cut with a diameter of 8.0 mm and a length of 25.0 mm as shown in Fig. 39.

4.2.1. ^1H spin density image

In the ^1H NMR imaging experiments, the polymer network of a PMAA gel is not detected using the conventional technique due to its large dipole broadening, but successfully detected are the ^1H signals of water contained in the PMAA gel due to the removal of dipole broadening by fast isotropic molecular motion. Figure 39 shows the transverse slice to be observed in a PMAA gel.

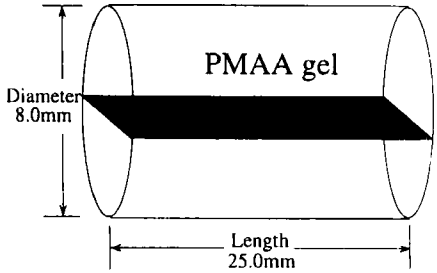

Fig. 39. A PMAA gel and image of transverse slice to be observed.

The shrinkage process of a PMAA gel is initiated by the application of an electric field. The application of an electric field to a PMAA gel leads to shrinkage of the gel with the exhaustion of water. Shrinkage around the positive electrode is larger than that around the negative electrode. The gel part in contact with the negative electrode is swollen.

Figure 40 shows the elapsed-time (T_e) dependencies for the shape and the spatial distribution of ^{1}H spin density of the PMAA gel with and without the application of an electric field. Hereafter, PMAA gel samples with and without the application of an electric field (3 V) are expressed by PMAA gel (3 V) and PMAA gel (0 V), respectively. The magnitude of the ^{1}H spin density is differentiated using 256 steps between the lowest and highest densities, and the observed ^{1}H spin density image is represented by colours from dark blue, representing the lowest density, to white, representing the highest density. The colour intensity scale is shown on the right.

The electric field effect on the shrinkage of a PMAA gel can be clarified by comparing the ^{1}H spin density image experiments for PMAA gel (3 V) with those for PMAA gel (0 V). The ^{1}H spin density image experiments for PMAA gel (0 V) are represented in Fig. 40(b), where some different coloured regions from blue to white are distributed. From the observed images, it is obvious that the ^{1}H spin density distribution is heterogeneous in the gel at elapsed time $T_e = 0$ min after the application of an electric field and the blue region is quite large. The magnitude of ^{1}H spin density increases in going from the right end of the gel to the left end, in the order blue → green → light green → yellowish green → yellow → bright orange → orange → red → white. At $T_e = 20$ min, the yellow region becomes large. The magnitude of ^{1}H spin density increases in going from the centre of the gel to the outside of the gel in the order yellow → bright orange → orange → red → white. At $T_e = 240$ min, the change in the magnitude of ^{1}H spin density reaches a steady state.

The ^{1}H spin density images for PMAA gel (3 V) are represented in Fig. 40(a). Before the application of an electric field ($T_e = 0$ min), the polymer

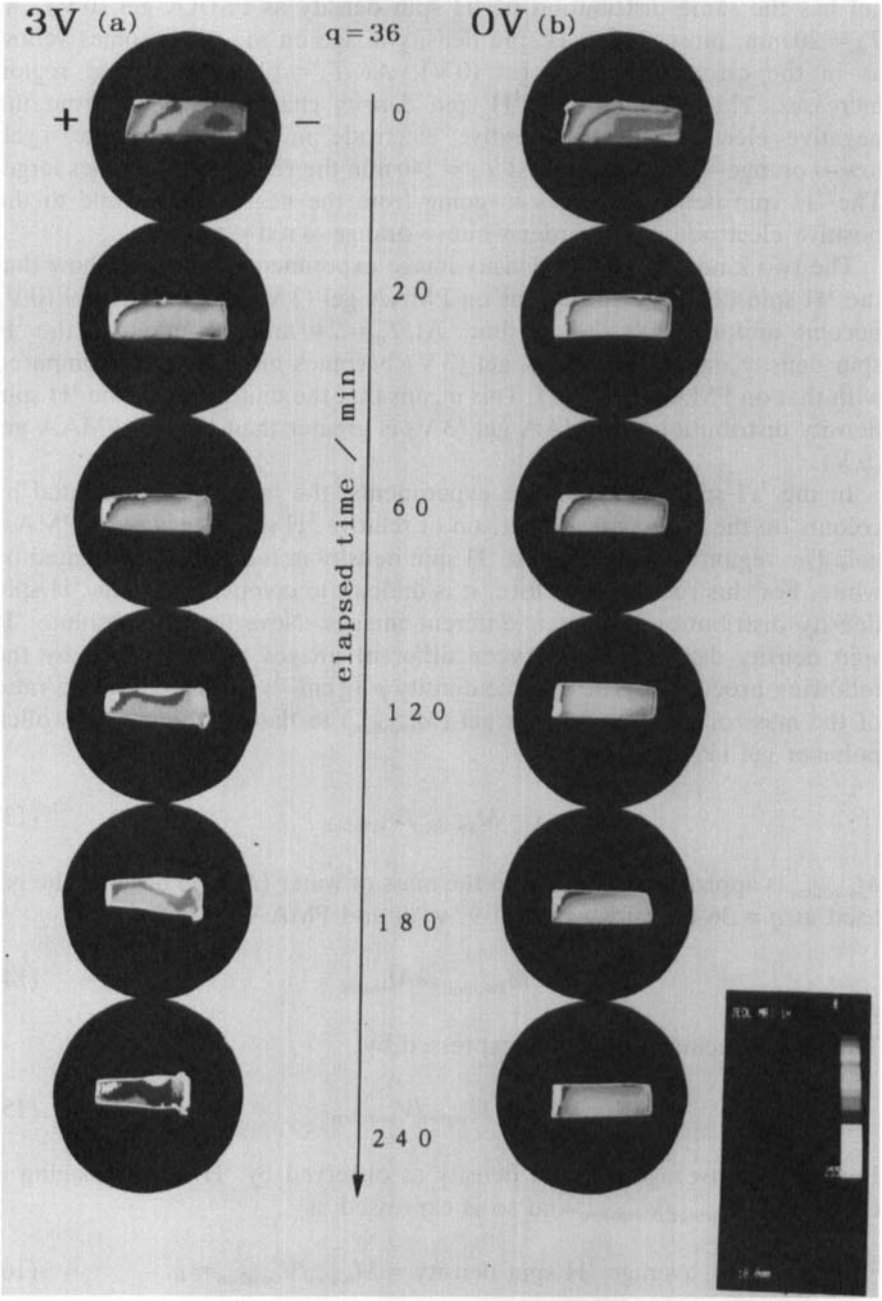

Fig. 40. Elapsed-time dependence of images for ^{1}H spin density distribution of a PMAA gel (a) with and (b) without the application of an electric field.

gel has the same distribution of ^{1}H spin density as PMAA gel (0 V). At $T_e = 20$ min, most of the ^{1}H spin density image on the gel becomes yellow as in the case for PMAA gel (0 V). At $T_e = 120$ min the red region increases. The magnitude of ^{1}H spin density changes in going from the negative electrode to the positive electrode in the order white → yellow → orange → red → white. At $T_e = 240$ min the red region becomes large. The ^{1}H spin density changes in going from the negative electrode to the positive electrode in the order white → orange → red → white.

The two kinds of ^{1}H spin density image experiments described show that the ^{1}H spin density distributions on PMAA gel (3 V) and PMAA gel (0 V) become uniform with elapsed time. At $T_e = 240$ min the colour in the ^{1}H spin density image on PMAA gel (3 V) becomes more uniform compared with that on PMAA gel (0 V). This means that the uniformity of the ^{1}H spin density distribution on PMAA gel (3 V) is greater than that on PMAA gel (0 V).

In the ^{1}H spin density image experiments, the image is represented by colours on the basis of a comparison of relative ^{1}H spin density in a PMAA gel. The region with the highest ^{1}H spin density in the gel is represented by white. For this reason, therefore, it is difficult to compare absolute ^{1}H spin density distributions between different images. Nevertheless, absolute ^{1}H spin density distributions between different images are compared by the following procedure. The specific density ρ (g cm^{-3}) is defined by the ratio of the mass of swollen polymer gel ($M_{swollen}$) to that of volume of swollen polymer gel ($V_{swollen}$) as

$$\rho = M_{swollen}/V_{swollen} \tag{13}$$

$M_{swollen}$ is approximately equal to the mass of water (M_{water}) because the gel used at $q = 36$ contains water of 97 wt% and PMAA of 3 wt% as

$$M_{swollen} \approx M_{water} \tag{14}$$

Thus, the specific density ρ is expressed by

$$\rho \approx M_{water}/V_{swollen} \tag{15}$$

Further, the average ^{1}H spin density as observed by ^{1}H NMR imaging is defined by $M_{water}/V_{swollen}$ and so is expressed as

$$\text{average } ^1\text{H spin density} = M_{water}/V_{swollen} \approx \rho \tag{16}$$

From this relation, the change in density (g cm^{-3}) of a PMAA gel against the elapsed time after the application of an electric field corresponds to that of average ^{1}H spin density in a PMAA gel (Fig. 41). Using these reference

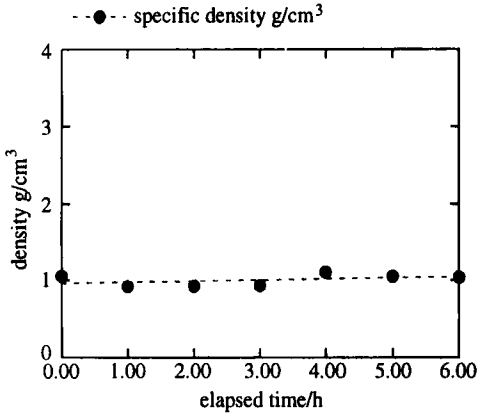

Fig. 41. Elapsed-time dependence of specific density of a PMAA gel.

data the ^{1}H spin density distributions of a PMAA gel between different images can be quantified and compared with each other. As seen from this figure, the average ^{1}H spin density of the gel does not change significantly with elapsed time after the application of an electric field.

In order to analyse clearly the ^{1}H spin density in detail, the images for the ^{1}H spin density distributions of PMAA gel (3 V) and PMAA gel (0 V) are shown in Fig. 42 as a three-dimensional profile. Also, the two-dimensional profiles of the ^{1}H spin density of PMAA gel (3 V) are shown in Fig. 43. The decrease of the ^{1}H spin density means a decrease in the population of water molecules in any specified region. In the white region of the image the population of water molecules in the gel is higher than that in the other regions. These profiles show that the observed ^{1}H spin density distribution can be divided into four regions after the application of an electric field. The change in the ^{1}H spin density distribution pattern as a result of the application of the electric field is shown by the schematic diagram in Fig. 44. The first region, at the left-hand side of the gel (the region around the positive electrode), has the highest ^{1}H spin density, the second region occupies most of the gel region and has almost the same ^{1}H spin density, the third region has the lowest ^{1}H spin density, and the fourth region, at the right-hand side of the gel (the region around the negative electrode), has the second highest density.

The above-mentioned results show that an electric stimulus leads to not only the uniformity of the ^{1}H spin density distribution but also the unique distribution pattern of ^{1}H spin density. The average ^{1}H spin density does not change significantly after a long elapsed time following the application of an electric field.

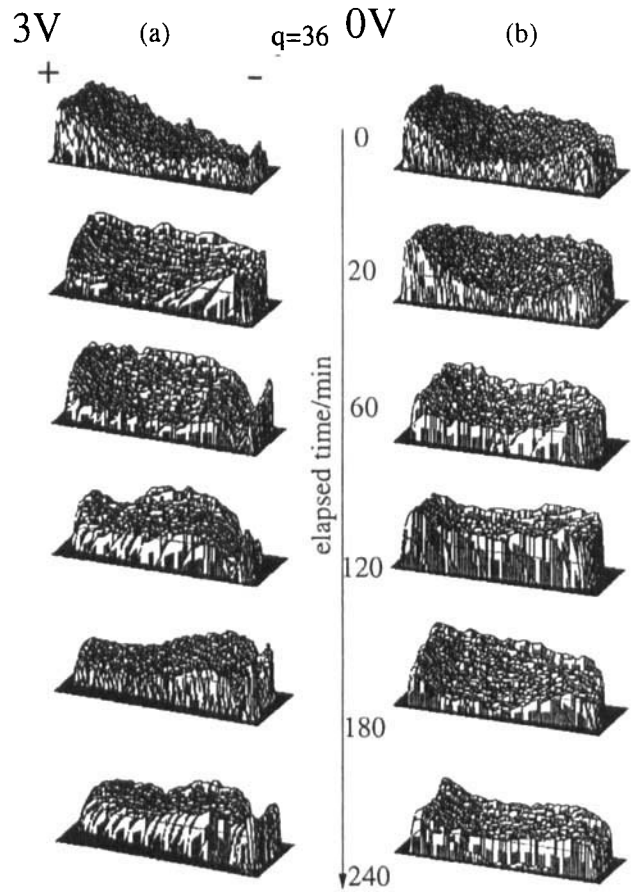

Fig. 42. Three-dimensional histograms of elapsed-time dependence for ^1H spin density distribution of a PMAA gel (a) with and (b) without the application of an electric field.

4.2.2. Spin–spin relaxation time T_2 *image*

It is important to have information on the ^1H T_2 value of water molecules in a PMAA gel, in order to analyse the dynamic behaviour of water molecules in the gel under electric stimulus.

The ^1H T_2 distributions for a PMAA gel with and without the application of an electric field were measured. The ^1H T_2 image experiment on the gel without the application of an electric field provided reference data to clarify the shrinkage process of the gel with the application of an electric field. Figure 45 shows the ^1H T_2 distribution images on PMAA gel (3 V) and PMAA gel (0 V) at elapsed time T_e = 0 min and 4 h after the application of an electric field, where figures show T_2 values for the part indicated by an

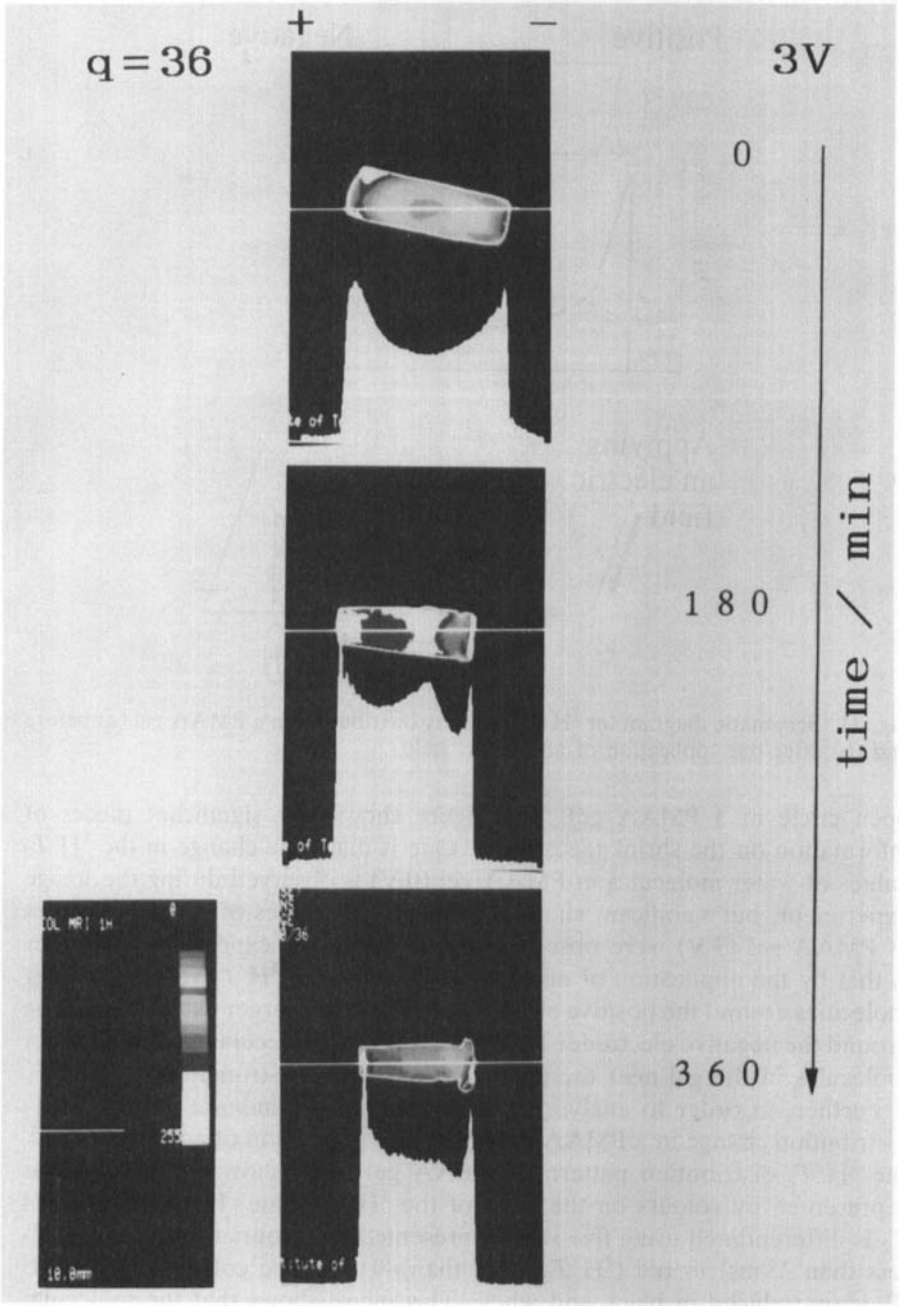

Fig. 43. Two-dimensional histograms of time dependence for ^1H spin density distribution of a PMAA gel with the application of an electric field.

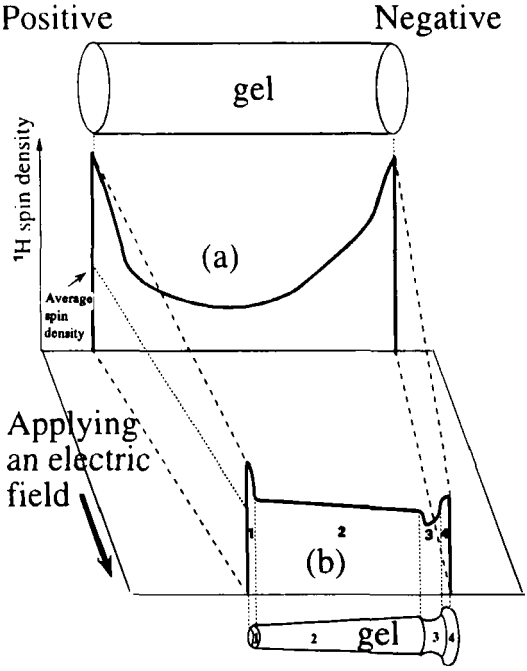

Fig. 44. Schematic diagram for ^{1}H spin density distribution in a PMAA gel (a) before and (b) after the application of an electric field.

open circle in a PMAA gel. This figure shows two significant pieces of information on the shrinkage process. One is that little change in the ^{1}H T_2 values of water molecules in PMAA gel (0 V) is observed during the image experiment, but significant changes in the ^{1}H T_2 values of water molecules in PMAA gel (3 V) were observed during the image experiment. Another is that by the application of an electric stimulus, the ^{1}H T_2 values of water molecules around the positive electrode decrease to a larger extent than those around the negative electrode. This means that the molecular motion of water molecules in the gel near the positive electrode was strongly restrained.

Further, in order to analyse the elapsed-time dependence of the ^{1}H T_2 distribution change in a PMAA gel under the application of an electric field, the ^{1}H T_2 distribution pattern of PMAA gel (3 V) shown in Fig. 46 was represented by colours on the basis of the ^{1}H T_2 value. In this figure, ^{1}H T_2 is differentiated using five steps represented by colours from blue (^{1}H T_2 less than 25 ms) to red (^{1}H T_2 more than 40 ms). The colour scale for ^{1}H T_2 is reproduced in black and white. This figure shows that the molecular motion of water molecules in the gel is restrained with elapsed time, as seen from the observation of the decrease of the ^{1}H T_2 value. In other words, the molecular motion of water molecules in the gel is more restrained with an increase of the degree of shrinkage of the gel by the application of an

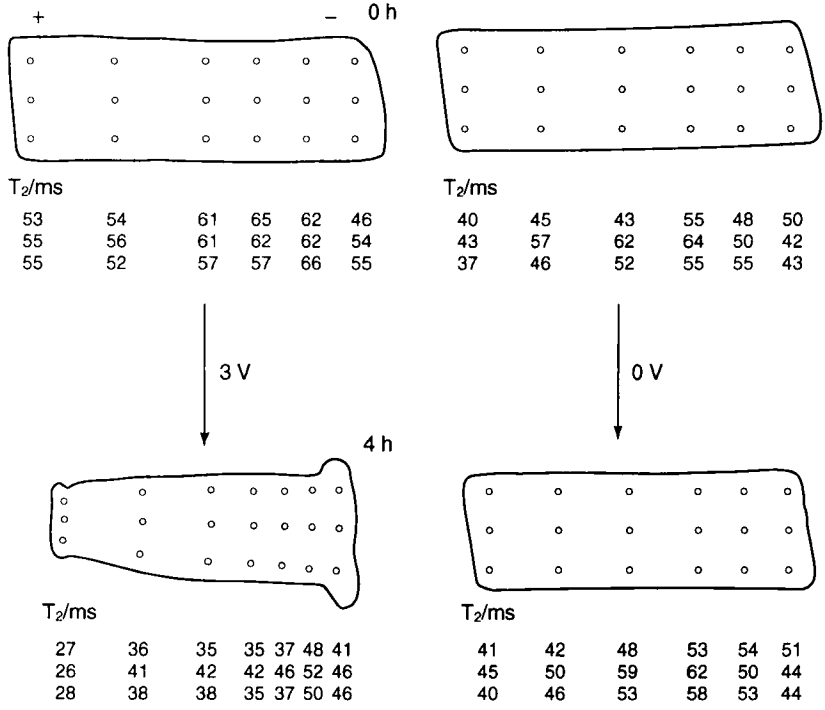

Fig. 45. ^{1}H T_2 distribution for transverse slice of a PMAA gel at $T_c = 0$ min and at $T_c = 4$ h with and without the application of an electric field.

electric field. From these results, the profile of the ^{1}H T_2 distribution image can be divided into four regions in a manner similar to the ^{1}H spin density distribution image. For convenience, a rough schematic representation of the ^{1}H T_2 distribution image is shown in Fig. 47.

In order to compare the ^{1}H T_2 weighted distribution image with the ^{1}H spin density distribution image, the three-dimensional histograms of elapsed-time dependence for the ^{1}H T_2 weighted image and the ^{1}H spin density image are shown in Fig. 48. From this figure it is clear that the region with large shrinkage in a PMAA gel has water molecules with low mobility, but in the third region the mobility of water molecules is high although the fraction of network is high.

4.3. Shrinkage analysis of a composite polymer gel under the application of an electric field

The shrinkage process under an applied electric field of a composite PMAA gel in the form of a double cylindrical rod (Fig. 49), in which the swelling

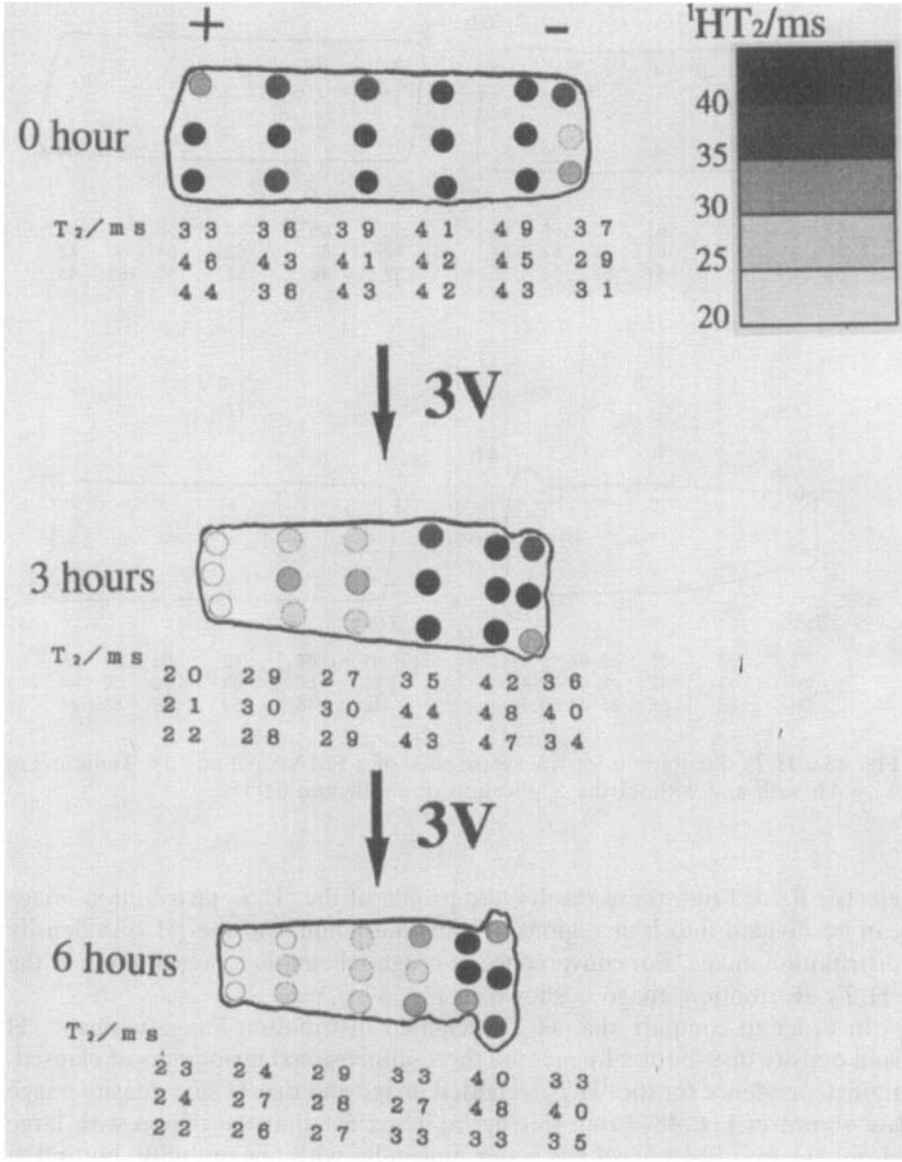

Fig. 46. ^{1}H T_2 distribution for transverse slice of a PMAA gel at $T_e = 0$ min, at $T_e = 3$ h and $T_e = 6$ h with the application of an electric field.

degrees of the outside and inside parts are different with each other, has also been studied.[66]

For the preparation of the double cylindrical rod, PMAA gel was formed by radical polymerization of MAA and MBAA in aqueous solution at 318 K for 24 h in a glass tube (inside diameter 8 mm), at the centre of which a glass

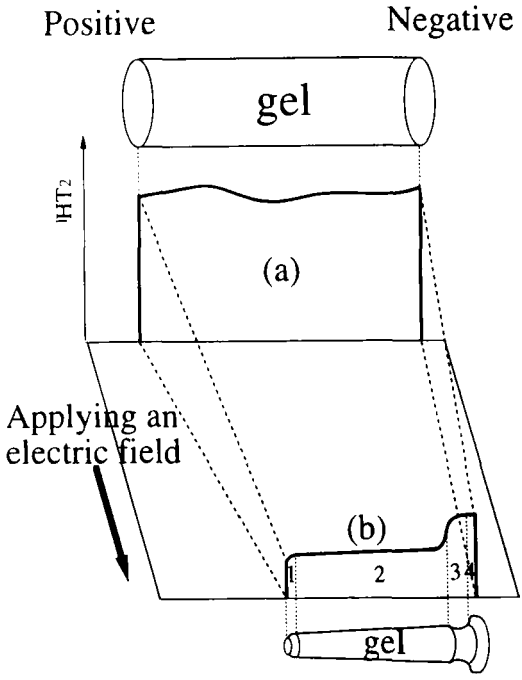

Fig. 47. Schematic diagram for change of ^1H T_2 distribution image in a PMAA gel (a) before and (b) after the application of an electric field.

rod (diameter 4 mm) was placed. After the first polymerization for the outside gel was completed, the glass rod was removed from the glass tube, and MAA, MBAA and $K_2S_2O_8$ were poured into the resulting cylindrical space to prepare the inside PMAA gel. The structural scheme of the composite PMAA gel is shown in Fig. 49. By varying the amount of MBAA used as the crosslinking monomer composite PMAA gels are obtained which consist of outer and inner gels exhibiting different degrees of swelling. In sample A the MBAA concentration was 0.25 mol% for the outside gel and 0.33 mol% for the inside gel, and in sample B it was 0.33 mol% for the outside gel and 0.25 mol% for the inside gel.

The PMAA gel samples obtained were soaked in excess deionized water for three weeks to remove remaining monomer, linear polymers formed as byproduct, and initiator. The water was changed repeatedly. The degree of swelling of the polymer gel (q) is defined by the ratio of the mass of swollen polymer gel to that of dried polymer. The degrees of swelling of polymer gels obtained at the MBAA concentrations of 0.33 and 0.25 mol% are 26 and 28, respectively.

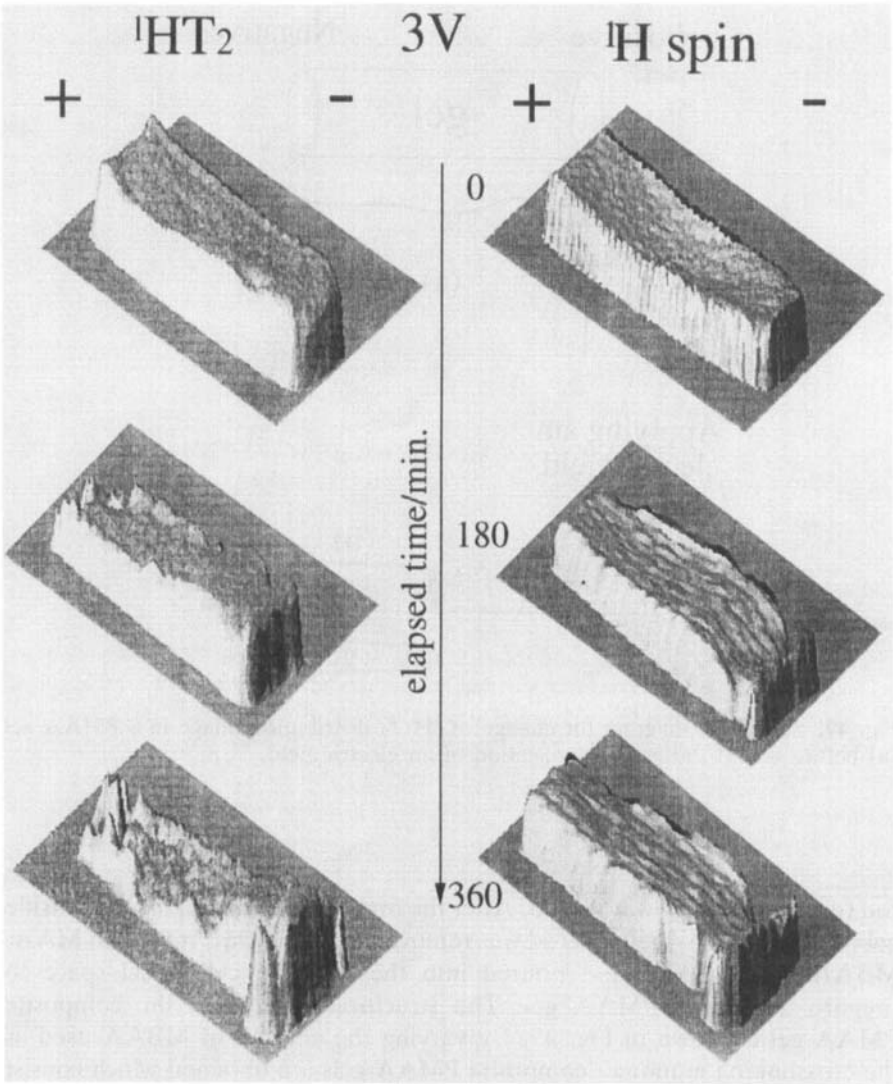

Fig. 48. Three-dimensional histograms of elapsed-time dependence for ^{1}H T_2 weighted image and ^{1}H spin distribution image of a PMAA gel with the application of an electric field.

4.3.1. Shrinkage process of sample A

In the ^{1}H NMR imaging experiments, the only detected ^{1}H signals are those of water contained in a composite gel due to the removal of dipolar broadening by fast isotropic molecular motion. When protonated water in the gel is replaced by deuterated water, no ^{1}H NMR signals are observed. The transverse slice of the gel is observed in a composite PMAA gel. The

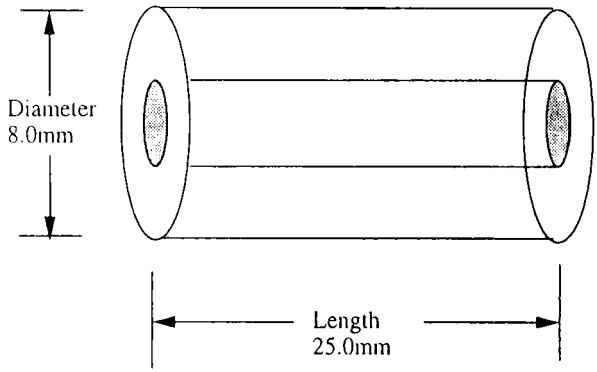

Fig. 49. Structural scheme of a composite PMAA gel where the degrees of swelling of the inside and outside gels are different from each other.

observed ^{1}H spin density images as a function of elapsed time (T_e) after the application of an electric field (3 V) are shown in Fig. 50. The relative magnitude of the ^{1}H spin density was represented by colours from dark blue (the lowest density) to white (the highest density). The colour intensity scale is shown on the right. At $T_e = 0$ min, most of the inside gel region is represented by yellow and most of the outside gel region is represented by red. This indicates that the ^{1}H spin density of the outside gel is higher than that of the inside gel. The experimental result is consistent with the fact that the degrees of swelling of the inside and outside gels are 26 and 28 respectively. As the elapsed time is increased, most of the inside and outside regions are represented by red except for the gel parts in contact with the negative and positive electrodes. At $T_e = 360$ min the inside gel region around the negative electrode becomes white and the region around the positive electrode becomes yellow. In the outside gel, the region around both the electrodes remains red.

It is convenient to represent the ^{1}H spin density distribution of a composite gel by a two-dimensional profile. The profiles of the ^{1}H spin density for the inside and outside gels, of which the positions are indicated by a white line on the image, are shown in Fig. 50 as a function of elapsed time after the application of an electric field. It is shown that the application of an electric field to a composite gel leads to shrinkage of the gel with exhaust of water from the negative electrode side. The shrinkage rate of the inside gel, which exhibits a smaller degree of swelling than the outside gel, is faster compared with the outside gel. For this, at $T_e = 360$ min it is clear that the inside gel with $q = 26$ shrinks more than the outside gel with $q = 28$, and the shrinkage in the region around the negative electrode is greater when compared with the region around the positive electrode. As seen from the two-dimensional

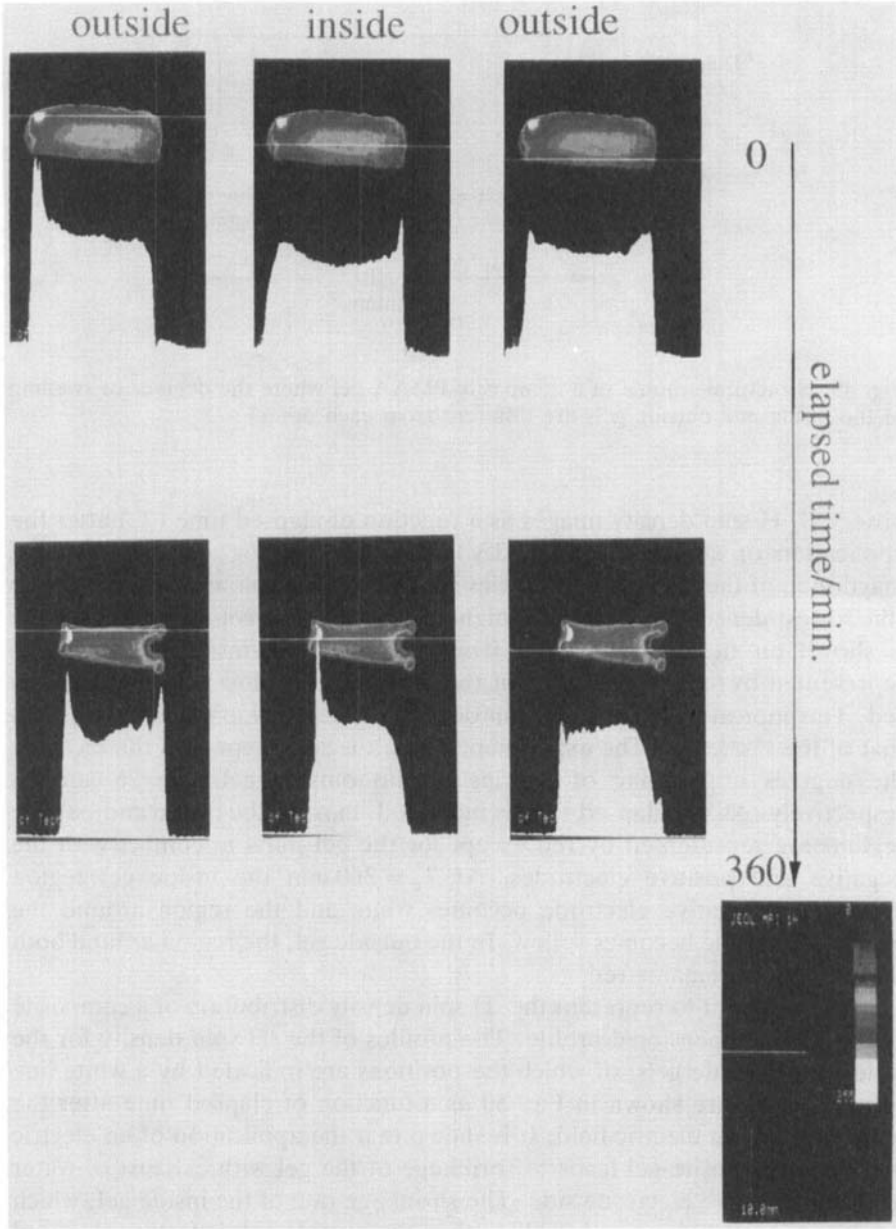

Fig. 50. Elapsed-time dependence of images for the ^{1}H spin density distribution and two-dimensional intensity profile of a composite PMAA gel (sample A) with the application of an electric field. The degrees of swelling q of the inside and outside gels are 26 and 28, respectively.

profiles, as the elapsed time after the application of an electric field is increased, the ^{1}H spin density of water in the region around the positive and negative electrodes becomes higher compared with the bulk region. Such a situation can be more clearly illustrated by the three-dimensional histograms as shown in Fig. 51. For convenience, the schematic diagram for the ^{1}H spin density distribution of the gel under the shrinkage process is shown in Fig. 52(a). The trend for the shrinkage process of the ^{1}H spin density distribution of a homogeneous gel by the application of an electric field as reported previously[65] is very similar to that of the outside gel rather than the inside gel. However, the whole shape of the shrunk composite gel is very different from that of the homogeneous gel which shrinks to form a "bottle-stopper" shape after a long elapsed time following the application of an electric field.

The ^{1}H T_2 weighted image (not shown) provides spatial information on the dynamical behaviour of water molecules in a composite PMAA gel under an electric stimulus. The three-dimensional histograms of elapsed-time dependence of the ^{1}H T_2 weighted image of water in the gel (sample A) after the application of an electric field are shown in Fig. 51. For convenience, the corresponding schematic diagram is shown in Fig. 52(b). Before the application of an electric field the ^{1}H T_2 weighted intensity is almost constant in the whole region of the gel. This means that the mobility of water in the whole region of the inside and outside gels is almost the same. However, at long elapsed times after the application of an electric field, the ^{1}H T_2 weighted intensity in the region around the negative electrode in both the inside and outside gels is somewhat more intense than that around the positive electrode. This means that molecular motion of water in the gel region around the negative electrode is somewhat faster than that in the other region. The trend is very similar to that for the case of a homogeneous PMAA gel discussed above.

4.3.2. Shrinkage process of sample B

The degrees of swelling of the inside and outside gels for sample B are opposite to those for sample A. Therefore, the degree of swelling of the inside gel for sample B is higher than that for sample A. The three-dimensional histogram of the ^{1}H spin density distribution of sample B as a function of elapsed time after the application of an electric field is shown in Fig. 53. For convenience, the schematic diagram of the ^{1}H spin density distribution of the gel is shown in Fig. 54(a). It is apparent that the shrinkage process of sample B with the application of an electric field is very different from the case of sample A. At long elapsed times after the application of an electric field the ^{1}H spin densities of water in the inside and outside gels around the negative and positive electrodes are more intense than those in the other regions. This trend is very similar to that for the homogeneous gel. Also,

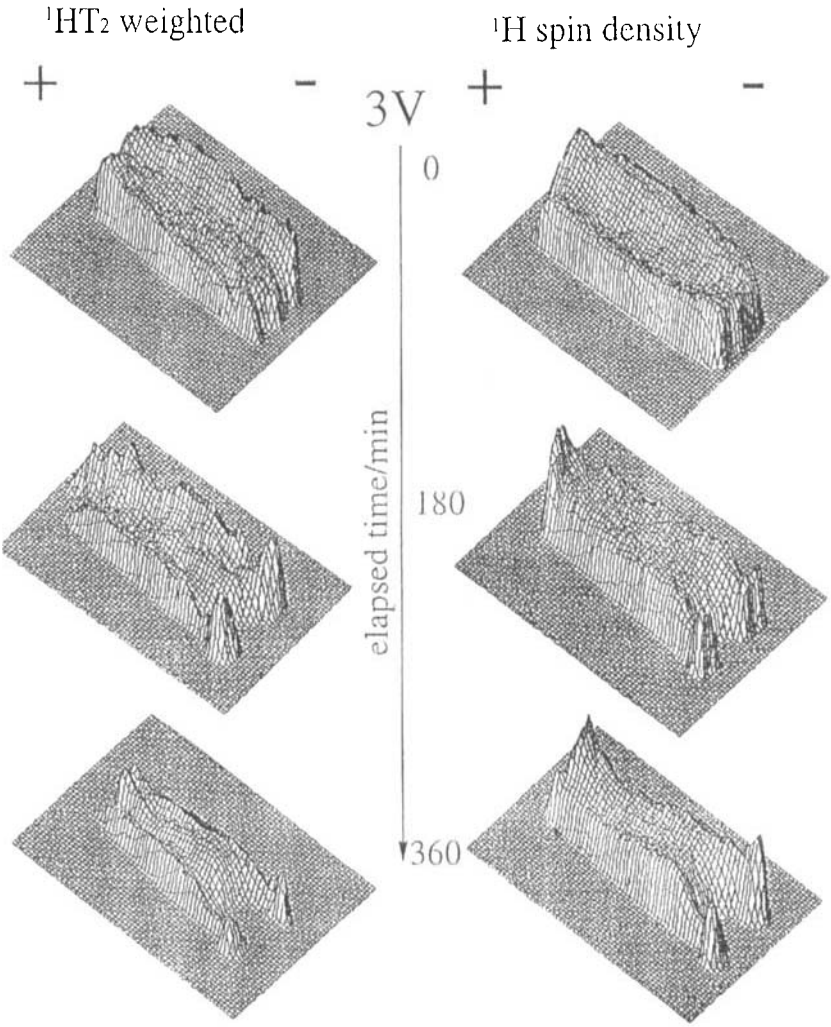

Fig. 51. Three-dimensional histograms of elapsed-time dependence for the ^1H spin–density distribution and ^1H T_2 weighted images of a composite PMAA gel (sample A) with the application of an electric field. The degrees of swelling q of the inside and outside gels are 26 and 28, respectively.

the shape after shrinkage is similar to that of the homogeneous gel, resulting in a "bottle-stopper" shape at long elapsed times. In Fig. 53 the three-dimensional histograms of elapsed-time dependence of the ^1H T_2 weighted image of water in the gel after the application of an electric field are shown. For convenience, the schematic diagram for the ^1H T_2 weighted image of water in the gel after the application of an electric field is shown in Fig. 54(b). Before the application of an electric field the ^1H T_2 intensity is almost

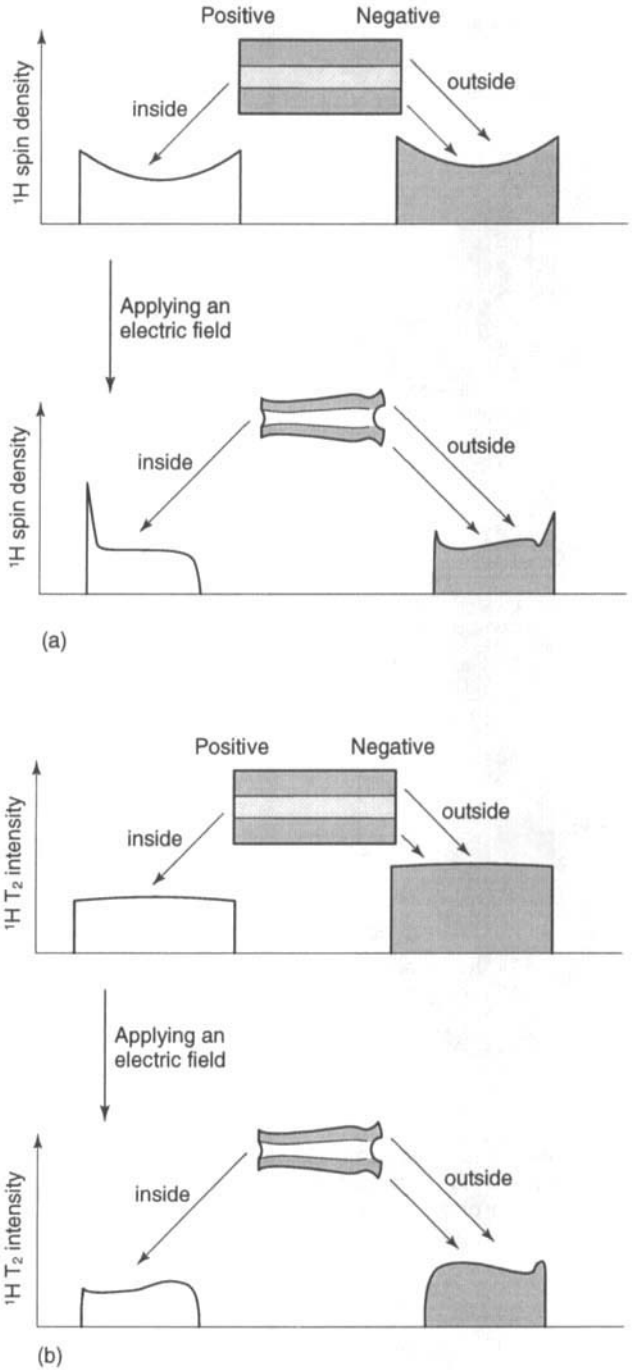

Fig. 52. A schematic diagram of the shrinkage process of a composite PMAA gel (sample A) with the application of an electric field, as viewed by (a) ^{1}H spin density and (b) ^{1}H T_2 weighted images. The degrees of swelling q of the inside and outside gels are 26 and 28, respectively.

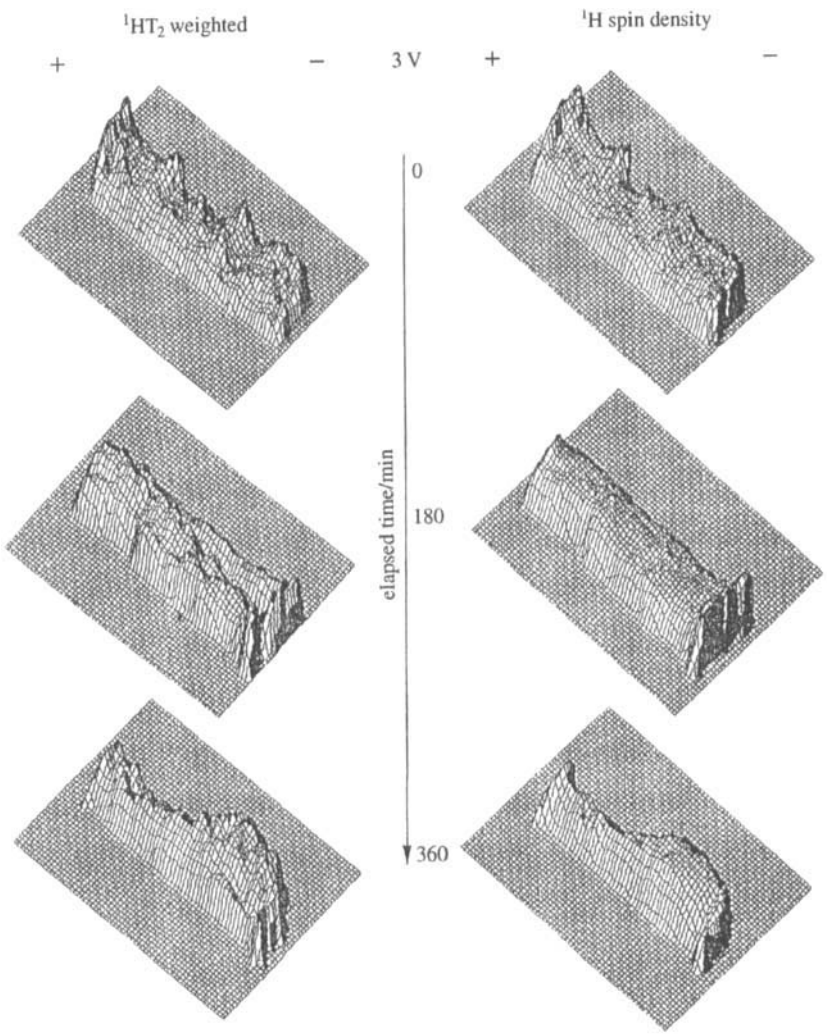

Fig. 53. Three-dimensional histogram of elapsed-time dependence for the ^1H spin density distribution and ^1H T_2 weighted images of a composite PMAA gel (sample B) with the application of an electric field. The degrees of swelling q of the inside and outside gels are 28 and 26, respectively.

constant in the whole region of the inside and outside gels. The mobilities of water in the whole region of the inside and outside gels are almost the same. After a long elapsed time following the application of an electric field the ^1H T_2 intensity of water in the inside and outside gels around the negative electrode is more intense compared with that around the positive electrode.

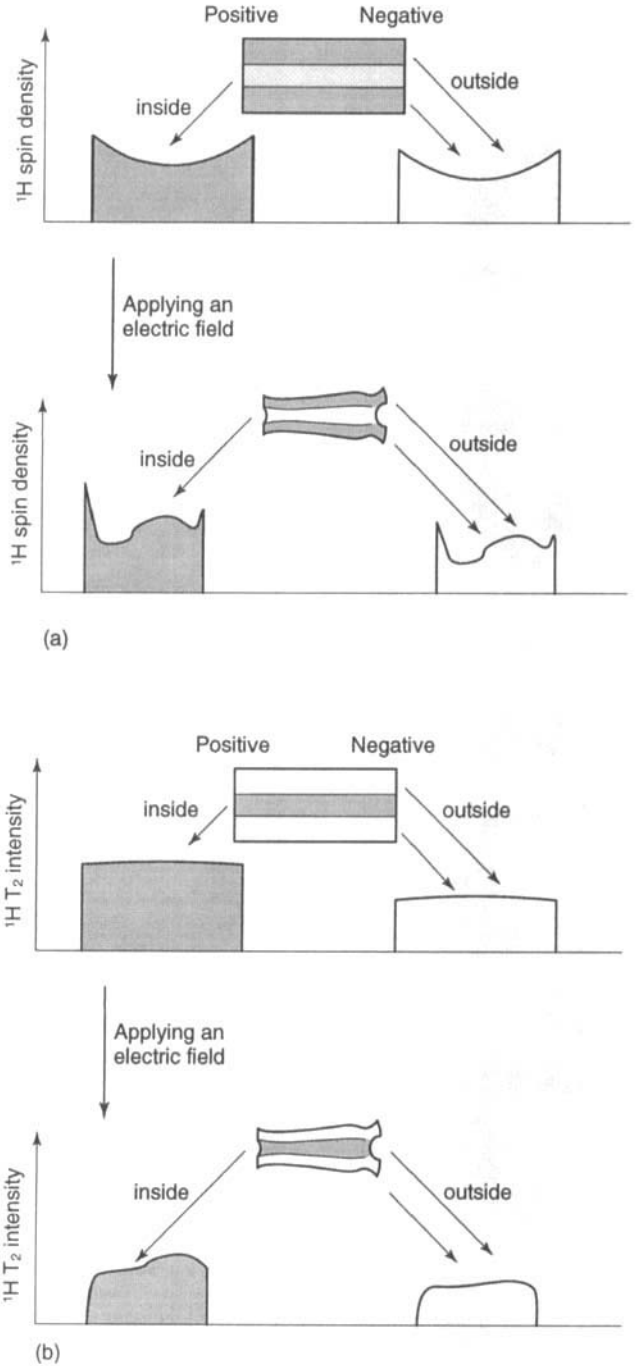

Fig. 54. Schematic diagram of the shrinkage process of a composite PMAA gel (sample B) by the application of an electric field, as viewed by (a) ^{1}H spin density and (b) ^{1}H T_2 weighted images. The degrees of swelling q of the inside and outside gels are 28 and 26, respectively.

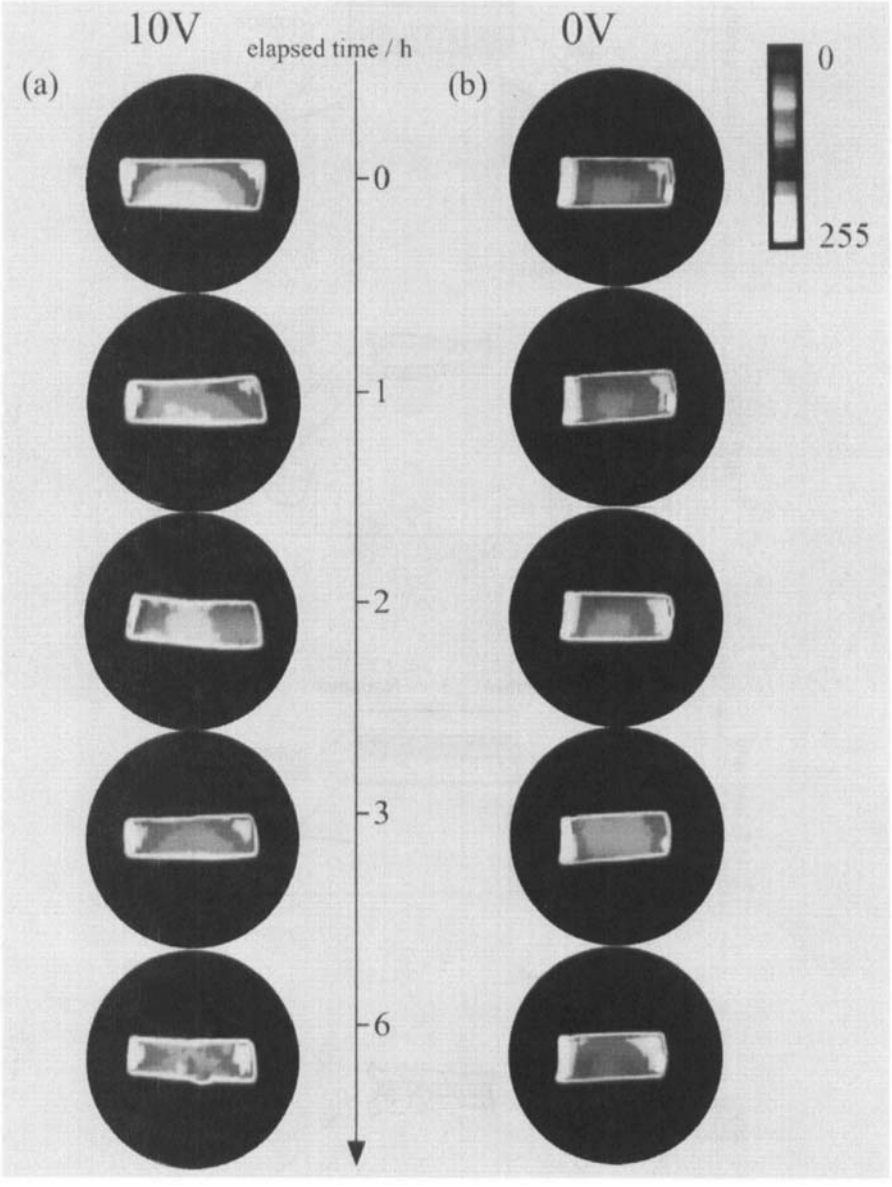

Fig. 55. Elapsed-time dependence of images for the ^{1}H spin density distribution of a PMAA gel (a) with and (b) without the application of an alternating current electric field.

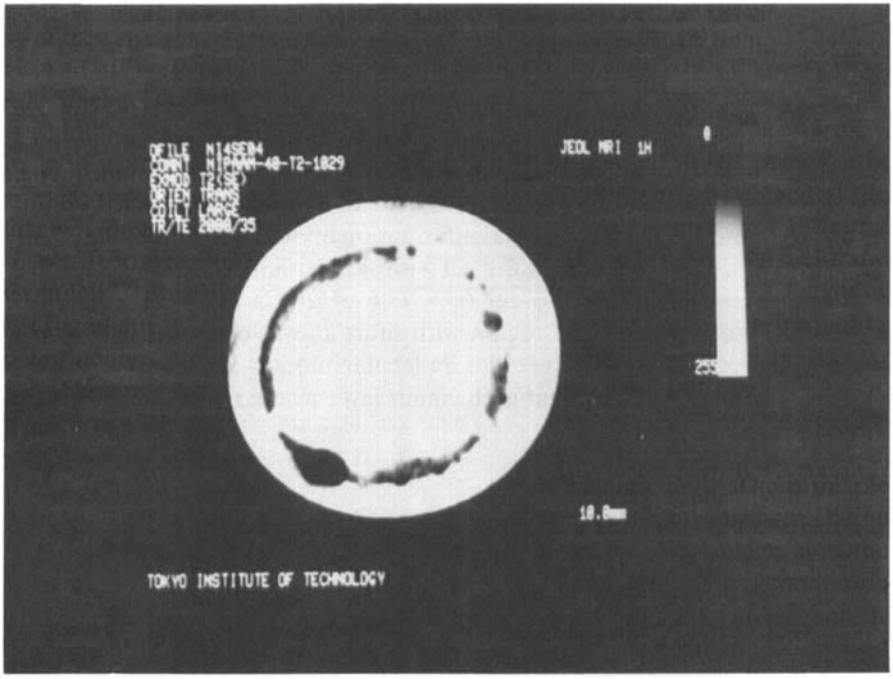

Fig. 56. Observed ^{1}H T_2 enhanced image of a PNIPAM gel ($q = 40$) after rapid temperature change from 20 to 40°C.

This means that the mobility of water in the inside and outside gels around the negative electrode is somewhat higher compared with that around the positive electrode. As discussed above, the ^{1}H T_2 values of water molecules around the negative electrode in a homogeneous cylindrical gel after the application of an electric field are much longer than that around the positive electrode. This trend is very similar to that of the composite gel, meaning that the shrinkage process is very similar to that of the composite gel.

The shrinkage process on application of alternating current electric field (10 V) has also been investigated.[67] Figure 55 shows the transverse slice observed in a PMAA gel under application of an alternating current electric field. The application of an alternating current electric field to a PMAA gel leads to shrinkage of the gel with exhaustion of water. However, the difference between application of a direct and alternating current electric field is the shape of the gel. As shown in Fig. 55, on application of an alternating current electric field to a PMAA gel, the whole shape remains unchanged apart from overall shrinkage.

PNIPAM gel is a well-known thermo-shrinkage gel which collapses at the transition temperature *ca.* 33°C. During the sjhrinkage process, in response

to the change of temperature crossing over the transition temperature, PNIPAM gels often show the so-called skin structure in which the inner unshrunken layer is surrounded by the outer shrunken layer and takes a very long time to complete the shrinkage process. In Section 3, it is shown that two components of T_2 for a PNIPAM gel are observed after increasing the temperature: a short T_2 component corresponding to the outer shrunken layer and a long T_2 component corresponding to the inner unshrunken layer. It would be interesting to have spatial information about the molecular mobility during the shrinkage process of the gel with skin structure.[68] Figure 56 shows a T_2 enhanced image for the gel ($q = 43.6$ at 20°C) in water after rapid increase in temperature. The region with short T_2 was observed in the outer layer of the gel. It is clear that the molecular motion in the outer layer is much more restrained than that in the inner layer where the polymer network does not shrink.

5. CONCLUSIONS

Polymer gels are widely used as functional materials because of their characteristic properties. However, the structure and dynamics of polymer gels associated with their properties are insufficiently clear. In this review, it has been demonstrated that NMR spectroscopy can provide a clear perspective for elucidating the structure and dynamics of polymer gels from both the microscopic and macroscopic aspects. It is expected that the position of new NMR techniques such as pulse NMR, solid-state high-resolution NMR, NMR imaging, etc. will increase in importance within the field of gel science.

REFERENCES

1. (a) P. J. Flory, *Principles of Polymer Chemistry*, Cornell University Press, Ithaca and London, 1953.
   (b) D. DeRossi, K. Kajiwara, Y. Osada and A. Yamauchi (eds), *Polymer Gels – Fundamentals and Biomedical Applications*, Plenum Press, New York, 1991.
   (c) K. Dusek (ed.), *Adv. Polym. Sci.*, 1993, **109**, 1–267.
   (d) K. Dusek (ed.), *Adv. Polym. Sci.*, 1993, **110**, 1–261.
   (e) Y. Osada and J. Gong, *Prog. Polym. Sci.*, 1993, **18**, 187–226.
   (f) T. Tanaka, Y. Osada, S. B. Ross-Murphy and R. A. Siegel (eds), *Polymer Gels and Networks – Special Issue: Tsukuba Symposium on Polymer Gels and Networks*, 1994, **2**, No. 3–4.
2. Y. Osada, *Adv. Polym. Sci.*, 1987, **82**, 1.
3. (a) R. A. Komoroski (ed.), *High Resolution NMR of Synthetic Polymers in Bulk*, VCH Publishers, Florida, 1986.
   (b) I. Ando, T. Yamanobe and T. Asakura, *Progress in NMR Spectroscopy* (eds J. W. Emsley, J. Feeney and L. H. Sutcliffe), Vol. 22, p. 349, Pergamon Press, Oxford, 1990.

(c) H. Kurosu, S. Ando, H. Yoshimizu and I. Ando, *Annual Reports on NMR Spectroscopy* (ed. G. A. Webb), Vol. 28, p. 189, Academic Press, London, 1994.
(d) I. Ando (ed.), *Kobunshi no Kotai NMR (Solid State NMR of Polymers)*, Kyouritu Press, Tokyo, 1994.
4. C. J. Ong and R. Saxon, *J. Appl. Polym. Sci.*, 1976, **20**, 1695.
5. M. Shibayama, H. Yoshizawa, H. Kurokawa, H. Fujiwara and S. Nomura, *Polymer*, 1988, **29**, 2066.
6. J. M. Guenet, *Thermoreversible Gelation of Polymers and Biopolymers*, Academic Press, London, 1992.
7. V. J. Morris, *Spec. Publ. – R. Soc. Chem.*, 1991, **82**, 310.
8. M. Watanabe and K. Nishinari, *Reol. Acta*, 1983, **22**, 580.
9. H. Yasunaga and I. Ando, *Polym. Gels Networks*, 1993, **1**, 83, 267.
10. D. E. Woessner and JR. B. S. Snowden, *J. Colloid Interface Sci.*, 1970, **34**, 290.
11. F. X. Quinn, E. Kampff, G. Symth and V. J. McBrierty, *Macromolecules*, 1988, **21**, 3191.
12. G. Symth, F. X. Quinn and V. J. McBrierty, *Macromolecules*, 1988, **21**, 3198.
13. H. Ohta, I. Ando, S. Fujishige and K. Kubota, *J. Polym. Sci.*, 1991, **B29**, 963.
14. N. Bloembergen, E. M. Purcell and R. V. Pound, *Phys. Rev.*, 1948, **73**, 679.
15. M. Heskins and J. E. Guillet, *J. Macromol. Sci. Chem.*, 1986, **A2**, 1441.
16. S. Hirotu, Y. Hirokawa and T. Tanaka, *J. Chem. Phys.*, 1987, **87(2)**, 1392.
17. J. Karger, H. Pfeifer and W. Heink, *Adv. Magn. Reson.*, 1988, **12**, 1.
18. T. Tanaka, *Phys. Rev. Lett.*, 1978, **40**, 820.
19. T. Tanaka, *Sci. Am.*, 1981, **244**, 110.
20. I. Omine and T. Tanaka, *J. Chem. Phys.*, 1982, **77**, 5725.
21. Y. Hirokawa and T. Tanaka, *J. Chem. Phys.*, 1984, **81**, 6379.
22. T. Tanaka, I. Nishio, S.-T. Sun and S. Ueno-Nishio, *Science*, 1982, **218**, 467.
23. Y. Osada and M. Hasebe, *Chem. Lett.*, 1985, 1285.
24. N. Bloembergen, E. M. Purcell and R. V. Pound, *Phys. Rev.*, 1948, **73**, 679.
25. A. Abragam, *The Principles of Nuclear Magnetism*, pp. 323–7. Oxford at the Clarendon Press, 1961.
26. P. S. Hubbard, *Phys. Rev.*, 1963, **131**, 275.
27. N. Tanaka, S. Matsukawa, H. Kurosu and I. Ando, submitted.
28. R. A. Michael and C. Claude, *Polymer* 1990, **31**, 778.
29. N. A. Rotstein and T. P. Lodge, *Macromolecules*, 1992, **25**, 1316.
30. S. Pajevic, R. Bansil and C. Konak, *Macromolecules*, 1993, **26**, 305.
31. H. Yoon, H. Kim and H. Yu, *Macromolecules*, 1989, **22**, 848.
32. J. M. Widmaier, T. E. Ouriaghli, L. Leger and M. F. Marmonier, *Polymer*, 1989, **30**, 549.
33. S. Matsukawa and I. Ando, *Macromolecules*, 1996, **22**, 7136
34. H. Fujita, *Adv. Polym. Sci.*, 1961, **3**, 1.
35. H. Yasuda, C. E. Lamaze and A. Peterlin, *J. Polym. Sci.*, 1971, **A9**, 1117.
36. J. A. Barrie, *Diffusion in Polymer* (eds J. Crank and G. S. Parks), p. 259, Academic Press, New York, 1968.
37. N. Nemoto, M. R. Landry, I. Noh, T. Kitano, J. Wesson and H. Yu, *Macromolecules*, 1985, **18**, 308.
38. R. Cukier, *Macromolecules*, 1984, **17**, 252.
39. P. G. de Gennes, *Macromolecules*, 1976, **9**, 594.
40. Y. Osada, *J. Polym. Sci.*, 1979, **A17**, 3485.
41. S. Matsukawa and I. Ando, submitted.
42. M. Kobayashi, I. Ando, T. Ishii and S. Amiya, *Macromolecules*, 1995, **28**, 6677.
43. D. R. Paul, *J. Appl. Polym. Sci.*, 1976, **11**, 439.
44. A. Takahashi and S. Hiramitsu, *Polym. J.*, 1974, **6**, 103.

45. (a) T. K. Wu and D. W. Ovenall, *Macromolecules* 1973, **6**, 582.
(b) Y. Inoue, R. Chujo and A. Nishioka, *J. Polym. Sci.*, 1973, **A11**, 393.
(c) Y. Inoue, R. Chujo, A. Nishioka, S. Nozakura and H. Iimuro, *Polym. J.*, 1973, **4**, 244.
46. T. Terao, S. Maeda and A. Saika, *Macromolecules*, 1983, **16**, 1535.
47. M. Kobayashi and I. Ando, submitted.
48. D. A. Torchia, *J. Magn. Reson.*, 1978, **30**, 613.
49. Y. Osada, R. Kishi and M. Hasebe, *J. Polym. Sci., Polym. Lett.*, 1987, **25**, 481.
50. A. Takizawa, T. Kinoshita, O. Nomura and Y. Tsujita, *Polym. J.*, 1985, **17**, 747.
51. H. Fushimi, I. Ando and T. Iijima, *Polymer*, 1991, **32**, 241.
52. P. C. Lauterbur, *Nature*, 1973, **242**, 190.
53. H. Yasunaga and I. Ando, *J. Mol. Struct.*, 1993, **301**, 125.
54. H. Yasunaga and I. Ando, *Polym. Gels Networks*, 1993, **1**, 267.
55. H. Ohta, I. Ando, S. Fujishige and K. Kubota, *J. Mol. Struct.*, 1991, **245**, 391.
56. H. Yasunaga and I. Ando, *J. Mol. Struct.*, 1993, **301**, 129.
57. P. Mansfield and P. G. Morris, *NMR Imaging in Biomedicine. Adv. Magn. Reson., Supplement 2*, Academic Press, New York, 1982.
58. V. R. McCready, M. Leach and P. J. Ell (eds), *Functional Studies Using NMR*, Springer-Verlag, Berlin, 1987.
59. P. Mansfield and E. L. Hahn (eds), *Phil. Trans. R. Soc. Lond. A*, 1990, **333**, 401.
60. P. T. Callaghan, *Principles of Nuclear Magnetic Resonance Microscopy*, Oxford Science Pub., Oxford, 1991.
61. L. A. Weisenberger and J. L. Koenig, *Macromolecules*, 1990, **23**, 2445.
62. L. A. Weisenberger and J. L. Koenig, *Macromolecules*, 1990, **23**, 2454.
63. D. G. Cory, J. C. de Boer and W. S. Veeman, *Macromolecules*, 1989, **22**, 1618.
64. H. Yasunaga, H. Kurosu and I. Ando, *Macromolecules*, 1992, **25**, 6505.
65. T. Shibuya, H. Yasunaga, H. Kurosu and I. Ando, *Macromolecules*, 1995, **28**, 4377.
66. H. Kurosu, T. Shibuya, H. Yasunaga and I. Ando, *Polym. J.*, 1996, **28**, 80.
67. Y. Hotta, H. Kurosu and I. Ando, *Polym. Gels Networks*, to be published.
68. N. Tanaka, S. Matsukawa, H. Kurosu and I. Ando, to be submitted.

NMR Studies of Crosslinked Polymers

ANDREW K. WHITTAKER

Centre for Magnetic Resonance, University of Queensland, Queensland, 4072, Australia

ANNUAL REPORTS ON NMR SPECTROSCOPY
VOLUME 34 ISBN 0-12-505334-7

Crosslinks are introduced into polymers either deliberately so as to enhance material properties such as stiffness, stability and solvent resistance, or are formed as a result of degradation processes. In either case, the inherent insolubility of the materials limits the number of techniques available for characterization of the details of crosslinking. NMR spectroscopy has been applied to this problem for over 40 years. Chemical structure can be characterized using high-resolution solution NMR prior to gelation, or high-resolution MAS NMR after the material has gelled. A range of different experimental approaches are discussed in this review. Crosslink density can be determined using measurements of ^1H T_2 relaxation times, which are sensitive to changes in the motional state of the polymer chains after crosslinking. The relationship between NMR relaxation parameters and macroscopic properties such as crosslink density and the glass transition is of much interest. Changes in the relaxation parameters are used to provide contrast in recent NMR imaging experiments, which can provide maps not only of the crosslink density, but also of material properties.

1. INTRODUCTION

The study and characterization of crosslinked polymers has been one of the major challenges in polymer science. The difficulty in characterizing crosslinked polymers arises naturally from their effectively-infinite molecular weight, and consequent insolubility. Information on molecular mass and molecular mass distribution (and therefore on kinetics of polymerization), conformation, and often chemical structure are difficult to obtain by standard chemical and spectroscopic techniques. NMR spectroscopy, particularly in the solid state, is one technique which offers hope of obtaining these important molecular parameters. Since the initial broad-line ^{1}H NMR experiments on crosslinked polymers in 1953,[1] consistent advances have been made in the area of NMR of crosslinked polymers, punctuated by several major advances in techniques, such as NMR imaging in 1973, and CPMAS in 1976.

The aim of this review is to summarize the important papers in the field of NMR of crosslinked polymers, and to hopefully point to the areas where future advances will be made. The various types of crosslinking reactions are first described in brief, and then the application of the major techniques available at our disposal are summarized. Where appropriate the reader is referred to important reviews in each field. The final sections will summarize results obtained using the more recent techniques of pulsed field gradient (PFG) NMR and NMR imaging.

1.1. Crosslinking reactions

Crosslinking reactions can conveniently be divided into four categories. Firstly, reactions can occur between two or more components of a resin via a *step-growth reaction*. Initially linear chains tend to be formed, however, at higher conversion, if one or more of the monomers in the resin is multifunctional, then a crosslinked network results. This type of crosslinking occurs in the majority of the common resin materials such as epoxy, phenolic, polyester and urethane resins.

Chain-growth reaction is also an important method of producing crosslinked polymers. The polymerization of multifunctional vinyl monomers is an example of such a reaction. In this case the rates of polymerization and termination are high, and hence the material consists at any time only of reacted crosslinked-chain and residual monomer.

The third class of crosslinking reaction involves use of *crosslinking agent*. The agent may be a difunctional monomer, which can react with fully-polymerized chains to initiate crosslinking. In another example the crosslinking agent may be an external source of energy, such as ionizing radiation, which produces reactive centres on chains which can subsequently combine to form crosslinks. Examples of this important category of crosslinking include vulcanization reactions, crosslinking of poly(olefin)s by electron beam irradiation or by reaction with peroxy radicals.

The final class of reaction involves *combination reactions*, in which monomers react with each other, usually upon application of heat. These reactions form the basis of important new materials, such as crosslinked end-capped aromatic molecules.

1.2. Effects of crosslinking on polymer properties

1.2.1. Molecular weight

The first and most obvious result of crosslinking is an increase in molecular weight of the resin or polymer. As reaction proceeds, the viscosity gradually

increases until the gel point is reached, at which time the viscosity undergoes a sudden increase. The gel point is the point at which, on average, each polymer chain contains one crosslink to another chain. The molecular weight of the gel is effectively infinite. The molecular weight, M_w, as a function of conversion, x, up to the gel point has been calculated by Flory and others[2–8] to be:

$$M_w(x) = M_w(0)\frac{1+x}{1-x(f-1)} \tag{1}$$

where f is the functionality of the monomer. Gelation occurs when the conversion $x(\text{gel}) = 1/(f-1)$. The equivalent term for the conversion at the gel point for a chain-growth reaction is:[7,8]

$$x(\text{gel}) = \frac{1}{(DP_w - 1)\,f} \tag{2}$$

where DP_w is the weight-average degree of polymerization. For this category of polymerization, the soluble fraction after gelation consists only of monomer chains.

A similar relationship to equation (2) is obtained for the case of crosslinking of linear chains with a crosslinking agent. In the commercially important example of crosslinking by ionizing radiation the soluble fraction, S, above the gel point is given by the Charlesby–Pinner relationship:[9]

$$S + S^{1/2} = \frac{G(S)}{4G(X)} + \frac{2.404e^6}{G(X)\,M_w D} \tag{3}$$

where $G(S)$ and $G(X)$ are the yields of chain-scission and crosslinking per 16 aJ of energy, respectively, and D is the radiation dose in kGy. This equation takes into account the possibility of competing chain-scission reactions. These equations have been generalized to account for a range of initial molecular weight distributions by Sohma.[10]

1.2.2. Glass transition temperature

An important parameter of crosslinked polymers is the temperature, T_g, at which the polymer passes from the glassy to the rubbery state. Crosslinking has the general effect of increasing the glass transition temperature. For chain-growth reactions, the increase in glass transition temperature with conversion has been described by a number of expressions including the diBenedetto equation:[11]

$$\frac{T_g - T_{g0}}{T_{g0}} = \frac{\varepsilon_X}{\varepsilon_M} \cdot \frac{X_c}{1 - X_c} \tag{4}$$

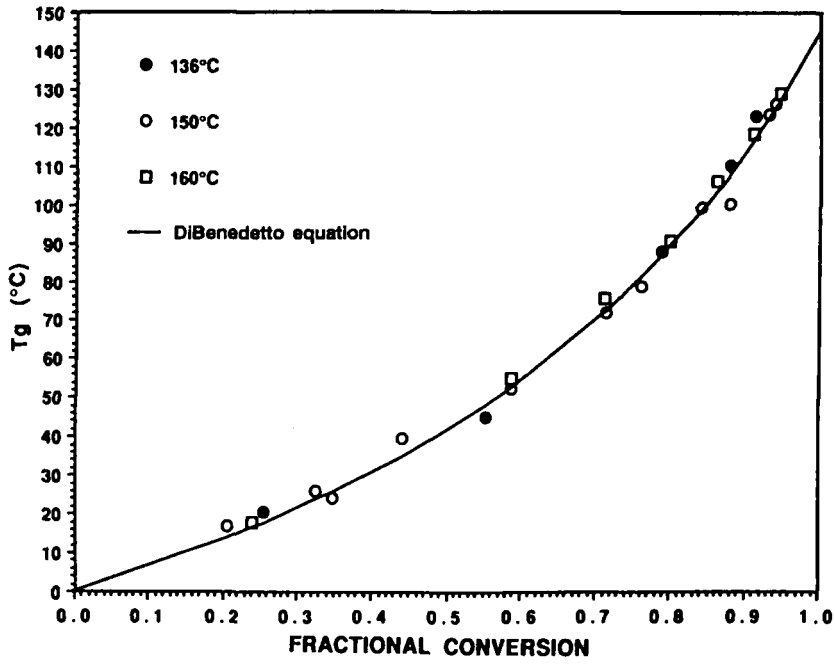

Fig. 1. The dependence of the glass transition temperature, determined by DSC, on fractional conversion, during the cure of diglycidyl ether of bisphenol A with trimethylene glycol di-*p*-aminobenzoate, and the result of the fit of the data to the diBenedetto equation. (Reproduced from reference 12 with permission. Copyright © 1990 American Chemical Society.)

where $\varepsilon_X/\varepsilon_M$ is the ratio of the lattice energies of the crosslinked and linear polymers, respectively, and can be estimated from solubility parameters.[11] Figure 1 shows the increase in glass transition temperature, as a function of conversion, during the cure of diglycidyl ether of bisphenol A with trimethylene glycol di-*p*-aminobenzoate,[12] and the result of the fit of the data to the diBenedetto equation (4). Other examples of investigations of the relationship of T_g with extent of crosslinking can be found in the references.[13–16]

1.2.3. Mechanical properties

Crosslinking tends to most profoundly affect low-frequency molecular motions. Long-time deformation or creep is dramatically reduced with increasing crosslinking density.[17] Similarly, stress relaxation tends to reach a plateau value at long times in crosslinked polymers rather than decay to zero. At slightly higher frequencies, the rubbery plateau observed by dynamic

mechanical analysis tends to flatten out and the plateau modulus to increase, due to a higher effective entanglement density compared with the un-crosslinked, but entangled material. The elastic modulus is indeed a sensitive measure of crosslink density. In stress–strain measurements the elongation to break decreases monotonically on crosslinking, while the tensile strength may initially increase and subsequently decrease. As discussed above, the glass transition temperature increases with crosslinking. Motions having frequencies up to the kilohertz range are all hindered by crosslinking, as discussed in the body of this review. High-frequency motions, generally associated with motion of side-chains, tend to be less dramatically affected by crosslinking. The effects of crosslinking on mechanical properties have been extensively discussed by Nielsen.[11,18]

1.2.4. Techniques for measuring crosslinking in polymers

Many of the techniques for measuring crosslinking are based on the changes in fundamental physical properties discussed briefly above. Many of these techniques have been reviewed recently.[11,19,20] The degree of swelling of the crosslinked polymer in a good solvent has long been used as a method for determining crosslink density.[21] Measurement of residual sol fraction is also a powerful technique for obtaining crosslinking densities.[20] As discussed above, measurement of modulus above T_g[22] leads to a measure of crosslink density. It is fair to say, however, that these methods rely on a number of fundamental assumptions, for example on the form of the initial molecular weight distribution, the distribution of crosslinking reactions, and knowledge of a variety of parameters, for example the solvent–polymer interaction parameters. Alternative methods such as measurement of glass transition temperature, or dynamic properties[19] are often difficult to interpret and make assumptions about the chemistry of cure.

Spectroscopic methods of analysis offer the opportunity of model-independent analysis of crosslinked polymers. Infrared spectroscopy has been applied with great success in the analysis of crosslinking thermosetting resins.[23–25] Not all crosslinking systems are amenable to infrared analysis; most notably filled samples cannot be readily analysed. Generally such limitations do not apply to the technique of NMR spectroscopy. A number of complementary approaches have been applied in the effort to use NMR to measure crosslinking. Firstly, attempts have been made to directly observe an NMR signal due to crosslinks. In highly crosslinked networks, such as thermosetting resins, this objective is relatively trivial; however, in materials with low crosslink density, such as poly(olefin)s crosslinked using ionizing radiation, the problem is more difficult. The number of crosslinks in these materials is generally only just greater than one crosslink per polymer chain, i.e. the polymer is usually crosslinked to just beyond the gel point. The concentration of crosslinks, therefore, is of the order of one crosslink per

10^4–10^5 total carbon atoms. These concentrations represent the limits of the sensitivity of modern solution-state NMR spectrometers. Often the mechanism of crosslinking is studied by crosslinking the materials to unrealistically high levels. Although peaks due to crosslinks can be observed in the NMR spectra, questions must be raised about the validity of these results at low crosslink levels. Despite these reservations, many important advances have been made in this area.

The second approach often adopted in the NMR study of crosslinking polymers is to measure changes in the dynamic properties which reflect the concentration of crosslinks. This most often means measurement of entanglement density in crosslinked polymers from the decays of transverse magnetization. With appropriate calibration, or by resorting to data analysis, rapid and accurate measurement of crosslink density is achievable. The results of these measurements are reviewed in Section 2.4.

The advent of NMR imaging has given NMR an advantage over other spectroscopic techniques. Most spectroscopic methods measure a macroscopic average over the sample of interest, whereas NMR imaging can give important information on the distribution of crosslinks throughout a material. Recent results in this area are summarized in Section 8.

The time-dependence of the NMR signal gives an additional advantage over the majority of other spectroscopic techniques. Studies of dynamic processes, and the relationship between mechanical properties and molecular motion, are amenable to study by NMR spectroscopy. Insight into the fundamental processes involved in relaxation processes has been obtained by NMR spectroscopy. Throughout this review the important papers concerned with studies of motion in crosslinked polymers will be discussed.

1.3. NMR texts and reviews

The field of NMR studies of crosslinking in polymers has already been the subject of several valuable reviews. Andreis and Koenig[26] provided an extensive review of the literature in 1989, including a comprehensive summary of background theory. Harrison and coworkers[19] have summarized the range of possible techniques for analysis of crosslinked polymers, including NMR spectroscopy. Bauer[27] and more recently Kinsey[28] have also reviewed the use of NMR to characterize crosslinked polymers. More general reviews of the application of NMR to the study of polymer structure are to be found in the references.[29–34] Several important books have also appeared, including those primarily concerned with the application of solution-state NMR to polymers,[35–37] while solid-state NMR studies of polymer are dealt with in three more recent texts.[38–40]

2. ^{1}H NMR SPECTROSCOPY

2.1. Background

^{1}H NMR spectroscopy was the first NMR technique applied to crosslinked polymers. The power of the method arises from the sensitivity of the linewidth of the NMR signal to molecular motion. Increasing amplitude and frequency of molecular reorientation results in a decrease in the NMR linewidth, as demonstrated in Fig. 2,[41] in which the NMR linewidth of crosslinked natural rubber has been measured as a function of temperature. Crosslinking has the effect of raising the glass transition temperature, as discussed in Section 1.2 above, and therefore if NMR measurements are made in the vicinity of T_g, dramatic changes in the linewidth are observed on crosslinking. The NMR linewidth measured at temperatures well above T_g also increases with increasing crosslink density, due to the reduced averaging of the dipole–dipole couplings by molecular motion. This is discussed in more detail in Section 2.2.

Before the advent of pulsed Fourier transform (FT) NMR spectrometers,

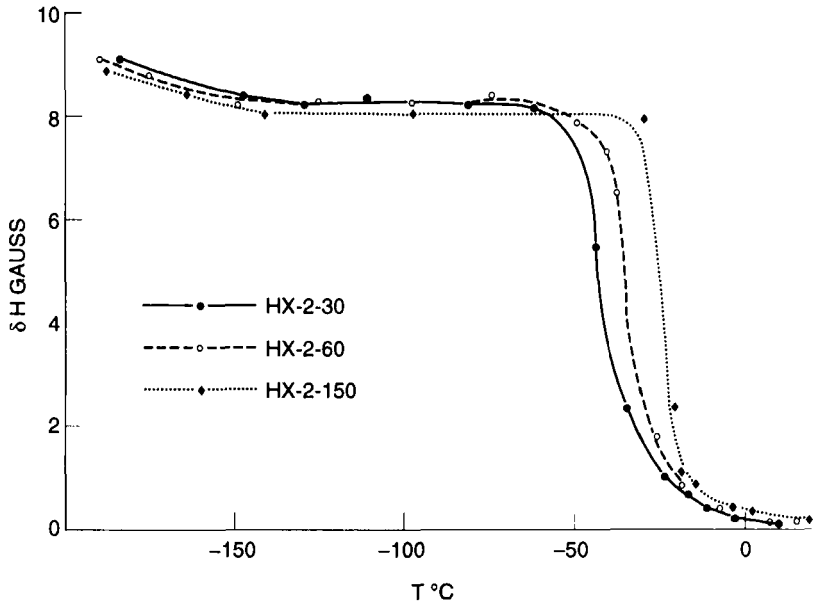

Fig. 2. Linewidths of the NMR spectra of natural rubber cured for 30, 60 and 150 min, and containing respectively 2.91%, 3.75% and 5.58% residual sulphur in crosslinks, as a function of measurement temperature. (Reproduced from reference 41 with permission. Copyright © 1957 American Institute of Physics.)

NMR spectra were obtained by sweeping the magnetic field across the whole NMR line, and recorded with a small modulating field, which resulted in a spectrum which is the first-derivative of the absorption spectrum. The introduction of pulsed FT instruments resulted in increases in signal-to-noise ratio via signal averaging, and an increase in the number of available experiments. Care must be taken however in accounting for the effects of finite pulse length. Powles and Mansfield[42] suggested the solid-echo experiment as a means of refocusing magnetization resulting from strongly dipole-coupled spin systems. For crosslinked systems above T_g, direct detection of the free induction decay (FID) is often possible after probe ring down, due to long T_2 relaxation times; however, in many cases the full NMR line shape can only be obtained using the solid-echo sequence.

2.2. ^{1}H NMR spectroscopy of crosslinked polymers

The first NMR studies of crosslinked polymers were performed by Gutowsky and Meyer in 1953 using CW ^{1}H NMR.[1] This study was concerned with measurement of the ^{1}H linewidth of sulphur-cured natural rubber as a function of temperature and curing time. Figure 3 shows the linewidth, measured as the separation of the maximum and minimum of the first derivative NMR spectra, for natural rubber cured to 30 and 90 min, and

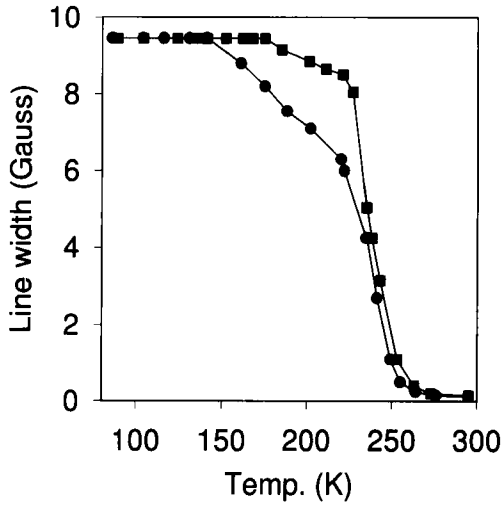

Fig. 3. Linewidths of the NMR spectra of natural rubber cured for 30 (●) and 90 (■) min, as a function of measurement temperature. (Adapted from reference 1 with permission. Copyright © 1953 American Institute of Physics.)

measured from 86 K up to 295 K. Two transitions are observed; the transition at approximately 150 K was assigned to the temperature of onset of rotation of methyl groups, while the more pronounced transition at 230 K was due to the onset of large scale cooperative motions associated with the glass transition. Crosslinking appears to affect the lower temperature transition more strongly than the T_g transition, and therefore, an intramolecular reaction was proposed as the main reaction.

In a later study, Gutowsky and coworkers[41] studied the changes in line shape and T_1 relaxation times in well-characterized samples of cured natural rubber. The temperature of the onset of the large-scale cooperative motions associated with the glass transition was seen to increase 5–10 K with increasing degree of crosslinking (see Fig. 2). On the other hand, Huggins *et al.*[43] reported that for irradiated poly(dimethyl siloxane) the temperature of line narrowing near the glass temperature decreases with increasing dose, due, it is suggested, to decreased chain rotational energy associated with this transition as a consequence of the formation of defects (i.e. crosslinks). At higher doses the linewidth increases as expected.

Other studies of changes in line shape as a result of crosslinking, include the study of Bamford *et al.*[44] of poly(vinyl trichloroacetate) crosslinked with methyl methacrylate. On crosslinking an increase in the temperature of onset of large-scale cooperative motions was observed; however, a decrease or an increase in the temperature (*ca.* 140 K) of onset of rotation of the α-methyl group was observed depending on the composition of the crosslinked polymer. These effects were related to the morphology of the crosslinked material. Eastmond and Smith also reported the decrease in linewidth of poly(vinyl trichloroacetate) crosslinked with methyl acrylate.[45] Morita *et al.*[46] have measured the ^{1}H NMR line width of plasma polymerized (crosslinked) poly(styrene). The line shape consists of superimposed broad and narrow lines, assigned to the crosslinked network and short branches, respectively. The narrow line appears at *ca.* 320 K, while the width of the broad line decreases gradually up to 470 K. The rapid decrease in linewidth at 390 K expected for uncrosslinked poly(styrene) is not observed for these materials. Banks and Ellis[47] have studied the changes in the NMR linewidth of cured epoxy resins as a function of temperature from 200 K to 400 K. A very broad transition from 200 K to 300 K was assigned to the onset of methyl group motion, and at higher temperatures flipping of the phenyl rings.

2.3. ^{1}H longitudinal relaxation times in crosslinked polymers

2.3.1. Background

The relationship between spin–lattice relaxation and molecular motion in polymers is well known and has been the subject of several reviews.[29–32] The

essential elements of the theory describing spin–lattice relaxation were developed by Bloembergen, Purcell and Pound in 1948.[48] For dipole–dipole relaxation, which tends to dominate ^{1}H spectroscopy, the rate of relaxation is given by

$$\frac{1}{T_1} = \frac{3\gamma^4 h^2}{10r^6} [J(\omega_0) + 4J(\omega_0)] \tag{5}$$

where $J(\omega_0)$ is the spectral density function and is related to the autocorrelation function, $G(\tau)$, by

$$J(\omega_0) = \frac{1}{2} \int_{-\infty}^{+\infty} G(\tau)\, e^{i\omega\tau} d\tau \tag{6}$$

For rapid isotropic motion of the internuclear vector $J(\omega_0)$ can be written as

$$J(\omega_0) = \frac{\tau_c}{1 + \omega^2 \tau_c^2} \tag{7}$$

In the case of polymers, however, molecular motions are coupled through the extended backbone and through space, and hence such a simple description of relaxation rarely suffices. A number of papers have dealt with the form of the autocorrelation function appropriate for conformational jumps responsible for polymer relaxation. These have been reviewed by Dejean de la Batie and coworkers.[49] Alternatively, the relaxation can be modelled by assuming a distribution of correlation times of motions:

$$\frac{1}{T_1} = A \left[\int_0^\infty \frac{\tau_c G(\tau_c) d\tau_c}{1 + \omega_0^2 \tau_c^2} + 4 \int_0^\infty \frac{\tau_c G(\tau_c) d\tau_c}{1 + 4\omega_0^2 \tau_c^1} \right] \tag{8}$$

where A contains γ and r. The appropriate form of the distribution function, $G(\tau_c)$, has been the subject of some debate.[41,50–57] Connor[53] has derived expressions for a large number of distribution functions with origins in dynamic mechanic analysis, including log-Gaussian, Fuoss–Kirkwood, Cole–Cole, and Cole–Davidson distributions. Schaefer[54] later introduced the log-χ^2 distribution and applied it with success to the spin–lattice relaxation of poly(styrene) in solution, as well as solid poly(isoprene) and poly(butadiene). In recent years the Kolrausch–Williams–Watt[55] and the Havriliak–Negami[56] distributions have also been considered. Asymmetric distributions having increased density of motions in the low frequency range are often more successful in describing NMR data.

For the case of crosslinked polymers, Roland and Labun[57] have compared the Weibull and log-Gaussian distributions for describing the temperature dependence of the spin–lattice relaxation times in lightly-crosslinked

poly(butadiene) rubber. The former distribution function was found to provide a more satisfactory fit to the data, especially on the high-temperature side of the minimum in T_1. At higher crosslink levels, the quality of the fit to the data was less satisfactory. The authors introduced a model in which T_1 was averaged by spin diffusion to crosslinking sites.

The spectral densities of motions at lower frequencies are responsible for relaxation in the rotating frame during a spin-locking experiment. The rate of spin–lattice relaxation in the rotating frame is given by[58]

$$\frac{1}{T_{1\rho}} = A\left[\frac{3}{2}\frac{\tau_c}{1+4\omega_1^2\tau_c^2} + \frac{5}{2}\frac{\tau_c}{1+\omega_0^2\tau_c^2} + \frac{\tau_c}{1+4\omega_0^2\tau_c^2}\right] \tag{9}$$

$T_{1\rho}$ is a sensitive measure of the higher frequency motions chain motions in rubbery polymers, and hence is generally more strongly affected by crosslinking than T_1 relaxation.

Finally it must be recognized that in ^{1}H NMR spectroscopy of ^{1}H-rich solids, such as crosslinked polymers, consideration should be given to the effects of spin diffusion. The transport of magnetization through solids via energy-conserving spin flip-flops can be exploited to measure the dimensions of domain structures in solid polymers.[59–62] The transport of magnetization may, however, lead to a complication of the interpretation of the relaxation time experiment.[41,59]

2.3.2. *Measurements of the effect of crosslinking on* T_1 and $T_{1\rho}$ *relaxation times*

Gutowsky and coworkers[41] measured the T_1 of cured natural rubber over a temperature range of 200–380 K. On crosslinking, the minimum in T_1 moved to higher temperatures, and the minimum T_1 increased. Simple Bloembergen–Purcell–Pound (BPP) theory was found to be inadequate to describe the relaxation behaviour; the authors suggest that a distribution of correlation times may be needed to describe the data adequately.

Eastmond and Smith have measured the spin–lattice relaxation times of poly(vinyl trichloroacetate) crosslinked with methyl acrylate.[45] Increases in the temperature of the minimum in T_1 were due to restriction of motion due to crosslinking, while a decrease in the apparent activation energy of motion below T_g, calculated from the slope of the plot of the logarithm of T_1 versus inverse temperature, was ascribed to an increase in the distribution of correlation times of motion on crosslinking. The effects of spin diffusion on these results are not considered.

In 1978, Rowland and Labun presented a detailed study of the effects of chemical crosslinking on the T_1 relaxation of poly(butadiene).[57] With increasing crosslinking density, the temperature of the minimum in T_1 increased, and a marked decrease in T_1 on the high-temperature side of the

minimum was observed. The authors suggested that a distribution of correlation times of motions was responsible for this behaviour, and that spin diffusion of magnetization to the crosslinked regions was important at all temperatures. A distribution of correlation times based on the Weibull function provided a superior fit to the experimental result compared with a log-Gaussian distribution. The distribution of correlation times covers several orders of magnitude.

In a related paper, Munie, Jonas and Rowland[63] measured, in addition to ^1H T_1, the rates of ^1H spin–lattice relaxation in the rotating frame in crosslinked poly(butadiene). Similar conclusions were reached from this work; however, the $T_{1\rho}$ measurements extended the frequency of motions measured to the kHz region. Activation energies for reorientation, obtained from the minima in plots $T_1/T_{1\rho}$ versus temperature, yield 15.8 kcal mol^{-1} for uncrosslinked polymer and 10.7 kcal mol^{-1} for a heavily crosslinked sample. Brown *et al.* also reported the T_1 relaxation of poly(butadiene) crosslinked in bulk and in solution.[64] The samples crosslinked in bulk have a high proportion of trapped entanglements, which was reflected in the $T_{1\rho}$ relaxation times but not the T_1 relaxation times.

Larsen and Strange have studied the changes in T_1 and $T_{1\rho}$ during the cure of DGEBA and MDA[65,66] at 327 K. A minimum in T_1 is observed after 4.5 hours of cure, while both $T_{1\rho}$ and T_2 decrease after 3.5 hours, at which time the resin has reached the gel point. Both $T_{1\rho}$ and T_2 are bi-exponential at this time. On further curing $T_{1\rho}$ increases and T_2 decreases abruptly as the polymer enters the vitreous state. The correlation times of motion are related to changes in the molecular weight during cure.

Other studies of spin–lattice relaxation in crosslinked polymers include chemically-crosslinked poly(propylene),[67] poly(ester) crosslinked with styrene,[68] and polyester resin.[69]

2.4. ^1H transverse relaxation times in crosslinked polymers

2.4.1. Background

The spin–spin relaxation time is measured usually by the Hahn echo,[70] or the Carr–Purcell–Meiboom–Gill (CPMG) sequence.[71,72] The Hahn sequence is more time consuming than the CPMG, in which the full echo train can be collected in one "shot". Care must be taken when using the CPMG sequence, since it has been reported that the time constants of the decay of magnetization depend on the separation of the π-refocusing pulses.[73–77] This has recently been attributed to the effects of diffusion during the NMR experiment. The microscopic voids present in polymers result in large local gradients in magnetic field in the neighbourhood of the voids.[73] Diffusion of chain segments through these gradients,[77] or diffusive motion of the voids

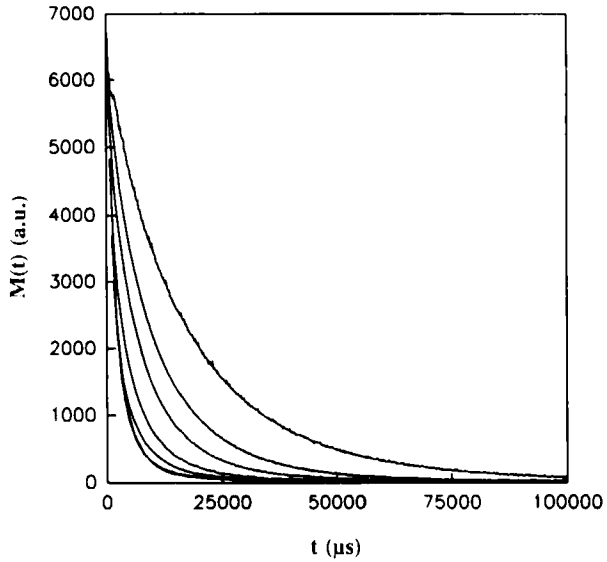

Fig. 4. T_2 decay curves for poly(butadiene) at 302 K measured using the CPMG sequence. The upper curve was collected using magic angle sample spinning, while the other curves were collected without sample spinning and with echo spacings of 1 ms, 800 μs, 600 μs, 400 μs, 200 μs and 100 μs in order of decreasing rate of decay. (Reproduced from reference 77 with permission. Copyright © 1992 Butterworth-Heinemann.)

themselves,[73–76] results in dephasing of the magnetization during the echo experiment. The extent of dephasing increases within certain limits with increasing pulse spacing. Figure 4 shows that increasing the pulse spacing in CPMG experiments on poly(butadiene) at 302 K increases the rate of decay of magnetization.[77] The uppermost curve was obtained with high-speed sample spinning, when the decay time constants were not affected by changing the pulse spacing. The results of the study of poly(butadiene) and other polymers[77] suggest that meaningful results can be obtained in a comparative study if a constant set of conditions is chosen, i.e. a constant pulse spacing. Care must also therefore be taken using the Hahn echo sequence, where similar effects are also operating.

2.4.2. Measurements of the effect of crosslinking on T_2 relaxation times

(i) Measurements of crosslink density. As discussed in Section 2.2, crosslinking has a profound effect on transverse relaxation times above the glass transition. The reduction in amplitude and frequency of molecular reorientation results in residual dipole–dipole couplings, which lead to line broaden-

ing. The decrease in segmental mobility is most important at sites adjacent to crosslink points, so that the amplitude of motion of a particular chain segment increases the further that point is from the crosslink. This results in a decrease in T_2 close to the crosslink point. In practice the decay of transverse relaxation can be decomposed into usually two or, in the case of crosslinked poly(ethylene), three decay times. The more rapid decay process is assigned to segments close to crosslinks, and the slower decay to segments well removed from the crosslinks. Therefore the decay of magnetization is described by

$$M(t) = \sum M_i(0)\mathrm{e}^{-t/T_2^i} \tag{10}$$

where M_i and T_2^i are the amplitude and time constant of the ith decay process, respectively, and i can take the values 1,2,3, etc. It is important to note that M_1, i.e. the amplitude of the fastest decay, does not give a direct measure of the number of crosslinks, but rather the number of segments adjacent to the crosslinks.

Charlesby and coworkers have been foremost in pursuing the use of measurements of T_2 to follow crosslinking reactions. For example, poly(dimethyl siloxane) was crosslinked by exposure to gamma rays, and the change in T_2 relaxation, measured using the Hahn echo sequence, followed as a function of radiation dose and initial molecular weight.[78] The initial molecular weights of all polymers investigated were above the critical molecular weight for entanglement, and therefore prior to irradiation the T_2 decay was decomposed into two separate decays. The proportion of protons having a long T_2 was labelled f by Charlesby. The initial proportion of entanglements $(1-f)$ was modelled by the concept of a virtual radiation dose, i.e. the physical entanglements in the unirradiated polymers were suggested to be equivalent to chemical crosslinks formed by a virtual radiation dose. This virtual radiation dose was added to the actual radiation dose, to allow analysis of the radiation chemical processes. Figure 5 shows the plot of the fraction f of the slowly relaxing protons, plotted as a function of "corrected" radiation dose divided by the gel dose, for all four polymers analysed. The solid line in the figure is the result of fitting the data to the Charlesby–Pinner equation (3). The agreement between experimental and theory is excellent, and yields a G-value for crosslinking of $G(X) = 2.8$ $(G(S) = 0.0)$, in concord with results obtained with more traditional methods. The figure also demonstrates that the yield of crosslinks is independent of molecular weight, as expected for high molecular weight polymers.

In a similar paper,[79] the effect of gamma irradiation on *cis*-poly(isoprene) was also studied, and the $G(X)$ value of 0.81–0.88 obtained from NMR was in good agreement with the value of $G(X) = 0.8$ previously reported. In addition the magnitude of the virtual dose, as described above, allowed an

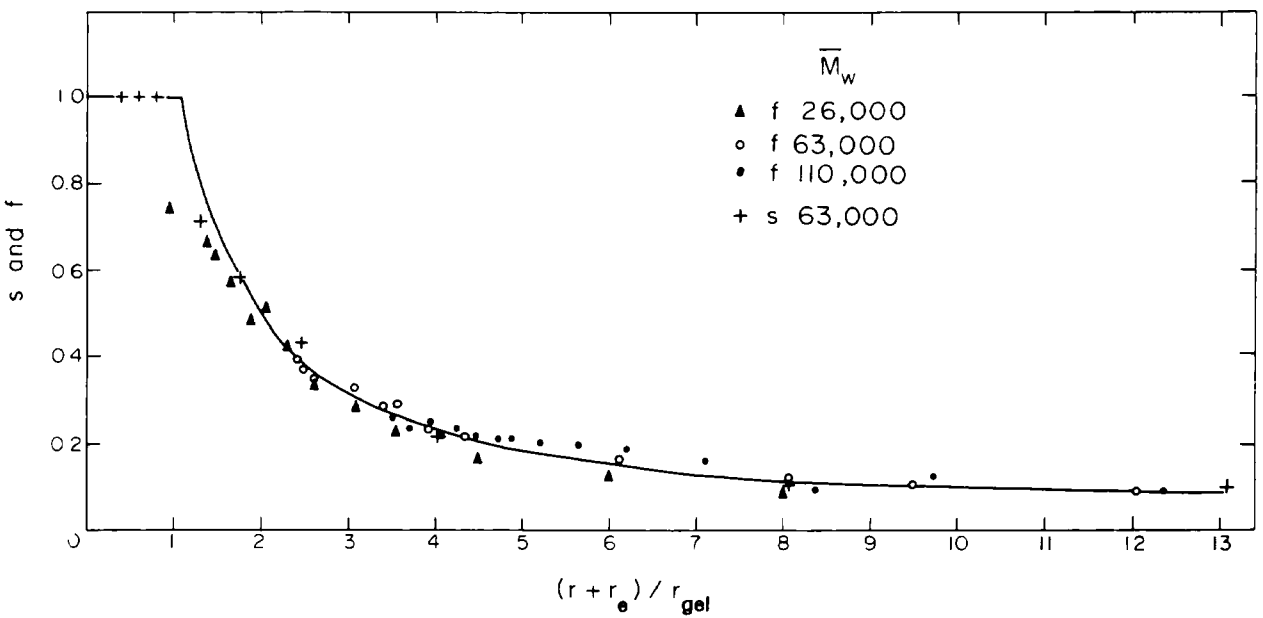

Fig. 5. Plot of the fraction f of the slowly relaxing protons in irradiated poly(dimethyl siloxane), obtained from measurements of the T_2 decays, as a function of the corrected radiation dose, and the best fit of the data to the Charlesby–Pinner equation. (Reproduced from reference 78 with permission. Copyright © 1977 Elsevier Science.)

estimate of the initial molecular weight between entanglements to be 40 000 at 423 K. This was compared with the estimate of $M_c = 30\,000$ also obtained by measurement of T_2 relaxation times.[80]

The analysis of the effects of radiation on poly(ethylene) having very high molecular weight was also investigated by Charlesby and coworkers,[81] and was complicated by the difficulty in fitting the T_2 decay of the molten irradiated polymer in an unambiguous manner. The decay could be described by the Kolrausch–Williams–Watt or stretched exponential:

$$M(t) = M(0)e^{(-t/T_2)^{\alpha}} \tag{11}$$

or fitting to the sum of three exponential decay processes. For ease of description the decay curves were fitted to two exponential decay processes, despite the fit being less adequate than that obtained assuming three processes. The two processes could not be assigned to protons in entangled and unentangled chains in the manner described above. This was ascribed to either non-random crosslinking, or the possibility that the short T_2 decay does not represent radiation-induced crosslinks.

Very recently this problem was revisited by Whittaker.[82] The decay curves, obtained using the CPMG sequence, were fitted to the sum of three exponential processes. The most rapid decay was ascribed to residual order in the molten phase, as suggested for unirradiated poly(ethylene) by previous workers.[83–85] The two longer decay processes were assigned to chains in a transition zone, and chains distant from both regions of order and crosslinks, in order of increasing T_2. Figure 6 shows the proportion of the three decay curves as a function of radiation dose, while Fig. 7 shows the heat of fusion of the polymer over the same dose range. The similarity of the two curves suggests that at low radiation doses the crystalline regions of poly(ethylene) are especially sensitive to radiation degradation, and that crosslinking occurs within or at the surface of the crystalline regions.

In a more recent study, Simon and coworkers[86] have examined the T_2 decay of irradiated *cis*-poly(butadiene) using the Hahn echo sequence. The decay curves were not exponential in nature, and the initial part of the decay was assigned as having contributions from near-static dipole–dipole interactions, which are refocused by the Hahn echo. The value of T_2 was related to the second moment of the rigid lattice line shape, and the correlation time of motion. The trends with radiation dose are reasonable. Similar conclusions were made with end-linked poly(dimethyl siloxane)[87] and filled and unfilled styrene–butadiene rubber.[88] More recently, Simon and Schneider have compared the values of M_c determined by such an analysis of the T_2 decay in filled and unfilled various elastomers, with M_c derived from measurements of ^2H quadrupolar splittings of drawn elastomers,[89] or from measurements of ^2H T_2 relaxation times.[90] Munie and coworkers[63] have also reported a "solid-like" component to the T_2 relaxation of crosslinked poly(butadiene).

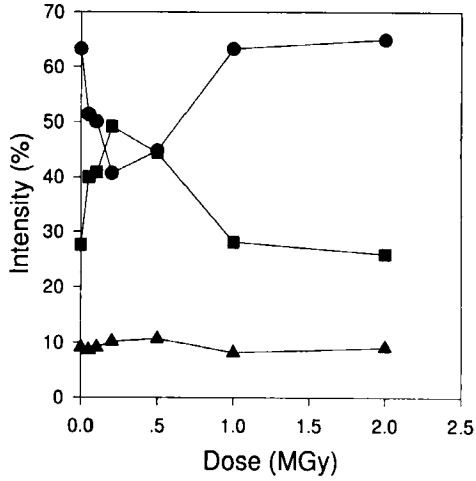

Fig. 6. Relative proportions (%) of the fast (●), intermediate (■) and slow (▲) relaxation decays in irradiated linear low-density poly(ethylene) as a function of radiation dose, measured at 430 K. (Reproduced from reference 82 with permission. Copyright © 1996 Elsevier Science.)

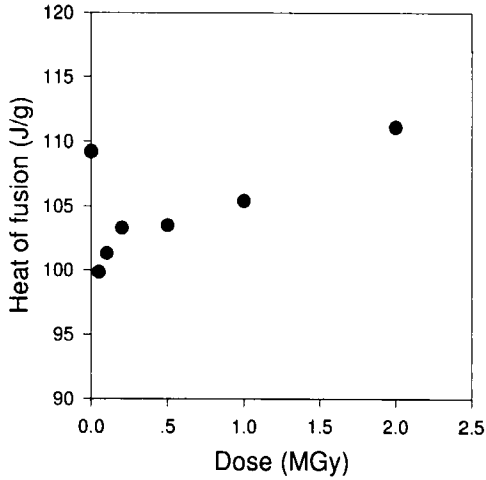

Fig. 7. The heat of fusion of irradiated linear low-density poly(ethylene) as a function of irradiation dose, measured by DSC. (Reproduced from reference 82 with permission. Copyright © 1996 Elsevier Science.)

Other T_2 studies of crosslinked polymers include crosslinking in chemically-crosslinked poly(butadiene),[64] determination of crosslink density in epoxy thermosetting resins,[91] a study of the motion in cured poly(imide) resins,[92] the study of crosslinked and linear poly(urethane) resins,[93,94] curing in phenolic resins,[95] and motion in poly(urethane) IPNs.[96]

Cohen-Addad and coworkers have used extensively the so-called pseudo-solid echo experiment,[97] which measures the residual dipole–dipole couplings not averaged by anisotropic chain reorientation. The presence of crosslinks will increase the proportion of chain segments undergoing such anisotropic motion, and hence increase the amplitude of the echo. In this manner the kinetics of crosslinking of poly(ethylene) by a free radical initiator were measured in real time.[98] The pseudo-solid echo decay curve was decomposed into two decays, corresponding to the decays for the uncrosslinked material, and the fully crosslinked polymer, respectively. The proportion of the decay due to the crosslinked material was seen to increase linearly with gel content.

In a more complete paper, the sulphur crosslinking of poly(butadiene) was studied by measurements of the decay of the amplitude of the pseudo-solid echo.[99] The decay functions described above were related to the distance between chain entanglements, being physical entanglements in uncrosslinked polymer, and chemical crosslinks after vulcanization. For poly(butadiene), however, the decays of the crosslinked material could not be described by the summation of these two functions. The low molecular weight fraction of the poly(ethylene) sample studied in reference[98] was said to play the role of a solvent, and therefore, the behaviour of the material while crosslinking was much more heterogeneous than for the poly(butadiene) sample of narrow molecular weight distribution.[99] The behaviour of the chain segments on crosslinking was therefore much more uniform in poly(butadiene), and hence separation of relaxation decays for fully-crosslinked and uncrosslinked polymer was not possible.

(ii) Measurements of T_2 *in swollen and elongated networks.* Cohen-Addad and coworkers have also studied extensively the swelling of polymer networks.[100–104] For example, the swelling behaviour of crosslinked poly(ethylene) in xylene was studied[100] in a manner similar to the above-mentioned study of the crosslinked melt.[98] The relaxation functions of the uncrosslinked melt, and the crosslinked swollen gel were modelled by a moment expansion to M_4. The residual dipolar energy was thus derived for a range of swelling ratios, and found to initially decrease at low swelling ratios, and subsequently increase at swelling ratios above $Q = 3.5$. A two-stage model is suggested for the swelling; at low swelling ratios the elementary chains remain Gaussian; however, at higher swelling ratios the network structure becomes stretched. The point at which the behaviour changes over corresponds to the swelling ratio at which the NMR lattice constant corresponds to the average distance between crosslinks. A similar study was conducted on poly(dimethyl siloxane).[101] A shift factor was used to superimpose the relaxation decays at different gel fractions, and was related to the decrease in free volume on crosslinking.

In a series of papers,[102–104] Cohen-Addad and coworkers have studied the effect of elongation of crosslinked swollen networks on the transverse

relaxation decays. Calculations demonstrate an expected dependence of the residual dipolar order on the term $\lambda^2 - 1/\lambda$.[102] Experimental validation of this dependence was obtained for crosslinked poly(butadiene).[103,104] In this final paper[104] Cohen-Addad and Soyez demonstrate the dependence of the NMR parameters on the angle the sample was aligned with respect to the magnetic field.

Von Meerwall and Ferguson[105] have studied the effect of stretching on the relaxation times of poly(butadiene) in the dry and swollen states. ^1H T_1 relaxation times of the dry rubber were found to be insensitive to orientation of the sample with respect to the magnetic field, however, T_2 showed a small dependence on orientation. Very similar results were obtained for the ^{19}F T_1 and T_2 relaxation times of a penetrant molecule C_6F_6. Analysis of the angular-dependence of T_2 of the penetrant showed that allowance had to be made for a distribution of orientations of polymer segments about the stretch direction. As expected the width of the distribution of angles decreased with increasing elongation, and could be modelled by assuming a diffusive path for the penetrant, and affine deformation of the elastomer. Finally, the self-diffusion coefficients for the penetrant molecules were measured by PFG NMR, and found to be isotropic. This indicates that sufficient diffusion pathways exist perpendicular to the draw direction, up to an elongation as high as $\lambda = 10$.

More recently, Brereton[106,107] has presented a reinterpretation of the above results. Brereton[106] points out that the term "nematic" applied to the ordering of chain segments in strained networks implies spontaneous ordering of the polymer at some lower temperature, despite the networks polymer being considered being disordered materials. However, this point appears debatable. Nonetheless, Brereton derives an expression for the NMR line shape due to the effects of constraints, i.e. network points, based on a scaling argument. The assumption of a Gaussian distribution of vectors connecting junction points leads to a line shape which does not show splittings. Brereton then calculates the effect of neighbouring chain segments on the NMR line shape using excluded volume arguments. The inclusion of deformation into the system results in splitting of the resonance line. These studies of elongated networks are closely related to the ^2H NMR studies discussed in Section 5.

3. ^{13}C NMR STUDIES OF CROSSLINKED POLYMERS

3.1. ^{13}C NMR studies of polymers swollen with solvents

3.1.1. Polymers swollen with organic solvents

High-resolution ^{13}C NMR spectra of crosslinked polymers can be obtained without resorting to magic angle spinning and high power ^1H decoupling by

swelling the polymer with a solvent, and thereby effectively reducing the glass temperature well below the measurement temperature. The molecular motions thus liberated are efficient at reducing the strength of the dipole–dipole couplings to acceptable levels. Schaefer[108] first demonstrated this for crosslinked ethylene–maleic anhydride copolymer swollen with dimethylformamide.

A number of groups have studied the limits and applicability of this method. Manatt and coworkers[109] obtained excellent high-resolution ^{13}C spectra of crosslinked chloromethylated poly(styrene)s, with the aim of determining the extent of substitution of the chloromethyl and hydroxymethyl groups. Measurements of the nuclear Overhauser enhancement (NOE) were made. Ford and coworkers[110–113] have produced a series of papers also concerned with poly(styrene) resins. In the initial study[110] a series of poly(styrene) resins were prepared with a range of concentrations of divinyl benzene crosslinking agent. The samples were swollen to equilibrium with deuterated chloroform and measurements were made of T_1, ^{13}C linewidths, and NOE factors using a conventional solution-state NMR spectrometer. T_1 was relatively unaffected by crosslinking, indicating no change in the spectral density of motions in the MHz frequency range. On the other hand the linewidth increased with increasing crosslink density. Most significantly, the intensity of the peaks decreased significantly, with the peaks associated with the aliphatic backbone being more strongly affected than those due to the aromatic side chains. The loss of intensity was ascribed to inefficient decoupling of the dipole–dipole interactions both by the low-power ^1H decoupler used, and by restricted molecular motion. It was concluded that this experiment is only observing parts of the structure removed from the crosslinks.

In a later study, Mohanraj and Ford[111] have attempted to account for the decrease in intensity in the ^{13}C spectra of crosslinked chloromethylpoly(styrene)s in a more quantitative manner. The results indicate that carbon nuclei in crosslinks are not detected by solution-state NMR methods, and that uncrosslinked units with either one or two adjacent units which are crosslinked are also not observed. Errede *et al.*[114] have examined further the experimental dependence of linewidth on crosslink density in poly(styrene) crosslinked with divinylbenzene. They find that the linewidth is proportional to the crosslink density raised to the power 1.6, an exponent larger than predicted by other workers. In other studies of this type, Marchall and Wilson have examined swollen crosslinked poly(ester) resins,[115,116] while Hodgkin has reported high-resolution spectra of crosslinked poly(3,4-pyrrolidinediylethylene)s.[117]

The problem of residual dipolar couplings in swollen crosslinked polymers has been addressed by Stöver and Fréchet[118,119] who have shown that magic angle spinning (MAS) and dipolar decoupling reduces the residual linewidth to values similar to those observed for uncrosslinked polymers. The relative

peak intensities in the spectra are close to those predicted from the known structure of the polymer. In a second paper[119] the authors suggest the use of cross-polarization to measure selectively the crosslink points in the polymer gels.

Several groups have reported studies of solvents in crosslinked networks.[112,113,116,120–122] Ford and coworkers have studied the ^{13}C spectra of toluene in crosslinked poly(styrene) gels.[112] Two sets of peaks are observed in the ^{13}C spectra, due to toluene inside and outside the gel structure. T_1 measurements suggested a reduction in the rate of rotational diffusion of the solvent within the gel. The T_1 of the toluene molecules outside the gel was affected by exchange with toluene within the gel. In a second paper,[113] the rate of exchange was measured by selective inversion of the magnetization of one of the components using the DANTE pulse sequence. Marshall and Wilson[116] have reported that the difference in chemical shift between solvent internal and external to network structures depends on the degree of crosslinking. They suggest the use of the ^{13}C technique to measure swelling rates. Similar observations have been made using ^{1}H NMR spectroscopy.[123,124] Other studies of linewidth and relaxation times of small organic molecules in crosslinked gels have been reported by Simon and coworkers[120] and Ogino and Sato.[121]

3.1.2. Polymers swollen with water

The observation of improved resolution in ^{13}C spectra of swollen polymers has also been applied to hydrogel materials. Yokota and coworkers[124] examined a number of crosslinked hydrogel materials including poly(*N*-vinylpyrrolidone), copolymers of *N*-vinylpyrrolidone with methylmethacrylate (MMA), and poly(hydroxyethyl methacrylate). Linewidths were seen in decrease with increasing water content (corresponding to decreasing crosslink density) and increasing temperature. Spectra of the copolymers swollen with water did not show any peaks due the hydrophobic MMA monomers. The peaks were visible, however, when the polymer was swollen with a good solvent for poly(MMA). In a more recent study, Bain and coworkers[125] have examined the mechanism of line broadening in the ^{13}C spectra of poly(sodium acrylate) swollen with water. The NMR linewidth was found to depend linearly on field strength, and was confirmed to be inhomogeneous using a hole burning experiment. It was concluded that chemical shift dispersion was a major contributor to the linewidth of the materials under study. Other studies have concluded that, particularly at higher crosslink densities, dipole–dipole interactions become significant.[118,119] McBrierty and colleagues[126] have shown further that molecular motion in hydrated gels can interfere with the efficiency of decoupling as suggested by Rothwell and Waugh[127] and Takagoshi.[128] The ^{13}C linewidth of α,ω-dicarboxylatopolybutadiene gels increases with increase temperature from 200 K

to 290 K and subsequently decreases, indicative of molecular fluctuations of frequencies close to the frequency of the decoupling field.

Allen and coworkers[129] have studied the effect of hydration on the ^{13}C $T_{1\rho}$ times of crosslinked poly(hydroxyethyl methacrylate). Increasing water content decreases the ^{13}C $T_{1\rho}$ of main-chain and side-chain carbons. Increasing the level of crosslinking has the reverse effect. The results are consistent with changes in the spectral density of motions in the mid-kHz range observed on plasticization and crosslinking, respectively. Yasunaga and Ando[130] have studied motions in the MHz range by measuring ^{13}C T_1 of gels of poly(methacrylic acid). Changes in T_1 were observed for all carbon types, and indicated restriction of motion on crosslinking.

The range of techniques discussed in this section have been utilized by Kobayashi *et al.*[131] in a study of poly(vinyl alcohol) gels. Figure 8 shows the effect of measurement technique on the ^{13}C NMR spectra. The resolution in the spectrum of the swollen gel (Fig. 8(B)) is inferior to the spectrum of the dilute solution (Fig. 8(A)), however, magic angle spinning of the gel does lead to an improvement in resolution. The use of cross-polarization results in the detection of the immobile component of the gel (Fig. 8(D)) as detected in the rigid solid (Fig. 8(E)). The significance of H-bonding on the gel formation was discussed by these authors.

3.2. ^{13}C solid state NMR

3.2.1. Background

The technique of magic angle spinning (MAS) was introduced by Andrew and coworkers[132] and Lowe[133] in 1959. The aim of the experiment at that time was to partially average homonuclear dipole–dipole couplings in ^1H-rich materials. It was not until more than a decade later that MAS was first used in ^{13}C NMR spectroscopy. At this time Pines, Gibbey and Waugh[134] had introduced the experiment now known as cross-polarization (CP). The combination of the two techniques, as well as the use of high-power ^1H decoupling was first applied to solid polymers by Schaefer and Stejskal in 1976,[135] and revolutionized the field of analysis of insoluble materials, including crosslinked polymers.

In the absence of isotropic motion, the ^{13}C NMR line shape is dominated by strong dipole–dipole couplings to neighbouring protons, and the relatively large anisotropy of the chemical shift tensor. The technique of MAS deals effectively with the latter of these effects, since rapid rotation of the sample around the magic angle leaves only the trace of the tensor, i.e. the isotropic chemical shift, observable. Rotation at intermediate spinning speeds results in a series of rotational echoes in the FID, which on Fourier transformation results in the familiar spinning side bands.[136] Magic angle spinning also

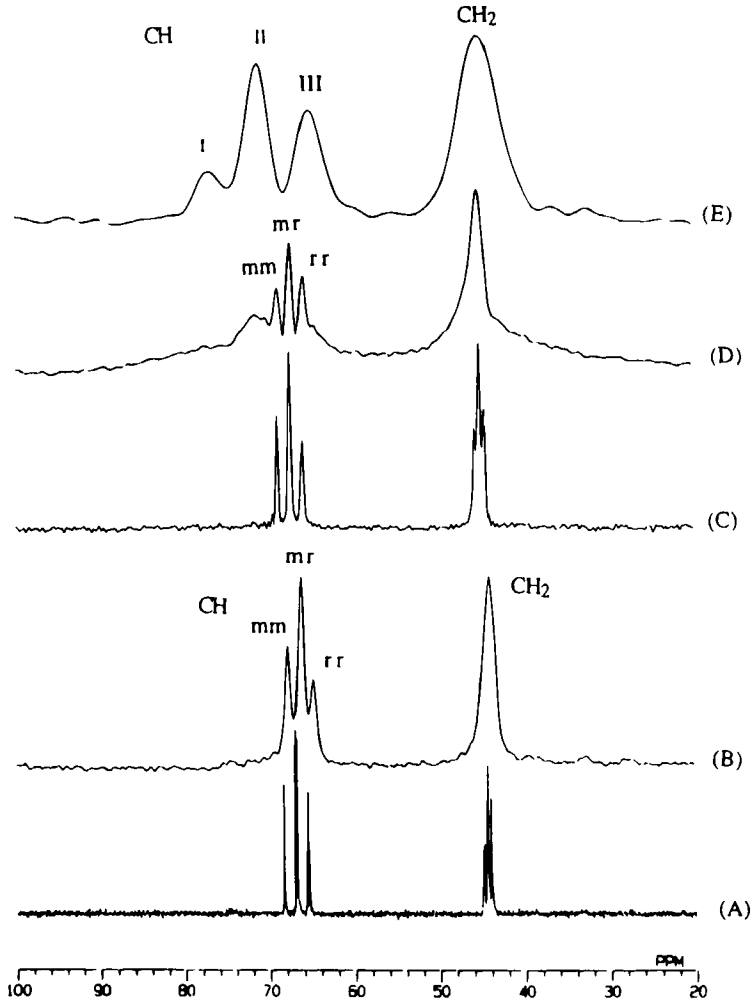

Fig. 8. ^{13}C NMR spectra of poly(vinyl alcohol) recorded under different experimental conditions: (A) solution-state spectrum of solution; (B) solution-state spectrum of gel; (C) spectrum of gel using high-power decoupling and MAS; (D) CPMAS spectrum of the gel; (E) CPMAS spectrum of solid poly(vinyl alcohol). (Reproduced from reference 131 with permission. Copyright © 1995 American Chemical Society.)

partially averages the heteronuclear dipole–dipole couplings, however, high-power proton decoupling during acquisition is required to fully remove this contribution to the ^{13}C NMR line. The combination of MAS and high-power ^{1}H decoupling is sufficient to achieve high-resolution ^{13}C NMR spectra of solid polymers.

The sensitivity of the ^{13}C NMR experiment is limited by the often very long spin–lattice relaxation times of the ^{13}C nuclei. Values of ^{13}C T_1 of up over 1000 s have been measured in solid poly(ethylene).[137] Pulse repetition times, and hence total scan times are often prohibitively long. The technique of cross-polarization overcomes this problem since the spin temperature of the protons and not the ^{13}C nuclei has to re-equilibrate before pulse repetition. In addition the signal-to-noise ratio is increased by a factor of up to four, due to the larger Boltzmann population of the proton nuclei. The method of cross-polarization is dealt with in more depth in the next section.

3.2.2. Quantitative aspects of cross-polarization

In the cross-polarization experiment a number of different relaxation time constants need to be accounted for to obtain quantitative peak intensities. The experiment consists of a $\pi/2$ ^1H pulse to cool the proton spin temperature followed by spin-locking of the proton magnetization in the rotating frame. During this time, spin–lattice relaxation processes at *ca.* 50–100 kHz frequencies occur which are described by the time constant, ^1H $T_{1\rho}$. Cross-polarization is effected by applying a ^{13}C pulse of matched amplitude during the ^1H spin-lock period. Magnetization is created in the ^{13}C spin reservoir due to transfer from the ^1H spin reservoir at a rate described by the time constant, T_{CH}. This process is due to static dipole–dipole interactions, and hence is at a maximum in the absence of motion. A competing relaxation mechanism during cross-polarization is relaxation of the ^{13}C magnetization in the rotating frame, described by ^{13}C $T_{1\rho}$, which is also sensitive to motions of frequencies around 50–100 kHz, and in addition coupling to the dipolar reservoir.[138,139] After cross-polarization the ^{13}C signal is observed with simultaneous ^1H high-power decoupling. Finally, the experiment can be repeated after allowing for relaxation of the ^1H spins, described by ^1H T_1. It is generally accepted that the process of spin diffusion during the recycle delay produces an average ^1H T_1, and therefore incomplete ^1H relaxation does not usually influence the relative peak intensities.

The rate of change of ^{13}C magnetization in the cross-polarization experiment described in the previous paragraph has been shown to be described by[140]

$$M_S = \frac{M_{IO}}{T_{CH}} \cdot \left[\frac{1}{T_{CH}} + \frac{1}{T_{1\rho}^C} - \frac{1}{T_{1\rho}^H} \right] \cdot \left[e^{-1/T_{1\rho}^H} - e^{-t(1/T_{CH} + 1/T_{1\rho}^C)} \right] \qquad (12)$$

where $M_S(t)$ is the ^{13}C signal as a function of time, M_{IO} is the initial proton spin temperature, and T_{CH}, $T_{1\rho}^H$ and $T_{1\rho}^C$ are the time constants defined above. Note that the rate of build up of magnetization may not necessarily be exponential.[141]

It follows from the above that knowledge of the rate of cross-polarization T_{CH}, and relaxation times $T_{1\rho}$ is necessary before quantitative intensities can be obtained in ^{13}C CPMAS spectra. It is often assumed that ^{13}C $T_{1\rho}$ is very long compared with T_{CH} and $T_{1\rho}$, and therefore its influence on the relaxation dynamics can be ignored. This is despite some evidence to the contrary. Schaefer *et al.*[139] have shown that in many glassy polymer systems there is a strong dispersion in ^{13}C $T_{1\rho}$, and therefore the assumption of a single long ^{13}C $T_{1\rho}$ may not always hold.

The two additional simplifying assumptions often made in the analysis of the cross-polarization dynamics are that (1) $T_{1\rho}$ (^{13}C) > $T_{1\rho}$ (^{1}H) and (2) $T_{CH} << T_{1\rho}$ (^{1}H), leading to the often-used simplified equations (13) and (14), respectively.

$$M_S = \frac{M_{IO}}{T_{CH}} \cdot \left[\frac{1}{T_{CH}} - \frac{1}{T_{1\rho}^{H}}\right] \cdot [e^{-1/T_{1\rho}^{H}} - e^{-1/T_{CH}}] \tag{13}$$

$$M_S = M_{IO}[e^{-1/T_{1\rho}^{H}} - e^{-1/T_{CH}}] \tag{14}$$

In highly heterogeneous materials, such as many crosslinked polymers, knowledge of the full behaviour of the magnetization as a function of cross-polarization contact time is necessary. In many rigid polymers, effective spin diffusion results in a constant rate of ^{1}H $T_{1\rho}$ across the range of ^{13}C nuclei present in the polymer. In this case, it is often stated that quantitative intensities can be obtained by collecting a single cross-polarization spectrum with a contact time beyond the maximum in the plot of intensity versus contact time. These conditions tend to only apply in crosslinked systems once the glass transition temperature of the polymer has increased to above the measurement temperature. In special cases, however, the effects of spin diffusion, for example in the case of the presence of strongly relaxing relaxation sinks, may lead to distortion of the signal intensities. The more typical behaviour is shown in Fig. 9, which shows the signal intensity of individual peaks resolved in the ^{13}C CPMAS spectra of crosslinked poly(butadiene) as a function of contact time.[142] The value of the ^{1}H $T_{1\rho}$ for the peak due to the crosslinked parts of the matrix is considerably shorter than that for the peak due to uncrosslinked chains, which appears to have a bi-exponential $T_{1\rho}$ decay. Analysis of such data is difficult, and relies on the assumption that spin diffusion does not strongly distort the peak intensities during the CP experiment. It is important that the data are checked for internal consistencies based on knowledge of the structures formed during crosslinking; for example in this case, the area of the peak due to carbons in crosslinked structures should be comparable to the decrease in area of the peak due to carbons in double bonds.[142]

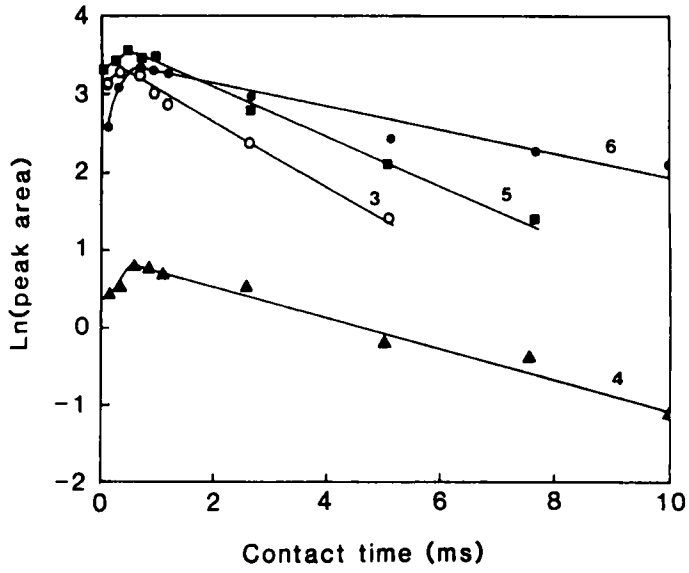

Fig. 9. Variation in intensity of individual peaks resolved in the ^{13}C CPMAS spectra of crosslinked poly(butadiene) irradiated to 3 MGy, as a function of contact time. The curves are due to (3) methine carbons in crosslinked structures, (4) methylene carbons adjacent to *trans* double bonds, (5) methylene carbons adjacent to crosslinks, and (6) methylene adjacent to *cis* double bonds. (Reproduced from reference 142 with permission. Copyright © 1992 John Wiley & Sons.)

3.3. ^{13}C NMR studies of crosslinked polymers

3.3.1. Crosslinking of poly(olefin)s

(i) Radiation crosslinking. One of major aims in the study of radiation crosslinking of polymer has been the direct observation and quantification of crosslinks. Polymers, particularly poly(olefin)s, are crosslinked by electron beam or gamma rays to improve abrasion resistance and reduce high-temperature distortion in applications such as coatings for wires and hot water pipes. As discussed in Section 1.2, once the level of crosslinks reaches approximately one link on average per chain, the polymer reaches the gel state, and is largely insoluble. The concentration of crosslinks at the gel point for polymers with initially high molecular weight is very small, of the order of one carbon per 10^4 to 10^5 carbons in the main-chain. For this reason model compounds were initially studied. Bennett *et al.*[143] reported the formation of H-type crosslinks in irradiated liquid *n*-hexadecane and *n*-eicosane. H-links are believed to form by the mutual recombination of main-chain

alkyl radicals,[144] which are highly mobile due to the efficient H-hopping mechanism. Bovey *et al.*[145] observed H-links and long-chain branching (Y-links) in n-$C_{44}H_{99}$ irradiated in the melt, whereas irradiation in the crystalline state gave only linear dimers, apparently through end-linking of the chains at surface of the crystals.

Randall and coworkers[146] were the first to report the identification of crosslinks on the NMR spectra of irradiated high molecular weight polymers. Y-links were detected in linear poly(ethylene) irradiated to below the gel dose at 298 K. On the other hand, H-links were observed when the irradiation temperature was increased to 450 K, i.e. in the molten state. The authors suggested that the major linking reaction at low doses involved addition of main-chain alkyl radicals to terminal double bonds initially present in linear poly(ethylene). This mechanism was previously suggested by Lyons *et al.*[147]

Horii and coworkers[148,149] have irradiated low molecular weight fractions of linear poly(ethylene) to below the gel dose at a range of temperatures, and identified both H- and Y-links using ^{13}C solution-state NMR.[148] New peaks were identified for three types of carbons in H-link structures, while the formation of Y-links was inferred from an increase in the peaks due to long-chain branches. The yields of H- and Y-links were G(H-link) = 0.74 and G(Y-link) = 0.27, for irradiation in the molten state. The authors also presented measurements of changes in concentration of other structures. For example, terminal vinyl groups were completely consumed during irradiation, possibly resulting in the formation of Y-links. In a second paper from this group,[149] the effect of irradiation temperature on the yield of crosslinks is studied. At low temperatures H-linking predominates over Y-linking, while at higher temperatures the situation is reversed. The decrease in stability of the primary radical at higher temperatures is suggested to account for this effect.

The presence of H-links in irradiated ethylene–propylene rubbers was demonstrated by O'Donnell and Whittaker[150] in a ^{13}C solution-state NMR study. The width of the line due to the methine carbon in H-crosslinks increased with increasing level of crosslinking, and eventually this line disappeared in the rising baseline in the spectrum. It was not possible to quantify the level of crosslinking from these spectra. It is evident that, at higher levels of crosslinking, solid state NMR techniques need to be utilized.

Sohma and coworkers[151] were the first to use solid state NMR to analyse radiation-crosslinked poly(olefin)s. The ^{13}C CPMAS spectrum of irradiated ethylene–propylene rubber showed an increase in intensity at 37 ppm on crosslinking, due to the methine groups of crosslinks, as well as a new peak at 24 ppm due to the products of main-chain scission. The peak at 37 ppm was poorly resolved, and the low signal-to-noise level made definite assignment difficult. O'Donnell and Whittaker[152] applied the same technique

to ethylene–propylene rubbers irradiated to an even higher radiation dose, and were able to estimate yields for crosslinking and scission which were in excellent agreement with values obtained from measurement of the soluble fractions. The authors concluded that the assumption of random crosslinking implicit in the Charlesby–Pinner equation (3) was valid in this case.

Havens *et al.*[153] have reported that irradiation crosslinking in poly(1,11-dodecadiyne) proceeds through cross-polymerization of the acetylene groups, resulting in alternating double and triple bonds. The crosslinking occurs in the crystalline state of the macromer, where the reactive groups have favourable conformations for the free radical chain reaction.

The radiation-crosslinking of *cis*-1,4-poly(butadiene) proceeds, on the other hand, through a chain reaction involving consumption of double bonds. Barron and coworkers[142,154] have measured the ^{13}C CPMAS spectra of samples irradiated to various doses up to 10 MGy. Figure 10 shows the changes in the CPMAS spectra as a function of radiation dose. The peak at 130.5 ppm due to double bonds decreases on irradiation, while a new broad peak at 45.8 ppm assigned to methine carbons in crosslinks appears. The peak due to methine groups adjacent to crosslinks appears at 30.5 ppm, as shown in the simulation of the aliphatic region of the spectrum in Fig. 11. Spectra were recorded at a range of cross-polarization contact times up to 25 ms, and the results analysed as described in Section 3.2.2 to yield quantitative yields of crosslinks, and for loss of double bonds. *G*-values were of the order of 28,[142] indicating a chain reaction was involved in the crosslinking. The clusters of crosslinking so-produced explain the relatively low *G*-values for crosslinking ($G(X) = 3–6$) determined from gel contents and swelling measurements. A *cis–trans* isomerization reaction was also characterized, and emphasized the importance of allyl radicals in the initial stage of crosslinking. In the second of these papers, O'Donnell and Whittaker[142] examined the effect of chemical composition, and dose on a range of different poly(butadiene) samples. Similar results were obtained for *cis*- and *trans*-1,4-poly(butadiene), however, even large *G*-values were measured for 1,2-poly(butadiene), presumably because of a zipping chain reaction of the pendant vinyl groups. This group[155,156] has also examined the crosslinking in butyl rubber,[157] natural rubber sensitized with acrylates,[158] chloroprene,[159] chlorobutyl rubber[160] and nitrile rubber.[161]

Patterson and Koenig[162] have reported the radiation crosslinking of natural rubber, *cis*-poly(isoprene), studied by solid state ^{13}C NMR. A highly heterogeneous structure was evidenced by differences in the spectra obtained by direct polarization of the ^{13}C nuclei, and those obtained using CP. CPMAS spectra showed resonances due to crosslinks, and new chain ends formed by degradation processes. The isomerization of *cis* double bonds to the *trans* configuration was also followed. A lower yield of isomerized double bonds was measured compared with a peroxide-cured sample.

Up to this point the aim of detecting peaks in the solid state NMR spectrum

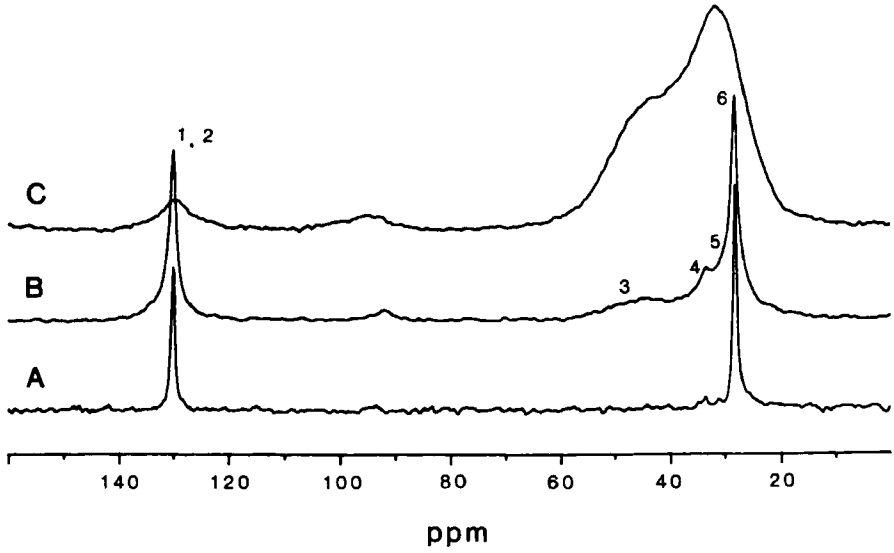

Fig. 10. ^{13}C CPMAS spectra of irradiated poly(butadiene) as a function of radiation dose: (A) 0.44 MGy; (B) 3 MGy; (C) 10 MGy. (Reproduced from reference 142 with permission. Copyright © 1992 John Wiley & Sons.)

due to crosslinks in poly(ethylene) had not been achieved. The solid state ^{13}C NMR spectrum of poly(ethylene) is dominated by a peak at 32.5 ppm due to methylene units in chain segments having all-*trans* configurations, and a broad peak centred on 29.0 ppm due to chains with *gauche* configurations.[163,164] The broad shoulder of the peak at 32.5 ppm, and the appearance of a peak at 34.0 ppm due to all-*trans* chains in monoclinic unit cells[165] made observation of a new peak due to the methine group of the crosslink (expected at 35–45 ppm) problematic. Cholli and coworkers[166] were the first to convincingly demonstrate the direct observation of crosslinks in poly(ethylene) by solid state NMR. ^{13}C CPMAS NMR spectra of high-density poly(ethylene) irradiated to 6 MGy showed two small new peaks at 43 ppm and 39.7 ppm, assigned to methine carbons in Y- and H-links respectively. The formation of Y-links or branches was confirmed by the appearance of new peaks at 30.0, 7.8 and 15.4 ppm due to branch structures.

O'Donnell and Whittaker[167] have also studied this problem, and reported the changes in crystalline content and dimensions from DSC and spin diffusion measurements. A peak at 39.5 ppm was also observed by these authors, and also assigned to methine carbons in H-crosslinks. Spectra were recorded as a function of cross-polarization contact time up to 25 ms, and it was found that the methine carbons had a very long ^1H $T_{1\rho}$, and therefore the peak became more prominent at longer contact times. The long ^1H $T_{1\rho}$

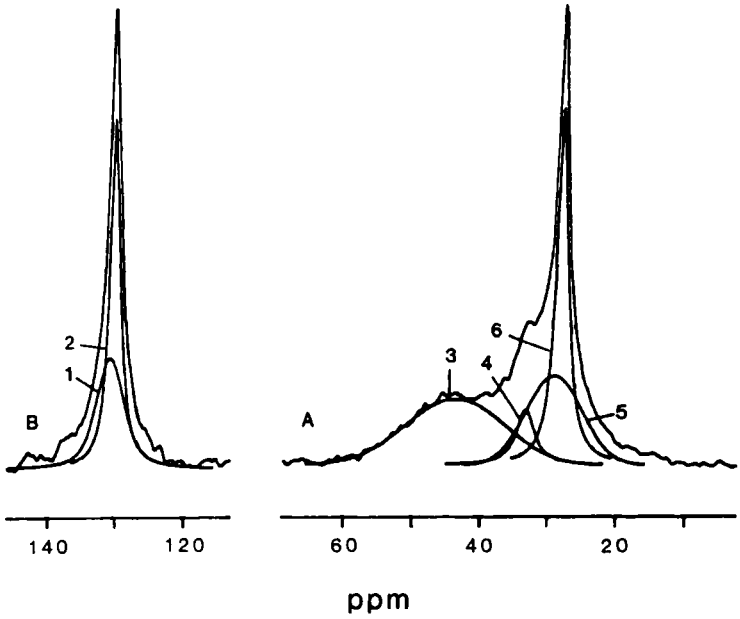

Fig. 11. Computer simulation of the aliphatic region of the spectrum of poly(butadiene) irradiated to 3 MGy. The peaks which appear in the spectrum after crosslinking are labelled 1, 3 and 5. (Reproduced from reference 142 with permission. Copyright © 1992 John Wiley & Sons.)

is consistent with a very rigid structure, since the intrinsic ^1H $T_{1\rho}$ of the rigid protons in the crystalline domains of poly(ethylene) are also reported to be very long.[e.g.168] The yield of crosslinks obtained from analysis of the NMR spectra was very close to the yield obtained from analysis of the soluble fraction. It was therefore concluded that crosslinking occurs randomly throughout the amorphous phase of poly(ethylene). Pérez and VanderHart[169] have also used ^{13}C CPMAS to study irradiated poly(ethylene), however, were unable to observe peaks due to crosslinks in samples irradiated up to 2 MGy. Their elegant study was on the other hand concerned with characterizing the partitioning of chain-end structures into the crystalline and amorphous phases.

Cholli and coworkers[170,171] have studied the effect of crosslinking on the motion of chains in irradiated poly(ethylene oxide). The ^{13}C CPMAS spectra of irradiated polymer showed an increase in the intensity of a broad resonance at 71.9 ppm due to chains within crystalline regions.[170] This was attributed to crystallization of chains arising from local rearrangement of polymer chains. Irradiation in vacuum resulted in a crosslinked material; however, main-chain scission was the major event observed after irradiation in air, as confirmed by solution-state ^{13}C NMR. No new peaks due to

crosslinks were observed. In a second paper the authors investigate in detail the changes in motion of the chains within the crystalline regions upon crosslinking. The ^{13}C CPMAS NMR signal of chains within the crystalline regions of poly(ethylene oxide) is usually attenuated strongly compared with the peak due to chains within the amorphous regions. This is a result of the very short ^{1}H $T_{1\rho}$ of carbon nuclei in the crystalline regions of poly(ethylene oxide), due in turn to the proximity of the alpha relaxation (motion of the chain within the crystalline region) to the measurement temperature.[172,173] An increase in ^{1}H $T_{1\rho}$ of the protons within the crystalline regions is observed upon crosslinking, due to restriction of this motion by the formation of crosslinks at the surface of the crystalline lamellae. This was further confirmed by melting and recrystallization of the sample. The NMR spectrum of this sample was nearly identical to that of the unirradiated material, due to a redistribution of the crosslinks throughout the amorphous phase.

The effect of crosslinking on molecular motion was exploited by Beckham and Spiess[174] to identify the location of crosslinks in irradiated poly(1,23-tetracosadiyne) and poly(ethylene). A two-dimensional wide-line separation experiment called "WISE"[175] was used to measure the ^{1}H wide-line spectrum associated with each carbon type represented in the ^{13}C CPMAS spectrum (see Fig. 12). In this way the motion of the particular carbons could be studied from changes in the widths of the ^{1}H NMR spectra associated with each carbon. Crosslinking reactions in poly(1,23-tetracosadiyne) occur within the well-ordered crystalline regions, as suggested by Havens *et al.* in a much earlier study.[153] The width of the ^{1}H NMR spectrum associated with carbon nuclei within the amorphous regions is unaffected by crosslinking, indicating no change in the molecular motion of these chains. The same experiment was conducted on irradiated poly(ethylene). It was observed that the ^{1}H spectrum associated with chains within the amorphous region is substantially broader in the irradiated material compared with the unirradiated polymer, and therefore it was concluded that crosslinking occurred predominantly within the amorphous regions of poly(ethylene).

(ii) Sulphur and peroxide curing of poly(olefin)s. The vulcanization of natural rubber with sulphur was first performed in 1841, and since then has become the basis of the enormous automobile tyre industry. Initially the process consisted of simply mixing rubber and sulphur and heating to approximately 410 K for several hours. The cure time, and hence competing oxidative reactions, have been reduced by the use of so-called accelerators, such as aromatic amines, guanidine derivatives, and dithiocarbamates, in conjunction with activators such as zinc oxide and stearic acid. Despite much study, the mechanism of crosslinking is complex and remains unresolved. Addition of the sulphur can occur at the double bonds, as in unaccelerated cure, or at one of the allylic positions, as in accelerated vulcanization. Solid

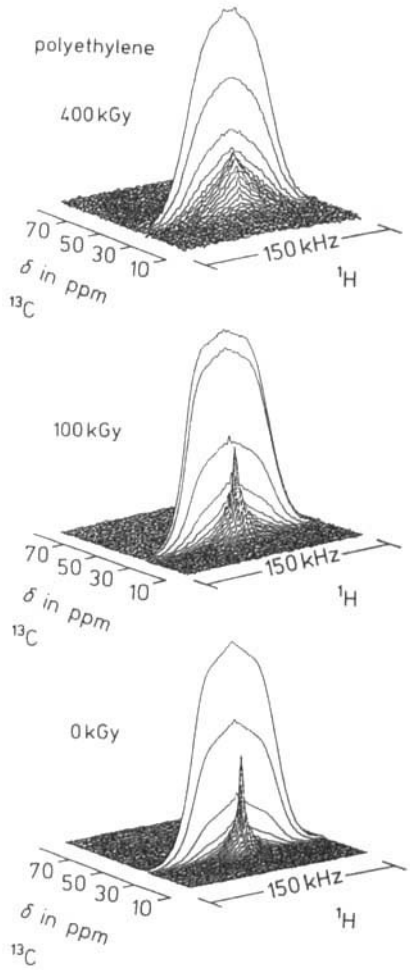

Fig. 12. 2D "WISE" spectra of poly(ethylene); unirradiated, and irradiated to 100 kGy and 400 kGy. (Reproduced from reference 174 with permission. Copyright © 1994 Hüthig and Wepf Verlag.)

state NMR has made a significant contribution to the characterization of vulcanization reactions.

The analysis of the sulphur vulcanization of rubber materials has been the subject of an extensive series of publications by Koenig and coworkers.[176–192] The authors have attempted to cover the very wide range of reactions which occur in vulcanization reactions. In early work, Zaper and Koenig[177,178] studied the reaction of sulphur with natural rubber. As shown in Fig. 13, profound changes in the ^{13}C NMR spectra were observed on curing. The increase in linewidth on curing reflects the decrease in segmental motion on

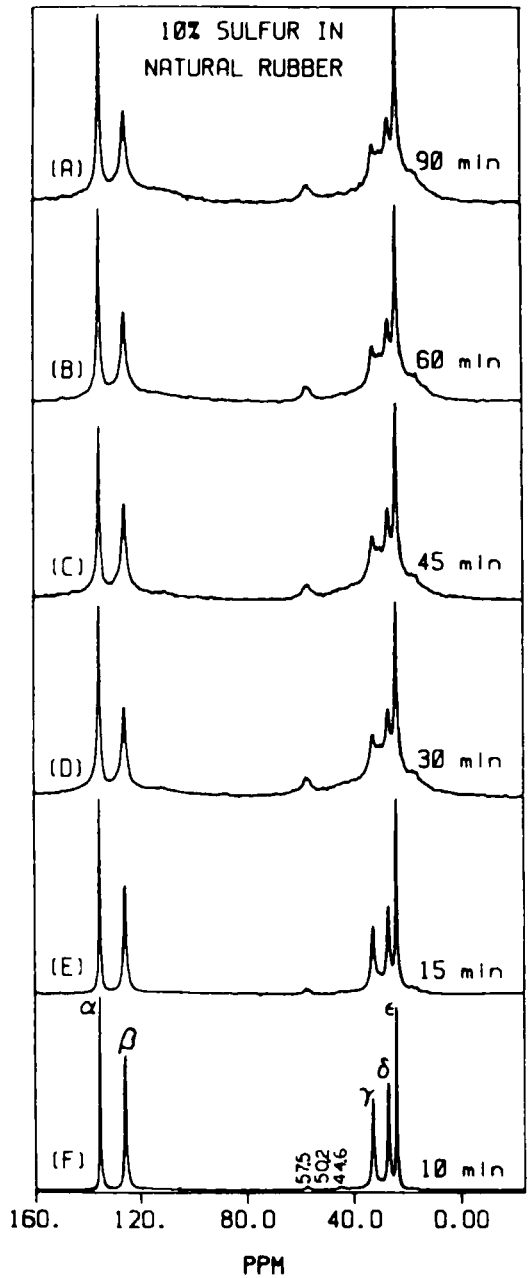

Fig. 13. ^{13}C single-pulse NMR spectra of natural rubber cured with 10% sulphur at 423 K for times ranging from 10 to 90 min. (Reproduced from reference 178 with permission. Copyright © 1987 American Chemical Society.)

crosslinking. New peaks were observed on both the high-field and low-field sides of the peaks in the aliphatic region. At higher levels of cure, however, the resolution deteriorates and chemical information is lost. Cross-polarization was used to obtain spectra of the immobile component of the crosslinked rubber. The major new peak at 58 ppm is assigned to methine groups in polysulphidic crosslinks, on the basis of comparisons with model compounds. The intensity of this peak was shown to be inversely proportional to the swelling ratio. Other new peaks in the spectra were assigned to carbons in crosslinks in which addition of sulphur occurs at all four possible sites adjacent to the double bonds. In addition the presence of cyclic structures was confirmed. The use of accelerator resulted in a more simple network structure containing less cyclic structures.[178]

Zaper and Koenig[179] have confirmed a similar mechanism for the vulcanization of *cis*-1,4-butadiene rubber. Again addition of the sulphur at the methylene unit adjacent to the double bond was observed. Peaks indicative of *cis–trans* isomerization and cyclic structures were also observed. In a more detailed paper, Clough and Koenig[182] measured the changes in the peak intensities in the ^{13}C spectra of cured poly(*cis*-1,4-butadiene) as a function of curing time. The spectra were recorded using single-pulse excitation, and with a recycle delay of seven seconds, longer than five times the longest T_1. Under these conditions quantitative spectra were obtained. The data suggest that the curing reactions are virtually complete after curing at 423 K for 100 min. In this paper the use of the DEPT pulse sequence to obtain sub-spectra of the different carbon types is also demonstrated.

The use of the single-pulse excitation experiment to obtain quantitative signal intensities in the ^{13}C NMR spectra is predicated on the assumption that the ^{13}C spins have relaxed fully during the recycle delay. As a background to this, Andreis and coworkers[183] have conducted a variable temperature study of ^{13}C T_1 in crosslinked natural rubber as a function of cure time (also discussed in Section 3.5.1). After curing, the minima in the plots of T_1 versus inverse temperature become broader for all carbon types, and both the temperature of the minimum, and the value of T_1 at the minimum increase on curing. These observations are consistent with an increase in T_g on curing, an increase in the anisotropy of motions, and a coupling of motions throughout the network. The motion of the methyl group is less affected by crosslinking than the motion of the main-chain.

In more recent years, Koenig and coworkers have studied a large range of modified crosslinking reactions. These studies include the use of tetramethylene thiuram disulphide as a sulphur donor agent,[185] sulphur vulcanization of poly(isoprene) in the presence of *N*-*t*-butyl-2-benzothiazole sulphenamide (TBBS)[186,187] or *N*-*t*-butyl benzothiazole sulphenimide[188] acting as an accelerator, vulcanization of poly(butadiene) having a high content of vinyl groups,[189] and the vulcanization of carbon-black-filled natural rubber in the presence of TBBS.[190]

An alternative to sulphur curing is crosslinking by initiation with peroxy radicals. The ^{13}C solid state NMR spectra of chemically-crosslinked poly(isoprene) and poly(butadiene)[191,192] are similar to that reported for the gamma-irradiated materials. *Cis–trans* isomerization was confirmed for both materials, indicating the participation of allylic radicals in the crosslinking reaction. A broad resonance at 44 ppm was assigned to new carbon types in crosslinked structures, while a small amount of chain scission was indicated by a new peak at 15 ppm assigned to methyl groups in new chain-ends. Spectra obtained by swelling showed a marked decrease in linewidth, which the authors ascribed to motional averaging of carbon–proton dipolar coupling. The spectrum of the swollen material was collected using a single-pulse excitation, and so comparison with the cross-polarization spectrum of the unswollen material is problematic. No attempt was made to quantify the peak intensities.

Very recently, Fulber and coworkers[193] have demonstrated the utility of an experiment which correlates the decay of transverse magnetization of the ^1H spins with the ^{13}C chemical shift, by cross-polarizing residual ^1H magnetization to the ^{13}C nuclei. This experiment is equivalent to the "WISE" experiment,[175] with the difference that the ^1H decay is examined in the time domain, rather than after Fourier transformation as in the "WISE" experiment. Figure 14 shows the evolution of ^1H magnetization for sulphur-cured poly(styrene-co-butadiene) rubber. The decay of ^1H magnetization was fitted to the sum of Gaussian and Lorentzian decays, corresponding to relatively rigid and mobile parts of the polymer, respectively. The second

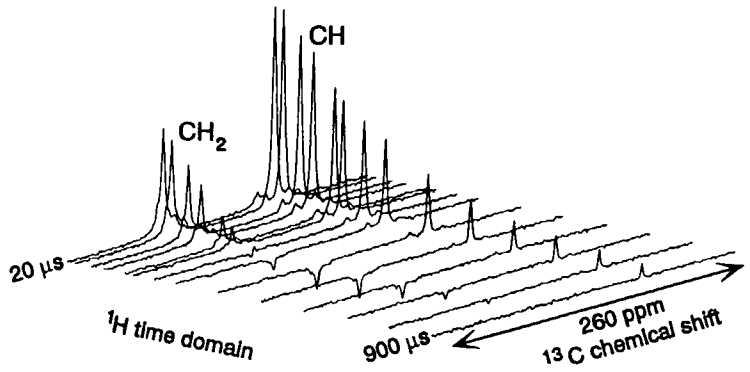

Fig. 14. Evolution of ^1H magnetization in the time-domain version of the wide-line separation experiment applied to sulphur-cured poly(styrene–co–butadiene) rubber. The width of the spectrum in the ^{13}C dimension is 260 ppm, while the decay of proton magnetization is plotted from 20 to 900 μs. (Reproduced from reference 193 with permission. Copyright © 1996 Hüthig and Wepf Verlag.)

moment of the Gaussian line shape, and the inverse of the T_2 of the Lorentzian line shape were seen to increase with increasing crosslinking density, consistent with restriction of motion of the main- and side-chains on crosslinking.

3.3.2. Curing of thermosetting resins

(i) Epoxy resins. Characterization of chemistry of curing. Epoxy resins are an important class of materials used extensively in coatings and structural applications. Largely-aliphatic coatings can be cured at ambient temperature over a long period of time, and are used extensively to improve corrosion resistance of metals in marine environments. Higher-temperature-cured resins generally have improved solvent resistance. Approximately 50% of production of epoxy resins is destined for use in structural components, often as the matrix in composite materials. The many applications include use in glass-filled wiring boards, and more recently, in carbon-fibre-reinforced composites in the aerospace industry. Questions of interest to the chemist which can be resolved by NMR spectroscopy include the mechanism of cure, and extent of reaction of the secondary amine groups, and in particular the effect of filler on curing chemistry, a problem not easily accessible to other spectroscopic techniques.

The role of NMR spectroscopy in the study of curing of epoxy resins has been primarily to confirm the structure of resins after curing. At low conversions it is possible to follow the cure of resins using conventional solution-state NMR;[194–199] however, when the viscosity of the resin increases and the ^{13}C lines broaden considerably, resort must be made to solid state techniques. Nonetheless, important contributions to the understanding have been made by solution NMR studies. The kinetics of reaction of diglycidyl ether of bisphenol A (DGEBA) with piperidine,[194] DGEBA with *m*-phenylenediamine,[195,196] model epoxy compounds with amines,[197] DGEBA with diols,[198] and model epoxy compounds with cyanates[199] have been followed up to moderate conversions. The importance of 2D NMR techniques for the identification of new chemical species was demonstrated by Fyfe *et al.*[199]

The changes in the ^{13}C NMR spectra which occur during curing have been demonstrated by Haw and Johnson[200] who have attempted to follow the cure of DGEBA and tetraethylene tetraamine at 323 K from the liquid state through the gel state and into the solid state. All spectra were recorded with high-speed magic angle spinning. Initially the high-resolution solution spectrum gave information comparable to that obtained by conventional high-resolution spectroscopy; however, as the reaction proceeded, the overall signal intensity increased and the lines became progressively broader. In the gel region a spectrum (single-pulse excitation or CPMAS) could not be observed at all. This was ascribed to a decrease in the efficiency of decoupling

as the frequency of motion became comparable to the frequency of the dipolar decoupling field.[127,128] At longer curing times CPMAS was used to measure changes in the spectra.

The first solid state NMR study of an epoxy resin was presented by Garroway *et al.* in 1979.[138] In this work they were concerned with investigating the quantitative aspects of the NMR technique as applied to resins of DGEBA cured with four amine–anhydride mixtures. While all the features of the solution-state spectra at low conversion are replicated in the solid state spectra, the much larger linewidth in the solid state limits the amount of chemical information available from the ^{13}C NMR spectra. The increase in linewidth is ascribed mainly to increased dispersion of isotropic chemical shifts due to the presence of a large number of frozen conformations in the glassy cured matrix. A general discussion of the origin of line broadening in solid state ^{13}C MAS NMR has been presented by VanderHart *et al.*[201]

An obvious method for reducing the linewidth in ^{13}C NMR spectra of glassy polymers is to record the spectra above the glass transition temperature. Until recently most commercial MAS probes were limited to a maximum temperature of 423 K, often well below the T_g of epoxy resins, which are usually post-cured at close to 473 K. Recent advances in probe design have, however, allowed much higher temperatures to be reached in the MAS rotor. Sterna and Smith[202] were the first to demonstrate the advantages of improved resolution in ^{13}C spectra of epoxy resins recorded above T_g. The spectra of co-reacted DGEBA and bisphenol A recorded at 473 K display liquid-like resolution. These workers were able to identify a small peak at 77 ppm due to the methine carbon in etheric crosslink structures. Very recently Harris *et al.*[203] studied the structure of the matrix formed by reaction of DGEBA with diamino diphenyl sulphone (DDS). Figure 15 shows the ^{13}C MAS spectra recorded at 563 K, as well as the spectrum recorded at 296 K. The increase in resolution due to averaging of conformations is dramatic. In addition, Harris *et al.*[203] demonstrated that multipulse solution-state techniques such as APT and DEPT can be successfully applied to crosslinked epoxy resins above T_g.

Grenier-Loustalot and Grenier[204] have studied the chemistry of the cure of DGEBA and derivatives with diamino diphenyl methane (DDM) and DDS. The solid state NMR spectra allowed the peaks due to unreacted epoxy groups, amine addition products, and hydroxy groups to be identified. It is suggested that the extent of cure can be followed by solid state ^{13}C NMR. In an associated paper, this group reported the ^{13}C CPMAS spectra of DGEBA cured with DDS under the influence of microwave heating.[205] The overall extent of cure was somewhat diminished in the microwave cure compared to a nominally-comparable thermal cure; however, the extent of cure was affected by the mode of application of the microwave radiation. Higher cure rates were observed for the pulsed microwave field compared

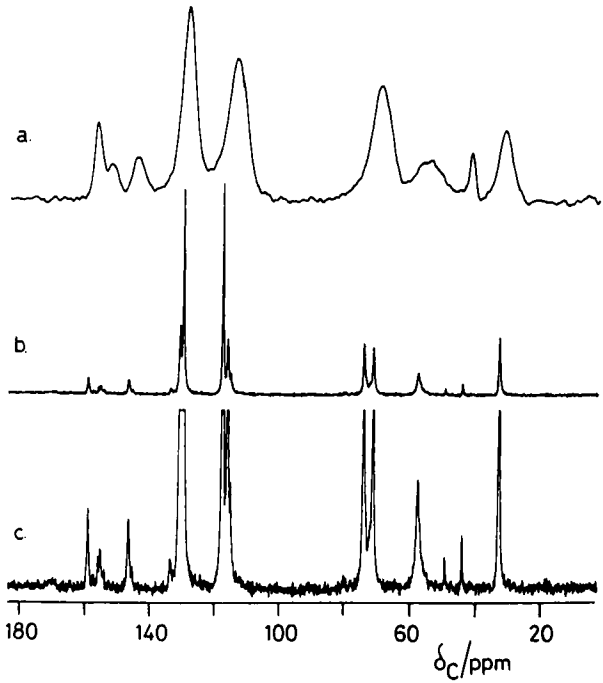

Fig. 15. ^{13}C MAS spectra of DGEBA reacted with DDS recorded at (A) 296 K and (B) 563 K; (C) expanded view of spectrum (B). (Reproduced from reference 203 with permission. Copyright © 1996 Elsevier Science.)

with a CW field. The quantitative aspects of this work must be questioned in light of the work of Mijovic who claims identical cure kinetics for thermal and microwave curing of this system.[206,207] The group of Grenier-Loustalot and Grenier have published further work on the cure of DGEBA and DDS in the presence of benzyldimethylamine and BF_3 catalysts,[208] as well as DGEBA cured with aniline, *N*-methylanaline, and DDS.[209] In general, agreement with the results of infrared measurement of conversion was good.

Attias and coworkers have published the results of a quantitative study of the mechanism of cure of *N*,*N*,*N*′,*N*′-tetraglycidyl 4,4′-diaminodiphenylmethane (TGDDM) with DDS and DDM.[210,211] In the first paper[210] the factors important for obtaining quantitative peak intensities in the CPMAS spectroscopy are discussed. In particular, it is pointed out that in a homogeneous polymers, such as a glassy cured epoxy resin, spin diffusion is efficient in averaging ^1H $T_{1\rho}$ for all carbon nuclei, and therefore, a single spectrum provides quantitative intensities. The use of the TOSS sequence is reviewed, and it is pointed out that distortion of intensity due to decay of magnetization during the pulse sequence is less pronounced for the peaks

due to the aliphatic carbons compared with the aromatic carbons. The complex composite peak due to the aliphatic region was resolved into individual peaks by spectral simulation.[211] The chemical shifts of carbons in predicted structures are obtained from spectra of model compounds, and from the literature. The analysis allows the determination of the proportion of unreacted epoxy group, primary amine, secondary amine and etheric structures formed on curing.

Similar studies of the structure of cured epoxy resins include the use of ^{13}C CPMAS to identify the hardener type in DGEBA-based resins,[212] reaction of TGDDM with DDS and masked isocyanates,[213] DGEBA cured with dicyandiamide,[214] DGEBA cured with hexamethylenediamine and hexamine[215] and butanediol diglycidyl ether cured with phthalic anhydride.[216]

Molecular motion and phase structure. Molecular motion in cured epoxy resins has been studied by a number of authors. In their early paper, Garroway and coworkers[138] discussed the possibility of using measurements of ^{13}C $T_{1\rho}$ to study molecular motion in epoxy resins. As discussed in Section 3.5.2, they caution that the dipole–dipole mechanism may provide non-motional pathways for $T_{1\rho}$ relaxation; however, they conclude that the spin–lattice mechanism dominates for glassy cured resins. In an earlier paper,[217] Garroway *et al.* discuss the broadening at low temperatures of the peak due to methyl groups in the ^{13}C CPMAS spectra of DGEBA cured with piperidine. At lower temperatures the frequency of methyl reorientation slows to approach the frequency of the decoupling field, and so the decoupling becomes less efficient.[127,128] At even lower temperatures the peak due to the methyl groups is expected to become narrow again.

A later study by these authors focused on motion of the phenyl ring in DGEBA resins cured with a range of diamines.[218] It was noted that at low temperatures (< 250 K), two peaks were observed for both of the protonated aromatic carbons of DGEBA. The splitting, which is assigned to two different conformations in the glassy state, disappears at high temperature (> 300 K), due to increasing rates of exchange of the conformations. Simulation of the behaviour of the NMR lines assuming a single correlation time of motion gave results at variance with the results of dynamic mechanical analysis. A distribution of correlation times was therefore considered. Simulations were performed using the Kolrausch–Williams–Watts distribution function, with a width parameter of $\alpha = 0.28$. Both an inhomogeneous and a homogeneous distribution of correlation times adequately described the data, and were superior to the model of a single correlation time of motion; the experimental data could not be used to distinguish between the case of inhomogeneous and homogeneous distributions of correlation times. The activation energy of *ca.* 60 kJ mol^{-1} was in agreement with the activation energy obtained from dynamic mechanical analysis; however, the rate of motion was several orders of magnitude lower than that measured by the mechanical measurements.

To reconcile this difference the authors suggested a mechanism of flipping motion involving diffusive reorientation.

Udagawa *et al.*[219] have measured the rates of ^{13}C $T_{1\rho}$ relaxation in cycloaliphatic epoxy resins cured either thermally with the aid of a sulphonium catalyst, or with ultraviolet (UV) light in the presence of the photoinitiator triphenylsulphonium hexafluorantimonate. ^{13}C $T_{1\rho}$ was found to initially increase, and then decrease for the UV-initiated system; however, it increased only slightly for thermal cure. This was ascribed to initial anti-plasticization and subsequent plasticization in the UV-initiated system. The ^{13}C T_1 of the butyl group was observed to be shorter than the cyclohexyl group for these polymers, and hence the butyl group has a shorter correlation time of motion than the cyclohexyl group.

Laupretre and coworkers[220] have measured the rate of cross-polarization as a measure of the extent of molecular motion in DGEBA and diglycidyl ether of butanediol (DGEBU) crosslinked with hexamethylenediamine (HMDA), isophoronediamine (IPD) and DDM. The rates of cross-polarization were measured for carbons in the hydroxypropyl ether groups, the methylene adjacent to the crosslinks, and the methylene carbons in the centre of the HMDA unit. The centre of the methylene sequence was the most mobile part of the molecule, followed by the hydroxypropyl ether groups and the crosslink points. Motion of the centre of the methylene group was associated with the low-temperature γ-relaxation reported from dynamic mechanical analysis of these polymers, while motion of the hydroxypropyl ether groups was suggested to be involved in the β-relaxation process. A model for the motion of fast jumps between *trans* and *gauche* conformations was used, and lead to the conclusion that for the DGEBA–HMDA, 70% of the hydroxypropyl ether groups were undergoing this molecular rearrangement; however, in the more rigid DGEBA–DDM system, only 20% of these groups were involved in jumps between conformations. For the DGEBA–HMDA, 20% of crosslink points were undergoing conformational jumps; however, at the centre of the methylene sequence, 100% of the groups were moving rapidly. The effect of incorporation of mono-substituted amine was also investigated.

Finally, the phase structure of epoxy resins has been characterized by measurements of spin diffusion.[221] Samples of a cycloaliphatic epoxy, crosslinked with flexible propylene glycols in the presence of aryl sulphonium salts, were prepared with different ratios of epoxy to propylene glycol units. The dipolar filter experiment[221] was used to select magnetization only in the mobile regions of the resins. Spin diffusion was allowed to proceed during a variable mixing time, and then the magnetization was observed after cross-polarization to the ^{13}C spins. The evolution of magnetization throughout the resin as a function of mixing time was simulated by solving the diffusion equations for a three-dimensional spherical model of domain structure, which included an intermediate phase between the hard and soft

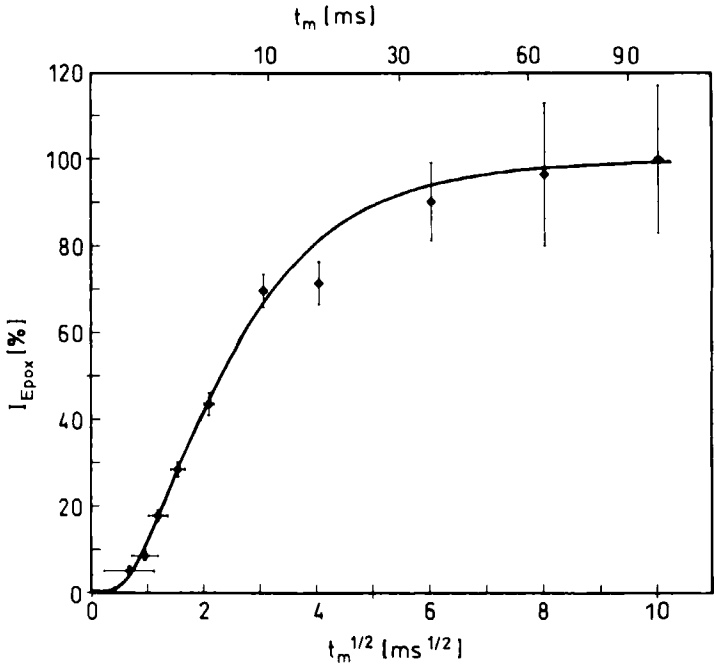

Fig. 16. Intensity of the ^{13}C NMR signal due to epoxy (19 to 44 ppm) in crosslinked epoxy resin, measured as a function of mixing time in the spin diffusion experiment, and the fit of the data to a spherical model of morphology including an interface (solid line). (Reproduced from reference 221 with permission. Copyright © 1992 John Wiley & Sons.)

components. Figure 16 shows a sample set of experimental results and the result of fitting the data to the model. The domain sizes are of the order of 0.5–5 nm in size, and correspond, for example, to only a few polyol chains.

(ii) Phenol–formaldehyde and related amino resins. Chemistry of phenol–formaldehyde resins. Phenolic resins, formed by the reaction of phenol and formaldehyde either in the presence of acid or base catalyst, have been used for over 80 years in applications such as mouldings, coatings, adhesives and laminates. The basic chemistry has been modified over time with the use of substituted phenols, and in combination with hexamethylenetetramine or other resins such as poly(ester), epoxy or alkyd resins. The associated class of materials known as amino resins are formed by the reaction of an aliphatic amine with an aldehyde, as in urea–formaldehyde and melamine–formaldehyde resins, and are used primarily as adhesives.

The chemistry of phenol–formaldehyde and related resins has been the

subject of a number of solution-state NMR studies (see examples in the references[222–229]). Important information on the early stages of the reactions has thus been obtained. However, the problems of limited solubility, and the extensive use of model compounds has limited this research. When the reaction proceeds to high conversion the need for solid state NMR methods arises. Fyfe and coworkers[230] were the first to apply solid state NMR techniques to the curing of phenol–formaldehyde resins. Peaks due to substituted and unsubstituted aromatic carbons were clearly identified, as well as peaks due to paraformaldehyde, methanolic carbons and methylene-bridging carbons, thus allowing measurement of the degree of conversion. The use of ^{13}C-labelled formaldehyde simplified the spectra of the methylene carbons. The authors also used the dipolar-dephasing experiment[231] to identify the non-protonated aromatic carbons, and by subtraction obtain a sub-spectrum of the protonated carbons. The quantitative aspects of this last experiment must be questioned.

Bryson and coworkers[232] have measured cured phenol–formaldehyde resins at three different field strengths, and reported no appreciable improvement in resolution at higher field. In fact at higher fields the presence of overlapping spinning side bands necessitated the use of the TOSS sequence for suppression of side bands. This resulted in a decrease in the intensity of the peaks due to methylene carbons, which was partially attributed to the shorter T_2 of these carbons. Slightly narrower peaks were observed at the early stages of cure, and hence the freezing of conformations on vitrification was suggested as the dominant mechanism of line broadening. In a later paper[233] this group reports the curing of resol-type phenol–formaldehyde resins. Extensive use is made of the dipolar-dephasing experiment, and measurements of the rate of cross-polarization, $1/T_{CH}$, to identify new structures. For example, the relative magnitude of these parameters enables the authors to differentiate aromatic carbons attached to hydroxyl and etheric groups, and identify methylene bridges and methyl groups formed during cure. A third paper[234] was concerned with identification of the reaction mechanisms during the curing of the above resin with ^{13}C-labelled hexamethylenetetramine. The spectrum prior to curing was dominated by the peak at 75 ppm due to unreacted hexamine. As the curing temperature was raised, a new peak at 55 ppm appeared, as well as a shoulder at 83 ppm, and finally at still higher curing temperature (433–463 K) a peak at 30 ppm became predominant. The three peaks appearing during curing are assigned to benzoxazine and tribenzylamine (83 and 55 ppm), and bridging methylene carbons (33 ppm). ^{15}N NMR was used to aid assignment of the spectra.

Several other groups have reported the solid state ^{13}C NMR spectra of phenol–formaldehyde resins.[229,235–237] Sinha and coworkers[238] have studied the structure of substituted-phenolic resins. The NMR method allowed facile identification of the resin structure. Spectra obtained using the dipolar dephasing experiments were more highly resolved, indicating a distribution

of strengths of dipolar couplings. Spectra of thermally-degraded samples indicate that the methylene bridges degrade preferentially.

Other formaldehyde-based resins. Bauer *et al.*[239] have reported the ^{13}C NMR spectra of coatings based on acrylic copolymers crosslinked with a melamine–formaldehyde resin. Comparison of the peak intensities in spectra obtained using cross-polarization, and by direct polarization of the ^{13}C nuclei, have enabled the relative rigidity of various structures to be estimated. The effect of structure and of degradation on the rigidity of the crosslinked groups was therefore assessed. In a recent study, Andreis and coworkers have used solid state ^{15}N[240] and ^{13}C NMR[241] to study melamine–formaldehyde resins. Both sets of results indicate highly heterogeneous curing mechanisms.[240,241] In the ^{13}C NMR study[241] three different types of methyloxy group were identified, on the basis of differences in rates of cross-polarization, and spectral deconvolution. The peaks due to methylene groups were found to be broadened by coupling to the attached ^{14}N nuclei, particularly at lower temperatures. The problems associated with obtaining quantitative peak intensities were also discussed.

Chuang and Maciel[242] have studied the hydrolytic degradation of a wide range of urea–formaldehyde resins using ^{13}C CPMAS NMR. The relative sensitivity of various structural entities to degradation were assessed by measuring ^{13}C CPMAS spectra of the degradation residues. Degradation was seen to occur at crosslinked sites predominantly, while resins prepared with an excess of formaldehyde had significant concentrations of dimethyl ether, poly(oxymethylene glycols) and methyloyl groups which were sensitive to hydrolysis. The temperature and pH dependence of the degradation reactions have been assessed.

Other solid state ^{13}C NMR studies of the chemistry of formaldehyde-based resins include a study of urea–formaldehyde-furfuryl alcohol resins,[226] and starch crosslinked with urea-formaldehyde resins.[243]

(iii) Poly(ester) resins. Despite the commercial importance of poly(ester) resins in the field of composites, relatively little has been reported on the characterization of these materials by ^{13}C NMR. Paci and coworkers[244] have studied the reaction of styrene with poly(ester) resins based on maleic anhydride and phthalic anhydride and propylene glycol, using ^{13}C solid state NMR. At higher styrene contents there was evidence for substantial runs of poly(styrene). The spectra were fully consistent with their known composition. Subsequently Paci and Campana[245] studied the hydrolysis of these same polymers by ^{13}C solution NMR. Finally, Bergmark and Florin,[246] have reported a study of the ^{13}C $T_{1\rho}$ relaxation of resins consisting of fumaric and adipic acids with propylene glycol and styrene, as a function of cure temperature. A maximum in ^{13}C $T_{1\rho}$ was observed for all carbons at approximately 363 K, indicating cooperative motions of the main-chains. The results reflect changes in the structure of the resin with curing temperature.

(iv) Poly(imide)s. Acetylene–terminated oligomers have come to occupy an important niche market as matrix resins for high-performance composite materials. Curing of these materials does not liberate volatile molecules, and therefore the formation of voids is not significant. Imides oligomers are often used for their excellent mechanical properties and stability at high temperatures. This class of materials has therefore found application in the aerospace industry.

Sefcik and coworkers[247] were the first to use solid state ^{13}C NMR to study the curing of oligomers terminated with reactive groups. The authors observed a clearly-resolved peak at 84 ppm in the spectrum of the unreacted polyimide resin, Thermid 600, due to terminal acetylene groups. The decrease in intensity of this peak on curing at 450–640 K allowed facile analysis of the extent of cure. Additional structures formed during curing were identified by subtraction of the spectrum of the uncured resin, after artificial broadening of the peaks, from the spectrum of the cured sample. New peaks in the region of 120–150 ppm were assigned to the products of trimerization of the acetylene groups, and addition of acetylene groups onto the imide backbone.

Swanson and coworkers[248] have studied the cure of acetylene–terminated poly(imide)s selectively-labelled at various positions with ^{13}C nuclei. Curing of the sample labelled at the imide carbonyl group confirmed the completion of the imidization reaction on heating. Four new peaks were identified in the spectrum of the cured sample labelled at the C1-acetylene group, while a similar result was obtained for the sample labelled at the C2-acetylene position. Analysis of these results rules out the participation of coupling reactions and the biradical mechanism, but confirms the presence of the product of cyclotrimerization and Friedel–Crafts reactions.

Wong *et al.*[249] have used ^{13}C solution and solid state NMR to study the cure of the norbornene end-capped polyimides 2NE/MDA and PMR-15. The formation of a three-dimensional network by retro-Diels–Alder and Diels–Alder reactions was confirmed. Spectra obtained at higher fields did not show improved resolution, once again indicating that the dominant mechanism for line broadening in these materials is dispersion of isotropic chemical shifts resulting from frozen conformations.

The mechanism of cure of bismaleimide–styrene resins were studied by Winter and van der Velden[250] using ^{13}C solution and solid state NMR. An alternating structure was confirmed by comparison with spectra of model linear copolymers. Finally Gambogi and Blum[251] have reported the ^{13}C CPMAS spectra of a bismaleimide reactive group attached to a silica surface via an (aminoalkyl)silane coupling agent. The bulk of this work consists of an ^{2}H NMR study of the molecular motion of the coupling agent, and will be discussed in Section 5.

(v) Isocyanate and poly(urethane) resins. Poly(urethane) resins, formed by

the reaction of diisocyanates and polyols, are used extensively as coatings, due to their excellent abrasion resistance, hardness, chemical resistance, and weatherability. Curing is usually effected by reaction with water, on evaporation of solvents, or by UV or electron beam curing. Resins based on aliphatic isocyanates tend to have superior stability to UV degradation than the aromatic analogues, which have superior mechanical properties. The large number of competing reactions which occur on curing are especially amenable to study by ^{13}C and ^{15}N NMR.

Duff and Maciel[252–254] have studied in detail the cure of 4,4′-methylenebis(phenyl isocyanate) (MDI) resins using a combination of solid-state ^{13}C and ^{15}N NMR spectroscopy. The ^{13}C NMR spectra consist of a single peak in the aliphatic region due to methylene carbons and heavily overlapping signals in the aromatic region. Assignments to the spectra were made by comparison with model compounds and by using the dipolar dephasing experiment to increase resolution. For pure MDI resins,[252] the formation of isocyanurate crosslinks was confirmed and was a maximum for a cure temperature of 393 K, while a decrease at higher temperatures was suggested to be due to decomposition of the catalyst. The carbonyl region of the ^{13}C spectra was complicated by three overlapping resonances, and distinction cannot be made between biuret or urea linkages. The concentration of biuret linkages formed on reaction of MDI with formic acid[253] was studied as a function of resin composition and cure temperature. The formation of biuret crosslinks and the consumption of isocyanate linkages was favoured at higher formic acid contents, while the temperature of reaction had little effect. Finally, the effect of prolonged storage in air on the cured isocyanurate resins was also studied.[254] Decreases in the concentration of the isocyanate groups are evidenced by a decrease in the intensity of the peak at 125 ppm on ageing, while a polyurea peak at 137 ppm increases in intensity. All three of these studies are complemented by ^{15}N NMR experiments which will be discussed in Section 4.2.

Fyfe and coworkers[255] have also used ^{13}C and ^{15}N NMR to study the curing reactions in bisphenol A diisocyanate. Their results agree generally with those of Duff and Maciel,[252] in that the major product of the curing reaction is the isocyanurate crosslink. Curing in solution resulted in the formation of unidentified side-products; however, curing of the neat resin resulted in a cleaner reaction.

Clayton and colleagues[256] have characterized the cross-polarization time constants in a series of urethane acrylates formed by curing of toluene 2,4-diisocyanate and 2-hydroxyethyl acrylate with poly(tetramethylene oxide) (PTMO) of varying size. The last molecule forms the soft segments of the polymer. ^{13}C $T_{1\rho}$ and T_{CH} were shown to increase with increasing length of the soft segment. This is consistent with an increase in flexibility of the chains within the soft segment with increasing size. Comparisons were made with results of dynamic mechanical measurements.

(vi) Other thermosetting resins. A number of other studies of crosslinked resins by ^{13}C NMR are summarized here briefly. Maciel and coworkers[257,258] have reported a solid state ^{13}C NMR analysis of the cure of furfuryl alcohol resins. Linear chain extension occurs through condensation of the methyloyl group with an adjacent furfuryl alcohol group. Crosslinking occurs through cleavage of the methylene linkage and subsequent reaction.

Laupretre and coworkers[259,260] have characterized the structure of a series of poly(styrylpyridine) resins by solution and solid state ^{13}C NMR. Linear products formed by the addition of terephthalic aldehyde with trimethylpyridine, were identified by solution NMR. Further curing resulted in crosslinking via reaction of the bridging double bonds. The presence of residual aldehyde groups was confirmed.[260] The method of solid state ^{13}C NMR has also been applied to the study of cured alkyl paint resins,[261] and the reaction of dicyclopentadiene resins.[262]

3.4. ^{13}C NMR studies of crosslinking of other polymers

A number of other ^{13}C NMR studies of crosslinked polymers have been reported in the literature. For example, Dejean de la Batie and coworkers[263] have measured the ^{13}C T_1 relaxation times of linear and crosslinked poly(ethylene oxide)s well above the glass transition temperature. The authors have used a modified autocorrelation function to obtained reasonable fits to the experimental T_1 relaxation times as a function of temperature. A comparison with the linear polymer indicates that the orientation diffusion process is interrupted by the presence of crosslinks, and in addition the motion of central units of the PEO chains is retarded by crosslinking.

The molecular mobility of crosslinked poly(*N*-alkylacrylamide) resins was measured by Yu and Brown[264] using the dipolar dephasing experiment. In chemically-similar environments the rate of decay of ^{13}C magnetization on cessation of dipolar decoupling is a measure of the strength of the dipole–dipole couplings at that site, and hence in a heterogeneous system is a measure of molecular mobility. For these polymers Yu and Brown[264] found that *N-n*-hexyl acrylamide side-chains were undergoing fast segmental motion, while the main-chain was restricted by crosslinking. The incorporation of bulkier side-chain groups slowed the motion of the side-chain also. In another study of chain mobility in crosslinked polymers, Du Prez *et al.*[265] have used a range of different ^{13}C NMR techniques, such as variable contact time measurements, cross-depolarization, and measurements of ^{1}H $T_{1\rho}$ to study motion in crosslinked poly(1,3-dioxolane). A highly heterogeneous network was demonstrated by the first two techniques. Increases in ^{1}H $T_{1\rho}$ were observed with decreasing chain mobility. Crosslinking had little affect on the mobility of the crystalline regions of the polymer.

Other studies of the structure of crosslinked polymers include the

observation of crosslinks in functionalized poly(styrene)s,[266] a study of crosslinks in poly(vinyl cinnamate),[267] and the measurement of residual unsaturation in crosslinked methacrylate dental resins.[268] Allen and coworkers have also studied the molecular mobility of unreacted double bonds in crosslinked methacrylates,[269] as well as motion of the cured crosslinked network.[270,271] Reichert and Mathias[272] have recently reported a ^{13}C CPMAS study of the cured resin of an acetylene derivative of adamantane.

3.5. Measurement of ^{13}C relaxation times in crosslinked polymers

3.5.1. ^{13}C spin–lattice relaxation in the laboratory frame

As discussed in Section 2.3 of this review, both ^{1}H and ^{13}C T_1 relaxation times in crosslinked polymers are dominated by dipole–dipole interactions. The rate of spin–lattice relaxation of the carbon nuclei is given by[273]

$$\frac{1}{T_1} = \frac{\gamma_C^2 \gamma_H^2 h^2}{10r^6}[J(\omega_H - \omega_C) + 3J(\omega_C) + 6J(\omega_H + \omega_C)] \qquad (15)$$

The low natural abundance of ^{13}C nuclei eliminates complications due to spin diffusion inherent in measurement of ^{1}H longitudinal relaxation times, as discussed briefly in Section 2.3, and therefore ^{13}C T_1 relaxation is a measure of molecular motion of the carbon type in question. In rigid polymers below the glass transition temperature, ^{13}C T_1 is often long, for example a value of T_1 of over 1000 s has been recorded for carbon nuclei in the crystalline regions of poly(ethylene).[137] The low spectral density of motions in the MHz range below T_g, apart from motion of side-chains which tend to be less affected by crosslinking, has meant that T_1 measurements of crosslinked polymers have tended to be made above T_g.

Komoroski and Mandelkern[274] found that ^{13}C T_1 at 298 K for crosslinked butyl rubber does not change with increasing extent of crosslinking, indicating no change in the spectral density of motions at 70 MHz under these conditions. Zaper and Koenig[178,179] reported similar observations for crosslinked natural rubber. Andreis and coworkers[181] have made extensive use of inversion recovery T_1 measurements to aid resolution of the ^{13}C spectra of sulphur-vulcanized natural rubber; however, the authors did not report values of T_1. A later study from the same group[183] reported values of ^{13}C T_1 for natural rubber crosslinked for varying lengths of time, and measured over a range of temperatures. A complex model of motion, in which the backbone carbons undergo combined random diffusional motion and librational motion, and in which the correlation times of motion are described by a log-χ^2 distribution function, was used to describe the results. On

crosslinking, the plot of T_1 versus inverse temperature broadened considerably, and the minimum moved to higher temperature. It was found that the correlation time for the isotropic component of the motional model was most strongly affected by crosslinking. As the authors point out, these results should be regarded as semi-quantitative, since a nine-parameter model is used to describe a set of results consisting of just six points. Nonetheless, important conclusions can been made from such a study. Dejean de la Batie and coworkers,[263] in a ^{13}C T_1 study of crosslinked poly(ethylene oxide), have used a similar autocorrelation function, and found that crosslinking interrupts the diffusion of conformations along the PEO chain.

More recently, Udagawa *et al.*[219] have studied fully-cured thermosetting cycloaliphatic epoxy resins, and found an increase in ^{13}C T_1 with increasing initiator concentration, despite plasticization of the network with initiator fragments. Values of ^{13}C $T_{1\rho}$ were seen to initially increase and then decrease with increasing initiator concentration, due to initial antiplasticization and subsequent plasticization. The participation of the cyclohexane rings in the β-relaxation was confirmed. Evidently plasticization only affects the mid- and low-frequency region of the frequency spectrum.

3.5.2. *^{13}C spin–lattice relaxation in the rotating frame*

As discussed in Section 2.3, molecular motions in the mid-kHz frequency range are more strongly affected by crosslinking than the higher frequency motions important for T_1 relaxation. For this reason measurements of ^{13}C spin–lattice relaxation in the rotating frame (^{13}C $T_{1\rho}$) promise to provide much information on motion in crosslinked polymers. The rate of $T_{1\rho}$ relaxation is given by[275,276]

$$\frac{1}{T_{1\rho}} = \frac{\gamma_C^2 \gamma_H^2 h^2}{20r^6} [4J(\omega_1) + J(\omega_H - \omega_C) + 3J(\omega_C) + 6J(\omega_H + \omega_C) + 6J(\omega_H)] \quad (16)$$

In general for many systems in which the distribution of correlation times is not excessively broad, only the first spectral density term is required.

A major possible complication of the interpretation of ^{13}C $T_{1\rho}$ data, which may have restricted the use of the technique, is the possibility that relaxation can proceed partially via fluctuations of the dipolar field due to mutual ^1H–^1H spin flip-flops.[138,139] The ^{13}C $T_{1\rho}$ relaxation time measured by spin-locking (^{13}C $T^*_{1\rho}$) is therefore the sum of two components:

$$\frac{1}{^{13}C\,T^*_{1\rho}} = \frac{1}{^{13}C\,T_{1\rho}} + \frac{1}{T^D_{CH}} \quad (17)$$

where ^{13}C $T_{1\rho}$ and T^D_{CH} are the time constants for the spin–lattice and the spin–spin relaxation processes, respectively. The former processes are

associated with motion of the ^{13}C–^{1}H bond vector with frequency components in the mid-kilohertz range. T_{CH}^{D}, however, is a function of the ^{1}H dipolar field strength and provides no direct information about motion of the ^{13}C nuclei. The issue of the relative contribution of the two mechanisms to ^{13}C $T_{1\rho}$ relaxation is of some importance, and therefore is discussed below.

Stejskal *et al.*[277] and Schaefer *et al.*[278] have suggested that the spin–lattice contribution to ^{13}C $T_{1\rho}^{*}$ can be determined by adiabatic alignment of protons in the dipolar field; however, this experiment is difficult to implement on most commercial NMR spectrometers, and in addition, the uncertainties associated with these measurements are also estimated to be large, *ca.* $\pm 30\%$.[278] A semi-qualitative method of calculating T_{CH}^{D}, based on measurements of the proton local field (H_L) and known values of T_{CH}^{D} and H_L for a model polymer, has been proposed by Schaefer *et al.*[278] A more simple method for determining the relative importance of the two mechanisms is the measurement of ^{13}C $T_{1\rho}^{*}$ as a function of the spin-locking field strength.[138,139,278–281] For relaxation dominated by the spin–lattice mechanism, ^{13}C $T_{1\rho}^{*}$ will increase as the square of the rotating-frame field strength.[48] However, if ^{13}C $T_{1\rho}^{*}$ is dominated by spin–spin processes then an exponential dependency of ^{13}C $T_{1\rho}^{*}$ on the rotating frame field is expected.[138] This method suffers in its turn by the limited range of field strengths achievable while maintaining spin-locking. More fundamentally, the observation of a minimum in ^{13}C $T_{1\rho}^{*}$ as a function of temperature is good evidence that relaxation is dominated by spin–lattice processes. The importance of the spin–spin contribution to ^{13}C $T_{1\rho}^{*}$ may be expected to decrease, but not increase, with increasing temperature as there is an increase in frequency and amplitude of motion which in turn modulates the dipole–dipole interactions.

A number of groups have confirmed that ^{13}C $T_{1\rho}$ is dominated by spin–lattice processes in amorphous polymers in both the glassy and rubbery states. The polymers examined include poly(styrene), poly(methyl methacrylate), poly(phenylene oxide),[277] poly(carbonate), poly(ethylene terephthalate),[279] poly(α-methyl styrene),[278] cured DGEBA epoxy resin[138] and rubbery poly(butyl acrylate).[282] The spin–spin processes, generally, only become significant in determining the ^{13}C $T_{1\rho}^{*}$ of the crystalline regions in highly rigid and highly crystalline polymers, e.g. poly(oxymethylene),[277] poly(ethylene)[278,283] and poly(propylene).[280]

The earliest studies of ^{13}C $T_{1\rho}$ in crosslinked polymers were those of Garroway and coworkers,[138,284,285] who studied the field-dependence of ^{13}C $T_{1\rho}$. For field strengths above 40 kHz, ^{13}C $T_{1\rho}$ was dominated by molecular motions. Therefore the potential usefulness of the method was established at an early stage. Despite this, there have been few reports of the measurement of ^{13}C $T_{1\rho}$ in crosslinked polymers. Dickinson *et al.*[286,287] have studied the effect of crosslink density on motion in crosslinked poly(propylene oxide) (PPO). $T_{1\rho}$ for the linear polymers passed through a

minimum at approximately 298 K with increasing measurement temperature; however, $T_{1\rho}$ for the more heavily crosslinked materials was generally much longer, and did not reach a minimum at to 340 K. In addition, the network materials were somewhat heterogeneous, since $T_{1\rho}$ values measured using direct excitation of the ^{13}C spins were shorter than those measured using cross-polarization preparation. The two experiments evidently discriminate between units either close to, or removed from, the rigid crosslinking unit. $T_{1\rho}$ for the lightly-crosslinked PPO showed similar behaviour, as a function of temperature to the linear polymer, and in fact $T_{1\rho}$ was lower in the network material. The authors suggest that either a dipolar contribution to the relaxation was responsible, or that the motion of the phenyl or methyl groups contributes to the relaxation.

Other studies of ^{13}C $T_{1\rho}$ have included a study of the effect of cure temperature on this parameter for cured poly(ester) resins.[246] In addition, Allen and coworkers[288,270,271] have similarly reported that ^{13}C $T_{1\rho}$ increases during the cure of tetra(ethylene glycol)dimethacrylate. The effect of cure and length of the ethylene glycol chain on the dynamic properties of these polymers was studied by ^{13}C NMR and dynamic mechanical analysis.[270]

4. CPMAS STUDIES UTILIZING NUCLEI OTHER THAN ^{13}C

4.1. ^{31}P NMR studies of crosslinked polymers

^{31}P is a very favourable nucleus for studies of molecular motion, particularly because of its high sensitivity and large chemical shift anisotropy. Despite this there are relatively few reports of the use of ^{31}P NMR to study crosslinked polymers. This of course reflects the small number of important polymeric materials which contain appreciable concentrations of phosphorous. In an elegant series of papers, Dickinson and coworkers[289–292] have used ^{31}P relaxation times and line shapes to study motion of junction points in urethane-type polymers. Changes in the chemical shift anisotropy demonstrated that the temperature for the onset of motion of the junction points increased with decreasing molecular weight between crosslinks.[289,290] For the sample with the highest crosslink density studied, the crosslinks did not show signs of motion even at 40°C above the T_g determined by DETA. It was concluded that the crosslinks did not participate in the segmental motion of the propylene oxide soft segments. In a later paper,[291] the authors have examined in detail the changes in NMR line shape by assuming a model of isotropic diffusion motion. The model was confirmed by performing two-dimensional exchange NMR experiments.[292] A distribution of correlation times, described by the Kolrausch–Williams–Watts distribution function with exponent equal to 0.45, was required to describe the data. Excellent agreement was obtained between the NMR data and the results of

measurements of dynamic mechanical and dielectric relaxation. The authors have also reported extensive studies of ^{31}P T_1 and $T_{1\rho}$ for these materials.

4.2. ^{15}N NMR studies of crosslinked polymers

The application of ^{15}N NMR to the study of polymers has recently been reviewed by Andreis and Koenig.[293] Although the low-natural abundance of ^{15}N necessitates expensive isotopic enrichment, the wealth of information obtained from the NMR spectra more than compensates. The power of ^{15}N NMR is the relatively large range of chemical shifts compared with the ^{15}N linewidth, thus spectra are often relatively simple. Cross-polarization can be used to enhance the signal-to-noise ratio of this low gyromagnetic ratio nucleus.

Andreis and coworkers have used solid state ^{15}N NMR[240] to study ^{15}N-labelled melamine–formaldehyde resins. Spectra obtained using cross-polarization or direct polarization of the ^{13}C nuclei demonstrate the heterogeneous nature of the network. The poorly-revolved spectra were resolved into four resonances, due to three non-protonated and one protonated nitrogen structure. There is evidence of at least two types of protonated nitrogen group having differing molecular mobility. Measurements were also made of $T_{1\rho}$ and T_1 relaxation times.

Hatfield and Maciel have studied the curing of a phenolic resin with ^{15}N-labelled (and ^{13}C-labelled) hexamethylentetramine[234] using ^{15}N (and ^{13}C) NMR. As discussed in Section 3.3.2(ii), the authors were able to identify benzoxazine and tribenzlamine intermediates, and crosslinked methylene groups in fully cured materials. Chuang *et al.*[294] have also reported the observation of peaks due to secondary and tertiary amide nitrogens in the ^{15}N spectra of cure urea–formaldehyde resins. Measurements of the rate of cross-polarization, and dipolar dephasing confirmed these assignments.

Murphy *et al.*[295] have studied the cure and degradation of an acetylene-terminated ^{15}N-labelled poly(imide) using ^{15}N CPMAS NMR. Initially the conversion of the amic acid to the imide precursor was followed. Four resolved peaks were observed due to amide and imide either attached to a phenyl ring or at the terminal position. Measurements of the rate of cross-polarization, and the dipolar dephasing experiment assisted in these assignments. Very different rates of cross-polarization ($1/T_{NH}$), and values of ^1H $T_{1\rho}$ were measured for the various structures. After heating to higher temperatures (670 K) the imidization reaction was still incomplete, a result at variance with infrared measurements. A cured sample of poly(isoimide) also revealed incomplete imidization. The effects of temperature and humidity on the stability of the imide groups were also reported. Duff and Maciel have reported a similar ^{15}N NMR study of the degradation of MDI-based isocyanate resins.[296]

Duff and Maciel[252–254] and Fyfe *et al.*[255] have studied in detail the cure of isocyanate resins using a combination of solid state ^{13}C and ^{15}N NMR spectroscopy. Aspects of the ^{13}C NMR study are discussed in Section 3.3.2(iv). The ^{15}N NMR spectra are relatively simple by comparison with the ^{13}C spectra, due to larger dispersion of chemical shifts. Peaks due to the isocyanurate and cyanurate nitrogens, polyurea and biuret nitrogens were identified. The conclusions of these ^{13}C and ^{15}N NMR studies are summarized in Section 3.3.2(iv).

4.3. ^{29}Si NMR studies of crosslinked polymers

^{29}Si NMR is a convenient technique for the analysis of silicon-containing polymers. The disadvantage of the long T_1 relaxation times of ^{29}Si is somewhat offset by the high natural abundance of that nucleus. Engelhardt and Janke,[297] and Newmark and Copley[298] have demonstrated that conventional solution-state NMR can provide a wealth of information on the chemical structure of linear and crosslinked siloxane polymers, although more heavily crosslinked networks require the use of cross-polarization and magic angle spinning.[297,299,300] Beshah and coworkers[299,300] have used these last techniques to study model siloxane networks. Well-resolved axially-symmetric powder patterns were observed in the spectra collected in the absence of sample spinning, and could potentially be used to study motion of the polymer backbone.[301–303] The authors have identified three types of crosslink structures from the CPMAS spectra, and assigned them to silicon in true crosslinks, and silicon with one or two attached short loops.

5. ^{2}H NMR STUDIES OF CROSSLINKED POLYMERS

5.1. Background

^{2}H NMR is acknowledged as one of the most important methods for studying dynamic processes in polymers.[304–306] The sensitivity of the ^{2}H nuclei to motion is due to its large quadrupolar coupling constant. In the general case the ^{2}H NMR line shape is given by the expression

$$\omega = \omega_0 \pm \tfrac{3}{8}\delta(3\cos^2\theta - 1 - \eta\sin^2\theta\cos\phi) \tag{18}$$

where δ is the quadrupolar coupling constant, η is the asymmetry parameter, and θ and ϕ are the polar angles describing the orientation of the coupling tensor with respect to the magnetic field. In most cases the quadrupolar coupling is axially symmetric, and the principal axis of the coupling tensor

lies along the C–D bond.[306] In disordered polymers the ^2H nuclei do not possess a preferred orientation with respect to the static magnetic field, and so the total NMR line shape is the summation of the individual line shapes corresponding to each orientation in the powder weighted by the probability of that orientation occurring. The resultant ^2H spectrum is the familiar Pake doublet.

The effect of molecular motion on the ^2H NMR spectrum has been dealt with in depth by Mehring[307] and Spiess.[308] Three specific regimes have been identified, namely the slow motional regime in which the correlation time of motion (τ_c) is much larger than the inverse of the quadrupolar coupling constant ($1/\delta$), the intermediate regime where $\tau_c \approx 1/\delta$, and finally the fast motion regime where $\tau_c < 1/\delta$. In the majority of cases discussed in this review, motions are occurring in the fast motion regime, where an averaged line shape is observed which reflects the geometry of motion of the ^2H-labelled segments of the polymer chain.

Recent advances in the field of ^2H NMR have concentrated on the area of exchange spectroscopy, first applied to ^2H NMR by Schmidt and coworkers.[309] These very powerful experiments provide a direct measure of the geometry and rate of slow molecular reorientation. As yet they have not been applied to crosslinked polymers. For a comprehensive overview of the field of ^2H NMR of polymers the reader is referred to the reviews of Jelinksi[304] and Spiess and coworkers.[40,305,306]

5.2. Experimental results

5.2.1. Swollen crosslinked networks

Deloche and Samulski[310] have studied the effect of orientation on residual quadrupolar splitting of deuterated solvents in swollen strained poly(isoprene). The splitting was seen to depend linearly on $\lambda^2 - 1/\lambda$ over a very large range of swelling ratios and extents of elongation. The results are consistent with a lattice model of affine deformation, and highlight the importance of nematic-like interactions in strained elastomers. Gronski *et al.*[311] have made similar measurements on partially-deuterated poly(butadiene), and concluded that at higher extension ratios, the non-Gaussian nature of the network leads to non-affine behaviour. Gottlieb and Luz,[312] on the other hand, observed a linear relationship between the quadrupolar splitting and elongation for deuterated benzene in stretched poly(ethylene). Other ^2H NMR studies on the deformation of crosslinked polymers have been reported by Lifshits,[313] Gronski *et al.*[314] and Yang *et al.*[315] These papers are related to the equivalent measurements of ^1H dipolar coupling discussed in Section 2.4 above.

5.2.2. *Molecular motion in bulk crosslinked polymers*

Changes in the ^2H NMR spectra, and ^2H T_1 relaxation times, during curing of deuterated phenol–formaldehyde resins were reported by Kelusky *et al.*[316] The spectra of the prepolymers consisted of a superposition of a narrow, motionally-averaged line and a broad quadrupolar pattern with splitting of 130 kHz, indicating that approximately 50% of the prepolymer was extensively crosslinked, and hence rigid on the NMR time scale. On curing at 343 K for 150 min, the spectra indicated restriction of motion of the phenyl rings and the formaldehyde unit. A narrow peak in the spectrum of the cured resin labelled at the formaldehyde unit was attributed to the presence of small molecules. Curing at higher temperatures (393 K) introduced an additional partially-averaged line shape to the spectrum, which was assigned to labelled methyl groups formed by degradation processes. Finally the increase in ^2H T_1 during the cure indicated a decrease in the spectral density of motions at 30 MHz. A similar study was reported by Jahroni[317] of the changes in the ^2H spectra during the cure of partially-deuterated liquid crystalline epoxy resins. An increase in orientational order on curing was reflected in an increase in the quadrupolar splitting with curing time. ^2H NMR measurements of reaction kinetics agreed well with those determined from measurements of molecular weight.

Very recently Shi and coworkers[318] have studied the ^2H NMR spectra of partially-deuterated DGEBA cured with 4,4′-methylenedianiline (MDA). The DGEBA monomers were labelled either on the phenyl ring, or at the methylene unit on the epoxy group. ^2H spectra were recorded at a range of temperatures, and with a range of quadrupolar echo delay times, so as to sample as wide as possible a range of frequencies of motion. The experimental data were fitted assuming a Kolrausch–Williams–Watts distribution, with an exponent of $\alpha = 0.6$ or 0.7. The correlation time of the 180° flipping motion of the phenyl groups was shorter by approximately an order of magnitude than that for the methylene units. An activation energy of 48–51 kJ mol^{-1} was calculated for the phenyl ring motion, in agreement with previous reports; however, the activation energy for *trans–gauche* isomerization of the methylene groups of 55–58 kJ mol^{-1} is higher than previous reported values and may reflect decreased mobility due to hydrogen bonding. The effect of crosslinking was to increase the activation energies of motion for both processes by on average 3 kJ mol^{-1}. The NMR data were used to predict the mechanical response of this resin, as shown in Fig. 17. The agreement between the predicted and experimental result is good at high frequencies; however, it is apparent that an additional low-frequency motion contributes to the mechanical relaxation at 1 Hz. It is suggested that this may be motion of the MDA unit. This result importantly demonstrates that the very large distributions of correlation times obtained by dynamic mechanical analysis, or dielectric relaxation, may be in part due to the

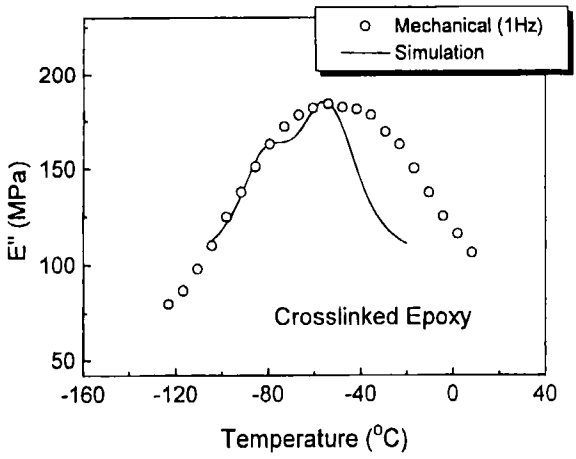

Fig. 17. Comparison of experimental mechanical relaxation at 1 Hz with simulated mechanical response based on motion of main-chain and phenyl rings in a crosslinked DGEBA–MDA epoxy resin, measured using ^{2}H NMR. (Reproduced from reference 318 with permission. Copyright © 1996 American Chemical Society.)

superposition of individual motions with different characteristic frequencies of motion.

Gambogi and Blum[251] have used ^{2}H NMR to study the molecular motion of the interface between a bismaleimide (BMI) attached to a silica surface via a deuterated (aminoalkyl)silane coupling agent. Spectra were recorded for chemisorbed coupling agent before and after reaction with BMI in two molar ratios. Changes in the ^{2}H NMR shape, as a function of temperature and BMI content were explained in terms of either a model of two-site jumping motion coupled with slow anisotropic Brownian diffusion, or at lower temperatures, by jumping motion on a tetrahedral lattice. A single correlation time of motion was used, and a small activation energy of motion deduced from variable temperature measurements. Polymerization with an excess of BMI did not appreciably affect the NMR spectra.

Mathias and Colletti[319] have reported an ^{2}H NMR study of the motion of crosslinked poly(acrylate)s of various structure. A rigid lattice line shape is observed below T_g; however, at higher temperatures a motionally-averaged spectrum is obtained. At low crosslink densities, the temperature of the onset of motion of the crosslink site is lower than that for motion of the polymer backbone. The onset temperature increased with increasing crosslink densities.

6. MULTINUCLEAR NMR STUDIES OF CROSSLINKED POLYMERS

NMR spectroscopy has an important role to play in the study of molecular motion in ion-conducting polymer electrolytes. Many polymer electrolytes are crosslinked to improve mechanical integrity; however, crosslinking invariably leads to an increase in glass transition temperature, and hence a decrease in molecular mobility of solute molecules. The factors influencing molecular mobility of dissolved ions are of significant commercial importance.

Several papers have appeared reporting spin–lattice relaxation of ions in polymer electrolytes. The value of T_1 (or $T_{1\rho}$) is related to the correlation time for motion of that species, and hence may reflect the ionic conductivity of the polymer. For example, Adamic *et al.*[320] have reported T_1 relaxation times for ^{23}Na nuclei in crosslinked dimethylsiloxane–ethylene oxide copolymers. The ^{23}Na NMR spectra consisted of two components of differing molecular mobility. The temperature dependence of the T_1 relaxation times of the two signals is well described by the Arrhenius relationship, despite the relationship of the conductivity with temperature being best described by a Vogel–Tammann–Fulcher (VTF) relationship. This difference reflects the very different time scales of motion responsible for T_1 relaxation, and ionic conductivity. Nonetheless, valuable information on relative ionic mobility can be obtained from NMR measurements.[320,321]

Spindler and Shriver[322,323] have reported NMR measurements on similar materials. The authors suggest that ^{13}C T_1 of the polymer matrix depends on a similar relationship to the VTF equation, i.e. molecular mobility depends on the reduced temperature related to the glass temperature of the system. Measurements were also made of ^{7}Li and ^{23}Na linewidth and chemical shift. The ^{23}Na chemical shift was shown to depend on temperature and ionic concentration, due, it is suggested, to changes in the strength of the ionic interactions.

Kim *et al.*[324] have shown that ^{7}Li NMR is a useful probe of motion in doped crosslinked poly(ether urethane) elastomers. T_2 measurements showed that the proportion of mobile Li ions increased with increasing poly(ethylene oxide) (PEO) content in the polymer, due to greater solvating properties of the PEO units. Measurements of T_1 versus temperature were used to obtained values of the activation energy for the motion of the Li ion, which were 30% lower than those obtained from measurements of conductivity. This difference is again ascribed to the short-range nature of the motions responsible for the T_1 relaxation.

A similar approach was adopted by Forsyth and coworkers,[325,326,327] in studies of motion of sodium triflate ions in polymer electrolytes based on poly(ether urethane). The spectra of their materials were consistent with full solvation of the sodium triflate species.[325] The width of the ^{23}Na resonance was investigated as a function of temperature, salt concentration, and

plasticizer concentration, and shown to be consistent with the line shape being dominated by quadrupolar interactions. T_1 relaxation times were shown to reflect mobility of the salts. In a second paper[326] measurements were made of both ^{23}Na and ^{19}F chemical shifts for a range of samples. Changes in chemical shift were related to cation–anion electrostatic interactions, which were found to increase with increasing salt content, and decrease on addition of plasticizer. Plots of ^{19}F relaxation times versus temperature showed two minima in T_1, due to the freezing of large scale motions associated with the glass transition, and motion of the CF_3 group at lower temperatures. The activation energy of motion above T_g was unaltered by addition of plasticizer. In the third paper in this series[327] the authors report measurements of ^{13}C T_1 relaxation times for the PEO component of the polymer electrolyte, as a function of temperature and plasticizer concentration. On addition of dimethyl formamide as a plasticizer, T_1 relaxation times are seen to increase, consistent with an increase in the spectral density of MHz motions; however, when propylene carbonate (PC) is added as a plasticizer to the electrolyte, T_1 decreases. This unexpected observation is suggested to result from screening of the coulombic interactions by PC, and hence increased binding of the cation to the polymer.

7. PFG NMR STUDIES OF CROSSLINKED POLYMERS

7.1. Background

In recent years the technique of PFG NMR has become increasingly important for measuring self-diffusion in polymers, and mixtures of small molecules and polymers. The technique was presaged in 1950 by Hahn,[70] who described the formation of echoes after the application of refocusing pulses. His aim was to reduce the effect of inhomogeneous magnetic fields on the T_2 decay. Hahn recognized the importance of dephasing of the magnetization due to diffusion of molecules during the echo refocusing delays. It was not until 1965 that Stejskal and Tanner[328] suggested the pulsed field gradient (PFG) experiment, and showed that the echo amplitude was described by the following expression, provided that the self-diffusion was due to simple Brownian motion:

$$I(2\tau) = I(0) \cdot e^{-\gamma^2 D\delta^2(\Delta - 1/3\delta)g^2} \tag{19}$$

where I is the echo amplitude, D is the self-diffusion coefficient, δ is the width of the gradient pulse, Δ is the separation of the two gradient pulses, and g is the strength of the gradient pulses.

In recent years, Callaghan and coworkers[329–331] have demonstrated that the PFG NMR experiment is analogous to a scattering experiment, and has shown that in solids with regular repeating structures, a peak in the plot of

echo attenuation versus scattering vector may be seen.[329] Callaghan has also applied the PFG NMR method to a wide range of materials problems, including diffusion in restricted geometries, such as within lamellar structures, plant tissue, and porous glasses.[329–331]

The essential limit of the PFG experiment is the need for very large and precisely balanced field gradients, as well as elimination of the effects of eddy currents on the echo amplitude. This usually limits in practice the lower limit of measurable diffusion coefficients to $10^{-11}\,m^2\,s^{-1}$; however, recent developments of the use of very high pulsed field gradients[330,332,333] have reduced this limit to $10^{-15}\,m^2\,s^{-1}$. In any case, the measurement of self-diffusion of entangled or crosslinked polymers is at the limit of the most advanced current technology. PFG NMR experiments conducted so far on crosslinked polymers have concentrated on measurements of self-diffusion of small molecules within the network of the crosslinked structure, and have important applications in the fields of polymerization kinetics, membrane science, and diffusion in hydrogel materials.

7.2. Experimental results

The initial PFG experiments concerned with diffusion of small molecules within crosslinked networks were conducted by Von Meerwall and Ferguson,[105] who measured self-diffusion coefficients of *n*-hexadecane and hexafluorobenzene in elongated samples of crosslinked *cis*-poly(isoprene). The self-diffusion coefficient did not depend on the orientation of the sample with respect to the diffusion gradients, and it was concluded, therefore, that in rubber samples elongated up to 10 times the initial dimension there were sufficient pathways for diffusion perpendicular to the draw direction to allow isotropic diffusion over the time of the diffusion experiment.

Von Meerwall and Palunas[334] have also measured the self-diffusion of low-molecular weight poly(butadiene) reacted with a chain extender. The echo attenuation plot for the unreacted polymer was highly non-linear and was interpreted in terms of a sum of diffusion terms arising from the distribution of molecular weights, and corrections for chain entanglements. On curing, the diffusion coefficient of the chain extender was relatively unaffected, and that of the polymer initially decreased by a factor of three. In a later related paper, Galiatsatos and Von Meerwall[335] measured the diffusion of the sol fraction out of a crosslinked poly(dimethyl siloxane) sample having an initially bimodal molecular weight distribution. The non-linear echo attenuation plots were again interpreted as having contributions from low and higher molecular weight material. The sol fraction was monitored over an extended period of time and was seen to decay to zero after five days extraction. The smaller, more rapidly diffusing molecules were extracted within one hour diffusion time.

More recently, Yasunaga and Ando[336,337] have measured the self-diffusion coefficient of water in crosslinked poly(methacrylic acid) gels. The equilibrium water content was controlled by varying the level of *N,N'*-methylenebisacrylamide crosslinking agent. The value of the self-diffusion coefficient was seen to increase with increasing water content to the power 1/3. Similar relationships were observed for ^1H T_1 and T_2 relaxation times with water content, and was consistent with the self-diffusion coefficients being proportional to the distance between chains, which is in turn proportional to the third power of the total volume, and hence mass, of the swollen gel. Expressed in other terms, the self-diffusion coefficient decreases with increasing crosslink density.[337]

Finally, Skirda and coworkers[332] have measured segmental fluctuations in crosslinked poly(butadiene) swollen with deuterated benzene. Very high field gradients of $50\,T\,m^{-1}$ were used in these experiments. The mean-squared displacement of the segments was observed to be independent of diffusion time, as indicated in Fig. 18, indicating restricted diffusion around an attractive centre. The mean-squared displacement decreased with increasing crosslinking density and was approximately equal to the mean-squared collective fluctuations calculated for these polymers.

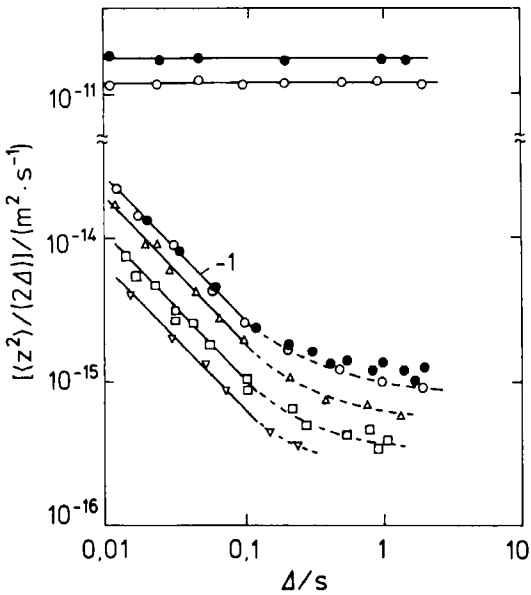

Fig. 18. Mean-squared displacement of polymer segments in crosslinked poly(butadiene) as a function of diffusion time, measured using PFG NMR. The self-diffusion coefficient, $\langle z^2\rangle/2\Delta$, decreases with increasing crosslink density. The upper two curves are for the uncrosslinked sol fraction. (Reproduced from reference 332 with permission. Copyright © 1988 Hüthig and Wepf Verlag.)

8. NMR IMAGING OF CROSSLINKED POLYMERS

8.1. Background

In 1954, Carr and Purcell[71] noted that the FID obtained in the presence of a linear gradient reflects the shape of the sample, and in fact calculated the form of the FID in the case of linear gradients over samples of different shape. It was not until 1973, however, that Lauterbur[338] and Mansfield and Grannell[339] obtained the first NMR images. As is well known a magnetic field gradient, G, applied across a sample results in the precession frequency being dependent of position, r, within the sample:

$$\omega(r) = \gamma B_0 + \gamma G \cdot r \tag{20}$$

where γ is the gyromagnetic ratio, B_0 the static magnetic field. The principle can be applied in two dimensions, with the gradient strength being incremented in a two-dimensional experiment. Finally, slice-selection in the third dimension can be achieved by applying a shaped pulse[340] in combination with a magnetic field gradient in the final dimension. The above simple experiment is one of a very large number of possible experiments[331] devised for obtaining two- or three-dimensional representations of the density of protons in the mobile phase of a sample.

The ultimate resolution obtainable in an NMR image depends on several factors. As lucidly explained by Blümich and Blümler,[341] discrimination of two points in space separated by the distance Δx is only possible if the following inequality is satisfied:

$$|\Delta\omega| < |\gamma \cdot G_x \cdot \Delta x| \tag{21}$$

where $\Delta\omega$ is the width of the resonance line. In mobile liquids, the ^{1}H NMR line can be less than 1 Hz in width, although for liquids in heterogeneous materials, a linewidth of 10 Hz is more typical, due to the broadening of the signal resulting from differences in magnetic susceptibility of the liquid and solid parts of material. The ^{1}H NMR linewidth in rigid ^{1}H-rich solids, is up to 100 kHz, due to the strong dipole–dipole coupling of the protons. In rubbers and elastomers, and the amorphous phase of semicrystalline polymers, an intermediate linewidth of 100 to 1 kHz is typical. A typical maximum gradient field strength obtainable from a conventional set of imaging gradients might be 100 mT m^{-1}. Equation (21) above therefore sets limits on the maximum attainable resolution as being 30 μm in liquids, 30 mm in an elastomer, and 3 m in a rigid solid! Efforts to reduce the last two limits have concentrated on either using very large field gradients including the utilization of gradients in the stray field of the NMR magnet,[342,343] or

alternatively narrowing the line with multi-pulse sequences,[339,344–351] or by sample spinning.[352,353] Examples of the use of some of these techniques will be mentioned in the next section. Of equal significance are the problems associated with the short T_2 relaxation times of ^1H nuclei in solids.

The field of NMR imaging has been the subject of a number of important texts and review articles of relevance to the polymer spectroscopist. The interested reader is directed to the text of Callaghan for the background to the techniques of NMR imaging and PFG NMR,[331] and of Mansfield and Morris for the principles of imaging in general, and biomedical applications in particular.[354] Recent reviews of interest include those by Blümich and Blümler[341] of application to polymeric, primarily elastomeric, materials, imaging of elastomers by Koenig,[355] applications to rigid solid materials by Jezzard *et al.*,[356] a specific review by the same authors dedicated to polymers and polymer composites,[357] non-medical applications of NMR imaging by Komoroski,[358] application of NMR imaging to materials of importance in chemical engineering by Gladden,[359] and NMR microscopy by Kuhn.[360] Of particular interest is the text edited by Blümich and Kuhn,[361] which covers background theory, and application of NMR imaging to the fields of materials science, plant science, and biomedicine.

8.2. Experimental results

8.2.1. Direct imaging of the polymer

Chingas and coworkers[345] were the first to report NMR images of crosslinked polymers. They examined a sample of the plastic crystal adamantane (^1H linewidth of 30 kHz) surrounded by a section of crosslinked neoprene rubber tubing. An MREV-8 sequence[362,363] applied to achieve line narrowing, in the presence of an incremented gradient, provided encoding in the x-direction. To allow sufficient time for switching of the gradients, the magnetization was stored after the first gradient, either in the Zeeman field or in the rotating RF field. Discrimination of the two solids forming the phantom could, therefore, be made by varying the storage time and taking account of differences in T_1 or $T_{1\rho}$. Finally the magnetization was acquired in the presence of a gradient in the y-direction. The two-dimensional images resulting from this pulse sequence demonstrate clearly the ability of NMR imaging both to produce images of dipolar-coupled solids, and to distinguish between parts of the sample on the basis of differences in relaxation parameters.

Cory and coworkers[353] combined magic angle spinning and back projection reconstruction to obtain images of poly(isoprene) rubber, as well as blends of poly(styrene) and poly(butadiene). The ^1H linewidth of poly(isoprene) was reduced from 1500 Hz to 100 Hz under the influence of magic angle

spinning at 5 kHz. Small features deliberately introduced into the rubber sample were accurately reproduced in the NMR images. The large linewidth of the poly(styrene) component of the blend precluded detection of this component, and so images of the distribution of poly(butadiene) through the blend were obtained.

Chang and Komoroski[364] have reported the NMR imaging of a range of different elastomers with differing ^1H T_2 relaxation times. Both the spin echo and gradient echo sequences were used. A sample of uncrosslinked *cis*-poly(butadiene) ($T_2 = 13$ ms) gave strong images using both imaging sequences, with void structures apparent in the images. The method was also applied to smoked natural rubber ($T_2 = 9$ ms) and cured filled *cis*-poly(butadiene) ($T_2 = 4$ ms); however, an image could not be obtained for poly(isobutylene) ($T_2 < 1$ ms). These results demonstrate the potential and limitations of the method using conventional imaging systems. In a later demonstration of the practical application of NMR imaging, Sarkar and Komoroski[365] measured samples of automobile tyre composites. A range of morphological features were identified, including voids and fibres, and layers of rubber having different T_2 relaxation times. An inner layer with very short T_2 was identified as consisting of butyl rubber. A study of blends of *cis*-poly(butadiene) (BR) with styrene–butadiene rubber (SBR), as a function of blend composition indicated that the approximate composition of blends could be determined from T_2-weighted images. Finally measurements were made of the dispersion of carbon black in several samples. Similar images of fibre-reinforced rubber have been reported by Cory *et al.*[366] The use of differences in T_2 to discriminate between rubber samples of differing crosslinking density has also been demonstrated by Strange.[367]

Kuhn and coworkers[368] have investigated the effect of crosslinking of natural rubber on the transverse relaxation times, and consequently the NMR images of these samples. The images were obtained of three samples of differing crosslinking density sandwiched together, using a Hahn echo acquired in the presence of an incremented gradient, and reconstructed using back-projection techniques. The decay of transverse magnetization was fitted to the sum of Gaussian and Lorentzian decay. Histograms displaying the populations of the T_2 relaxation times throughout the whole sample allow clear identification of the three rubber components as shown in Fig. 19. Samples consisting of filled crosslinked rubbers displayed similar relaxation characteristics; however, the absolute values of T_2 were decreased, and the distribution of relaxation times narrower in the filled samples. In a similar paper, Hafner and Barth[369] correlated the measured distribution of T_2 relaxation times in crosslinked natural rubber with the average molecular weight between crosslinks (M_c), and hence produced a histogram of the distribution of M_c throughout the polymer.

Jezzard *et al.*[370] demonstrated that increasing the temperature often dramatically increases the T_2 relaxation time of polymers including a

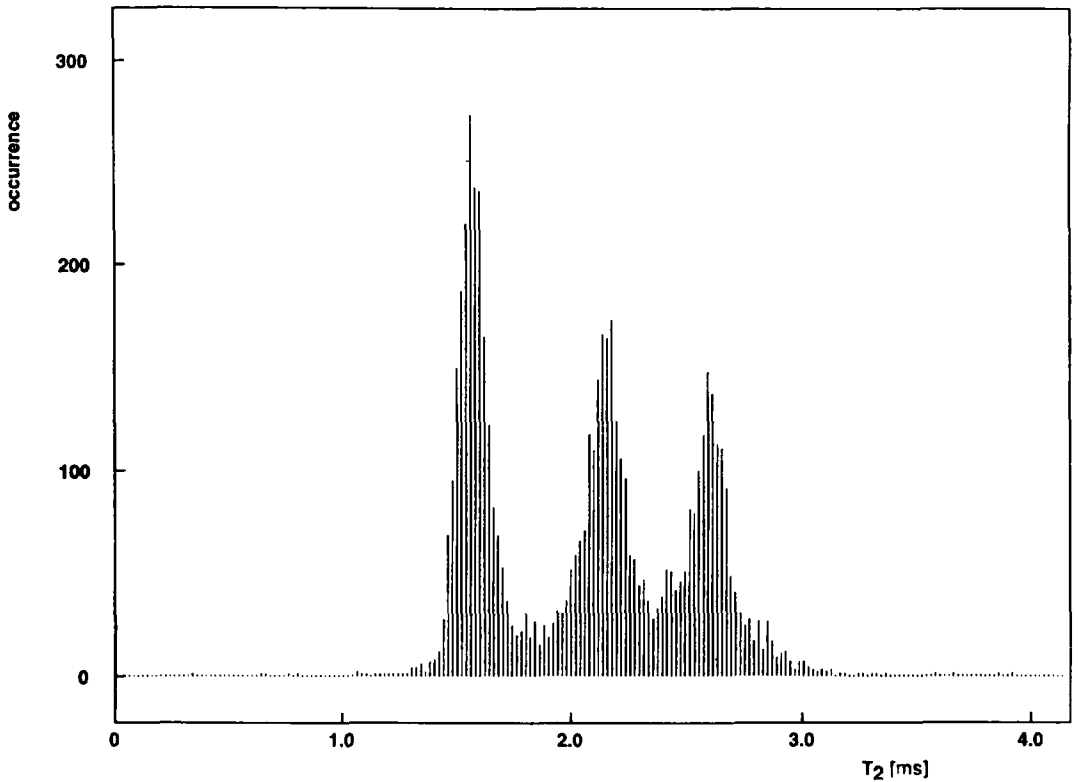

Fig. 19. Histograms of the occurrence of T_2 relaxation times throughout a sample of crosslinked natural rubber consisting of three samples of different crosslink density sandwiched together. (Reproduced from reference 368 with permission. Copyright © 1994 American Chemical Society.)

crosslinked elastomer. For example the T_2 of the elastomer increased from 1.1 ms to 1.7 ms on heating from 300 K to 340 K. Samples of water in nylon, and poly(vinyl alcohol) showed more dramatic increases on heating. The effect of collecting images at higher temperatures was demonstrated for the nylon–water system.

An alternative method of increasing the mobility of a crosslinked polymer, and hence lengthen the ^1H T_2, is to swell the material with a solvent. Smith and Koenig[371] have obtained excellent images of sulphur-vulcanized poly(butadiene) swollen with deuterated cyclohexane. On increasing the extent of cure, an overall reduction in signal-to-noise ratio was observed, consistent with a decrease in the T_2 relaxation time. The authors also collected T_2-maps, i.e. images in which the intensity of the image is equal to the T_2 at each pixel. These images are highly heterogeneous, presumably reflecting the heterogeneous nature of the crosslinking reaction. The values of T_2 are discussed in terms of the equilibrium dimensions of the crosslinked network. The authors also discuss the effects of a distribution of chemical shifts on the images.

The effects of ageing on crosslinked natural rubber have been reported by Blümler and Blümich.[372] Samples were heated to 400 K in air for varying periods of time, and spin echo images taken. An outer layer of heavily oxidized rubber with short T_2 was identified using a contrast agent around the sample. The kinetic of growth of the oxidized layer were consistent with previous reports. T_2-maps also identified regions in which low molecular weight oxidization products collected. In addition, these authors also report images taken during the phase separation of a blend of poly(styrene) and poly(isoprene). A similar study of degraded poly(isoprene) and rubber-modified poly(styrene) was reported by Chudek and Hunter.[373]

Very recently, Barth and coworkers[374] have reported the application of spin locking the ^1H magnetization prior to the imaging sequence to obtain $T_{1\rho}$ maps of crosslinked rubber. The value of $T_{1\rho}$ was related to local segment motion using a defect diffusion model, and provided a measure of the anisotropy of the segmental motion. $T_{1\rho}$ maps were obtained of a sample consisting of three rubbers of differing crosslink density.

An important area of application of NMR imaging will be the study of the rates and distribution of curing reactions in polymer resins. Jackson[375] has demonstrated that the intensity of T_2-weighted images can be related to the local viscosity and hence extent of cure in carbon-fibre-filled epoxy resins during curing. The method has application in process design and control.

8.2.2. Imaging of small molecules in crosslinked polymers

NMR imaging has also been applied to small molecules in crosslinked polymers. Solvents have been incorporated to enhance the resolution of the NMR image, to provide contrast necessary for observation of voids in rigid

polymers, and for studies of the rate of diffusion of small molecules through a crosslinked polymer. Clough and Koenig[376] measured the heterogeneity of crosslinking in sulphur-cured poly(butadiene) by imaging of the dioxane in the rubber swollen with that solvent. A more complete study of sulphur-cured high-1,2-poly(butadiene) was reported by Rana and Koenig.[377] Images were obtained of materials swollen with cyclohexane. Yasunaga *et al.*[378] have used the dependence of T_2 of water in swollen gels on applied stress to produce images of water density and stress in crosslinked poly(methacrylic acid) gels. A lower water density having a shorter T_2 relaxation time is observed close to the point of application of the stress.

A potential application of NMR imaging is measurement of void spaces in solid materials, including crosslinked polymers. For example, Rothwell and coworkers[379] reported images of glass-fibre-reinforced epoxy resins after immersion in water. The total increase in mass after immersion was less than 1%. The images of the two materials were highly heterogeneous, and provided evidence for crack propagation as a mechanism for diffusion of water. Jezzard and coworkers[380] have measured voids in carbon-fibre reinforced epoxy resin composites by imaging water trapped in voids of the composite. The results were in excellent agreement with void distributions measured by ultrasound methods. The advantage of NMR lies in the ability to obtain three-dimensional images, and images of irregularly-shaped objects. Problems with the conductive carbon fibres were encountered when the fibre direction was parallel with the B_1 field direction.

NMR imaging has an important contribution to make in the field of measurement of diffusion of solvents into polymers. Weisenberger and Koenig[381] have characterized the Case II diffusion of methanol in poly(methyl methacrylate) (MMA), including crosslinked PMMA. The kinetics have been identified not only from the characteristic sharp diffusion front from measured by imaging, but also from the linear dependence of the position of the diffusion front with time.[381] An initial rapid Fickian component to the diffusion was suggested to account for the non-zero intercept of the plot of position of the diffusion front against time. In a similar paper, the diffusion of acetone and methanol into crosslinked PMMA cylinder is studied.[382] At lower temperatures (303 K) the diffusion of methanol into PMMA is described by Case II kinetics, while at 333 K the kinetics are Fickian. At intermediate temperatures a combination of these two types of behaviour is observed. The authors also demonstrate the spatial dependence of the spin–spin relaxation time. In a third paper in this series, Weisenberger and Koenig[383] have measured T_1, T_2 and the self-diffusion coefficient of methanol in PMMA as a function of distance into the partially-swollen polymer. All three parameters decrease towards the glassy core, despite the concentration of solvent being constant across this swollen annulus. The glassy core is suggested to act as an anchor for the polymer

chains, thereby restricting motion towards the centre of the sample. These important results are at variance with current theories of diffusion of small molecules in polymers.

Webb and Hall have also measured the diffusion of small molecules into crosslinked polymers.[384–386] The diffusion of acetone into crosslinked natural rubber[384] was shown to follow Fickian diffusion kinetics, despite the shape of the profiles of concentration of acetone in the rubber giving evidence for the diffusion coefficient being dependent on concentration. This concentration-dependence of the diffusion coefficient is ascribed to the plasticization of the polymer chains by the small molecules. In the mixed solvent system,[385] benzene and acetone, diffusing into crosslinked natural rubber, images of the individual solvents were obtained by selective excitation of the ^{1}H resonances by replacing the 90° excitation pulse with a binomial excitation pulse sequence. The rates of ingress are identical for the two solvents, and were intermediate between the values measured for the pure solvents. The limitations of this chemical-shift selection method are discussed in this paper.[385] These results are reviewed in a third paper by these authors,[386] which also presents the results of editing images by utilizing scalar couplings.

Recent reports of measurement of diffusion of small molecules into crosslinked polymers include the diffusion of dioxane into crosslinked poly(styrene),[387] decalin into crosslinked ultra-high molecular weight poly(ethylene),[388] water in ion-exchange resins,[389] and water into hydroxypropyl methylcellulose gels.[390]

9. ^{129}Xe NMR STUDIES OF CROSSLINKED POLYMERS

^{129}Xe NMR is a potentially powerful method of measuring density of chain packing in crosslinked polymers. The technique has been applied to a number of uncrosslinked polymers, including polymer blends,[391,392] poly(ethylene),[393,394] block copolymers,[395] and a range of glassy and rubbery polymers.[396] Miller and coworkers[396] have demonstrated that the ^{129}Xe chemical shift in polymers is dominated by van der Waals dispersion interactions. Thus the ^{129}Xe chemical shift is a measure of the free volume available for the gas molecules within the polymer matrix.

A single paper has appeared reporting ^{129}Xe NMR of xenon absorbed into a crosslinked polymer. The spectrum of 8 atm xenon in uncrosslinked ethylene–propylene–diene rubber[397] shows at least two peaks, and possibly up to four overlapping peaks assignable to regions having different packing density. The precise nature of these regions is not discussed. On crosslinking the composite peak is shifted to lower field, consistent with an increase in density on crosslinking.

10. CONCLUSIONS

Three major challenges confront the experimental scientist engaged in research in the field of crosslinked polymers: determining the chemical structure of crosslinks, measuring the concentration of crosslinks, and characterizing the distribution of crosslinking reaction. The first of these aims has been readily achieved by NMR techniques. At early times in the crosslinking reaction, solution-state NMR provides a wealth of chemical information familiar to all chemists. The advent of spectrometers operating at even higher magnetic field strengths promises resolution and signal-to-noise ratio beyond the results so far reported, and hence a deeper understanding of the chemistry of crosslinking. Solid state NMR, particularly of ^{13}C nuclei, has been applied with great success to samples crosslinked beyond the gel point. The quantitative aspects of these experiments are well understood. A difficulty for this spectroscopy is the very large linewidths due largely to frozen conformations in the crosslinked or vitreous state. Recent advances in design of high-temperature MAS probes promise to largely overcome this disadvantage; however, there remain the obvious pitfalls of oxidative degradation, or continuation of curing, at higher temperatures.

It is fair to say that the uncertainties associated with the determination of the concentration of structures in any form of NMR spectroscopy are generally greater than in some other forms of spectroscopy, for example, infrared spectroscopy. For example, this latter form of spectroscopy may be the method of choice when determining rates of cure of unfilled epoxy resins. The advantage of NMR lies in the much higher chemical resolution, and in the flexibility of use. For example, filled polymers are often not readily accessible to analysis by vibrational spectroscopy, whereas NMR spectroscopy is generally not affected by non-conducting fillers. Despite the reservations on the quantitative nature of NMR, methods such as ^{13}C solid state NMR have given important information of the extent of crosslinking reactions. Measurements of the ^{1}H T_2 decay is a very powerful, rapid and flexible method for determining crosslink density in polymers, and should find greater application in industry.

The issue of the distribution of crosslinking reactions has been addressed by a number of workers. The approach taken has been to compare the yield of crosslinks determined by, for example, ^{13}C solid state NMR, with that obtained by a non-spectroscopic technique which relies on changes in a physical property, such as swelling ratio, or sol content. The results from the latter techniques are analysed assuming random crosslinking reactions, and so the often much larger yields determined by NMR spectroscopy are taken to indicate non-random crosslinking. Such general conclusions are often supported by knowledge of the chemical processes involved. However, this qualitative approach will be replaced by the use of new NMR

experiments, such as the dipolar filter and spin diffusion experiments, which have yet to be applied to this problem in detail.

NMR imaging has enormous potential for studying the distribution of crosslinking reactions. The images obtained so far have tended to show gross differences in crosslinking density due to inhomogeneous mixing of curing agent, or phase separation during crosslinking. In many crosslinked polymers the material will appear homogeneous over the smallest volume element resolved in the NMR images. However, it appears that many chemically-cured elastomers, including those used in commercial products, display gross heterogeneity. Differences in the relaxation times due to differences in crosslink density, or to degradation processes, can be used to provide contrast in imaging experiments. Combination of the knowledge of the behaviour of ^{1}H NMR relaxation times on crosslinking, and the spatial resolution derived from the imaging experiment, is especially powerful.

The time dependence of the NMR signal lends NMR spectroscopy a powerful advantage over other spectroscopic techniques. On the other hand, the chemical selectivity of the NMR signal provides an advantage over other methods for studying motion, such as DMA or dielectric relaxation. The effect of crosslinking on molecular motion has been studied in great detail. As confirmed by other techniques, the lower frequency motions tend to be most strongly influenced by the introduction of crosslinks. Measurements of NMR relaxation times have shown an increased coupling of relaxation processes on crosslinking, particularly at the low-frequency end of the frequency spectrum. The analysis of the relaxation behaviour has tended to rely on models for the type of motion or the form of the distribution of correlation times of motion. The future application of solid state exchange NMR will help resolve this problem by providing model-free information on the geometry of slow molecular reorientation. The improved resolution of the separation spectroscopies will also aid identification of the motions which contribute to mechanical relaxation in crosslinked polymers.

REFERENCES

1. H. S. Gutowsky and L. H. Meyer, *J. Chem. Phys.*, 1953, **21**, 2122.
2. P. J. Flory, *J. Am. Chem. Soc.*, 1943, **63**, 3083.
3. P. J. Flory, *J. Am. Chem. Soc.*, 1943, **63**, 3091.
4. P. J. Flory, *J. Am. Chem. Soc.*, 1943, **63**, 3096.
5. W. H. Stockmayer, *J. Polym. Sci.*, 1951, **9**, 69.
6. W. H. Stockmayer, *J. Polym. Sci.*, 1953, **11**, 424.
7. C. W. Macosko and D. R. Miller, *Macromolecules*, 1976, **9**, 199.
8. D. R. Miller and C. W. Macosko, *Macromolecules*, 1976, **9**, 206.
9. A. Charlesby and S. H. Pinner, *Proc. Roy. Soc. Lond. A*, 1959, **249**, 369.
10. O. Saito, *The Radiation Chemistry of Macromolecules*, Vol. 1, Ch. 11 (ed. M. Dole), Academic Press, New York, 1973.
11. L. E. Nielsen, *J. Macromol. Sci., Rev. Macromol. Chem.*, 1969, **C3**, 69.

12. G. Wisanrakkit and J. K. Gillham, *ACS Sympos. Ser.*, 1990, **227**, 143.
13. T. G. Fox and S. Loshaek, *J. Polym. Sci.*, 1955, **15**, 371.
14. S. Lunak, J. Vladyka and K. Dusek, *Polymer*, 1978, **19**, 931.
15. H. E. Adabbo and R. J. J. Williams, *J. Appl. Polym. Sci.*, 1982, **27**, 1327.
16. A. Hale, C. W. Macosko and H. E. Blair, *Macromolecules*, 1991, **24**, 2610.
17. L. E. Nielsen, *J. Appl. Polym. Sci.*, 1964, **8**, 511.
18. L. E. Nielsen and R. F. Landel, *Mechanical Properties of Polymers and Composites*, Marcel Dekker, New York, 1994.
19. D. J. P. Harrison, W. R. Yates and J. F. Johnson, *J. Macromol. Sci., Macromol. Chem. Phys.*, 1985, **C25**, 481.
20. D. M. French, *J. Macromol. Sci. – Chem.*, 1977, **A11**, 643.
21. P. J. Flory and J. Rehner, *J. Chem. Phys.*, 1943, **11**, 521.
22. E. F. Cluff, E. K. Gladding and R. Praiser, *J. Polym. Sci.*, 1960, **45**, 341.
23. R. A. H. Strecker, *J. Appl. Polym. Sci.*, 1969, **13**, 2439.
24. D. M. French, R. A. H. Strecker and A. S. Tompa, *J. Appl. Polym. Sci.*, 1970, **14**, 599.
25. C. J. de Bakker, N. A. St. John and G. A. George, *Polymer*, 1993, **34**, 716.
26. M. Andreis and J. L. Koenig, *Adv. Polym. Sci.*, 1989, **89**, 69.
27. D. R. Bauer, *Prog. Org. Coat.*, 1986, **12**, 155.
28. R. A. Kinsey, *Rubber Chem. Technol.*, 1990, **63**, 407.
29. D. W. McCall, *Acc. Chem. Res.*, 1971, **4**, 223.
30. V. J. McBrierty, *Polymer*, 1974, **15**, 503.
31. V. J. McBrierty and D. C. Douglass, *Phys. Rep.*, 1980, **83**, 61.
32. V. J. McBrierty and D. C. Douglass, *J. Polym. Sci., Macromol. Rev.*, 1981, **16**, 295.
33. V. J. McBrierty, *Magn. Reson. Rev.*, 1983, **8**, 165.
34. J. R. Havens and J. L. Koenig, *Appl. Spectrosc.*, 1983, **37**, 226.
35. F. A. Bovey, *High Resolution NMR of Macromolecules*, Academic Press, New York, 1972.
36. J. C. Randall (ed.), *NMR and Macromolecules: Sequence, Dynamics and Domain Structure*, ACS, Washington D.C., 1984.
37. J. L. Koenig, *Spectroscopy of Polymers*, ACS, Washington, 1992.
38. R. A. Komoroski (ed.), *High-resolution NMR Spectroscopy of Synthetic Polymers in Bulk*, VCH, Deerfield Beach, FL, 1986.
39. L. J. Mathias (ed.), *Solid-state NMR of Polymers*, Plenum Press, New York, 1991.
40. K. Schmidt-Rohr and H. W. Spiess, *Multidimensional Solid-state NMR and Polymers*, Academic Press, London, 1994.
41. H. S. Gutowsky, A. Saika, M. Takeda and D. E. Woessner, *J. Chem., Phys.*, 1957, **27**, 534.
42. J. G. Powles and P. Mansfield, *Phys. Lett.*, 1962, **2**, 58.
43. C. M. Huggins, L. E. St. Pierre and A. M. Bueche, *J. Polym. Sci., Part A*, 1963, **1**, 2731.
44. C. H. Bamford, G. C. Eastmond and D. Whittle, *Polymer*, 1975, **16**, 377.
45. G. C. Eastmond and E. G. Smith, *Polymer*, 1977, **18**, 245.
46. S. Morita, M. Shen and G. S. M. Ieda, *J. Polym. Sci., Polym. Phys. Ed.*, 1976, **14**, 1917.
47. L. Banks and B. Ellis, *J. Polym. Sci., Polym. Phys. Ed.*, 1982, **20**, 1055.
48. N. Bloembergen, E. M. Purcell and R. V. Pound, *Phys. Rev.*, 1948, **73**, 679.
49. R. Dejean de la Batie, F. Laupretre and L. Monnerie, *Macromolecules*, 1988, **21**, 2045.
50. A. Mirake, *J. Polym. Sci.*, 1958, **28**, 477.
51. D. W. McCall, D. C. Douglass and E. W. Anderson, *J. Chem. Phys.*, 1959, **30**, 1272.
52. K. Luszczynski and J. G. Powles, *Proc. Physic. Soc.*, 1959, **74**, 408.

53. T. M. Connor, *Trans. Faraday Soc.*, 1964, **60**, 1574.
54. J. Schaefer, *Macromolecules*, 1973, **6**, 882.
55. J. I. Kaplan and A. N. Garroway, *J. Magn. Reson.*, 1982, **49**, 464.
56. J. Colmenero, A. Alegría, J. M. Alberdi, F. Alvarez and B. Frick, *Phys. Rev.*, 1991, **44**, 7321.
57. T. J. Rowland and L. C. Labun, *Macromolecules*, 1978, **11**, 466.
58. G. P. Jones, *Phys. Rev.*, 1966, **148**, 332.
59. D. C. Douglass and V. J. McBrierty, *J. Chem. Phys.*, 1971, **54**, 4085.
60. D. E. Demco, A. Johansson and J. Tegenfeldt, *Solid State Nucl. Magn. Reson.*, 1995, **4**, 13.
61. K. Takagoshi, *Ann. Rep. NMR Spectrosc.*, 1995, **30**, 97.
62. J. Clauss, K. Schmidt-Rohr and H. W. Spiess, *Acta Polym.*, 1993, **44**, 1.
63. G. C. Munie, J. Jonas and T. J. Rowland, *J. Polymer. Sci., Polym. Chem. Ed.*, 1980, **18**, 1061.
64. D. R. Brown, G. C. Munie and J. Jonas, *J. Polymer. Sci., Polym. Phys. Ed.*, 1982, **20**, 1659.
65. D. W. Larsen and J. H. Strange, *J. Polymer. Sci., Polym. Phys. Ed.*, 1973, **11**, 65.
66. D. W. Larsen and J. H. Strange, *J. Polymer. Sci., Polym. Phys. Ed.*, 1973, **11**, 1453.
67. A. Jurkiewicz, N. Pislewski and K. A. Kunert, *J. Macromol. Sci.-Chem.*, 1982, **A18**, 511.
68. M. Andreis, Z. Veksli, F. Ranogajec and P. Hedvig, *Polymer*, 1989, **30**, 1498.
69. M. Pacl, E. D. Vecchio and F. Campana, *Polym. Bull.*, 1986, **15**, 21.
70. E. Hahn, *Phys. Rev.*, 1950, **80**, 580.
71. H. Y. Carr and E. M. Purcell, *Phys. Rev.*, 1954, **94**, 630.
72. S. Meiboom and D. Gill, *Rev. Sci. Instr.*, 1958, **29**, 688.
73. H. Koch, R. Bachus and R. Kimmich, *Polymer*, 1980, **21**, 1009.
74. R. Bachus and R. Kimmich, *Polym. Commun.*, 1983, **24**, 317.
75. A. Singer and D. Geschke, *Acta Polym.*, 1989, **40**, 86.
76. D. Geschke and G. Fleischer, *Acta Polym.*, 1991, **42**, 362.
77. A. K. Whittaker, T. Bremner and F. O. Zelaya, *Polymer*, 1995, **36**, 2159.
78. R. Folland and A. Charlesby, *Radiat. Phys. Chem.*, 1977, **10**, 61.
79. R. Folland and A. Charlesby, *Polymer*, 1979, **20**, 211.
80. R. Folland and A. Charlesby, *Polymer*, 1979, **20**, 207.
81. A. Charlesby, P. Käfer and R. Folland, *Radiat. Phys. Chem.*, 1978, **11**, 83.
82. A. K. Whittaker, *Radiat. Phys. Chem*, in press.
83. I. Kamel and A. Charlesby, *J. Polym. Sci., Polym. Phys. Ed.*, 1981, **19**, 803.
84. W. L. Gölz and H. G. Zachmann, *Makromol. Chem.*, 1975, **176**, 2721.
85. T. Bremner and A. Rudin, *J. Polym. Sci., Polym. Phys. Ed.*, 1992, **30**, 1247.
86. G. Simon, H. Schneider and K.-G. Häusler, *Prog. Coll. Polym. Sci.*, 1988, **78**, 30.
87. G. Simon, A. Birnsiel and K.-H. Schimmel, *Polym. Bull.*, 1989, **21**, 235.
88. G. Simon, B. Götschmann, D. Matzen and H. Schneider, *Polym. Bull.*, 1989, **21**, 475.
89. G. Simon and H. Schneider, *Makromol. Chem., Macromol. Symp.*, 1991, **52**, 233.
90. G. Simon, K. Baumann and W. Gronski, *Macromolecules*, 1992, **25**, 3624.
91. C. G. Fry and A. C. Lind, *Macromolecules*, 1988, **21**, 1292.
92. D. S. Bradley, E. D. von MeerWall, G. D. Roberts and J. Kamvouris, *J. Polym. Sci., Polym. Phys. Ed.*, 1995, **33**, 1545.
93. I. I. Nazarova, Yu. A. Ol'Khov and S. M. Baturin, *Polym. Sci. USSR*, 1980, **22**, 433.
94. I. I. Nazarova, V. B. Nazarov and S. M. Baturin, *Polym. Sci. USSR*, 1982, **24**, 1967.
95. T. G. Neiss and E. J. Vanderheiden, *Macromol. Symp.*, 1994, **86**, 117.
96. N. Parizel, G. Meyer and G. Weill, *Polymer*, 1993, **34**, 2495.
97. J. P. Cohen-Addad and C. Schmidt, *Polymer*, 1988, **29**, 883.
98. J. P. Cohen-Addad and C. Schmidt, *J. Polym. Sci., Polym. Phys. Ed.*, 1987, **25**, 487.

99. J. P. Cohen-Addad, E. Soyez, A. Vaillat and J. P. Queslel, *Macromolecules*, 1992, **25**, 1259.
100. C. Schmidt and J. P. Cohen-Addad, *Macromolecules*, 1989, **22**, 142.
101. J. P. Cohen-Addad and O. Girad, *Macromolecules*, 1992, **25**, 593.
102. J. P. Cohen-Addad, *Macromolecules*, 1989, **22**, 147.
103. J. P. Cohen-Addad and P. Huchot, *Macromolecules*, 1991, **24**, 6591.
104. J. P. Cohen-Addad and E. Soyez, *Macromolecules*, 1992, **25**, 6855.
105. E. Von Meerwall and R. D. Ferguson, *J. Polym. Sci., Polym. Phys. Ed.*, 1981, **19**, 77.
106. M. G. Brereton, *Macromolecules*, 1993, **26**, 1152.
107. M. G. Brereton, *Makromol. Chem., Macromol. Symp.*, 1993, **76**, 249.
108. J. Schaefer, *Macromolecules*, 1971, **4**, 110.
109. S. L. Manatt, D. Horowitz, R. Horowitz and R. P. Pinnell, *Anal. Chem.*, 1980, **52**, 1529.
110. W. T. Ford and T. Balakrishnan, *Macromolecules*, 1981, **14**, 284.
111. W. T. Ford, M. Periyasamy and H. O. Spivey, *Macromolecules*, 1984, **17**, 2881.
112. S. Mohanraj and W. T. Ford, *Macromolecules*, 1985, **18**, 351.
113. W. T. Ford, M. Periyasamy, H. O. Spivey and J. P. Chandler, *J. Magn. Reson.*, 1985, **63**, 298.
114. L. A. Errede, R. A. Newmark and J. R. Hill, *Macromolecules*, 1986, **19**, 651.
115. G. L. Marshall and S. J. Wilson, *Eur. Polym. J.*, 1988, **24**, 933.
116. G. L. Marshall and S. J. Wilson, *Eur. Polym. J.*, 1988, **24**, 939.
117. J. H. Hodgkin, R. I. Willing and R. Eibl, *J. Polym. Sci., Polym. Chem. Ed.*, 1981, **19**, 1239.
118. H. D. H. Stöver and J. M. J. Fréchet, *Macromolecules*, 1989, **22**, 1574.
119. H. D. H. Stöver and J. M. J. Fréchet, *Macromolecules*, 1991, **24**, 883.
120. G. P. Simon, P. E. M. Allen, D. R. G. Williams and E. H. Williams, *Eur. Polym. J.*, 1985, **21**, 877.
121. K. Ogino and H. Sato, *J. Polym. Sci., Polym. Phys. Ed.*, 1995, **33**, 189.
122. K.-J. Liu and W. J. Burlant, *J. Polym. Sci., Polym. Chem. Ed.*, 1967, **5**, 1407.
123. K. Ogino and H. Sato, *J. Appl. Polym. Sci.*, 1995, **58**, 1015.
124. K. Yokota, A. Abe, S. Hosaka, I. Sakai and H. Saito, *Macromolecules*, 1978, **11**, 95.
125. A. D. Bain, D. R. Eaton, A. E. Hamielec, M. Mlekuz and B. G. Sayer, *Macromolecules*, 1989, **22**, 3561.
126. V. J. McBrierty, X. Zhang, D. C. Douglass, J. X. Zhang and R. Jerome, *Polymer*, 1994, **35**, 3811.
127. W. P. Rothwell and J. S. Waugh, *J. Chem. Phys.*, 1981, **74**, 2721.
128. K. Takagoshi and K. Hikichi, *J. Chem. Phys.*, 1991, **94**, 3200.
129. P. E. M. Allen, D. J. Bennett, A. M. Hounslow and D. R. G. Williams, *Eur. Polym. J.*, 1992, **28**, 1179.
130. H. Yasuaga and I. Ando, *J. Mol. Struct.*, 1993, **301**, 129.
131. M. Kobayashi, I. Ando, T. Ishii and S. Amiya, *Macromolecules*, 1995, **28**, 6677.
132. E. R. Andrew, A. Bradbury and R. G. Eades, *Nature*, 1959, **183**, 1802.
133. I. J. Lowe, *Phys. Rev. Lett.*, 1959, **2**, 285.
134. A. Pines, M. G. Gibby and J. S. Waugh, *J. Chem. Phys.*, 1973, **59**, 569.
135. J. Schaefer and E. O. Stejskal, *J. Am. Chem. Soc.*, 1976, **98**, 1031.
136. J. Herzfeld and A. Berger, *J. Chem. Phys.*, 1979, **73**, 6021.
137. D. E. Axelson, L. Mandelkern, R. Popli and P. Mathieu, *J. Polym. Sci., Polym. Phys. Ed.*, 1983, **21**, 2319.
138. A. N. Garroway, W. B. Moniz and H. A. Resing, *ACS Symp. Ser.*, 1979, **103**, 67.
139. J. Schaefer, E. O. Stejskal and R. Buchdahl, *Macromolecules*, 1977, **10**, 384.
140. M. Mehring, *Principles of High Resolution NMR in Solids*, Springer-Verlag, Berlin, 1983.

141. X. Wu and K. W. Zilm, *J. Magn. Reson.*, 1991, **93**, 265.
142. J. H. O'Donnell and A. K. Whittaker, *J. Polym. Sci., Polym. Chem. Ed.*, 1992, **30**, 185.
143. R. L. Bennett, A. Keller, J. Stejny and M. Murray, *J. Polym. Sci., Polym. Chem. Ed.*, 1976, **14**, 3027.
144. M. Dole, *Crystalline Olefin Polymers*, (ed. R. A. V. Raff and K. W. Doak) Interscience, New York, 1965, Part 1, p. 845.
145. F. A. Bovey and F. C. Schilling, *ACS Symposium Series*, 1978, **169**, 131.
146. J. C. Randall, F. J. Zoepfl and J. Silverman, *Makromol. Chem., Rapid Commun.*, 1983, **4**, 149.
147. B. J. Lyons, *Polym. Prep.*, 1967, **8**, 672.
148. F. Horii, Q. Zhu, R. Kitamaru and H. Yamaoka, *Macromolecules*, 1990, **23**, 977.
149. Q. Zhu, F. Horii, R. Kitamaru and H. Yamaoka, *J. Polym. Sci., Polym. Chem. Ed.*, 1990, **28**, 2741.
150. J. H. O'Donnell and A. K. Whittaker, *Polymer*, 1992, **33**, 62.
151. J. Sohma, M. Shiotani, S. Murakami and T. Yoshida, *Radiat. Phys. Chem.*, 1983, **21**, 413.
152. J. H. O'Donnell and A. K. Whittaker, *Br. Polym. J.*, 1985, **17**, 51.
153. J. R. Havens, M. Thankur, B. Jerome and J. L. Koenig, *Macromolecules*, 1984, **17**, 1071.
154. P. F. Barron, J. H. O'Donnell and A. K. Whittaker, *Polym. Bull.*, 1985, **14**, 339.
155. D. J. T. Hill, J. H. O'Donnell, M. C. S. Perera, P. J. Pomery and A. K. Whittaker, *Macromol. Symp.*, 1995, **98**, 689.
156. D. J. T. Hill, J. H. O'Donnell, M. C. S. Perera, P. J. Pomery and A. K. Whittaker, *J. Macromol. Sci. – Pure Appl. Chem.*, 1993, **A30**, 633.
157. D. J. T. Hill, J. H. O'Donnell, M. C. S. Perera and P. J. Pomery, *Radiat. Phys. Chem.*, 1992, **40**, 127.
158. D. J. T. Hill, J. H. O'Donnell, M. C. S. Perera, P. J. Pomery and P. Smetsers, *J. Appl. Polym. Sci.*, 1995, **57**, 1155.
159. D. J. T. Hill, J. H. O'Donnell, M. C. S. Perera and P. J. Pomery, *ACS Symp. Ser.*, 1993, **527**, 74.
160. D. J. T. Hill, J. H. O'Donnell, M. C. S. Perera and P. J. Pomery, *Polymer*, 1995, **36**, 4185.
161. D. J. T. Hill, J. H. O'Donnell, M. C. S. Perera and P. J. Pomery, *J. Polym. Sci., Polym. Chem. Ed.*, 1996, **34**, 2439.
162. D. J. Patterson and J. L. Koenig, *Appl. Spectrosc.*, 1987, **41**, 441.
163. C. A. Fyfe, J. R. Lyerla, W. Volksen and C. S. Yannoni, *Macromolecules*, 1979, **19**, 757.
164. W. L. Earl and D. L. VanderHart, *Macromolecules*, 1979, **19**, 763.
165. D. L. VanderHart and F. Khoury, *Polymer*, 1984, **25**, 1589.
166. A. L. Cholli, W. M. Ritchey and J. L. Koenig, *Appl. Spectrosc.*, 1987, **41**, 1418.
167. J. H. O'Donnell and A. K. Whittaker, *Radiat. Phys. Chem.*, 1992, **39**, 209.
168. I. J. Colquhoun and K. J. Packer, *Br. Polym. J.*, 1987, **19**, 151.
169. E. Pérez and D. L. VanderHart, *J. Polym. Sci., Polym. Phys. Ed.*, 1988, **26**, 1979.
170. A. L. Cholli, F. C. Schilling and A. E. Tonelli, *Solid State NMR of Polymer* (ed. L. J. Mathias), Plenum, New York, 1991, p. 117.
171. F. C. Schilling, A. E. Tonelli and A. L. Cholli, *J. Polym. Sci., Polym. Phys. Ed.*, 1992, **30**, 91.
172. J. T. Dechter, *J. Polym. Sci., Polym. Lett. Ed.*, 1985, **23**, 261.
173. A. Johansson and J. Tegenfeldt, *Macromolecules*, 1992, **25**, 4712.
174. H. W. Beckham and H. W. Spiess, *Macromol. Chem. Phys.*, 1994, **195**, 1471.
175. K. Schmidt-Rohr, J. Clauss and H. W. Spiess, *Macromolecules*, 1992, **25**, 3273.

176. J. L. Koenig and D. J. Patterson, *Elastomerics*, 1986, **118**, 21.
177. A. M. Zaper and J. L. Koenig, *Polym. Mater. Sci. Eng.*, 1987, **56**, 189.
178. A. M. Zaper and J. L. Koenig, *Rubber Chem. Technol.*, 1987, **60**, 252.
179. A. M. Zaper and J. L. Koenig, *Rubber Chem. Technol.*, 1987, **60**, 278.
180. A. M. Zaper and J. L. Koenig, *Makromol. Chem.*, 1988, **189**, 1239.
181. M. Andreis, J. Liu and J. L. Koenig, *J. Polym. Sci., Polym. Phys. Ed.*, 1989, **27**, 1389.
182. R. S. Clough and J. L. Koenig, *Rubber Chem. Technol.*, 1989, **62**, 908.
183. M. Andreis, J. Liu and J. L. Koenig, *Rubber Chem. Technol.*, 1989, **62**, 82.
184. J. L. Koenig and M. Andreis, *Solid-state NMR of Polymer* (ed. L. J. Mathias), Ch. 11, Plenum Press, New York, 1991.
185. S. R. Smith and J. L. Koenig, *Rubber Chem. Technol.*, 1992, **65**, 176.
186. M. R. Krejsa and J. L. Koenig, *Rubber Chem. Technol.*, 1992, **65**, 427.
187. M. R. Krejsa, J. L. Koenig and A. B. Sullivan, *Rubber Chem. Technol.*, 1994, **67**, 348.
188. M. R. Krejsa and J. L. Koenig, *Rubber Chem. Technol.*, 1993, **66**, 73.
189. M. A. Rana and J. L. Koenig, *Rubber Chem. Technol.*, 1993, **66**, 242.
190. M. Mori and J. L. Koenig, *Rubber Chem. Technol.*, 1995, **68**, 551.
191. D. J. Patterson, J. L. Koenig and J. R. Shelton, *Rubber Chem. Technol.*, 1983, **56**, 971.
192. D. J. Patterson and J. L. Koenig, *ACS Symp. Ser.*, 1984, **243**, 205.
193. C. Fulber, D. E. Demco, O. Weintraub and B. Blümich, *Macromol. Chem. Phys.*, 1996, **197**, 581.
194. S. A. Sojka and W. B. Moniz, *J. Appl. Polym. Sci.*, 1976, **20**, 1977.
195. M.-F. Grenier-Loustalot and P. Grenier, *Makromol. Chem.*, 1983, **184**, 2477.
196. M.-F. Grenier-Loustalot and P. Grenier, *J. Polym. Sci., Polym. Chem. Ed.*, 1984, **22**, 4011.
197. J. Francillette, P. J. Madac and P. A. Hoarau, *Makromol. Chem., Macromol, Symp.*, 1987, **9**, 131.
198. K. Schlothauer, W. Tänzer, A. Fischer and M. Fedtke, *Polym. Bull.*, 1989, **22**, 221.
199. C. A. Fyfe, J. Nui, S. J. Rettig, D. W. Wang and M. D. Poliks, *J. Polym. Sci., Polym. Chem. Ed.*, 1994, **32**, 2203.
200. J. F. Haw and N. A. Johnson, *Anal. Chem.*, 1986, **58**, 3256.
201. D. L. VanderHart, W. L. Earl and A. H. Garroway, *J. Magn. Reson.*, 1981, **44**, 361.
202. L. L. Sterna and H. C. Smith, *J. Magn. Reson.*, 1988, **79**, 528.
203. R. K. Harris, R. R. Yeung, P. Johncock and D. A. Jones, *Polymer*, 1996, **37**, 721.
204. M.-F. Grenier-Loustalot and P. Grenier, *Eur. Polym. J.*, 1986, **22**, 457.
205. F. M. Thuillier, H. Jullien and M.-F. Grenier-Loustalot, *Polym. Commun.*, 1986, **27**, 206.
206. J. Mijovic and J. Wijaya, *Macromolecules*, 1990, **23**, 3671.
207. J. Mijovic, A. Fishbain and J. Wijaya, *Macromolecules*, 1992, **25**, 986.
208. A. Sabra, T. M. Lam, J. P. Pascault, M.-F. Grenier-Loustalot and P. Grenier, *Polymer*, 1987, **28**, 1030.
209. M.-F. Grenier-Loustalot, P. Grenier, P. Horny and Y.-Y. Chenard, *Br. Polym. J.*, 1988, **20**, 463.
210. A. J. Attias, B. Bloch and F. Laupretre, *J. Chim. Phys.*, 1987, **84**, 1223.
211. A. J. Attias, B. Bloch and F. Laupretre, *J. Polym. Sci., Polym. Chem. Ed.*, 1990, **28**, 3445.
212. A. A. Chalmers and P. Perlstein, *Eur. Polym. J.*, 1987, **22**, 887.
213. S. S. Sankar, S.V. Lonikar, R. D. Gilbert, R. E. Fornes and E. O. Stejskal, *J. Polym. Sci., Polym. Phys. Ed.*, 1990, **28**, 293.
214. A. Fischer, K. Schlothauer, A. Pfitzmann and J. Spèvácek, *Polymer*, 1992, **33**, 1370.

215. F. Gallouedec, F. Costa-Torro, F. Laupretre and B. Jasse, *J. Appl. Polym. Sci.*, 1993, **47**, 823.
216. L. A. Weisenberger and J. L. Koenig, *J. Polym. Sci., Polym. Phys. Ed.*, 1988, **26**, 771.
217. A. N. Garroway, D. L. VanderHart and W. L. Earl, *Phil. Trans. R. London A*, 1981, **299**, 609.
218. A. N. Garroway, W. M. Ritchey and W. B. Moniz, *Macromolecules*, 1982, **15**, 1051.
219. A. Udagawa, Y. Yamamoto, Y. Inoue and R. Chujo, *Polymer*, 1991, **32**, 2947.
220. F. Laupretre, R.-P. Eustache and L. Monnerie, *Polymer*, 1995, **36**, 267.
221. N. Egger, K. Schmidt-Rohr, B. Blümich, W.-D. Domke and B. Stapp, *J. Appl. Polym. Sci.*, 1992, **44**, 289.
222. P. W. Kopf and E. R. Wagner, *J. Polym. Sci., Polym. Chem. Ed.*, 1973, **11**, 939.
223. E. Dradi, G. Casiraghim G. Satori and G. Casnati, *Macromolecules*, 1978, **11**, 1295.
224. S. A. Sojka, R. A. Wolfe, E. A. Deitz and B. F. Dannels, *Macromolecules*, 1979, **12**, 767.
225. S. A. Sojka, R. A. Wolfe and G. D. Guenther, *Macromolecules*, 1981, **14**, 1539.
226. I. Ya. Slonin, S. G. Alekseyeva, B. M. Archava, S. L. Pokrovskii and P. A. Okunev, *Polym. Sci. USSR*, 1985, **27**, 1993.
227. L. E. Bogan, *Macromolecules*, 1991, **24**, 4807.
228. R. A. Fitzgerald, S. P. Tadros, R. F. Almeida, G. A. Sienko, K. Honda and T. Sarubbi, *J. Appl. Polym. Sci.*, 1992, **45**, 363.
229. T. G. Neiss and E. J. Vanderheiden, *Macromol. Symp.*, 1994, **86**, 117.
230. C. A. Fyfe, A. Rudin and W. Tehir, *Macromolecules*, 1980, **13**, 1320.
231. S. J. Opella and M. H. Frey, *J. Am. Chem. Soc.*, 1979, **101**, 5854.
232. R. L. Bryson, G. R. Hatfield, T. E. Early, A. E. Palmer and G. E. Maciel, *Macromolecules*, 1983, **16**, 1669.
233. G. E. Maciel, I.-S. Chuang and L. Gollob, *Macromolecules*, 1984, **17**, 1081.
234. G. R. Hatfield and G. E. Maciel, *Macromolecules*, 1987, **20**, 608.
235. S. So and A. Rudin, *J. Polym. Sci., Polym. Lett. Ed.*, 1985, **23**, 403.
236. A. Pizzi and P. Tekely, *J. Appl. Polym. Sci.*, 1995, **56**, 1645.
237. C. A. Fyfe, M. S. McKinnon, A. Rudin and W. Tehir, *Macromolecules*, 1983, **16**, 1216.
238. S. Sinha, F. D. Blum and D. O'Connor, *J. Appl. Polym. Sci.*, 1989, **38**, 163.
239. D. R. Bauer, R. A. Dickie and J. L. Koenig, *J. Polym. Sci., Polym. Phys. Ed.*, 1984, **22**, 2009.
240. M. Andreis, J. L. Koenig, M. Gupta and S. Ramesh, *J. Polym. Sci., Polym. Phys. Ed.*, 1995, **33**, 1449.
241. M. Andreis, J. L. Koenig, M. Gupta and S. Ramesh, *J. Polym. Sci., Polym. Phys. Ed.*, 1995, **33**, 1461.
242. I.-S. Chuang and G. E. Maciel, *Macromolecules, J. Appl. Polym. Sci.*, 1994, **52**, 1637.
243. P. G. Shukla, S. Sivaram and B. Mohanty, *Macromolecules*, 1992, **25**, 2746.
244. M. Paci, V. Crescenzi and F. Campana, *Polym. Bull.*, 1982, **7**, 59.
245. M. Paci and F. Campana, *Eur. Polym. J.*, 1985, **21**, 717.
246. P. Bergmark and P. Flodin, *Polymer*, 1987, **28**, 1657.
247. M. D. Sefcik, E. O. Stejskal, R. A. McKay and J. Schaefer, *Macromolecules*, 1979, **12**, 423.
248. S. A. Swanson, W. W. Fleming and D. C. Hofner, *Macromolecules*, 1992, **25**, 582.
249. A. C. Wong, A. N. Garroway and W. M. Ritchey, *Macromolecules*, 1981, **14**, 832.
250. H. Winter and G. P. M. van der Velden, *Macromolecules*, 1992, **25**, 4285.
251. J. E. Gambogi and F. D. Blum, *Macromolecules*, 1992, **25**, 4526.
252. D. W. Duff and G. E. Maciel, *Macromolecules*, 1990, **23**, 3069.
253. D. W. Duff and G. E. Maciel, *Macromolecules*, 1990, **23**, 4367.

254. D. W. Duff and G. E. Maciel, *Macromolecules*, 1991, **24**, 387.
255. C. A. Fyfe, J. Nui, S. J. Rettig, N. E. Burlinson, C. M. Reidsema, D. W. Wang and M. Poliks, *Macromolecules*, 1992, **25**, 6289.
256. A. B. Clayton, P. E. M. Allen, B. J. Keon and D. R. G. Williams, *Eur. Polym. J.*, 1993, **29**, 1283.
257. G. E. Maciel, I.-S. Chuang and G. E. Myers, *Macromolecules*, 1982, **15**, 1218.
258. I.-S. Chuang, G. E. Maciel and G. E. Myers, *Macromolecules*, 1984, **17**, 1087.
259. F. Laupretre, L. Monnerie and B. Bloch, *Anal. Chim. Acta*, 1986, **189**, 117.
260. R. Menif, B. Jasse, F. Laupretre and B. Bloch, *J. Appl. Polym. Sci.*, 1989, **38**, 1065.
261. G. L. Marshall, M. E. A. Cudby, K. Smith, T. H. Stevenson, K. J. Packer and R. K. Harris, *Polymer*, 1987, **28**, 1093.
262. Y.-S. Yang, E. Lafontaine and B. Mortaigne, *J. Appl. Polm. Sci.*, 1996, **60**, 2419.
263. R. Dejean de la Batie, F. Laupretre and L. Monnerie, *Macromolecules*, 1988, **21**, 2052.
264. Y. Yu and G. R. Brown, *Macromolecules*, 1993, **26**, 4872.
265. F. E. Du Prez, E. J. Goethals, P. J. Adriaensens, J. M. Gelan and D. J. M. Canderzande, *Macromolecules*, 1996, **29**, 4000.
266. T. W. Skloss and J. F. Haw, *Macromolecules*, 1994, **27**, 6998.
267. J. P. Gao, F. G. Morin and G. D. Darling, *Macromolecules*, 1993, **26**, 1196.
268. R. G. Earnshaw, C. A. Price, J. H. O'Donnell and A. K. Whittaker, *J. Appl. Polym. Sci.*, 1986, **32**, 5337.
269. G. P. Simon, P. E. M. Allen, D. J. Bennett, D. R. G. Williams and E. H. Williams, *Macromolecules*, 1989, **22**, 3555.
270. P. E. M. Allen, G. P. Simon, D. R. G. Williams and E. H. Williams, *Eur. Polym. J.*, 1986, **22**, 549.
271. P. E. M. Allen, G. P. Simon, D. R. G. Williams and E. H. Williams, *Macromolecules*, 1989, **22**, 809.
272. V. R. Reichert and L. J. Mathias, *Macromolecules*, 1994, **27**, 7030.
273. A. Allerhand, D. Doddrell and R. Komoroski, *J. Chem. Phys.*, 1971, **55**, 189.
274. R. A. Komoroski and L. Mandelkern, *J. Polym. Sci., Polym. Lett. Ed.*, 1976, **14**, 253.
275. E. M. Menger, W. S. Veeman and E. de Boer, *Macromolecules*, 1982, **15**, 1406.
276. G. P. Jones, *Phys. Rev.*, 1966, **148**, 332.
277. E. O. Stejskal, J. Schaefer and T. R. Steger, *Faraday Soc. Symp.*, 1979, **13**, 56.
278. J. Schaefer, M. D. Sefcik, E. O. Stejskal and R. A. McKay, *Macromolecules*, 1984, **17**, 1118.
279. J. Schaefer, E. O. Stejskal, T. R. Steger, M. D. Sefcik and R. A. McKay, *Macromolecules*, 1980, **13**, 1121.
280. W. W. Fleming, J. R. Lyerla and C. S. Yannoni, *ACS Symp. Ser.*, 1984, **247**, 83.
281. J. Schaefer, M. D. Sefick, E. O. Stejskal, R. A. McKay, W. T. Dixon and R. E. Cais, *Macromolecules*, 1984, **17**, 1107.
282. R. Voelkel, *Angew. Chem. Int. Ed. Engl.*, 1988, **27**, 1468.
283. D. L. VanderHart and A. N. Garroway, *J. Chem. Phys.*, 1979, **71**, 2773.
284. A. N. Garroway, W. B. Moniz and H. A. Resing, *Faraday Symp. Chem. Soc.*, 1979, **13**, 63.
285. A. N. Garroway, D. L. VanderHart and W. L. Earl, *Phil. Trans. R. London A*, 1981, **299**, 609.
286. L. C. Dickinson, P. L. Morganelli, W. J. MacKnight and J. C. W. Chien, *Makromol. Chem., Rapid Commun.*, 1987, **8**, 425.
287. L. C. Dickinson, P. Morganelli, C.W Chu, Z. Petrović, W. J. MacKnight and J. C. W. Chien, *Macromolecules*, 1988, **21**, 338.
288. P. E. M. Allen, G. P. Simon, D. R. G. Williams and E. H. Williams, *Polym. Bull.*, 1984, **11**, 593.

289. C. L. Dickinson, W. J. McKnight, J. C. W. Chien, *J. Polym. Sci., Polym. Lett. Ed.*, 1988, **26**, 191.
290. L. C. Dickinson, J. C. W. Chien and W. J. McKnight, *Macromolecules*, 1988, **21**, 2959.
291. L. C. Dickinson, J. C. W. Chien and W. J. McKnight, *Macromolecules*, 1990, **23**, 1279.
292. J. F. Shi, C. L. Dickinson, W. J. McKnight, J. C. W. Chien, C. Zhang, Y. Liu, Y. H. Chin, A. A. Jones and P. T. Inglefield, *Macromolecules*, 1993, **26**, 1008.
293. M. Andreis and J. L. Koenig, *Adv. Polym. Sci.*, 1995, **124**, 191.
294. I.-S. Chuang, B. L. Hawkins, G. E. Maciel and G. E. Myers, *Macromolecules*, 1985, **18**, 1482.
295. P. D. Murphy, R. A. Di Pietro, C. J. Lund and W. D. Weber, *Macromolecules*, 1994, **27**, 279.
296. D. W. Duff and G. E. Maciel, *Macromolecules*, 1991, **24**, 651.
297. G. Engelhardt and H. Janke, *Polym. Bull.*, 1981, **5**, 577.
298. R. A. Newmark and B. C. Copley, *Macromolecules*, 1984, **17**, 1973.
299. K. Beshah, J. E. Mark and J. L. Ackerman, *Macromolecules*, 1986, **19**, 2194.
300. K. Beshah, J. E. Mark, J. L. Ackerman and A. Himstedt, *J. Polym. Sci., Polym. Phys. Ed.*, 1986, **24**, 1207.
301. V. M. Litvinov, A. K. Whittaker, A. Hagemeyer and H. W. Spiess, *Coll. Polym. Sci.*, 1989, **267**, 681.
302. G. Kögler, A. Hasenhindl and M. Möller, *Macromolecules*, 1989, **22**, 4190.
303. G. Kögler, K. Loufakis and M. Möller, *Polymer*, 1990, **31**, 1538.
304. L. W. Jelinski, *High-resolution NMR Spectroscopy of Synthetic Polymers in Bulk* (ed. R. A. Komoroski), Ch. 10, VCH, Deerfield Beach, FL, 1986.
305. H. W. Spiess, *Coll. Polym. Sci.*, 1983, **261**, 193.
306. H. W. Spiess, *Chem. Rev.*, 1991, **91**, 1321.
307. M. Mehring, *Principles of High Resolution NMR in Solids*, Springer-Verlag, Berlin, 1983.
308. H. W. Spiess, *NMR Basic Princ. Progr.*, 1978, **15**, 59.
309. C. Schmidt, S. Wefing, B. Blümich and H. W. Spiess, *Chem. Phys. Lett.*, 1986, **130**, 84.
310. B. Deloche and E. T. Samulski, *Macromolecules*, 1981, **14**, 575.
311. W. Gronski, R. Stadler and M. M. Jacobi, *Macromolecules*, 1984, **17**, 741.
312. H. E. Gottlieb and Z. Luz, *Macromolecules*, 1984, **17**, 1959.
313. M. I. Lifshits, *Polymer*, 1987, **28**, 454.
314. W. Gronski, F. Forster, W. Pyckhout-Hintzen and T. Springer, *Makromol. Chem., Macromol. Symp.*, 1990, **40**, 121.
315. D. Yang, F. Li and Z. Qiu, *J. Macromol. Sci., Chem.*, 1990, **A27**, 149.
316. E. C. Kelusky, C. A. Fyfe and M. S. McKinnon, *Macromolecules*, 1986, **19**, 329.
317. S. Jahroni, *Macromolecules*, 1994, **27**, 2804.
318. J.-F. Shi, P. T. Inglefield, A. A. Jones and M. D. Meadows, *Macromolecules*, 1996, **29**, 605.
319. L. J. Mathias and R. F. Colletti, *Macromolecules*, 1991, **24**, 5515.
320. K. J. Adamic, S. G. Greenbaum, M. C. Wintersgill and J. J. Fontanella, *J. Appl. Phys.*, 1986, **60**, 1342.
321. M. C. Wintersgill, J. J. Fontanella, M. K. Smith, S. G. Greenbaum, K. J. Adamic and C. G. Andeen, *Polymer*, 1987, **28**, 633.
322. R. Spindler and D. F. Shriver, *Macromolecules*, 1988, **21**, 648.
323. R. Spindler and D. F. Shriver, *J. Am. Chem. Soc.*, 1988, **110**, 3036.
324. D.-W. Kim, J.-K. Park, H.-W. Rhee and H.-D. Kim, *Polym. J.*, 1994, **26**, 993.
325. M. Forsyth, M. E. Smith, P. Meakin and D. R. MacFarlane, *J. Polym. Sci., Polym. Phys. Ed.*, 1994, **32**, 2077.
326. M. Forsyth, D. R. MacFarlane, P. Meakin, M. E. Smith and T. J. Bastow, *Electrochim. Acta*, 1995, **40**, 2343.

327. M. Forsyth, P. Meakin and D. R. MacFarlane, *Electrochim. Acta*, 1995, **40**, 2339.
328. E. O. Stejskal and J. E. Tanner, *J. Chem. Phys.*, 1965, **42**, 288.
329. P. T. Callaghan, A. Coy, D. MacGowan, K. J. Packer and F. O. Zelaya, *Nature*, 1991, **351**, 467.
330. P. T. Callaghan, *Aust. J. Phys.*, 1984, **37**, 359.
331. P. T. Callaghan, *Principles of Nuclear Magnetic Resonance Microscopy*, Oxford University Press, Oxford, 1991.
332. V. D. Skirda, M. M. Doroginitskii, V. I. Sundukov, A. I. Maklakov, G. Fleischer, K. G. Häusler and E. Straube, *Makromol. Chem., Rapid Commun.*, 1988, **9**, 603.
333. J. Kärger and H. Spindler, *J. Am. Chem. Soc.*, 1991, **113**, 7571.
334. E. Von Meerwall and P. Palunas, *J. Polym. Sci., Poly. Phys. Ed.*, 1987, **25**, 1439.
335. V. Galiatsatos and E. D. Von Meerwall, *Macromolecules*, 1990, **23**, 3551.
336. H. Yasunaga and I. Ando, *Polym. Gels Networks*, 1993, **1**, 83.
337. H. Yasunaga and I. Ando, *Polym. Gels Networks*, 1993, **1**, 267.
338. P. C. Lauterbur, *Nature*, 1973, **242**, 190.
339. P. Mansfield and P. K. Grannell, *J. Phys. C.*, 1973, **6**, L422.
340. R. Damadian, M. Goldsmith and L. Minkoff, *Physio. Chem. Phys.*, 1977, **9**, 97.
341. B. Blümich and P. Blümler, *Makromol. Chem.*, 1993, **194**, 2133.
342. A. A. Samoilenko, D. Yu. Artemov and L. A. Sibeldina, *JETP Lett.*, 1988, **47**, 348.
343. A. A. Samoilenko and K. Zick, *Bruker Rep.*, 1990, **1**, 40.
344. P. Mansfield and P. K. Grannell, *Phys. Rev. B*, 1975, **12**, 3618.
345. G. C. Chingas, J. B. Miller and A. N. Garroway, *J. Magn. Reson.*, 1986, **66**, 530.
346. F. De Luca, C. Nuccetelli, B. C. De Simone and B. Maraviglia, *J. Magn. Reson.*, 1986, **69**, 496.
347. J. B. Miller and A. N. Garroway, *J. Magn. Reson.*, 1988, **77**, 187.
348. J. B. Miller and A. N. Garroway, *J. Magn. Reson.*, 1989, **82**, 529.
349. P. J. McDonald and P. F. Tokarczuk, *J. Phys. E.*, 1989, **22**, 948.
350. D. G. Cory, J. B. Miller, R. Turner and A. N. Garroway, *Mol. Phys.*, 1990, **70**, 331.
351. D. G. Cory, A. M. Reichwein, J. W. M. Van Os and W. S. Veeman, *Chem. Phys. Lett.*, 1988, **143**, 467.
352. D. G. Cory, J. W. M. Van Os and W. S. Veeman, *J. Magn. Reson.*, 1988, **76**, 543.
353. D. G. Cory, J. C. de Boer and W. S. Veeman, *Macromolecules*, 1989, **22**, 1618.
354. P. Mansfield and P. G. Morris, *NMR Imaging in Biomedicin', Adv. Magn. Reson.*, Suppl. 2, Academic Press, New York, 1982.
355. J. F. Koenig, *Macromol. Symp.*, 1994, **86**, 283.
356. P. Jezzard, J. J. Attard, T. A. Carpenter and L. D. Hall, *Prog. NMR Spectrosc.*, 1991, **23**, 1.
357. P. Jezzard, C. J. Wiggins, T. A. Carpenter, L. D. Hall, P. Jackson, N. J. Clayden and N. J. Walton, *Adv. Mater.*, 1992, **4**, 82.
358. R. A. Komoroski, *Anal. Chem.*, 1993, **65**, 1068.
359. L. F. Gladden, *Chem. Eng. Sci.*, 1994, **49**, 3339.
360. W. Kuhn, *Angewandte Chem.*, 1990, **29**, 1.
361. B. Blümich and W. Kuhn (eds), *Magnetic Resonance Microscopy*, VCH Publishers, Weinhein, 1992.
362. P. Mansfield, *J. Phys. C.*, 1971, **4**, 1444.
363. W.-K. Rhim, D. D. Elleman and R. W. Vaughan, *J. Chem. Phys.*, 1973, **58**, 1772.
364. C. Chang and R. A. Komoroski, *Macromolecules*, 1989, **22**, 600.
365. S. N. Sarkar and R. A. Komoroski, *Macromolecules*, 1992, **25**, 1420.
366. D. G. Cory, J. B. Miller and A. N. Garroway, *Macromol. Symp.*, 1994, **86**, 259.
367. J. H. Strange, *Phil. Trans. Roy. Soc. A*, 1990, **333**, 427.
368. W. Kuhn, P. Barth, S. Hafner, G. Simon and H. Schneider, *Macromolecules*, 1994, **27**, 5773.

369. S. Hafner and P. Barth, *Magn. Reson. Imaging*, 1995, **13**, 739.
370. P. Jezzard, T. A. Carpenter, L. D. Hall, P. Jackson and N. J. Clayden, *Polym. Commun.*, 1991, **32**, 74.
371. S. R. Smith and J. L. Koenig, *Macromolecules*, 1991, **24**, 3496.
372. P. Blümler and B. Blümich, *Macromolecules*, 1991, **24**, 2183.
373. J. A. Chudek and G. Hunter, *J. Mater. Sci. Lett.*, 1992, **11**, 222.
374. P. Barth, S. Hafner and P. Denner, *Macromolecules*, 1996, **29**, 1655.
375. P. Jackson, *J. Mater. Sci.*, 1992, **27**, 1302.
376. R. S. Clough and J. L. Koenig, *J. Polym. Sci., Polym. Lett. Ed.*, 1989, **27**, 451.
377. M. A. Rana and J. L. Koenig, *Macromolecules*, 1994, **27**, 3727.
378. H. Yasunaga, H. Kurosu and I. Ando, *Macromolecules*, 1992, **25**, 6505.
379. W. P. Rothwell, D. R. Holecek and J. A. Kershaw, *J. Polym. Sci., Polym. Lett. Ed.*, 1984, **22**, 241.
380. P. Jezzard, C. J. Wiggins, T. A. Carpenter, L. D. Hall, J. A. Barnes, P. Jackson and N. J. Clayden, *J. Mater. Sci.*, 1992, **27**, 6365.
381. L. A. Weisenberger and J. L. Koenig, *J. Polym. Sci., Polym. Lett. Ed.*, 1989, **27**, 55.
382. L. A. Weisenberger and J. L. Koenig, *Appl. Spectrosc.*, 1989, **43**, 1117.
383. L. A. Weisenberger and J. L. Koenig, *Macromolecules*, 1990, **23**, 2445.
384. A. G. Webb and L. D. Hall, *Polymer Commun.*, 1990, **31**, 422.
385. A. G. Webb and L. D. Hall, *Polymer Commun.*, 1990, **31**, 425.
386. A. G. Webb and L. D. Hall, *Polymer*, 1991, **32**, 2926.
387. M. Ing, B. Pfleiderer, K. Albert, W. Rapp and E. Beyer, *Macromolecules*, 1994, **27**, 2778.
388. T. M. Hyde, L. F. Gladden, M. R.Mackley and P. Gao, *J. Polym. Sci., Polym. Chem. Ed.*, 1995, **33**, 1795.
389. A. S. Wallner and W. M. Ritchey, *J. Appl. Polym. Sci.*, 1995, **57**, 1.
390. A. R. Rajabi-Siahboomi, R. W. Bowtell, P. Mansfield, M. C. Davies and C. D. Melia, *Pharm. Res.*, 1996, **13**, 376.
391. J. H. Walton, J. B. Miller and C. M. Roland, *J. Polym. Sci., Polym. Phys. Ed.*, 1992, **30**, 527.
392. M. Tomaselli, B. H. Meier, P. Robyr, U. W. Suter and R. R. Ernst, *Chem. Phys. Lett.*, 1993, **205**, 145.
393. A. P. M. Kentgens, H. A. van Boxtel, R.-J. Verweel and W. S. Veeman, *Macromolecules*, 1991, **24**, 3712.
394. T. R. Stengle and K. L. Williamson, *Macromolecules*, 1987, **20**, 1430.
395. S. K. Brownstein, J. E. L. Roovers and D. J. Worsfled, *Magn. Reson. Chem.*, 1988, **26**, 392.
396. J. B. Miller, J. H. Walton and C. M. Roland, *Macromolecules*, 1993, **26**, 5602.
397. G. J. Kennedy, *Polym. Bull.*, 1990, **23**, 605.

This Page Intentionally Left Blank

The Conformational Connection Between the Microstructures of Polymers and Their NMR Spectra

ALAN E. TONELLI

Fiber and Polymer Science Program, College of Textiles, North Carolina State University, P.O. Box 8301, Raleigh, North Carolina 27695-8301, USA

The connections between the NMR spectra and microstructures of polymers are examined from the point of view of the microstructurally-sensitive local conformations of polymer chains. This approach is rendered fruitful by application of the conformationally-sensitive γ-gauche effect method of predicting chemical shifts. Through knowledge of the conformational characteristics of polymers and their sensitivity to polymer microstructure, we may more readily assign their NMR spectra to their underlying microstructures. By means of several examples, we illustrate the types of detailed structural and conformational information that can be obtained for polymer samples from their high-resolution NMR spectra when analysed in terms of their local chain conformations.

1. INTRODUCTION

The resonance or Larmor frequency of a spin-1/2 nucleus is highly sensitive to the local molecular environment in which it resides. When placed in a strong, static magnetic field B_0 of several tesla, the cloud of electrons about the nucleus produce orbital currents, resulting in the creation of small local magnetic fields which are proportional to B_0, but are opposite in direction.

ANNUAL REPORTS ON NMR SPECTROSCOPY
VOLUME 34 ISBN 0-12-505334-7

These local induced magnetic fields effectively screen or shield the nucleus from B_0 and result in the nucleus experiencing a net local magnetic field $B_{loc} = B_0(1 - \sigma)$, where σ is the screening constant. σ is highly sensitive to chemical structure, i.e., the numbers and types of atoms and groups of atoms attached to or near the observed nucleus. It is the dependence of σ upon molecular structure that lies at the heart of NMR's utility as a probe of molecular structure.

Any structural feature that alters the electronic environment around a nucleus will affect its screening constant σ and lead to an alteration in its resonance frequency or chemical shift δ. Consequently, to predict the chemical shift of, say a ^{13}C nucleus in a particular molecular environment, the electronic wave function of the molecular system in the presence of the strong applied field B_0 must be known. For this reason it has been extremely difficult to make *a priori* predictions of the resonance frequencies or chemical shifts of spin-1/2 nuclei.[1–4] If, for example, we wish to calculate the relative chemical shifts of the ^{13}C nuclei in methane and methylfluoride, we must be able to accurately determine the electronic wave functions of both molecules in the presence of B_0.

To date it has not been possible to make accurate predictions of the chemical shifts observed for spin-1/2 nuclei, even when applying the most sophisticated *ab initio* quantum mechanical methods. Instead the empirically observed effects of substituents and local conformation have been used to correlate chemical shifts (usually ^{13}C) with the microstructures of molecules, including polymers.[5]

2. SUBSTITUENT EFFECTS ON ^{13}C CHEMICAL SHIFTS

Substituent effect rules, useful in predicting the ^{13}C chemical shifts observed in the ^{13}C NMR spectra of paraffinic hydrocarbons, have been derived.[6–9] ^{13}C chemical shifts are ordered in terms of the effects produced by substituents attached to the observed carbon at the α, β, and γ positions. Some of the data used to establish these rules are reproduced in Tables 1–3,[10] where it is apparent that each carbon substituent added, α and/or β, to the observed carbon, C^o, deshields it by *ca.* 9 ppm. On the other hand, each carbon γ-substituent results in a *ca.* -2 ppm shielding of the observed carbon. Using these substituent rules makes it possible to assign the ^{13}C NMR spectra of paraffinic hydrocarbons, including their highly branched members.

We may understand why the ^{13}C nuclei in head-to-tail (H-T) polypropylene (PP) (Fig. 1) resonate in the order CH_2, CH, CH_3 from high to low frequency (Table 4) in terms of their α-, β-, and γ-substituent effects. Methine carbons have two additional α- (+18 ppm) and two additional γ-substituents (-4 ppm) compared to methyl carbons and should resonate $18 - 4 = 14$ ppm downfield. Methylene carbons have two additional β- (+18 ppm), one fewer

Table 1. α-Substituent effect on δ ^{13}C (Bovey[10]).

		δ ^{13}C from TMS (ppm)	α-effect (ppm)
(a)	$C^{\circ}H_3$——H	−2.1	—
(b)	$C^{\circ}H_3$——$C^{\alpha}H_3$	5.9	8.0
(c)	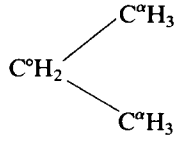	16.1	10.2
(d)	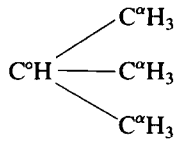	25.2	9.1
(e)	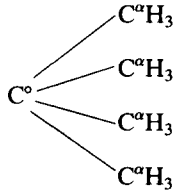	27.9	2.7

α- (−9 ppm), and two fewer γ-substituents (+4 ppm) compared with the methine carbons, and should resonate 18 − 9 + 4 = 13 ppm further downfield.

Suppose that PP possesses head-to-head (H-H) and tail-to-tail (T-T) units in addition to the predominant H-T enchainment of monomer units. As seen in Fig. 1, the H-H methine carbons have an additional β- (+9 ppm) and two fewer γ-substituents (+4 ppm) than H-T methine carbons, and should resonate 9 + 4 = 13 ppm downfield from their H-T counterparts. T-T methylene carbons have one fewer β- (−9 ppm) and two more γ-substituents (−4 ppm) than the H-T methylene carbons, and should move −9 −4 = −13 ppm upfield from the H-T methylene resonances. H-H methyls should resonate −2 ppm upfield from the H-T methyls, because they have a single additional γ-substituent. Note in Table 4 that all these expectations are borne out in the ^{13}C NMR spectra of H-T PP[11] and H-H:T-T PP,[12] and

Table 2. β-Substituent effect on δ ^{13}C (Bovey[10]).

		δ ^{13}C from TMS (ppm)	β-effect (ppm)
(a)	$C^{\gamma}H_3-\overset{1}{-}C^{\alpha}H_3$	5.9	—
(b)	$C^{\gamma}H_3-C^{\alpha}H_2-C^{\beta}H_3$	15.6	9.7
(c)	$C^{\gamma}H_3-C^{\alpha}H_3$ ($C^{\beta}H_3$, $C^{\beta}H_3$)	24.3	8.7
(d)	$C^{\gamma}H_3-C^{\alpha}$ ($C^{\beta}H_3$, $C^{\beta}H_3$, $C^{\beta}H_3$)	31.5	7.2

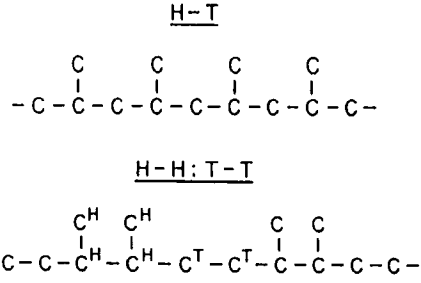

Fig. 1. Possible regiosequences of monomer units in PP.

are consistent with the α-, β-, and γ-substituent effects on ^{13}C chemical shifts derived from paraffins.

However, it is clear from the ^{13}C NMR spectra of three PP samples presented in Fig. 2[14] that the multiple resonances appearing in the spectrum of atactic PP, which are well-known to be produced by different stereosequences,[11] cannot be explained by the usual α-, β-, and γ-substituent effects. Each methyl carbon in PP has one α-, two β-, and two γ-substituents,

Table 3. γ-Substituent effect on δ ^{13}C (Bovey[10]).

		δ ^{13}C from TMS (ppm)	γ-effect (ppm)
(a)	$C^{\circ}H_3-C^{\alpha}H_2-C^{\beta}H_3$ $C^{\circ}H_3-C^{\alpha}H_2-C^{\beta}H_2-C^{\gamma}H_3$	15.6 13.2	– −2.4
(c)	$C^{\circ}H_3-C^{\alpha}H_2$ $C^{\beta}H$ ($C^{\gamma}H_3$, $C^{\gamma}H_3$)	11.5	−1.7
(d)	$C^{\circ}H_3-C^{\alpha}H_2-C^{\beta}$ ($C^{\gamma}H_3$, $C^{\gamma}H_3$, $C^{\gamma}H_3$)	8.7	−2.8
(e)	$C^{\alpha}H_3-C^{\circ}H_2-C^{\alpha}H_2-C^{\beta}H_3$	25.0	
(f)	$C^{\alpha}H_3-C^{\circ}H_2-C^{\alpha}H-C^{\beta}H_3-C^{\gamma}CH_3$	22.6	−2.4
(g)	$C^{\alpha}H_3-C^{\circ}H_2-C^{\beta}H_2-C^{\beta}H$ ($C^{\gamma}CH_3$, $C^{\gamma}CH_3$)	20.7	−1.9
(h)	$C^{\alpha}H_3-C^{\alpha}H_2-C^{\alpha}H_2-C^{\beta}$ ($C^{\gamma}CH_3$, $C^{\gamma}CH_3$, $C^{\gamma}CH_3$)	18.8	−1.9

each methine carbon has two α-, two β-, and four γ-substituents, and each methylene carbon has two α-, four β- and two γ-substituents independent of stereosequence. Some factor other than numbers and types of α-, β-, and γ-substituents, and which depends on PP stereosequence, must be responsible for the multiplicity of resonances observed in the atactic-PP spectrum. As we shall shortly see, that other factor is the stereosequence-dependent local conformation of the PP chain.[11,13,14]

Table 4. δ ^{13}C's observed in the spectra of H-T and H-H:T-T PPs.[13]

Carbon	δ^{13}C *vs.* TMS[a] (ppm)		
	H-T[b]	H-H[c]	T-T[c]
CH	28.5	37.0	—
CH_2	46.0	—	31.3
CH_3	20.5	15.0	—

[a]All δ ^{13}C values are averaged over the different stereosequences.[13]
[b]Schilling and Tonelli.[11]
[c]Möller *et al.*[12]

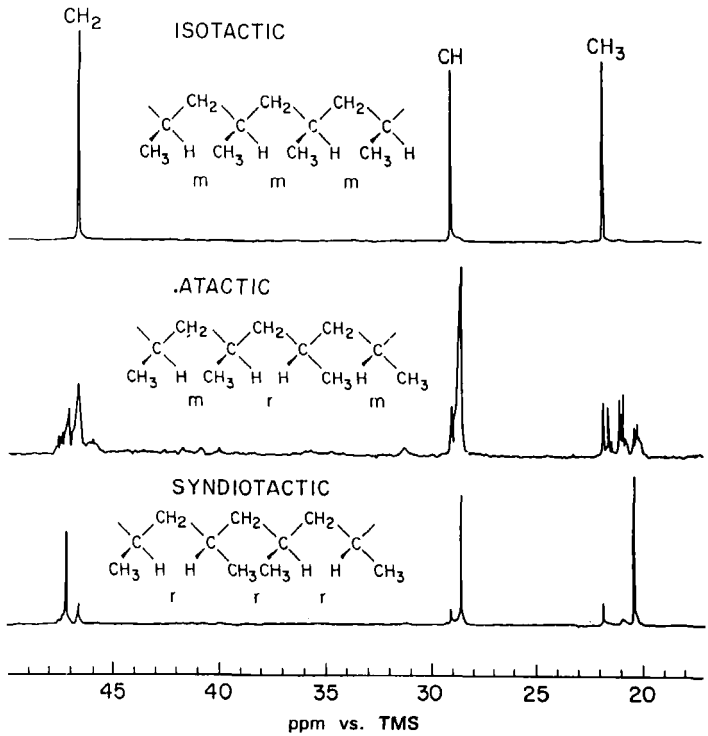

Fig. 2. 25 MHz ^{13}C NMR spectra of isotactic, atactic, and syndiotactic PP.[14]

3. *γ-GAUCHE* EFFECT METHOD OF PREDICTING NMR CHEMICAL SHIFTS

We have mentioned that γ-substituents in paraffinic hydrocarbons shield carbon nuclei relative to unsubstituted carbons. In Fig. 3 it is apparent that the observed carbon C^{α} and its γ-substituent (C^{γ}) can alter their mutual

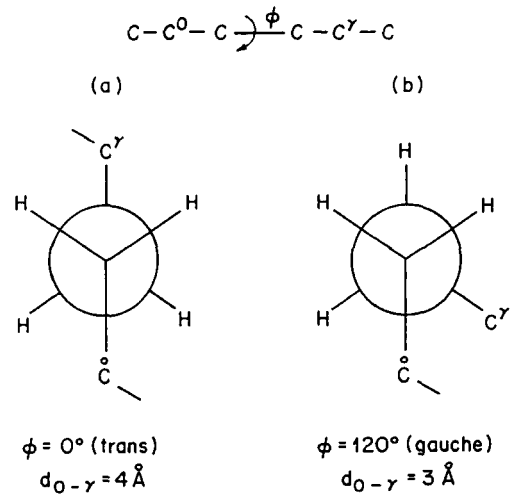

Fig. 3. Newman projections of an *n*-alkane chain in the (a) *trans* ($\phi = 0°$) and *gauche* ($\phi = 120°$) conformations.

arrangement (distance and orientation) via rotation about the central of the three bonds which separate them. Note the distance between C^o and C^γ ($d_{o-\gamma}$) is reduced from 4 to 3 Å on changing their arrangement from *trans* to *gauche*.

Grant and Cheney[15] first suggested a conformational origin for the γ-substituent effect on δ ^{13}C. Polarization of the C^o–H and C^γ–H bonds as a result of their compression by proton–proton (o–γ) repulsion was suggested as the source of *γ-gauche* shielding. More recently, Li and Chestnut[16] have suggested that the shielding γ-effects correlate with attractive van der Waals forces and not repulsive steric interactions, though they still suggest that the *gauche* arrangement of the observed carbon and its γ-substituent is required for shielding. Seidman and Maciel[17] concluded, based on semiempirical and *ab initio* quantum mechanical calculations, that the γ-substituent effect is conformational in origin, but is not exclusively attributable to the proximity of the interacting C^o and C^γ groups. Most recently, Barfield and Yamamura[4] concluded that nuclear shielding of the methyl carbons in *n*-butane is dominated by changes in the paramagnetic contributions for the C_1–C_2 and C_1–H bonds, rather than the steric compression of C^1–H bonds produced by the crowding of terminal methyl groups in the *gauche* conformation.

Though its fundamental origins remain uncertain, the γ-substituent effect on δ ^{13}C's has a conformational sensitivity and is, as we will shortly demonstrate, potentially useful in characterizing both the conformations and microstructures of polymers.

For a carbon nucleus to be shielded by a γ-substituent we have suggested

that they must be in a *gauche* arrangement (see Fig. 3). This suggestion is supported by comparing the δ ^{13}C's observed for the methyl carbons in *n*-alkanes. The methyl carbons in *n*-butane and higher *n*-alkanes have a single γ-substituent, while the methyl carbons in *n*-propane have no γ-substituents, but the same number and kinds of α- and β-substituents as the higher *n*-alkanes. In their crystals the *n*-alkanes adopt the extended, all-*trans* conformation where both methyl carbons are *trans* to their γ-substituents. If the γ-substituents are *trans* to the methyl carbons in the higher solid *n*-alkanes, then we would expect δ $^{13}CH_3$ (solid $C_n H_{2n+2}$, $n \geq 4$) = δ $^{13}CH_3$ (liquid *n*-propane). VanderHart[18] has observed the methyl carbons in the solid *n*-alkanes with n = 19,20,23,32 to resonate between 15–16 ppm (relative to TMS), while the methyl carbon in liquid *n*-propane resonates at 15.6 ppm.[19]

On the other hand, in the liquid state the methyl carbons in the higher *n*-alkanes ($n \geq 4$) resonate upfield at 13.2–14.1 ppm.[19] Of course in the liquid state the C–C bonds in *n*-alkanes possess a significant *gauche* content, and this results in the shielding of δ $^{13}CH_3$ for *n*-butane and the higher *n*-alkanes compared to that observed for the methyl carbons in *n*-propane or the higher solid *n*-alkanes in the all-*trans* conformation.

If we know how much *gauche* character, P_g, is possessed by the central bond between C^o and X^γ (C^o–C)–C–X^γ), then we can estimate the shielding produced by X^γ, $\gamma_{c,x}$, when in a *gauche* arrangement with C^o. This procedure is illustrated in Fig. 4, where the *gauche* shielding effects of the γ-substituents C, OH, and Cl are derived. As an example, the shielding produced at the methyl carbon in *n*-butane by the other methyl group (its γ-substituent), i.e., $\Delta\delta$ $^{13}CH_3$ = δ $^{13}CH_3$ (*n*-butane) $-\delta$ $^{13}CH_3$ (*n*-propane) = 13.2 − 15.6 = −2.4 ppm, is divided by the *gauche* character of the intervening bond, P_g = 0.46: $\gamma_{c,c} = \Delta\delta$ $^{13}CH_3/P_g$ = −2.4/0.46 = −5.2 ppm.

When this procedure is applied to *n*-butane, 1-propanol, and 1-chloropropane, the following γ-*gauche* shielding effects are derived: $\gamma_{c,c}$ = −5.2 ppm, $\gamma_{C,OH}$ = −7.2 ppm, and $\gamma_{c,cl}$ = −6.8 ppm. We now see that the shielding at a carbon nucleus produced by a γ-substituent in a *gauche* arrangement can be comparable in magnitude (−5 to −7 ppm) to the deshielding (+9 ppm) caused by the more proximal α and β substituents. More important, however, is the conformational dependence of the γ-substituent effect on ^{13}C NMR chemical shifts. Any variation in the microstructure of a molecule which effects its local conformation can be expected to be reflected in its δ ^{13}C's via the γ-*gauche* effect.

Let us complete our discussion of the conformational connection between the microstructures and NMR spectra of polymers, which is provided by the conformationally sensitive γ-*gauche* effect, by considering the non-equivalent δ ^{13}C's for the isopropyl methyl carbons in several branched alkanes[8,20,21] as presented in Table 5. Even though the isopropyl methyl carbons in each alkane have the same α, β, and γ substituents, we note in column 2 that the

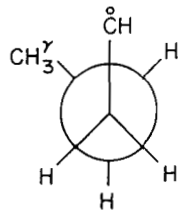

$\overset{\circ}{C}H_3 - CH_2 - CH_2 - CH_3^{\gamma}$

% gauche = 46

$\gamma_{C-C} = \frac{-2.4}{.46} = -5.2$ ppm

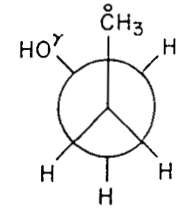

$\overset{\circ}{C}H_3 - CH_2 - CH_2 - OH^{\gamma}$

% gauche = 74

$\gamma_{C-O} = \frac{-5.3}{.74} = -7.2$ ppm

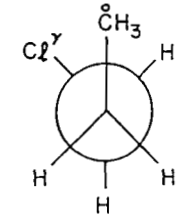

$\overset{\circ}{C}H_3 - CH_2 - CH_2 - Cl^{\gamma}$

% gauche $\cong$ 60.0

$\gamma_{C-Cl} \cong \frac{-4.1}{.60} \cong -6.8$ ppm

Fig. 4. Derivation of the *γ-gauche* shielding produced by the γ-substituents C, OH, and Cl (see text).

observed non-equivalence progressively decreases as the number of carbons separating the terminal isopropyl group from the asymmetric centre is increased. This behaviour can be understood[22] if we focus on the source of the non-equivalent δ ^{13}C's observed for the isopropyl methyl carbons in 2,4-dimethylhexane (2,4-DMH).

In Fig. 5 we have illustrated the possible staggered conformations about the C_2–C_3 backbone bond in 2,4-DMH, since these determine whether or not the isopropyl methyl carbons C^{sc}, C^{bb} are *γ-gauche* to the asymmetric carbon C_4. From the probabilities of finding bond C_2–C_3 in the *trans* (*t*), *gauche*+ (*g*+), and *gauche*− (*g*−) rotational states (P_t, P_{g+}, P_{g-}), we obtain $P_t + P_{g+}$, $P_{g+} + P_{g-}$ as the probabilities for *gauche* arrangements between C^{sc} and C^{bb}, respectively, and their γ-substituent C_4. Bond rotation probabilities are obtained from the conformational model developed by Mark[23] for ethylene–propylene copolymers: $P_t = 0.38$, $P_{g+} = 0.01$, and $P_{g-} = 0.61$. Thus, C_4 is *γ-gauche* to C^{sc} with probability 0.39 and to C^{bb} with probability 0.62. We expect the non-equivalence between C^{sc} and C^{bb} to be $\Delta\delta$ $^{13}C = (0.39 - 0.62)X\ \gamma_{c,c} = -0.23\ (-5.2\,\text{ppm}) = 1.1$ ppm, where we have adopted the value $\gamma_{c,c} = -5.2$ ppm derived from *n*-butane.

Table 5. Non-equivalent ^{13}C NMR chemical shifts for the isopropyl methyl carbons in branched alkanes.

Alkaline	$\Delta\delta$ (ppm)	
	Observed	Calculated
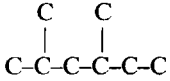	1.0 (1.9, 1.1, 0.9)[b]	1.6, 1.1, 0.9
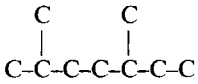	0.2	0.2
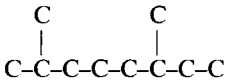	0.1	0.04
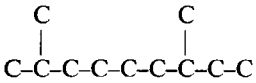	0.0	0.0

[a]Observed between ambient temperature and 48°C (Kroschwitz *et al.*,[20] Lindeman and Adams,[8] Carman *et al.*[21]).
[b]Observed at −120, 25, and 90°C (Tonelli *et al.*[22]).

The observed non-equivalence (1.0–1.1 ppm) is in close agreement with the value expected from the *γ-gauche* conformational calculation. The temperature dependence of the observed magnetic non-equivalence is also successfully reproduced by the *γ-gauche* effect calculations, leaving little doubt that its origin is the conformationally sensitive *γ-gauche* effect.

From the Newman projections in Fig. 5 it might be expected that the t and $g-$ conformations would be equally populated. However, it is well known[24] that rotational-state probabilities for the backbone bonds in linear chain molecules depend on the conformations, or rotational states, of neighbouring bonds. The asymmetric centre at C_4 generates intramolecular interactions which depend simultaneously on ϕ and neighbouring bond rotations (Fig. 5(a)), which render $P_t \neq P_{g-}$. The values of P_t and P_{g-} approach each other as the asymmetric centre is further removed from the terminal isopropyl group, leading to a reduction in the expected non-equivalence of the isopropyl methyl carbons. This expectation is borne out in Table 5, where it is both observed and predicted that the magnetic non-equivalence of isopropyl methyl carbons vanishes once they are separated by more than four carbons from the asymmetric centre.

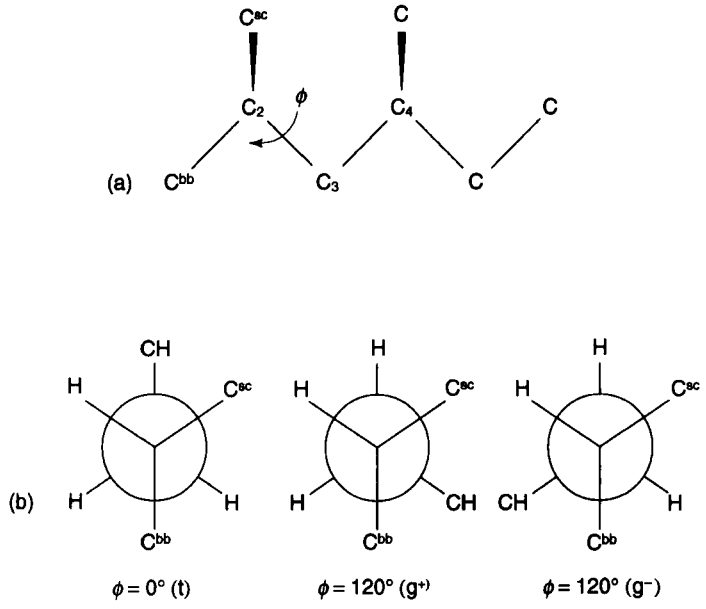

Fig. 5. (a) 2,4-DMH in the all-*trans* conformation. (b) Newman projections illustrating rotational states about the C_2–C_3 backbone bond of 2,4-DMH.[22]

It is apparent from this example that the microstructural sensitivity of ^{13}C NMR chemical shifts can have a conformational origin. δ ^{13}C depends on the local magnetic field, which is influenced by the local conformation in the vicinity of the resonating carbon nucleus. The local conformation is determined by the neighbouring microstructure. Hence, the microstructural sensitivity of ^{13}C NMR has its basis in the dependence of the local conformation on microstructure:

$$\text{microstructure} \rightarrow \text{conformation} \rightarrow H_{loc} \rightarrow \delta\ ^{13}C$$

The shielding of ^{13}C nuclei by γ-substituents in a *gauche* arrangement (γ-*gauche* effect) enables us to both complete and simplify the conformational connection between the microstructures and NMR spectra of polymers.

$$\text{microstructure} \xrightarrow{\gamma\text{-gauche effect}} \delta\ ^{13}C$$

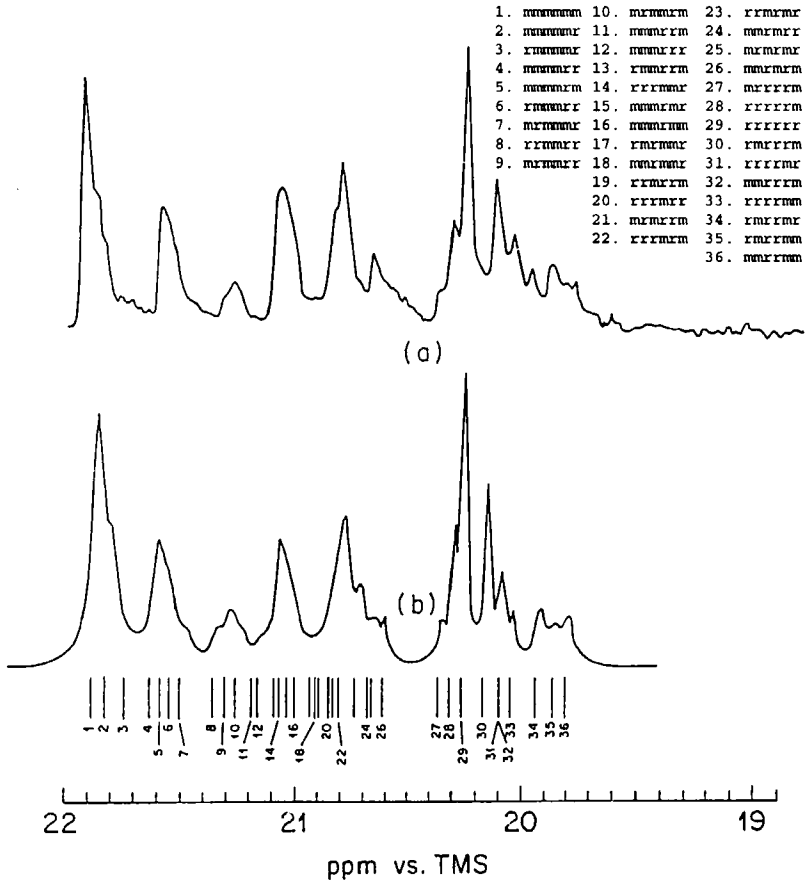

Fig. 6. (a) ^{13}C NMR spectrum at 90.52 MHz of the methyl carbon region in atactic PP in 20% w/v *n*-heptane solution at 67°C. (b) Simulated spectrum obtained from calculated chemical shifts, as represented by the line spectrum below, assuming Lorentzian peaks < 0.1 ppm width at half height.[14]

4. APPLICATIONS OF *γ-GAUCHE* EFFECT ANALYSIS OF POLYMER MICROSTRUCTURES

4.1. Polypropylene (PP)

We are now in a position to understand the stereosequence sensitivity of the δ ^{13}C's observed[11] for atactic PP (Fig. 2(b)). When the methyl carbon region of this spectrum is expanded[14] we see in Fig. 6(a) that over 20 resonances are observed. Because there are 10 and 36 distinct pentad and heptad

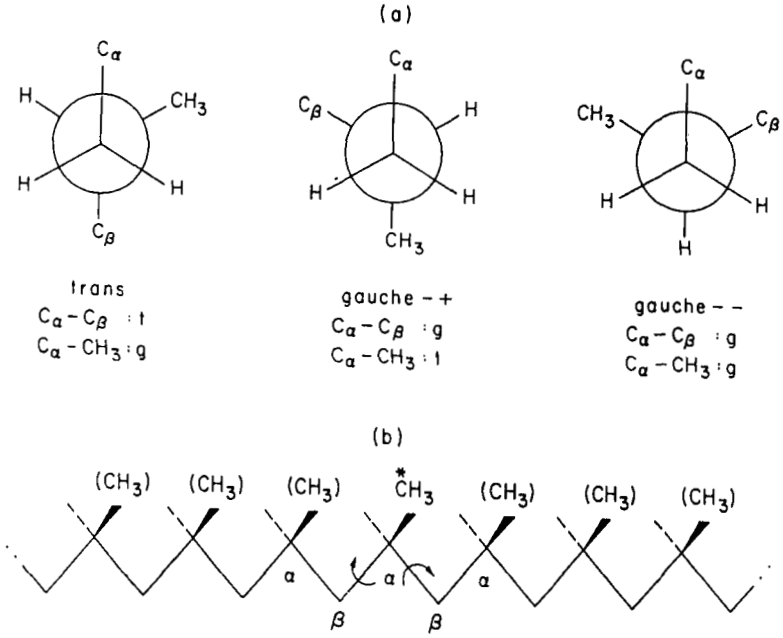

Fig. 7. (a) Conformations of a four carbon fragment of a PP chain; (b) heptad of PP; observed methyl is marked by "*".

stereosequences,[25] the ^{13}C NMR spectrum of atactic PP shows sensitivity to heptad stereosequences in the methyl region. An atactic-PP heptad is illustrated in Fig. 7 along with Newman projections detailing the *γ-gauche* interactions involving the methyl group. It is clear that in the *t*- and *g*-backbone conformations the methyl group is *gauche* to its γ-substituents, the backbone methine carbons (α). To predict the ^{13}C chemical shifts expected for the methyl carbons in atactic PP we simply have to calculate the *trans/gauche* probabilities for these backbone bonds in each of the 36 heptad stereosequences. When this is carried out with the Suter–Flory[26] RIS model for PP, and the resultant probabilities of finding CH_3 in a *gauche* arrangement with its γ-substituents C_α are multiplied by the shielding produced by this arrangement (γCH_3, $C_\alpha = -5$ ppm), we obtain[13] the predicted methyl ^{13}C chemical shifts presented in the form of a stick spectrum at the bottom of Fig. 6(b).

Because the *γ-gauche* effect method of calculating ^{13}C chemical shifts only leads to the prediction of stereosequence-dependent relative chemical shifts, we are free in the comparison with observed spectra to translate the calculated shifts to obtain the best agreement with the observed δ ^{13}C's. This has been done in Fig. 6, where the agreement between the observed and

calculated methyl δ ^{13}C's has been used to make the stereosequence assignments indicated there. The *γ-gauche* effect method of assigning resonances in the methyl region of the ^{13}C NMR spectrum of atactic PP to heptad stereosequences has been achieved without recourse to the study of PP model compounds or stereoregular PP's (see Fig. 2(a) and (c)) and without assuming a particular statistical model to describe the frequencies or populations of stereosequences produced during polymerization.

By achieving agreement between the observed ^{13}C chemical shifts and those predicted by the *γ-gauche* effect method we have not only determined the microstructure (stereosequence) of this polymer, but in addition we have stringently tested its conformational characteristics as embodied in the RIS model. Clearly then it is possible to use ^{13}C NMR spectroscopy to test or derive the conformational characteristics of vinyl polymers by comparison of observed ^{13}C NMR spectra with the δ ^{13}C's calculated via the *γ-gauche* effect method. This approach has been pursued with success to test the local conformational characteristics of several vinyl polymers[13,27,28] and provides the basis for the discussion presented in the following sections.

Having established the assignment of resonances observed in the methyl region of the ^{13}C NMR spectrum of atactic PP to the appropriate heptad stereosequences, one might ask what use can be made of this detailed configurational information. Through an analysis of the intensities of the observed resonances we may learn if any simple statistical model, such as Bernoullian or Markovian statistics, can describe the polymerization of atactic PP. In Fig. 6 we compare the observed and simulated ^{13}C NMR spectra of the methyl region of atactic PP. The simulated spectrum was obtained[14] by assuming Lorentzian peaks of <0.1 ppm width at half height for each of the 36 heptad chemical shifts calculated by the *γ-gauche* effect method. The relative intensities or heights of these heptad peaks were then adjusted to obtain the best simulation of the observed spectrum.

The comparison presented in Fig. 6 makes apparent that we have been able to successfully simulate the methyl region of the ^{13}C NMR spectrum of atactic PP based on our ability to calculate and assign all of the heptad stereosequence resonances. Thus, from this successful simulation we know how much of each heptad stereosequence is present in our atactic-PP sample. When we compare these heptad stereosequence populations with those predicted by simple statistical models, we are able to conclude that our atactic-PP sample cannot be described by any simple statistical polymerization model, such as Bernoullian or first-order Markovian.

It has been subsequently shown by Inoue *et al.*[29] that a two-site model of Ziegler–Natta polymerization of propylene[30] adequately describes the distribution of stereosequences observed in atactic PP. At one of the catalyst sites the monomer addition obeys Bernoullian statistics, and at the other site a predominance of monomer units are added in only one of the two possible configurations (R,S or d,l).

As we can see, the *γ-gauche* effect prediction of ^{13}C NMR chemical shifts in vinyl polymers permits assignment of their ^{13}C NMR spectra, provides an opportunity to test or derive a RIS model description of their conformational characteristics, and may also permit a test of their polymerization statistics.

4.2. Propylene–vinyl chloride copolymers (P–VC)

Though propylene (P) does not homopolymerize under free-radical initiation,[31] it can be incorporated to a minor degree in a copolymerization with vinyl chloride (VC) leading to P–VC copolymers with up to 15 mol% P units. The combination of low P content and the inability of P to homopolymerize under these conditions results in P–VC copolymers where all P units are isolated by long uninterrupted runs of VC units. Consequently, we may study the stereochemistry of the comonomer sequences containing the isolated P units, i.e., . . .VC-VC-VC-VC-VC-VC-P-VC-VC-VC-VC-VC-VC. . ., and compare them with the stereosequences found in the two homopolymers PP and PVC.

The methyl carbon regions of the ^{13}C NMR spectra of two PP samples are compared to the methyl carbon region observed in the P–VC copolymer[32] in Fig. 8. Sample A (Fig. 8(a)) is a typical commercial atactic material,[11] while sample B (Fig. 8(b)) is a heptane-soluble fraction of a research-grade material.[33] The stick spectrum in Fig. 8(b) was calculated as just described, while the *γ-gauche* effect ^{13}C chemical shifts calculated for the methyl carbons in the P–VC copolymers (Fig. 8(c)) were obtained by employing Mark's[34] RIS conformational model of P–VC copolymers.

Comparison of the methyl resonances in P–VC and PP reveals a decreased sensitivity to stereosequence for the P–VC copolymer. The methyl carbon resonances in P–VC are sensitive to pentad stereosequences, while in PP heptad sensitivity is observed. In Table 6 the ^{13}C chemical shifts calculated for the methyl carbons in several heptad stereosequences of P–VC and PP are compared. As observed, the methyl carbon chemical shifts calculated for P–VC are sensitive to pentads, while PP methyl carbons show significant heptad sensitivity. This difference in stereosequence sensitivity between the methyl carbons in P–VC and PP is directly attributable to differences in their conformational behaviours as embodied in their RIS models. Local bond conformations reflect pentad sensitivity in P–VC and heptad dependence in PP. In addition, note that the overall spreads in methyl carbon chemical shifts observed in P–VC and PP are 2.7 and 2.0 ppm, respectively, with the P–VC methyl carbons resonating about 1 ppm upfield from those in PP. These observations are also reproduced by the calculated chemical shifts, which employ the same γ-effect ($\gamma_{CH_3,CH} = -5$ ppm) and further indicate differences in the conformational behaviour between P–VC copolymer[34] and PP homopolymer.[26]

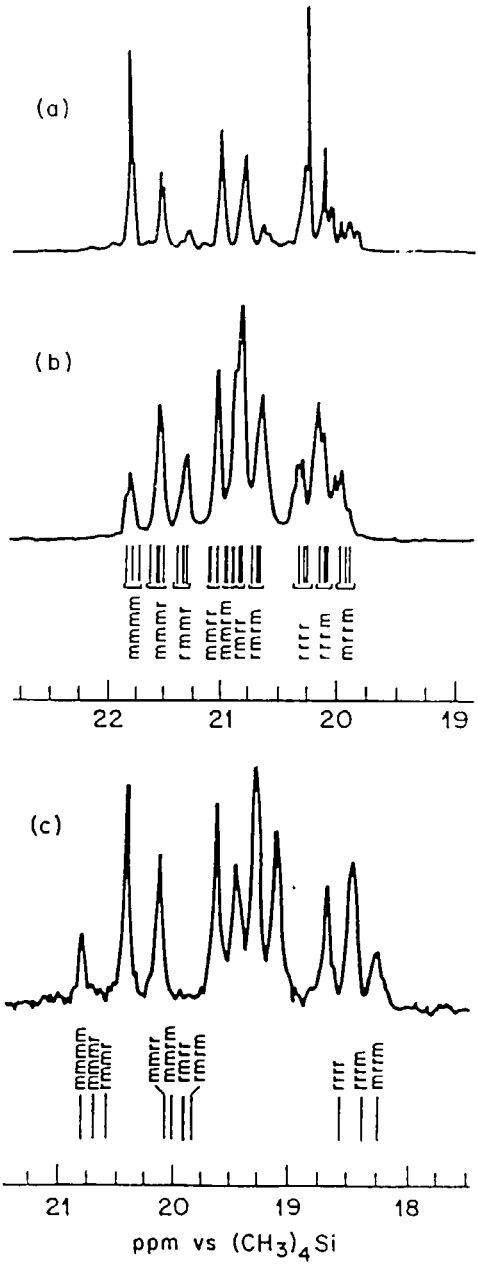

Fig. 8. (a) Methyl carbon region of the 50 MHz ^{13}C NMR spectrum of PP sample A. (b) Methyl carbon region of the 50 MHz ^{13}C NMR spectrum of PP sample B with stick spectrum of chemical shifts calculated for the methyl carbons in atactic PP. (c) P-methyl carbon region of the 50 MHz ^{13}C NMR spectrum of P–VC copolymer with stick spectrum of ^{13}C chemical shifts calculated for the methyl carbons in P–VC.

Table 6. ^{13}C NMR chemical shifts calculated for the methyl carbons in several heptad stereosequences of P–VC and PP.[a]

Heptad	$\Delta\delta^b$ (ppm)	
	P–VC	PP
r(*rmrm*)*r*	0	0
m(*rmrm*)*r*	−0.01	−0.07
r(*rmrm*)*m*	−0.01	−0.05
m(*rmrm*)*m*	−0.03	−0.10
r(*mrrm*)*r*	0	0
m(*mrrm*)*r*	−0.04	−0.07
m(*mrrm*)*m*	−0.07	−0.12

[a]Tonelli and Schilling.[32]
[b]$\Delta\delta$ is the difference in chemical shift among the various heptads containing the same central pentad stereosequence. $\gamma_{CH_3,CH} = -5$ ppm was used for both PP and P–VC.

4.3. Poly(propylene oxide) (PPO)

Propylene oxide,

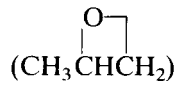

exists in both R and S optical forms due to its asymmetric methine carbon. If during polymerization only one of the C–O bonds in the cyclic monomer is cleaved, then it is possible to generate four different stereochemical triads in the regioregular head-to-tail (H-T) PPO polymer. These H-T triads are presented in Fig. 9(a) planar zigzag projections below.

If, however, during the ring-opening polymerization[35,36] both C–O bonds in propylene oxide are subject to cleavage, then, in addition to the H-T PPO triads above, three additional structural triads or regiosequences are possible for PPO. These are illustrated here for the all-R regioisomers, where H-T, H-H, T-T, and T-H refer to the directions of neighbouring monomers, and where H is the methine end and T is the methylene end of the monomer unit.

Each of these regioirregular triads, with H-H and T-T additions, can be further subdivided on stereochemical grounds as was done for the regioregular H-T triads. Thus, when both regiosequence and stereosequence are considered, 16 unique structural triads can potentially exist in PPO. It is worth mentioning that independent of regiosequence (H-T, H-H, T-T), an *m*-diad consists of RR or SS neighbouring units, while an *r*-diad consists

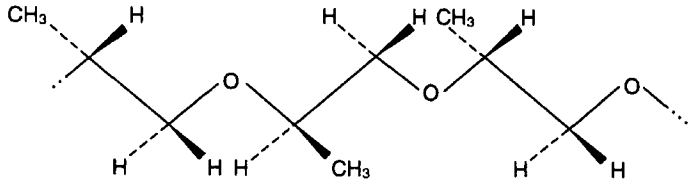

ISOTACTIC, RRR OR SSS

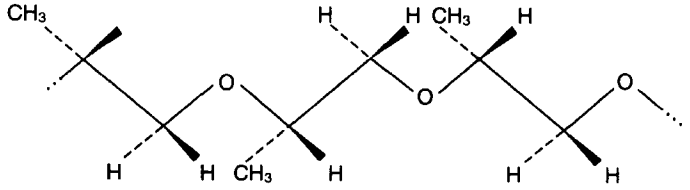

SYNDIOTACTIC, RSR OR SRS

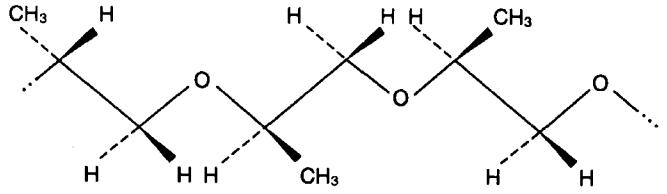

HETEROTACTIC-1 RRS OR SSR

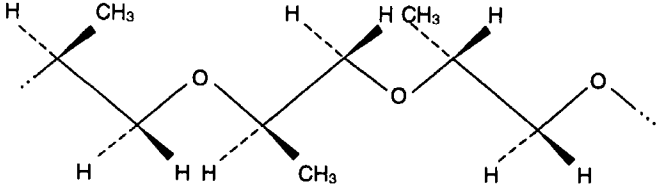

HETEROTACTIC-2 SRR OR RSS

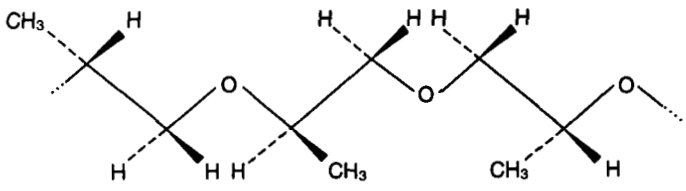

(T–H : T–T)

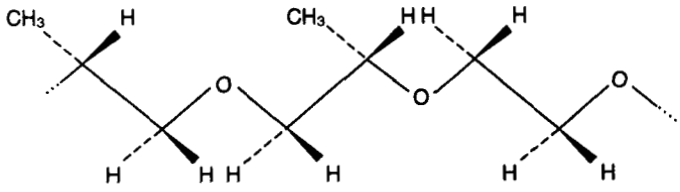

(T–T : H–H)

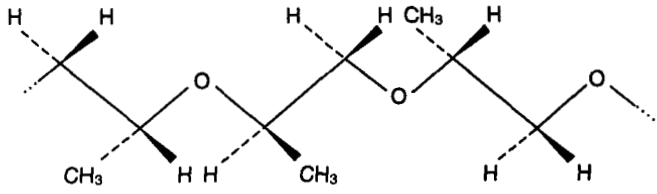

(H–H : T–H)

of RS or SR neighbouring units. However, the methyl groups in an H-T *m*-diad are on opposite sides of the planar zigzag projection, while in H-H and T-T diads they are on the same side. The methyl groups in *r*-diads are on the same side of the backbone when the diad is H-T, but are on opposite sides in both the H-H and T-T *r*-diads. This is a direct consequence of the number of bonds separating asymmetric centres in H-T (three bonds) and in H-H,T-T (two, four bonds) regiosequences.

Because the PPO repeat unit contains three protons (two methylene and one methine) whose resonances overlap extensively, it has not been possible to use ^{1}H NMR spectroscopy,[37–42] even at 500 MHz, to determine the microstructure of PPO. Deuteration at the methine carbon simplifies the ^{1}H NMR spectra of PPO,[38–41] and 2D ^{1}H NMR spectroscopy[42] also leads to greater separation of the overlapping proton resonances. However, even the application of these special synthetic and spectroscopic techniques has not

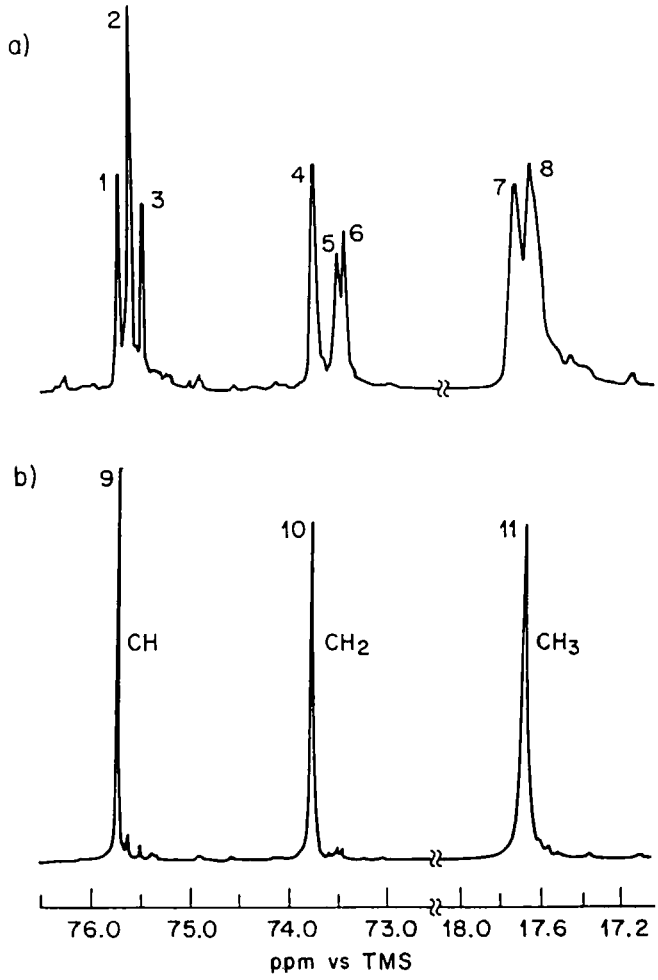

Fig. 9. 50.31 MHz ^{13}C NMR spectra of (a) atactic PPO 4000 and (b) isotactic PPO, observed[48] at 23°C in C_6D_6 (see Table 8).

been completely successful in establishing the microstructures present in PPO.

^{13}C NMR generally offers the potential for greater spectroscopic resolution than ^{1}H NMR and might be expected to be better suited for the analysis of PPO microstructure.[43–47] This expectation is realized for regioregular (all H-T) PPO, where CH and CH_2 carbon resonances are separated by 2 ppm, and permits the unambiguous assignment[45] of PPO stereosequences. However, as we will demonstrate here, the methine and methylene carbon resonances in regioirregular (H-T,H-H,T-T) PPO do overlap.[48]

The methine and methylene carbons in PPO have the same numbers and types of α and β substituents (CH $\rightarrow$ 2 α-C, 1 α-O, 1 β-C, and 1 β-O; $CH_2 \rightarrow$ 1 α-C, 1 α-O, 2 β-C, and 1 β-O) independent of whether or not they are part of H-T, H-H, or T-T units (see Fig. 9). Because the deshielding of a carbon nucleus produced by α- and β-carbon substituents is very similar (*ca.* +9 ppm), the relative ^{13}C chemical shifts of both CH and CH_2 carbons in PPO should depend solely on their γ-*gauche* interactions. In regioregular PPO the H-T methine carbons have two γ-substituents (2 CH) and the methylene carbons three γ-substituents (2 CH_2, 1 CH_3). We therefore expect, as is observed,[45] that the methylene carbons resonate upfield (*ca.* −2 ppm) from the methine carbons. In regioirregular PPO the H-H methine carbons have three γ-substituents (2 CH_2 and 1 CH_3 or 1 CH, 1 CH_2, and 1 CH_3), as do the H-T methylene carbons, and the T-T methylene carbons have two γ-substituents (2 CH or 1 CH and 1 CH_2), like the H-T methine carbons.

We therefore expect the H-H methine and H-T methylene carbon resonances and the T-T methylene and H-T methine resonances to overlap, based on their having the same numbers and types of α-, β-, and γ-substituents. In earlier studies of PPO using ^{13}C NMR,[45] confusion developed in assigning resonances to carbons of the H-H:T-T defects that result from the catalyst occasionally cleaving the CH–O linkage instead of the CH_2–O bond when opening the propylene oxide ring. The possible mixing of overlapping methine and methylene carbon resonances was not considered. Additionally, spectral analysis of lower-molecular-weight samples must take into account the contributions of carbon nuclei in the chain-end structures.

Our approach[48] in analysing the ^{13}C NMR spectra of PPO was first to define the type of carbon represented by each resonance, i.e., methine, methylene, or methyl. Application of the DEPT and INEPT pulse editing techniques[49] permitted achievement of this objective. Second, by analysis of PPO samples differing in molecular weight we were able to assign those resonances belonging to end-group carbons. The third and final step in the analysis was to assign the H-H and T-T defect resonances using the γ-*gauche* effect method to calculate δ ^{13}C's.

The carbon nuclei in PPO are shielded by carbon and oxygen γ-substituents. From ^{13}C NMR studies of alkanes and their oxygenated derivatives[19] $\gamma_{c,c} = -4$ to -5 ppm and $\gamma_{c,o} = -6$ to -8 ppm seem likely for the shieldings produced by C and O γ-substituents when in a *gauche* arrangement with carbon nuclei in PPO.

The numbers of such γ-*gauche* arrangements were determined from the bond conformation probabilities calculated for PPO with the RIS model developed by Abe *et al.*[50] This conformational description developed for regioregular (H-T) PPO was modified[48] so as to permit the calculation of bond conformation probabilities in the H-H and T-T portions of PPO as well. Effects of both regiosequence and stereosequence were explicitly considered

Table 7. Calculated ^{13}C NMR chemical shifts for poly(propylene oxide)[48] at 23°C.

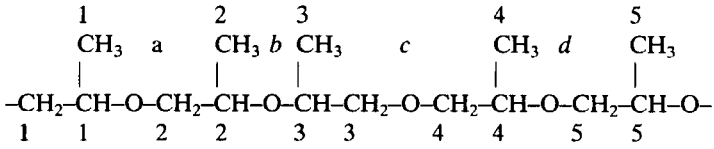

Carbon	Diad[a] a	b	c	d	Chem. shift (ppm)[b]
CH_3 1	*m*	—	—	—	0.00
2	*r*	*r*	—	—	+0.45
2	*m*	*r*	—	—	+0.49
2	*r*	*m*	—	—	+0.75
2	*m*	*m*	—	—	+0.79
3	—	*r*	—	—	+0.53
3	—	*m*	—	—	+0.82
4	—	—	—	*m*	+0.02
4	—	—	—	*r*	+0.04
5	—	—	—	*m*	0.00
CH_2 1	*m*	—	—	—	0.00
2	*m*	*m*	—	—	−0.15
2	*r*	*m*	—	—	−0.19
2	*r*	*r*	—	—	+0.20
2	*m*	*r*	—	—	+0.25
3	—	*m*	—	—	+4.40
3	—	*r*	—	—	+4.73
4	—	—	—	*r*	+4.75
4	—	—	—	*r*	+4.78
5	—	—	—	*m*	0.00
CH 1	*m*	—	—	—	0.00
2	*m*	*m*	—	—	−4.49
2	*r*	*m*	—	—	−4.45
2	*m*	*r*	—	—	−4.49
2	*r*	*r*	—	—	−4.45
3	—	*m*	—	—	−4.48
3	—	*r*	—	—	−4.48
4	—	—	—	*r*	−0.25
4	—	—	—	*m*	−0.27
5	—	—	—	*m*	0.00

[a]The dash — indicates either *m* or *r* diad placement.
[b]The + and − indicate downfield and upfield shifts, respectively, relative to the position of the 1 or 5 (H–T) carbons.

Table 8. ^{13}C NMR chemical shifts and relaxation data[48] for head-to-tail carbons in poly(propylene oxide) at 23°C (Fig. 10).

Resonance	Chem. shift (ppm)	T_1(s)	Carbon type	Stereosequence
1	75.75	0.78	CH	*mm*
2	75.64	0.80	CH	*mr* + *rm*
3	75.50	0.81	CH	*rr*
4	73.78	0.51	CH_2	*m*
5	73.54	0.50	CH_2	*r*
6	73.47	0.50	CH_2	*r*
7	17.79	1.03	CH_3	*rm*, *mr*, *rr*
8	17.71	1.03	CH_3	*mm*, *rm*, *mr*, *rr*
9	75.73		CH	*mm*
10	73.77		CH_2	*m*
11	17.72		CH_3	*mm*

when calculating relative ^{13}C NMR chemical shifts in PPO via the *γ-gauche* effect method. The results of these calculations for the carbon nuclei in the H-H and T-T defect structures of PPO are presented in Table 7. Note the significant differences between the δ ^{13}C's predicted for the regular H-T and defect H-H and T-T carbons. ^{13}C NMR spectra of PPO 4000 (M = 4000) and isotactic PPO (M = 14 500) are presented in Fig. 9. All three carbon types display chemical shift sensitivity to the stereochemistry of the polymer chain. The assignment of resonances to the regioregular portions of PPO (see Table 8) are made by comparison of the two spectra, and agree with earlier work.[44,45] In contrast with ^{13}C NMR observations for most vinyl polymers, the observed sensitivity of the PPO carbon chemical shifts to stereochemistry is very small. The total spread of δ ^{13}C's is only 0.12, 0.20, and 0.25 ppm for the methyl, methine, and methylene carbons, respectively. This can be contrasted with atactic PP[11] where the range of chemical shifts due to stereosequences is 2.0, 0.5, and 2.0 ppm for the same carbon types. The reduced sensitivity in PPO reflects the presence of three bonds between chiral centres in contrast to the two bonds in vinyl polymers. The limited chemical shift sensitivity is predicted by the RIS model for PPO.[50] On the basis of *γ-gauche* shielding interactions a spread of H-T chemical shifts of *ca.* 0.5 ppm is predicted for each of the three carbon types.

The DEPT technique[49,51] permits spectral editing in such a manner that spectra containing only a specific carbon type can be produced. In Fig. 10 we show results of DEPT measurements on atactic PPO 4000 for the methine and methylene carbons only. At the vertical gain used in acquiring these spectra the H-T resonances are off scale, and we are observing the resonances of the defect H-H and T-T structures as well as the chain-end carbons. In (a) all CH and CH_2 resonances are observed, while in (b) and (c) only the

CH and CH_2 resonances, respectively, are observed. The most striking feature of these DEPT editing spectra is the observation that there are clearly methine carbon resonances in the upfield region previously thought to contain exclusively methylene resonances, and there also are methylene resonances in the downfield portion of the spectra previously thought to contain only methine resonances. (These observations are confirmed by INEPT spectra (not shown)[48] in which methylene resonances can be observed with negative intensity while methine signals appear as positive peaks.) Certain H-H:T-T and/or end-group resonances at about 73.5 and 75.6 ppm can only be observed in the edited spectra, as they are completely obscured by the H-T peaks in a normal Fourier transform (FT) spectrum. The comparison of resonances in the three spectra of Fig. 10 permits us to identify each resonance as to carbon type, methine or methylene.

To assign resonances produced by various end-groups we compare the spectra observed for PPO 4000 (DP = 69) and PPO 1000 (DP = 17) as presented in Fig. 11. Results of a DEPT measurement on PPO 1000 agree with those of PPO 4000 in establishing the carbon type represented by each resonance. All of the visible resonances in Fig. 11(a), other than the labelled H-T peaks, can be attributed to the end-groups, because the number of such groups is about three times that of the H-H:T-T defects in the low-molecular-weight PPO 1000. All of the CH_2 and CH end-group resonances occur in the H-T methine region between 75.0 and 76.5 ppm.

DEPT spectra of PPO 1000 (not shown)[48] indicate that no end-group CH resonances are hidden by the H-T methylene resonance at 73.5 ppm. Comparison of DEPT spectra permits the specific assignment of end-group methine (1) and methylene (2) resonances. Note in Fig. 11(a) the end-group methylene resonances at *ca.* 75.6 ppm, which add to the complexity of the H-T CH region. Comparison of the spectra in Fig. 11 permits the identification of end-group resonances in PPO 4000, and by elimination, those resonances that are crosshatched must result from carbons in the H-H:T-T structures. These H-H:T-T peaks are identified as to carbon type from the DEPT spectra in Fig. 10. A summary of the methine and methylene carbon resonances and their assignment to H-H:T-T defects or end-groups appears in Table 9. The methyl regions of both atactic PPO samples are displayed in Fig. 12. Resonances attributable to methyl carbons in or adjacent to an end-group can be assigned by comparison of (a) and (b), where it can be seen that all H-H:T-T defect resonances occur downfield from the H-T peaks. A summary of the methyl carbon data is given in Table 10.

In order to make the assignments of the carbon nuclei in the H-H:T-T structures, a comparison was made between the experimental chemical shift data (Figs 10 and 11 and Tables 9 and 10) and the relative chemical shifts for each carbon type resulting from the *γ-gauche* effect calculations (Table 7). The calculated data indicate a lack of sensitivity for all carbons to the nature of the stereochemistry across the T-T portion of the chain (diad *c* in

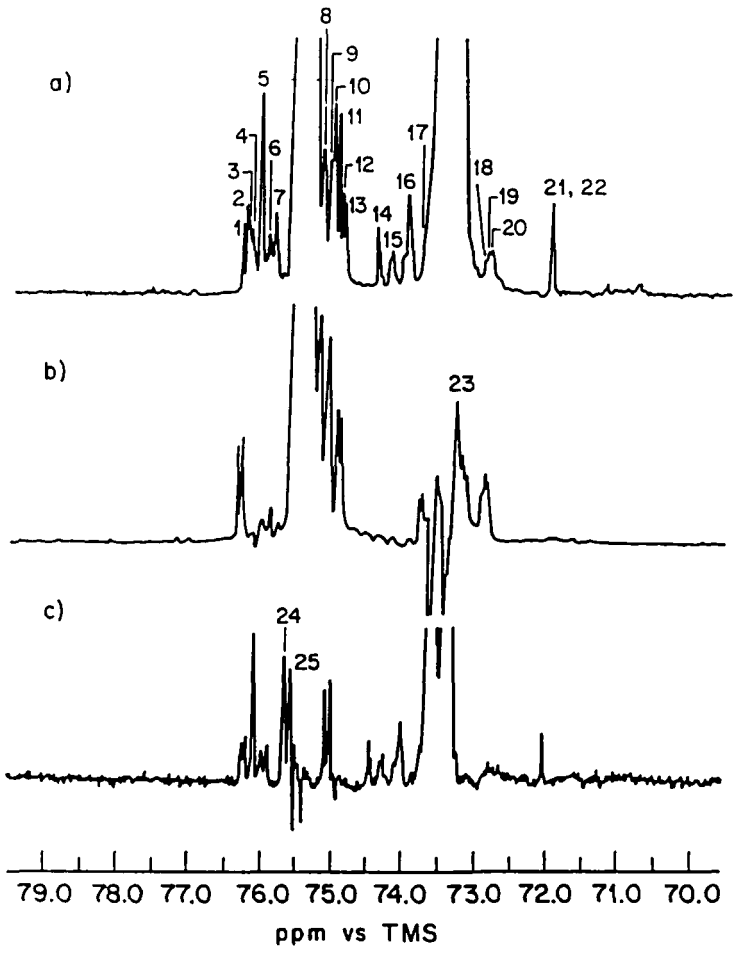

Fig. 10. 50.31 MHz ^{13}C NMR DEPT spectra of atactic PPO 4000 observed[48] at 23°C in C_6D_6: (a) methine and methylene; (b) methine only; (c) methylene only.

Table 7). In addition, for the H-H methyl and methylene carbons 2 and 3, diad *b* strongly affects their chemical shifts while diad *a* has a much smaller influence. The H-H methine carbons, however, are expected to show only a very minor stereochemical dependence.

Using the calculated shift data of Table 7, it is possible to make the specific assignments given in Tables 9 and 10. The H-H methine carbons 2 and 3 are predicted to be significantly upfield of the H-T CH resonances (at *ca.* 72.8–73.8 ppm) and are observed most clearly in the DEPT editing spectrum (Fig. 10(b)). Methine carbon 4 cannot be resolved from the H-T CH resonances.

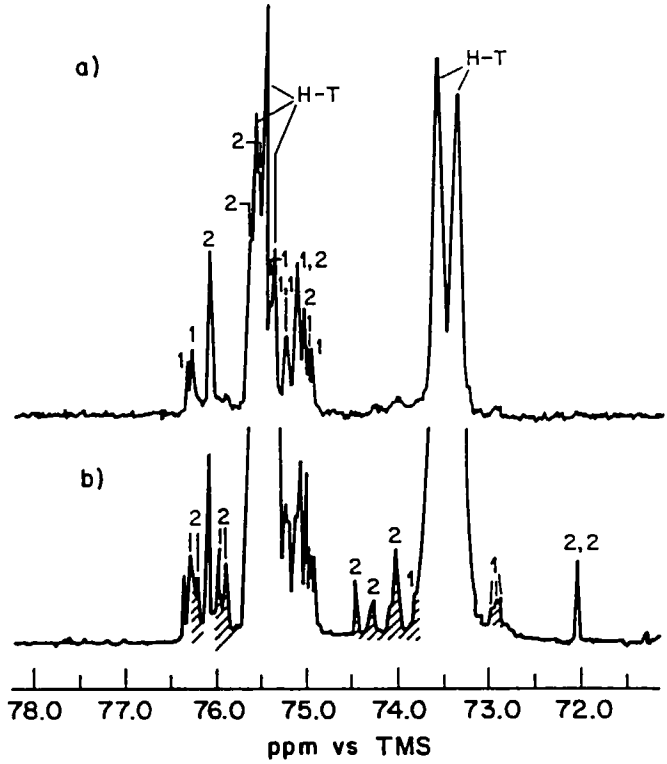

Fig. 11. 50.31 MHz ^{13}C NMR spectra of (a) atactic PPO 1000 and (b) atactic PPO 4000 observed[48] at 23°C in C_6D_6 (1 indicates methine and 2 indicates methylene). The crosshatched resonances result from the H-H:T-T structure.

For the CH_2 carbons (Fig. 10(a)) the group of resonances slightly downfield from the H-T methylene resonances are assigned to carbon 2, while the methylene resonances (3,4,6,7) shifted downfield into the H-T CH region are assigned to carbons 3 and 4. Despite differences in the magnitudes of calculated and observed shifts for the H-H:T-T *vs.* H-T methine and methylene carbons (see below), the predicted direction of relative *γ-gauche* shielding for each carbon permits a consistent set of assignments as given in Table 9.

These results illustrate the difficulties faced by early workers in assigning the ^{13}C NMR spectrum of PPO. At first glance one is tempted to simply divide the 73–76 ppm region into two parts, methine and methylene. However, a careful interpretation of the chemical-shift effects produced by the H-H:T-T structures shows that a large number of the methine and methylene resonances should overlap, and that the identity of carbon types can only

Table 9. ^{13}C NMR chemical shifts and relaxation data[48] for the methine and methylene carbons of atactic PPO 4000 at 23°C (Fig. 11).

Resonance	Chem. shift, ppm		Assignment[a]	T_1 (s)
1	76.36	–CH–	E	0.93
2	76.29	–CH–	E	0.80
3	76.26	$-CH_2-$	3,4	0.80
4	76.21	$-CH_2-$	3,4	0.77
5	76.10	$-CH_2-$	E	1.19
6	75.98	$-CH_2-$	3,4	0.56
7	75.88	$-CH_2-$	3,4	0.59
8	75.24	–CH–	E	0.82
9	75.13	–CH–	E	0.81
10	75.08	–CH–, $-CH_2-$	E	0.81
11	75.02	$-CH_2-$	E	0.90
12	74.96	–CH–	E	1.08
13	74.91	–CH–	E	1.18
14	74.46	$-CH_2-$	2	1.04
15	74.26	$-CH_2-$	2	0.50
16	74.02	$-CH_2-$	2	0.51
17	73.82	–CH–	2,3	
18	72.97	–CH–	2,3	0.61
19	72.93	–CH–	2,3	0.64
20	72.87	–CH–	2,3	0.68
21	72.06	$-CH_2-$	E	2.16
22	72.03	$-CH_2-$	E	2.16
23	73.30	–CH–	2,3	
24	75.65	$-CH_2-$	E	
25	75.57	$-CH_2-$	E	

[a]E indicates chain end structure; 2,3,4 indicate H-H:T-T defect structure (see Table 7).

be ascertained by DEPT or INEPT editing experiments.[51] In addition, the comparison of PPO samples differing in molecular weight is necessary to identify the chain-end carbon resonances.

The differences in the magnitudes of the δ ^{13}C's observed and calculated for methine and methylene carbons in the H-H:T-T and H-T PPO structures may stem from the slightly different β-substituents[19] present in each of these structural environments. The methine and methylene carbons in both H-T and H-H:T-T structures are β to oxygen (CH–CH_2–O and CH_2–CH–O), and the methylene carbons are β to methyl carbons (CH_2–CH–CH_3). However, the H-T methine and H-H:T-T methylene carbons are β to methylene carbons (CH–O–CH_2 and CH_2–O–CH_2), while H-T methylene and H-H:T-T methine carbons are β to methine carbons (CH_2–O–CH and CH–O–CH) (see Table 7). On the other hand, H-H:T-T and H-T methyl carbons have

Table 10. ^{13}C NMR chemical shift assignments and relaxation data[48] for the methyl carbons of atactic PPO 4000 at 23°C (Fig. 12).

Resonance	Chem. shift (ppm)	Assignment[a]	T_1 (s)
1	19.27	E	1.65
2	19.24	E	1.65
3	18.99	E	1.80
4	18.74	2,3	0.99
5	18.51	2,3	0.96
6	18.38	2,3	0.92
7	17.29	E	1.09
8	19.31	E	
9	19.26	E	
10	19.02	E	
11	17.31	E	

[a]E indicates chain-end structure; 2,3 indicate H-H:T-T defect structure (see Table 9).

precisely the same α-, and β-substituents. The fact that the calculated and observed δ ^{13}C's agree so closely for the methyl carbons (see below) lends support to the suggestion that slightly different β-substituents for H-T and H-H:T-T methine and methylene carbons may be the source of the disparity between the magnitudes of their measured and calculated δ ^{13}C's.

The methyl carbon resonances of the H-H:T-T structures are assigned in Table 10. Both the calculated magnitudes and the directions of the methyl resonances relative to H-T resonances agree with the observed results (Fig. 12(a)). The three defect resonances (peaks 4,5,6) are assigned to carbons 2 and 3 (Table 7). Because of the predicted overlap resulting from stereosequences, we cannot make further specific assignments in this region of the PPO spectrum.

Note that in Tables 8–10, values of the spin–lattice relaxation time T_1 are presented for each resonance. These were determined by the inversion recovery method and were utilized to ensure that quantitative spectra were obtained. From the methyl carbon data (Fig. 12(a)) we are able to estimate that PPO 4000 contains 2.2% inverted or defect, H-H:T-T units and has a number-average molecular weight $M_n = 5400$, or DP = 93, based on the end-group resonance intensities. This may be compared with $M_v = 4000$, or DP = 69, provided by the manufacturer and based on KOH hydroxyl number.

With the aid of multiple-pulse editing techniques (DEPT, INEPT) and the *γ-gauche* effect calculations of relative ^{13}C NMR chemical shifts, we[48] have assigned the ^{13}C NMR spectrum of PPO, including the determination of

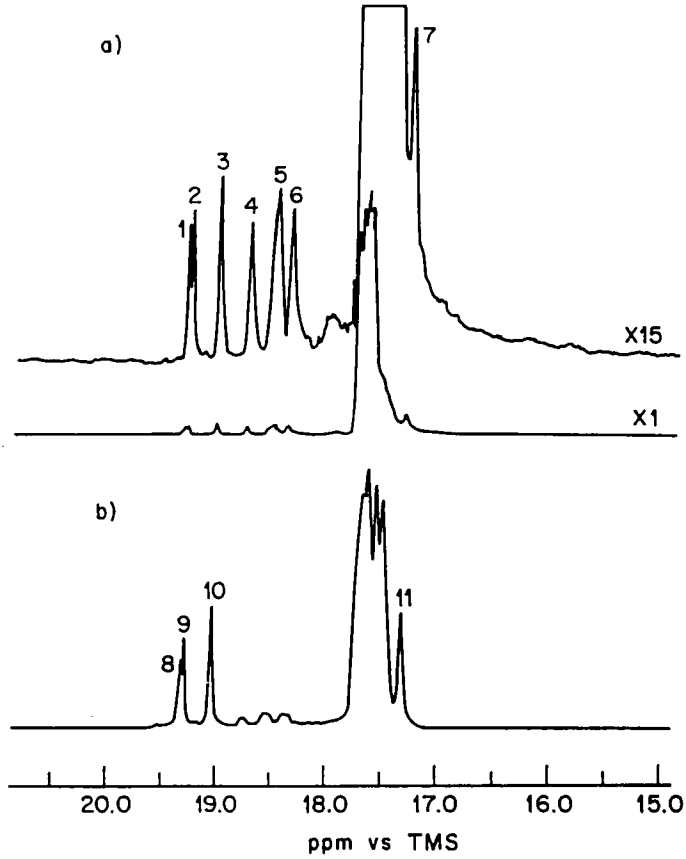

Fig. 12. Methyl region of the 50.31 MHz ^{13}C NMR spectra of (a) atactic PPO 4000 and (b) atactic PPO 1000 observed[48] at 23°C in C_6D_6 (see Table 10).

carbon resonances resulting from chain-end structures. Analysis of the expected differences between the *γ-gauche* interactions of the methine and methylene carbons in H-T and H-H:T-T PPO structures indicated that H-H:T-T methine resonances should overlap with the H-T methylene signals and that H-H:T-T methylene and H-T methine peaks should also overlap. It was this analysis that prompted our reinvestigation and assignment of the ^{13}C NMR spectrum of PPO. From these assignments it was possible to quantitatively determine the number of H-H:T-T defects incorporated in PPO through occasional ring opening of propylene oxide monomer at the CH–O bond. In addition, identification of chain-end structures permitted an estimate of the number-average molecular weight, and (though not discussed here) determination of specific terminal structures also provided insight concerning the polymerization mechanism of PPO.

4.4. Poly(vinylidene fluoride) (PVF_2)

With the application of a triple-resonance scheme,[52] which simultaneously broad-band decouples both proton and fluorine nuclei while observing carbon nuclei, it was possible to obtain ^{13}C NMR spectra of fluoropolymers that were free of both ^{13}C–^{1}H and ^{13}C–^{19}F J-couplings. As an example, the triple-resonance ^{13}C NMR spectrum of poly(vinylidene fluoride) (PVF_2) was successfully interpreted with *γ-gauche* effects of $\gamma_{c,c} = -2$ ppm and $\gamma_{c,F} = -(2 \text{ to } 4)$ ppm, and an estimate of 3.2% was made for the content of H-H:T-T defect structures shown below:

$$-CF_2{}^{a}CH_2{}^{b}\overset{1}{C}F_2{}^{c}CH_2{}^{d}\overset{2}{C}F_2{}^{e}\overset{3}{C}F_2{}^{f}CH_2{}^{g}CH_2{}^{h}\overset{4}{C}F_2{}^{i}CH_2{}^{j}CF_2{}^{k}CH_2-$$

Having successfully analysed[53] the ^{13}C NMR spectrum of PVF_2 containing a small number of inverted units (3.2% H-H:T-T monomer additions as observed by integration of defect (H-H:T-T) and normal (H-T) resonances), we now attempt to assign and analyse the ^{19}F NMR spectrum of the same PVF_2 sample. The ^{19}F NMR spectrum of PVF_2 measured at 84.6 MHz is presented in Fig. 13(a).[54] Three small resonances appear 3.2, 22.0, and 24.0 ppm upfield from the main H-T fluorine resonance at 91.9 ppm (relative to $CFCl_3$) and are attributed to the fluorine nuclei belonging to H-H:T-T inverted units.[55,56]

We may write expressions for the relative ^{19}F NMR chemical shifts (δ_F) of the H-T and H-H:T-T fluorines in terms of their *γ-gauche* effects ($\gamma_{F,F}$ and $\gamma_{F,C}$) and the bond rotation probabilities (P) which determine the frequencies of *γ-gauche* interactions:

$$\delta_F^{H\text{-}T} = (1 + P_t)\,\gamma_{F,C} \tag{1}$$

$$\delta_F^2 = (1 + 0.5P_{t,d} + 0.5P_{t,c})\,\gamma_{F,C} + (1.5 - 0.5P_{t,c})\;\gamma_{F,F} \tag{2}$$

$$\delta_F^3 = (1 + 0.5P_{t,c} + 0.5P_{t,f})\,\gamma_{F,C} + (1.5 - 0.5P_{t,c})\;\gamma_{F,F} \tag{3}$$

$$\delta_F^4 = (1 + 0.5P_{t,h} + 0.5P_{t,i})\,\gamma_{F,C} \tag{4}$$

Comparison of equations (1) and (4) reveals that $\delta_F^{H\text{-}T}$ and δ_F^4 are most similar. Thus, $\delta_F^4 - \delta_F^{H\text{-}T} = 3.2$ ppm, which leads directly to $\delta_{F,C} = +30$ ppm (shielding). By elimination, $|\delta_F^2 - \delta_F^3| = 2$ ppm, which yields $\delta_{F,F} = +15$ ppm. Substitution of $\delta_{F,F} = 15$ ppm and $\delta_{F,C} = 30$ ppm into equations (1)–(4) leads to calculated δ_F's shown as sticks in Fig. 13(c), and which compare well with the observed spectrum in Fig. 13(a) recorded at low field strength.

At 188 MHz, four additional defect resonances (1, 5, 6, and 7) appear in the ^{19}F NMR spectrum of PVF_2 (see Fig. 13(b)). Ferguson and Brame[57] also observed these additional defect peaks and tentatively assigned them to defect

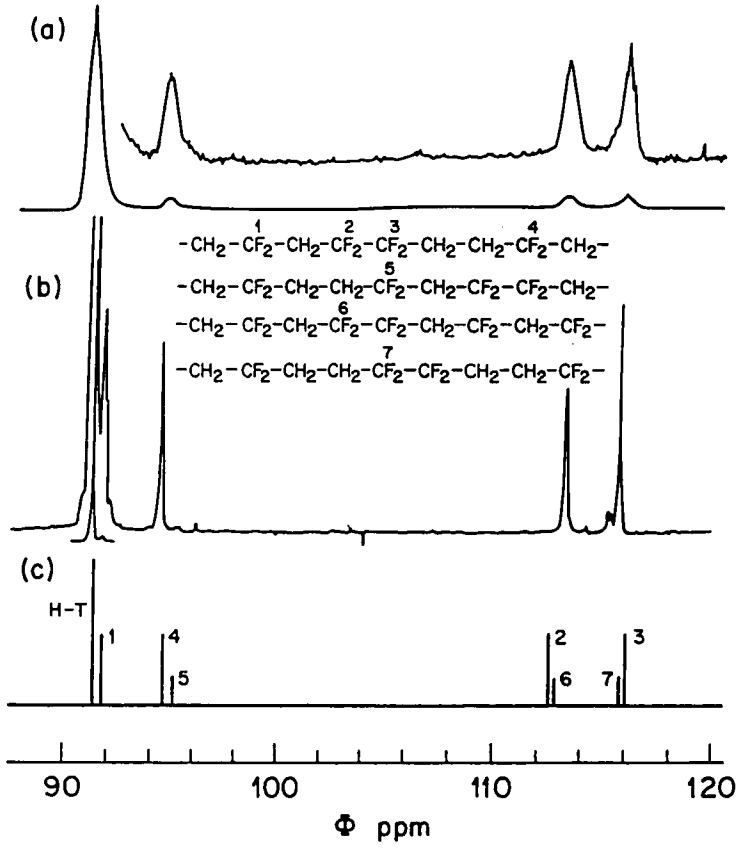

Fig. 13. Observed and calculated[54] ^{19}F NMR spectra of PVF_2: (a) measured at 84.6 MHz; (b) measured at 188.2 MHz; (c) calculated. Vertical expansion in (a) is ×8, in (b) ×40.

structures drawn in Fig. 13(b) based on α, β, and γ substituent effects derived from the CF_2 resonances observed in various saturated, partially fluorinated linear alkanes. In addition to $\delta_F^{H\text{-}T}$, δ_F^2, δ_F^3, and δ_F^4, ^{19}F chemical shifts were also calculated for the defect fluorines 1, 5, 6, and 7. ^{19}F γ-effects (γ_{F,CH_2}, γ_{F,CF_2}, and $\gamma_{F,F}$) were least squares fitted to produce the best agreement between observed and calculated δ_F's (see Fig. 13(b) and (c)). Best agreement was achieved for $\gamma_{F,CH_2} = \gamma_{F,CF_2} = \gamma_{F,C} = 25$–$30$ ppm and $\gamma_{F,F} = 15$ ppm, confirming the assignments proposed by Ferguson and Brame[57] and the γ-effects derived from the more prominent defect resonances 2, 3, and 4 observed at lower field strength.

Measurement of the intensities of the defect resonances and comparison with the total intensity of all observable resonances yields an estimate of 3.4%

defect H-H:T-T addition in this sample of PVF_2. This compares well with the 3.2% defect estimate described earlier using ^{13}C NMR analysis.

The ^{19}F NMR spectra of poly(vinyl fluoride), poly(fluoromethylene), and poly(trifluoroethylene) were also successfully interpreted[54] with very similar *γ-gauche* effects ($\gamma_{F,F} = 15$ ppm and $\gamma_{F,C} = 25$–30 ppm) leading to a detailed accounting of the stereo- and regiosequences.

In addition to eliminating the need for triple-resonance observation[52] of ^{13}C NMR spectra, ^{19}F NMR spectra of fluoropolymers[54] are much more sensitive to their microstructures, because the conformationally-sensitive *γ-gauche* shieldings of their ^{19}F nuclei are nearly an order of magnitude greater than the shieldings observed for their ^{13}C nuclei. Clearly ^{19}F NMR provides a vastly superior means for characterizing the microstructures of fluoropolymers compared with ^{13}C NMR observations.

5. NMR SPECTROSCOPY AS A MEANS TO PROBE POLYMER CONFORMATIONS

5.1. Styrene–methyl methacrylate copolymers (S–MM)

The advent of 2D NMR techniques[58–61] has resulted in a rebirth of ^1H NMR as a means to study molecular structure. Extensive J-coupling of protons, which unduly complicate 1D ^1H NMR spectra, are used to advantage in 2D ^1H NMR to map the connectivity of molecules. Those protons that are scalar J-coupled, and therefore interact between the 90° RF pulses, exhibit crosspeaks in a 2D ^1H COSY spectrum. If an additional 90° RF pulse is inserted between the two 90° RF pulses of the 2D ^1H COSY experiment, then the correlating influence or interaction between proton spins which results in crosspeaks is their direct, through space, dipolar coupling or NOE. This 2D technique is referred to as NOE correlated spectroscopy (NOESY) and permits a mapping of all proton spins in the sample which are closer than *ca.* 4 Å. Let us illustrate how the NOESY technique can be applied to regularly alternating styrene–methyl methacrylate (S–MM) copolymer to learn about its conformational characteristics.

The methylene region of the 500 MHz 2D-NOESY spectrum of the regularly alternating S–MM copolymer is presented in Fig. 14. The stippled crosspeaks correspond to the intermethylene interactions occurring in the S-centred co-hetero S–MM triad shown in Fig. 16. These intermethylene NOE crosspeaks appear to fall into three categories based on their intensities: one strong (S), H_e'-H_t, two medium (M), H_e-H_e' and H_t-H_t', and one weak (W), H_e-H_t', corresponding to short, medium, and longer interproton distances, respectively (see Heffner *et al.*[62] for the details of the proton peak assignments).

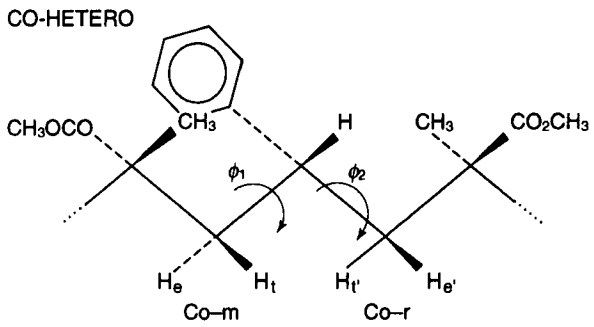

By combining portions of the conformational descriptions derived for styrene, methyl acrylate, and methyl methacrylate homopolymers,[63–66] Koinuma *et al.*[67] developed an RIS model for the 1:1 alternating S–MM copolymer. When this RIS model is utilized to calculate the conformational probabilities for the bond pair flanking the styrene methine carbon in the co-hetero S–MM triad illustrated above it is possible to calculate[62] the average intermethylene proton distances corresponding to the four crosspeaks in Fig. 14. This procedure is illustrated in Fig. 15 and Table 11. The only three conformations allowed for the co-hetero S–MM triad are drawn in Fig. 15 along with the probability calculated for each. The intermethylene proton distances, r_{HH}, calculated for the same S–MM triad are listed for each conformation in Table 11.

When these r_{HH} values are raised to the power -6 and averaged over the three possible conformers shown in Fig. 15 according to the calculated probabilities also listed there, the entries in the next-to-last row of Table 11 are obtained. These values should be proportional to the strengths of the intermethylene proton–proton crosspeaks seen in Fig. 14, and this is indeed the case.

The agreement between the predicted and observed pattern of NOESY crosspeaks for the co-hetero triad of 1:1 alternating S–MM copolymer confirms the validity of the Koinuma *et al.*[67] conformational model. It is particularly noteworthy that this agreement requires the assumption of *ca.* 20° displacements from the perfectly staggered rotational states as predicted

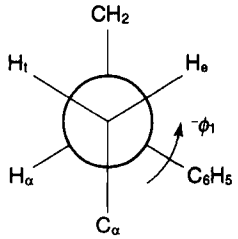

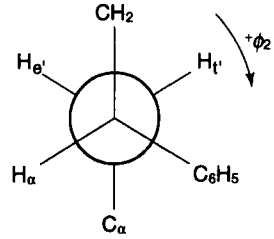

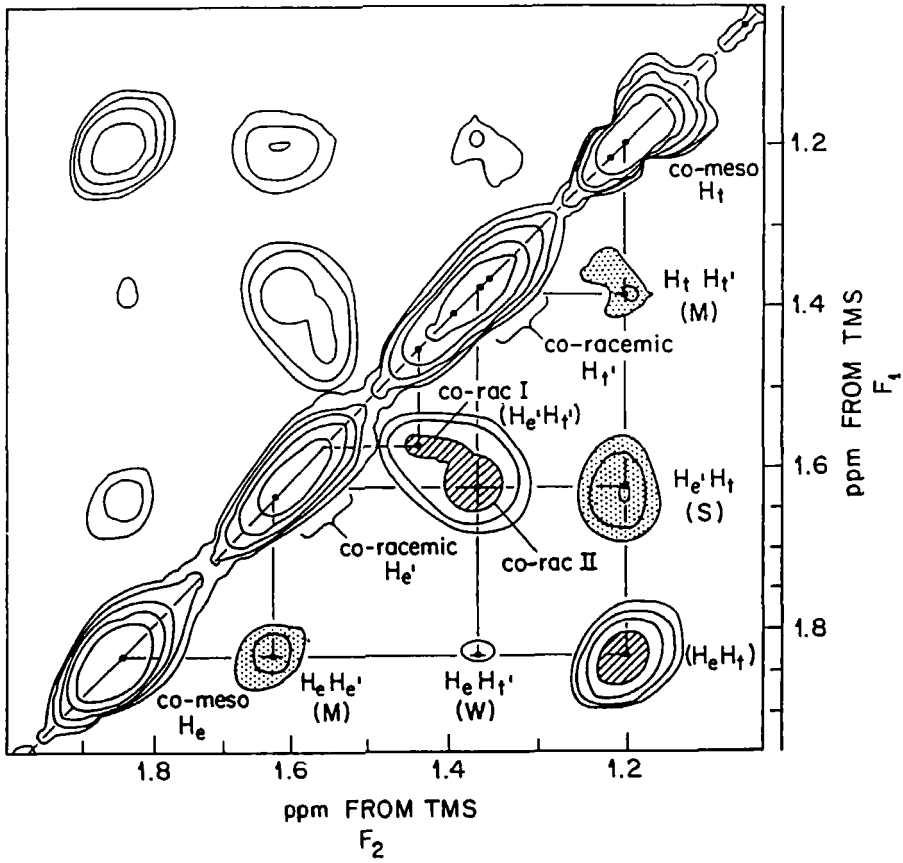

Fig. 14. Expansion of the phase-sensitive proton NOESY spectrum at 500 MHz and 80°C, showing only the methylene region.[62] Geminal interactions are indicated by crosshatched crosspeaks, and intermethylene interactions by stippled crosspeaks. The designations S, M, and W refer to the strengths (crosspeak volumes) of the intermethylene proton interactions.

for the backbone bonds in polystyrene by Yoon *et al.*[63] (see the Newman projections in Fig. 18). As an example, in the *t,t* conformation (see Fig. 15) $\phi,\phi_2 = -20°,20°$ because this produces relief from steric interactions of the phenyl ring and the methyl methacrylate C_α, as seen in the following Newman projections.

If perfectly staggered states *t* (0°), $g\pm(\pm 120°)$ are assigned in the calculation of intermethylene proton–proton distances, then the results in the bottom row of Table 11 are obtained, i.e., all interactions ($<r_{HH}^{-6}>$) are approximately the same. It is apparent from Fig. 14 that this is not the case.

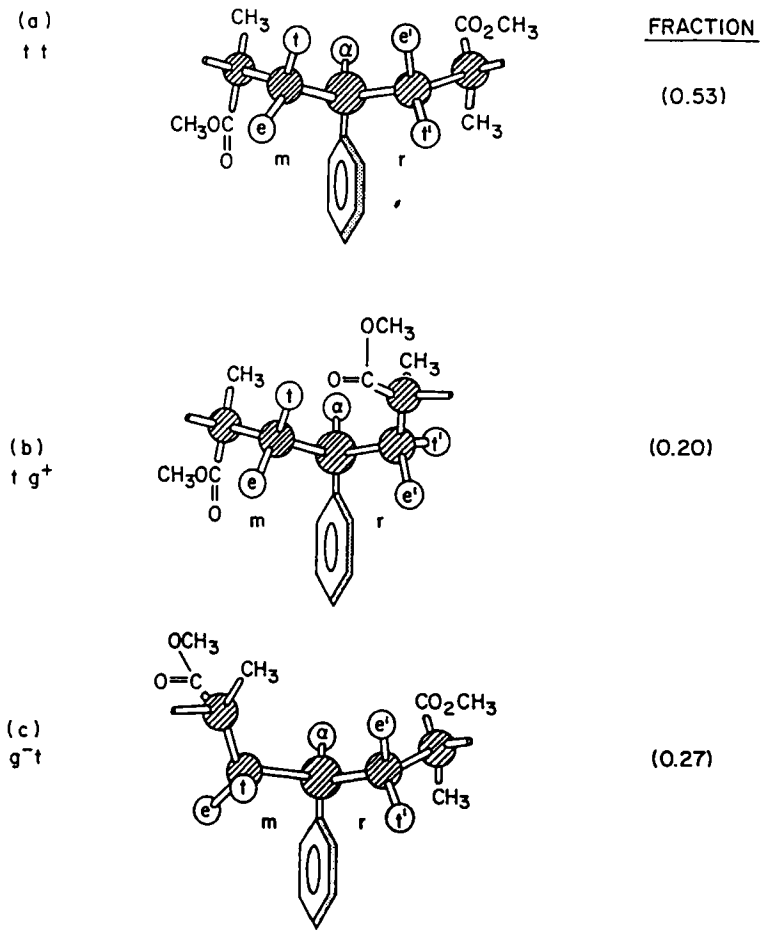

Fig. 15. Ball-and-stick models of the styrene-centred MM–S–MM co-hetero triad, showing the *t,t*, *t,g+*, and *g−,t* conformations, with 20° deviations from exact staggering.[62]

More recently, Mirau *et al.*[68] have derived intermethylene proton–proton distances r_{HH} directly from the NOESY spectra of 1:1 alternating S–MM. A comparison was made with the distances r_{HH} of Table 11 after conformationally averaging according to the Koinuma *et al.*[67] RIS model. Reasonable agreement was obtained, as indicated by the following observed and (calculated) conformer populations: $t,t = 0.58 \pm 0.05(0.53)$, $t,g+ = 0.24 \pm 0.05(0.20)$, and $g-,t = 0.18 \pm 0.05(0.27)$. In addition, it was found that an 11° displacement from perfectly staggered rotational states

Table 11. Intermethylene H–H distances (r_{HH}) calculated[62] for the co-hetero styrene-centred triad (Fig. 17).

	r_{HH} (Å)			
ϕ_1, ϕ_2	H_e–$H_{t'}$	H_e–$H_{e'}$	H_t–$H_{t'}$	$H_{e'}$–H_t
t, t (−20°. 20°)	2.89	3.10	3.10	2.20
t, $g+$ (−20°, 100°)	3.74	2.63	3.68	2.59
$g-$, t (−100°, 20°)	3.74	3.68	2.63	2.59
$\langle\phi_1, \phi_2\rangle$	0.0010[a]	0.0016[a]	0.0016[a]	0.0063[a]
$\langle\phi_1, \phi_2\rangle$	(0.0027)[b]	(0.0016)[b]	(0.0020)[b]	(0.0030)[b]

[a] r_{HH}^{-6} averaged over all three (ϕ_1, ϕ_2) conformations.
[b] As above, except ϕ_1, $\phi_2 = 0, \pm 120°$ in the t, $g \pm$ states (Heffner *et al.*[62]).

produced r_{HH} values in closest agreement with those obtained from NOESY crosspeak intensities, adding further support to the Koinuma *et al.*[67] RIS model, which assumed 20° displacements. This 2D NOESY ^{1}H NMR study of 1:1 alternating S–MM copolymer marked the first attempt to derive the conformational characteristics of a flexible polymer in solution through a direct measure of conformationally-averaged interproton distances.

5.2. Ethylene–vinyl acetate (E–VAc) copolymers

Recently, a conformational description (RIS model) has been developed for ethylene–vinyl acetate (E–VAc) copolymers[69] by merging the RIS model descriptions of the constituent homopolymers.[70,71] Unfortunately, no measurements of microstructurally and conformationally sensitive properties have been reported for these copolymers. Traditional global measures of polymer conformations, such as mean-square end-to-end distances and dipole moments, are not yet available for E–VAc copolymers. However, the ^{13}C NMR spectra of a complete series of atactic E–VAc copolymers have been assigned.[72–74] Through comparison of δ ^{13}C's calculated[28] via the *γ-gauche* effect method to those previously observed and assigned in E–VAc ^{13}C NMR spectra, we may evaluate the ability of the RIS model derived for E–VAc copolymers to describe the microstructural sensitivity of the local copolymer conformation, thereby providing an alternative means for testing its validity.

Wu *et al.*[72,73] assigned the low-field (22.6 MHz for ^{13}C) ^{13}C NMR spectra of E-VAc copolymers by comparison to the ^{13}C NMR spectra recorded for the E–VAc model compounds presented below. Later Sung and Noggle,[74]

CH

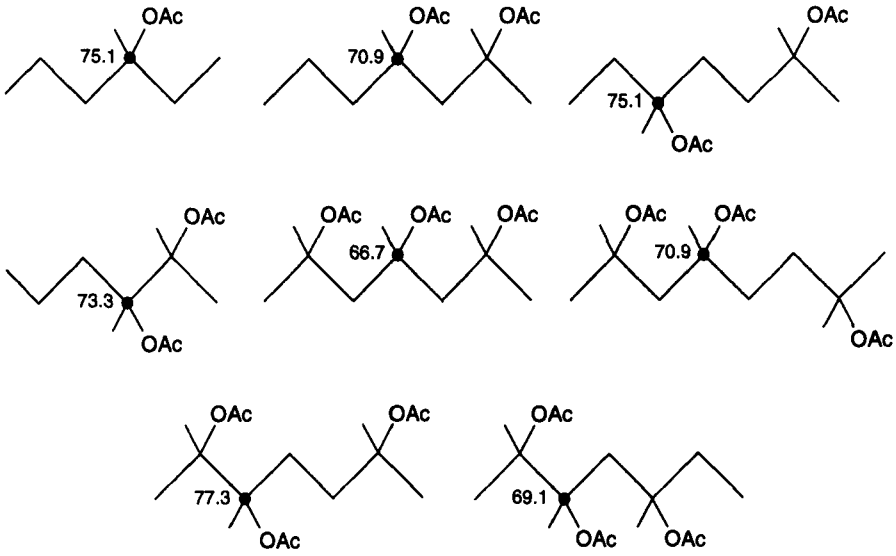

CH_2

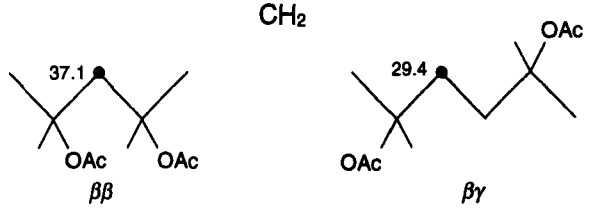

$\beta\beta$ $\beta\gamma$

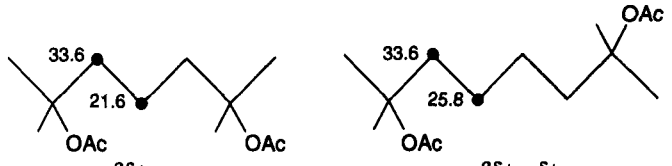

$\beta\delta^+, \gamma\gamma$ $\beta\delta^+, \gamma\delta^+$

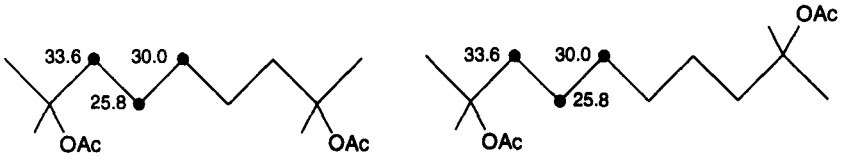

$\beta\delta^+, \gamma\delta^+, \delta^+\delta^+$ $\beta\delta^+, \gamma\delta^+, \delta^+\delta^+$

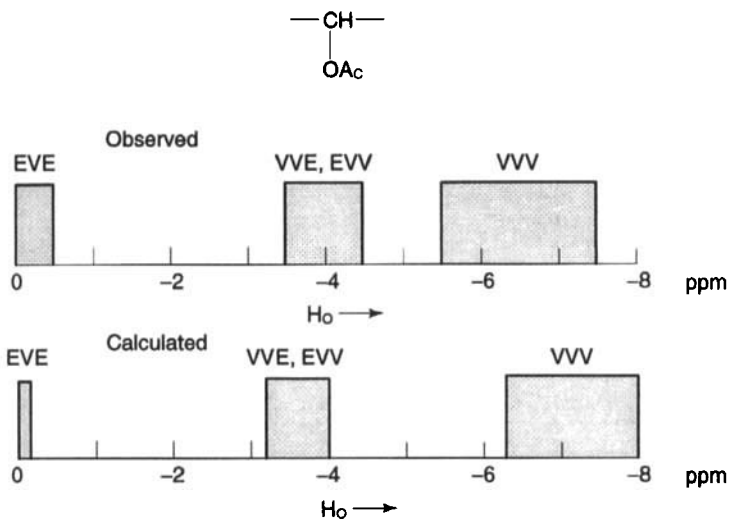

Fig. 16. Comparison of observed[74] and calculated[28] ^{13}C chemical shifts for the methine carbons in E–VAc copolymers.

employing higher-field observations (62.9 MHz for ^{13}C) and using paramagnetic shift reagents, corrected some of the earlier assignments made by Wu *et al.*[72,73] Even so, they were not able to conclusively discriminate between the assignment of resonances belonging to the methine carbons in the *mrmr*, *rrrr*, and *mrrm* stereosequence pentads of atactic PVAc.

We calculated[28] the δ ^{13}C's expected for the methylene and methine carbons in the complete series of E–VAc copolymers using $\gamma_{c,c} = -3$ ppm and $\gamma_{c,o} = -5$ ppm and the RIS model recently developed for these copolymers.[69]

Figure 16 presents a schematic comparison of methine carbon δ ^{13}C's observed and calculated for E–VAc copolymers. A similar comparison of E–VAc methylene carbon δ ^{13}C's is displayed in Fig. 17. While the chemical shifts calculated for the methine carbons in E–VAc copolymers only reflect differences in the numbers and kinds ($\gamma_{c,c}$ and $\gamma_{c,o}$) of magnetic shieldings produced by their microstructurally sensitive *gauche* arrangements with C and O γ-substituents (see Fig. 16), the methylene carbon chemical shift (see Fig. 17) reflect in addition different numbers of β-OAc substituents. Wu *et al.*[72,73] found β-OAc = +5 ppm from their model compound studies and this value was employed in the calculation of E–VAc methylene carbon chemical shifts.

Note the close agreement between δ ^{13}C's observed and calculated for the backbone carbon nuclei in E–VAc copolymers. This provides strong support for the efficacy of the RIS model[69] recently developed for these copolymers.

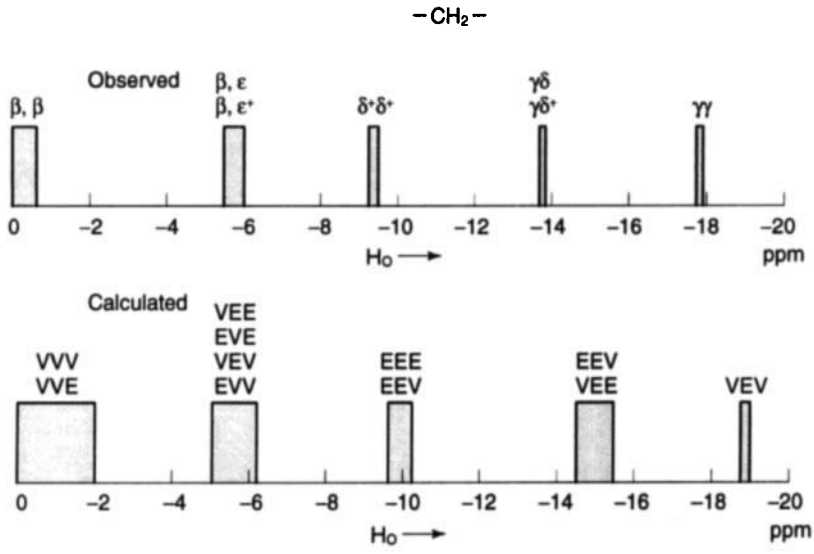

Fig. 17. Comparison of observed[74] and calculated[28] ^{13}C chemical shifts for the methylene carbons in E–VAc copolymers.

In addition, δ ^{13}C's calculated for the backbone carbon nuclei in atactic PVAc using the homopolymer RIS model[71] and the same γ-*gauche* effects employed for E–VAc copolymers, generally agree with those appearing in the observed spectrum.[74] This agreement permitted a conclusive assignment of those methine carbon resonances belonging to the *mrmr*, *rrrr*, and *mrrm* pentad stereosequences which Sung and Noggle[74] had been unable to assign unambiguously.

6. NMR OBSERVATION OF RIGID POLYMER CONFORMATIONS

Though we have dealt exclusively with the analysis of polymer microstructures and conformations by comparison of chemical shifts (δ ^{13}C, δ ^{19}F) calculated via the γ-*gauche* effect method and ^{1}H–^{1}H distances, averaged over all conformations available to them, with their observed solution spectra, high-resolution, solid-state NMR observations can also probe rigidly fixed polymer conformations. It has been demonstrated[75,76] that the ^{13}C chemical shifts observed in CPMAS/DD ^{13}C NMR spectra of solid polymers are also sensitive to the local rigid conformations of their constituent chains. This has been demonstrated in several instances for crystalline polymers able to

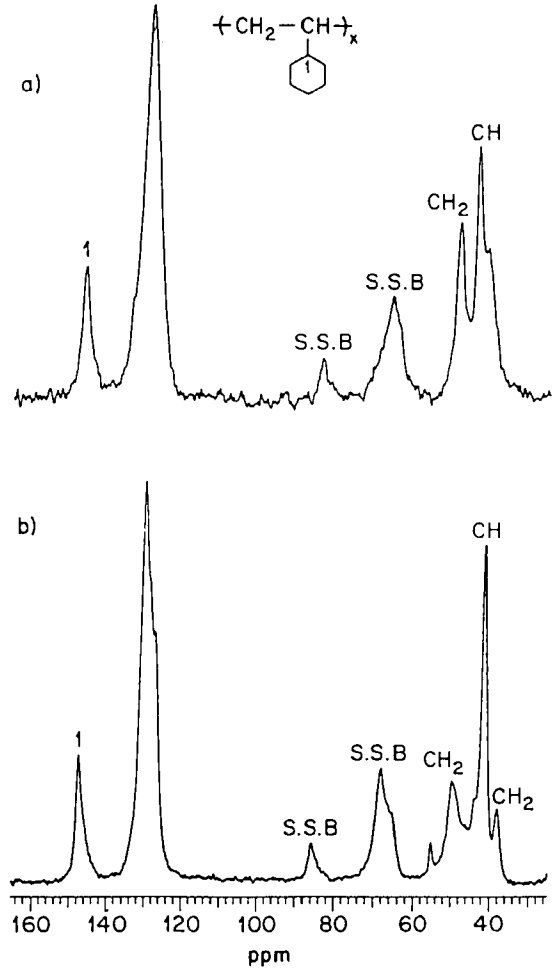

Fig. 18. CPMAS/DD ^{13}C NMR spectra[76] of (a) form I and (b) form II s-PS. The form II sample of (b) was obtained by absorption of dichloromethane into an amorphous, melt-quenched film of s-PS.

crystallize in two or more polymorphs which are distinguishable for the different conformations adopted by their polymer chains.

As an example, syndiotactic polystyrene (s-PS)[76] can be crystallized in two conformationally distinct polymorphs, form I with all *trans*, planar zigzag chains and form II where the chains adopt the helical . . .*ttggttgg*. . . conformation, very similar to that observed[77] in syndiotactic polypropylene (s-PP) crystals. CPMAS/DD ^{13}C NMR spectra of both s-PS polymorphs are shown in Fig. 18. Note in the form II spectrum (b) two methylene carbon resonances appear at 49.1 and 38.1 ppm (*vs.* TMS). Since half of the

methylene carbons in form II s-PS are *trans* to both of their γ-substituents (CH's), while the other half are *gauche* to both of theirs, it is not surprising that two methylene carbon resonances separated by *ca.* $2\gamma_{c,c}$ (11 ppm) are observed. Identical behaviour is observed[78] for s-PP which also crystallizes in the . . .*ttggttgg*. . . helical conformation. All the methylene carbons in the all-*trans* form I crystalline chains are *trans* to their γ-substituents, consistent with the single CH_2 resonance observed for this polymorph at 48.4 ppm, which is virtually coincident with that half of the methylene carbons in form II crystals (49.1 ppm) that are also not shielded by their γ-substituents.

S-PP can also be crystallized in the all-*trans* conformation[79,80] when a molten sample is rapidly cooled from the melt and then cold drawn at 0°C. Sozzani *et al.*[81] have recorded the CPMAS/DD ^{13}C NMR spectra of several different portions of such a quenched, cold drawn s-PP sample with the results shown in Fig. 19. It is apparent that in that portion of the cold drawn s-PP specimen observed in Fig. 19(d) the s-PP chains are crystallized in the all-*trans*, planar zigzag conformation as evidenced by a single CH_2 resonance at 49.1 ppm (see Fig. 18(a) for comparison to form I s-PS). in the portion of the cold drawn s-PP sample examined in Fig. 19(c) both the all-*trans* and helical . . .*ttggttgg*. . . crystals are evident giving two CH_2 resonances at 49.1 and 39.6 ppm, respectively, once again caused by 0 and $2\gamma_{c,c}$ *gauche* shieldings.

More recently two studies[82,83] concerning the NMR observation of the rigid conformations adopted by amorphous polymer chains in their glassy phases have appeared. Sozzani *et al.*[82] have interpreted the methylene portion of the MAS/DD ^{13}C NMR spectra of s-PP observed below T_g in terms of the rigid conformations adopted by the glassy, amorphous s-PP chains. The s-PP chains in the crystalline regions of this sample adopt the usual helical . . .*ttggttgg*. . . conformation. They identified resonances at 50.2, 48.7, 45.5, and 40.2 ppm with *tttt*, *tggt*, *gttt* or *tttg*, and *gttg* conformations, respectively, and discussed their intensities in terms of their populations.

Born *et al.*[83] have compared the CPMAS/DD ^{13}C NMR spectrum of amorphous polyisobutylene (PIB) recorded[84] below T_g with the ^{13}C chemical shifts they calculated for PIB using the *ab initio* IGLO (Individual Gauge for Localized Orbitals) quantum mechanical approach.[85,86] They considered the central diad in a PEB tetrad terminated with 4 methyl groups in their chemical shift calculations, and accounted for the $(6)^4 = 1296$ conformations adopted by the four central dihedral angles according to the six-state RIS model for PIB developed by Vacatello and Yoon.[87]

Their results are presented in Fig. 20, where simulated ^{13}C NMR spectra of CH_2 and $-C-/CH_3$ carbons are compared to the observed CPMAS/DD ^{13}C NMR spectrum of glassy PIB. The leftmost subpeak of the methylene resonances was attributed to $t,*,*,t$ conformations ($0\gamma_{c,c}$), the central subpeak to $g,*,*,t$ or $t,*,*,g$ conformations ($1\gamma_{c,c}$), and the rightmost (upfield) subpeak to $g,*,*,g$ conformations ($2\gamma_{c,c}$). Note that the overall spread in methylene

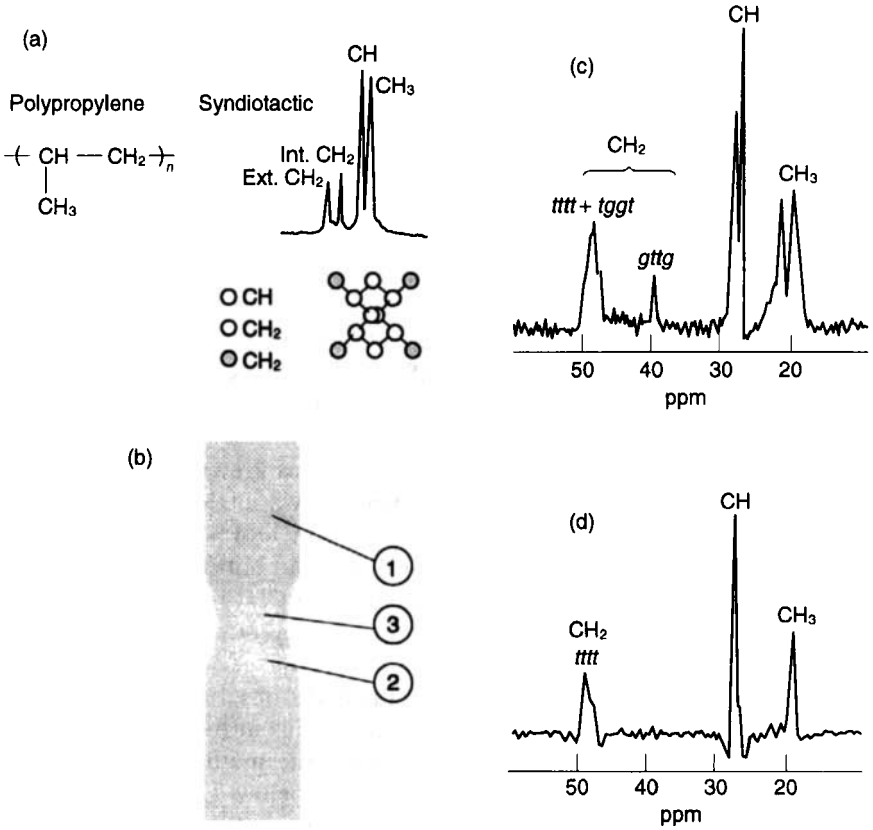

Fig. 19. CPMAS/DD ^{13}C NMR of s-PP: (a) crystalline powder spectrum; (b) sample of cold drawn s-PP showing elongation; (c) spectrum of a sample far from elongation point (1 or 2); (d) spectrum of sample near elongation point (3). (Adapted from Sozzani *et al.*[82])

carbon chemical shifts (*ca.* 20 ppm observed and calculated) is twice that observed in s-PS and s-PP. The authors attribute this to a dependence of CH_2 chemical shifts upon the conformations of the interior dihedral angles *,* (*t* or *g*,*,*,*t* or *g*), different packing environments, and variations in local geometries, such as bond lengths and valence angles. As noted by Born *et al.*,[83] the calculated separation of CH_2 and $-C-/CH_3$ chemical shifts is underestimated, a result they believe is caused by the finite basis set used in their IGLO calculations.

This and many other examples[75] clearly demonstrate the utility of high-resolution NMR as a probe of polymer chain conformations as they occur in rigid, solid samples.

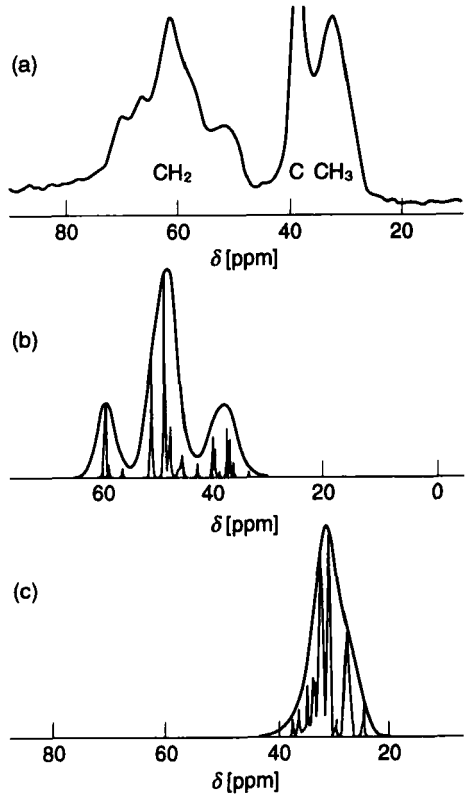

Fig. 20. Comparison of observed MAS/DD ^{13}C NMR spectrum of glassy PIB in (a), with the chemical shifts calculated by Born *et al.*[83] for the CH_2 (b), and $-C-/CH_3$ (c) carbons in a PIB tetramer fragment in different rigid conformations which were used to produce simulated spectra. (Adapted from Born *et al.*[83]).

REFERENCES

1. R. Ditchfield, *Nucl. Magn. Reson.*, 1976, **5**, 1.
2. P. V. Schastnev and A. A. Cheremisin, *J. Struct. Chem.*, 1982, **23**, 440.
3. D. B. Chestnut, *Annual Reports on NMR Spectroscopy* (ed. G. A. Webb), Vol. 21, p. 51. Academic Press, New York, 1989.
4. M. Barfield and S. H. Yamamura, *J. Am. Chem. Soc.*, 1990, **112**, 4747.
5. H. Duddeck, *Topics in Stereochemistry* (ed. E. L. Eliel, S. H. Wilen and N. L. Allinger), Vol. 16, p. 219. Wiley-Interscience, New York, 1986.
6. H. Spiesecke and W. G. Schneider, *J. Chem. Phys.*, 1961, **35**, 722.
7. D. M. Grant and E. G. Paul, *J. Am. Chem. Soc.*, 1964. **86**, 2984.
8. L. P. Lindeman and J. Q. Adams, *Anal. Chem.*, 1971, **43**, 1245.
9. D. E. Dorman, R. E. Carhart and J. D. Roberts, cited in reference 10, 1974.
10. F. A. Bovey, *Proceedings of the International Symposium on Macromolecules*, Rio de Janeiro, 26–31 July, 1974 (ed. E. B. Mano), p. 169. Elsevier, New York, 1974.

11. F. C. Schilling and A. E. Tonelli, *Macromolecules*, 1980, **13**, 270.
12. M. Moller, W. Ritter and H.-J. Cantow, *Polym. Bull.*, 1981, **4**, 609.
13. A. E. Tonelli, *NMR Spectroscopy and Polymer Microstructure: The Conformational Connection*, VCH, New York, 1989.
14. A. E. Tonelli and F. C. Schilling, *Accts. Chem. Res.*, 1981, **14**, 233.
15. D. M. Grant and B. V. Cheney, *J. Am. Chem. Soc.*, 1967, **89**, 5315.
16. S. Li and D. B. Chestnut, *Magn. Reson. Chem.*, 1985, **23**, 625.
17. K. Seidman and G. E. Maciel, *J. Am. Chem. Soc.*, 1977, **99**, 659.
18. D. L. VanderHart, *J. Magn. Reson.*, 1981, **44**, 117.
19. J. B. Stothers, *Carbon-13 NMR Spectroscopy*, Ch. 3. Academic Press, New York, 1972.
20. J. I. Kroschwitz, M. Winokur, H. J. Reid and J. D. Roberts, *J. Am. Chem. Soc.*, 1969, **91**, 5927.
21. C. J. Carman, A. R. Tarpley, Jr. and J. H. Goldstein, *Macromolecules*, 1973, **6**, 719.
22. A. E. Tonelli, F. C. Schilling and F. A. Bovey, *J. Am. Chem. Soc.*, 1984, **106**, 1157.
23. J. E. Mark, *J. Chem. Phys.*, 1972, **57**, 2541.
24. P. J. Flory, *Statistical Mechanics of Chain Molecules*, Wiley-Interscience, New York, 1969.
25. H. L. Frisch, C. L. Mallows and F. A. Bovey, *J. Chem. Phys.*, 1966, **45**, 1565.
26. U. W. Suter and P. J. Flory, *Macromolecules*, 1975, **8**, 765.
27. A. E. Tonelli, *Macromolecules*, 1978, **11**, 565, 634; *ibid.*, 1979, **12**, 255; *ibid.*, 1985, **18**, 1086.
28. E. Tart, G. Wood, D. Wernsman, U. Sangwatanaroj, C. Howe, Q. Zhou, S. Zhang and A. E. Tonelli, *Macromolecules*, 1993, **26**, 4283.
29. Y. Inoue, Y. Itabashi, R. Chujo and Y. Doi, *Polymer*, 1984, **25**, 1640.
30. V. A. Zakharov, G. P. Bukatov and Y. I. Yermakov, *Adv. Polym. Sci.*, 1983, **51**, 61.
31. R. D. Deanin, *SPE J.*, 1967, **23**, 59.
32. A. E. Tonelli and F. C. Schilling, *Macromolecules*, 1984, **17**, 1946.
33. D. L. Plazek and D. J. Plazek, *Macromolecules*, 1983, **16**, 1469.
34. J. E. Mark, *J. Polym. Sci., Polym. Phys. Ed.*, 1973, **11**, 1375.
35. C. C. Price and M. Osgun, *J. Am. Chem. Soc.*, 1956, **78**, 4787
36. C. C. Price, R. Spectro and A. Tunolo, *J. Polym. Sci., Part A-1*, 1967, **5**, 407, 19.
37. K. C. Ramey and N. D. Field, *Polym. Lett.*, 1964, **2**, 461.
38. H. Tani, N. Oguni and S. Watanabe, *Polym. Lett.*, 1968, **6**, 577.
39. T. Hirano, P. H. Khanh and T. Tsurata, *Makromol. Chem.*, 1972, **153**, 331.
40. N. Oguni, S. Maeda and H. Tani, *Macromolecules*, 1973, **6**, 459.
41. N. Oguni, S. Watanabe, M. Maki and H. Tani, *Macromolecules*, 1973, **6**, 195.
42. M D. Bruch, F. A. Bovey, R. E. Cais and J. H. Noggle, *Macromolecules*, 1985, **18**, 1253.
43. J. Schaefer, *Macromolecules*, 1969, **2**, 533.
44. N. Oguni, K. Lee and H. Tani, *Macromolecules*, 1972, **5** 819.
45. N. Oguni, S. Shinohara and K. Lee, *Polym. J. (Tokyo)*, 1979, **11**, 755.
46. W. Lapeyre, H. Cheradame, N. Spassky and P. Sigwalt, *J. Chim. Phys.*, 1973, **70**, 838.
47. T. Uryu, H. Shimazu and K. Matsuzuki, *Polym. Lett.*, 1973, **11**, 275.
48. F. C. Schilling and A. E. Tonelli, *Macromolecules*, 1986, **19**, 1337.
49. A. E. Derome, *Modern NMR Techniques for Chemistry Research*, Ch. 4. Pergamon, New York, 1987.
50. A. Abe, T. Hirano and T. Tsurata, *Macromolecules*, 1979, **12**, 1092.
51. C. J. Turner, *Prog. Nucl. Magn. Reson. Spectrosc.*, 1984, **16**, 27.
52. F. C. Schilling, *J. Magn. Reson.*, 1982, **47**, 61.
53. A. E. Tonelli, F. C. Schilling and R. E. Cais, *Macromolecules*, 1981, **14**, 560.
54. A. E. Tonelli, F. C. Schilling and R. E. Cais, *Macromolecules*, 1982, **15**, 849.
55. C. W. Wilson, III, *J. Polym. Sci., Part A-1*, 1963, 1305.

56. C. W. Wilson, III and E. R. Santee, Jr., *J. Polym. Sci., Part C*, 1965, **8**, 97.
57. R. C. Ferguson and E. G. Brame, Jr., *J. Phys. Chem.*, 1979, **83**, 1397.
58. A. Bax, *Two-Dimensional Nuclear Magnetic Resonance in Liquids*, Delft University Press, Delft, Reidel, Amsterdam, 1982.
59. K. Wuthrich, *NMR of Proteins and Nucleic Acids*, Wiley, New York, 1986.
60. A. Bax and L. Lerner, *Science*, 1986, **232**, 1960.
61. F. A. Bovey and P. A. Mirau, *Accts Chem. Res.*, 1988, **21**, 37.
62. S. A. Heffner, F. A. Bovey, L. A. Verge, P. A. Mirau and A. E. Tonelli, *Macromolecules*, 1986, **19**, 1628.
63. D. Y. Yoon, P. R. Sundararajan and P. J. Flory, *Macromolecules*, 1975, **8**, 776.
64. D. Y. Yoon, U. W. Suter, P. R. Sundararajan and P. J. Flory, *Macromolecules*, 1975, **8**, 784.
65. P. R. Sundararajan and P. J. Flory, *J. Am. Chem. Soc.*, 1974, **96**, 5025.
66. P. R. Sundararajan and P. J. Flory, *J. Polym. Sci. Polym. Lett. Ed.*, 1977, **15**, 699.
67. H. Koinuma, T. Tanabe and H. Hirai, *Makromol. Chem.*, 1980, **181**, 383.
68. P. A. Mirau, F. A. Bovey, A. E. Tonelli and S. A. Heffner, *Macromolecules*, 1987, **20**, 1701.
69. T. D. Rathke, M. W. Frey, D. Guthrie, R. Graham, W. Simendinger, B.-C. Wang, T. Shepard, R. Jones and A. E. Tonelli, *Comp. Polym. Sci.*, 1993, **3**, 61.
70. A. Abe, R. L. Jernigan and P. J. Flory, *J. Am. Chem. Soc.*, 1966, **88**, 631.
71. P. R. Sundararajan, *Macromolecules*, 1978, **11**, 256.
72. T. K. Wu, *J. Polym. Sd., Part A-2*, 1970, **8**, 167.
73. T. K. Wu, and D. W. Ovenall, *Macromolecules*, 1974, **7**, 776.
74. H. N. Sung and J. H. Noggle, *J. Polym. Sci., Polym. Phys. Ed.*, 1981, **19**, 1593.
75. See Ch. 11 in reference 13 and the references cited there.
76. M. A. Gomez and A. E. Tonelli, *Macromolecules*, 1990, **23**, 3385; 1991, **24**, 3533.
77. G. Natta, I. Pasquon, P. Corradini, M. Peraldo, M. Pegoraro and A. Zambelli, *Atti. Accad. Naz. Lincei, Cl. Sci. Fis. Mat. Nat. Rend.*, 1960, **28**, 539.
78. A. Bunn, E. A. Cudby, R. K. Harris, K. J. Packer and B. Say, *J. Chem. Soc., Chem. Commun.*, 15, 1981.
79. P. Corradini, G. Natta, P. Ganis and P. A. Temussi, *J. Polym. Sci., Part C*, 1967, **16**, 2477.
80. Y. Chatani, H. Maruyama, K. Naguchi, T. Asanuma and T. Shiomura, *J. Polym. Sci., Part C; Polym. Lett.*, 1990, **28**, 393.
81. P. Sozzani, M. Galimberti and G. Balbontin, *Makromol. Chem., Rapid Commun.*, 1992, **13**, 305.
82. P. Sozzani, R. Simonutti and M. Galimberti, *Macromolecules*, 1993, **26**, 5782.
83. R. Born, H. W. Spiess, W. Kutzelnigg, U. Fleischer and M. Schindler, *Macromolecules*, 1994, **27**, 1500.
84. K. Zemke, K. Schmidt-Rohr and H. W. Spiess, *Acta. Polym.*, 1994, **45**, 148.
85. W. Kutzelnigg, U. Fleischer and M. Schindler, *NMR Basic Princ. Prog.*, 1991, **23**, 165.
86. W. Kutzelnigg, *J. Mol. Struct. (THEOCHEM)*, 1989, **202**, 11.
87. M. Vacatello and D. Y. Yoon, *Macromolecules*, 1992, **25**, 2502.

This Page Intentionally Left Blank

A Review of High-Resolution NMR Studies of Vulcanized Elastomers

MAKIO MORI and JACK L. KOENIG

Department of Macromolecular Science, Case Western Reserve University, Cleveland, Ohio 44106-7202, USA

Recent advances are reviewed concerning the application of high-resolution NMR solid-state spectroscopy to the characterization of network structures and vulcanization chemistry for elastomers. Included are several vulcanization systems cured with sulfur, peroxides or radiation, with and without accelerators and cure activators. The major findings are the type, number and distribution of crosslinks and main-chain modifications induced by the vulcanization reactions. Contributions to an understanding of the vulcanization mechanisms are reported.

1. INTRODUCTION

Elastomeric systems are one of the most important classes of materials in industry because of their specific dynamic properties. Elastomers are typically crosslinked to a greater or lesser degree in order to improve their properties. The crosslinking process termed vulcanization prevents permanent deformation under load and ensures elastic recovery on removal of the load. The introduction of crosslinking, however, limits the ability to characterize these systems because of the insolubility of the resulting network. Additionally, the extremely low concentration of the chemically modified structures induced by the vulcanization challenges many of the traditional analytical techniques. Many approaches, including physical tests and chemical analysis, have been attempted in an effort to relate the chemical microstructure to the physical properties of both raw and cured elastomers.

ANNUAL REPORTS ON NMR SPECTROSCOPY
VOLUME 34 ISBN 0-12-505334-7

^{13}C and ^{1}H NMR spectroscopy are powerful methods to directly observe the chemical species and types of molecular connections existing in polymeric materials. The information obtainable from high-resolution NMR spectroscopy includes main-chain microstructures, comonomer composition and sequence, terminal structures, branching, abnormal structures (cyclic and isomerized structures), bonding direction, tacticity, and the crosslink structure in the sample. In the modern solid-state NMR spectroscopy, high-resolution spectra with sharp resonance lines are obtainable in solid bulk samples by applying specific line narrowing techniques. Under magic angle spinning (MAS) conditions, high-quality spectra can be recorded for the lightly crosslinked elastomers above the glass transition temperature. Recently, solid-state ^{13}C NMR has been widely applied to the characterization of vulcanized rubber systems. Several reviews have been published in terms of the solution and solid-state NMR analysis of crosslinked polymers[1,2] and uncrosslinked and crosslinked elastomers.[3–8]

Recent literature will be reviewed on the study of vulcanized elastomers using high-resolution NMR spectroscopy. After an introduction to the various NMR techniques to characterize the elastomers, solution NMR studies of cured rubbers are briefly reviewed. An extensive discussion is focused on the solid-state NMR studies of several vulcanized elastomers. The detailed mechanisms of the individual vulcanization reactions will not be discussed here. The references listed in the preceding paragraph provide related studies as well as the reviews that deal specifically with vulcanization reactions.[2,9,10]

2. NMR TECHNIQUES TO CHARACTERIZE VULCANIZED ELASTOMERS

High-resolution solution ^{1}H and ^{13}C NMR have usually been used to characterize the structure of soluble, uncured elastomers.[3,4,6] The main advantages of using NMR compared to the other analytical techniques are the high spectral selectivity and the capability of measuring quantitatively the structural components in the sample without using any external calibration. The spectral sensitivity is more pronounced in ^{1}H NMR due to the high natural abundance and higher gyromagnetic ratio of hydrogen relative to ^{13}C. However, ^{13}C NMR has a greater spectral selectivity due to the larger dispersion of the chemical shifts compared to ^{1}H NMR, enabling more detailed structural characterization. The quantitative nature of the results can be compromised in conventional solution ^{13}C NMR by the presence of heteronuclear spin decoupling, but it can be overcome in the gated decoupling pulse mode with some sacrifice in the sensitivity.

In the ^{13}C NMR of polymer solutions, high-resolution spectra with very narrow linewidths are obtained because rapid, random molecular motions

in the solution average several line-broadening interactions to zero. The resulting narrow lines enable not only the identification of the rubber backbone type but also more detailed characterization of the sample chemistry such as the tacticity and branching distribution of the backbone sequence.

There are several difficulties in characterizing vulcanized elastomers in solution NMR due to the limited solubility of the cured network structure. Efforts have been made to swell the networks and examine the NMR spectra using normal solution NMR conditions.[11] Although the spectra obtained by this solvent-swelling method can provide valuable information, the broader resonance lines (relative to lines in true solutions) limit the details of the structural information compared to the high-resolution solution spectra.

The two main factors which determine the broadening of the resonance lines in the NMR of the nuclei with $I = 1/2$ are the homo- or heteronuclear dipolar interactions (DI) and the chemical shift anisotropy (CSA). In modern solid-state ^{13}C NMR spectroscopy, these strong interactions can be reduced or removed by utilizing special instrumental techniques.

High-power dipolar decoupling (HPD) is typically applied to average the strong heteronuclear dipolar C–H interactions (~30–40 kHz) in the solid state. This HPD technique is the high-power analogue of scalar decoupling (~1–3 kHz) in solution. In the single radiofrequency pulse ^{13}C NMR mode, a series of short decoupling pulses can be intermittently applied during the acquisition period in order to enhance the sensitivity of the spectra via the generation of the nuclear Overhauser effect (NOE) (pulse saturation). In a quantitative analysis, the decoupling is gated off during the acquisition in order that the NOE fades out (gated high power decoupling or GHPD).

Magic angle sample spinning utilizes the fact that anisotropic solid interactions arising from chemical shifts have an angular dependence of $3\cos^2\theta - 1$, where θ is the orientation of the interaction vector with respect to the external magnetic field. The magnetic interactions responding to this geometrical dependence can be removed by mechanically rotating the solid sample at the magic angle, $\theta = 54.44°$.[12,13]

In rigid solids, cross-polarization (CP) is typically used instead of a single radiofrequency pulse sequence to enhance the sensitivity of the ^{13}C NMR. CP is a double-resonance experiment in which the energy levels of the ^{1}H and ^{13}C spins are matched to the Hartman–Hahn condition in the rotating frame. Under this condition, energy may be exchanged between the two coupled spin systems. The result is a growth of the ^{13}C magnetization at the expense of the ^{1}H magnetization. The delay time between the CP pulse depends on the shorter ^{1}H spin-lattice relaxation time (T_1), which allows shorter pulse sequences and the collection of more signal which further improves the sensitivity in the CP experiment.[14] By combining CP with HPD and MAS, narrow lines and enhanced sensitivity can be obtained for rigid polymers in the solid state.

Typically, the CP–MAS–HPD experiment is a valuable technique to examine crystalline and/or glassy polymers which have large dipolar interactions induced by highly restricted molecular motions. However in rubbery materials, the CP technique is not so efficient due to the reduced dipolar interactions and shorter ^{13}C T_1 times arising from the extensive reorientational motion in the molecule. The CP experiment is difficult to accomplish under these circumstances and the contact is difficult to maintain. Usually, the single-pulse GHPD–MAS mode is utilized for mobile materials under conditions well above (+70°C~) the glass transition temperature.[15,16] Most of the uncured and lightly crosslinked elastomers are sufficiently mobile when they are measured at room temperature. Since the efficiency of CP increases with decrease in the molecular mobility, CP–MAS is also valuable to study more highly crosslinked and/or filled elastomer systems.

The comparison of the GHPD–MAS and CP–MAS spectra for sulfur vulcanized natural rubber (10% sulfur) is shown in Fig. 1. The GHPD–MAS experiment is more sensitive to the mobile portions (uncrosslinked or lightly cured sample), while the CP–MAS–GHPD experiment measures the spectra of the more rigid or highly crosslinked parts of the network.[17] Typically, the GHPD technique has an advantage compared to the CP in that quantitative results can be obtained by interpretation of the resonance areas and linewidths.

Several experimental and instrumental techniques have been proposed to enhance the resolution of the ^{13}C NMR spectra for crosslinked polymer systems. The spectral resolution can be greatly improved by increasing the measurement temperature in the GHPD–MAS experiment. The increased temperatures induce additional mobility in the sample molecules which narrows the resonance bandwidths, enabling the observation of more solution-like spectra in the solid state.[17]

Three spectral editing techniques, dipolar-dephasing (or interrupted decoupling),[18] attached proton test (APT)[19,20] and distortionless enhancement by polarization transfer (DEPT),[21–23] are useful to distinguish carbons with different degrees of protonation. Another unique technique to separate the highly overlapping peaks is the inversion recovery experiment, where the carbons with different spin–lattice relaxation times (T_1) are resolvable.[24]

Obtaining high-resolution spectra for ^{1}H NMR in the solid-state is typically more difficult than ^{13}C NMR. The line broadening in solid-state ^{1}H NMR is dominated by strong homonuclear dipolar interactions (~30–80 kHz) which cannot be removed by GHPD or MAS except at very high spinning rates (typically not available for routine use). Multiple-pulse techniques such as REV-8, BR-24 and CRAMPS must be used to reduce the homonuclear dipolar interactions and narrow the resonance lines. A series of intense synchronous pulses are applied to average the nuclear spin magnetization.[25] Figure 2 illustrates the ^{1}H NMR spectra of polyisoprene obtained under

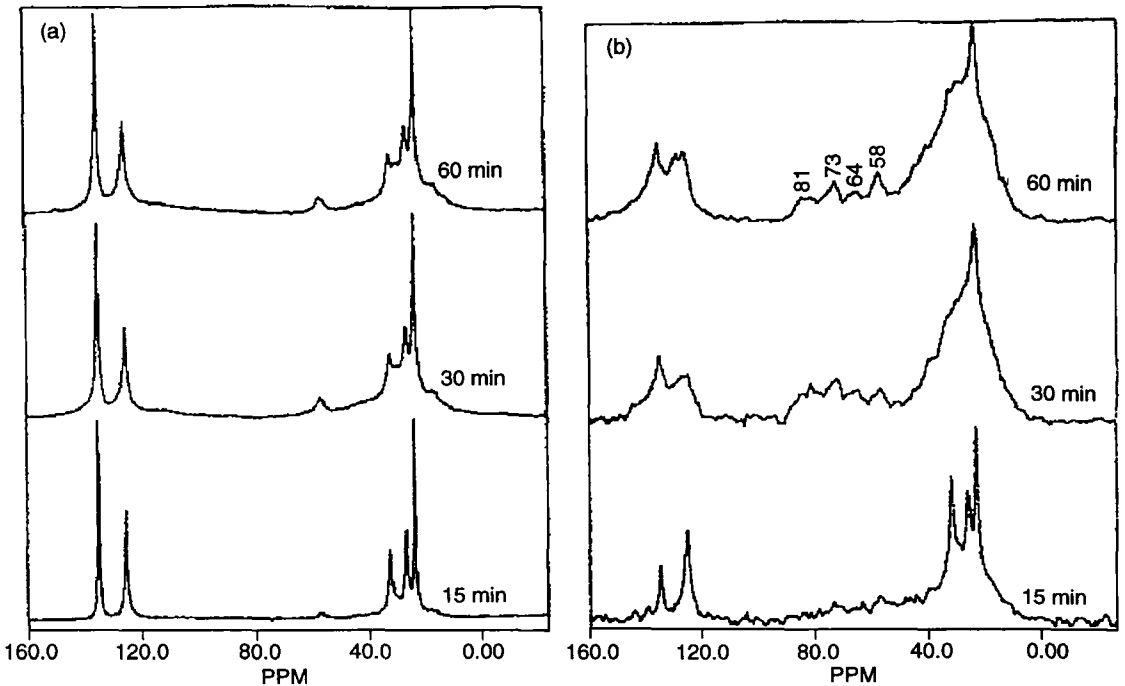

Fig. 1. ^{13}C MAS NMR spectra of NR cured with 10% sulfur at 150°C for 15, 30 and 60 min: (A) GHPD spectra; (B) CP spectra. (Reprinted from ref. 17.)

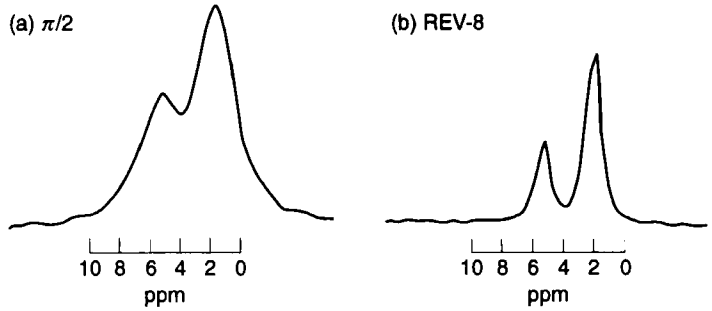

Fig. 2. (a) Conventional and (b) multiple-pulse proton NMR spectra of *cis*-1,4-polyisoprene acquired at a frequency of 56.41 MHz. (Reprinted from ref. 26 with permission.)

the standard $\pi/2$ pulse and REV-8 conditions. The linewidths have been further narrowed by combining with the MAS.[26]

Pulsed ^{1}H NMR is often used to characterize the structural and molecular dynamics of elastomeric systems via the NMR relaxation information obtained from the unresolved resonance lines.[27] Although no chemical shift information is obtainable, it is a valuable technique to study changes in molecular mobility due to rubber-to-filler interactions, rubber degradation, crosslink density and the interfacial region in the heterogeneous systems.

3. STUDY OF VULCANIZED ELASTOMERS USING SOLUTION NMR TECHNIQUES

Because of the high chain mobility, solid elastomers can be observed using the standard Fourier transform (FT) NMR method. Resonances are broadened by the decrease in molecular motion which occurs when the elastomer system is cured, but the line broadening can be partially decreased by increasing the measurement temperature. Comparisons of the ^{13}C NMR spectra of solution rubber and bulk rubber obtained by the solution NMR method were made for several elastomers in the presence and absence of carbon black.[28]

Figure 3 shows the ^{13}C NMR spectra obtained from various portions of typical rubber tyres. These samples were cut from the tyre, placed in an NMR tube without solvent, and spectra obtained at an elevated temperature. The data show that polyisoprene (IR) and an IR–polybutadiene (IR–BR) rubber blend can be quickly identified in the materials.

The chemistry of sulfur vulcanization of natural rubber was studied by using standard ^{13}C FT-NMR without MAS.[16] Prior to the observation of

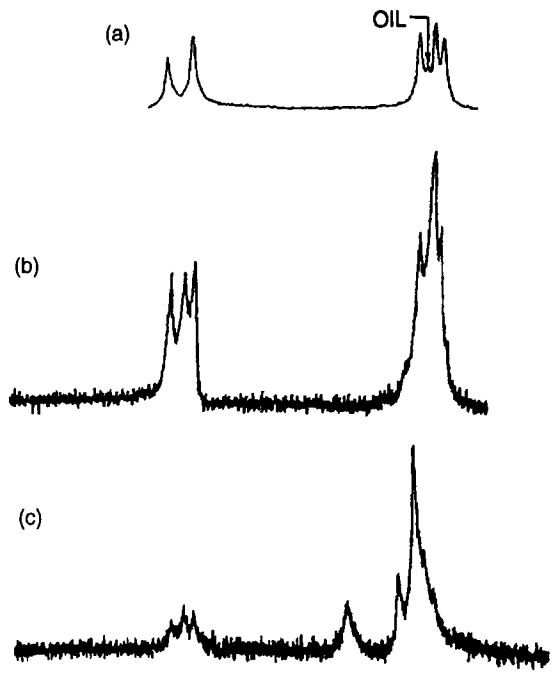

Fig. 3. ^{13}C NMR spectra of rubber fabricated materials run on solids at 90°C using normal pulsed FT technique: (a) tyre tread; (b) tyre compound; (c) liner material. (Reprinted from ref. 28 with permission.)

the natural rubber vulcanizates, model compounds were examined to determine where the chemical shifts of the crosslink sites occur, and how different crosslink structures may be resolved. Based on the chemical shifts of the model compounds having different levels of sulfurization, it is found that the chemical shift of the α-carbon in a disulfide is about 7 ppm down field compared to the corresponding monosulfide. Hence, one could expect to resolve monosulfidic and disulfidic crosslinks attached to the polymer chain. On the other hand, there is usually little difference between the α-carbon chemical shift in a trisulfide and the corresponding disulfide.

Figure 4 shows some of the more likely structures occurring in the vulcanization of the natural rubber. The approximate chemical shifts for carbons in these structures have been calculated by using ^{13}C chemical shift substituent effects. The initial substituent-effect values used are taken from reference 29, but were slightly modified, based on model compound studies. The values are: monosulfidic, $\alpha = +18$ ppm, $\beta = +6$ ppm, $\gamma = -4$ ppm; di- and polysulfide, $\alpha = +25$ ppm, $\beta = +6$ ppm, $\gamma = -4$ ppm.

Figure 5 shows the aliphatic-carbon region of the ^{13}C spectrum of natural rubber (NR) cured with sulfur for 6 hours at 138°C using standard pulsed

FT techniques at 90°C. A number of new peaks are seen in the spectrum. Two of these can be assigned to *trans*-polyisoprene units in the predominantly *cis*-polyisoprene chain. This assignment confirms that isomerization of the double bonds from *cis* to *trans* occurs in the sulfur vulcanization of NR. The other new resonances are due to the sulfur crosslink sites themselves. However, there is substantial overlap among the various resonances due to the crosslink sites at this field strength.

Additional discrimination of the spectra is done by the distortionless enhancement by polarization transfer (DEPT)[21–23] experiment. The value of the DEPT sequence lies in its ability to provide relatively pure subspectra, each of which arises from only one type (CH_3, CH_2 or CH) of carbon. Figure 6 is the aliphatic region of the DEPT subspectra of NR cured with sulfur alone. There is reasonably good separation among the subspectra, enabling discrimination and identification of the types of the crosslinks. The peak at 59 ppm appears to be exclusively CH, suggesting di- or polysulfidic crosslinks of structure II (in Fig. 4), or possible structure IV. The peak at 46 ppm for this sample is a CH_2 carbon, suggesting di- or polysulfidic crosslinks of structure III, although in this case structures V and VI are also possibilities.

Many valuable insights are obtained directly from the bulk rubber vulcanizates in the standard ^{13}C FT-NMR; however, it is concluded that additional studies under higher resolution conditions are necessary to resolve the types and amounts of crosslinks occurring in the complex vulcanization reactions.[16]

An estimation of the crosslink densities in the vulcanized elastomers and their blends have been made by conventional ^1H FT-NMR in the swollen state. This technique is based on the fact that signals in NMR spectra of polymers become broader as the crosslink density increases, as seen in Fig. 7, by the reduction in the chain mobility.[11,30] Adequate spectra of vulcanizates cannot normally be obtained by using solution NMR instrumentation, but swelling the vulcanizates permits observation of spectra with sufficient resolution to identify some signals from nuclei in different environments, although much broader than the normal bandwidths for polymer solutions or in the high-resolution solid-state NMR.

The half-widths of particular peaks in a swollen elastomer vulcanizates are given by the signal strength at a reference position on the side of the peak expressed as a percentage of the peak signal strength, and is designated

---

Fig. 4. Predicted chemical shifts for some structures expected in the sulfur vulcanization of NR. The top three structures are known models. For the bottom six structures, the chemical shifts are derived from the models and α-, β- and γ-substituent effects for monosulfidic crosslinks. Values in parentheses are for di- and polysulfidic crosslinks for the α-carbons. (Reprinted from ref. 16 with permission.)

CIS–PIP

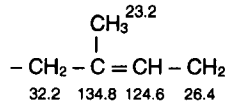

TRANS–PIP

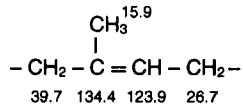

EP–COPOLYMER SEGMENT

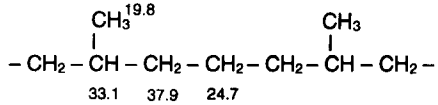

I

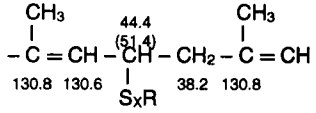

II

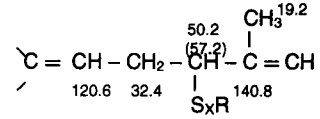

III

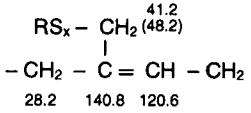

IV

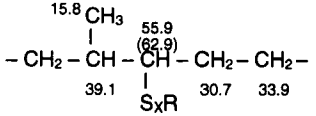

V

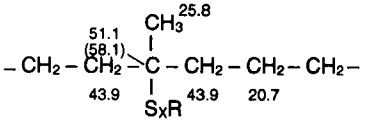

VI

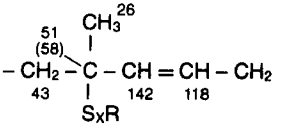

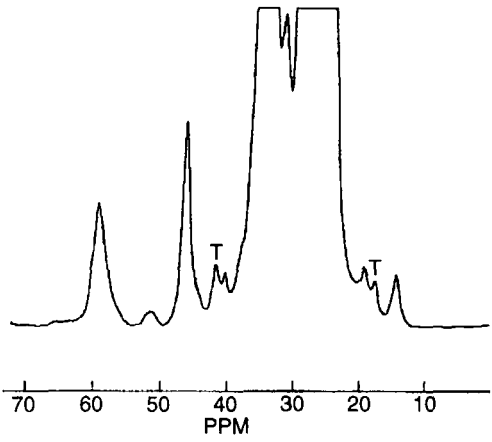

Fig. 5. Standard ^{13}C NMR spectrum at 90°C of a sulfur-cured NR (6 h at 138°C). The label "T" indicates peaks from *trans*-isoprene units. (Reprinted from ref. 16 with permission.)

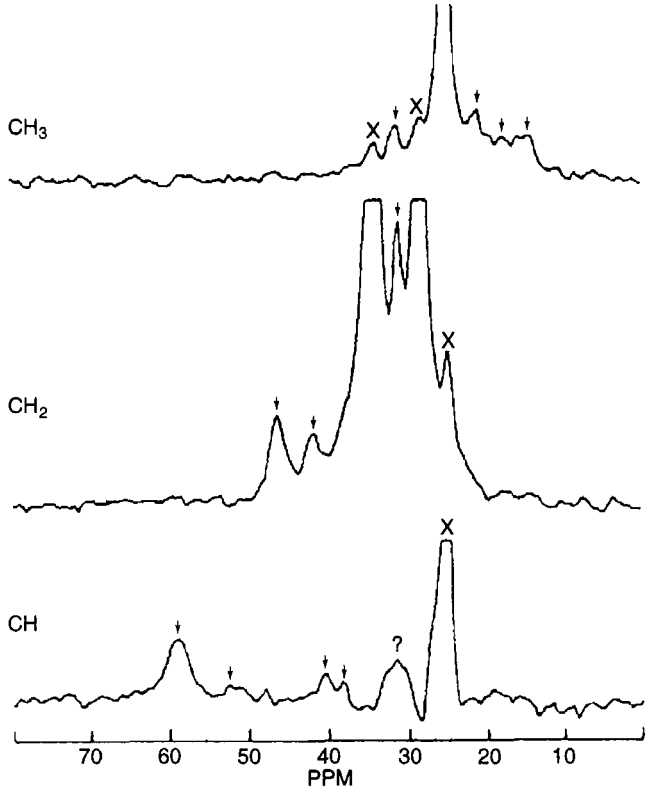

Fig. 6. DEPT spectra of the sulfur-cured NR of Fig. 5. "X" marks residual peaks from other subspectra. Arrows indicate peaks due to crosslink sites. (Reprinted from ref. 16 with permission.)

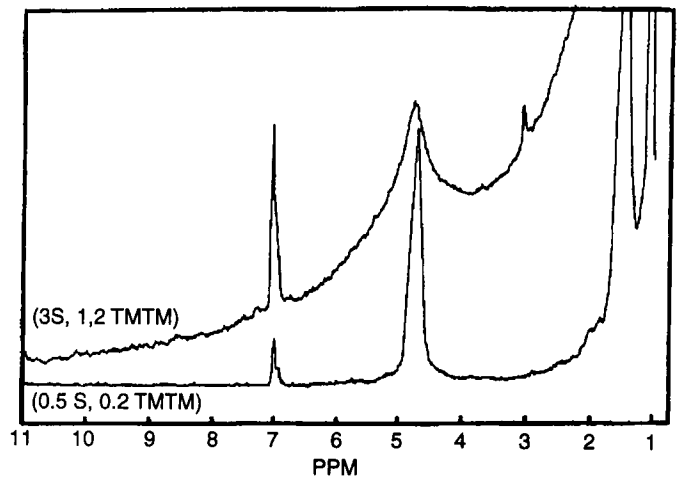

Fig. 7. ^{1}H NMR spectra of NR vulcanizates swollen to equilibrium in deuterochloroform: vulcanizates with high crosslink density (upper) and low crosslink density (lower). (Reprinted from ref. 30 with permission.)

H%. *H*% can be correlated with physical crosslink density as estimated by the equilibrium swelling measurements.

Correlations have been observed between *H*% and the crosslink density for NR,[11,30–34] IR,[31] epoxidized natural rubber (ENR),[35] *cis*-polybutadiene (BR),[11,31,35] acrylonitrile butadiene rubber (NBR),[11,30,32,33] and ethylene–propylene–diene terpolymer (EPDM).[11,34] Figure 8 shows the dependence of olefinic ^{1}H peak widths, *H*%, on the physical crosslink density for NR vulcanizates. The spectra of the binary blends are then analysed to provide estimates of the crosslink density in the two phases. These studies showed that there is a heterogeneous distribution of the crosslinking between the two phases of NR–BR,[11,31] ENR–BR,[35] NR–NBR[30,32,33] and NR–EPDM[34] blends. This trend is particularly notable when there is a difference in polarity between the two rubbers. Both in NR–NBR and ENR–BR blends there is a marked bias in the crosslink distribution in favour of the more polar polymer.

Using a higher frequency FT-NMR spectrometer (300 MHz) rather than the continuous-wave 90 MHz spectrometer, additional observations have been made. The frequency of the ^{1}H olefinic resonances from the elastomer is dependent on crosslink density due to differences in the local field within the swollen gel. Also, two resonances are observed for small molecules such as TMS (internal standard) and residual protonated solvent. The smaller resonance of each pair changes in shape and position in synchrony with the polymer signals and originates from the solvent within the swollen polymer.[11]

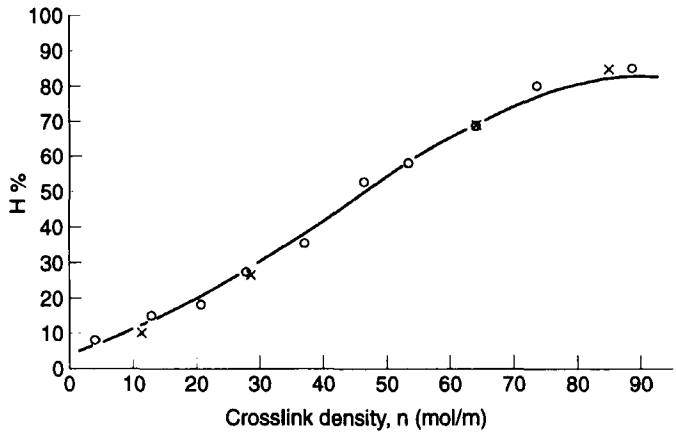

Fig. 8. *H*% *vs* crosslink density for NR vulcanizates. ○: calculated from V_r via modified Flory–Rehner equation; ×: calculated from C_1 data.[15] The curve represents best-fit third-order polynomial to the data. (Reprinted from ref. 31 with permission.)

The frequencies of the smaller resonances of each pair in the spectra of filled vulcanizates are found to depend on the amount of curatives, black loading and black surface area.[11] A study was also attempted using ^{13}C NMR at 75 MHz for an NR–BR blend, and similar trends have been observed.[11]

The utilization of the ortho-dichlorobenzene (ODCB)-solubilization method, which is commonly used in infrared spectroscopic study,[36] is an attempt to overcome the solubility limitations of vulcanized elastomers in solution ^{13}C NMR studies.[37] The microstructural compositions in the filled and unfilled elastomer vulcanizates can be analysed by solution ^{13}C NMR using this technique. Several rubber blends including NR, IR, BR, styrene–butadiene copolymer (SBR), butyl rubber (IIR), polychloroprene (CR) and EPDM with known microstructural and blend compositions have been tested using solution ^{13}C NMR. The ^{13}C NMR data are in good agreement with the known values, which enables the quantitative analysis of the unknown elastomer blend products.[37]

However, the chemical shift assignments used in this study for BR and SBR with high content of vinyl(1,2)-butadiene and/or styrene units must be updated for BR[38] and SBR.[39] The chemical shifts between 40 and 45 ppm are more complicated, reflecting the effect of tacticity in the multi-sequence of vinyl–butadiene and styrene units, which may disable the simple calculation of the structural compositions for the modern solution-polymerized materials containing unique sequence distributions.

Another technique to solubilize vulcanized elastomer in the commonly used NMR solvent has been proposed.[40] Di- and polysulfidic crosslinks present in elastomer vulcanizates can be cleaved by treatment with

hexane-1-thiol/piperidine,[41] enabling solution ^{1}H NMR analysis of rubber containing exclusively di- and polysulfidic crosslinks. Natural rubber was sulfur-vulcanized with *N-t*-butylbenzothiazole-2-sulfenamide (TBBS) at low cure temperatures (80 to 100°C) and short cure times (5 to 8 min) to avoid the formation of monosulfide. Figure 9 shows the ^{1}H NMR spectrum of solubilized rubber vulcanizate. The crosslink residues were identified by correlation of the chemical shift, splitting pattern and coupling constants of the α-protons with those of model thiols having very similar structures. Yields of crosslinks agreed well with values obtained from the physical measurements.

4. HIGH-RESOLUTION SOLID-STATE ^{13}C NMR STUDIES OF VULCANIZED ELASTOMERS

4.1. Peroxide and γ-irradiation cured NR

The chemical structure of natural rubber crosslinked with dicumyl peroxide has been studied by high-resolution solid-state ^{13}C NMR with and without the use of the CP technique at 37.7 MHz.[42,43] Figure 10 shows a series of normal FT-NMR (GHPD) spectra of natural rubber cured with different amounts of dicumyl peroxide. As the level of peroxide increases (increase in crosslink density), the peak widths at half-height increase along with the decrease in the peak heights for the backbone carbons in the natural rubber. The observed chemical shifts in this study are calibrated by the polyoxymethylene rotor peak at 89.1 ppm, which results in 1 to 2 ppm downfield shift in the peak positions compared to TMS calibrated spectra in solution.

Evidence of the new structures occurring in the vulcanization can be characterized by the new resonances in the spectra. The two carbon resonances at 17.3 and 41.5 ppm in Fig. 10(A) and (C) are attributable to the carbons in the *trans*-isoprene unit in the sample, which are typically observed at 16 and 40 ppm from TMS in the solution ^{13}C NMR.[44] The intensities of the two peaks increase with the level of peroxide, suggesting the occurrence of *cis*-to-*trans* configurational isomerization during the cure by the rearrangement of the allylic free radical.

No additional new peaks are observed in the spectra recorded by the single-pulse GHTD experiments with a moderate pulse repetition delay times. The absence of the peaks from the crosslinked structures may suggest the existence of rigid network junctions in the system. The use of dicumyl peroxide as a curative for the diene polymers produces a network that contains only carbon–carbon crosslinks. The junctions of carbon–carbon crosslinks will have longer longitudinal relaxation times (T_1), which disable the detection of the crosslinks in the single-pulse experiment.

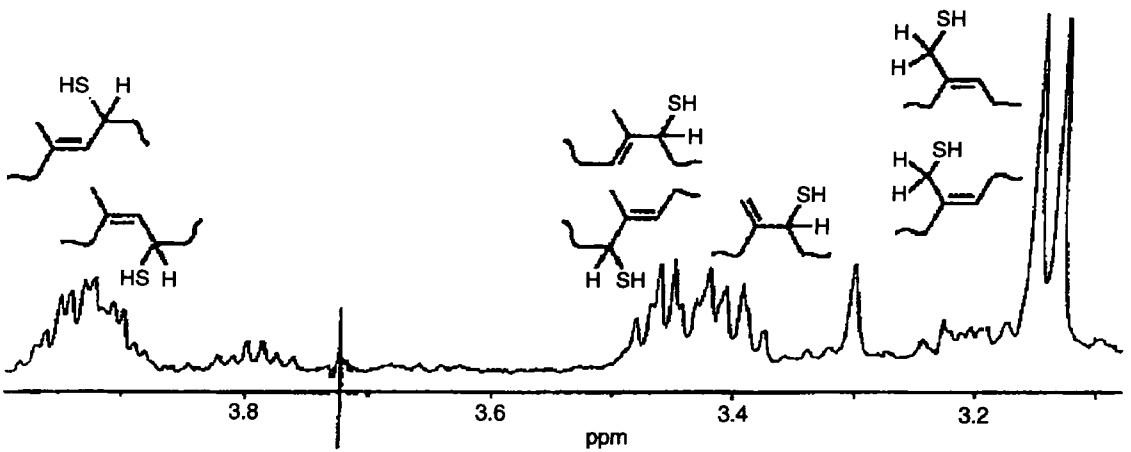

Fig. 9. ^{1}H NMR spectrum of soluble rubber from NR vulcanizate. (Reprinted from ref. 40 with permission.)

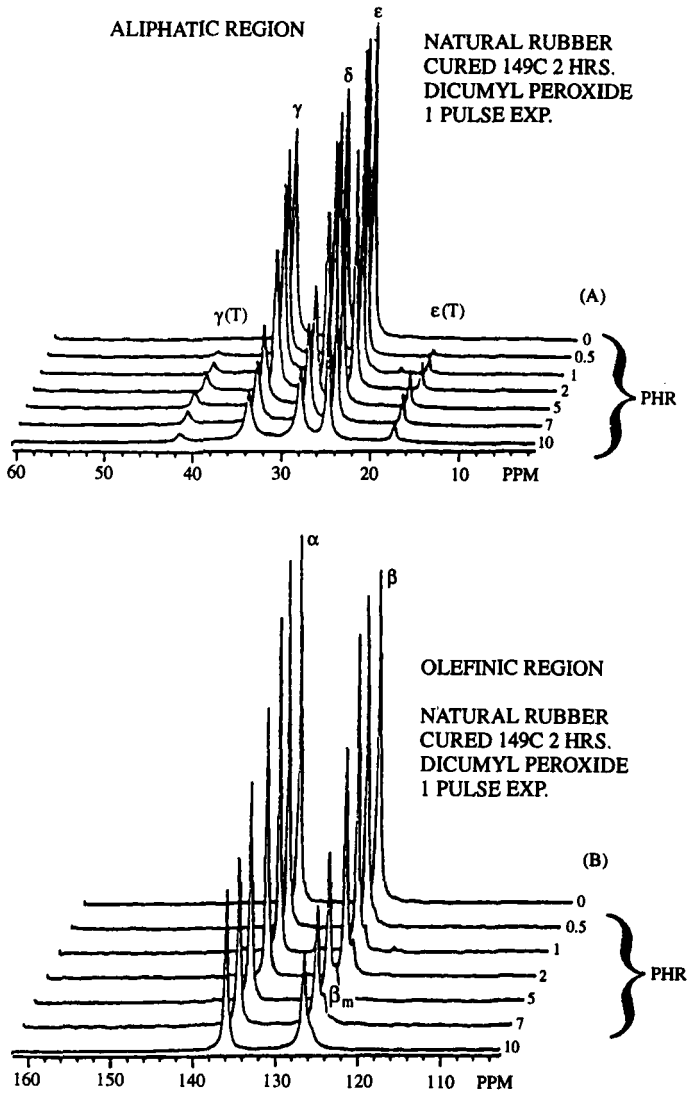

Fig. 10. ^{13}C NMR spectra of NR crosslinked with dicumyl peroxide: (A) aliphatic region; (B) olefinic region; (C) NR crosslinked with higher amount of peroxide. Amount of peroxide indicated at the high field side of the spectra. (Reprinted from ref. 42.)

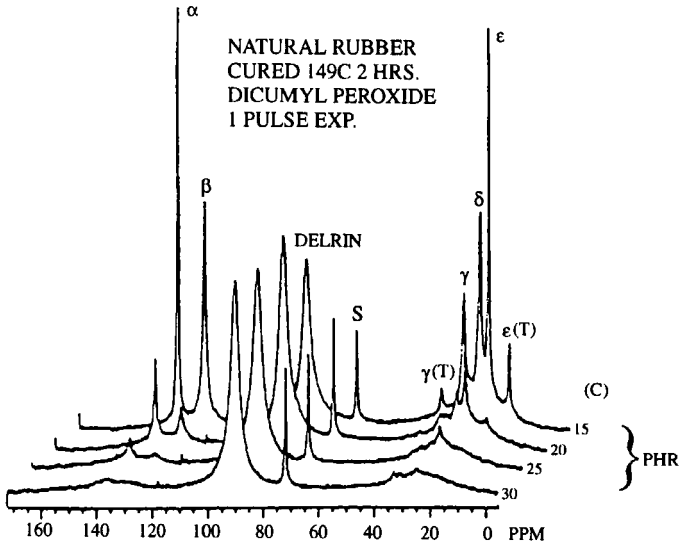

Fig. 10. *continued.*

Figure 11 shows the CP–MAS spectra of NR cured with dicumyl peroxide. The CP experiment is more sensitive to rigid structures which have larger dipolar interactions and longer T_1 relaxation times. In addition to the resonances observed in the GHPD spectra that depict *cis* and *trans* structures, resonances at 14.9, 21.4, 30.6, 37.5 and 45.0 ppm are observed in the CP–MAS experiment. By comparison with the CP-PCS test, where the carbons without attached protons (or less proton-coupled carbons) are discriminated by the modified CP pulse program,[45,46] the 45 ppm peak was assigned to the quaternary carbon which results from double-bond migration. The other four peaks were assigned in this study to the methyl carbons; however, at least two of them (30.6 and 37.5 ppm) now appear to be less probable.

In trying to increase the resolution of the spectra of the highly crosslinked rubber networks, the samples were swollen in benzene to equilibrium and the measurements were performed with MAS. Figure 12 shows the spectra of swollen natural rubber vulcanizate (25 phr peroxide), obtained from the CP–MAS (A) and GHPD (B) experiments. By swelling the rigid network, increased segmental motion is implied and hence, a further narrowing of

Fig. 11. (A) CP–MAS spectra of the aliphatic region of NR cured with dicumyl peroxide. (B) Olefinic region. The amount of peroxide indicated on the high field side of spectra. The arrow indicates an artifact of the carrier. Greek letters represent NR backbone carbons. (Reprinted from ref. 42.)

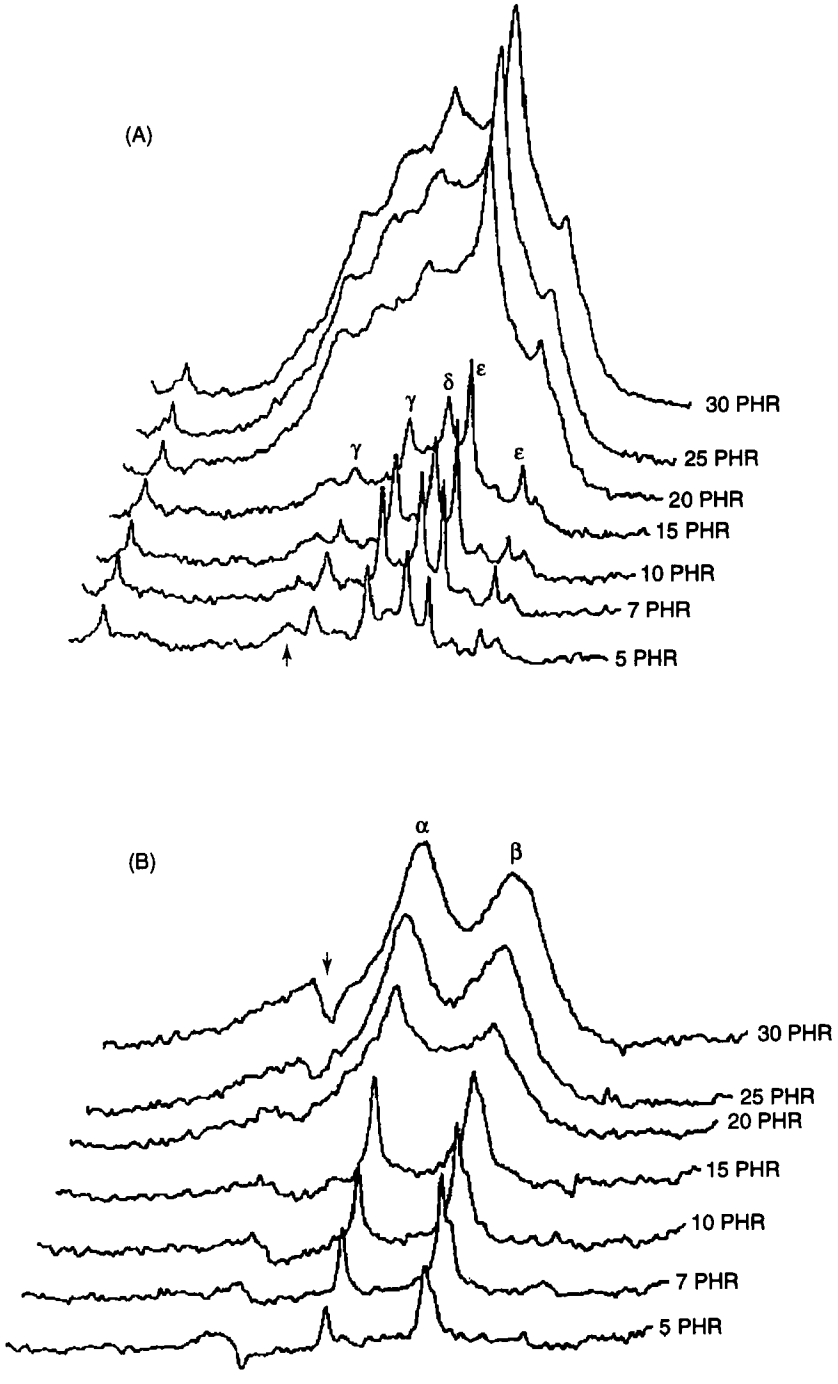
(A)
γ
δ
ε
γ
ε
30 PHR
25 PHR
20 PHR
15 PHR
10 PHR
7 PHR
5 PHR
(B)
α
β
30 PHR
25 PHR
20 PHR
15 PHR
10 PHR
7 PHR
5 PHR

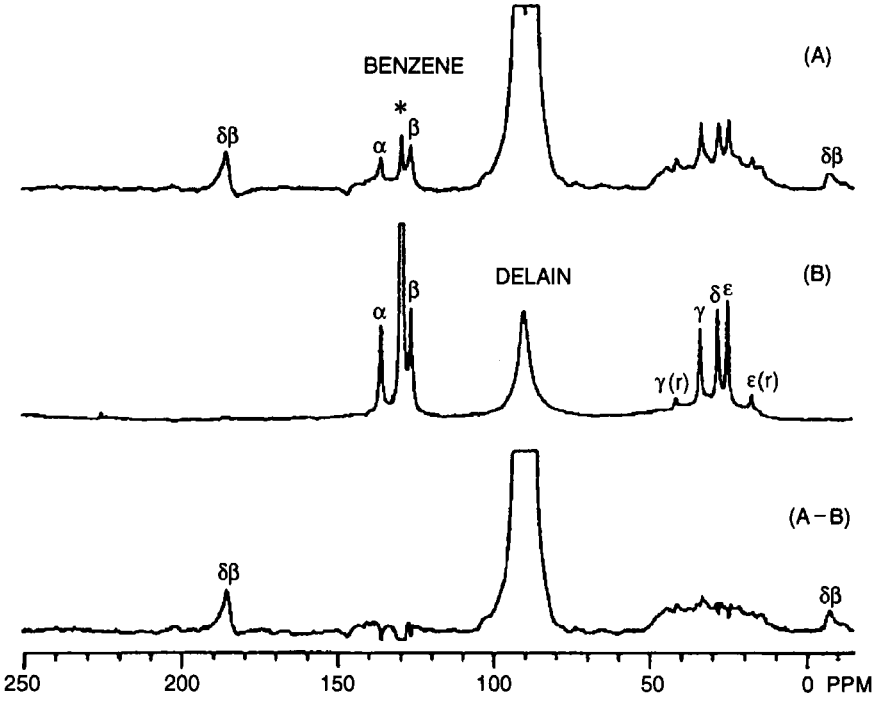

Fig. 12. Spectra of NR crosslinked with 25 phr dicumyl peroxide. Spectrum (A), swollen in benzene to equilibrium swelling. Spectrum obtained under conditions of NFT experiment. Spectrum (B) (same sample as (A)) obtained under CP–MAS. The asterisk marks resonance of benzene solvent. Spectrum (C), the difference between (A) and (B). (Reprinted from ref. 42.)

the resonance lines is expected. Figure 12(C) is the spectrum of (B) subtracted from (A). The spectrum leaves a broad resonance from 10 to 50 ppm, indicating the presence of multiple chemical structures in the crosslinked network. Models for crosslinked networks are proposed from the results of NMR and Fourier transform infrared (FT-IR) investigations.[42,43]

The ^{13}C NMR spectrum of dicumyl peroxide-cured natural rubber was recorded using MAS and low-power decoupling conditions at 75.45 MHz.[47] Seven new resonances are observed in the region between 34 and 60 ppm, at the positions of 34.2, 35.5, 36.8, 37.9, 38.7, 42.7 and 46.4 ppm (see Fig. 13). In this study, the chemical shifts are calibrated by the methylene carbon peak of the *cis*-polyisoprene backbone at 32.5 ppm (from TMS in solution). The resonances originate from tertiary or quaternary carbons of carbon–carbon crosslinks at various positions of the monomer unit and neighbouring CH_2 groups. An assignment by chemical shift calculations is not given because an unequivocal assignment does not appear to be possible.[47]

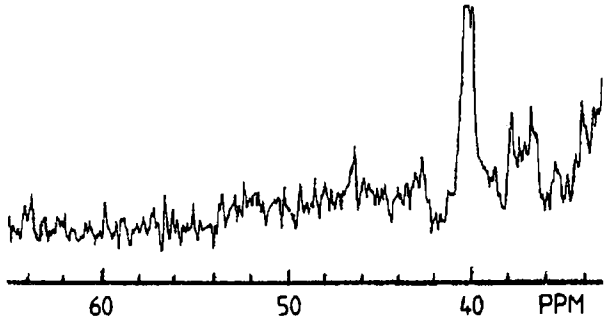

Fig. 13. ^{13}C NMR spectrum of NR vulcanized with dicumyl peroxide. (Reprinted from ref. 47 with permission.)

Natural rubber cured with γ-irradiation was studied by solid-state ^{13}C NMR and the results were compared with those for the peroxide-cured natural rubber.[48] The γ-irradiation also forms a network of carbon–carbon crosslinks in the rubber. Thus, similar results are expected as in the peroxide-cured natural rubber. Like the peroxide-cured natural rubber, the only resonances, other than the *cis*-isoprene backbone observed in the GHPD experiment, are due to *trans*-isoprene units. The amount of *trans* structure, relative to the *cis* structure, is found to increase with the dose of γ-irradiation, suggesting the occurrence of *cis*-to-*trans* isomerization with cure. The γ-irradiation-cured natural rubber has a lower amount of *trans* structure after cure than does the peroxide-cured natural rubber at the same crosslink density.

Figure 14 shows the CP–MAS spectra of the γ-irradiated natural rubber with different irradiation doses, where the rigid components in the network are visualized. The resonance at 44 ppm is due to the quaternary carbon formed during crosslinking. The methine crosslinked carbon is observed at 38 ppm. The methyl group attached to the quaternary aliphatic carbon is observed at 21 ppm. The weak resonances at 109 and 140 ppm are observed in the olefinic region. These are due to vinyl end-groups, which are possibly byproducts of main-chain scission caused by disproportion of the allylic radical. The spectral features of both peroxide-cured and γ-irradiation-cured natural rubber are similar but the γ-irradiated sample has a less complicated structure than the peroxide-cured sample.[48]

4.2. Peroxide and γ-irradiation cured BR

Structural changes occurring in the dicumyl-peroxide-cured *cis*-polybutadiene (BR) were studied by solid-state ^{13}C NMR.[42,43] Experiments were performed for both dry (bulk) and benzene-swollen samples with and

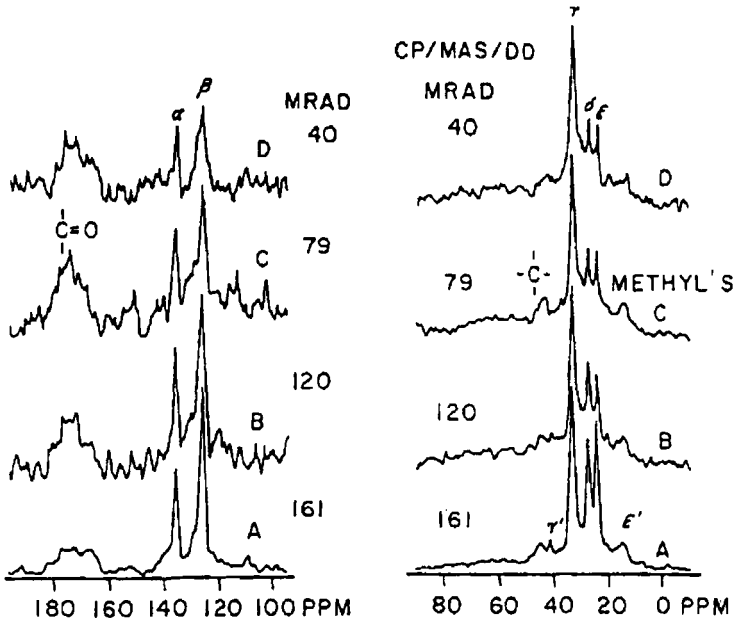

Fig. 14. ^{13}C NMR spectra of the (A) olefinic region and (B) aliphatic region of γ-irradiated NR. (Reprinted from ref. 48.)

without CP at 37.7 MHz. Figure 15 illustrates the GHPD–MAS spectra of cured BR in the dry state with varying amount of dicumyl peroxide. The methylene carbon of the *trans*-butadiene unit is seen at 34 ppm, on the shoulder of the aliphatic main peak at low peroxide concentrations. As the peroxide level increases, the resonance lines broaden, which totally obscures the *trans* peak at high peroxide concentration.

The GHPD experiment in the swollen state visualizes the *trans* peak for the 5 phr peroxide-cured sample, but the change in *trans* content was not examined because of the poor separation of the peaks from the *cis* and *trans* structures. No evidence of the crosslinking is detected in the GHPD experiments for both dry and swollen BR vulcanizates, possibly due to the rigid structure of carbon–carbon crosslinks.

Figure 16 shows the CP–MAS spectra of BR cured with different amounts of dicumyl peroxide. New resonances are observed at 35 and 44 ppm with cure, which are assigned to methylene and methine carbons present in the crosslinked network, respectively. A small number of methyl groups, possibly formed by chain scission, are also detected in the vulcanizates at 15 ppm.[42,43]

The structures of γ-irradiation cured *cis*-polybutadiene (BR) were studied both qualitatively and quantitatively by solid-state ^{13}C NMR at 75.46 MHz.[49]

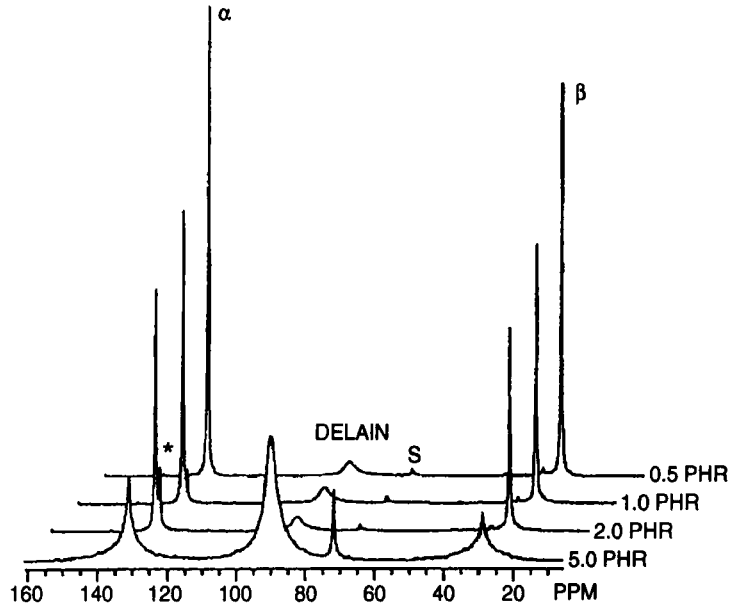

Fig. 15. Superposed ^{13}C NMR spectra of *cis*-polybutadiene crosslinked with varying amounts of dicumyl peroxide. Spectra were obtained under NFT conditions with magic angle spinning. Sample was cured at 149°C for 2 h in a hot press. (Reprinted from ref. 42.)

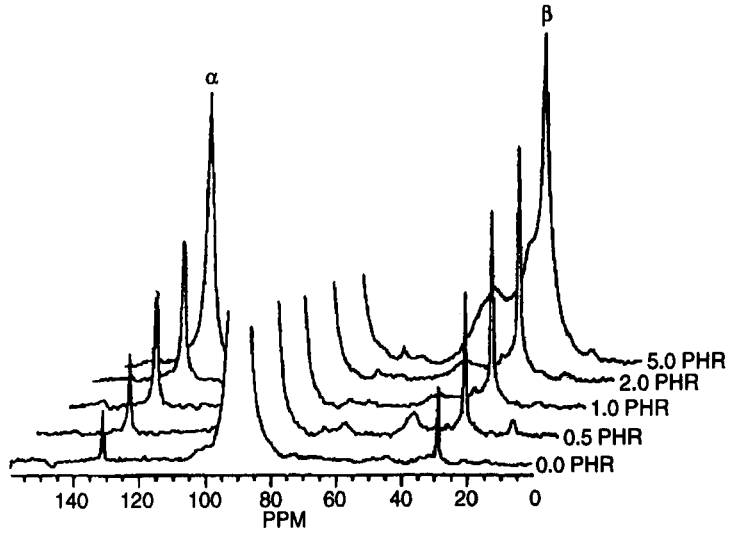

Fig. 16. Superposed ^{13}C CP–MAS spectra of *cis*-polybutadiene cured with varying amounts of dicumyl peroxide. Sample was cured at 149°C for 2 h in a hot press. (Reprinted from ref. 42.)

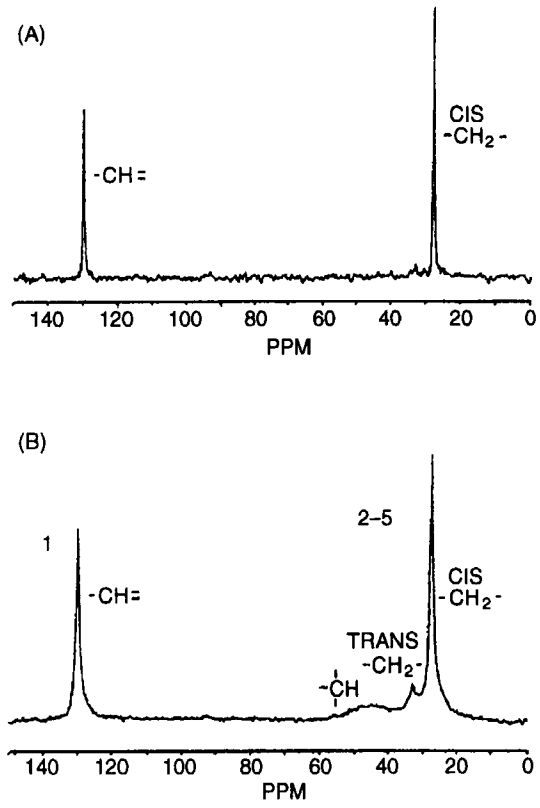

Fig. 17. Solid-state ^{13}C CP–MAS NMR spectra of *cis*-polybutadiene after (A) 0.44 MGy and (B) 3 MGy of γ-irradiation at 30°C. (Reprinted from ref. 49 with permission.)

The TOSS (total suppression of sidebands) sequence[50] was used with CP-MAS to suppress the spinning sidebands. Figure 17 illustrates the ^{13}C NMR spectra of BR after 0.44 MGy (A) and 3 MGy (B) of γ-irradiation. A slight increase in the intensity of the *trans* peak at 33.6 ppm is observed with cure, which postulates the occurrence of *cis*-to-*trans* isomerization. The formation of carbon–carbon crosslinks (*H*-crosslinks) is observed as a broad resonance centred at 45.8 ppm. The loss of backbone C=C double bonds is observed quantitatively from the decrease in intensity of the –CH= resonance at 130.1 ppm.

The yield of crosslinks (G) and the loss of double bonds ($G - (C{=}C)$) are obtained from quantitative measurements of peak intensities. These two values, obtained independently, are in close agreement. Main-chain scission does not occur during irradiation, in contrast to crosslinking of BR by

peroxide. The aliphatic region of Fig. 17(B) was analysed by computer simulation in order to decompose the overlapping peaks. The simulation confirms the presence of the broad resonance at 30.5 ppm, which seems likely to arise from a change in the chemical shift of methylene groups that are adjacent to crosslinks.

The G values for formation of carbon–carbon crosslinks by γ-irradiation of BR obtained in this study are considerably higher than the values reported in the literature based on swelling and soluble fraction measurements. This difference indicates that radiation-induced crosslinking occurs by a chain reaction, similar to that proposed for peroxide-initiated crosslinks, so that clustering of crosslinks occurs.[49]

It has been shown that the CP technique along with MAS is a more efficient method to detect rigid junctions of carbon–carbon crosslinks formed by peroxide and γ-irradiation vulcanization even above the T_g of the sample than using single-pulse FID experiments. However, in such rigidly crosslinked elastomers containing only carbon–carbon crosslinks, the residual mobile nature of the sample obscures the Hartmann–Hahn match in the CP experiment when measured in combination with the MAS. It is found that polybutadiene (PB) cured with dicumyl peroxide exhibits maximum polarization transfer rates when the carbon spin-locking radio frequency is offset from the exact Hartmann–Hahn match in the CP–MAS experiments. High-speed MAS is shown to amplitude modulate (AM) the static C–H dipolar interactions and frequency modulate (FM) the homonuclear proton dipolar decoupling in mobile solids. It was proposed that the FM part of the pattern can be used to characterize the physical mobility of the crosslinked elastomers.[51]

4.3. Unaccelerated sulfur vulcanization of NR

Among the many available vulcanizing agents, sulfur is the most widely used. Although vulcanization with sulfur alone is not practical compared to the accelerated sulfur vulcanization in terms of the slower cure rate and inferior physical properties of the end products, many fundamental aspects can be learned from such a simply formulated vulcanization system. The use of sulfur alone to cure natural rubber (NR) is typically inefficient, i.e., requiring 45–55 sulfur atoms per crosslink,[52] and tends to produce a large portion of intramolecular (cyclic) crosslinks. However, such ineffective crosslink structures are of interest in the understanding of complex nature of vulcanization reactions.

The reaction of diene rubber with sulfur produces a variety of sulfurized structures. A schematic representation of different types of sulfurized structures is shown in Fig. 18. The type of sulfurization occurring in NR has been designated as A1, A2, B1, B2 and C1 types depending on the

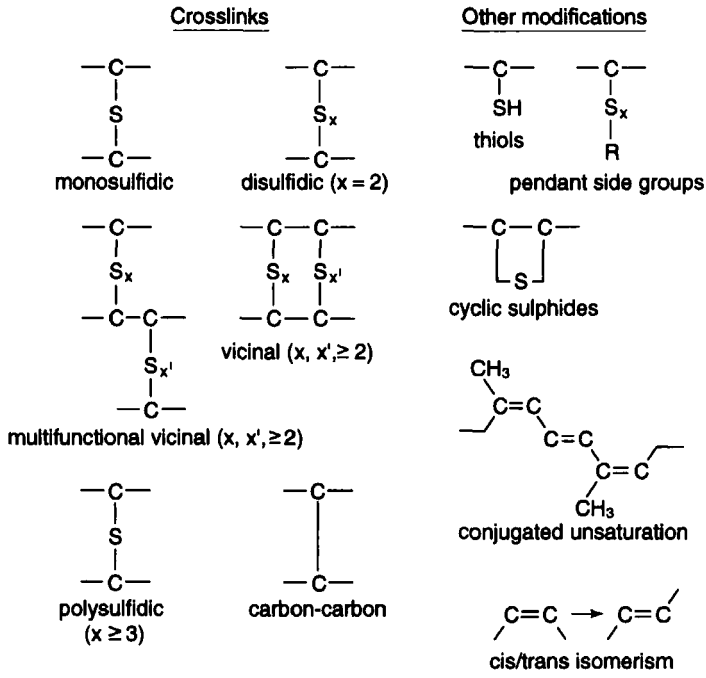

Fig. 18. Schematic representation of different types of sulfur crosslinks. (Reprinted from ref. 53.)

positions of sulfide attachment as seen in Fig. 19. Carbon numbers in 1,4-isoprene units in NR have been designated as follows:

$$-C1-C2(-C5)=C3-C4- \text{ or } -C\gamma-C\alpha(-C\varepsilon)=C\beta-C\delta-$$

Sulfur vulcanization of NR was studied by solid-state ^{13}C NMR under several different experimental conditions at 37.7 MHz.[53] The ^{13}C NMR with MAS and scalar decoupling (MAS–SD) yields the spectra of NR cured with 10% sulfur at different times of cure (see Fig. 20). An increase in linewidths and decrease in the resolution are observed with increase in cure time. A dominant new resonance is observed at 58 ppm which is assigned to the polysulfide or vicinal crosslink. Other new resonances are at 47 and 129 ppm which are assigned to monosulfide and *trans*-butadiene-like species, respectively. Broad resonances are observed in 18–21 ppm and 30–33 ppm which are attributed to the products of chain scission and cyclic structures, respectively.[53]

The resolution of the spectra is improved by applying the high-power dipolar decoupling along with MAS.[17] The GHPD spectra of NR cured with 10% sulfur at 150°C for variations of cure times are shown in Fig. 21. New

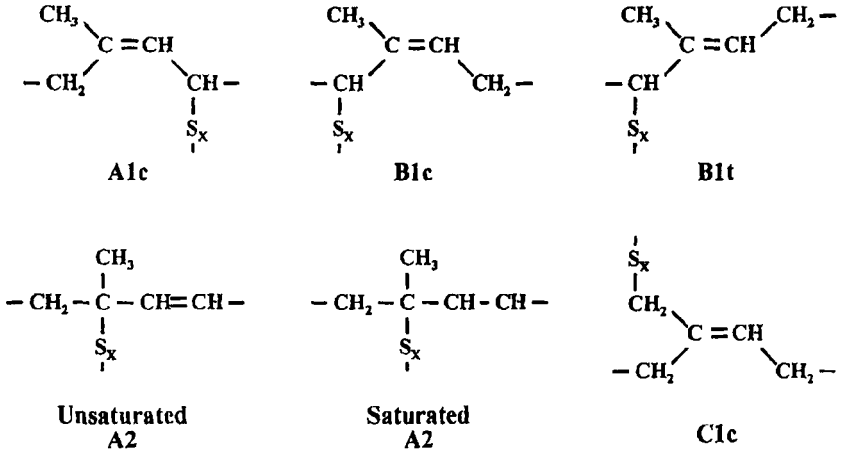

Fig. 19. Designation of nomenclature for structures occurring upon vulcanization of NR and *cis*-polyisoprene.

resonances observed in this experiment upon vulcanization are at 14.0, 16.1, 18.0, 30.0, 40.1, 44.6, 50.2 and 57.5 ppm. The peaks at 40.1 and 16.1 ppm have been assigned to the C1 and C5 carbons of the *trans*-isoprene units. The increases in these two resonances with cure suggest the occurrence of *cis*-to-*trans* isomerization. Intensities of the peaks at 14.0, 44.6 and 57.5 ppm also increase with cure time. The peak at 50.2 ppm which is observed in the lightly cured sample disappears after 30 min cure.

Further improvement of the spectral resolution was attempted by increasing the measurement temperature to 80C°.[17] In the spectra obtained at 80°C, additional small peaks are observed at 36.1 and 38.6 ppm and at the shoulder of 43 ppm. The peak at 58 ppm split into two peaks in the high-temperature measurements.

The effect of sulfur content on the spectra is examined by the GHPD measurements at 80°C for NR cured with 10%, 20% and 30% sulfur for 60 min[17] (see Fig. 22). The areas of two peaks observed at 58 and 45 ppm increase significantly with increasing sulfur content. The resonances which appear at 18.0, 30.0, 36.1 and 38.6 ppm also increase. The remaining three resonances of interest which appear at 14, 16.1 and 40.1 ppm increase only when the sulfur content is increased from 10% to 20%.

To aid in the NMR peak assignments of the ^{13}C NMR spectra, a series of model compounds for sulfur-vulcanized NR have been studied by solution ^{13}C NMR spectroscopy.[17] Figure 23 represents the model compounds for sulfur-vulcanized NR based on 2-methyl-2-pentene. In addition to the ^{13}C NMR observations of the model compounds, the chemical shifts of the carbons for these structures were calculated using the shielding parameters

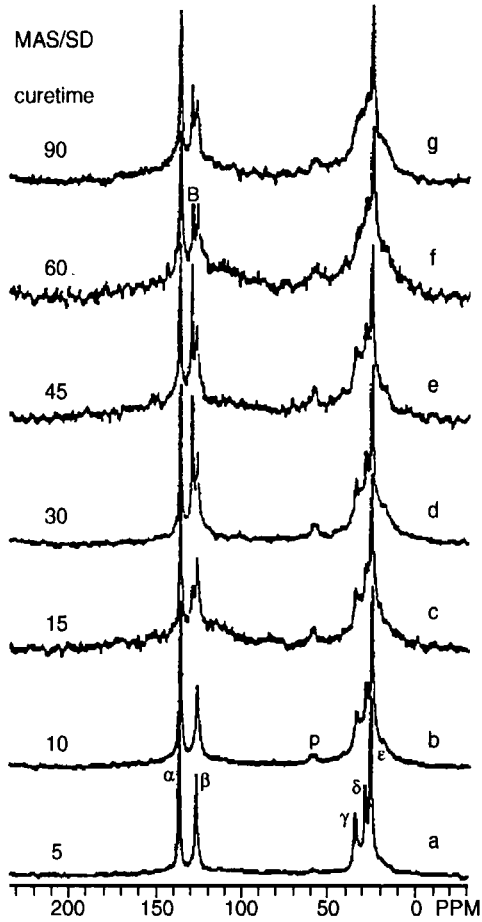

Fig. 20. Stack plots of 10% sulfur-cured NR for different times of cure. B: butadiene-like species; p: polysulfidic crosslinks. (Reprinted from ref. 53.)

shown in Table 1. The aliphatic additivity constants for the various sulfur groups were obtained from *The Sadtler Guide to Carbon-13 NMR Spectra*.[54] The sulfur shielding values were added to the initial chemical shift values of the *cis*-1,4-polyisoprene carbons to determine the chemical shifts for the sulfurized species. For the case where the crosslinking reaction may result in a saturated system, the starting chemical shift values corresponding to a portion of the ethylene–propylene copolymer were used. Table 2 shows the observed and calculated ^{13}C chemical shifts of the model structures. These data indicate that monosulfidic and disulfidic crosslinks should be distinguishable in the ^{13}C NMR spectra of sulfur-vulcanized NR. However, it may not be possible to distinguish disulfidic crosslinks from crosslinks of higher sulfur rank (polysulfide).

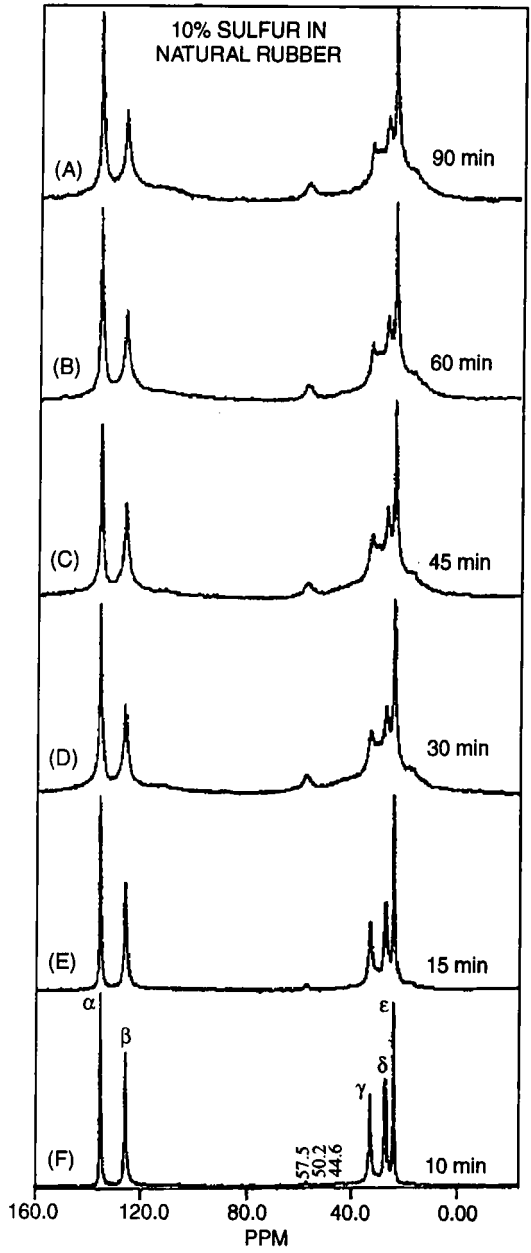

Fig. 21. ^{13}C GHPD–MAS NMR spectra of NR cured with 10% sulfur at 150°C for times ranging between 10 and 90 min. (Reprinted from ref. 17.)

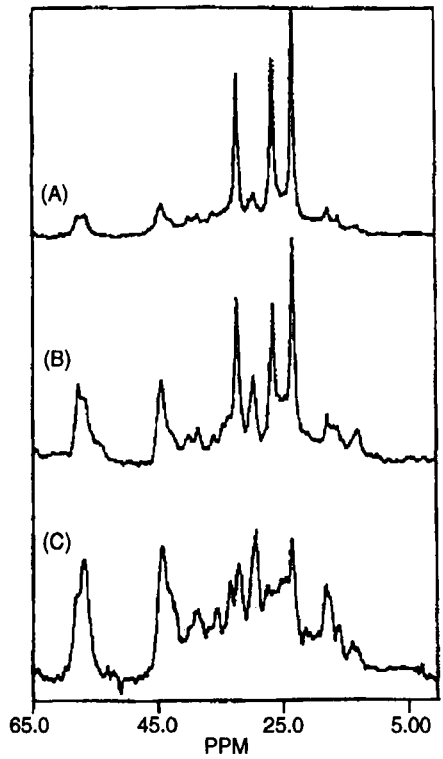

Fig. 22. The ^{13}C GHPD–MAS NMR spectra of sulfur-cured NR (60 min at 150°C) with measurement temperature of 80°C. (A) 10% sulfur, (B) 20% sulfur, and (C) 30% sulfur by weight in the formulation. (Reprinted from ref. 17.)

Table 1. Aliphatic additivity constants.[54]

HS–	C1 = + 10.5	C2 = +11.4	C3 = −3.6	C4 = −0.2
CH_3–S–	C1 = + 20.4	C2 = +6.2	C3 = −2.7	C4 = +0.3
R–S–S–	C1 = + 25.2	C2 = +6.6	C3 = −3.4	C4 = −0.1
R–S–	C1 = + 17.9	C2 = +7.1	C3 = −3.0	C4 = −0.1

Source: ref. 17.

Based on these data, the chemical shifts of the new resonances were assigned. The peak at 50 ppm is assigned to the carbons involved in the polysulfidic crosslinks of the A1-type structure in Fig. 19. The resonance peak which appears at roughly 45 ppm in the spectra can be assigned to the polysulfidic crosslinks of B1-type structure. The carbon–sulfur groups of the monosulfidic A1-type crosslinks may also overlap with this resonance peak. The peak at 58 ppm is assigned to the crosslink point found in B1-type

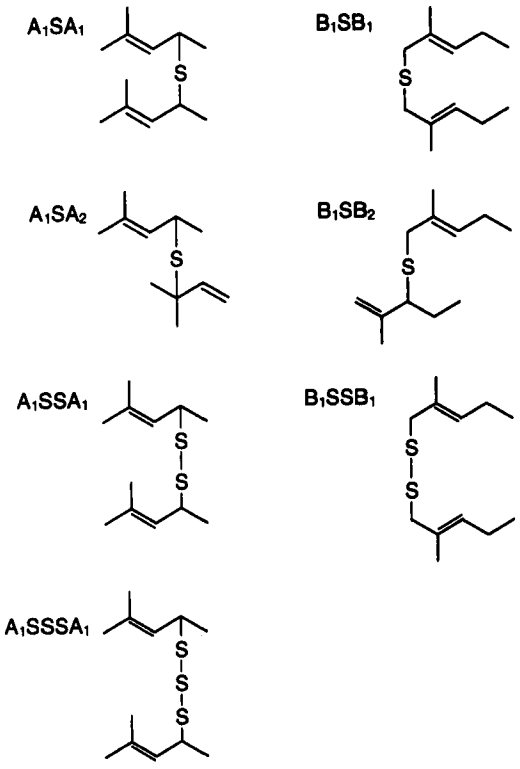

Fig. 23. Compounds based on 2-methyl-2-pentene, studied as models for sulfur-vulcanized NR. (Reprinted from ref. 17.)

Table 2. Observed and calculated chemical shifts (ppm).

Model compound	C–S bond	Observed chemical shift	Calculated chemical shift
A_1SA_1	HC–S–	36.8	21.5 + 17.9 = 39.4
A_1SA_2	HC–S–	36.8	21.5 + 17.9 = 39.4
	H_3C–C–S–	47.1	26.4 + 17.9 = 44.3
A_1SSA_1	HC–S–S–	43.6; 44.0	21.5 + 25.2 = 46.7
A_1SSSA_1	HC–S–S–S–	44.1	21.5 + 25.2 = 46.7
B_1SB_1	H_2C–S–	40.0	25.7 + 17.9 = 43.6
B_1SSB_1	H_2C–S–S–	48.9	25.7 + 25.2 = 50.9
B_1SB_2	H_2C–S–	40.0; 40.4	25.7 + 17.9 = 43.6
	HC–S–	53.2; 54.7	40.3 + 17.9 = 58.2

Source: ref. 17.

polysulfide structure. The splitting of this peak observed in the high-temperature measurement may arise from the difference in carbon configurations or conformations in the same type of structure. The small peaks found at 30.0, 36.1 and 38.6 and at the shoulder of 43 ppm, which are resolved in the high-temperature measurement, are most probably due to cyclic sulfides. The peaks at 14.0 and 18.0 ppm is possibly due to the chain-end methyl groups occurring by chain scission.[17]

The CP–MAS ^{13}C NMR spectra are recorded for NR cured with 10%,[17,53] 20% and 30% sulfur.[17] Figure 24 shows the CP–MAS spectra of NR cured with 10% sulfur at 150°C for 15, 30 and 60 min. Considerable broadening is observed compared to the counterparts from the GHPD experiments seen in Fig. 21. The lower signal-to-noise ratios of the CP spectra indicate that only a small portion of the sample is highly crosslinked in this sample. The new resonances are observed at 58, 64, 73 and 81 ppm. For the NR cured with 20% and 30% sulfur, where zinc oxide and stearic acid are added to stabilize the vulcanization, the peaks at 64, 73 and 81 ppm are not observed, which suggests that these peaks are occurring from the oxidation products. Figure 25 illustrates the comparison of the CP spectrum with the GHPD spectrum for the NR cured with 30% sulfur at 150°C for 60 min. Almost identical features of the spectra from CP and GHPD suggest that most of this sample is highly crosslinked.[17]

The complementary application of the NMR inversion recovery measurements ($180°$–τ–$90°$–t_R) and the computer fitting of the overlapping region is found to be a useful method for structural analysis of vulcanized natural rubber in the solid state.[24] Since the linewidths in ^{13}C NMR spectra of solids are relatively broad compared with the differences between chemical shifts, some weak signals are completely obscured in the resulting spectra. If the resonances have sufficiently different relaxation times, such as with methyl and methylene carbons, it is possible to detect neighbouring overlapped signals by using the inversion recovery delay τ value at which the interfering strong resonance has null intensity.

Figure 26 shows the aliphatic part of inversion recovery spectra for NR cured with 10% sulfur at 150°C for 120 min simulated with 18 resonances. Difference spectra between the experimental and calculated spectra are also shown in Fig. 26, indicating that the results of fitting the aliphatic region with 18 resonances are in good agreement with the experimental data. The proposed sulfurization products are shown in Fig. 27, and the resonance assignments for the decomposed peaks are given in Table 3. The detection of the proposed structures and the quantitative analysis of peak areas suggest the existence of the following reaction types in the vulcanization process:

(1) formation of sulfur crosslinks at C1 (B1c-type), C4 (A1c-type) and C5 (C1c-type) carbons;

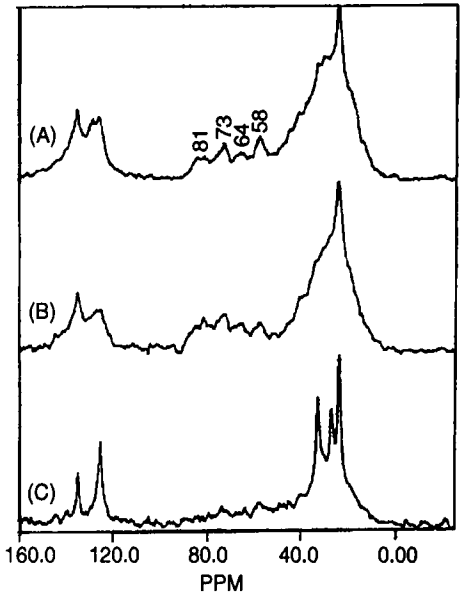

Fig. 24. ^{13}C CP–MAS NMR spectra of NR cured with 10% sulfur at 150°C for (A) 60, (B) 30, and (C) 15 min. (Reprinted from ref. 17.)

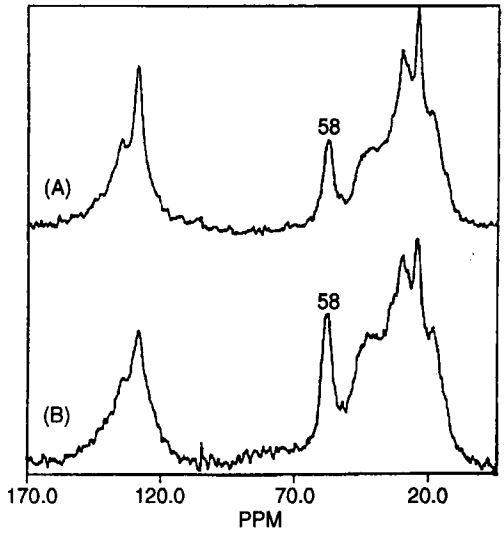

Fig. 25. ^{13}C MAS NMR spectra of NR cured with 30 phr sulfur, 5 phr zinc oxide, 1 phr antioxidant, and 2.5 phr stearic acid at 150°C for 60 min: (A) GHPD spectrum; (B) CP spectrum. (Reprinted from ref. 17.)

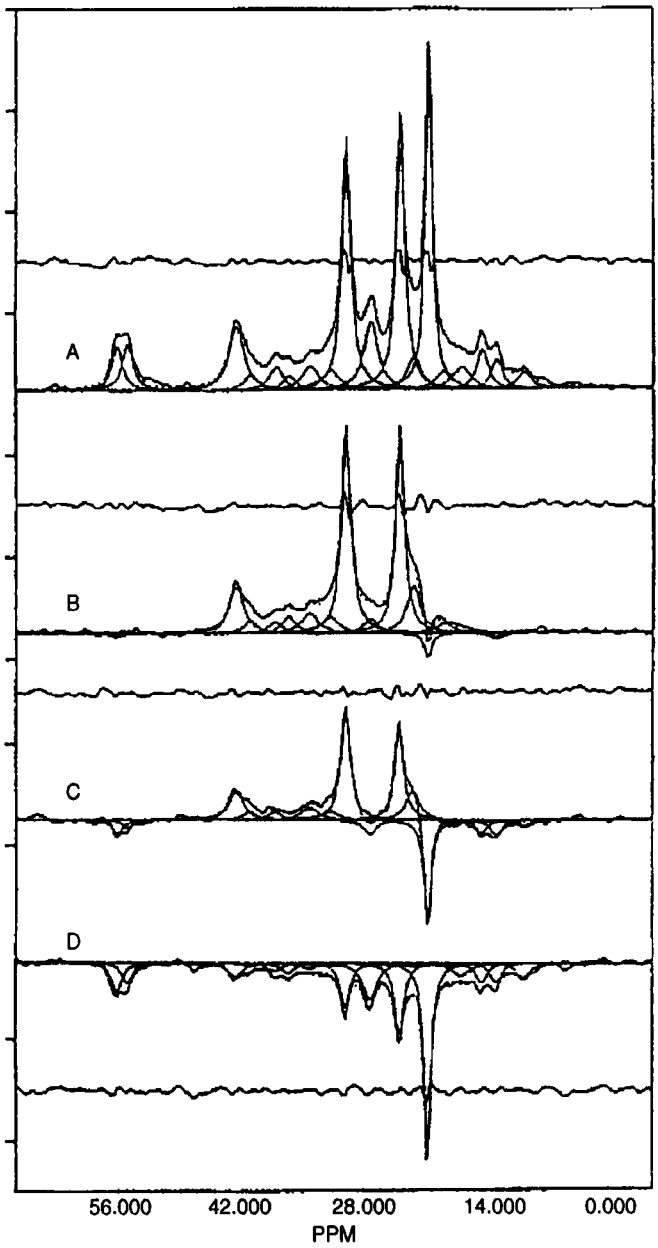

Fig. 26. The ^{13}C NMR inversion recovery spectra of NR cured with 10% sulfur at 338 K for 120 min. τ values: (A) 4 s; (B) 0.2 s; (C) 0.1 s; (D) 0.03 s. (Reprinted from ref. 24.)

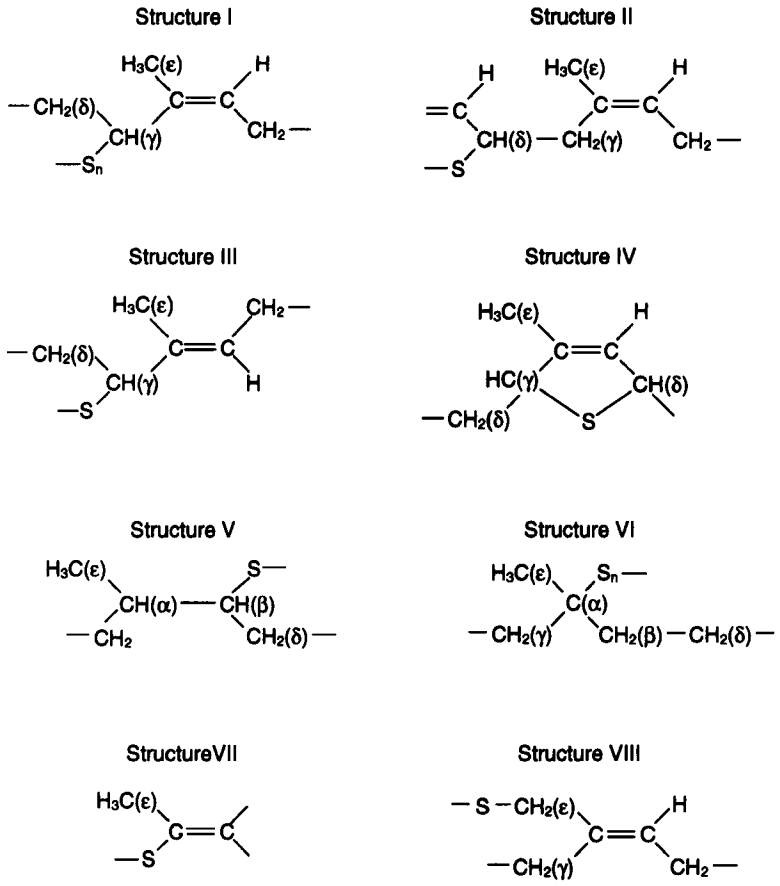

Fig. 27. Proposed structural units for a sulfur-vulcanized natural rubber. -S- indicates monosulfidic, $-S_n-$ indicates disulfidic/polysulfidic. (Reprinted from ref. 24.)

(2) formation of sulfur crosslinks at C2 (A2-type) and C3 (B2-type) with the saturation of the double bond;

(3) crosslinking with the sulfur at the C2 carbon associated with breaking of the polyisoprene main chain;

(4) formation of five-membered heterocyclic rings (unsaturated and saturated);

(5) *cis*-to-*trans* isomerization;

(6) formation of sulfur crosslinks at the C1 carbon of the *trans* isomer (B1t-type);

(7) chain scission.[24]

Table 3. ^{13}C chemical shifts (δ) of structural units in a sulfur-vulcanized rubber.

δ (ppm)	C atom	Structural unit
134.8	C-α	*Cis*-1,4-polyisoprene
134.4[a]	C-α	*Trans*-1,4-polyisoprene
125.3	C-β	*Cis*-1.4-polyisoprene
123.9[a]	C-β	*Trans*-1,4-polyisoprene
57.9	CH(γ)	Structure III
57.9	C(α)	Structure VI
56.8	CH(γ)	Structure I
56.8	CH(δ)	Structure IV
56.8	CH(β)	Structure V
44.6	CH(δ)	Structure II
44.6	CH_2(β)	Structure VI
44.6	CH_2(γ)	Structure VI
42.9	CH_2(ε)	Structure VIII
40.1	C-γ	*Trans*-1,4-polyisoprene
40.1	CH_2(γ)	Structure II
38.8	CH(α)	Structure V
36.4	CH_2(δ)	Structure III
34.2	CH_2(δ)	Structure I
32.5	C-γ	*Cis*-1,4-polyisoprene
32.5[b]	CH_2(δ)	Structure IV
~31.0	CH_2(δ)	Structure VI
~30.5	CH_2(δ)	Structure V
30.0	C-δ	*Trans*-1,4-polyisoprene
~30.0	CH_3(ε)	Structure VII
~30.0	CH_2(γ)	Structure VIII
26.7	C-δ	*Cis*-1,4-polyisoprene
25.2[c]	CH_2	Cyclic sulfide structures
23.6	C-ε	*Cis*-1,4-polyisoprene
~23.5	CH_3(ε)	Structure II
~21.8[c]	CH_3(ε)	Cyclic sulfide structures
~20.0	CH_3(ε)	Structure I
18.0[c]	CH_3–	Cyclic sulfide structures
16.1	C-ε	*Trans*-1,4-polyisoprene
16.1	CH_3(ε)	Structure IV
16.1	CH_3(ε)	Structure V
13.1	CH_3(ε)	Structure III

[a]The small amount of *trans*-olefinic absorption is not resolved from the corresponding *cis*-olefinic resonances.
[b]See Table 1.
[c]See text.
Source: ref. 24.

Solid-state ^{13}C NMR spectroscopy has been applied to analyse the effect of crosslinking on the molecular dynamics in NR by the measurement of the temperature dependence of spin–lattice relaxation times (nT_1s) at 37.7 MHz.[55] Figure 28 shows the temperature dependence of ^{13}C nT_1 values

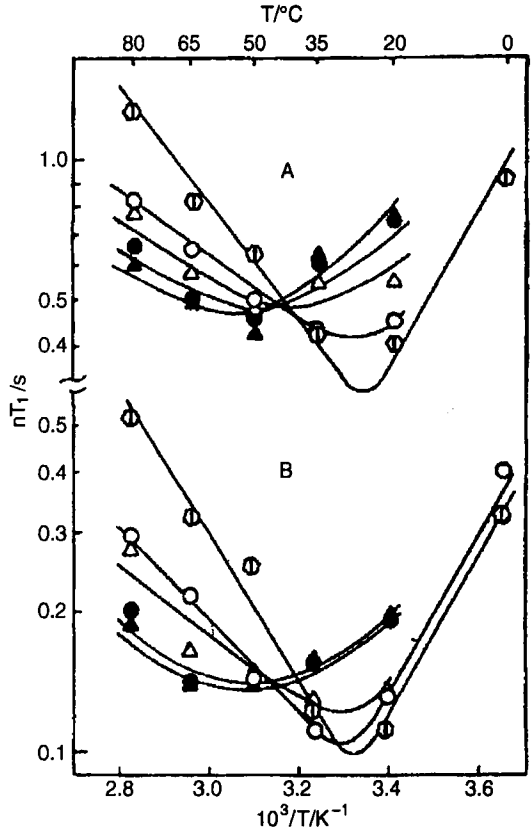

Fig. 28. The temperature dependence of ^{13}C nT_1 values for the (A) C-ε (C-5) and (B) C-β (C-3) carbons of NR cured with 10% sulfur for 0 (⊕), 15 (○), 22 (△), 60 (●) and 120 (▲) min. (Reprinted from ref. 55.)

at C5 (A) and C3 (B) carbon resonances for NR vulcanized with 10% sulfur at 150°C for different cure times. The nT_1 curves for the backbone carbons in the crosslinked samples cross each other and have similar T_1 values at about 313 K. However, the temperature dependence over a wider range clearly reflects the motional restrictions induced by the crosslinking. The general trends with increased cure time are T_1 curve broadening, shifts of the T_1 minima to higher temperatures, and increase in the T_1 minima values. At shorter cure times, motional restrictions for the methyl side group (C5) are more pronounced compared to the other main-chain carbons, although the methyl group is not directly involved in the crosslinked structures. It can be assumed that the relatively short crosslinks (mono- and di-sulfide) at the neighbouring carbons impose spatial restrictions on the methyl group reorientation. The V-curve (nT_1 *vs* $1/T$) for resonances associated with the

network structure generally follows the trends observed in the backbone carbons, with T_1 minimum in a similar temperature range.[55]

4.4. Accelerated sulfur vulcanization of NR and IR

Accelerated sulfur formulations are the most common vulcanization systems used in commercial and industrial applications. Because of this, there is a large body of ongoing works in both the fundamental and applied aspects of accelerated sulfur vulcanization. Several reviews of the chemistry and/or physics of accelerated sulfur vulcanization of elastomers have been published.[2,9,10,56] In this section, attention will be focused on the application of high-resolution solid-state ^{13}C NMR spectroscopy to the characterization of accelerated sulfur vulcanization of natural rubber (NR) and synthetic *cis*-1,4-polyisoprene (IR).

The structure of natural rubber vulcanized with sulfur and *N*-oxydiethylene-2-benzothiazole sulfenamide (MOR) was studied by solid-state ^{13}C NMR.[57] MOR is categorized in benzothiazolesulfenamides and is more popularly called 2-(4-morpholonothio)benzothiazole (MBS). New resonances are observed upon vulcanization at around 15, 31, 34, 45, 58 and 130 ppm and at the shoulder of 30 and 41 ppm along with the *trans* isomers appearing at 17 and 41 ppm.[53] The study including the resonance assignments and the quantitative considerations was updated in a subsequent paper from the same group.[60]

Model compounds based on 2-methyl-2-pentene were studied to supplement the ^{13}C chemical shift assignments of the products from accelerated sulfur vulcanization of NR.[57] Rubber–accelerator complex structures have been added to the previously used model structures seen in Fig. 23. The chemical shifts observed in solution ^{13}C NMR measurements are given in Table 4 along with the calculated shifts reported in the preceding paper.[17] It is observed in the model compound data that it may not be possible to distinguish between a ^{13}C NMR resonance which is due to disulfidic crosslinks and a peak due to pendant accelerator groups, while a large chemical shift difference (~3 ppm) is observed for the monosulfidic bonds.

The structure of accelerated sulfur-vulcanized NR was compared with that of the vulcanizate cured with sulfur alone.[57] The NR was vulcanized both with 0.01 moles sulfur and tetramethylthiuram disulfide (TMTD) to 100 parts NR and with 0.01 moles sulfur alone at 150°C for 120 min. Figure 29 shows the GHPD–MAS ^{13}C NMR spectra of (A) sulfur–TMTD-cured and (B) sulfur-cured NR. Dominant new resonances from both spectra are at 16.1, 30.0, 40.1, 44.6 and 57.5 ppm. The peaks at 16.1, 30.0 and 40.1 ppm are due to the products of *cis*-to-*trans* isomerization. The peaks at 44.6 and 57.5 ppm are assigned to polysulfidic crosslink or pendant structures in C1- and B1-type, respectively. It is concluded here that similar spectra are obtained

Table 4. Observed and calculated chemical shifts.

Model compound[a]	C–S bond[a]	Chemical shift (ppm)	
		Observed	Calculated
A_1SA_1	HC–S–	36.8	21.5 + 17.9 = 39.4
A_1SSA_1	HC–S–S–	43.6; 44.0	21.5 + 25.2 = 46.7
A_1SSX	HC–S–S–*X*	44.9	
B_1SB_1	H_2C–S–	40.0	25.7 + 17.9 = 43.6
B_1SSB_1	H_2C–S–S–S	48.9	25.7 + 25.2 = 50.9
B_1SX	H_2C–S–*X*	42.9	
B_1SSX	H_2C–S–S–*X*	49.2	

[a]*X*: accelerator residue of TMTD.
Source: ref. 57.

from both sulfur-TMTD- and sulfur-cured systems with the same level of cure, but slight differences in the intensities of the new resonances are seen. It must be pointed out that the sulfur–TMTD-cured sample seen in Fig. 29(A) has been overcured. TMTD is one of the ultrafast accelerators which may cure the NR in 30 min or less at 150°C in the moderate formulations. However, the system has been cured for 120 min at 150°C for comparison purposes with the vulcanization by sulfur alone. These cure conditions make an extremely overcured state in this sample which results in the slight decrease in sulfurized products and an increase in the *trans* structure seen in Fig. 29(A).

The spectrum in Fig. 29 (A) was compared with the GHPD results for the NR cured with high content of sulfur (10%) shown in Fig. 21.[17] It is concluded that the NR systems crosslinked with accelerated formulations appear to show a simpler network structure than the vulcanizates cured with high sulfur levels.

The effect of accelerator level was studied using GHPD. Three sets of NR formulations containing 2 phr sulfur and 2, 10 and 20 phr TMTD were cured at 150°C for 90 min. The qualitative aspects of the new structures are identical among these three samples, but the variations in the resonance intensities are observed. Generally, an increase in the amount of TMTD accelerator used in the formulation results in an increase in the areas of the new resonances. The NR vulcanizate (2 phr sulfur and 10 phr TMTD cured at 150°C for 90 min) was further cured at 180°C for an additional 60 min to examine the effect of postcure. Further structural modifications are observed by the postcuring: an increase in *trans* structure and the appearance of the 36.4 ppm peaks. The peak at 36.4 ppm is assigned to cyclic structure in this reference; however, the possibility also exists for oxidation products for this resonance, in which the methylene group next to the carbonyl bond is expected to occur around this region.

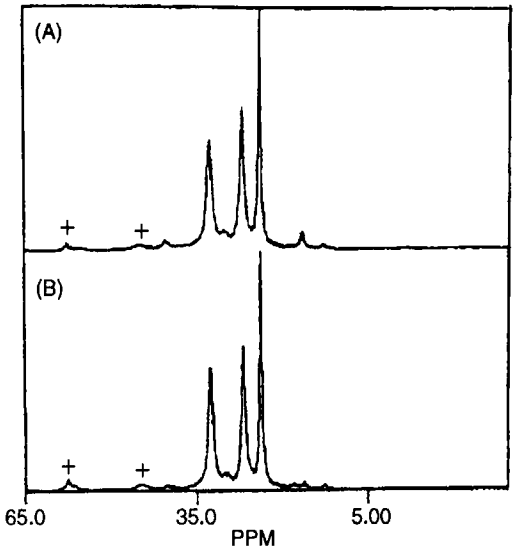

Fig. 29. The ^{13}CC GHPD–MAS spectra of NR vulcanized with 0.01 mol sulfur to 100 phr NR for 2 h at 150°C: (A) spectrum of sample cured with equal amounts of sulfur and TMTD; (B) spectrum of sample cured with elemental sulfur. (Reprinted from ref. 57.)

The effects of different accelerator systems was also investigated.[57] Figure 30 shows the ^{13}C GHPD NMR spectra of (A) NR cured with *N*-cyclohexyl-benzothiazole-2-sulfhenamide (CBS) (0.4 phr sulfur and 6 phr CBS) at 140°C for 120 min and (B) NR cured with MBS (MOR) (5 phr sulfur and 1 phr MBS) at 150°C for 90 min. Minimal spectral changes are observed in Fig. 30(A) compared to the ^{13}C NMR spectrum of uncured NR. The highly efficient formulation (CBS/sulfur = 15) with small sulfur levels may result in a crosslink density too low to be observed by NMR. The MBS-accelerated sample shows similar new resonances as seen in the TMTD accelerated systems. In this comparison however, the quantitative aspects of the data might be again obscured due to the differences in the state of cure among the different formulations.

The ^{13}C chemical shifts were assigned in more detail for monosulfidic and polysulfidic crosslinks occurring in the accelerated sulfur vulcanization of NR.[47] The NR was cured with a pure thiuram formulation (TMTD alone) in order to predominantly prepare monosulfidic bridges in the network. A CBS-accelerated formulation was also prepared, which was cured to only 65% rheometer torque increase so that the predominant crosslinks are polysulfidic bonds. The ^{13}C NMR experiments were performed using the

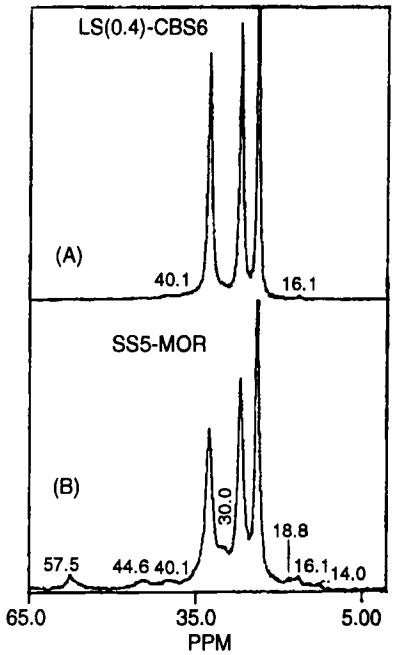

Fig. 30. ^{13}C GHPD–MAS NMR spectra of NR cured with (A) CBS at 140°C for 2 h and (B) MOR at 150°C for 90 min. (Reprinted from ref. 57.)

MAS and low power decoupling conditions at 75.5 MHz. Figure 31 illustrates the typical ^{13}C NMR spectra of the two NR vulcanizates. Several new resonances are seen in both spectra.

The DEPT experiments, in which carbons with different levels of protonation can be distinguished,[21–23] were performed for NR cured with extended levels of sulfur. Based on the DEPT results and previously reported model compound results,[17,57] the chemical shifts of the resonances occurring in the spectra (Fig. 31) were assigned. Some of the assignments proposed in the previous studies[17,57] have been updated due to the mismatch in the DEPT results.

In the DEPT experiments, both peaks around 50 and 58 ppm are divided into three components and the levels of the protonation for these six individual resonances are evaluated. The peaks at 57.4, 58.0 and 58.6 ppm are assigned to the polysulfidic crosslinks in the A1-, B1- and B2-type structures, respectively. The peaks at 37.2 and 50.7 ppm are due to A1-type polysulfidic crosslinks. There is no apparent structural match for the quaternary peak at 50.2 ppm.

It is proposed that the chemical shifts due to the monosulfidic crosslinks are influenced not only by the position on the monomeric unit to which it

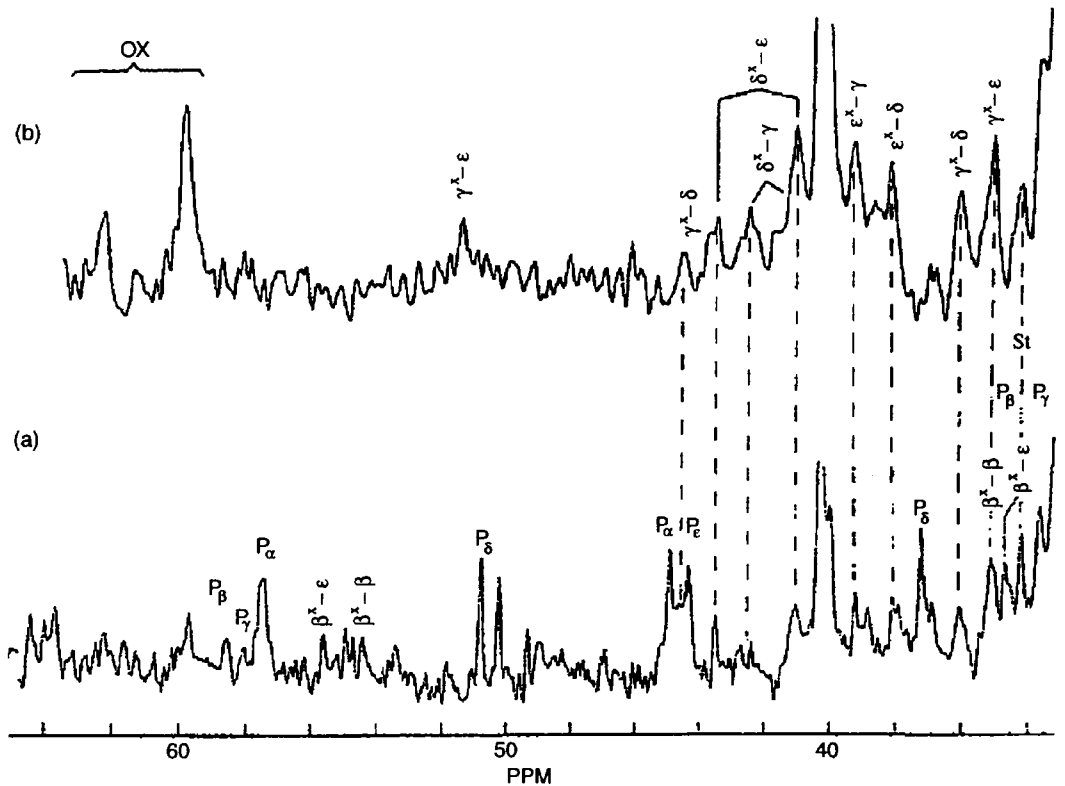

Fig. 31. ^{13}C NMR spectra of sulfur vulcanized NR: samples were formulated and cured to expect predominant amount of (a) polysulfidic and (b) monosulfidic crosslinks (see ref. 47). (Reprinted from ref. 47 with permission.)

Table 5. Chemical shifts of monosulfidic crosslinks.

Observed C atom (*) and crosslink structure	C_1 calc.	C_1 exp	C_2 calc.	C_2 exp	C_1 ref. [5]	C_2 ref. [5]
β^*	55.4[a]	—	34.7[a]	—	56.8	39.8
β^*–β^c	52.7	54.9	36.4	35.1	—	—
β^*–$\varepsilon^{b,c}$	55.4	55.6	36.1	34.7	—	—
γ^*	50.4[a]	—	33.8[a]	—	57.9	36.4
γ^*–$\delta^{b,c}$	47.4	44.5	35.5	36.0	—	—
γ^*–ε^b	50.4	51.3	35.2	35.0	—	—
δ^*	44.6[a]	—	39.6[a]	—	44.6	40.1
δ^*–$\gamma^{b,c}$	41.9	42.4	41.0	41.0	—	—
δ^*–δ^c	41.6	42.6	41.3	40.6	—	—
δ^*–$\varepsilon^{b,c}$	44.6	43.5	41.0	41.0	—	—
ε^*	41.5[a]	42.9				
ε^*–β, γ^c	38.8	39.2				
ε^*–$\delta^{b,c}$	38.5	38.1				

[a]Chemical shifts calculated by Zaper and Koenig [57].
[b]Figs 1(b), 2(b).
[c]Figs 1(c), 2(a).
Source: ref. 47. Used with permission.

belongs, but also by the position of the carbon atom of the monomeric unit on the other side of the bridge. The shielding parameters of monosulfide substitution on the individual carbons of the isoprene unit have also been determined. The chemical shift assignments for monosulfidic crosslinks are shown in Table 5. It is shown that resolvable polysulfidic crosslink resonances exist in all positions of the backbone carbons, while monosulfidic crosslinks appear only between C1 and C4 carbons with detectable intensity.[47]

Another approach in the ^{13}C NMR technique has been utilized to assign the peaks for the sulfurized structures occurring in the accelerated sulfur-vulcanization of NR.[58] The NR formulations with a variation of accelerator (CBS) to sulfur ratio were cured at 150°C to t_{90} (90% of the rheometer torque increase) plus 10 min. The attached proton test (APT) experiment[19,20] was performed for those vulcanizates, in which carbons with an even number of hydrogens (methylene or quaternary carbon) and carbons with an odd number of hydrogens (methine or methyl carbon) can be distinguished. In addition, the ^{13}C spin–lattice relaxation times (T_1) for individual carbons in both backbone and sulfurized structures were measured. The carbons with an odd number of hydrogens can be easily distinguished between methine and methyl carbons by observing the region where the resonance is occurring.

The carbons which have an even number of hydrogens with long T_1 (~ 1 s) are assignable to the quaternary carbons while those with short T_1s are due to the methylene carbons.

The resonances at 57.5 and 50.4 ppm are assigned to the polysulfide and monosulfide of B2-type structures, respectively. The peaks at 50.8 and 55.6 ppm are due to the polysulfidic bonds of A1 and B1-type structures, respectively; however, the monosulfidic counterparts for these structures which fit the APT results are missing. None of the structures can explain the splitting of the peaks near 64 ppm. The T_1 value of 1.1 s of these coupled peaks suggests that the resonances are due to oxidation products. The *trans* structures increase with increasing number of sulfide attachments to the polymer backbone. The peaks appearing at 12.9 and 14.3 ppm are possibly due to the end groups of hydrocarbon fragments formed during the mixing and crosslinking steps of sample preparation.

The crosslink densities of the rubber networks were determined by the quantitative treatment of the ^{13}C NMR spectra.[58] In this study, the peaks at 37.3, 44.7, 48.2, 49.6, 50.6, 52.5, 54.8 and 57.5 ppm are involved in crosslinks according to the peak assignments. Half the sum of these areas should give the crosslink density of the sample as determined by ^{13}C MAS NMR. The results were compared to the network chain densities obtained by *n*-heptane swelling methods to examine the efficiency of the intermolecular crosslinking reactions for the individual formulation. For the efficient cure system (EV; higher accelerator concentration relative to sulfur), nearly 100% of the sulfurization is monosulfide and is involved in crosslinks. However, for conventional cure systems or systems containing predominantly polysulfidic bonds, about 50% of the sulfide units are not involved in crosslinking.

Solid-state ^{13}C MAS NMR has been applied for quantitative determination of crosslink density in accelerated sulfur-vulcanized NR.[59] The concepts used to calculate the crosslink density by ^{13}C NMR are the same as the one mentioned above,[58] but different resonances were employed for the quantitative treatment based on the different assignments of the ^{13}C resonances.[47] The crosslink density of the network is evaluated by

$$\mu_C = \frac{I(S_X)}{I_0} \cdot \frac{\rho}{M_0}$$

$$I(S_X) = \frac{1}{2}\,[I(58.6) + I(58.0) + I(57.4) + I(44.4) + I(44.5) + I(40.7)]$$

where I_0 is the reference intensity of the monomer unit, ρ is the density of the vulcanizates and M_0, is the molar mass of the monomer unit. The peaks at 40.7 and 44.5 ppm are due to monosulfides and the others are from polysulfides. If the overlapping peak around 45 ppm can be precisely decomposed to polysulfidic (44.5 ppm) and monosulfidic (44.4 ppm)

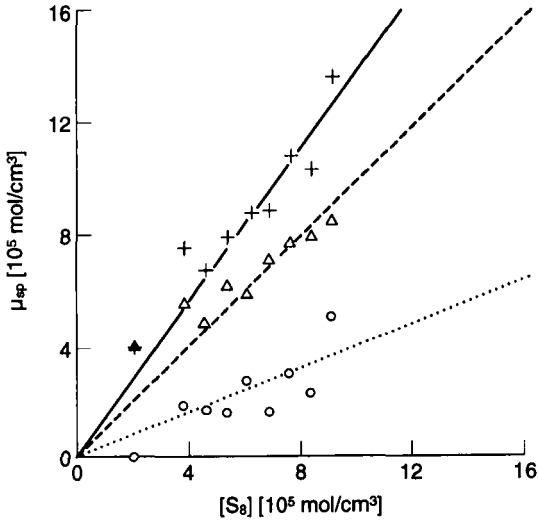

Fig. 32. Crosslink densities of sulfur-vulcanized NR determined from ^{13}C NMR: ○, monosulfidic, △, polysulfidic, +, total. (Reprinted from ref. 59 with permission.)

contributions, the densities of poly- and monosulfidic crosslinks are individually determined by ^{13}C NMR.

Figure 32 illustrates the crosslink densities of NR vulcanizates from polysulfide, monosulfide and total sulfide contributions as a function of the sulfur concentration. The relative amount of polysulfidic bonds among all sulfurization is determined to be 71% in the sample examined.

The ^{13}C NMR crosslink density results were compared with the crosslink density obtained by the mechanical measurements. In the determination of the crosslink density by mechanical methods, the contributions of the topological constraints on the results were neglected and the density was expressed as $G/2RT$. The ^{13}C and mechanical-crosslink densities were obtained for both sulfur and dicumyl peroxide (DCP)-cured samples to ensure the effect of wasted crosslinks (pendant or intramolecular type sulfurizations) which are expected in the typical sulfur-vulcanization of NR. Figure 33 illustrates the comparison of the mechanical-crosslink densities ($G/2RT$) *vs* the ^{13}C NMR-crosslink densities for sulfur and DCP-cured vulcanizates. In the major range of crosslink densities, the crosslink densities for those two systems are described by the same linear function with a slope of 1.0. Based on this observation, it is shown that the crosslink density of the sulfur-vulcanized NR as determined by ^{13}C is identical with the true crosslink density, and the influence of the wasted or ineffective crosslinks (pendant and cyclic crosslinks) and chain ends is negligible. However, this conclusion seems to be only valid if the effect of topological constraints or entrapped entanglements on the mechanical modulus is negligible, which is

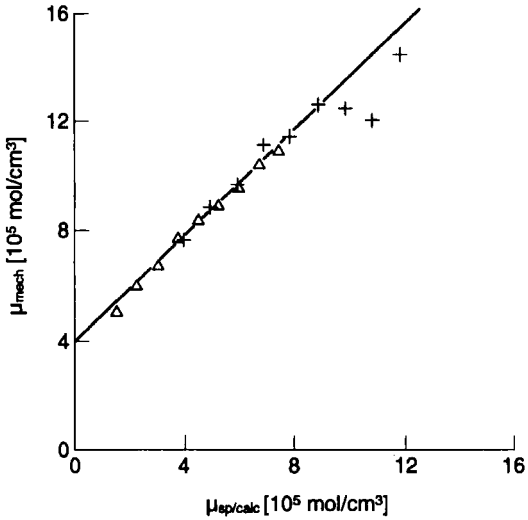

Fig. 33. Mechanical-crosslink density $(2C_1 + 2C_2)/2RT$ *vs* calculated crosslink densities, μ, of peroxide-cured NR vulcanizates (△) and *vs* spectroscopically (^{13}C) determined crosslink densities of sulfur-cured NR vulcanizates (+). (Reprinted from ref. 59 with permission.)

rarely the case in real systems. The slope of 1.0 obtained in the relationship between mechanical and ^{13}C NMR-crosslink densities might be arising from the mutual compensation of the possible effects of physical crosslinks and the effects of ineffective crosslinks. For the DCP-cured sample, the relatively short bridges of carbon–carbon crosslinks forming in this system may enhance the influence of the entrapped entanglements, which may result in the further increase in the mechanical-crosslink densities, making them comparable to those of sulfur-cured systems.

The crosslink densities of the network were also determined by ^1H transversal relaxation measurements in this study.[59] By the comparison to the results of NR by the ^{13}C method, it is shown that the same crosslink density is derived from ^1H NMR relaxation. However, also in these results, it is assumed that the effect of wasted or ineffective crosslinks which was not accounted in the ^{13}C method may compensate for the effect of possible physical crosslinks which should be included in the crosslink densities from the ^1H relaxation technique.[59]

The chemical microstructures of *cis*-polyisoprene (IR) vulcanized with sulfur and *N*-*t*-butyl-2-benzothiazole sulfenamide (TBBS) accelerator were studied as a function of extent of cure and accelerator to sulfur ratio in the formulations by solid-state ^{13}C NMR spectroscopy at 75.5 MHz.[60] Conventional (TBBS/sulfur = 0.75/2.38), semi-efficient (SEV) (= 1.50/1.50) and

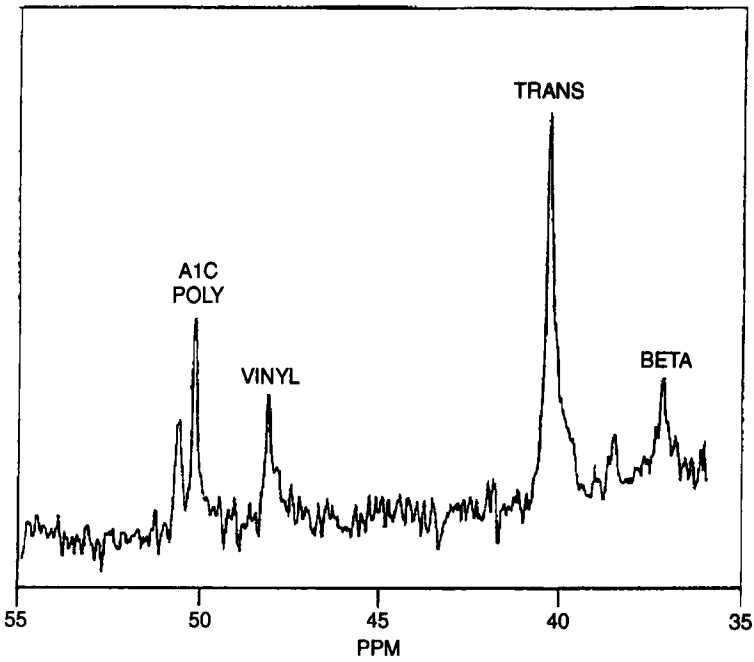

Fig. 34. ^{13}C NMR spectrum of conventionally formulated (TBBS–sulfur) IR cured for 32 min, illustrating the new α-carbon resonance at 51 ppm and the β-carbon resonance at 38 ppm. C, *cis*. (Reprinted from ref. 60.)

efficient (EV) (= 3.00/1.08) formulations were prepared, which were cured to several cure states according to the rheometer torque increase. Figures 34 and 35 show the magnified GHPD–MAS spectra typical of shortly and highly cured IR, respectively.

The content of *trans* isomer found at 16 and 40 ppm remains constant for all three formulations at all cure times, suggesting no *cis*-to-*trans* isomerization occurring in IR formulations, unlike in NR. New sulfurization resonances appear at 38 and 51 ppm at short cure times (Fig. 34) in all three systems, both of which weaken and disappear at longer cure times. The sulfurization resonances at long cure times (Fig. 35) are the peaks at 12, 14, 17, 45 and 58 ppm. The peak at 64 ppm is a weak resonance which is detected in the conventional system, barely discernible in the SEV system and could not be detected in the EV system. The ^{13}C NMR chemical shift assignments are shown on the spectra of Figs 34 and 35, although some of the assignments are updated in a subsequent study.[61] The order and types of the sulfurization products formed are constant in all the formulation systems with different accelerator to sulfur ratios. However, the amount of sulfurization has been found to vary directly with the concentration of elemental sulfur.[60]

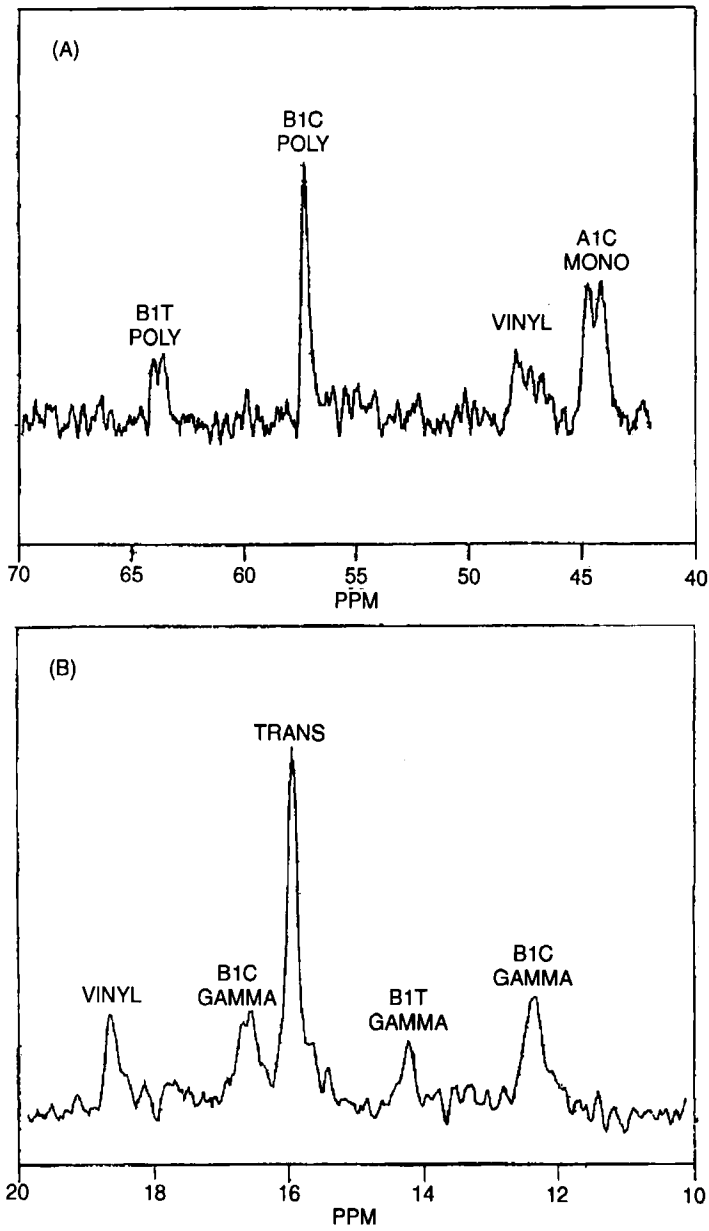

Fig. 35. ^{13}C NMR spectra of conventionally formulated (TBBS–sulfur) IR cured for 300 min: (A) 70–40 ppm region, illustrating the new resonances at 64, 58 and 45 ppm, (B) 20–10 ppm region, illustrating new γ-carbon resonances at 17, 14 and 12 ppm. C, *cis*; T, *trans*. (Reprinted from ref. 60.)

Similar vulcanization chemistry is observed with the *N-t*-butyl-2-benzothiazole sulfenimide (TBSI) accelerated sulfur-vulcanization of IR[61] compared to the TBBS accelerated system.[60] Almost identical ^{13}C GHPD spectra (as seen in Figs 34 and 35) are presented in Fig. 36 for the TBSI-accelerated IR systems. At low cure times, only A1c and A2c polysulfidic structures (50 ppm) are observed. At longer cure times, A1c and A2c polysulfidic structures reduce in sulfur rank to monosulfide (45 ppm) and B1c (58 ppm). B1t (64 ppm) and C1c (45 ppm) polysulfidic structures are observed. A small amount of *cis*-to-*trans* isomerization was observed, which increased with sulfur content. The reversion reactions of TBSI-accelerated systems result in a lower degree of sulfurization as opposed to TBBS-accelerated samples. Based on the equilibrium swelling measurements, TBSI is found to be a less efficient accelerator than TBBS.[61]

The ^{13}C NMR chemical shifts occurring in the 40 to 70 ppm region of the TBBS-cured IR system were further examined by the DEPT experiments.[62] Based on the DEPT data along with the attached proton test (APT)[58] and chemical measurements, the peak assignments for the resonances at 45.0, 50.2, 50.7 and 58.0 ppm in the previous study[61] were confirmed. The peaks at 50.2 and 50.7 ppm are due to polysulfidic A1c and A2c structures, respectively. The monosulfidic counterparts of these structures are expected at approximately 45 ppm. Thus, the 45 ppm resonance contains contributions from A1c and A2c monosulfides as well as C1c polysulfides. According to observations in the chemical network analysis, it is postulated that the peak at 45 ppm is most likely due initially to the A1c and A2c structures, while at longer cure times, it reflects the formation of polysulfidic C1c structures. The peak at 58 ppm has been assigned to a B1c polysulfide. The resonance at 64 ppm, which has been assigned to a B1t polysulfide[60] could not be detected in the DEPT experiments, probably due to the low concentration.

The mechanism of the network formation was proposed, based on the data of ^{13}C NMR[62] and chemical network analysis. Figure 37 illustrates the concentration profile of (A) accelerator intermediates and (B) accelerator, sulfur and byproducts during the vulcanization of IR, obtained by HPLC analysis.[63] Figure 38 gives the structures and abbreviations used for the accelerators and cure intermediates. Initially, BtS_xBt, which is the product of the TBBS–sulfur reaction, reacts with rubber to form A1c and A2c-polysulfidic intermediates along with BtSH. At the later extent of cure, the BtS_xZnS_xBt structure is produced by the consumption of BtSH with Zn–sulfur, which reacts with the rubber to form B1c and B1t-polysulfidic intermediates. In the reversion period, reduction in sulfur rank and the formation of C1c structure occurs via the following scheme:[62]

$$\text{Blc–}S_x\text{–Blc} + [\text{BtS}]_2\text{Zn} \quad \longleftrightarrow \quad \text{Blc–}S_{x-y}\text{–SBt} + \text{Blc–}S_y\text{ZnSBt}$$

$$\text{Blc–}S_{x-y}\text{–SBt} + \text{Rubber} \quad \rightarrow \quad \text{Blc–}S_{x-y}\text{–Clc} + \text{BtSH}$$

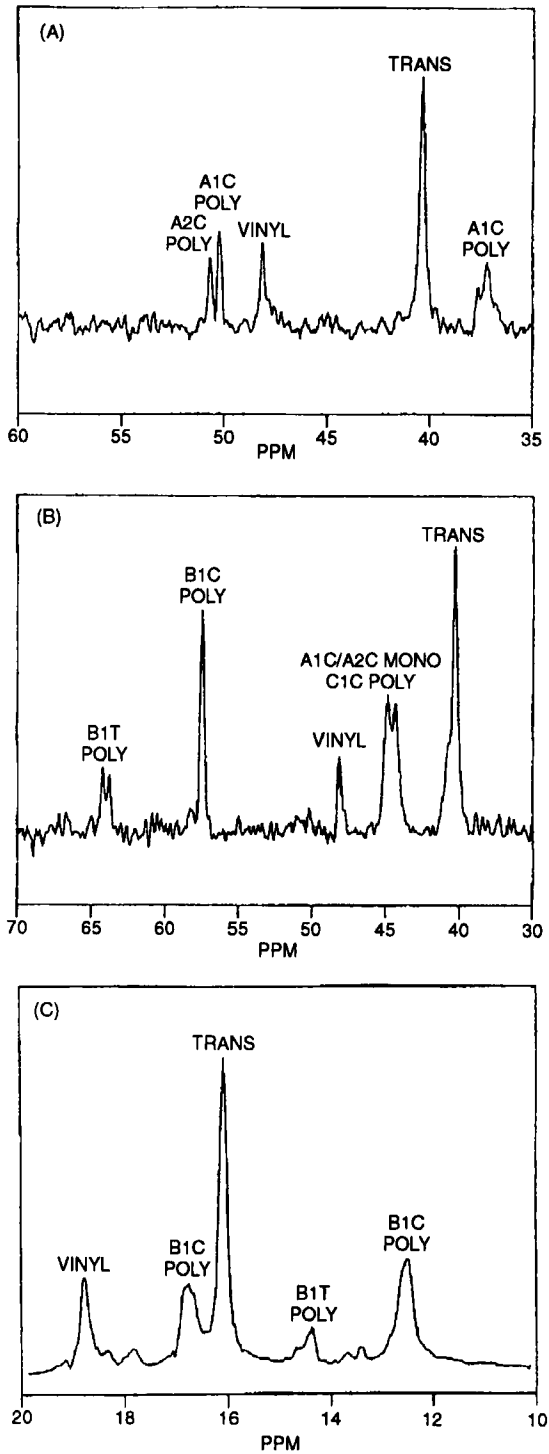

Fig. 36. ^{13}C NMR spectra of conventionally formulated (TBSI-sulfur) IR cured for (A) 50 min and (B) (C) 300 min. (Reprinted from ref. 61.)

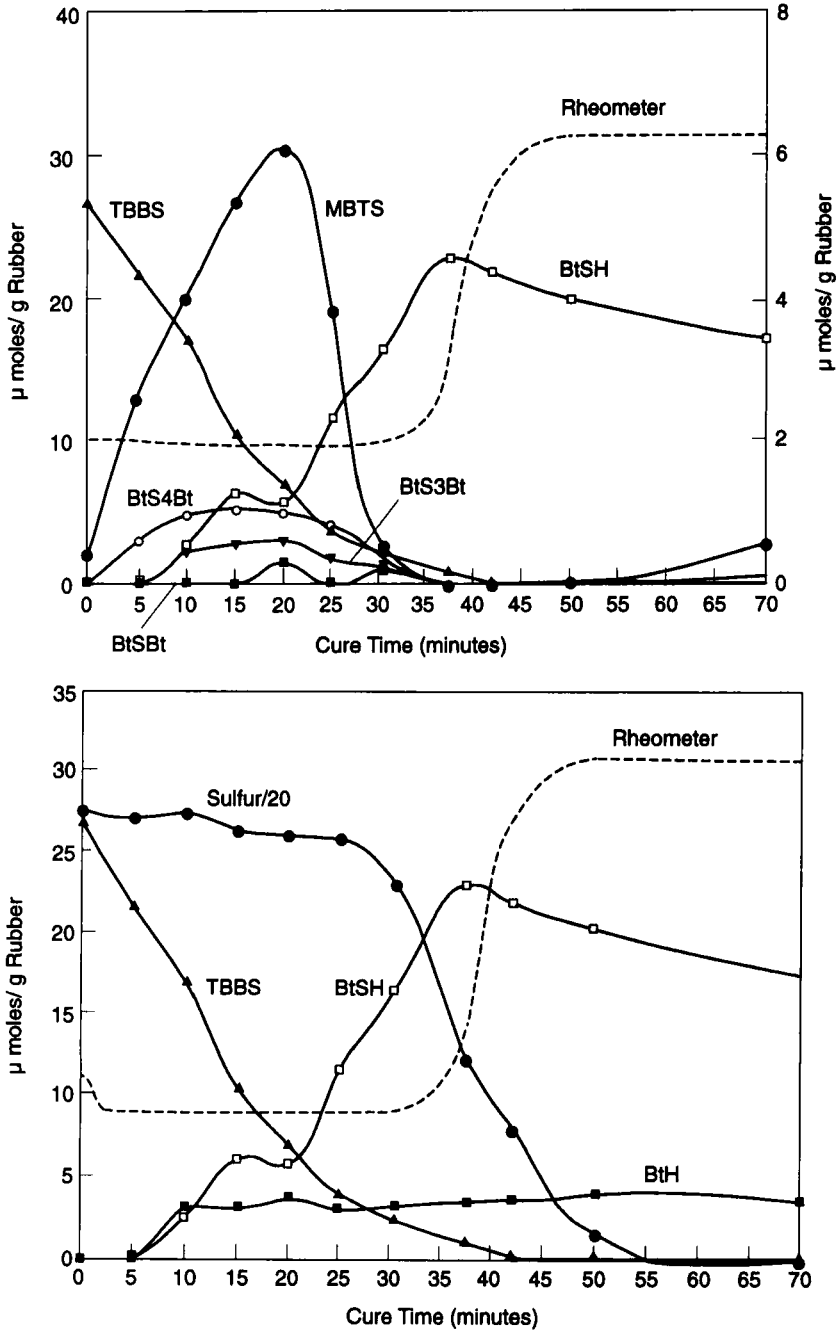

Fig. 37. (A) Accelerator intermediate and (B) accelerator, sulfur and byproduct concentration profiles during IR vulcanization for the conventional formulation. (Reprinted from refs 62 and 63 with permission.)

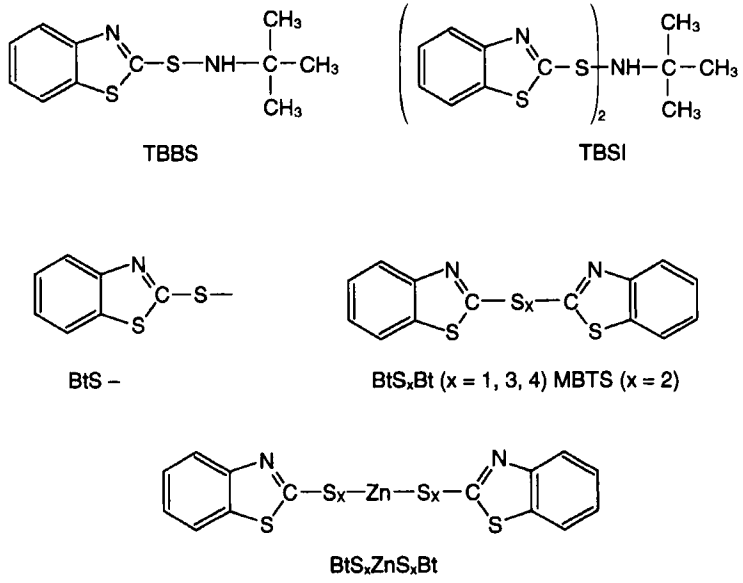

Fig. 38. Structures and abbreviations used for accelerators and cure intermediates. (Reprinted from ref. 62.)

The network chain density (ν_e) and the density of the chains between sulfurizations ($2[S]_{chem}$) for the natural rubber (NR)[64] and high-*cis*-polyisoprene (IR)[65] vulcanized with TBBS were determined by equilibrium swelling and solid-state ^{13}C NMR measurements, respectively. The proportion of the intermolecular crosslinks over a whole range of sulfurization reactions (E_c) was estimated by the comparison of the chemical network chain density (ν_{chem}) calculated from the ν_e using Mullins's approach[66] with the $2[S]_{chem}$ obtained by NMR. The E_c in the NR system plotted as a function of cure is shown in Fig. 39. The E_c is zero until the scorch cure (t_{10}; 10% of rheometer torque increase) increases with cure during the curing periods and hits the maximum, 59.8%, at the optimum cure state (t_{90}). The E_c then decreases with time in the overcuring and drops to 23.4% at 120 min cure.[64] The maximum E_c of 57.6% is obtained at t_{90} for the TBBS–sulfur–IR system.[65]

4.5. Sulfur vulcanization of BR

Solid-state ^{13}C NMR spectroscopy was used to study accelerated[67] and unaccelerated[67,68] sulfur-vulcanization and sulfur donor (TMTD)[69] vulcanization of *cis*-polybutadiene (BR). The structures of TMTD-accelerated and

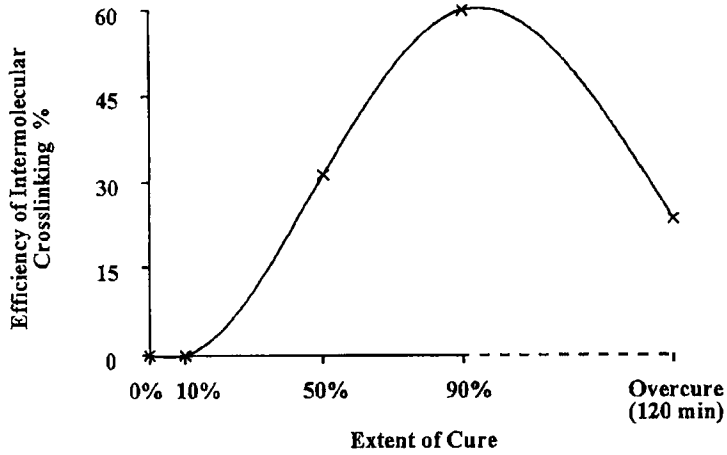

Fig. 39. Efficiency of the intermolecular crosslinking over the whole sulfurization reactions for NR gum formulation. (Reprinted from ref. 64.)

unaccelerated, sulfur-vulcanized BR were compared using solid-state ^{13}C NMR with and without CP at 37.7 MHz. Figure 40 shows (A) GHPD and (B) CP ^{13}C NMR spectra of BR cured with 20% sulfur at 150°C for 90 min. Olefinic and methylene carbons of the *cis*-polybutadiene repeating unit typically resonate at 129.5 and 27.5 ppm, respectively. The dominant products occurring in the vulcanization with sulfur alone are the resonances at 33, 38 and 50 ppm in both GHPD and CP experiments. Similar new resonances are observed in the TMTD-accelerated sulfur-cure systems. In the system where zinc oxide was formulated in addition to the elemental sulfur and TMTD, simpler spectra are obtained in which the peaks at 38 and 50 ppm are missing.

The peak at 33 ppm is assigned to the *trans* structure of 1,4-polybutadiene. An increasing intensity at 33 ppm peak with cure in both sulfur-cured and accelerated sulfur-cured BR postulates the occurrence of *cis*-to-*trans* chain isomerization in these systems. The resonances at 38 and 50 ppm are assigned to cyclic monosulfide and polysulfidic crosslink structures. The expected monosulfidic junctions are not detected in this study, possibly due to the low concentration of these species.[67]

At 75.5 MHz, improved resolution is attained in the GHPD spectra of sulfur-vulcanized BR. Figure 41 is the magnified spectrum of the high-*cis* BR cured with 10 phr sulfur at 150°C for 30 min. Twenty-five new peaks are obtained with cure which are labelled in Fig. 41. According to the DEPT experiments, peaks 1–7 are due to methine carbons and all other resonances are due to methylene carbon.[68]

Similar vulcanization products with reduced structural modification are

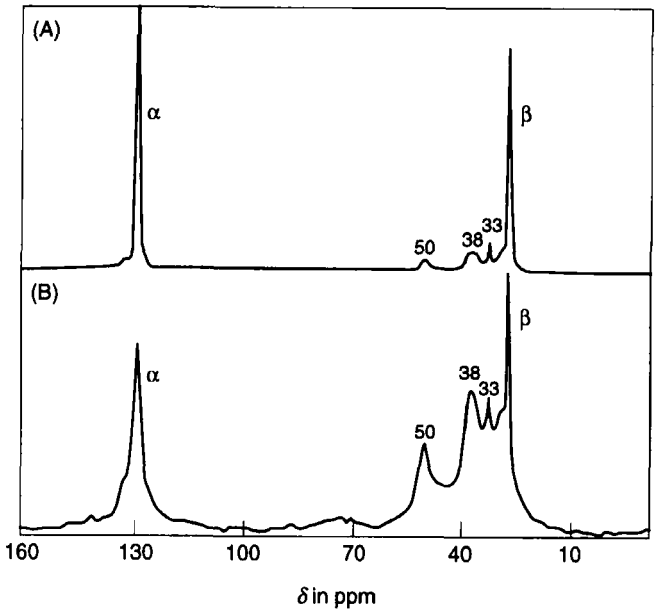

Fig. 40. ^{13}C MAS NMR spectra of *cis*-polybutadiene cured with 20 wt% sulfur at 150°C for 90 min: (A) GHPD NMR spectrum; (B) CP NMR spectrum. (Reprinted from ref. 67.)

obtained in the sulfur-donor (TMTD) vulcanized BR.[69] By comparing the GHPD and DEPT results of sulfur-vulcanized BR[68] with the results of sulfur-donor vulcanization,[69] detailed chemical shift assignments are possible where the peaks from inter- and intra-molecular sulfurizations and those from accelerator fragments can be distinguished. Figure 42 illustrates the expected network reaction products for the sulfur-vulcanized BR. The calculated chemical shifts for these structures are presented in Table 6. The chemical shift assignments for sulfur- and TMTD-cured BR based on these calculations[69] and the DEPT results[68] are shown in Table 7.

A considerable number of side reactions including *cis*-to-*trans* isomerization and sulfidic cyclization are observed along with the formation of crosslinks in the BR cured with sulfur alone.[68] In the sulfur-donor vulcanization of BR, *cis*-to-*trans* isomerization is the predominant feature of the vulcanization reaction sequence and seems to obey first-order kinetics with respect to the concentration of accelerator.[69]

The chemical crosslink densities determined from the NMR were obtained for both sulfur-cured[68] and sulfur donor-cured[69] BR by computing the crosslink densities as half the sum of all sulfurized structures, which were then compared with the corresponding crosslink densities obtained by the swelling experiments (modified Flory–Rehner equation). The NMR crosslink

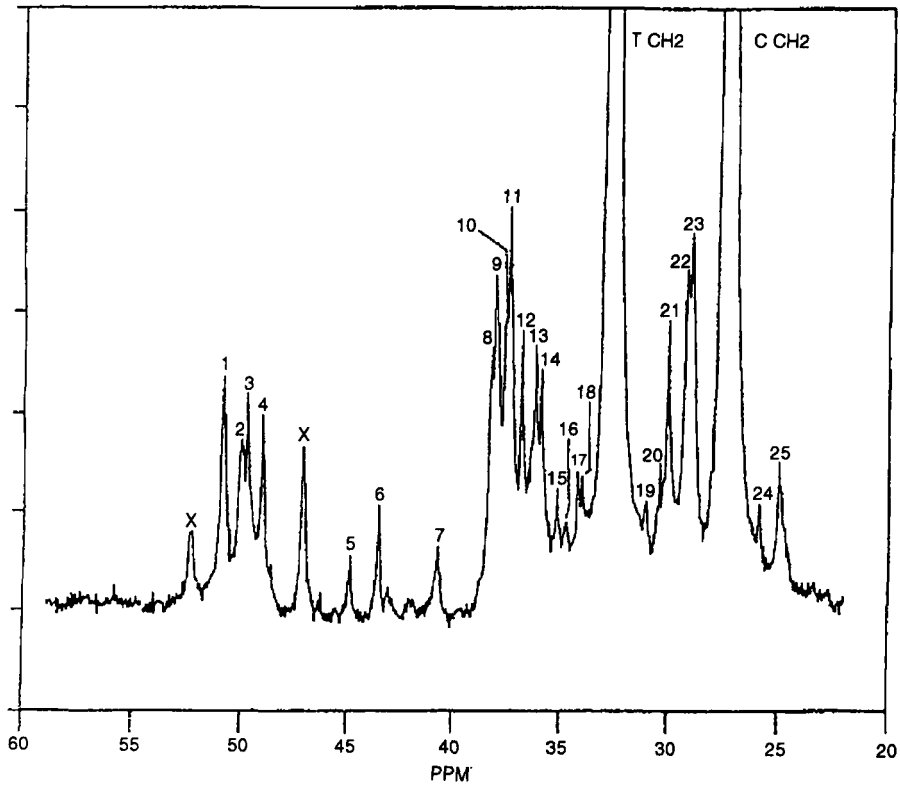

Fig. 41. The aliphatic region of the ^{13}C GHPD–MAS spectrum of *cis*-polybutadiene cured with 10 phr sulfur at 150°C for 30 min. (Reprinted from ref. 68.)

densities of the vulcanizates are routinely an order of magnitude greater than the swelling crosslink densities in both systems. It was concluded that sulfur- or TMTD-vulcanized BR networks must possess a significant proportion of mechanically ineffective vicinal and/or cyclic crosslink structures.[68,69] Either a free-radical chain reaction mechanism of crosslink induction or the phase-solubility isolation of crosslinking within discrete localized domains in the rubber would account for the formation of a high percentage of elastically inefficient crosslink structures.[69]

The chemistry of the TBBS-accelerated sulfur-vulcanization of high-vinyl BR was studied by solid-state ^{13}C NMR at 75.5 MHz.[70] The ^{13}C NMR study of high-vinyl BR (or high-styrene SBR) is challenging, since the regions between 30 and 45 ppm are typically overlapped by the backbone resonances arising from the complex tacticity distribution in the vinyl–vinyl (or vinyl–styrene, styrene–styrene) sequences. Furthermore, the inherent rigid nature of the vinyl-BR (or styrene sequence) structure broadens the

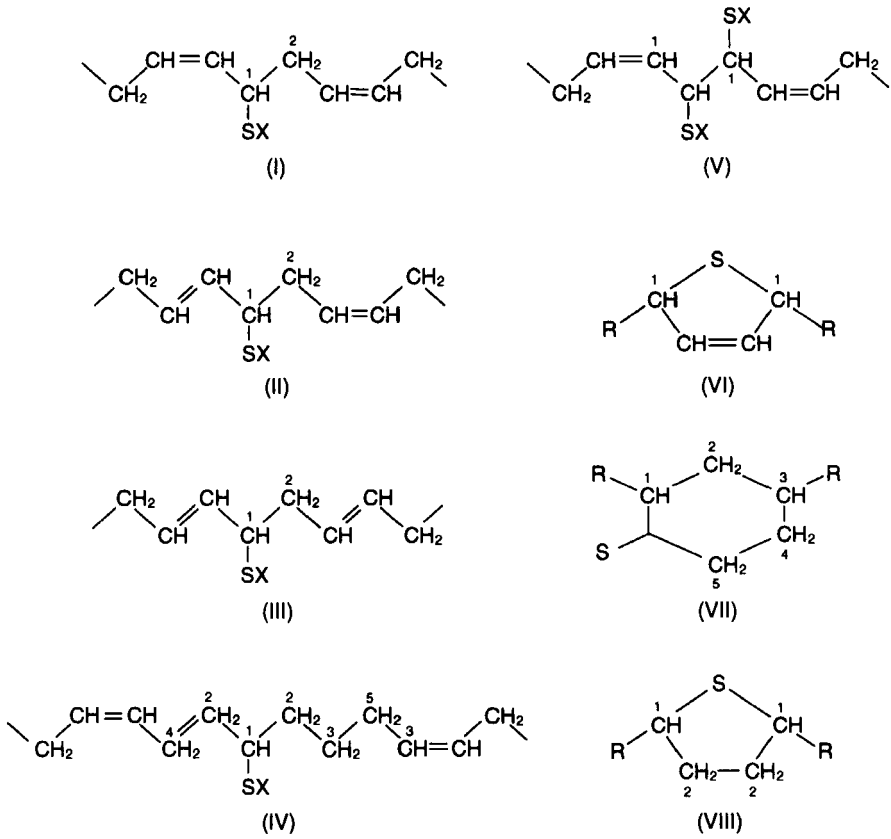

Fig. 42. Network reaction structures expected for TMTD vulcanization of *cis*-BR. (Reprinted from ref. 69.)

resonance lines, which decreases the resolution in the particular region where the sulfurization products are expected.

Figure 43 illustrates the series of GHPD spectra of the high-vinyl BR vulcanized with TMTD–sulfur for various cure times. By careful comparison with the spectrum from the raw rubber, new peaks are found at 33.3, 36.3, 43.9, 45.4 and 54.8 ppm along with the considerable broadening of the backbone resonances. The resonance at 54.8 ppm, which appears only at the initial stage of cure, is due to the accelerator fragments. The DEPT experiment was performed to aid in the peak assignments. The chemical shifts of the new resonances were assigned based on the DEPT results and the chemical shift calculations. The assignments for both new and backbone resonances are shown in Table 8. The peaks at 33.3 and 43.9 ppm are due to polysulfidic structures. The resonances at 36.3 and 45.4 ppm are assigned to the monosulfidic bond and cyclic structure, respectively.

Table 6. Calculated chemical shift values expected for numbered carbons of structures indicated in Fig. 42.

Structure	Carbon	Base shift	Calculated shift for X =				
			–SAc[a]	–SR[b]	–Ac	–R	–H
I	1	27.6	51.0	49.9	44.8	42.9	35.9
	2	27.6	33.6	33.9	34.4	34.8	38.5
II	1	32.9	56.3	55.2	50.1	48.2	41.2
	2	27.6	33.6	33.9	34.4	34.8	38.5
III	1	32.9	56.3	55.2	50.1	48.2	41.2
	2	32.9	38.9	39.2	39.7	40.1	43.8
IV	1	29.1	52.8	51.7	45.8	43.9	37.8
	2	29.1	35.2	35.5	36.3	36.7	41.1
	3	29.1	26.9	26.9	26.8	26.8	27.5
	4	28.5	26.3	26.3	26.2	26.2	26.9
	5	28.5	28.5	28.5	28.5	28.5	28.5
V	1	27.6	57.0	56.2	51.6	50.1	46.8
VI	1	39.1	—	—	—	57.1[c]	—
VII	1	29.1	—	—	—	46.4[d]	—
	2	27.8	—	—	—	45.8[d]	—
	3	26.5	—	—	—	42.0[d]	—
	4	27.8	—	—	—	36.8[d]	—
	5	29.1	—	—	—	29.5[d]	—
VIII	1	31.7	—	—	—	51.7[d]	—
	2	31.1	—	—	—	38.9[d]	—

[a]–Ac = 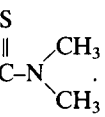

[b]–R =  .
[c]Measured value for –R = $-CH_2-CH_3$.
[d]Calculated value for –R = $-CH_2-CH_3$.
Source: ref. 69.

However, it is assumed that, in the assignments given in Table 8, the effect of the vinyl sequences on the dispersion of resonance peaks in the aliphatic region is underestimated. The peaks at 33.3, 36.3 and 43.9 ppm must totally overlap with the backbone peaks due to vinyl–vinyl–*cis*, 1.4–vinyl–vinyl and 1.4–vinyl–1.4 sequences in the high-vinyl BR structure,[38] which obscures to some extent the quantitative treatment of the resonances.

The amount of polysulfidic crosslink (33.3 ppm) decreases with cure time, while the monosulfidic crosslink (36.3 ppm) goes through a maximum for a fully cured state and decreases for 120 min cure. In addition to the vulcanization reactions, *cis*-to-*trans* isomerization, chain scission and chain saturation are observed in this system.

Table 7. Summary of tentative assignments of new resonances found in the ^{13}C-NMR spectra of BR vulcanizates cured with 2 phr TMTD, 10 phr TMTD, and 2 phr S

2 phr S	2 phr TMTD	10 phr TMTD	Tentative assignment
—	53.9	53.9	Trans di- and/or polysulfidic fragment >CH–
—	53.7	53.7	
51.0	51.0	51.0	Sat'd disulfidic crosslink >CH– or cyclic >CH–
—	50.5	—	*Trans* monosulfidic fragment >CH–
50.1	50.1	50.1	Vicinal monosulfidic >CH–
49.8	49.8	49.8	*Cis* disulfidic crosslink >CH–
49.1	—	—	Cyclic >CH–
—	47.8	—	*Trans* monosulfidic crosslink >CH–
45.0	—	—	Possible cyclic >CH–
—	44.7	44.7	Fragment $-CH_3$
42.8	42.8	42.8	*Cis* monosulfidic >CH–
40.9	40.9	40.9	Fragment $-CH_3$ in TMTD-cured/possible-SH fragment >CH– in S-cured
—	39.3	—	*Trans* monosulfidic fragment $-CH_2-$
38.3	38.3	38.3	Possible cyclic $-CH_2-$
38.2	38.2	38.2	Possible cyclic $-CH_2-$
37.7	37.7	37.7	Unassigned $-CH_2-$
37.5	37.5	37.5	Unassigned $-CH_2-$
36.9	36.9	36.9	Unassigned $-CH_2-$
36.0	36.0	—	Unassigned $-CH_2-$
—	35.5	—	Unassigned $-CH_2-$
35.3	—	—	Unassigned $-CH_2-$
34.9	**	34.9	Sat'd crosslink $-CH_2-$
34.2	34.2	34.2	*Cis* monosulfidic crosslink $-CH_2-$
—	33.9	33.9	*Trans* disulfidic fragment $-CH_2-$
**	**	33.4	*Cis* disulfidic crosslink $-CH_2-$
—	32.1	—	Sat'd vinyl or end-group $-CH_2-$
31.3	31.2	31.2	Unassigned $-CH_2-$
—	29.9	—	Sat'd vinyl or end-group $-CH_2-$
—	29.6	—	Sat'd vinyl or end-group $-CH_2-$
29.4	29.4	29.4	Unassigned $-CH_2-$
29.1	29.1	29.1	Sat'd crosslink $-CH_2-$
26.0	26.0	26.0	Sat'd crosslink $-CH_2-$
—	22.9	—	Sat'd vinyl or end-group $-CH_2-$
—	14.3	—	Sat'd vinyl or end-group $-CH_3$

**Not observed.
Source: ref. 69.

The effect of the accelerator-to-sulfur ratio on the vulcanization chemistry was also investigated by comparing the vulcanization products from conventional, semi-efficient (SEV) and efficient (EV) formulation systems. With increase in accelerator-to-sulfur ratio (from conventional to EV) there is a lowering in the sulfur rank. Also, the *cis*-to-*trans* isomerization increases with the amount of accelerator.[70]

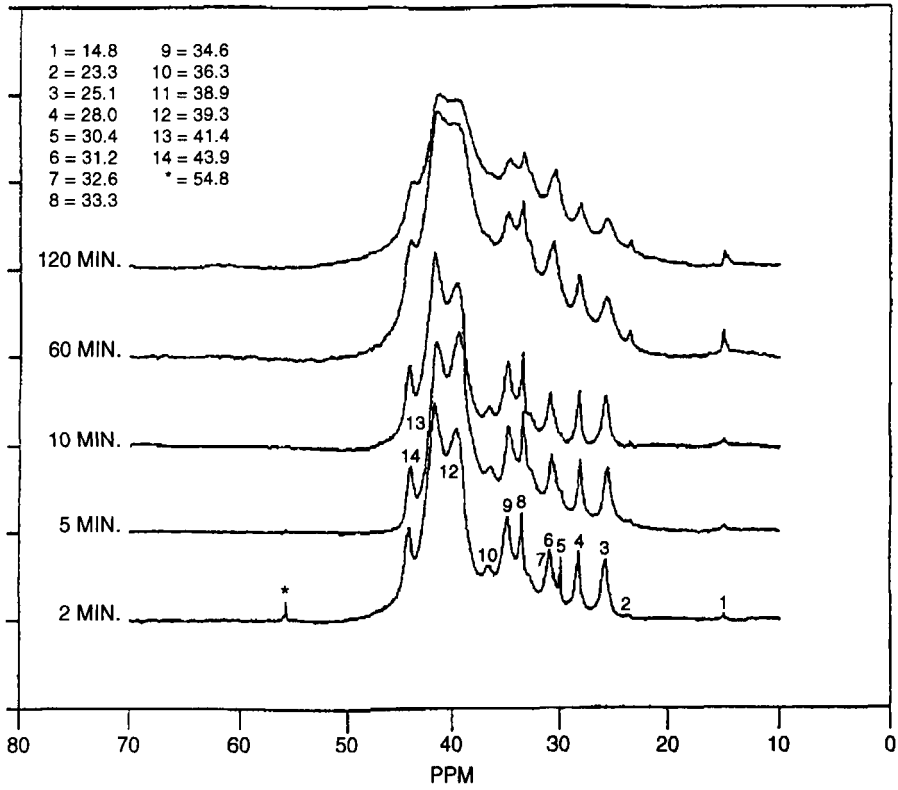

Fig. 43. Magnified ^{13}C GHPD NMR spectra of conventionally formulated high-vinyl BR cured for 2, 5, 10, 60, and 120 min. (Reprinted from ref. 70.)

4.6. Vulcanization of other elastomer systems

Chemical microstructural changes of an accelerated sulfur vulcanization of butyl rubber (IIR) with TMTD–ZnO–sulfur have been studied by solid-state ^{13}C NMR spectroscopy.[71] The IIRs containing 2% isoprene and 98% isobutylene were efficiently (EV) formulated and cured at 160°C for several cure times. ^{13}C NMR spectra were recorded under low-power continuous decoupling and high-power gated decoupling (GHPD) conditions at 75.5 MHz. Figure 44 illustrates the possible structures occurring in the vulcanization reaction along with the unreacted backbone structure of IIR (I). Chemical shifts of the expected chemical species were calculated by using the shielding parameters.

Figure 45 shows the ^{13}C NMR spectra of IIR cured for a variety of cure times. The resonances at 20.3 and 24.4 ppm, which are due to *trans*-isoprene units in the IIR (I in Fig. 44), decrease with cure, while the resonances at

Table 8. Comparison of peak assignments[a] for TBBS/sulfhur, DEPT, TMTD, and pure sulfur.

Assignments	Present work (ppm)	DEPT (ppm)	TMTD[b] (ppm)	S[c] (ppm)
Methyl ($-CH_3$)	14.8	14.6 (CH_3)	14.3	—
Methylene ($-CH_2-$)	23.3	23.2 (CH_2)	22.9	—
Cis (CV)	25.1	25.0 (CH_2)	25.1	25.1
Cis CCC ($-CH_2-$)	28.0	27.9 (CH_2)	27.6	27.6
TBBS (CH_3)	30.4	30.0 (CH_3)	30.5	—
Trans (TV)	32.6	32.5 (CH_2)	32.9	32.9
Cis (di/poly S)	33.3	33.1 (CH_2)	33.9	33.9
Vinyl ($-CH_2-$)	34.6	34.3 (CH_2)	34.4	34.4
Mono $S_1\beta$ to *trans*	36.3	36.2 (CH_2)	—	—
Vinyl (–CH–)	39.3	39.2 (CH–)	39.3	39.8
Vinyl (>CH–)	41.4	41.2 (CH–)	40.9	40.9
Di/poly S	43.9	43.8 (CH–)	43.7	43.8
Fragments (TBBS)	54.8	—	53.9	—
Vinyl ($=CH_2$)	114.9	114.6 ($=CH_2$)	114.5	—
Cis (=CH–)	128.1	128.0 (=CH–)	127.9	—
Cis (VCV, CCV)	129.8	129.7 (=CH–)	129.5	129.6
Trans (–CH=)	130.5	130.5 (–CH=)	130.1	130.1
Vinyl (=CH–)	143.1	143.0 (=CH–)	142.3	—

[a]Error in values = ±1.0 ppm.
[b]Data from ref. 57.
[c]Data from ref. 53.
Source: ref. 70.

26.9 and 25.2 ppm, which arise from *cis*-isoprene units (II), increase with cure time. The *cis/trans* ratio increases up to a maximum of approximately 4:1 at a cure time of 60 min. New resonances are observed at 15, 21, 23.6 and 49 ppm. The peak at 49 ppm is assigned to the mixture of the isoprene units in *cis*-IIR (II), polysulfidic A1t (III) and polysulfidic A1c (VI) structures. The resonance peaks at 15, 21 and 23.6 ppm are due to the isoprene units in mono- and polysulfidic B1t (IV), mono- and polysulfidic B1c (VII) and polysulfidic A1t (III) structures, respectively.

The quantitative data show that the sulfurization initially results in A1t (III) and A1c (VI) substitutions on the isoprene units and is polysulfidic in nature. At cure times greater than 75 min, desulfurization of III and VI occurs and mono- and polysulfidic sulfurization giving B1t (IV) and B1c (VII) structures occurs. No reaction occurs in the isobutylene units. No migration of the double-bond saturation, internal cyclization or sulfurization resulting in C1t (V) and C1c (VIII) structures is observed.[71]

Solid-state ^{13}C NMR has been used to identify elastomers in binary blends of chloroprene (CR) and NR, CR and chlorosulfonated polyethylene (CSM), NR and CSM, and styrene–butadiene rubber (SBR) and acrylonitrile–

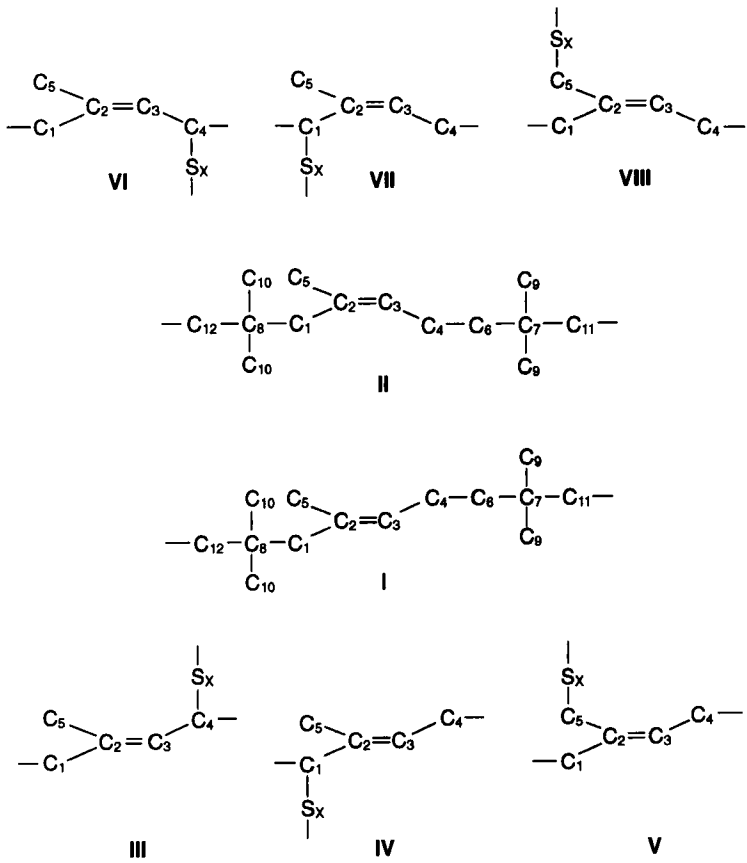

Fig. 44. Possible structures resulting from accelerated sulfur vulcanization of IIR. (Reprinted from ref. 71.)

butadiene rubber (NBR). The type of NBR can be determined by identifying the sequences of acrylonitrile and butadiene. The tertiary blend of NR–SBR–BR was also studied.[72] High-temperature ^{13}C solid-state NMR identified EPDM and fluoro and nitrile rubbers.[73]

Elastomeric components and compositions in the BR–SBR and NR–BR–SBR blends have been studied by ^{13}C solid-state NMR. The MAS spectra are of sufficient quality for polymer identification of the carbon-black-filled vulcanizates in most cases.[15]

Vulcanized SBR–EPDM diblends were quantitatively characterized by solid-state ^{13}C NMR spectroscopy. The SBR–EPDM blend ratio can be determined as well as the *cis*-1,4, *trans*-1,4 and vinyl-1,2 butadienes and styrene ratios in the SBR and the ethylene and propylene contents in the EPDM. No evidence for homo- and co-vulcanization has been obtained in

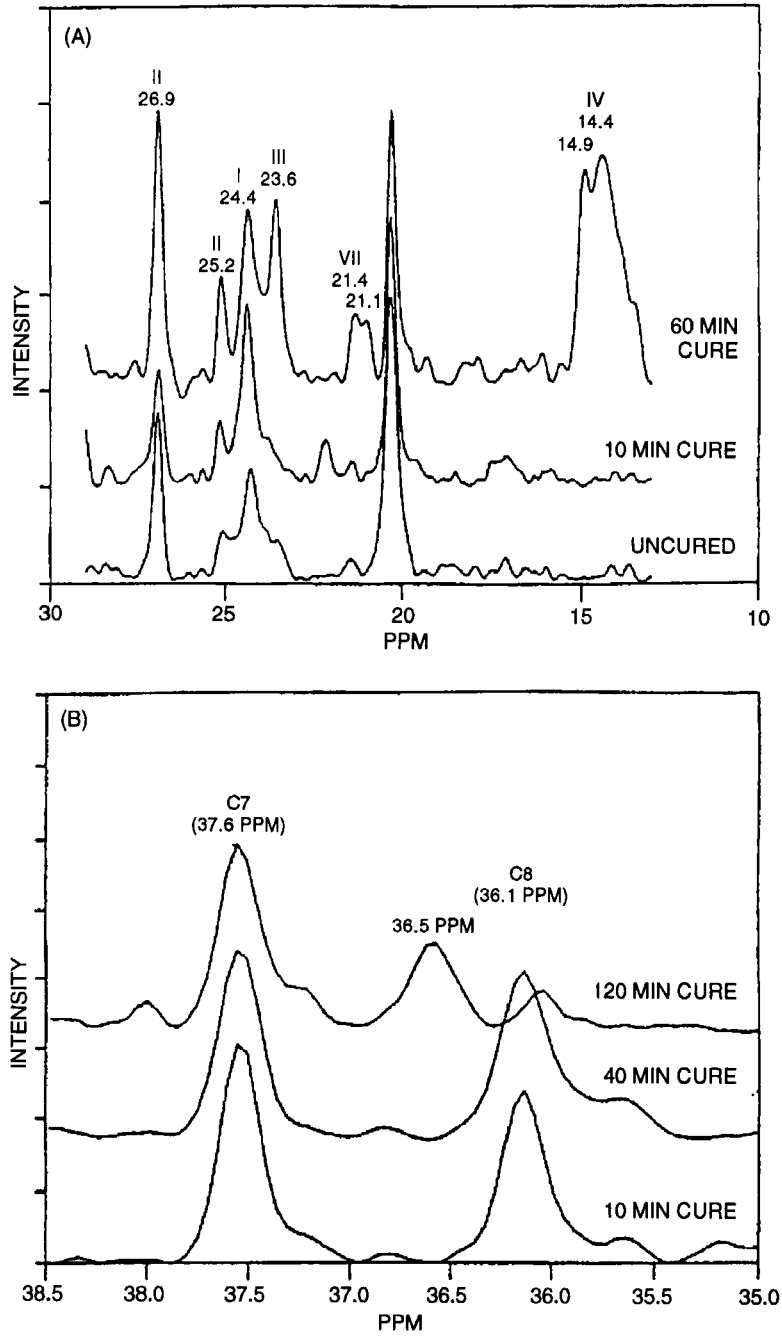

Fig. 45. The ^{13}C NMR spectra of uncured and cured IIR: (A) uncured sample and cured for 10 and 60 min; (B) quaternary region of the spectra for samples cured for 10, 40, and 120 min. (Reprinted from ref. 71.)

these systems, nor has evidence been found for the change in *cis/trans* ratio in SBR upon vulcanization.[74]

4.7. Vulcanization of carbon-black-filled elastomers

The incorporation of carbon black into elastomeric systems is a process of significant commercial importance. However, the additional stiffness of the sample imparted by the reinforcement effect of fillers is not favourable in terms of the experimental conditions for high-resolution NMR spectroscopy. Electric conductivity of the carbon black may also interfere to some extent. Under these circumstances, filled formulations are not widely employed for the study of elastomer vulcanizations where high resolution and signal-to-noise ratios are required to detect small amounts of vulcanization products.

Solid-state ^{13}C NMR spectra of carbon-black-filled, uncured and sulfur vulcanized *cis*-polyisoprene (IR) were recorded at 22.6 MHz. It was indicated that the line broadening of the filled polymer relative to the unfilled polymer is attributed to incomplete motional narrowing of the NMR lines.[75,76] Incorporation of filler also results in decrease in the signal-to-noise ratios in the spectra, but fundamentally it does not obscure the qualitative and quantitative nature of the spectra for the moderately cured elastomer systems.[15,72,77,78]

Carbon-black-filled NR vulcanizates have been studied by high-resolution solid-state ^{13}C NMR at 75.5 MHz. It is shown that the detection of poly- and monosulfidic crosslinks with ^{13}C MAS spectroscopy is also possible in the case of carbon-black-filled NR vulcanizates. Quantitative results suggest that the addition of carbon black leads to a decrease in crosslink density with increasing filler content.[77]

The effect of carbon black on the vulcanization chemistry has been studied for sulfur-cured NR systems by ^{13}C solid-state GHPD experiments at 75.5 MHz.[78] Figure 46 shows the ^{13}C NMR spectra of carbon-black-(N347)-filled NR cured to t_{50} (50% of rheometer torque increase) (A) and for 120 min (B). Similar new resonances are observed as compared to the results for unfilled *cis*-polyisoprene systems.[62] Increase in the 16 ppm peak in the overcuring period is attributed to the *cis*-to-*trans* isomerization. Incorporation of carbon black do not affect the level of this isomerization reaction. The peaks at 51 and 45 ppm are due mainly to polysulfidic A1c and monosulfidic A1c structures depicted in Fig. 19, respectively. Figure 47 illustrates the change in peak intensities at 51 ppm (A) and 45 ppm (B) for four formulations with different carbon-black loading as a function of cure. The amount of A1c polysulfide decreases with increase in carbon black (Fig. 47(A)), while more monosulfidic A1c structures are occurring after t_{90} with higher amounts of filler (Fig. 47(B)).

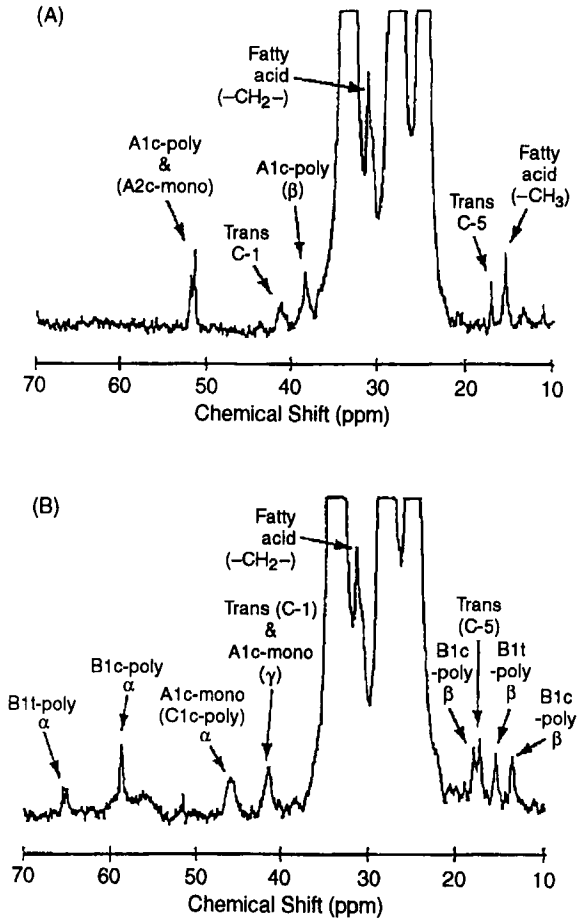

Fig. 46. ^{13}C NMR spectra of carbon-black-filled NR cured for (A) 26 min and (B) 120 min. (Reprinted from ref. 78.)

The peaks at 58 and 64 ppm are assigned to the polysulfidic B1c and B1t structures seen in Fig. 19, respectively. Changes in the peak intensities at 58 and 64 ppm are illustrated in Fig. 48(A) and (B), respectively. The occurrence of the B1-type sulfides increases with the level of carbon-black loading. These changes in the quantitative nature of the vulcanization are partially explained by the preferential adsorption of the rubber molecules on the surface of the carbon-black aggregates.[78]

Similar trends have been observed in the carbon-black-(N347)-filled, TBBS-accelerated sulfur-vulcanization of high-*cis*-polyisoprene (IR). In contrast to the NR–CB system, the reversion reactions, i.e., the *cis*-to-*trans*

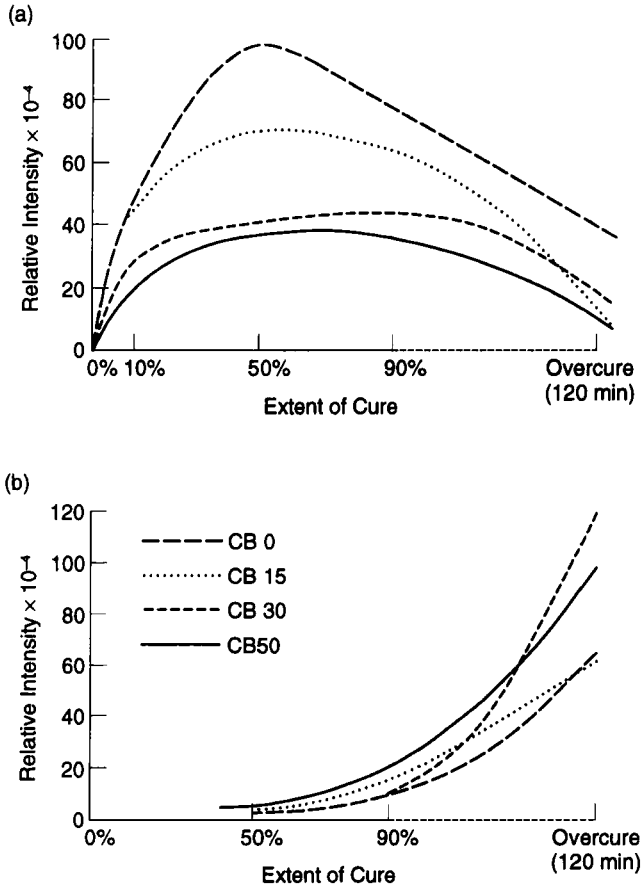

Fig. 47. Concentration of NMR peaks *vs* cure percentage for NR vulcanizates with variable carbon black concentrations: (a) 51 ppm peak (mainly for A1c polysulfide), (b) 45 ppm peak (mainly for A1c monosulfide). (Reprinted from ref. 78.)

isomerization and the chain scission at 3,4-isoprene units, increase with black content during the overcuring.[65]

The amount of the sulfurization occurring in the carbon-black-(N347)-filled, TBBS-accelerated sulfur vulcanization of NR[64] and IR[65] have been determined by quantitative measurements in the solid-state ^{13}C NMR. The density of the chains between sulfurizations ($2[S]_{chem}$) obtained from the ^{13}C NMR was then compared with the effective network chain density (ν_e) determined by the equilibrium swelling measurements (modified Flory–Rehner equation). The $2[S]_{chem}$ and ν_e for four NR formulations with different levels of carbon-black loading are shown in Figs 49 and 50, respectively. The four curves in Fig. 49 constantly increase with cure even

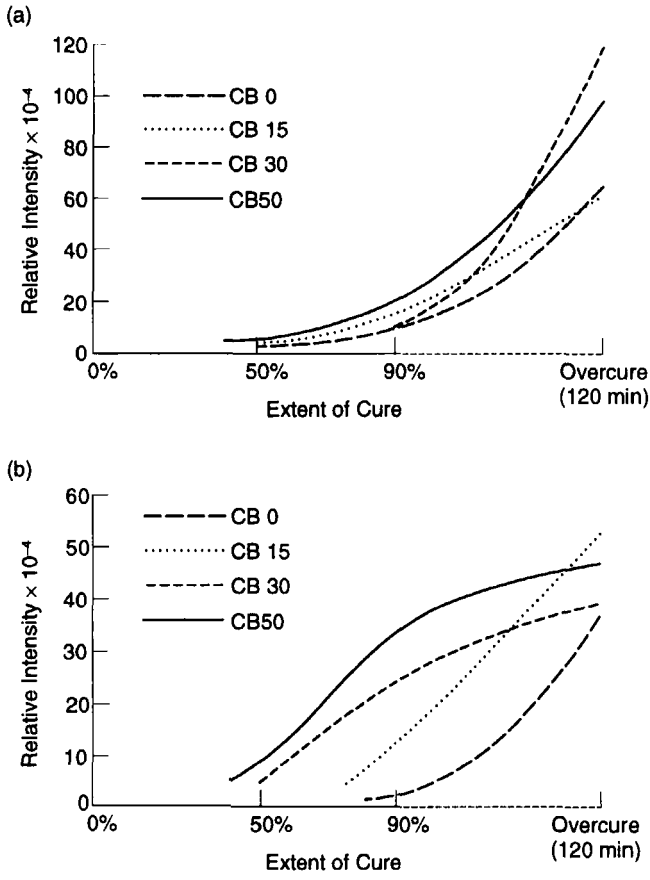

Fig. 48. Concentration of NMR peaks *vs* cure percentage for NR vulcanizates with variable carbon-black concentrations: (a) 58 ppm peak (B1c polysulfide), (b) 64 ppm peak (B1t polysulfide). (Reprinted from ref. 78.)

in the overcuring, while the ν_e reaches the maximum after t_{90} (Fig. 50). The $2[S]_{chem}$ are almost constant for all formulations with different contents of carbon black (Fig. 49), suggesting that the incorporation of carbon black does not affect the total number of chemical sulfurization reactions.

The physical network chain density (ν_{ent}) was estimated from the comparison of the NMR and swelling results. A plot of the ν_{ent} in the NR system as a function of carbon-black content is shown in Fig. 51. The linear relationship obtained in Fig. 51 suggests that the physical adsorption plays a major role in the polymer–filler interactions.[64,65]

The slope of the plot seen in Fig. 51 was assumed to represent the degree of filler reinforcement effect. Similar NR formulations using N110, N220, N326, N330, N550 and N765 carbon black have been studied by solid-state

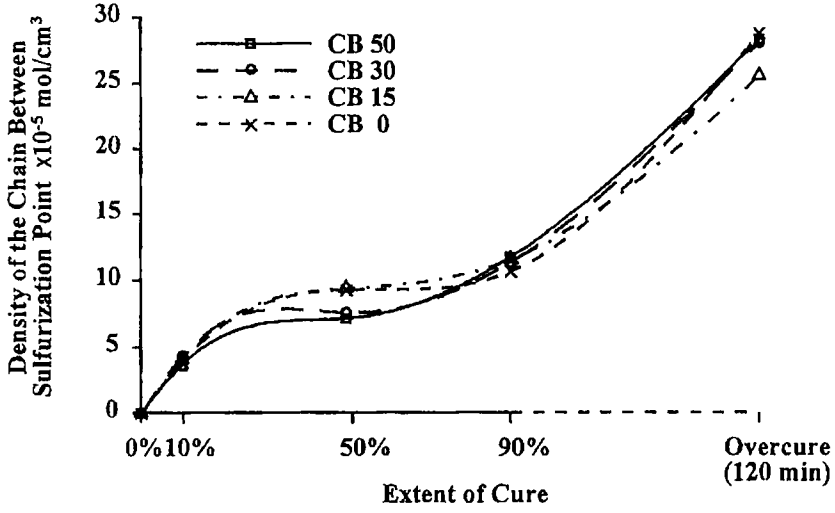

Fig. 49. Density of the chains between sulfurization points of NR with variable carbon-black content obtained by ^{13}C NMR quantitative analysis as a function of cure percentage. (Reprinted from ref. 64.)

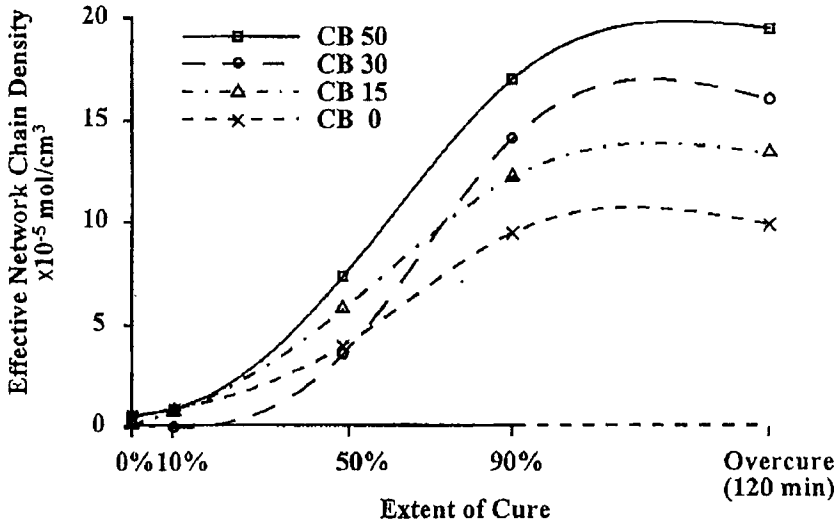

Fig. 50. Effective network chain densities of NR with variable carbon-black content obtained by equilibrium swelling measurements as a function of cure percentage. (Reprinted from ref. 64.)

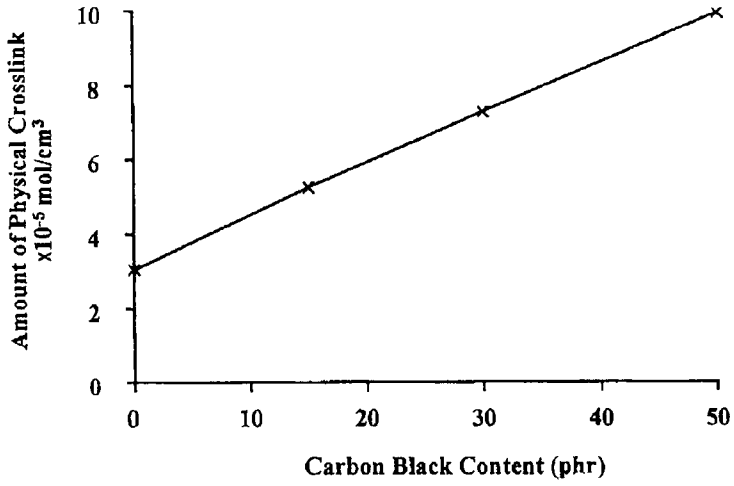

Fig. 51. Estimated amount of physical crosslinks (physical network chain density of NR cured to t_{90} as a function of carbon black content. (Reprinted from ref. 64.)

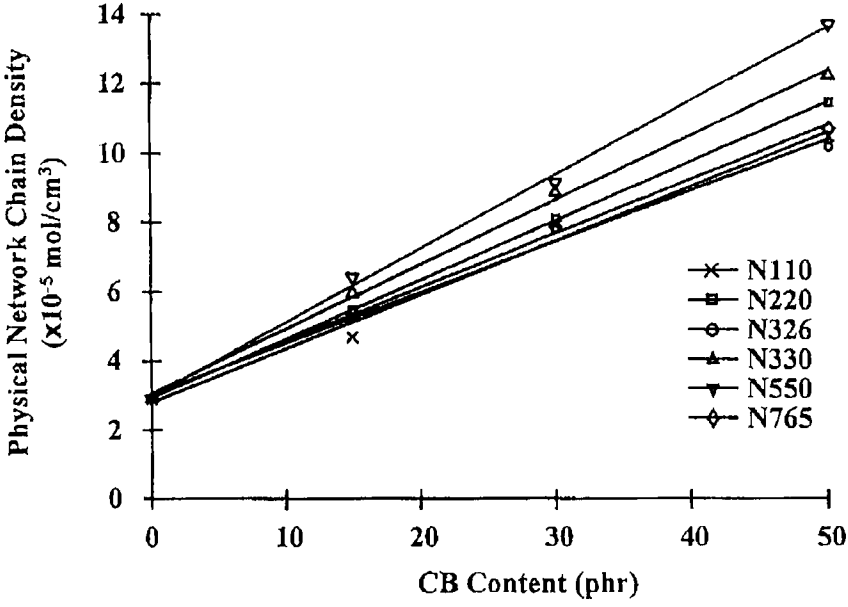

Fig. 52. Physical network chain densities of NR cured to t_{90} with variety of carbon-black as a function of carbon-black content. (Reprinted from ref. 79.)

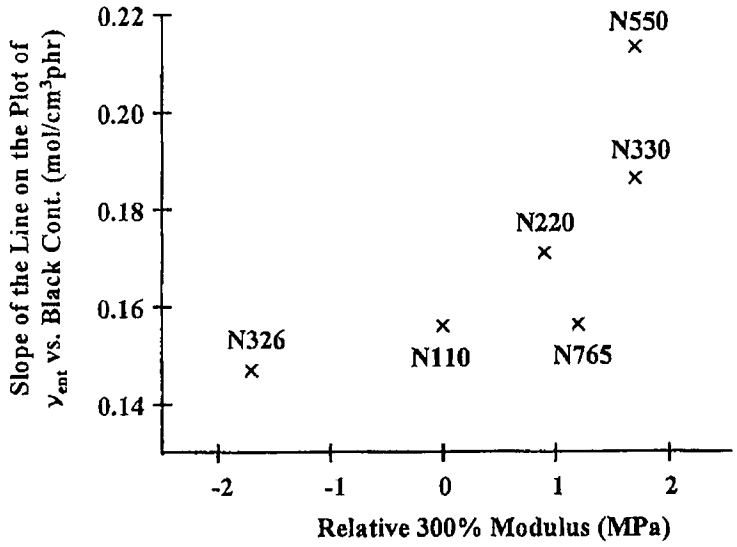

Fig. 53. Comparison between the slope of the line in Fig. 52 and relative 300% modulus (ASTM 1765) of filled NR vulcanizates. (Reprinted from ref. 79.)

^{13}C NMR and equilibrium swelling measurements.[79] Changes in the structural parameters (surface area and structure) of carbon black do not affect the amount of sulfurization reactions. The ν_{ent} at t_{90} were obtained for each formulation and are plotted as a function of carbon-black content in Fig. 52. A comparison of the slopes of the plots and the 300% modulus data (ASTM D1765, D3192) is illustrated in Fig. 53. The relationship between the slopes and the static modulus suggests the use of the plot as a method of evaluating filler reinforcement effects.[79]

REFERENCES

1. M. Andreis and J. L. Koenig, *Adv. Polym. Sci.*, 1989, **89**, 71.
2. M. R. Krejsa and J. L. Koenig, *Rubber Chem. Technol.*, 1993, **66**, 376.
3. C. J. Carman and K. C. Baranwal, *Rubber Chem. Technol.*, 1975, **48**, 705.
4. H. J. Harwood, *Rubber Chem. Technol.*, 1982, **55**, 769.
5. R. A. Kinsey, *Rubber Chem. Technol.*, 1990, **63**, 407.
6. Y. Tanaka, *Rubber Chem. Technol.*, 1991, **64**, 325.
7. J. L. Koenig, *Spectroscopy of Polymers*, ACS, Washington DC, 1992.
8. J. L. Koenig, Paper No. 28, *Educational Symp., ACS Rubber Div. Meet.*, May 1992.
9. M. R. Krejsa and J. L. Koenig, *Elastomer Technology Handbook*, Ch. 11. CRC Press, 1993.
10. A. Y. Coran, *Rubber Chem. Technol.*, 1995, **68**, 351.
11. P. S. Brown, M. J. R. Loadman and A. J. Tinker, *Rubber Chem. Technol.*, 1992, **65**, 744.

12. I. J. Lowe, *Phys. Rev. Lett.*, 1959, **2**, 285.
13. E. R. Andrew, A. Brandbury and R. G. Eades, *Nature*, 1959, **183**, 1802.
14. A. Pines, M. G. Gibby and J. S. Waugh, *J. Chem. Phys.*, 1972, **56**, 1776.
15. R. A. Komoroski, *Rubber Chem. Technol.*, 1983, **56**, 959.
16. R. A. Komoroski, J. P. Schockcor, E. C. Gregg and J. L. Savoca, *Rubber Chem. Technol.*, 1986, **59**, 328.
17. A. M. Zaper and J. L. Koenig, *Rubber Chem. Technol.*, 1987, **60**, 252.
18. S. J. Opella and M. H. Frey, *J. Am. Chem. Soc.*, 1979, **101**, 5854.
19. S. L. Patt and J. N. Schoolery, *J. Magn. Reson.*, 1982, **46**, 535.
20. J. Beloeil, C. L. Cocq and L. Lallemand, *Organic Magn. Reson.*, 1982, **19**, 112.
21. D. T. Pegg, M. R. Bendall and D. M. Doddrell, *J. Magn. Reson.*, 1981, **44**, 238.
22. M. R. Bendall, D. T. Pegg, D. M. Doddrell and D. M. Thomas, *J. Magn. Reson.*, 1982, **46**, 43.
23. D. M. Doddell, D. T. Pegg, M. R. Bendall, *J. Magn. Reson.*, 1982, **48**, 323.
24. M. Andreis, J. Liu and J. L. Koenig, *J. Polym. Sci., Phys. Ed.*, 1989, **27**, 1389.
25. J. S. Waugh, L. M. Huber and U. Haeberlin, *Phys. Rev. Lett.*, 1968, **20**, 180.
26. A. D. English and C. R. Dybowski, *Macromolecules*, 1984, **17**, 446.
27. S. Kaufman, W. P. Slichter and D. D. Davis, *J. Polym. Sci., Part A-2*, 1971, **9**, 829.
28. C. J. Carman, *Carbon-13 NMR in Polymer Science*, Ch. 6, ACS Symp. No. 103, 1979.
29. F. W. Wehrli and T. Wirthlin, *Interpretation of Carbon-13 NMR Spectra*, Heyden, London, 1978.
30. M. J. R. Loadman and A. J. Tinker, *Rubber Chem. Technol.*, 1989, **62**, 234.
31. P. S. Brown and A. J. Tinker, *J. Nat. Rubber Res.*, 1990, **5**, 286.
32. A. J. Tinker, *Rubber Chem. Technol.*, 1990, **63**, 503.
33. P. S. Brown and A. J. Tinker, *Proc. Commun. Int. Rubber Conf.*, p. 48, Paris, 1990.
34. P. S. Brown and A. J. Tinker, *J. Nat. Rubber Res.*, 1990, **5**, 157.
35. P. S. Brown and A. J. Tinker, *J. Nat. Rubber Res.*, 1991, **6**, 87.
36. H. L. Dinsmore and D. C. Smith, *Rubber Chem. Technol.*, 1949, **22**, 572.
37. D. D. Werstler, *Rubber Chem. Technol.*, 1981, **53**, 1191.
38. H. Sato, K. Takebayashi and Y. Tanaka, *Macromolecules*, 1987, **20**, 2418.
39. H. Sato, T. Ishikawa, K. Takebayashi and Y. Tanaka, *Macromolecules*, 1989, **22**, 1748.
40. D. S. Campbell, A. V. Chapman and P. S. Farley, *Phosph. Sulf. Silic.*, 1993, **74**, 475.
41. D. S. Campbell, *J. Appl. Polym. Sci.*, 1969, **13**, 1201.
42. D. J. Patterson, J. L. Koenig and J. R. Shelton, *Rubber Chem. Technol.*, 1983, **56**, 971.
43. D. J. Patterson and J. L. Koenig, *ACS Symp. No.* 243, p. 205, Seattle, 1984.
44. W. Gronski, N. Murayama, H. J. Cantow and T. Miyamoto, *Polymer*, 1976, **17**, 358.
45. R. J. Abraham and P. Loftus, *Proton and Carbon-13 NMR Spectroscopy*, Heyden, Philadelphia, 1979.
46. G. L. Nelson and G. C. Levy, *Carbon-13 Nuclear Magnetic Resonance*, John Wiley, NY, 1980.
47. W. Gronski, H. Hasenhindl, B. Freund and S. Wolff, *Kautsch. Gummi, Kunstst.*, 1991, **44**, 119.
48. D. J. Patterson and J. L. Koenig, *Appl. Spectrosc.*, 1987, **41**, 441.
49. P. F. Barrow, J. H. O'Donnell and A. K. Whittaker, *Polym. Bull.*, 1985, **14**, 339.
50. W. T. Dixon, *J. Magn. Reson.*, 1981, **44**, 220.
51. S. A. Curran and A. R. Padwa, *Macromolecules*, 1987, **20**, 625.
52. C. G. Moore, L. Mullins and P. M. Swift, *J. Appl. Polym. Sci.*, 1961, **5**, 293.
53. J. L. Koenig and D. J. Patterson, *Elastomers Rubber Technol.*, 1987, **32**, 31.
54. W. W. Simons, Ed., *The Sadtler Guide to C-13 NMR Spectra*, Sadtler Research Laboratories, 1983.
55. A. Andreis, L. Liu and J. L. Koenig, *Rubber Chem. Technol.*, 1989, **62**, 82.

56. A. Y. Coran, *Science and Technology of Rubber*, Ch. 7. Academic Press, 1994.
57. A. M. Zaper and J. L. Koenig, *Rubber Chem. Technol.*, 1987, **60**, 278.
58. R. C. Hirst, Paper No. 69, ACS Rubber Div. Meet., October 1991.
59. W. Gronski, U. Hoffmann, G. Simon, A. Wutzler and E. Straube, *Rubber Chem. Technol.*, 1992, **65**, 427.
60. M. R. Krejsa and J. L. Koenig, *Rubber Chem. Technol.*, 1992, **65**, 427.
61. M. R. Krejsa and J. L. Koenig, *Rubber Chem. Technol.*, 1993, **66**, 73.
62. M. R. Krejsa and J. L. Koenig, *Rubber Chem. Technol.*, 1994, **67**, 348.
63. A. B. Sullivan, C. J. Hahn and G. H. Huhls, *Rubber Chem. Technol.*, 1992, **65**, 488.
64. M. Mori and J. L. Koenig, *Macromolecules*, Submitted.
65. M. Mori and J. L. Koenig, *Macromolecules*, Submitted.
66. L. Mullins, *J. Appl. Polym. Sci.*, 1959, **4**, 1.
67. A. M. Zaper and J. L. Koenig, *Macromol. Chem.*, 1988, **189**, 1239.
68. R. S. Clough and J. L. Koenig, *Rubber Chem. Technol.*, 1969, **62**, 908.
69. S. R. Smith and J. L. Koenig, *Rubber Chem. Technol.*, 1992, **65**, 176.
70. M. A. Rana and J. L. Koenig, *Rubber Chem. Technol.*, 1993, **66**, 242.
71. M. R. Krejsa and J. L. Koenig, *Rubber Chem. Technol.*, 1991, **64**, 40.
72. D. Gross and J. Kelm, *Kautsch. Gummi, Kunstst.*, 1985, **38**, 1089.
73. D. Gross and J. Kelm, *Kautsch. Gummi, Kunstst.*, 1987, **40**, 13.
74. G. P. M. Van Del Velden and J. Lelm, *Rubber Chem. Technol.*, 1990, **63**, 215.
75. J. Schaefer, *Macromolecules*, 1972, **5**, 427.
76. J. Schaefer, S. H. Chin and S. I. Weissman, *Macromolecules*, 1972, **5**, 798.
77. U. Hoffmann, W. Gronski, G. Simon and A. Wutzler, *Angew. Makromol. Chem.*, 1992, **202/203**, 283.
78. M. Mori and J. L. Koenig, *Rubber Chem. Technol.*, 1995, **68**, 551.
79. M. Mori and J. L. Koenig, *Rubber Chem. Technol.*, Submitted.

This Page Intentionally Left Blank

Structural Analysis of Oriented Polymers by Solid-state NMR

TETSUO ASAKURA, MAKOTO DEMURA
and NAOKI NISHIKAWA

Department of Biotechnology, Tokyo University of Agriculture and Technology, Koganei, Tokyo 184, Japan

*A method for structural determination to elucidate atomic resolution details of the structures of ordered polymers with orientation-dependent NMR interactions, such as chemical shift, dipole–dipole and quadrupole, is described. This method has been applied to determine the torsion angles of peptide backbone of highly ordered silk fibroin fibre and to obtain structural information of oriented polyamide fibres such as poly(*p*-phenylene terephthalamide), poly(*m*-phenylene isophthalamide) and poly(4-methyl-*m*-phenylene terephthalamide). Oriented carbonyl-carbon-labelled poly(ethylene terephthalate) films have also been analysed using this method. In particular, more quantitative structural information is obtained for locally ordered domains which have been recognized as amorphous domains in X-ray diffraction analysis in heterogeneous polymer samples.*

1. INTRODUCTION

Many different experimental approaches have been used to characterize orientation in polymers, that is, birefringence, ultraviolet–visible light spectroscopy, infrared dichroism, sonic modulus measurements, various X-ray techniques and nuclear magnetic resonance (NMR).[1] Among these approaches, the rapid methodical development of solid-state NMR has opened up new possibilities in characterization.[1–7] Orientation-dependent NMR interactions such as dipole–dipole, quadrupole and chemical shielding yield structural information on polymers in the solid state. If these parameters are observed for each site in oriented polymers, the solid-state NMR methods can give even the atomic coordinates of the polymers. This is especially effective in the determination of the atomic coordinates of peptides or proteins in membrane systems, and fibrous proteins in which the X-ray technique gives only little structural information. The former application of solid-state NMR has been reviewed by Cross.[8]

Fibrous proteins are particularly difficult to study using standard structure determination techniques. The X-ray diffraction image from fibres in which proteins are aligned along the long axis of the fibre typically yields general features of molecular organization and packing, but lacks atomic resolution details. High-resolution solution NMR techniques are not applicable to fibrous proteins, since the solution-state structure is generally not representative of the structure in the fibrous state. On the other hand, the natural alignment of the protein within the fibre provides an important advantage that can be utilized by solid-state NMR.

First, the method for structural determination to elucidate atomic resolution details of the structures of ordered polymers with orientation-dependent NMR interactions, such as chemical shielding, dipole–dipole and quadrupole, will be described. Next, a solid-state NMR study which has been applied to determine the torsion angles of the peptide backbone of highly ordered silk fibroin fibre, a protein that has been studied extensively as a model for fibrous proteins, will be described.[9] Selective isotope labelling of the sample is usually required in these NMR experiments for getting site-specific structural information. This is possible for silk fibroin fibre by oral administration of isotope-labelled amino acids to silkworms or by cultivation of the silkglands which produce silk fibroin protein in the medium containing the isotope-labelled amino acids, as will be described below.

Then solid-state NMR studies of oriented polymer fibres or film other than silk will be described. The orientation-dependent chemical shielding tensors especially serve as probes with which the relative orientations of specific bond vectors can be determined.[10] This analytical method can be applied to obtain structural information of oriented polyamide fibres such as poly(*p*-phenylene terephthalamide) (PPTA),[11] and poly(*m*-phenylene isophthalamide) (PMIA) and poly(4-methyl-*m*-phenylene terephthalamide) (P4M-MPTA) fibres

without isotope labelling of the samples.[12] The oriented carbonyl carbon-labelled poly(ethylene terephthalate) (PET) films have also been analysed with this method.[13] Especially, more quantitative structural information will be obtained for a locally ordered domain which has been recognized as an amorphous domain in X-ray diffraction analysis in heterogeneous polymer samples.

As mentioned above, the determination of atomic level structure, that is, the backbone torsion angles for oriented protein fibre, is possible by using the solid-state NMR method described here. This is basically to obtain the "angle" information. Another structural parameter is "distance" between the nuclei for atomic coordinate determination. The observation of nuclear Overhauser enhancements (NOE) among hydrogen atoms is a well-known technique to determine the atomic coordinates of proteins in solution.[14] In the field of solid-state NMR, REDOR (rotational echo double resonance) for detection of weak heteronuclear dipole interactions such as those due to the ^{13}C and ^{15}N nuclei[15,16] or R^2 (rotational resonance) for detection of the distance between homonuclei are typical methods for internuclear distance determination.[17,18] The REDOR technique has been applied to structure determination of a silk fibroin model compound.[19] In general, this does not require the orientation of the samples in the analysis, but selective isotope labelling between specified nuclear pairs in the samples is required, which frequently becomes a problem. The review of these approaches has appeared elsewhere.[16]

Solid-state NMR is also one of the most powerful and informative probes of molecular dynamics of oriented polymers.[6] These have been reviewed elsewhere.[1-7]

2. METHOD FOR STRUCTURE DETERMINATION

The determination of polymer structure at the atomic level is possible by analysing the orientation-dependent NMR interactions such as dipole–dipole, quadrupole and chemical shielding anisotropy.[1] The outline of the atomic coordinate determination for oriented protein fibre used here is described. The chemical shielding anisotropy (CSA) interaction for ^{15}N nucleus in an amide (peptide) plane can be interpreted with the chemical shielding tensor transformation as shown in Fig. 1.[9,20] The ^{15}N CSA principal axis system (PAS) is a frame in which the ^{15}N CSA is diagonal, with principal components $\sigma_{11} < \sigma_{22} < \sigma_{33}$. When the molecular symmetry axis (MSA) system is used as a reference frame, the Euler angles that express the relative orientations of the ^{15}N CSA PAS and the MSA frames of reference are noted as α_D and β_D. Inherent in this orientation relation is the assumption that σ_{33} lies in the peptide plane (i.e., the xz plane), yielding the result that $\gamma_D = 0°$.[21-25] Here the fibre axis system (FAS) is a reference frame fixed in the aligned sample, and is defined such that the macroscopic fibre axis lies in the z direction.

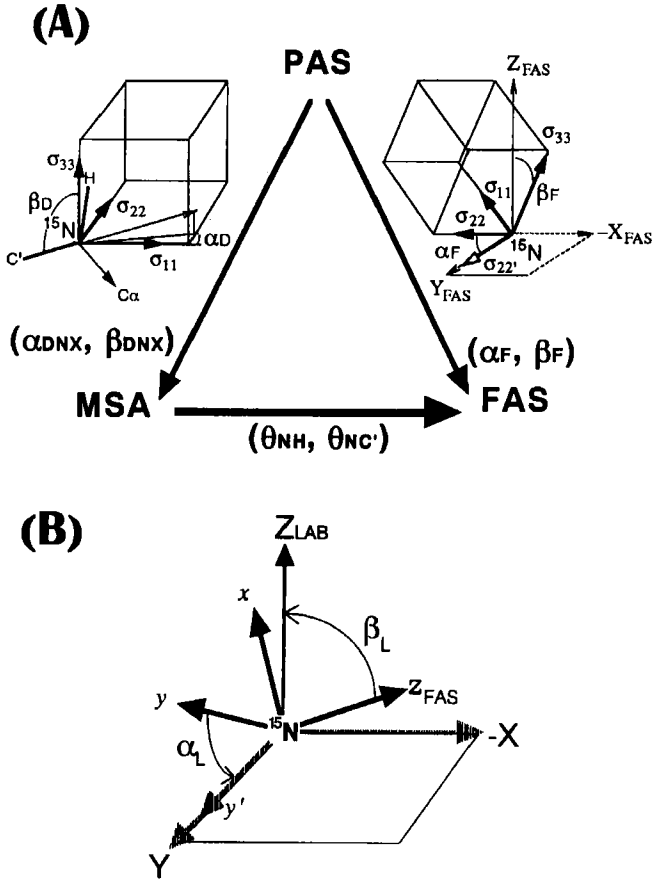

Fig. 1. (A) Transformation from the ^{15}N PAS to the MSA and to the FAS. The PAS is related to the MSA by the Euler angles α_D and β_D. The PAS is related to the FAB by the Euler angles α_F and β_F. The bond orientations θ_{NH} and θ_{NC} are obtained according to the transformation between PAS and MSA, and PAS and FAS. (B) Transformation from the FAS to the LAB frame of reference. The FAS is related to the LAB by the Euler angles α_L and β_L.

The ^{15}N CSA PAS is also at some orientation relative to the FAS, expressed by the Euler angles α_F and β_F. In this case, the location of x and y within the plane perpendicular to the fibre axis is defined such that σ_{33} lies in the xz plane, as illustrated in Fig. 1(A). This position also yields the convenient result that $\gamma_F = 0°$. The NMR spectra are observed in the laboratory frame of reference (LAB), in which the applied magnetic field (B_0) lies in the Z direction. The angles α_L and β_L are the Euler angles that transform the FAS into the LAB frame of reference (see Fig. 1(B)). Only two angles are required for this transformation because the NMR experiment is sensitive only to the component of the tensor parallel to B_0. Therefore, the position of the FAS

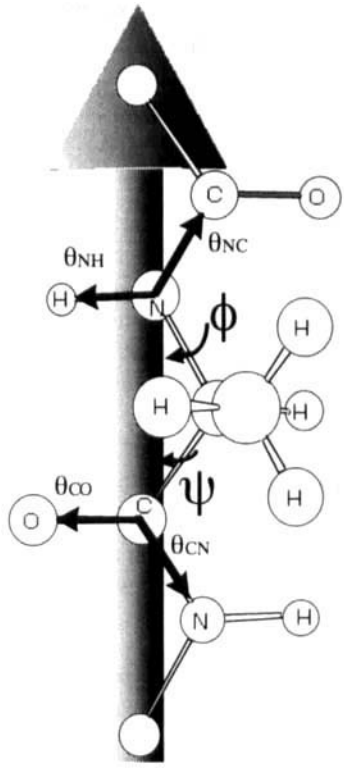

Fig. 2. Definition of the bond orientations, θ_{NH}, θ_{NC}, θ_{CO} and θ_{CN}. Each bond orientation is related to the angle between the N–H, N–C′, C′=O, and C′–N bond vectors and magnetic field B_0.

within the XY plane is arbitrary, and the third Euler angle, γ_L, can be conveniently set to zero. The angles α_L and β_L are set in the ^{15}N experiment performed here by placing the fibre axis parallel ($\alpha_L = 0°$, $\beta_L = 0°$) or perpendicular ($0° < \alpha_L < 360°$, $\beta_L = 90°$) to B_0. The specific orientations of the peptide plane, N–H, N–C′, C′=O, and C′–N bonds with respect to the fibre axis are illustrated in Fig. 2, and are calculated with these Euler angles α_F, β_F, α_D and β_D from the ^{15}N and ^{1}C solid-state NMR spectra. The torsion angles ϕ and ψ of the oriented protein fibres are determined by the combination of the bond orientations as described below.

2.1. Orientation of chemical shielding tensor elements with respect to the oriented axis

The ^{15}N CSA principal components ($\sigma_{11} < \sigma_{22} < \sigma_{33}$) of the chemical shielding tensor can be experimentally determined by observing the powder

pattern arising from a randomly dispersed sample.[20] Then the ^{15}N CSA tensor is rotated from the PAS through the FAS to the LAB frame of reference as follows:

$$\hat{\sigma}_{\mathrm{PAS}} \xrightarrow{R_{\mathrm{F}}(\alpha_{\mathrm{F}},\,\beta_{\mathrm{F}})} \hat{\sigma}_{\mathrm{FAS}} \xrightarrow{R_{\mathrm{L}}(\alpha_{\mathrm{L}},\,\beta_{\mathrm{L}})} \hat{\sigma}_{\mathrm{LAB}}$$

where R_i (α_i, β_i) represents the 3×3 unitary transformation matrix that rotates the original tensor to the i reference frame, where i denotes the frame to which the tensor is being rotated, (α_i, β_i) are the Euler angles as previously defined, and $\hat{\sigma}$ is the representation of the chemical shielding tensor in the reference frame denoted by its subscript. The explicit form of the above net transformation is expressed as the following series of matrix multiplications:

$$\hat{\sigma}_{\mathrm{LAB}} = R_{\mathrm{L}}(\alpha_{\mathrm{L}}, \beta_{\mathrm{L}}) \cdot R_{\mathrm{F}}(\alpha_{\mathrm{F}}, \beta_{\mathrm{F}}) \cdot \hat{\sigma}_{\mathrm{PAS}} \cdot R_{\mathrm{F}}(\alpha_{\mathrm{F}}, \beta_{\mathrm{F}})^{\mathrm{T}} \cdot R_{\mathrm{L}}(\alpha_{\mathrm{L}}, \beta_{\mathrm{L}})^{\mathrm{T}} \quad (1)$$

where σ_{LAB} denotes the final representation in the laboratory frame of the CSA, the superscript T denotes the transpose of the preceding matrix, and

$$\hat{\sigma}_{\mathrm{PAS}} = \begin{pmatrix} \sigma_{11} & 0 & 0 \\ 0 & \sigma_{22} & 0 \\ 0 & 0 & \sigma_{33} \end{pmatrix} \quad (2A)$$

$$R_i(\alpha_i, \beta_i) = \begin{pmatrix} \cos\beta_i & 0 & -\sin\beta_i \\ 0 & 1 & 0 \\ \sin\beta_i & 0 & \cos\beta_i \end{pmatrix} \times \begin{pmatrix} \cos\alpha_i & \sin\alpha_i & 0 \\ -\sin\alpha_i & \cos\alpha_i & 0 \\ 0 & 0 & 1 \end{pmatrix} \quad (2B)$$

The observed chemical shielding corresponds to the component of the transformed chemical shielding tensor that is parallel to B_0, which is the (3, 3) component of the resulting $\hat{\sigma}_{\mathrm{LAB}}$ matrix.

For the case where the fibre axis is parallel to B_0, $\alpha_{\mathrm{L}} = 0$ and $\beta_{\mathrm{L}} = 0$, and the observed chemical shielding obtained from equation (1) is given by

$$\sigma_{\mathrm{par}} = \sigma_{11} \sin^2\beta_{\mathrm{F}} \cos^2\alpha_{\mathrm{F}} + \sigma_{22} \sin^2\beta_{\mathrm{F}} \sin^2\alpha_{\mathrm{F}} + \sigma_{33} \cos^2\beta_{\mathrm{F}} \quad (3)$$

For the case where the fibre axis is perpendicular to B_0, $\beta_{\mathrm{L}} = 90°$ and $0° < \alpha_{\mathrm{L}} < 360°$ (all values of α_{L} will be equally represented in the spectrum). The observed chemical shielding for this situation can be obtained from equation (1) and is given by

$$\sigma_{\mathrm{per}}(\alpha_{\mathrm{F}}, \beta_{\mathrm{F}}, \alpha_{\mathrm{L}}) = F_{11} \cos^2\alpha_{\mathrm{L}} + 2F_{12} \cos\alpha_{\mathrm{L}} \sin\alpha_{\mathrm{L}} + F_{22} \sin^2\alpha_{\mathrm{L}} \quad (4)$$

where

$$F_{11} = \sigma_{11}\cos^2\beta_F\cos^2\alpha_F + \sigma_{22}\cos^2\beta_F\sin^2\alpha_F + \sigma_{33}\sin^2\beta_F \quad (5A)$$

$$F_{12} = (\sigma_{22} - \sigma_{11})\cos\beta_F\cos\alpha_F\sin\alpha_F \quad (5B)$$

$$F_{22} = \sigma_{11}\sin^2\alpha_F + \sigma_{22}\cos^2\alpha_F \quad (5C)$$

The F_{ij} terms are the i, j components of the CSA tensor expressed in the FAS reference frame. Equation (4) represents a family of curves that are manifested in the spectral line shape. The spectra obtained from oriented protein fibre samples aligned parallel and perpendicular to the magnetic field yield eight possible orientations of the peptide plane relative to the long axis of the fibre.[9] Note that it is necessary to consider only one set of α_F, β_F angles per site in the spectral simulations since the remaining seven possible pairs for each site will result in identical line shapes.

A trial-and-error process can be utilized to simulate the line shape by varying α_F and β_F. Full spectral simulations are performed in order to improve the accuracy of these two spectral frequencies as shown in Fig. 3. A Gaussian probability distribution of fibre axis orientations was employed to account for the spectral broadening observed in both the parallel and perpendicular cases. An error analysis is performed by summing the difference between the experimental and calculated points in the spectral line shape,

$$\chi^2 = \sum_{i=1}^{N} (I^{\text{calc}} - I^{\text{exp}})^2 \quad (6)$$

The minimum of this sum indicates the best fit of the α_F and β_F pair.

2.2. Orientation of chemical shielding tensor elements with respect to the molecular frame

The powder pattern spectrum of a dipolar coupled nuclear site can be expressed in the following form:[21]

$$S(\nu) = \sum_i S(\nu_i) = \sum \int_{\theta=0}^{180} \int_{\phi=0}^{360} g_i[\nu, \nu_i(\theta, \phi, \alpha_D, \beta_D)] \sin\theta\, \partial\theta\partial\phi \quad (7)$$

where θ and ϕ are polar angles that describe the orientation of the chemical shielding PAS with respect to the magnetic field fixed in the laboratory frame. ν is the observed frequency and ν_i is the transition frequency for a particular

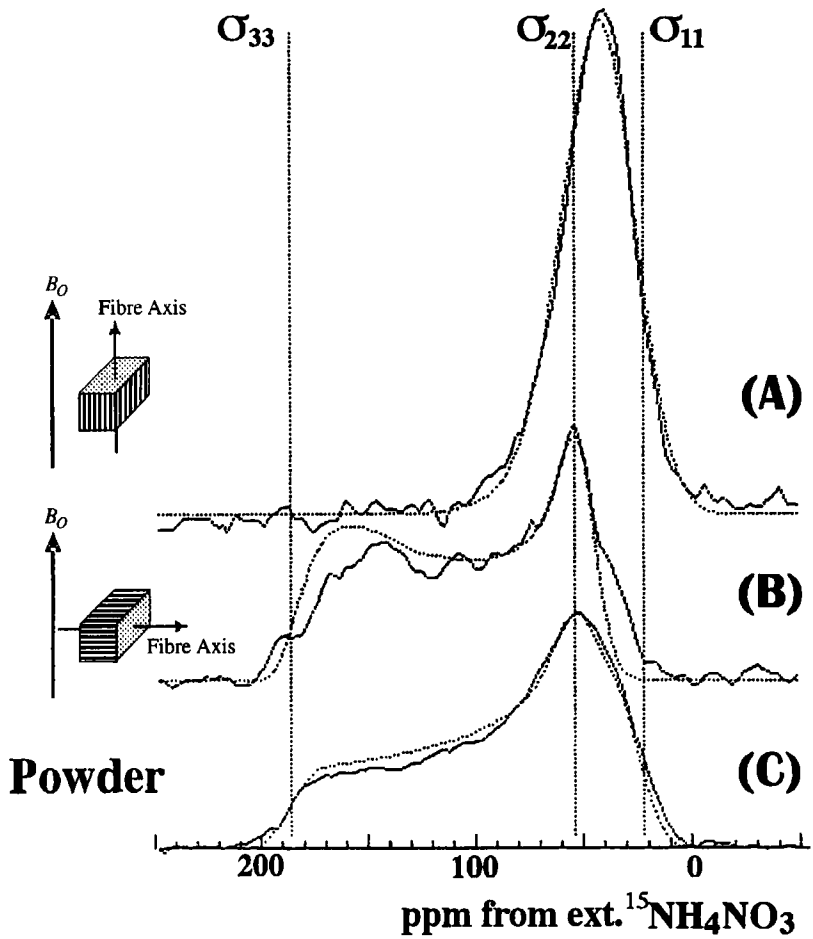

Fig. 3. Solid-state ^{15}N NMR spectra obtained from the oriented [^{15}N]Gly silk fibroin fibre sample. Spectra were observed with the fibre axis both (A) parallel and (B) perpendicular to the magnetic field. The powder pattern (C) is included for comparison. The best-fit simulated line shapes are superimposed on the experimental spectra.

orientation of the chemical shielding (ν_{CS}) and dipolar (ν_D) tensors. g_i is the line shape function for ν_i. The Euler angles α_D and β_D that express the relative orientations of the ^{15}N CSA PAS and the MSA frames of reference are determined from this spectral simulation. For example, the ^{13}C or ^{15}N powder patterns of [1-^{13}C]-[^{15}N] doubly labelled peptides are modulated by the dipolar interaction between ^{15}N and directly bonded ^{13}C nuclei, and thus the Euler angles α_D and β_D for [1-^{13}C]-[^{15}N] doubly labelled peptides are experimentally determined.

2.3. Orientation of the molecular frame with respect to the oriented axis

The orientation of the molecular frame with respect to the oriented axis defined as θ_{NH}, θ_{NC}, θ_{CO} and θ_{CN} in Fig. 2 can be calculated with these Euler angles described above. Simple equations can be derived for θ_{NH} and θ_{NC}, the N–H and N–C′ bond orientations to fibre axis, respectively. The resulting expression for the N–X bond angle relative to the fibre axis is as follows:[9,16]

$$\begin{aligned}\cos\theta_{NX} = {} & \cos\beta_F \cos\beta_{DNX} + \sin\beta_F \cos\alpha_F \cos\alpha_{DNX} \sin\beta_{DNX} \\ & + \sin\beta_F \sin\alpha_F \sin\alpha_{DNX} \sin\beta_{DNX}\end{aligned} \tag{8}$$

where α_{DNX} and β_{DNX} (X is H or C′), and α_F, β_F pairs are the Euler angles described above.

The determination of the molecular frame with respect to the oriented axis is possible from the observation of the dipolar coupling constant of uniaxially oriented [1-^{13}C]-[^{15}N] doubly labelled silk fibre. Namely, when the ^{13}C–^{15}N dipolar splitting is observed for the oriented protein fibre placed parallel to B_0, the angle between the ^{13}C–^{15}N bond and the oriented fibre axis can be directly obtained according to the following equation:[26,27]

$$\Delta\nu_{obs} = \nu_{\|} (3\cos^2\theta_{NC} - 1) \tag{9}$$

where $\nu_{\|}$ is the dipolar coupling constant ($= h\gamma_N\gamma_C/4\pi^2 r^2_{N-C}$; h: Planck constant; γ_N and γ_C: the gyromagnetic ratios of ^{15}N and ^{13}C nuclei, respectively; r_{N-C}: bond length of the N–C peptide bond).

The quadrupole splitting $\Delta\nu_Q$ observed in the solid-state ^{2}H NMR spectrum of oriented ^{2}H-labelled protein fibres depends on the angle, θ_{CD} of the C–^{2}H bond vector relative to B_0 when the oriented fibre axis is set parallel to the magnetic field:[28,29]

$$\Delta\nu_Q = \frac{1}{3}\frac{e^2qQ}{h}(3\cos^2\theta_{CD} - 1 + \eta\sin^2\theta_{CD}\cos 2\alpha) \tag{10}$$

where e^2qQ/h and η are the rigid lattice quadrupole coupling constant and asymmetry parameter (= 0–0.05 in a peptide), respectively.[3] Thus, the angle θ_{CD} is determined directly from observed quadrupole splitting $\Delta\nu_Q$.

2.4. Determination of torsion angles of peptide backbone

The relative orientations of the peptide planes in a protein are conveniently described with the torsion angles ϕ and ψ. As shown in Fig. 2, the orientation of a peptide plane with respect to the fibre axis, which is set parallel to B_0, is determined with the bond orientations, that is, θ_{NH} and θ_{NC} for C$\alpha(i-1)$–C′–N–C$\alpha(i)$ plane or θ_{CO} and θ_{CN} for C$\alpha(i)$–C′–N–C$\alpha(i+1)$ plane. In addition, θ_{CD} is also used for this purpose. The ϕ and ψ angles are

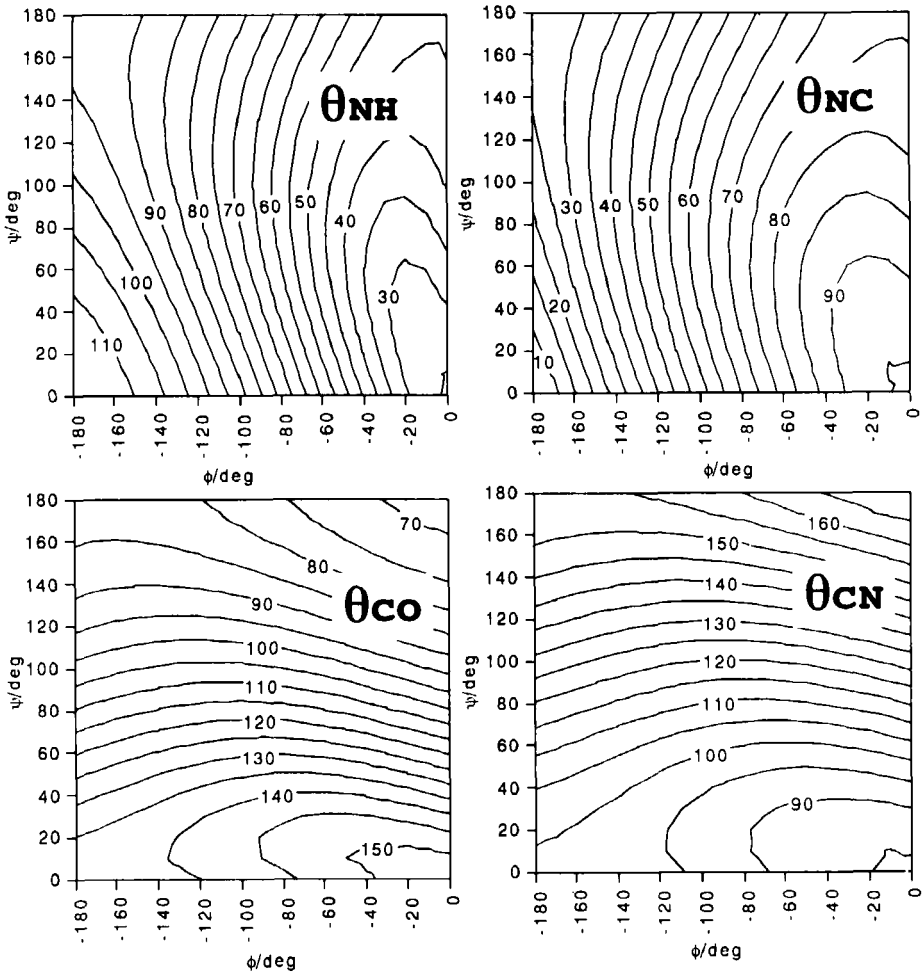

Fig. 4. Theoretical bond orientations of θ_{NH}, θ_{NC}, θ_{CO} and θ_{CN} for the i-residue with respect to FAS (i.e. C$\alpha(i-1)$–C$\alpha(i+1)$ direction) as a function of (ϕ, ψ).

determined from the relative orientation of two peptide plane linkages, and therefore the bond orientations, θ_{NH}, θ_{NC}, θ_{CO}, θ_{CN}, and θ_{CD} can be used for the determination. In a uniaxially oriented protein such as silk fibroin fibre, the angles ϕ, ψ are calculated under the following assumptions:[30]

1. Bond lengths and bond angles are fixed, and the standard values are used.
2. The angle ω of the peptide plane is fixed at 180°.
3. The C$\alpha(i-1)$–C$\alpha(i+1)$ direction with respect to FAS is known.

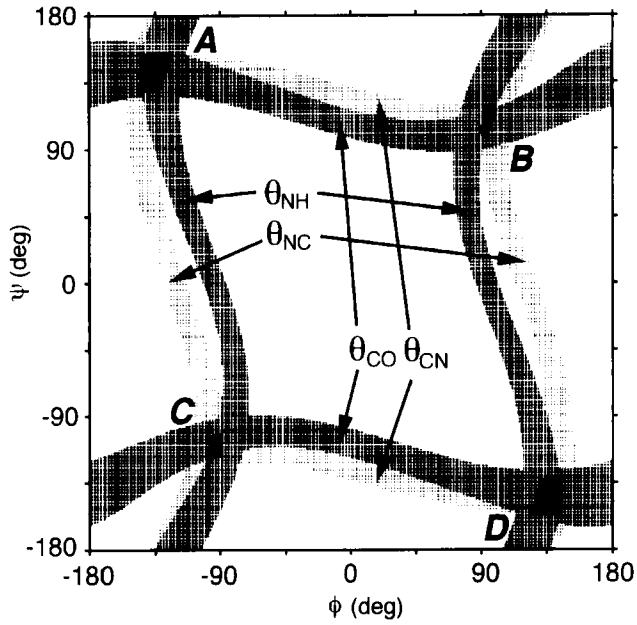

Fig. 5. Combination of four bond orientations (θ_{NH}, θ_{NC}, θ_{CO} and θ_{CN}) of Ala site of silk fibre within $-180° < \phi < 180°$ and $-180° < \psi < 180°$. The width of each line indicates experimental error (±5°). There are two lines indicated by arrows for each bond orientation. The black areas (A–D) indicate the most accurate ϕ–ψ angular constraints satisfied with all four bond orientations within experimental error.

At first, bond orientations, θ, with respect to the C$\alpha(i-1)$–C$\alpha(i+1)$ direction of the protein fibre are calculated as a function of (ϕ, ψ). Figure 4 shows the bond orientations in degrees calculated with standard geometrical parameters as an example. Possible (ϕ, ψ) pairs are compared with the observed bond orientations. In addition, the calculated bond angles directly correspond to the observed ones when the C$\alpha(i-1)$–C$\alpha(i+1)$ direction is parallel with respect to the FAS, such as in the oriented β-sheet structure which appears in the silk fibre. The most accurate (ϕ, ψ) values can be found from the combination of the calculated orientations which satisfy the observed bond orientations. Figure 5 shows a combination of the bond orientations, θ_{NH}, θ_{NC}, θ_{CO}, θ_{CN} for the case of the Ala site of silk fibre. Here, the experimental error for each θ value is introduced and shown as the width of the lines. The black areas indicate the most accurate ϕ–ψ regions which satisfy all of the observed bond orientations within experimental error. By addition of the angular constraint, θ_{CD}, to those obtained from ^{15}N and ^{13}C solid-state NMR, θ_{NH}, θ_{NC}, θ_{CO}, θ_{CN}, a further narrow ϕ–ψ region is determined.

3. PROTEIN FIBRE: SILK

The life cycle of *Bombyx mori* is summarized in Fig. 6.[31] In about 50 days it completes its life cycle of four different metamorphosizing phases; egg or embryo, larva, pupa and adult (moth). Of the life cycle, about half is the larval stage, the only stage at which they consume food (mulberry leaves). Pupation occurs at the end of spinning (or cocoon formation); the latter takes 3–4 days. Thus, silkworm silk is produced primarily at one stage in the life cycle, during the fifth larval instar just before moult to the pupa. The silk from each cocoon comprises a single thread ranging between 10 and 25 μm in diameter, and between 300 and 1200 m in length. Silks are of interest in textiles and other material applications due to their visual appearance, their texture (or "feel"), their environmental stability, and their unique mechanical properties.[31,32]

Silk fibroin from *Bombyx mori* silkworm is a fibrous protein whose primary structure consists largely of a repeating sequence of six residues (Gly–Ala–Gly–Ala–Gly–Ser) n.[33–37] Details of the primary structure are described in ref. 37. Two crystalline forms, silk I and silk II, have been reported as the dimorphs of silk fibroin from *B. mori* in the solid state on the

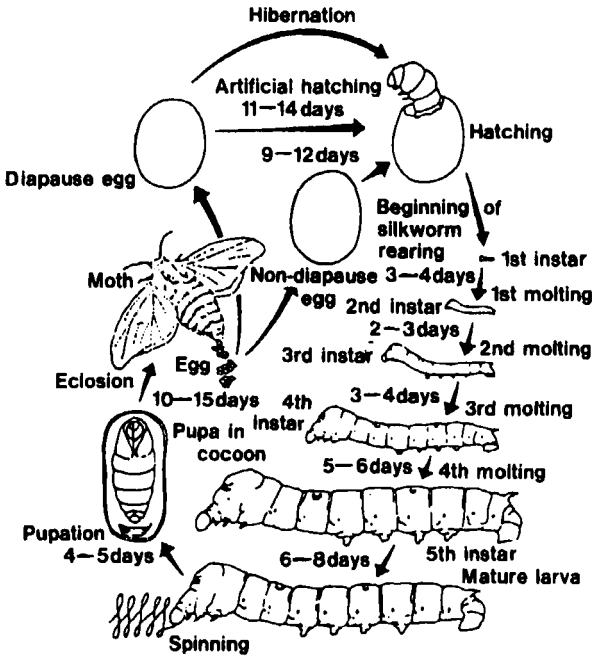

Fig. 6. Life cycle of *Bombyx mori*.

basis of X-ray fibre diffraction,[38–45] electron diffraction,[46] conformational energy calculations,[47,48] infrared,[44,49–51] and ^{13}C and ^{15}NCP/MAS NMR spectroscopies.[52–58] In 1955, Marsh *et al.*[40] reported a fibre diffraction study on native *B. mori* silk fibroin in which the antiparallel β-sheet model was first proposed for the silk II structure, although their proposed structure was based on the quantitative intensity estimation of only six equatorial reflections, and did not yield good agreement between the observed and calculated structure factors (discrepancy factor $R = 37\%$). The structural model was slightly revised by Fraser *et al.*[36,41] Takahashi *et al.*[45] reported a more detailed X-ray fibre diffraction analysis of the silk II structure of *B. mori* silk fibroin fibre with 35 quantitative intensities observed. They considered four kinds of β-sheet models, differing from one another in the mutual orientation of adjacent hydrogen bonded polypeptide chains (parallel *vs* antiparallel) and in the position of side chains on neighbouring stands relative to the plane of the sheet (polar *vs* antipolar). In this terminology, Marsh's model is of the polar–antiparallel type. Based on the R factor obtained for the four types of models, the antipolar–antiparallel β-sheet model was proposed. Fossey *et al.*[48] reproduced the antiparallel β-sheets that constitute the silk II structure from conformational energy computations on stacked sheet structures of poly(L–Ala–Gly). In this section, solid-state NMR analysis is applied to determine the torsion angles of the amino acid residues of silk fibroin fibre.

The less stable form, silk I, has remained poorly understood.[47] In general, attempts to induce orientation of its polymer chain tend to cause silk I to convert to the more stable silk II. If an oriented silk fibroin sample with silk I form can be obtained by the devised preparation method, solid-state NMR analysis for an oriented molecular system described here may be used to determine the atomic coordinate of silk fibroin with the silk I form.

3.1. ^{13}C, ^{15}N and ^{2}H labelling

Selective isotope labelling of silk fibroin is required in these NMR experiments to obtain site-specific structural information. The labelling is achieved biosynthetically through the use of an artificial diet supplemented with the isotope-labelled amino acids during the fifth instar larval stages.[44,59–64] The labelled silk fibroin samples are obtained as cocoon and used for NMR study after removing another silk protein, silk sericin coating the silk fibroin.[31] The method for removal of the silk sericin, that is, the degumming process, is described elsewhere.[44,53,56,59] Figure 7 shows the expanded carbonyl region in the solution ^{13}C NMR spectra of naturally abundant silk fibroin, and [1-^{13}C]Ala and [1–^{13}C]Gly labelled silk fibroins.[59,65] The assignment is described in detail in ref. 59. The labelling ratio was high for both isotope-labelled silk fibroin samples and can be used for the solid-state NMR

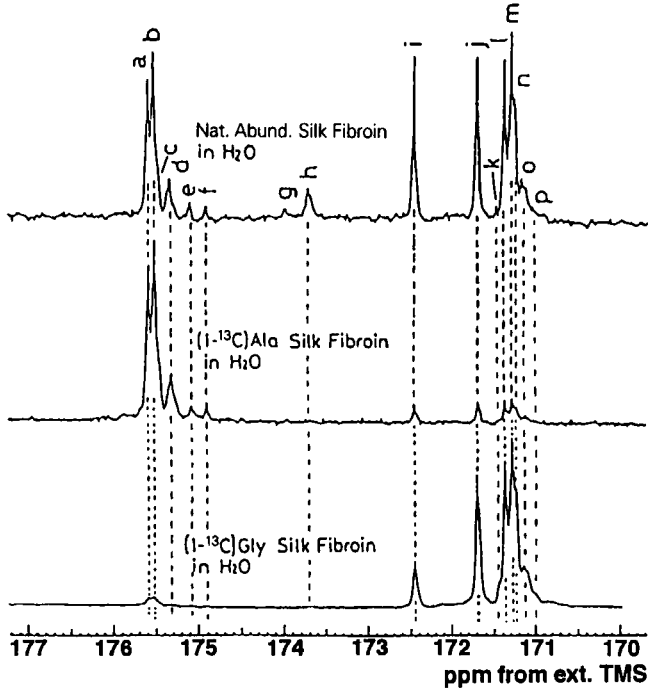

Fig. 7. Solution ^{13}C NMR spectra of naturally abundant and [1-^{13}C]Ala- and [1-^{13}C]Gly-labelled silk fibroin. (a) SGAGA; (b) AGAGS; (c) AGAGT; (d) TGAGA; (e) TGAGV; (f) VGAGT; (g) AGVGA; (h) AGTGA; (i) AGSGA; (j) GAGSG; (k) G; (l) GSGAG; (m) GAGAG; (n) GTGAG; (o) GAGTG; (p) G.

experiment. In the ^{15}N labelling, the [^{15}N]Gly-labelled silk fibroin sample with a sufficiently high labelling ratio was also obtained.[61] However, the labelling ratio was low in the case of [^{15}N]Ala labelling of the sample. This is due to the high activity of the transaminations in silkworms as follows:[66]

$$\text{Ala} + \alpha\text{-ketoglutaric acid} \rightarrow \text{pyruvic acid} + \text{glutamic acid}$$

$$\text{Ala} + \text{oxaloacetic acid} \rightarrow \text{aspartic acid} + \text{pyruvic acid}$$

Although glutamic acid or aspartic acid is added to the artificial diet containing [^{15}N]Ala, in order to avoid the transamination from Ala to these amino acids, the [^{15}N]Ala labelling of the sample was still low.[58] Thus, another isotope labelling method is required.

Cells of the silk gland from *Bombyx mori* silkworm synthesize enormous quantities of silk proteins, fibroin and sericin, during a brief period in larval development without cell division. Silk fibroin is exclusively synthesized in

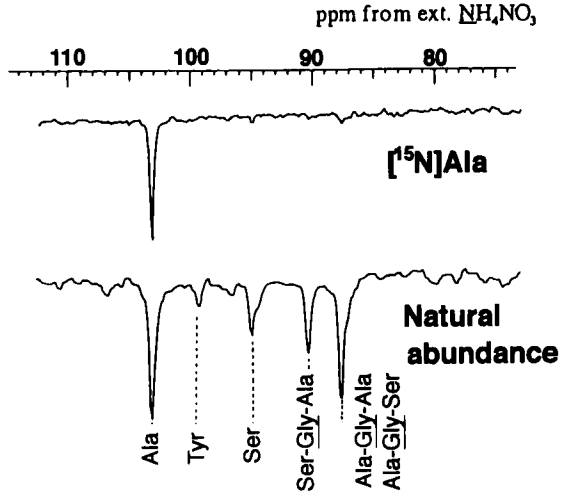

Fig. 8. Solution ^{15}N NMR spectra of natural abundance and [^{15}N]Ala labelled silk fibroins.

the posterior silk gland (each cell produces 1015 fibroin molecules, for example, about 80 μg during a period of only 3–4 days fifth instar larva).[67] Therefore, cultivation of the silk gland[31] was tried to prepare [^{15}N]Ala silk fibroin with a high isotope labelling ratio. The rotation culture of the silk gland was performed by adding [^{15}N]-labelled amino acid to the Grace medium[68] which has been currently used as a medium for insect cell culture.[69–74] The ^{15}N enrichment of the Ala residue in silk fibroin was 20 times with respect to the non-labelled sample, as shown in Fig. 8, which was sufficiently high for the solid-state ^{15}N NMR experiment.[58] Similarly, [^{15}N]Tyr, [^{15}N]Ser and [^{15}N]Val labelled silk fibroins including the ^{15}NGly labelled one with a high labelling ratio were obtained by the culture of the silk gland.[72,74]

The ^{2}H-labelled silk fibroin samples were prepared through the use of an artificial diet supplemented with the isotope-labelled amino acid during the fifth instar larval stage again. Interestingly, a highly ^{2}H-labelled sample of the methyl group of the Ala residue is obtained by only $^{2}H_2O$ administration. The possible metabolic pathway of the incorporation of $^{2}H_2O$ to silk fibroin is summarized in Fig. 9 where the incorporation occurs between fumarate and malate in the TCA cycle.

3.2. ^{13}C–^{15}N dipole–dipole interaction

If ^{13}C–^{15}N dipolar splitting is observed for the oriented fibre samples placed parallel to the magnetic field, the angle between the ^{13}C–^{15}N bond and the

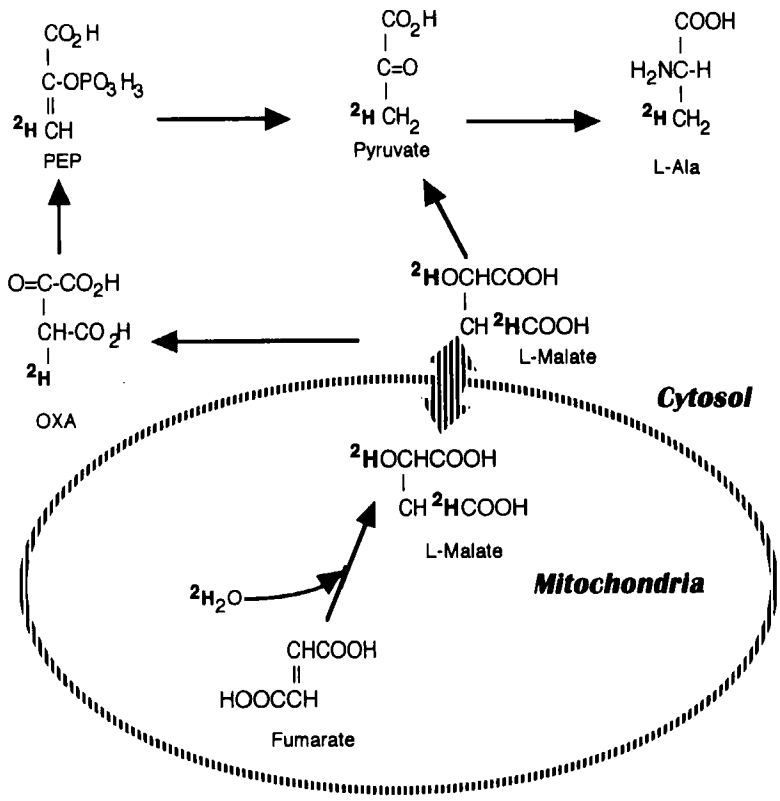

Fig. 9. The metabolic pathway from ^2H_2O to [3-^{2}H]Ala in silkworm larva. The arrow between mitochondria and cytosol indicates that L-malate is permeable. The pathway from fumarate to L-malate in mitochondria corresponds to TCA cycle.

oriented fibre axis can be directly obtained as described in Section 2. For this purpose, it is necessary to prepare a highly isotope doubly labelled [1-^{13}C]Gly–[^{15}N]Ala silk fibroin fibre. The cultivation of the silk glands is performed in the presence of both [1-^{13}C]Gly and [^{15}N]Ala in the medium.

Figure 10 shows the Ala region of the ^{15}N solution NMR spectra of the naturally abundant *B. mori* silk fibroin and the [1-^{13}C]Gly–[^{15}N]Ala doubly labelled silk fibroin in aqueous solution. The [1-^{13}C]Gly–[^{15}N]Ala direct coupling with 15 Hz[76] is observed clearly along with the [1-^{12}C]–[^{15}N]Ala peak in the latter spectrum. Figure 11 shows the ^{15}N solid-state NMR spectra (e) of the block of [1-^{13}C]Gly–[^{15}N]Ala silk fibroin rods whose macroscopic fibre axes were placed parallel to B_0 along with the [^{15}N]Ala powder (d) and the block of singly labelled [^{15}N]Ala silk fibroin rods (b), whose fibre axes were also placed parallel to B_0. Spectrum (c) is produced by the subtraction

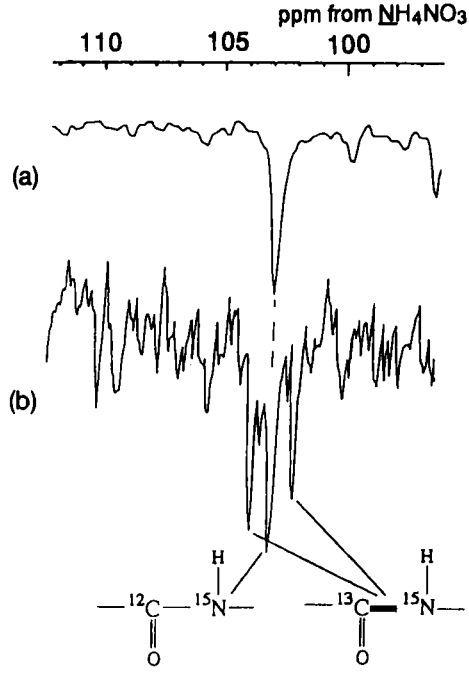

Fig. 10. Solution ^{15}N NMR spectra of (a) naturally abundant Ala residue of *B. mori* silk fibroin and (b) [1-^{13}C]Gly–[^{15}N]Ala doubly labelled silk fibroin in aqueous solution.

of the spectrum (d) from spectrum (e). In spectrum (e), the peak at about 20 ppm is assigned to free [^{15}N]Ala amino acid which is involved in the silk fibroin rods. It is difficult to remove the [^{15}N]Ala by only washing the silk gland after cultivation in water. By subtracting the spectrum (d) from the spectrum (e), the spectrum (c) without [^{15}N]Ala peak is easily obtained. The spectrum (c) consists of a peak of [^{15}N]Ala singly labelled silk fibroin (centre) and two peaks due to [1-^{13}C]Gly–[^{15}N]Ala dipolar splitting. By subtraction of the spectrum (b) from the spectrum (c) and by taking into account the ^{13}C–^{15}N double labelling ratio, the dipolar splitting is determined as $\Delta\nu_{obs} = 1.08 \pm 0.08$ kHz (spectrum (a)). The observed splitting directly reflects the angle, θ_{NC}, between the ^{15}N–^{13}C peptide bond and the macroscopic fibre axis. The angles were 39°, 141°, 76° and 104°. Among these angles, 141° is in agreement with the values, θ_{NC}, reported from X-ray diffraction analysis ($\theta_{NC} = 139.5°$ by Marsh *et al.*,[40] 140° by Takahashi *et al.*[45]). Although it is difficult to determine the structure of *B. mori* silk fibroin from only these dipolar coupling data, the number of unique orientations possible for a given site can be reduced, as will be described below.

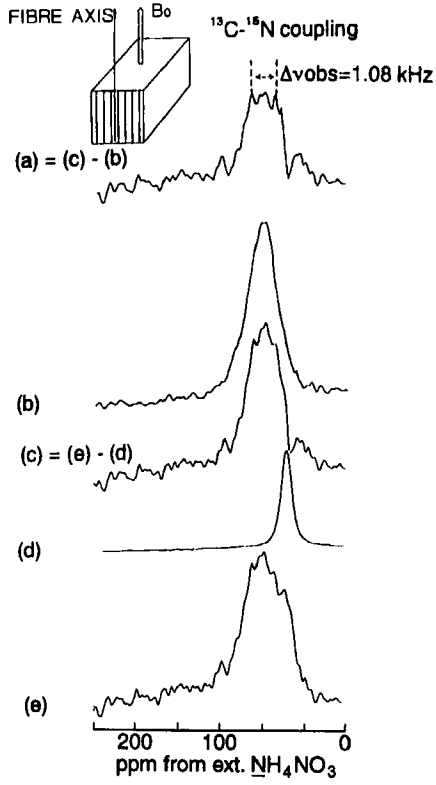

Fig. 11. Solid-state ^{15}N NMR spectra of the oriented block of [1-^{13}C]Gly-[^{15}N]Ala silk fibroin rods (e) whose macroscopic fibre axes were placed parallel to B_0. The spectra of [^{15}N]Ala powder (d) and the block of singly labelled [^{15}N]Ala silk fibroin rods (b), whose fibre axes are also placed parallel to B_0 are also shown. The spectra (a) and (c) are difference spectra, (c) = (e) − (d) and (a) = (c) − (b).

3.3. Solid-state ^{13}C and ^{15}N NMR

In this section, the solid-state NMR method described in Section 2 is applied to determine the torsion angles, ϕ and ψ of the Ala and Gly residues in *B. mori* silk fibroin. Biosynthetic labelling is employed to incorporate [^{15}N]Ala, [^{15}N]Gly, [1-^{13}C]Ala and [1-^{13}C]Gly into silk fibroin. In addition, several ^{13}C–^{15}N doubly labelled peptides synthesized as models of local structure of silk fibroin are used in order to observe the ^{13}C–^{15}N dipolar modulated powder pattern.[9,77]

Figure 12 shows the solid-state ^{13}C NMR spectra of the oriented block of [1-^{13}C]Gly silk fibroin fibres as a function of the angles between the oriented fibre axis and B_0 as an example.[30] The agreement between the simulated and

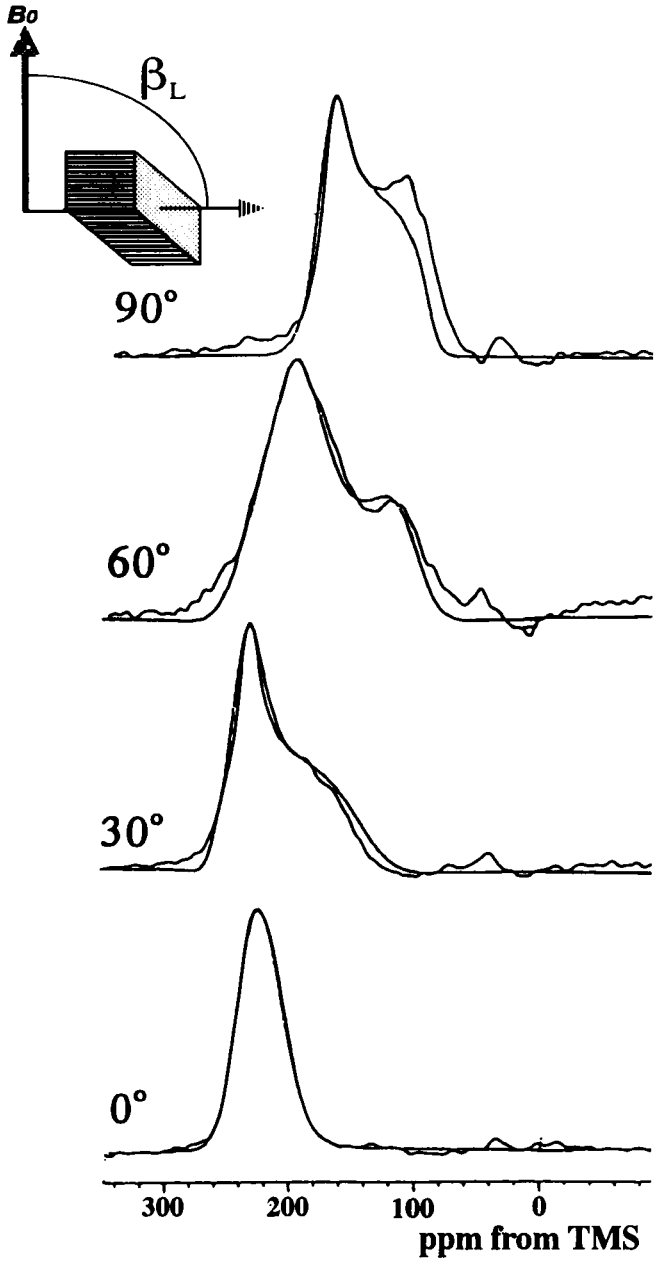

Fig. 12. Solid-state ^{13}C NMR spectra of the oriented block of [1-^{13}C]Gly fibroin fibres as a function of the setting angles, β_L, between the oriented fibre axis and B_0. The best fit theoretical line shapes are superimposed on the experimental spectra.

observed spectra is good, indicating the high reliability of the structural parameters. The Euler angles, α_F and β_F for the carbonyl carbon site of Gly residue are obtained by the simulation. The final values of the Euler angles, α_F and β_F for ^{13}C carbonyl carbons and ^{15}N nuclei of the Gly and Ala residues are summarized in Table 1 as well as the ^{13}C and ^{15}N chemical shielding tensors determined from the simulations of the powder pattern spectra.

Next, the Euler angles, α_D and β_D, are determined with two doubly labelled peptides:[77]

Boc–Gly–Ala-[1-^{13}C]Gly–[^{15}N]Ala–Gly–Ala–OPac

Boc–Ala–Gly-[1-^{13}C]Ala–[^{15}N]Gly–Ala–Gly–OPac

For example, the ^{13}C carbonyl carbon powder pattern of [1-^{13}C]Gly silk fibroin is modified by the dipolar interaction with the ^{15}N nucleus of the Ala residue bonded directly in the peptide. By the simulation which takes into account such a dipolar interaction, α_{DCN} and β_{DCN} values for the carbonyl carbon are determined. The results are also listed in Table 1 together with the values of other sites.

By the combination of α_F and β_F with α_{DNX} and β_{DNX} for the ^{15}N nucleus, the angle of the bond orientation, θ_{NH} between the N–H bond and the fibre axis, and θ_{NC} between the N–C′ bond and the fibre axis, can be determined for the Gly and Ala residues according to equation (8). Similarly, the angle, θ_{CO} between the C′=O bond and the fibre axis, and θ_{CN} between the C′–N bond and the fibre axis can be determined for the ^{13}C carbonyl carbons of the Gly and Ala residues. The values are summarized in Table 2. The error in these θ values is evaluated to be less than 5° by taking into account the experimental error in the simulation, $\alpha_F = \pm 5°$, $\beta_F = \pm 2°$, $\beta_{DX} = \pm 2°$. There is a total of eight possible sets from a pair of α_F and β_F values. A comparison of the θ_{NH} angles calculated from the combination of α_F, β_F, α_{DNH} and β_{DNH} for the ^{15}N site and those determined from ^{15}N–^{1}H dipolar coupling data can

Table 1. ^{13}C and ^{15}N chemical shielding tensors (ppm) and Euler angles (deg.) α_F and β_F determined from silk fibroin fibre sample, and the Euler angles (deg.) α_D and β_D determined from silk model compounds for Gly and Ala residues.

Residue	σ_{11}	σ_{22}	σ_{33}	σ_{iso}	α_F	β_F	α_{DNH}	β_{DNH}	α_{DNC}	β_{DNC}	α_{DCO}	β_{DCO}	α_{DCN}	β_{DCN}
[^{15}N]Gly[a]	22	54	186	87.3	25	72	0	−18	0	104	—	—	—	—
[^{15}N]Ala[a]	33	56	208	99.0	2	70	0	−13	0	109	—	—	—	—
[1-^{13}C]Gly[b]	99	179	245	174.3	0	152	—	—	—	—	90	81	90	35
[1-^{13}C]Ala[b]	96	186	242	174.7	6	165	—	—	—	—	90	89	90	31

[a]ppm from ext. $^{15}NH_4NO_3$.
[b]ppm from ext. TMS.

Table 2. Bond orientations (deg.) of Gly and Ala residues in the silk fibroin fibre determined from Euler angle transformation.

Residue	θ_{NH}	θ_{NC}	θ_{CO}	θ_{CN}
Gly	88.4	40.4	89.1	139.4
Ala	83.0	39.1	89.4	142.7

be used to select the possible sets.[9] In addition, on the basis of the fibre period along to *c* axis (fibre axis) observed from X-ray fibre diffraction[40,45] and conformational energy calculation,[48] corresponding to two residue repeat units along the peptide chain direction, i.e., parallel orientation of $C\alpha(i-1)$–$C\alpha(i+1)$ axis to fibre axis, the unique bond orientations are selected from the calculated bond orientation (Fig. 4). Within the conformational range, $-180° < \phi < 0°$ and $0° < \psi < 180°$, which include the β-sheet structure, the combinations of θ values are selected and listed in Table 2. The C′–N bond orientation of the oriented *B. mori* silk fibroin fibre is also obtained from the $^{13}C'$–^{15}N dipolar splitting of [1-^{13}C]Gly–[^{15}N]Ala doubly labelled sample using solid-state ^{15}N NMR.[26] The reasonable orientations are 39° or 141° for the θ_{NC} of Ala residue. These angles are in agreement with the angle, θ_{NC} for Ala residue selected from Fig. 4, indicating a high accuracy in the selection process of the angle, θ, in Section 2.3.

Figure 5 shows the combination of the bond orientations, θ_{NC}, θ_{NH}, θ_{CN}, θ_{CO} for Ala residue. The width of each line corresponds to the experimental error within ±5° for each θ value. There are four overlapped areas (A–D) which satisfy all of the θ constraints within experimental error, as shown in Fig. 5. However, only one region (A) can be considered to be the β-sheet structure. The best-fitted torsion angles (ϕ, ψ) of the Ala residue for this region A are obtained as (−140°, 142°) based on a minimum error of θ values. The Gly $C\alpha(i-1)$–Gly $C\alpha(i+1)$ distance, which corresponds to a unit cell length along the *c* axis (fibre axis) is calculated to be 6.98 Å by using the best-fitted torsion angles (ϕ, ψ) of Ala determined here, indicating a good agreement with the X-ray fibre diffraction data.[40,45] A similar combination for the Gly site is obtained.

Fujiwara *et al.*[78] applied solid-state NMR to a structural study on oriented [1-^{13}C]Ala silk fibroin fibre from *B. mori*. They found that the Euler angles obtained from the simulated line shapes of the Ala carbonyl group are slightly different from that of a typical antiparallel β sheet,[40] raising questions concerning the accuracy of the current models for silk II structure. However, our data are in agreement with the X-ray diffraction model within experimental error.

As mentioned above, [^{15}N]Ser, [^{15}N]Tyr and [^{15}N]Val *B. mori* silk fibroin were obtained by the cultivation of the silk gland. The torsion angles of these

residues have not been reported because these minor amino acid residues give basically no X-ray diffraction data. The solid-state NMR analysis described here is the only method for obtaining the torsion angles.[74]

3.4. Solid-state ^{2}H NMR

Deuterium solid-state NMR has frequently been used for the characterization of the orientation and dynamics of polymers including proteins during the last decade.[1–6] The advantage of a ^{2}H NMR study of a deuterium-labelled polymer is that its line shape and relaxation are determined principally by the quadrupolar interaction, the coupling between the deuterium nuclear quadrupole moment and the electric field gradients at the nucleus that are due to the electronic distribution of a particular bonding arrangement. Other interactions including the deuteron chemical shielding, together with deuteron–proton and deuteron–deuteron dipolar interactions are about 100 times smaller in magnitude.

In order to use solid-state ^{2}H NMR for the atomic coordinate determination, the angle of the C–^{2}H bond vector relative to the fibre axis is determined for [2,2-$^2H_2$]Gly- and [3,3,3-$^2H_3$]Ala-labelled silk fibroin fibres from *B. mori* with ^{2}H quadrupole echo NMR spectroscopies.[75] This structural information is used complementarily for the determination of the backbone chain conformation of the Gly and Ala residues obtained from solid-state ^{15}N and ^{13}C NMR studies. The ^{2}H-labelled silk fibroin samples are prepared by the oral administration of isotope-labelled amino acids or ^2H_2O to fifth instar larvae, as mentioned above.

Figure 13(A) shows the ^{2}H quadrupole echo spectrum of the oriented block of [2,2-$^2H_2$]Gly-labelled silk fibroin fibre when the fibre axis was set parallel to the magnetic field direction. The ^{2}H quadrupole echo spectrum, Fig. 13(B), of unaligned [2,2-$^2H_2$]Gly-labelled silk fibroin fibre is also observed as a powder pattern. Both spectra are split into doublets; these give the values of the quadrupole splitting, $\Delta\nu_Q$, 117.8 kHz for [2,2-$^2H_2$]Gly site; the values are the same in each case. The full rigid-lattice width of about 126 kHz should be observed when the motion is frozen.[79] Thus, it is concluded that the motion of the methylene groups of the Gly residue is almost frozen at room temperature, which is in agreement with the prediction from the intermolecular hydrogen bonding network in the silk fibroin backbone chain with an antiparallel β sheet conformation.

The quadrupole splittings, $\Delta\nu_Q$, depend on the angle, θ, of C–^{2}H bond vector relative to the magnetic field direction, B_0, according to equation (10). The quadrupole splitting, $\Delta\nu_Q$, 117.8 kHz observed for the oriented block of the [2,2-$^2H_2$]Gly-labelled silk fibroin fibre is the same as the value in the spectrum of unaligned sample as shown in Fig. 13(B). Therefore, if the latter quadrupole splitting is used as the constant, $3e^2qQ/4h$, the angle, θ_{CD}, of the

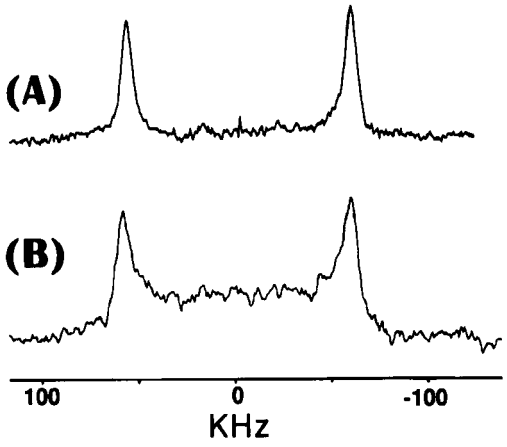

Fig. 13. Solid-state ^2H NMR spectra of (A) oriented and (B) randomly dispersed [2,2-$^2H_2$]Gly labelled silk fibroin fibre.

C–^2H bond vector of Gly residue relative to the fibre axis is calculated as 90°. By taking into account experimental error, ±0.2 kHz, in the determination of the constant because of slightly broader peak than the uniaxially aligned spectrum, the θ values are calculated as 90° ± 2°.

The ^2H solid-state NMR spectra of ordered blocks of the [2,2-$^2H_2$]Gly-labelled silk fibroin fibres are observed as a function of the angle between the fibre axis and B_0 in order to check the validity of the angle, $\theta = 90°$, obtained here. A series of observed spectra are shown in Fig. 14 along with the line shape simulations by assuming $\theta = 90°$. The details of the method of simulation are described elsewhere by Ulrich *et al.*[29,79] The agreement between the observed and simulated spectra is good.

The solid-state ^2H NMR spectrum of the oriented block of the [3,3,3-$^2H_3$]Ala-labelled silk fibroin fibre was also observed. The quadrupole splitting, $\Delta\nu_Q$, is 39.8 kHz and is the same as the value in the spectrum of the unaligned sample. This is the same as the case of the [2,2-$^2H_2$]Gly-labelled silk fibroin fibre. The smaller value of the quadrupole splitting for Ala site indicates the presence of the threefold fast rotation about the Cα–Cβ axis.[60,79] This has also been supported by the observation of the spin–lattice relaxation time, T_1, minimum at about −70 to −80°C in the 90 MHz ^1H pulsed NMR study of *B. mori* silk fibroin fibre.[80] For a rapidly spinning methyl group, the direction of the three individual bonds is time averaged, and the effective bond vector is that of the methyl rotor axis, that is, the C–C$^2H_3$ bond axis relative to the fibre axis. The angle of the Cα–Cβ bond vector of the Ala residue with respect to the fibre axis was calculated to be approximately 90° if the quadrupole splitting observed for the unaligned [3,3,3-$^2H_3$]Ala-labelled silk fibroin sample is used as a constant, $3e^2qQ/4h$.

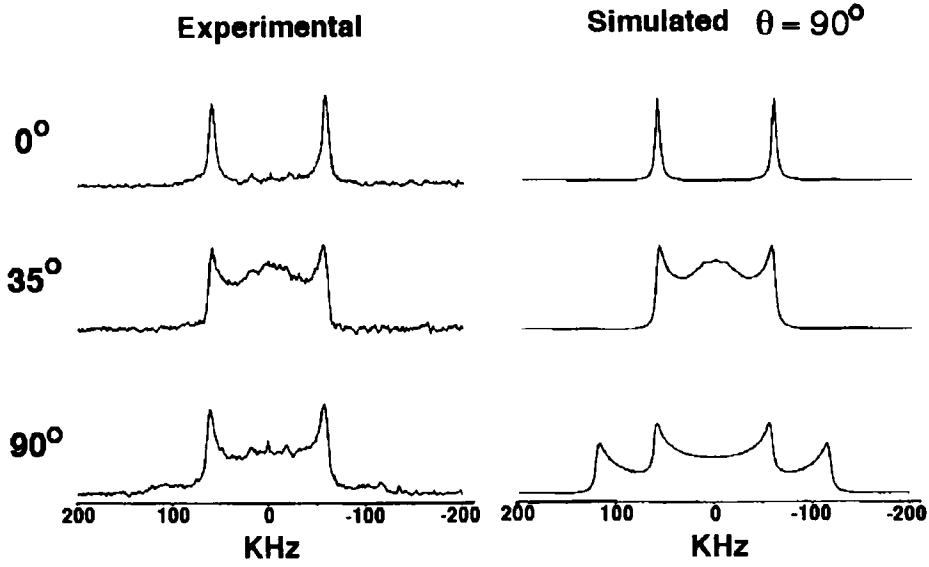

Fig. 14. Experimental and simulated solid-state ^2H NMR spectra of oriented [2, 2-$^2H_2$]Gly-labelled silk fibroin fibre as a function of the setting angles, β_L, between the oriented fibre axis and B_0.

The restricted (ϕ, ψ) region for Gly residue in the Ramachandran map ($-180° < \phi < 0°$, $0° < \psi < 180°$) was obtained as the overlapped region of each region obtained experimentally from the N–H, N–C, C–N, and C–O bond orientations as described above. The ^2H quadrupole echo spectrum of the oriented [2,2-$^2H_2$]Gly-labelled silk fibroin fibre yields the angle, $\theta = 90° \pm 2°$, for the C–$^2H_2$ bond vector of the Gly residue relative to the fibre axis. A further narrow restricted (ϕ, ψ) region for the Gly residue in Ramachandran map is obtained as shown in Fig. 15. Here the width of each line indicates the experimental error, $\pm 5°$ in the determination of the angle, θ, for each bond vector. An overlapping region is obtained for the antiparallel β sheet region. Thus, the angle constraints from solid-state ^2H NMR can be used effectively to narrow the allowed region obtained from previous solid-state ^{13}C and ^{15}N NMR studies. A similar result is obtained for the Ala residue.

4. ORIENTED SYNTHETIC POLYMERS

The solid-state NMR method described above is still useful in the determination of the local structure in oriented synthetic polymers. In this section, first

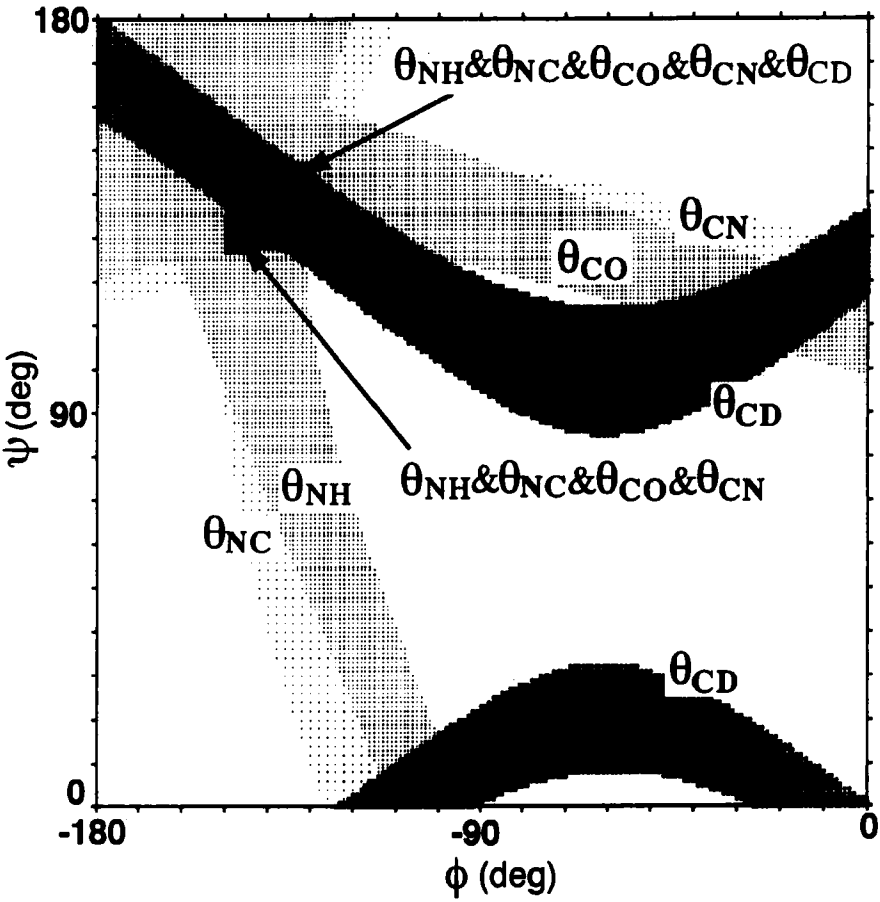

Fig. 15. Combination of bond orientations of Gly site of silk fibre. The black area ($\theta_{NH}\&\theta_{NC}\&\theta_{CO}\&\theta_{CN}\&\theta_{CD}$) indicates the most accurate angular constraints satisfied with both four bond orientations, θ_{NH}, θ_{NC}, θ_{CO} and θ_{CN}, within experimental error ($\pm 5°$) and θ_{CD}. The error of θ_{CD} was estimated within 2°.

the bond orientation will be used as a more simple matter in the structural determination on the basis of the chemical shielding. Namely, the N–H bond orientation relative to the oriented axis can be calculated from the ^{15}N chemical shielding when the oriented axis is set parallel to the magnetic field. Then the solid-state ^{15}N NMR method applied to the determination of silk fibre structure is shown to be also useful in the analysis of the local structure of polyamide fibres. In this case, the samples are not isotope labelled. On the other hand, a carbonyl carbon-labelled PET sample is used for elucidating the local structure of the oriented films with solid-state NMR.

4.1. Qualitative use of chemical shielding anisotropy *vs* bond orientation

The ^{15}N chemical shieldings of the oriented polymers are sensitive to the angle between the N–H bond vector and the fibre axis, θ_{NH}, when the oriented axis of the sample is set parallel to the magnetic field. Therefore, the relationship between the ^{15}N chemical shielding and the angle θ_{NH} can be used for obtaining structural information.

Figure 16 shows the solid-state ^{15}N NMR spectra (solid line) obtained from blocks of oriented natural abundance silk fibroin fibre, PPTA fibre and poly (γ-benzyl L-glutamate) (PBLG) film placed parallel to the magnetic field. Here the orientation film of PBLG was prepared under shearing stress on the glass plate.[81,82] The IR spectrum of the PBLG sample indicates an α-helical conformation,[83] where the angle between the N–H bond and the helix axis is approximately 13°.[36,84] The angle θ_{NH} of the oriented PPTA fibre is calculated from the coordinates reported from an X-ray diffraction analysis as 66°.[85] Thus, it is noted that the ^{15}N chemical shielding changes significantly when the angle θ_{NH} is changed from 13° to 90°.

The observed chemical shielding values of $\sigma_{par} - \sigma_{iso}$ for natural abundance silk fibroin, [^{15}N]Gly-labelled silk fibroin, PPTA, and PBLG are plotted against θ_{NH} for $0° < \theta_{NH} < 90°$ in Fig. 17. When the values α_{DNH} and β_{DNH}, determined for appropriate model compounds are used,[9,17] the angle θ_{NH} can be obtained as functions of α_F and β_F, as described in Section 2. The $\sigma_{par} - \sigma_{iso}$ values are calculated by searching all of the α_F and β_F space (0°–180°) for α_F and β_F pairs that yield simultaneous solutions to both equations (3) and (4) in Section 2. The orientational restriction for silk fibroins and PBLG are shown by the region shown by the horizontal lines in Fig. 17. Similarly, the region shown by the vertical lines is the case of PPTA. The latter region is considerably more narrow than the former one, due to the smaller β_{DNH} value.[17] Thus, the relationship between the ^{15}N chemical shielding and the angle θ_{NH} can be used for the determination of the local structure of polymers containing N–H bonds, such as polyamides. This method is used in Section 4.3.

4.2. Poly(*p*-phenylene terephthalamide) fibre

Poly(*p*-phenylene terephthalamide) (PPTA) is a well-known rigid polymer with high modulus and high tensile strength.[86] Two research groups have determined independently the crystal structure of PPTA fibres using X-ray diffraction.[82,87,88] All reflections of the diffraction pattern are satisfactorily indexed by assuming a monoclinic unit cell with a = 7.80–7.87 Å, b = 5.18–5.19 Å and c (fibre axis) = 12.9 Å. The molecular conformation in the crystalline region is found to be an all-*trans* fully extended structure. This conformation is primarily dictated by the extensive conjugation in the chain.

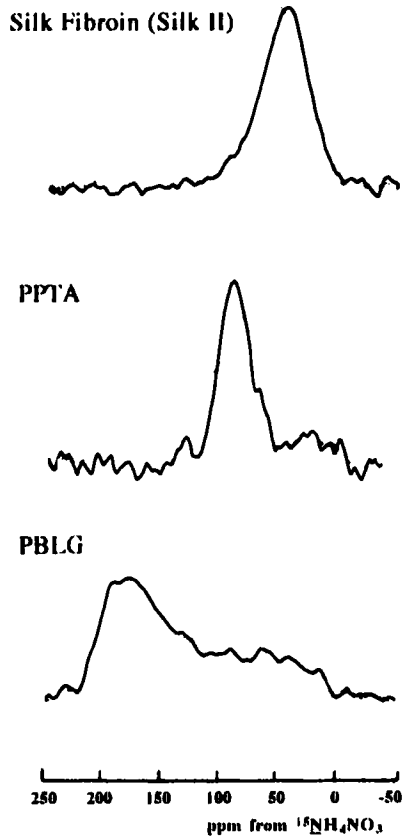

Fig. 16. Solid-state ^{15}N NMR spectra of the oriented block samples of natural abundance *B. mori* silk fibroin, poly(*p*-phenylene terephthalamide) (PPTA), and poly(γ-benzyl L-glutamate) (PBLG).

The resonance effect has the tendency to stabilize the coplanarity of the amide groups and the benzene rings. Counteracting this effect is the steric hindrance between the oxygen and hydrogen atoms of the amide group and the ortho-positioned hydrogen atoms of the *p*-phenylene diamine and terephthalic segments, respectively. Because of these restrictions, the polymer chain adopts an extended conformation with alternating amide group orientations.[86]

In this section, the solid-state ^{15}N NMR method developed here is used to elucidate the atomic resolution structure of PPTA fibres.[17] For this purpose, the N–H and N–C′ bond directions of PPTA have been determined with respect to the fibre axis, as well as the orientational distribution of the fibre axis, *p*. These structural parameters of the polymer chain are compared with those previously obtained by X-ray diffraction.[82]

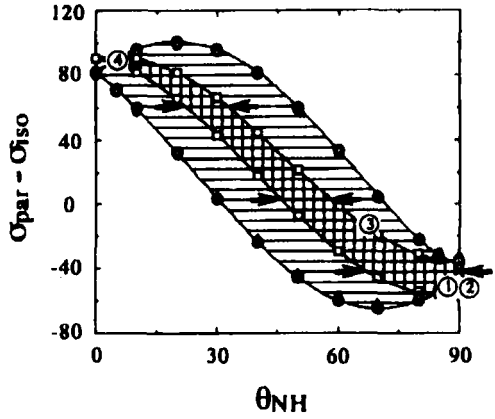

Fig. 17. Ranges of $\sigma_{par} - \sigma_{iso}$ *vs* θ_{NH} (0–90°) searched over all α_F and β_F space. The regions shown by the horizontal lines are for naturally abundant silk fibroin (○), [^{15}N]Gly-labelled silk fibroin (●) and PBLG (△), and the region shown by the vertical lines is for PPTA (□). The θ_{NH} values and the observed $\sigma_{par} - \sigma_{iso}$ values for (1) natural abundance silk fibroin, (2) [^{15}N]Gly-labelled silk fibroin, (3) PPTA and (4) PBLG are included. The three ranges for $\sigma_{par} - \sigma_{iso}$ determined from the spectrum of the block PMIA sample are represented by pairs of arrows.

From spectral simulation of the powder pattern, the chemical shielding tensor elements are determined as $\sigma_{11} = 48 \pm 3$ ppm, $\sigma_{22} = 68 \pm 3$ ppm, $\sigma_{33} = 195 \pm 5$ ppm and $\sigma_{iso} = 104 \pm 4$ ppm. The σ_{iso} value is consistent with the chemical shielding from the ^{15}N CP/MAS spectrum (107 ± 0.5 ppm). The Euler angles, $\alpha_{DN_{C'}}$ and $\beta_{DN_{C'}}$, which transform the ^{15}N chemical shielding tensor relative to the N–C′ bond direction are determined from the ^{15}N powder pattern of [1-^{13}C]-^{15}N doubly labelled benzanilide (Fig. 18) as 30° and 108°, respectively. Then the α_{DNH} and β_{DNH} values are calculated as 0° and −7° respectively, using 115° for the H–N–C′ bond angle.[82]

Figure 19 shows the ^{15}N CP NMR spectra of the oriented PPTA block sample, whose fibre axis is set parallel (A) and perpendicular (B) to B_0. Although the narrow line width of the peak in Fig. 19(A) indicates a highly oriented PPTA sample, if the fibres were perfectly aligned with respect to the magnetic field, a symmetric spectrum would be observed for both orientations. However, the observed line shape when the fibre axis is perpendicular to B_0 is clearly asymmetric and a fibre axis distribution is therefore introduced. The best-fit parameters determined from simulations (broken lines) of the observed spectra in Fig. 19 are $\alpha_F = 45°$, $\beta_F = 61°$ and $p = 19°$.[17]

Then the θ_{NH} and $\theta_{NC'}$ values were calculated. These coincide with data from an X-ray diffraction analysis: $\theta_{NH} = 68°$ and $\theta_{NC'} = 49°$ from NMR, and $\theta_{NH} = 66°$ and $\theta_{NC'} = 49°$ from X-ray diffraction analysis. A similar structural analysis with solid-state ^{15}N NMR was performed for poly(*m*-xylene-α,α'-diyladipamide) and nylon 66.[89]

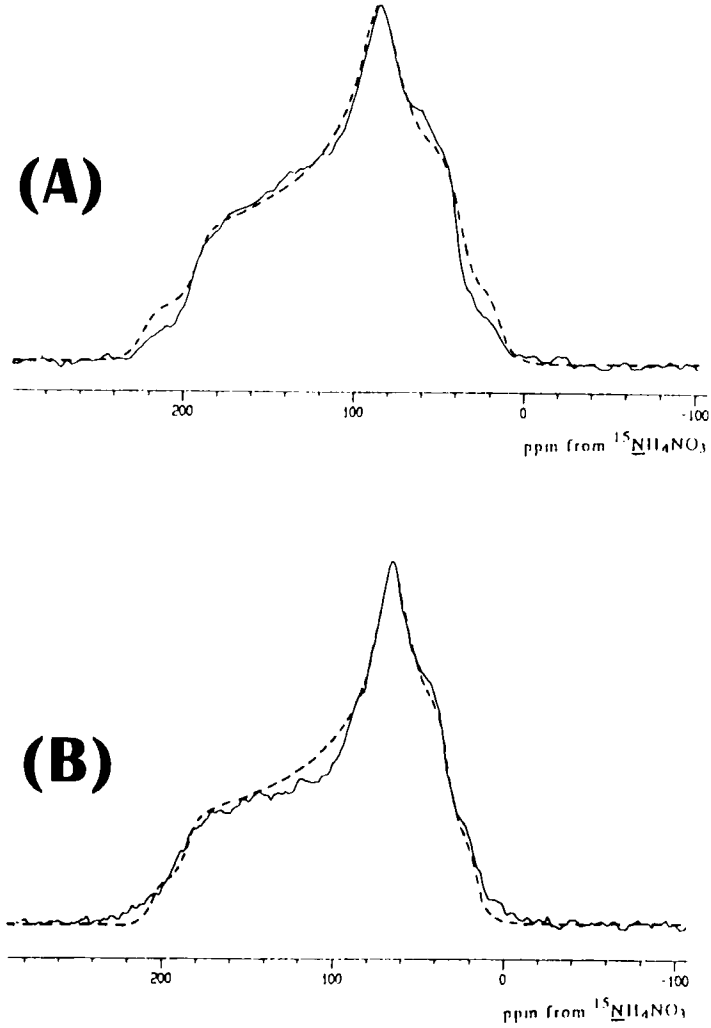

Fig. 18. Observed (solid line) and calculated (broken line) ^{15}N powder pattern spectra for [^{13}C–^{15}N]benzanilide at (A) 27.25 MHz and (B) 40.4 MHz.

Most recently, the influence of the application of macroscopic tensile stress to the PPTA fibre on the microscopic dynamic structure has been studied with deuterium NMR.[90] Figure 20 shows quadrupolar echo line shapes of the PPTA-T($^2H_4$) fibre at room temperature for the three delay times of 40, 80 and 160 μs between the pulses. No significant tension was applied to the sample for the spectra displayed in the left-hand column, while a tensile stress of approximately 8 g d $^{-1}$ or 55% of the breaking strength of the fibre bundle was applied for the data in the right column. By comparison of the stressed

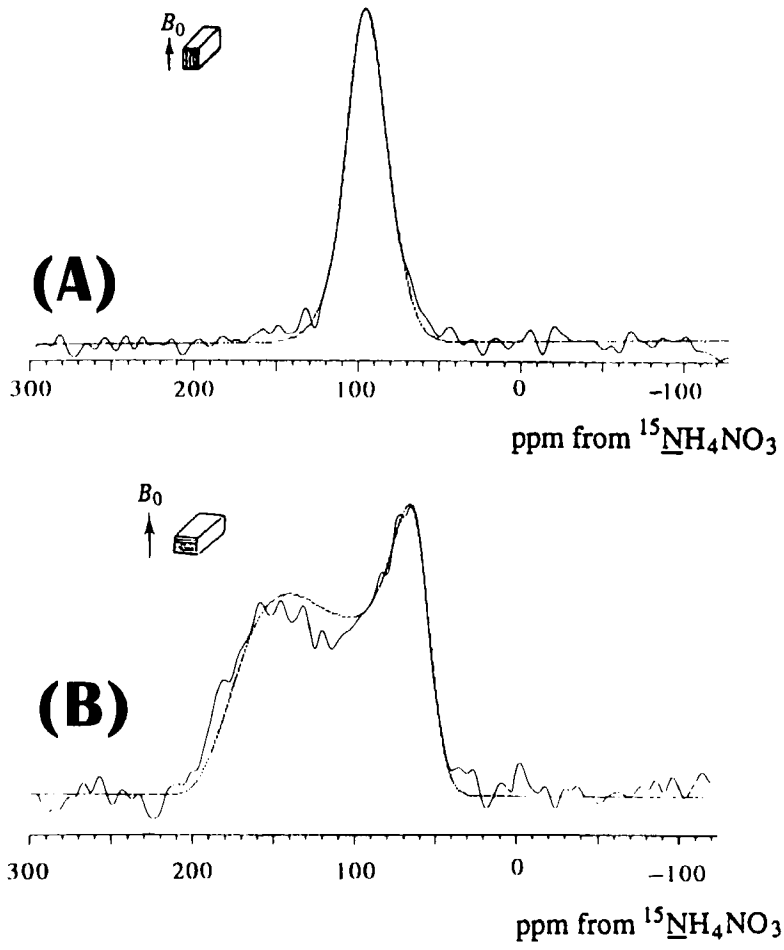

Fig. 19. Experimental (solid line) and calculated (broken line) ^{15}N solid-state NMR spectra of the oriented PPTA block sample set (A) parallel and (B) perpendicular to B_0.

and non-stressed line shapes for $\tau = 40\,\mu s$, it is obvious that tensile stress does not result in a significant change in the orientational distribution of the fibre, since the positions of the broad singularities in the line shapes are virtually unchanged. However, one visible effect is an increase, with stress, of the intensity of the inner singularities associated with fast flipping phenylene rings. In addition, the differences in the τ-dependence of the line shapes as a function of stress support the interpretation that the stress-induced changes of the line shape are caused mainly by differences in motional characteristics rather than by orientational aspects. Thus, informa-

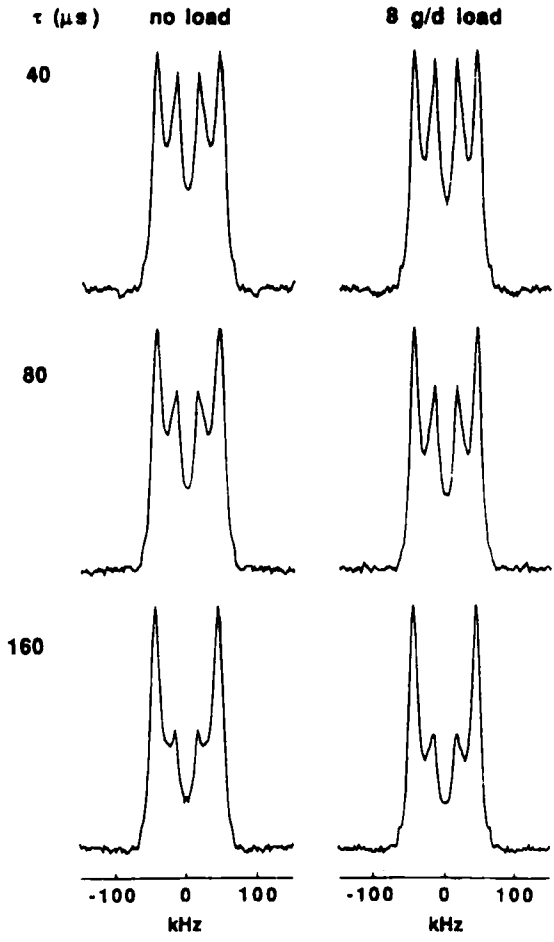

Fig. 20. Solid-state ^2H NMR spectra (symmetrized) of heat-treated PPTA-T(d_4) fibre oriented parallel to the external magnetic field as function of the pulse spacing between quadrupolar echo pulses at room temperature. Line shapes acquired with no applied tensile stress (left column) are compared to line shapes for the fibre under a tensile stress of the order of 55% of the breaking strength (right column).

tion on microscopic dynamics is required for the interpretation of the macroscopic mechanical deformation of PPTA fibre.

4.3. Poly(*m*-phenylene isophthalamide) and poly(4-methyl-*m*-phenylene terephthalamide) fibres

Aromatic polyamides, poly (*m*-phenylene isophthalamide) (PMIA) and poly (4-methyl-*m*-phenylene terephthalamide) (P4M-MPTA) have excellent thermal stability and high tensile modulus. The structures of these polyamides

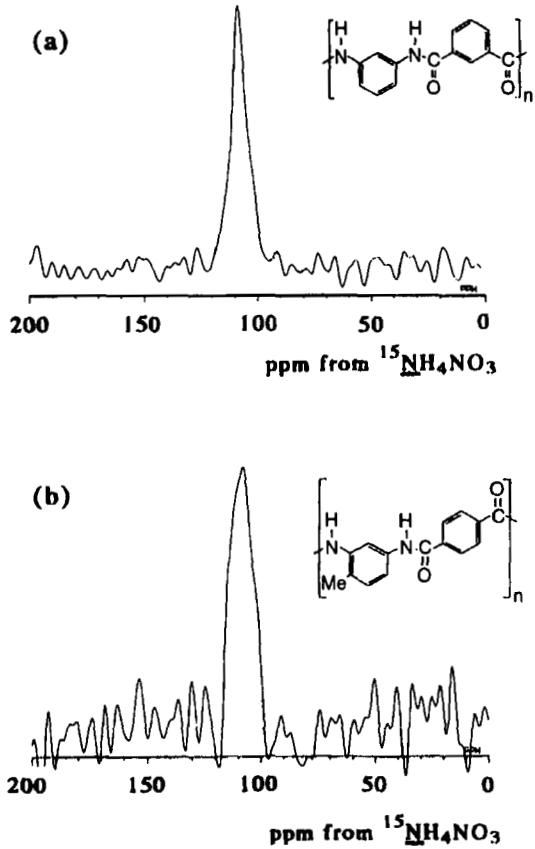

Fig. 21. ^{15}N CP/MAS NMR spectra of poly (*m*-phenylene isophthalamide) (a) (PMIA) and poly(4-methyl-*m*-phenylene terephthalamide) (b) (P4M-MPTA) powder samples.

in the crystalline domain have been reported by using X-ray diffraction methods.[91,92] However, the fraction of the non-crystalline domain has been reported as approximately 70% for PMIA[91] and 75% for P4M-MPTA.[92] Thus, the atomic level analysis of these polymer structures in the non-crystalline domain is especially required.

In this section, the solid-state ^{15}N NMR analyses of PMIA and P4M-MPTA fibres whose fibre axes are parallel to the magnetic field are described to clarify the non-crystalline domain structure through the determination of the angle θ_{NH} and the fraction of the assembly of the fibre axes which have different θ_{NH} values.

Figure 21 shows the ^{15}N CP/MAS NMR spectra of PMIA (a) and P4M-MPTA (b) powders. The ^{15}N chemical shielding values are 108 ppm

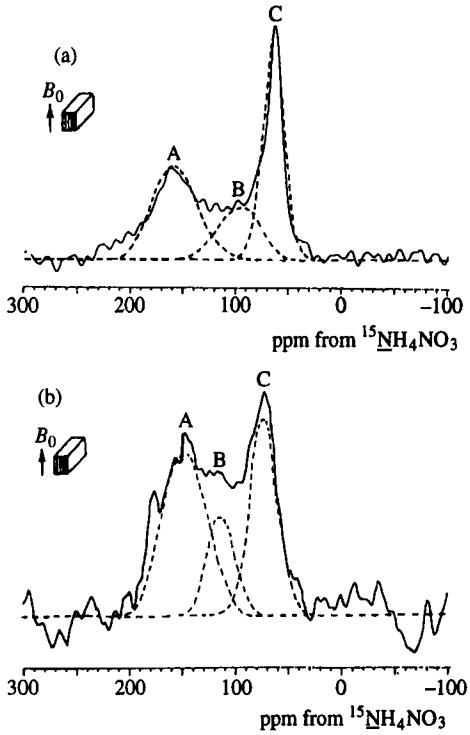

Fig. 22. Solid-state ^{15}N NMR spectral simulation of (a) PMIA and (b) P4M-MPTA oriented samples set parallel to B_0. The solid and broken lines represent observed and simulated spectra, respectively. The simulated peaks are composed of three components A, B and C.

(PMIA) and 107 ppm (P4M-MPTA). These peaks are asymmetric and broad (especially for P4M-MPTA), indicating the presence of a non-crystalline domain in addition to the crystalline domain. Actually, the oriented PPTA powder with more than 80% crystalline domain gives a sharp and narrow single peak.

Figure 22 shows the solid-state ^{15}N NMR spectra of oriented blocks of PMIA and P4M-MPTA fibres placed parallel to the applied magnetic field (solid line). There is a sharp peak at approximately 70 ppm with broad peaks towards higher frequencies for each spectrum. This spectral tendency is the same between both spectra, although the intensity of the broad peak increases in the P4M-MPTA sample. As mentioned in Section 4.1, the ^{15}N chemical shieldings of the oriented polymers placed parallel to the magnetic field are sensitive to the angle θ_{NH}, and the plot of the ^{15}N chemical shielding *vs* θ_{NH} (Fig. 17) can be used to determine this angle. In order to resolve the spectra, the peak simulations are performed by assuming them to be

Table 3. The ^{15}N CP parallel spectral parameters for oriented poly(*m*-phenylene isophthalamide) (PMIA) and poly(4-methyl-*m*-phenylene terephthalamide) (P4M-MPTA) block samples placed parallel to the supplied magnetic field. The fraction of each peak and the range of the angle θ_{NH} between the N–H bond and the fibre axis are also listed (see text).

Oriented block sample	Fraction (%)	δ (ppm)	Half-height width (Hz)	θ_{NH} range (deg.)
PMIA				
A	37	160	1000	25–35
B	20	105	880	46–58
C	43	68	400	67–90
P4M-MPTA				
A	61	149	1100	31–42
B	18	106	520	44–56
C	21	72	520	66–90

Gaussian. The presence of at least three peaks in each spectrum is suggested from the peak simulation (broken line) as shown in Fig. 22, where the three peaks are denoted A, B, C in order of decreasing frequency. The fraction of each peak determined by the simulation is summarized in Table 3, along with the chemical shielding and the half-height width. As indicated by arrows in Fig. 17, it is possible to determine the range of θ_{NH} values for each peak and these are also listed in Table 3. The angles θ_{NH}, 75° or 80° for PMIA, and 75° or 94° for P4M-MPTA are determined for the peak C in both spectra. These are in agreement with the X-ray diffraction data and therefore the peak C can be assigned to the ^{15}N nuclei of these samples in the crystalline domain. This assignment seems reasonable, judging from the fact that the peak C is the narrowest of the three peaks. However, the fraction of the peak C is slightly different from those of the crystalline domain determined by the X-ray diffraction method, 30% for PMIA and 25% for P4M-MPTA.[91,92] This difference between X-ray diffraction and the solid-state NMR results might come from ambiguity in the determination by the X-ray diffraction method, that is, in the determination of the base line coming from the non-crystalline domain. However, if the sequence of the chains with similar θ_{NH} values is too short to form the domain which is recognized as a crystalline domain from the viewpoint of X-ray diffraction, the disagreement between the NMR and X-ray diffraction can be interpreted. Namely, solid-state NMR gives more local structural information than does X-ray diffraction.

The peaks A and B in both spectra clearly originate from the non-crystalline domain in the samples, indicating that the non-crystalline domain reported from X-ray diffraction has relatively ordered structure rather than a randomly distributed one. This conclusion derived from NMR is also supported by the conclusion that the non-crystalline domain is highly oriented

in aromatic polyamides on the basis of the X-ray diffraction studies.[91,93] The relatively broad peaks show a wider distribution for each θ_{NH} value compared with the peak C, which is also reasonable. The chemical shieldings of the peaks A and B are almost the same between PMIA and P4M-MPTA. This indicates that the local structure in the non-crystalline domain is similar for these polyamide fibres. It has been reported that the fraction of non-crystalline domain in P4M-MPTA sample is higher than in the PMIA sample. The increase in the fraction of non-crystalline domain comes predominately from the contribution of peak A, that is, the structure with $\theta_{NH} = 31°–42°$, which is derived from the solid-state NMR experiment.

If the non-crystalline domain represents a random distribution of θ_{NH} values in the oriented PMIA and P4M-MPTA samples, the ^{15}N CP NMR spectrum would be a powder pattern. Clearly, the non-crystalline domains are not composed of randomly dispersed polymers, but exhibit a significant degree of order with remarkably well-defined θ_{NH} values. In addition, the ^{15}N CP/MAS NMR spectra shown in Fig. 21 give limited structural information because only a single peak is basically observed in each spectrum, but the solid-state ^{15}N NMR spectra of oriented blocks of these fibres give more fruitful structural information. The latter comes from the high sensitivity of the ^{15}N chemical shielding to the bond orientation, θ_{NH}.

4.4. Poly(ethylene terephthalate) film

Poly(ethylene terephthalate) (PET) is a synthetic polymer widely used for fibres, films, bottles, injection moulded parts, and other products.[94] The orientational ordering in deuterated PET films drawn by necking has been studied by ^{2}H NMR and the advantages of ^{2}H NMR are discussed in comparison with other methods, as regards characterizing the amorphous regions.[95] Multidimensional Direction Exchange with Correlation for Orientation-Distribution Evaluation and Reconstruction (DECODER) NMR experiments have also been applied to determine molecular orientation distributions in PET thin films and fibres.[5,96] For example, in PET fibres, direct reconstruction produces an orientation distribution that is at least bimodal, with 60% of the chains highly oriented with a full-width-at-half-maximum height (FWHM) of 20°. The angle between the phenylene *para* axis and the fibre axis is determined to be $18 \pm 4°$. For uniaxial films, the FWHM of the orientation distribution is measured as 85°.

However, ^{13}C CP/MAS NMR relaxation experiments have been applied to determine the molecular motions of PET samples by several researchers.[97–102] Most recently, on the basis of a relaxation study, Gabrielse *et al.*[102] have proposed a three-region model for semicrystalline PET yarns, these being NMR crystalline, rigid NMR amorphous, and the mobile NMR amorphous region.

In this section, solid-state ^{13}C NMR spectra of uniaxially oriented PET films with different draw ratios are reported as a function of the angle between the machine draw direction and the magnetic field, in order to allow analysis of the PET samples in terms of local structural ordering.[19] Our attention is focused on the carbonyl carbons (which have a large chemical shielding anisotropy) by the use of carbonyl carbon ^{13}C-labelled PET samples. Under these conditions the contribution of the aromatic carbon peaks which overlap with the carbonyl carbon peak in the natural abundance ^{13}C CP spectrum can be neglected in the analysis of the ^{13}C NMR results.[96,102–104] Here, the macroscopic fibre direction is assumed to be the same as that of the machine draw direction (MD) of PET films.

The determination of the angles between the ^{13}C PAS and the molecular symmetry axis frame of reference was made by FPT-INDO method[105] with the coordinates of PET.[106] As shown in Fig. 23, the σ_{11} axis is approximately perpendicular to the O–C=O plane. The σ_{33} makes an angle of 29° with the C–O bond direction and σ_{22} is very close to the C=O bond direction in the O–C=O plane. These are very close to the values reported for protonated carboxyl groups.[107,108]

PET polymers were prepared by a stagewise melt polymerization process which consists of transesterification, prepolymerization, and finishing polymerization steps. In the transesterification stage, carbonyl carbon ^{13}C-labelled dimethylterephthalate was used.

The chemical shielding tensor elements of the carbonyl carbon of PET are determined as $\sigma_{11} = 114$ ppm, $\sigma_{22} = 130$ ppm and $\sigma_{33} = 252$ ppm. The powder pattern spectrum of the PET powder prepared from uniaxially drawn films with a draw ratio of five is also determined as $\sigma_{11} = 117$ ppm, $\sigma_{22} = 131$ ppm and $\sigma_{33} = 254$ ppm. The σ_{iso} value is 167.3 ppm for PET powder prepared from film (draw ratio five), while the value is 165.3 ppm

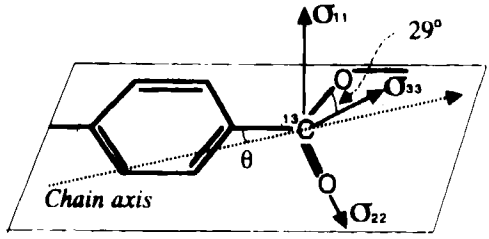

Fig. 23. The PAS orientation of carboxyl carbon relative to the bonds of interest in PET. The σ_{11} axis corresponds to the normal of the carbonyl (O–C=O) plane. The σ_{22} axis set parallel to the carbonyl direction (C=O) in the carbonyl plane. The σ_{33} axis is perpendicular to both σ_{11} and σ_{22} directions. These angles were determined from the results of an FPT-INDO calculation for the appropriate model compounds of PET. The angle θ between the phenylene *para*-C–C axis and the chain axis is also shown.

for amorphous PET powder. This is in agreement with the ^{13}C CP/MAS observation of PET where the carbonyl peak from the crystalline region is shielded slightly to low frequency from the corresponding resonance of the amorphous region.[102]

The solid-state ^{13}C NMR spectra of uniaxially oriented PET films (draw ratio 3, and drawn at 45°C) are shown in Fig. 24 as a function of the angle, β_L, between the machine draw direction (MD) and the magnetic field. The glass transition temperature T_g of PET has been reported to be about 68°C.[96,109] Thus, the oriented PET film used here was drawn at a temperature lower than T_g. It is clear from the angle-dependent spectra that they cannot be explained by assuming only a single angular-dependent component in the material examined. For example, the small peak at about 130 ppm between $\beta_L = 0°$ and 30° indicates strongly the presence of an angle-independent powder pattern component in this sample. By the use of spectral simulation (dotted lines in Fig. 24), the fraction of the powder pattern and the oriented components in the obtained spectra are determined as 35% and 65%, respectively. For the latter component, the structural parameters are determined as $\beta_F = 18 \pm 6°$ with $p = 22°$. The appearance of a series of simulated spectra as a function of β_L is strongly dependent on the angle β_F and, therefore, the angle β_F can be determined with a good precision by simulation. Chmelka *et al.*[96] have determined the angle (β_P in their paper) between the chain axis and σ_{33} direction at the carbonyl carbon site from the 2D ^{13}C DECODER spectra of drawn PET fibre as $18 \pm 7°$. Since β_F as defined in this case has the same direction as β_P, there is agreement between the two studies with regard to the angle between the chain axis and the σ_{33} direction at the carbonyl carbon site. However, the spectral change as a function of β_L is insensitive to the angle α_F in the simulation. Walls[110] applied ATR-IR to the examination of the conformational change by the sample orientation in uniaxially drawn PET films. A remarkable increase in the absorbance of the PET vibration at 1340 cm^{-1} (CH_2 wagging vibration from the glycol segments of the polymer chain in the *trans* conformation) and a decrease in the absorbance at 1370 cm^{-1} (*gauche*) are observed for a uniaxial draw ratio between 2 and 3. The most significant changes in extended *trans* content occur with samples in this uniaxial draw ratio range. In addition, the conjugated system

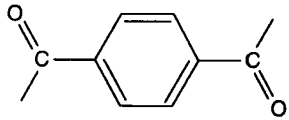

is substantially planar.[106] These considerations suggest that the angle α_F should be approximately 90°. In this case, $22 \pm 6°$ is obtained as the angle θ between the phenylene *para* axis and the chain axis in the oriented chain of uniaxially aligned PET films (draw ratio of 3, drawn at 45°C). Within experimental error, this is in agreement with the reported values, 20° by

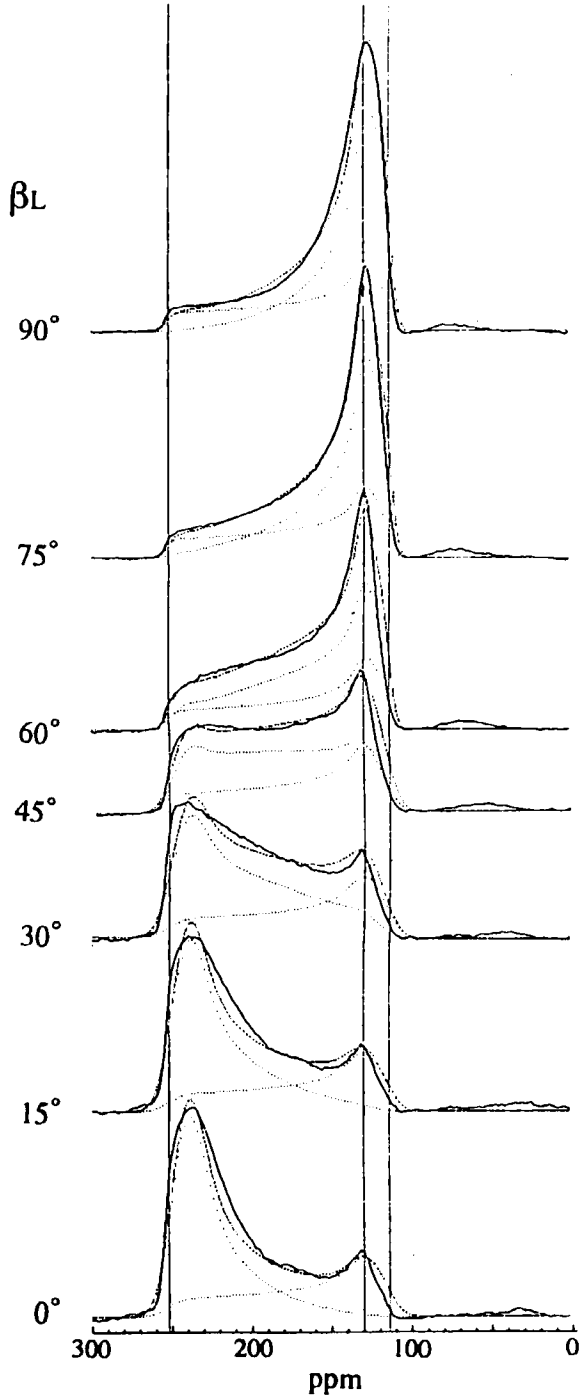
βL
90°
75°
60°
45°
30°
15°
0°
300
200
100
0
ppm

Arnott and Wonacott,[111] 24° by Rober and Zachmann[95] and Harbison *et al.*[104] and 18° by Chmelka *et al.*[96]

Next, the structures of the oriented samples with draw ratios 2, 3, 4, 5 and 5.66 drawn at 80°C (above T_g) are studied. The ^{13}C CP NMR spectra of a PET sample (draw ratio 2 when the sample is drawn at 80°C, i.e., above T_g) are independent of the angle β_L and are typical powder patterns. Thus, the structure of this sample is found to be completely disordered. On the other hand, the ^{13}C CP NMR spectra of PET samples with draw ratios 3 and 4 are analysed by assuming two components in the samples, which is similar to the case of uniaxially oriented PET films (draw ratio 3, drawn at 45°C) in Fig. 24.

The assumption of two components can no longer be retained when considering spectra obtained with a PET sample with a draw ratio of 5 (Fig. 25). There are additional broad peaks in these spectra (marked by arrows) for $\beta_L = 15°$ to 60°, indicating the presence of a highly oriented additional component beyond the oriented component observed in the spectra of the samples with draw ratios of 3 and 4. By assuming three components (one angle-independent, the remainder with spectra that are orientation angle-dependent), the spectra of the PET sample with a draw ratio of 5 could be simulated, as shown in Fig. 25. The contribution of the powder pattern to the spectrum was thus determined to be 55%. The oriented component which corresponds to the oriented portion of samples with draw ratios of 3 and 4 is found to be 33%, with $\alpha_F = 90°$, $\beta_F = 24 \pm 10°$, and $p = 24°$. The fraction of highly oriented component of the sample is 12% with the structural parameters $\alpha_F = 90°$, $\beta_F = 16° \pm 6°$ and $p = 5°$. The spectral character of the third component reproduces very well (the presence of the peaks is marked by arrows in Fig. 25). The fraction of this component is found to increase with heat treatment of the PET sample, as described below. The structural parameters obtained by analysis of ^{13}C spectra are the same for samples with draw ratios of 5 and 5.66 (data are not shown). However, the fraction of each component changes to 50% for the powder pattern, 38% for the low-oriented component, and 12% for the highly-oriented component.

The structural parameters obtained for uniaxially oriented PET films are summarized in Tables 4 and 5. The three components observed in the spectra of well-oriented PET samples might correspond to the three-region model

Fig. 24. Solid-state ^{13}C NMR spectra of carbonyl carbon ^{13}C-labelled uniaxially drawn (×3 at 45°C) PET film as a function of β_L, the angle between the draw direction and the magnetic field. Solid and dotted lines show observed and calculated spectra, respectively. The fractions of the two components, amorphous (35%) and oriented (65%) were determined from computer simulations of the observed NMR line shapes. The structural parameters $\alpha_F = 90°$, $\beta_F = 18 \pm 6°$, and distribution of FAS axis (p) = 22° are found to be characteristic of the oriented component.

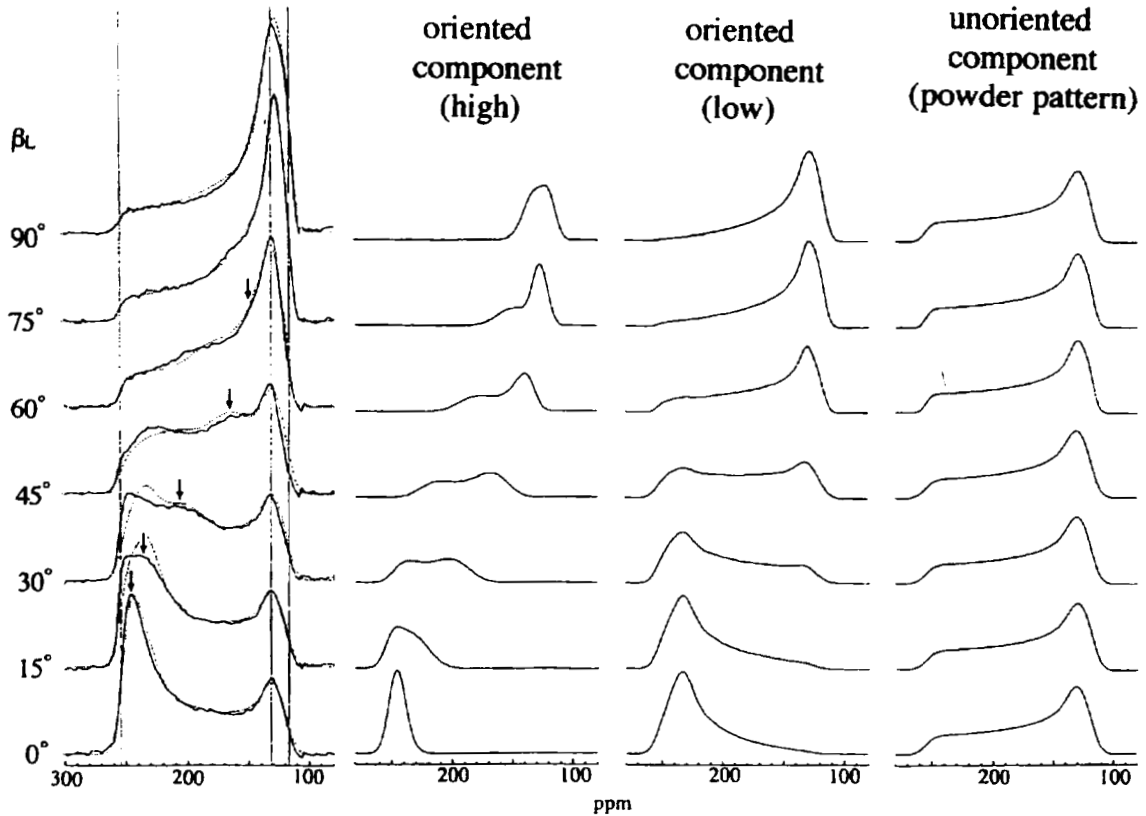

Fig. 25. Solid-state ^{13}C NMR spectra of carbonyl carbon ^{13}C-labelled uniaxially drawn (×5 at 80°C) PET film as a function of β_L, the angle between the draw direction and the magnetic field. Solid and dotted lines show observed and calculated spectra, respectively. The fractions of three components, one unoriented (55%) and two oriented (33 and 12%), were determined by simulation. The structural parameters were $\alpha_F = 90°$, $\beta_F = 24° \pm 10°$ and $p = 24°$ (low-oriented component), and $\alpha_F = 90°$, $\beta_F = 16° \pm 6°$ and $p = 5°$ (highly oriented component), respectively.

Table 4. Fraction (%) of unoriented and oriented components for uniaxially oriented PET films determined from ^{13}C CP NMR.

Film	Draw ratio	Unoriented	Oriented
Drawn at 45°C	3	35	65
Drawn at 80°C	2	100	0
	3	80	20
	4	70	30
	5	55	33,[a] 12[b]
	5.66	47	38,[a] 15[b]
Heat treatment	5	30	35,[a] 35[b]

[a]Low orientation.
[b]High orientation.

Table 5. Structural parameters[a] (deg.) of the ordered components for Uniaxially oriented PET samples determined from ^{13}C CP NMR (α_F is assumed to be 90°).

Film	Draw ratio	p	β_F	θ
Drawn at 45°C	3	22	18 ± 6	22 ± 6
Drawn at 80°C	3,4	24	20 ± 10	20 ± 10
	5, 5.66	24,[b] 5[c]	24 ± 10,[b] 16 ± 6[c]	16 ± 10,[b] 24 ± 6[c]
Heat treatment	5	8,[b] 2[c]	20 ± 10,[b] 11 ± 5[c]	20 ± 10,[b] 29 ± 5[c]

[a]The definitions of the angles α_F and β_F are shown in Fig. 1(A). p is the orientational distribution around the fibre axis (chain axis or MD); θ is the angle between the phenylene *para* C–C axis and the chain axis (or MD) or PET film.
[b]Low orientation.
[c]High orientation.

composed of an NMR crystalline (highly oriented) component, a rigid NMR amorphous (low oriented) component and a mobile NMR amorphous (unoriented) component proposed by Havens and VanderHart[99] and Gabrielse *et al.*[102] on the basis of ^{13}C CP/MAS NMR relaxation experiments.

5. CONCLUSIONS

The solid-state NMR approach on the basis of orientation-dependent NMR interactions such as chemical shielding anisotropy, dipole–dipole and quadrupoles has been developed to determine the atomic coordinate, that is, the torsion angles of the backbone chain of a protein fibre, silk fibroin fibre. This

approach is also applied to determine the local structure of oriented synthetic polymer containing a non-crystalline domain. We have concentrated on obtaining "static" detailed structural information of oriented polymers, but the spectra used for the analysis also include another important information, namely "dynamics", which have been currently obtained from solid-state NMR.[6]

Deformation such as drawing, compression, annealing, strain, creep and stress relaxation of polymers including fibres may produce quite different orientational behaviour, the results of which can be examined with solid-state NMR from both the static and dynamic viewpoints. Although we introduce only one paper (by English *et al.*[90]) published recently on these interesting problems, it is clear that solid-state NMR is a valuable tool for such studies. The accurate model produced on the basis of atomic resolution of the local structure and the local dynamics can be built up in order to interpret the mechanical properties of polymers and the deformation mechanisms.

Most recently, a double-quantum solid-state NMR technique has been reported.[112] This gives detailed structural information such as torsion angles for unoriented amorphous polymers including unoriented polypeptides with NMR tensor correlation in the ^{13}C–^{13}C-labelled segments. This new solid-state NMR technique can be used to cover the atomic level structural analyses of polymers from amorphous to crystalline, together with the analytical methods used for oriented polymers and described in this article as well as the REDOR or RR methods for "distance" determination.

ACKNOWLEDGEMENTS

We thank Profs T. A. Cross and T. Gullion at Florida State University, Prof. L. K. Nicholson at Cornell University, Dr M. P. Williamson at University of Sheffield, Dr A. S. Ulrich at Friedrich-Schiller-Universitaet, Prof. H. Saito at Himeji Institute of Technology, Prof. I. Ando at Tokyo Institute of Technology, Prof. M. Osanai at Kanazawa University and Prof. G. A. Webb at Surrey University for helpful discussions. T. A. acknowledges support from a Grant-in-Aid of the Ministry of Education, Science and Culture of Japan, Naito Science Foundation, Nissan Science Foundation, Yazaki Foundation, Ogasawara Foundation for the Promotion of Science and Engineering, Japan and The International Human Frontier Science Program.

REFERENCES

1. R. A. Komoroski (ed.), *High Resolution NMR of Synthetic Polymers in Bulk*, VCH Publishers, Deerfield Beach, FL, 1986.

2. J. L. Koenig, *Spectroscopy of Polymers*, ACS Professional Reference Book, American Chemical Society, Washington, DC, 1992.
3. V. J. McBrierty and K. J. Packer, *Nuclear Magnetic Resonance in Solid Polymers*, Cambridge Solid State Science Series, Cambridge, 1993.
4. R. N. Ibbett (ed.), *NMR Spectroscopy of Polymers*, Blackie Academic & Professional, Glasgow, 1993.
5. K. Schmidt-Rohr and H. W. Spiess, *Multidimensional Solid-State NMR and Polymers*, London, 1994.
6. R. Tycko (ed.), *Nuclear Magnetic Resonance Probes of Molecular Dynamics*, Kluwer Academic Publishers, Dordrecht, 1994.
7. A. H. Fawcett (ed.), *Polymer Spectroscopy*, John Wiley & Sons, Chichester, 1996.
8. T. A. Cross, *Annual Reports on NMR Spectroscopy*, Vol. 29 (ed. G. A. Webb), p. 123. Academic Press, London, 1994.
9. L. K. Nicholson, T. Asakura, M. Demura and T. A. Cross, *Biopolymers*, 1993, **33**, 847.
10. T. Asakura, J.-H. Yeo, M. Demura, T. Itoh, T. Fujito, M. Imanari, L. K. Nicholson and T. A. Cross, *Macromolecules*, 1993, **26**, 6660.
11. J.-H. Yeo, M. Demura, T. Asakura, T. Fujito, M. Imanari, L. K. Nicholson and T. A. Cross, *Solid State NMR*, 1994, **3**, 209.
12. T. Asakura, J.-H. Yeo and I. Ando, *Polym. J.*, 1994, **26**, 229.
13. T. Asakura, T. Konakazawa, M. Demura, T. Ito and Y. Maruhashi, *Polymer*, 1996, **37**, 1965.
14. K. Wuthrich, *NMR of Proteins and Nucleic Acids*, John Wiley & Sons, New York, 1986.
15. T. Gullion and J. Schaefer, *J. Magn. Reson.*, 1989, **81**, 196.
16. T. Gullion and J. Schaefer, *Adv. Magn. Reson.*, 1989, **13**, 57.
17. P. T. Lansbury, Jr, P. R. Costa, J. M. Griffiths, E. J. Simon, M. Auger, K. J. Halverson, D. A. Cocisko, Z. S. Hendsch, T. T. Ashburn, R. G. S. Spencer, B. Tidor and R. G. Griffin, *Nat. Struct. Biol.*, 1995, **2**, 990.
18. J. M. Griffiths, T. T. Ashburn, M. Auger, P. R. Costa, R. G. Griffin and P. T. Lansbury, Jr, *J. Am. Chem. Soc.*, 1995, **117**, 3539.
19. T. Asakura, A. Aoki, M. Demura, J. M. Joers, R. C. Rosanske and T. Gullion, *Polym. J.*, 1994, **26**, 1405.
20. M. Mehring, *Principles of High Resolution NMR in Solids*, 2nd revised edn, Springer-Verlag, Berlin, 1983.
21. Q. Teng and T. A. Cross, *J. Magn. Reson.*, **85**, 439.
22. G. S. Harbison, L. W. Jelinski, R. E. Stark, D. A. Torchia, J. Herzfeld and R. G. Griffin, *J. Magn. Reson.*, **60**, 79.
23. T. G. Oas, C. J. Hartzell, F. W. Dahlquist and G. P. Drobny, *J. Am. Chem. Soc.*, **109**, 5962.
24. C. J. Hartzell, M. Whitfield, T. G. Oas and G. P. Drobny, *J. Am. Chem. Soc.*, **109**, 5966.
25. C. J. Hartzell, T. K. Pratum and G. P. Drobny, *J. Chem. Phys.*, 1987, **87**, 4324.
26. T. Asakura, M. Demura, Y. Hiraishi, K. Ogawa and A. Uyama, *Chem Lett.*, 2249.
27. Q. Teng, L. K. Nicholson and T. A. Cross, *J. Mol. Biol.*, 1991, **218**, 607.
28. R. A. Kinsey, A. Kimtanar, M.-D. Isai, R. J. Smith, N. Janes and E. Oldfield, *J. Biol. Chem.*, 1981, **256**, 4146.
29. A. S. Ulrich, A. Watts, A. I. Wallat and M. P. Heyn, *Biochemistry*, 1994, **33**, 5370.
30. M. Demura, Y. Hiraishi, T. Asakura and T. A. Cross, Manuscript in preparation.
31. T. Asakura and D. L. Kaplan, *Encyclopedia of Agricultural Science* (ed. C. J. Arutzen), Vol. 4, p. 1. Academic Press, 1994.
32. D. L. Kaplan, S. J. Lombardi, W. S. Muller and S. A. Fossey. *Biomaterials*; *Novel Materials from Biological Sources* (ed. D. Byrom) 1. Silk. Stockton, New York, 1991.

33. D. J. Strydom, T. Haylett and R. H. Stead, *Biochem. Biophys. Res. Commun.*, 1977, **3**, 932.
34. F. Lucas, J. T. B. Shaw and S. G. Smith, *Biochem. J.*, 1962, **83**, 164.
35. T. Ohmachi and K. Shimura, *J. Biochem.*, 1981, **89**, 531.
36. R. D. B. Fraser and T. P. MacRae, *Conformation in Fibrous Proteins*, Academic Press, New York and London, 1973.
37. K. Mita, S. Ichimura and T. C. James, *J. Mol. Evol.*, 1994, **38**, 583.
38. M. Shimizu, *Bull. Imp. Seric. Stn., Tokyo*, 1941, **10**, 475.
39. O. Kratky, *Trans. Faraday Soc.*, 1955, **52**, 58.
40. R. E. Marsh, R. B. Corey and L. Pauling, *Biochim. Biophys. Acta*, 1955, **16**, 1.
41. R. D. B. Fraser, T. P. MacRae and F. H. Stewart, *J. Mol. Biol.*, 1966, **19**, 580.
42. K. Hirabayashi, M. Uchiyama, H. Ishikawa and Y. Go, *Sen'i Gakkaishi*, 1967, **23**, 538.
43. T. Konishi and M. Kurokawa, *Sen-i Gakkaishi*, 1968, **24**, 550.
44. T. Asakura, A. Kuzuhara, R. Tabeta and H. Saito, *Macromolecules*, 1985, **18**, 1841.
45. Y. Takahashi, M. Gehoh and K. Yuzuriha, *J. Polym. Sci., Polym. Phys. Ed.*, 1991, **29**, 889.
46. B. Lotz and H. D. Keith, *J. Mol. Biol.*, 1971, **61**, 201.
47. B. Lotz and F. C. Cesari, *Biochimie*, 1971, **61**, 205.
48. S. A. Fossey, G. Nemethy, K. D. Gibson and H. A. Scheraga, *Biopolymers*, 1991, **31**, 1529.
49. J. Magoshi, M. Mizuide, Y. Magoshi, K. Takahashi, M. Kubo and S. Nakamura, *J. Polym. Sci., Polym. Phys. Ed.*, 1979, **17**, 515.
50. T. Hayakawa, K. Kobo, S. Yamamoto and J. Noguchi, *Kobunshi Kagaku*, 1970, **27**, 300.
51. T. Miyazawa, T. Shimanouchi and S. Mizushima, *J. Chem. Phys.*, 1958, **29**, 611.
52. H. Saito, Y. Iwanaga, R. Tabeta, M. Narita and T. Asakura, *Chem. Lett*, 1983, 427.
53. H. Saito, R. Tabeta, T. Asakura, Y. Iwanaga, A. Shoji, T. Ozaki and I. Ando, *Macromolecules*, 1984, **17**, 1405.
54. T. Asakura and T. Yamaguchi, *J. Seric. Sci., Jpn.*, 1987, **56**, 300.
55. H. Saito, M. Ishida, M. Yokoi and T. Asakura, *Macromolecules*, 1990, **23**, 83.
56. M. Ishida, T. Asakura, M. Yokoi and H. Saito, *Macromolecules*, 1990, **23**, 88.
57. M. Demura and T. Asakura, *J. Membr. Sci.*, 1991, **59**, 39.
58. T. Asakura, M. Demura, T. Date, N. Miyashita, K. Ogawa and M. P. Williamson, *Biopolymers*, 1996, **41**, 193
59. T. Asakura, Y. Watanabe and T. Itoh, *Macromolecules*, 1984, **17**, 2421.
60. H. Saito, R. Tabeta, A. Kuzuhara and T. Asakura, *Bull. Chem. Soc. Jpn.*, 1986, **59**, 3383.
61. T. Asakura, H. Yoshimizu and F. Yoshizawa, *Macromolecules*, 1988, **21**, 2038.
62. T. Asakura, H. Suzuki and T. Tanaka, *J. Seric. Sci., Jpn*, 1985, **54**, 504.
63. T. Asakura, Y. Kawaguchi, M. Demura and M. Osanai, *Insect Biochem.*, 1988, **18**, 531.
64. T. Asakura, M. Nagashima, R. Sakaguchi, M. Demura and M. Osanai, *Insect Biochem.*, 1991, **21**, 743.
65. T. Asakura, Y. Watanabe, A. Uchida and H. Minagawa, *Macromolecules*, 1984, **17**, 1075.
66. F. Koide, H. Nagayama and K. Shimura, *Nippon Nogei Kagaku Kaishi*, 1955, **29**, 987.
67. Y. Suzuki, L. P. Gage and D. D. Brown, *J. Mol. Biol.*, 1972, **70**, 637.
68. T. D. C. Grace, *Nature (London)*, 1967, **261**, 613.
69. Y. Chinzei, *Appl. Ent. Zool.*, 1975, **10**, 136.
70. H. Inoue and J. Mitsuhashi, *J. Seric. Sci. Jpn.*, 1984, **53**, 108.
71. T. Asakura, H. Yamada, M. Demura and M. Osanai, *Insect Biochem.*, 1990, **20**, 261.

72. T. Asakura, R. Sakaguchi, M. Demura, T. Manabe, A. Uyama, K. Ogawa and M. Osanai, *Biotechnol. Bioeng.*, 1993, **41**, 245.
73. T. Asakura, M. Demura, A. Uyama, K. Ogawa, K. Komatsu, L. K. Nicholson and T. A. Cross. *Silk Polymers, Materials Science and Biotechnology* (ed. D. Kaplan *et al.*), p. 148. ACS Symposium Series, 1994.
74. T. Asakura, M. Demura and Y. Hiraishi, Manuscript in preparation.
75. T. Asakura, M. Minami, R. Shimada, M. Demura, M. Osanai, T. Fujito, M. Imanari and A. S. Ulrich. *Macromolecules*, in press.
76. M. Kainosho and T. Tsuji, *Biochemistry*, 1982, **21**, 6273.
77. T. Asakura, Y. Yamazaki, K. W. Seng, M. Demura and I. Ando, *Rep. Prog. Polym. Phys. Jpn.*, 1993, **36**, 633.
78. T. Fujiwara, Y. Kobayashi, Y. Kyogoku and K. Kataoka, *J. Mol. Biol.*, 1986, **187**, 137.
79. A. S. Ulrich and A. Watts, *Solid State NMR*, 1993, **2**, 21.
80. T. Asakura, M. Demura, Y. Watanabe and K. Sato, *J. Polym. Sci., B*, 1992, **30**, 693.
81. R. D. Orwoll and R. L. Vold, *J. Am. Chem. Soc.* 1971, **93**, 5335.
82. S. Sasaki and I. Uematsu, *J. Polym. Sci., Polym. Phys. Ed.*, 1985, **23**, 263.
83. Y. Masuda, K. Fukushima, T. Fujii and T. Miyazawa, *Biopolymers*, 1969, **8**, 91.
84. A. Elliott, R. D. B. Fraser and T. P. MacRae, *J. Mol. Biol.*, 1965, **11**, 821.
85. M. G. Notholt, *Eur. Polym. J.*, 1974, **10**, 799.
86. E. G. Chatzi and J. L. Koenig, *Polym. Plast. Technol. Eng.*, 1987, **26** (3 & 4), 229.
87. M. G. Northolt and J. J. van Aartsen, *J. Polym. Sci. B*, 1973, **11**, 333.
88. K. Tashiro, M. Kobayashi and H. Tadokoro, *Macromolecules*, 1977, **10**, 413.
89. J.-H. Yeo, T. Asakura and H. Shimazaki, *Makromol. Chem. Phys.*, 1994, **195**, 1423.
90. Dr A. D. English, private communication.
91. H. Kakida, Y. Chatani and H. Tadokoro, *J. Polym. Sci., Polym. Phys. Ed.*, 1976, **14**, 427.
92. K. Okuyama, H. Hidaka and H. Ichige, *Macromolecules*, 1989, **22**, 3776.
93. H. Tadokoro, *Sen-i Gakkaishi*, 1975, **31**, P-278.
94. I. M. Ward (ed.), *Developments in Oriented Polymers*, Applied Science Publishers, London, 1982.
95. S. Rober and H. G. Zachmann, *Polymer*, 1992, **33**, 2061.
96. B. F. Chmelka, K. Schmidt-Rohr and H. W. Spiess, *Macromolecules*, 1993, **26**, 2282.
97. M. D. Sefcik, J. Schaefer, E. O. Stejskal and R. A. McKay, *Macromolecules* 1980, **13**, 1132.
98. A. D. English, *Macromolecules* 1985, **17**, 2182.
99. J. R. Havens and D. L. VanderHart, *Macromolecules* 1985, **18**, 1663.
100. T. T. P. Cheung, B. C. Gerstein, L. M. Ryan, R. E. Taylor and D. R. Dybowsky, *J. Chem. Phys.*, 1980, **73**, 6059.
101. M. Ogasawara, K. Kouzai, H. Watanabe, T. Takada and F. Horii, *Kobunshi Ronbunshu*, 1992, **49**, 345.
102. W. Gabrielse, G. H. Angard, F. C. Feyen and W. S. Veeman, *Macromolecules*, 1994, **27**, 5811.
103. P. D. Murphy, T. Taki, B. C. Gerstein, P. M. Henrichs and D. J. Massa, *J. Magn. Reson.*, 1982, **49**, 99.
104. G. S. Harbison, V.-D. Vogt and H. W. Spiess, *J. Chem. Phys.* 1987, **86**, 1206.
105. I. Ando and G. A. Webb, *Theory of NMR Parameters*, Academic Press, London, 1983.
106. R. de P. Daubeny, C. W. Bunn and C. J. Brown, *Proc. R. Soc.*, London, 1954, **226A**, 531.
107. W. S. Veeman, *Prog. NMR. Spectrosc.*, 1984, **16**, 193.
108. B. A. Cornell, *J. Chem. Phys.*, 1986, **85**, 4199.

109. P. W. Jensen, *J. Polym. Sci.*, 1958, **28**, 635.
110. D. J. Walls, *Appl. Spectrosc.*, 1991, **45**, 1193.
111. S. Arnott and A. J. Wonacott, *Polymer*, 1966, **7**, 157.
112. K. Schmidt-Rohr, *Macromolecules*, 1996, **29**, 3975.

INDEX

This Page Intentionally Left Blank